IDŐJÁRÁS

QUARTERLY JOURNAL
OF THE HUNGARIAN METEOROLOGICAL SERVICE

CONTENTS

****

http://www.met.hu/Journal-Idojaras.php

VOL. 119 * NO. 1 * JANUARY – MARCH 2015

IDŐJÁRÁS

Quarterly Journal of the Hungarian Meteorological Service

Editorial Office: Kitaibel P.u. 1, H-1024 Budapest, Hungary
P.O. Box 38, H-1525 Budapest, Hungary
E-mail: journal.idojaras@met.hu
Fax: (36-1) 346-4669

Indexed and abstracted in Science Citation Index Expanded™ and Journal Citation Reports/Science Edition
Covered in the abstract and citation database SCOPUS®

Subscription by mail:
IDŐJÁRÁS, P.O. Box 38, H-1525 Budapest, Hungary
E-mail: journal.idojaras@met.hu

IDŐJÁRÁS

Quarterly Journal of the Hungarian Meteorological Service
Vol. 119, No. 1, January – March, 2015, pp. 1–21

Expected changes in mean seasonal precipitation and temperature across the Iberian Peninsula for the 21st century

Joan Ramon Coll[1], **Philip D. Jones**[2, 3], and **Enric Aguilar**[1]

[1] *Centre for Climate Change, Geography Department, Rovira i Virgili University, Av. Remolins 13-15, 43500 Tortosa, Spain.*

[2] *Climatic Research Unit, School of Environmental Sciences, University of East Anglia, Norwich, NR4 7TJ, UK.*

[3] *Center of Excellence for Climate Change Research, Department of Meteorology, King Abdulaziz University, Jeddah 21589, Saudi Arabia*

**Corresponding author E-mail: joanramon.coll@urv.cat*

(Manuscript received in final form April 24, 2014)

Abstract—Three different regional climate models (DMI-HIRHAM5, HadRM3, and KNMI-RACMO2) driven by ERA-40 reanalysis and also driven by global climate models (GCMs) obtained from the EU-Ensembles project have been compared to observed data over the Iberian Peninsula (IP) to assess the accuracy of simulated precipitation and temperature. KNMI-RACMO2 and DMI-HIRHAM5 were the best models for accurately simulating precipitation and temperature, respectively, although large uncertainties still affect their simulations. The same RCM simulations driven by GCMs have been used to project the seasonal expected changes in precipitation and temperature for the periods 2011–2050 and 2051–2090 relative to 1961–2000 under the A1B climate change scenario. From the results, a clear decrease in mean precipitation is expected in most IP for spring, summer, and autumn, but no clear signal was found in winter. Moreover, future projections showed a large increase in mean temperatures in all seasons being more evident in the interior of the IP especially in summer. The decrease in mean precipitation and the increase in mean temperature projected for the IP, could worsen current drought conditions especially for the second half of the 21st century.

Key-words: regional climate models, Iberian Peninsula, precipitation, temperature, model accuracy validation, future projections, drought

1. Introduction

Future climate will include simultaneous changes in temperature and precipitation for many regions of the world. For example, in the Iberian Peninsula (IP), the observed and projected increase in temperature is expected to be accompanied by a decrease in precipitation (*IPCC,* 2007; *Sousa et al.,* 2011; *IPCC,* 2012). This combination would have a negative impact on water availability.

Previous studies have confirmed a warming trend in the 20th century across the IP using observed data (*Brunet et al.,* 2006; *Brunet et al.,* 2007), while precipitation patterns showed a high inter-annual variability, but appreciable changes have not still been identified in annual precipitation totals (*Barrera-Escoda,* 2008; *CLIVAR*, 2010).

Being consistent with the observed trends, climate models project a large increase in temperatures, but also a future decrease in precipitation of roughly 20% in southern Europe by the end of 21st century (*IPCC,* 2007) including the whole IP (*Sánchez*, 2009; *Gómez-Navarro et al.,* 2010; *Rodríguez-Puebla* and *Nieto,* 2010; *Vicente-Serrano et al.,* 2011; *Jerez et al.,* 2012; *Jerez* and *Montavez*, 2012). Again, this warming/drying combination implies an increase of drought conditions over the wider Mediterranean region (*Blenkinsop* and *Fowler,* 2007; *Mariotti et al.,* 2008; *Dai*, 2011 and 2012; *IPCC,* 2012) and also over the IP (*Beniston et al.,* 2007; *Rodríguez-Puebla* and *Nieto,* 2010;; *Sanchez et al.,* 2012). These consistent results, obtained through the analysis of model output, have to be put in the context of the large uncertainties related to the reliability of model simulations affecting the projections of trends in temperature, precipitation, and drought conditions for the coming century (*Blenkinsop* and *Fowler,* 2007; *Sheffield* and *Wood*, 2008; *Rammukainen*, 2010; *Mishra* and *Singh*, 2011; *IPCC,* 2012; *Dai*, 2012).

This article focuses on investigating the capability of three regional climate models to correctly reproduce future temperature and precipitation in the IP. We used the outputs from the RCMs driven by ERA-40 reanalysis for the period 1958–2002 to make comparisons with observed data and the same RCMs driven by associated GCMs for future projections covering the period 1951–2100. We approach this analysis by comparing climate model output belonging to the A1B climate change scenario to an overlapping observational dataset of temperature and precipitation.

2. Data

Monthly simulated temperature and precipitation data from three regional climate models (RCMs) at 25 km resolution were obtained from the EU-Ensembles project (available at http://www.ensembles-eu.org). DMI-HIRHAM5 produced by the Danish Meteorological Institute (DMI) (*Christensen* and

Christensen, 2007), HadRM3 using the HC-Q0 (normal sensitivity) developed by the Hadley Centre for Climate Prediction and Research (HC) (*Collins et al.,* 2010), and KNMI-RACMO2 produced by the Royal Netherlands Meteorological Institute (KNMI) (*van Meijgaard et al.*, 2008) are the RCMs selected to assess changes in precipitation and temperature over the IP along the 21st century. These RCMs were selected because they are regarded as the best-performing models at handling precipitation variability in other European regions, with RACMO2 performing best overall for the UK (*Simpson*, 2011, *van der Linden* and *Mitchell*, 2009; *Christensen et al.,* 2010; *Kjellström et al.,* 2010). We used the outputs from the RCMs driven by ERA-40 reanalysis for the period 1958–2002 to make comparisons with observed data and the same RCMs driven by associated global climate models (GCMs) for future projections covering the period 1951–2100. The ERA-40 reanalysis is produced by the European Centre for Medium-Range Weather Forecasting (ECMWF), and it is based on observed data such as conventional observations or satellite data among others. Temperature from the ERA-40 reanalysis is well simulated in the Northern Hemisphere when compared with mean observed sea-level pressure and geopotential 500hPa temperatures (*ECMWF*, 2004), and precipitation is well-handled in the Northern Hemisphere continents (*Bosilovich et al.*, 2008). In this study, KNMI-RACMO2 and DMI-HIRHAM5 are coupled with ECHAM5-r3 as a GCM, while HadRM3 is associated with HadCM3. The A1B climate change scenario was chosen to project the expected changes in precipitation and temperature over the IP as it represents a medium greenhouse gases forcing to the climate system according to IPCC AR-4 (*IPCC,* 2007).

The observed data has been extracted from the Monthly Iberian temperature and precipitation series (MITPS, *Fig. 1*). The MITPS dataset updates to 2010 the Spanish daily adjusted temperature/precipitation series (SDATS/SDAPS) and adds to its 22 stations two new data points to represent the western part of the IP (Portugal). The SDATS – and its MITPS update - was quality controlled (QC) following *Aguilar et al.,* (2002) and were homogenized by the Centre for Climate Change (C3) (*Brunet et al.,* 2006; *Brunet* et al., 2007) applying the standard normal homogeneity test (SNHT) (*Alexandersson* and *Moberg*, 1997). The two Portuguese series (Lisboa and Porto) have been subjected to quality control procedure of raw data and tested using homogenization procedure based on the standard normal homogeneity test, to detect and adjust most prominent inhomogeneities on a monthly scale.

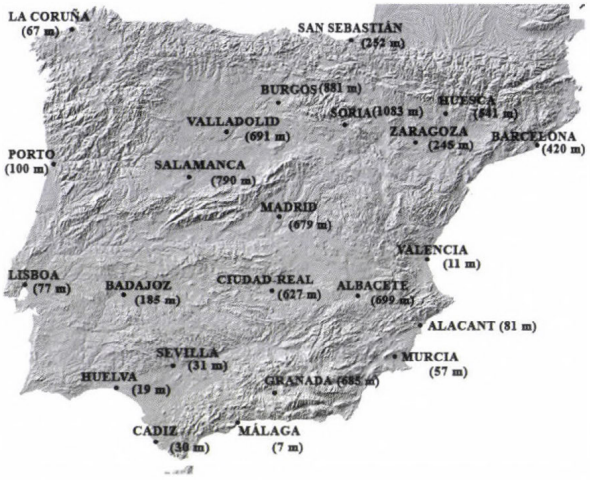

Fig. 1. MITPS station map: the closest city to each meteorological station is shown with the elevation (in brackets) of the last segment of record.

3. Methodology

The closest RCM grid box to each meteorological station has been selected to obtain the same geographical distribution of the Iberian simulated data according to observed data (MITPS) (*Fig. 1*). Monthly simulated precipitation and temperature data were obtained from DMI-HIRHAM5, HadRM3, and KNMI-RACMO2 model outputs driven by ERA-40 reanalysis and those driven by GCMs for each location. The RCMs outputs driven by ERA-40 reanalysis and by GCMs have been compared with the observed MITPS for the 1961–2010 period. All RCMs are more consistent when they are driven by ERA-40 reanalysis than by GCMs regarding precipitation and temperature simulation in the IP. Accumulated daily precipitation totals and mean temperature from observed and simulated data were totaled for Northern Hemisphere winter (DJF), spring (MAM), summer (JJA), and autumn (SON) seasons for the entire period. Based on the procedure applied by *Simpson* (2011), we computed the seasonal differences in precipitation totals, mean temperature, and the ratio between the standard deviations of simulated and observed data. Modeled and observed datasets have also been compared by computing the Pearson product-moment correlation coefficient and the root mean square error (RMSE). Finally, Kolmogorov-Smirnov test (K-S test) has been applied to evaluate the similarity between both statistical distributions.

Once the performance of the three RCMs is evaluated, simulations of seasonal precipitation and temperature from the RCMs driven by GCMs have been used to project the mean expected changes in precipitation and temperature over the IP for the periods 2011–2050 and 2051–2090 relative to 1961–2000 at seasonal time-scales under the A1B climate change scenario.

4. Results

4.1. Validation of the accuracy of precipitation simulations

The analysis of temperature and precipitation simulations showed quite different results, depending both on the model, the season of the year, and the different regions of the IP.

Precipitation simulations driven by ERA-40 tended to overestimate the observed data in central and north-western IP and also in the Ebro basin, especially in winter and spring (*Fig. 2*). Underestimated precipitation was found in the south, south-western IP and in the Mediterranean coast during all seasons, being more evident in summer and autumn. KNMI-RACMO2 showed the smallest deviations compared to observed data over the IP during all seasons except in summer, when it underestimated by between 20% and 40% of mean precipitation over most of the IP. HadRM3 produced overestimates of around 20–40% of mean precipitation in central, north-western area and in the Ebro basin, especially in spring and summer, and underestimated by 40% of mean precipitation in south-western areas and in the Mediterranean region for summer and autumn. DMI-HIRHAM5 showed large overestimates greater than 60% of mean precipitation in the Ebro basin and in the Sierra Nevada for winter and summer, respectively, and large underestimates towards 20–60% of mean precipitation for most of the IP, with higher anomalies located in the western and south-western area during all seasons.

Precipitation simulations from DMI-HIRHAM5 and KNMI-RACMO2 driven by ECHAM5-r3 and HadRM3 coupled with HadCM3 have also been compared with observed MITPS to check how the RCM simulations can be altered when they are driven by GCMs (*Fig. 3*). Large differences have been detected in mean seasonal precipitation from DMI-HIRHAM5 and KNMI-RACMO2 when they are driven by ERA-40 or by their associated GCMs (*Figs. 2* and *3*), but the simulations are closer in the case of HadRM3 in all seasons. All models have a tendency to overestimate mean precipitation in winter, spring, and autumn, while underestimates were found in summer. DMI-HIRHAM5 produced large overestimates greater than 80% of mean precipitation in central, north, and north-western IP for winter, spring, and autumn, while underestimates towards 20–40% of mean precipitation were focused in the south-western area and in the Mediterranean region for summer. HadRM3 and KNMI-RACMO2 overestimated by between 40–80% of mean precipitation in the Ebro basin and in the north-western IP mainly in winter and spring while underestimates around 40% of mean precipitation were primarily in the Mediterranean region for spring and summer. Note that large underestimates of greater than 60% of mean precipitation have been identified from KNMI-RACMO2 over most of the IP in summer.

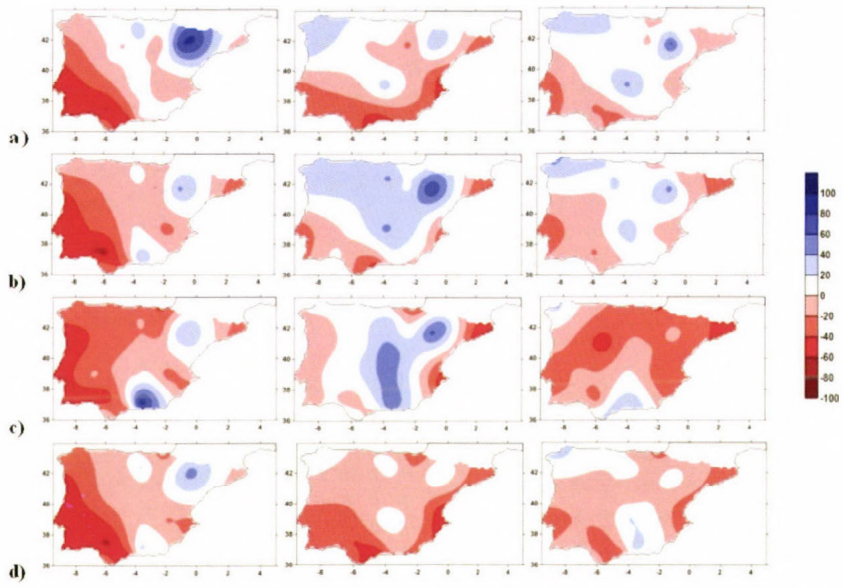

Fig. 2. Differences (in %) between simulated and observed mean seasonal precipitation totals (MITPS) in the IP for winter (DJF); **a)**, spring (MAM); **b)**, summer (JJA); **c)**, and autumn (SON); **d)** using the common period 1961–2000. The model outputs are derived from DMI-HIRHAM5 (left), HadRM3 (middle), and KNMI-RACMO2 (right), all driven by ERA-40 reanalysis.

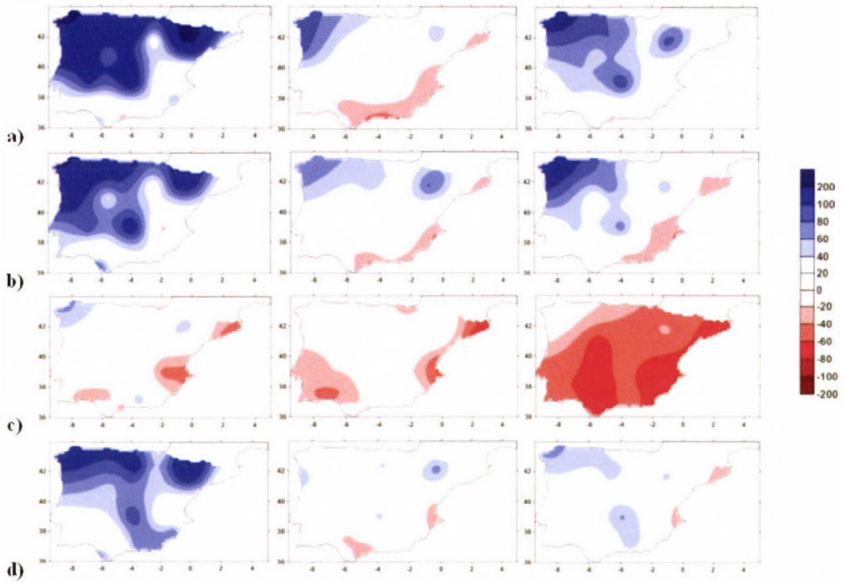

Fig. 3. Differences (in %) between simulated and observed precipitation seasonal totals (MITPS) in the IP for winter (DJF); **a)**, spring (MAM); **b)**, summer (JJA); **c)**, and autumn (SON); **d)** using the common period 1961–2000. The model outputs are derived from DMI-HIRHAM5 driven by ECHAM5-r3 (left), HadRM3 driven by HadCM3 (middle), and KNMI-RACMO2 driven by ECHAM5-r3 (right).

Simulated seasonal precipitation variability has been assessed from the ratio of standard deviations between mean simulated and observed precipitation from the three RCMs driven by ERA-40 reanalysis (*Fig. 4*). All RCMs exceeded 0.5 standard deviations for all seasons over most of the IP, while the ratio was greater than 1 standard deviation in some regions located in the north and central IP, especially for winter and spring. Otherwise, large differences in standard deviations could be appreciated from all RCMs driven by GCMs during all seasons (*Fig. 5*). All RCMs exceeded 1 standard deviation between mean simulated and observed precipitation over most of the IP, especially in spring and autumn.

The best correlations from the three RCMs driven by ERA-40 reanalysis between simulated and observed data were found in winter (*Fig. 6*), and the worst ones in summer with KNMI-RACMO2 the best-performing and DMI-HIRHAM5 second. The correlations were lower in the Mediterranean region than for the rest of the IP, especially in winter, summer, and autumn. Finally, the results from RMSE and K-S test (*Tables 1* and *2*) showed better fits between simulated and observed data using KNMI-RACMO2 during all seasons over most of the IP than DMI-HIRHAM5, which fitted better in the Mediterranean region.

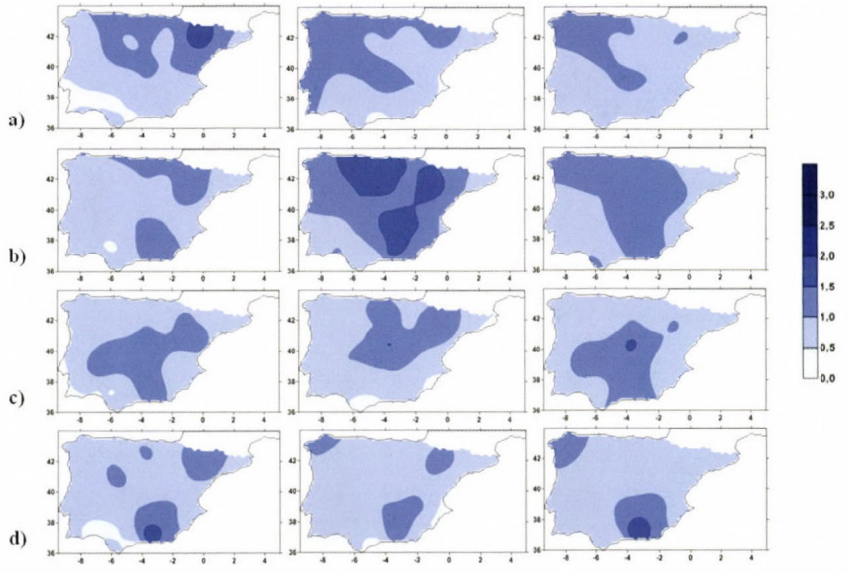

Fig. 4. Ratio of standard deviations between simulated and observed seasonal precipitation totals (MITPS) in the IP for winter (DJF); **a)**, spring (MAM); **b)**, summer (JJA); **c)**, and autumn (SON); **d)** using the common period 1961–2000. The model outputs are derived from DMI-HIRHAM5 (left), HadRM3 (middle), and KNMI-RACMO2 (right), all driven by ERA-40 reanalysis.

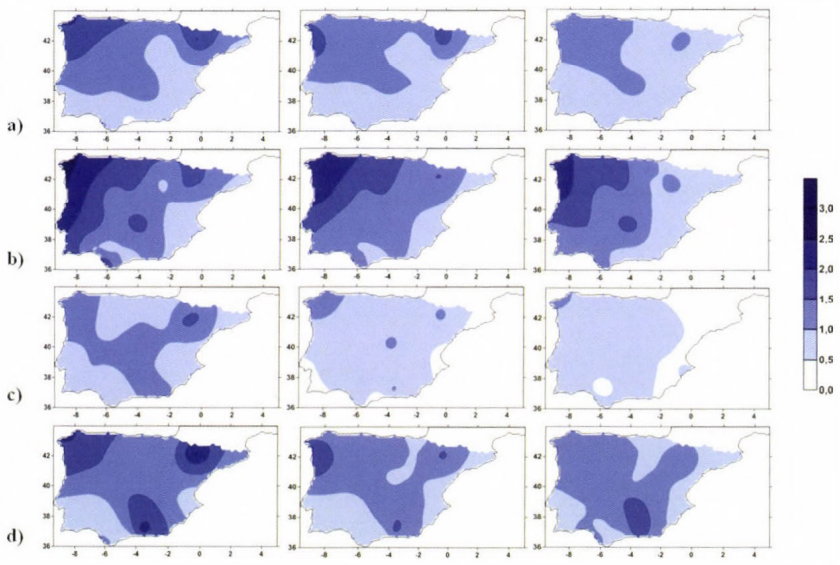

Fig. 5. Ratio of standard deviations between simulated and observed seasonal precipitation totals (MITPS) in the IP for winter (DJF); **a)**, spring (MAM); **b)**, summer (JJA); **c)**, and autumn (SON); **d)** using the common period 1961–2000. The model outputs are derived from DMI-HIRHAM5 driven by ECHAM5-r3 (left), HadRM3 driven by HadCM3 (middle), and KNMI-RACMO2 driven by ECHAM5-r3 (right).

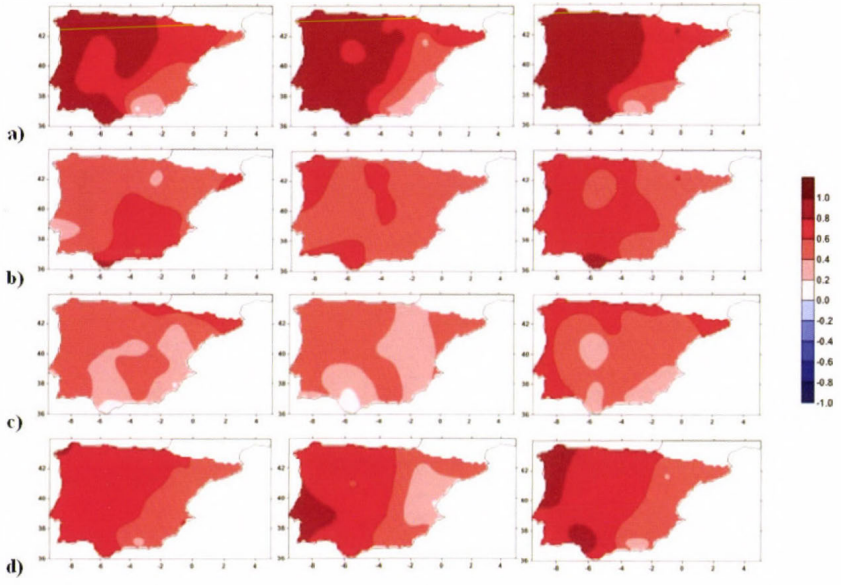

Fig. 6. Pearson Product-Moment Correlation coefficient between simulated and observed seasonal precipitation totals (MITPS) in the IP for winter (DJF); a), spring (MAM); b), summer (JJA); c), and autumn (SON); d) using the common period 1961–2000. The model outputs are derived from DMI-HIRHAM5 (left), HadRM3 (middle), and KNMI-RACMO2 (right), all driven by ERA-40 reanalysis. Correlations greater than 0.41 are statistically significant at the 99% level.

Table 1. Number of the best fitted RMSE values and K-S distances between simulated and observed precipitation and temperature for each season using the common period 1961–2000 for the 23 locations spread over the IP. The model outputs are derived from DMI-HIRHAM5, HadRM3, and KNMI-RACMO2, all driven by ERA-40 reanalysis. Values in bold refer to the maximum number of the best fitted values for each goodness of fit test and for the three RCMs assessed

		DMI-HIRHAM5		HadRM3		KNMI-RACMO2	
	Seasons	**Nº RMSE**	**Nº K-S distances**	**Nº RMSE**	**Nº K-S distances**	**Nº RMSE**	**Nº K-S distances**
Precipitation	Winter (DJF)	4	**10**	3	3	**16**	**10**
	Spring (MAM)	10	7	0	6	**13**	**10**
	Summer (JJA)	4	5	6	7	**13**	**11**
	Autumn (SON)	5	5	3	4	**15**	**14**
Temperature	Winter (DJF)	**14**	**14**	3	3	6	6
	Spring (MAM)	**15**	**14**	4	6	4	3
	Summer (JJA)	4	4	6	5	**13**	**14**
	Autumn (SON)	**11**	8	7	**11**	5	4

Table 2. Averaged RMSE values and averaged K-S distances between simulated and observed precipitation and temperature over the whole IP for each season using the common period 1961–2000. The model outputs are derived from DMI-HIRHAM5, HadRM3, and KNMI-RACMO2, all driven by ERA-40 reanalysis. Values in bold refer to the best fitted values for each goodness of fit test and for the three RCMs assessed

		DMI-HIRHAM5		HadRM3		KNMI-RACMO2	
	Seasons	**RMSE**	**K-S distances**	**RMSE**	**K-S distances**	**RMSE**	**K-S distances**
Precipitation	Winter (DJF)	92.69	0.29	81.45	0.28	**67.25**	**0.23**
	Spring (MAM)	69.33	0.35	77.63	0.32	**59.19**	**0.26**
	Summer (JJA)	46.02	0.35	48.91	0.33	**43.83**	**0.31**
	Autumn (SON)	97.19	0.33	90.85	0.31	**78.40**	**0.25**
Temperature	Winter (DJF)	**1.37**	**0.50**	1.65	0.58	1.76	0.58
	Spring (MAM)	**1.05**	**0.40**	1.27	0.46	1.52	0.57
	Summer (JJA)	1.65	0.59	1.88	0.59	**1.34**	**0.49**
	Autumn (SON)	**1.13**	0.43	1.25	**0.42**	1.57	0.61

From the results obtained above, KNMI-RACMO2 is the most suitable RCM for simulating precipitation in the IP when driven by ERA-40 data and by GCMs, although large uncertainties in mean precipitation should be appreciated for summer. All RCMs, including KNMI-RACMO2, are still affected by uncertainties in mean precipitation that have to be taken into account for future projections especially when the RCMs are driven by GCMs.

4.2. Validation of the accuracy of temperature simulations

The outputs from the RCMs driven by ERA-40 reanalysis and driven by GCMs for temperature were also compared with observed MITPS for each location applying the methodology described earlier for the common period 1961–2000 at seasonal time-scale.

Simulations of the RCMs driven by ERA-40 showed a bias in mean seasonal temperature relative to observed MITPS towards overestimates in north-eastern IP for winter and autumn and central IP, especially in summer (*Fig. 7*). Additionally, underestimates were detected in the north and north-western IP, especially in winter, spring, and autumn and in the south-eastern IP in summer. DMI-HIRHAM5 showed the smallest anomalies of 1 °C of mean simulated temperature in most of the IP during all seasons with HadRM3 the second best. DMI-HIRHAM5 overestimated between 2–3 °C of mean temperature mainly in north-eastern IP for winter and autumn and greater than 3 °C in central IP for summer. Underestimates of between 2–3 °C of mean temperature were focused in the north and north-western area in winter, spring, and autumn, while in the south-eastern IP, similar underestimates were found for summer. HadRM3 produced overestimates of between 3–4 °C of mean temperature in the central and in north-eastern corner of the IP (around 2 °C) in winter and summer, respectively, while underestimates of between 1–3 °C were identified in the central, north, and north-western areas during winter, spring, and autumn. KNMI-RACMO2 showed overestimates of around 2 °C for mean temperature in the central IP only for summer, but underestimates were detected in the most of the IP, but were more prominent (between 3–4 °C) in the north-western area in winter, spring, and autumn.

Additionally, temperature simulations from the RCMs coupled with associated GCMs were compared with observed MITPS in order to see whether RCM simulations are affected when they are driven by GCMs (*Fig. 8*). Some differences have been detected in mean seasonal temperature from DMI-HIRHAM5 and HadRM3 when they are driven by ERA-40 or by their associated GCMs (*Figs. 7* and *8*), but the simulations fitted better in the case of KNMI-RACMO2 driven by the associated GCM than those driven by ERA-40 in all seasons. All models have a tendency to overestimate by between 1–2 °C of mean temperature in the Mediterranean region in winter, while underestimates of between 1–2 °C for mean temperature were found in most of the IP, but were

more prominent in the north-western area during winter, spring, and autumn. DMI-HIRHAM5 showed overestimates of around 2–3 °C in the Mediterranean region for winter and autumn, while the underestimates of 2–3 °C were located in the central, north, and north-western parts of the IP in spring and summer. HadRM3 and KNMI-RACMO2 produced similar underestimates of 2–3 °C over most of the IP, mainly located in the north-western corner during winter, spring, and autumn.

Seasonal temperature variability has been figured out from the ratio of standard deviations between simulated and observed average temperatures from the three RCMs driven by ERA-40 reanalysis (*Fig. 9*). All RCMs exceeded 0.5 standard deviations over the IP for all seasons being greater than 1 standard deviation over most of the IP according to HadRM3. The seasonal temperature variability between simulated and observed data from the RCMs driven by GCMs produced similar differences than the simulations driven by ERA-40 (*Fig. 10*). All RCMs exceeded 0.5 standard deviations over the whole IP during all seasons with a ratio greater than 1 standard deviation for spring, summer, and autumn according to HadRM3.

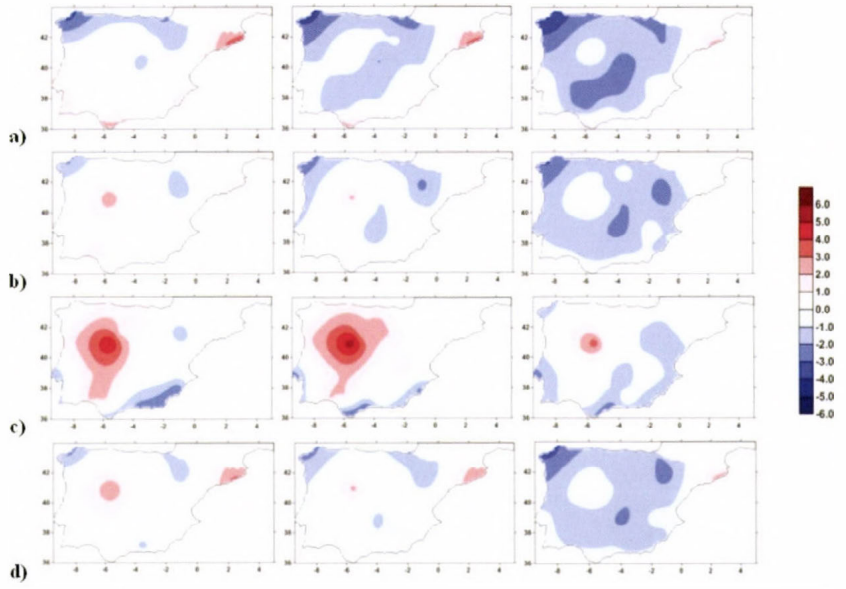

Fig. 7. Differences (in °C) between simulated and observed seasonal average temperatures (MITPS) in the IP for winter (DJF); **a)**, spring (MAM); **b)**, summer (JJA); **c)**, and autumn (SON); **d)** using the common period 1961–2000. The model outputs are derived from DMI-HIRHAM5 (left), HadRM3 (middle), and KNMI-RACMO2 (right), all driven by ERA-40 reanalysis.

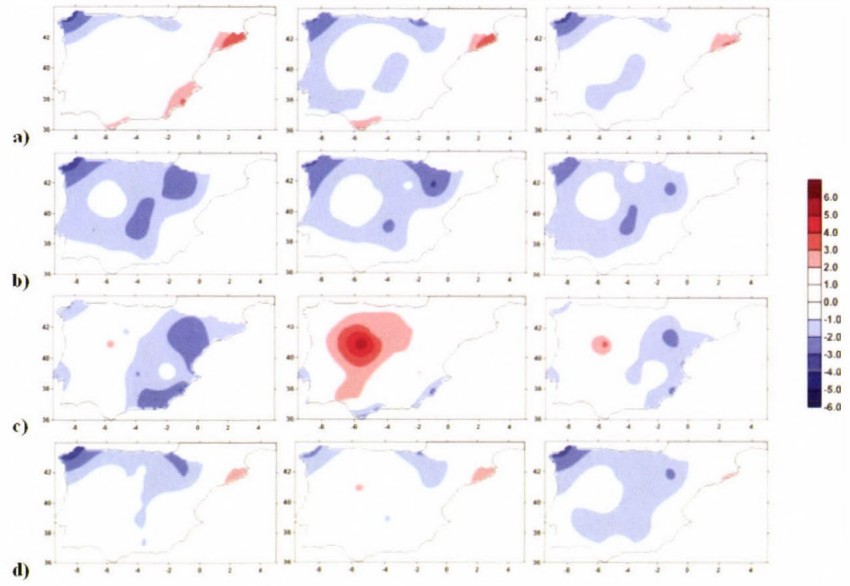

Fig. 8. Differences (in °C) between simulated and observed seasonal average temperatures (MITPS) in the IP for winter (DJF); **a)**, spring (MAM); **b)**, summer (JJA); **c)**, and autumn (SON); **d)** using the common period 1961–2000. The model outputs are derived from DMI-HIRHAM5 driven by ECHAM5-r3 (left), HadRM3 driven by HadCM3 (middle), and KNMI-RACMO2 driven by ECHAM5-r3 (right).

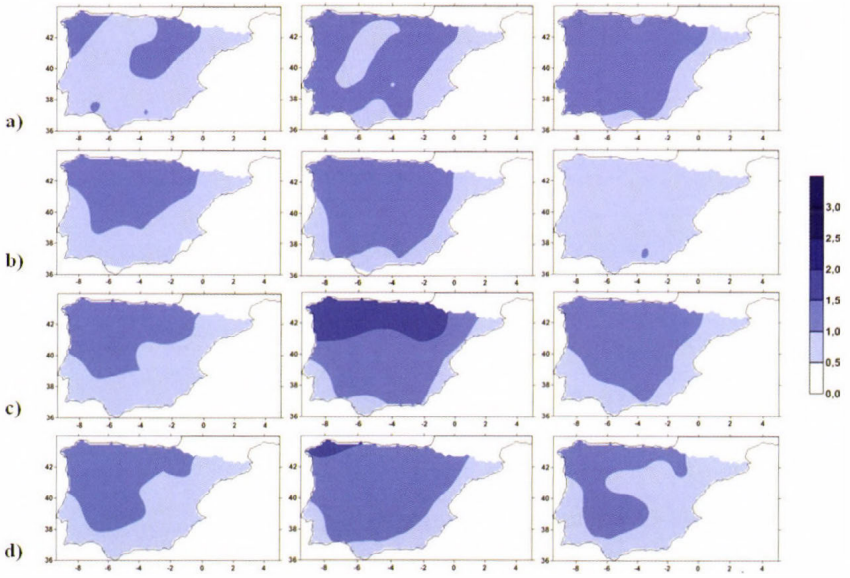

Fig. 9. Ratio of standard deviations between simulated and observed seasonal average temperatures (MITPS) in the IP for winter (DJF); **a)**, spring (MAM); **b)**, summer (JJA); **c)**, and autumn (SON); **d)** using the common period 1961–2000. The model outputs are derived from DMI-HIRHAM5 (left), HadRM3 (middle), and KNMI-RACMO2 (right), all driven by ERA-40 reanalysis.

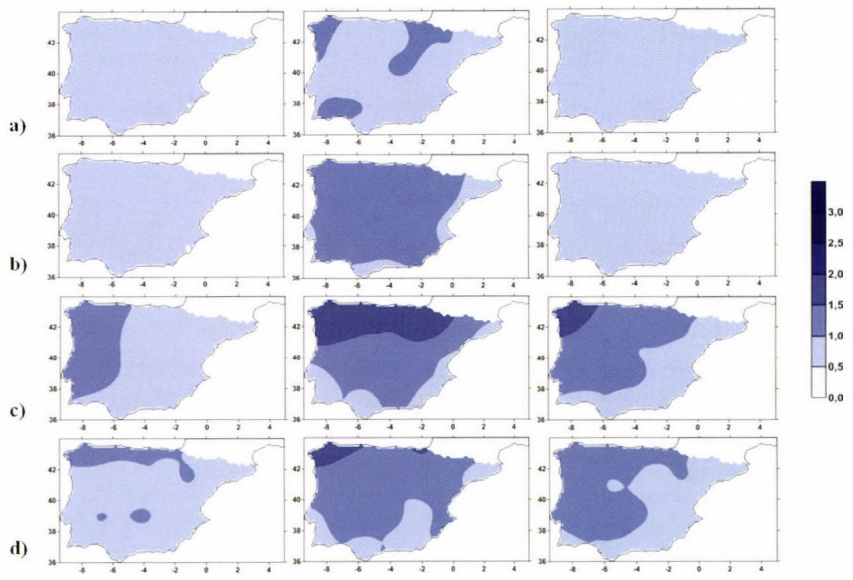

Fig. 10. Ratio of standard deviations between simulated and observed seasonal average temperatures (MITPS) in the IP for winter (DJF); **a)**, spring (MAM); **b)**, summer (JJA); **c)**, and autumn (SON); **d)** using the common period 1961–2000. The model outputs are derived from DMI-HIRHAM5 driven by ECHAM5-r3 (left), HadRM3 driven by HadCM3 (middle), and KNMI-RACMO2 driven by ECHAM5-r3 (right).

The three RCMs driven by ERA-40 reanalysis showed very high correlations between simulated and observed data during all seasons with DMI-HIRHAM5 the best-performing overall, although the correlations are lower in the Mediterranean region than in the rest of the IP, especially in summer and autumn (*Fig. 11*). Finally, the results from RMSE and K-S test showed a better fit between simulated and observed data using DMI-HIRHAM5 during winter and spring over most IP, while KNMI-RACMO2 fitted better in summer (see *Tables 1* and *2*).

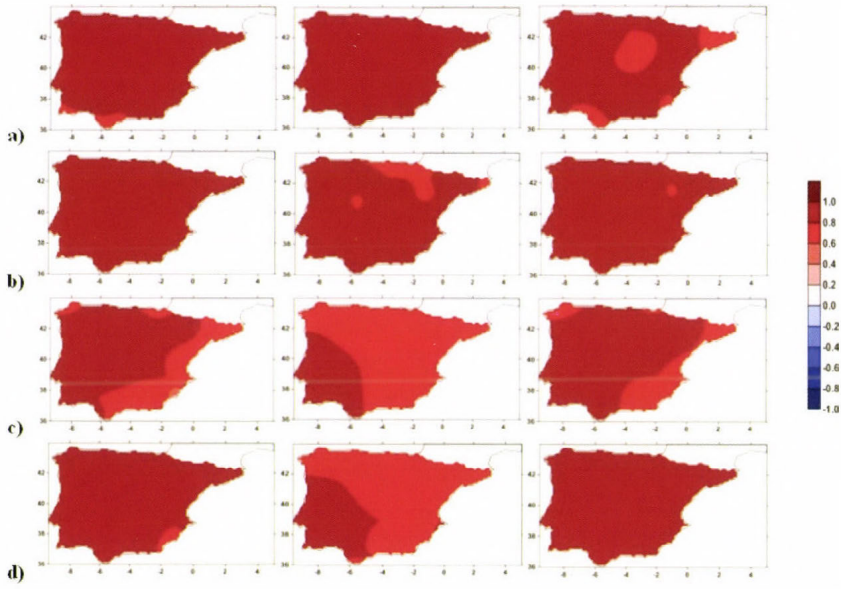

Fig. 11. Pearson product-moment correlation coefficient between simulated and observed seasonal average temperatures (MITPS) in the IP for winter (DJF); **a)**, spring (MAM); **b)**, summer (JJA); **c)**, and autumn (SON); **d)** using the common period 1961–2000. The model outputs are derived from DMI-HIRHAM5 (left), HadRM3 (middle), and KNMI-RACMO2 (right), all driven by ERA-40 reanalysis. Correlations greater than 0.34 are statistically significant at the 99% level.

From the measures considered above, DMI-HIRHAM5 is the best RCM of the three tested for the IP for simulating temperature, although large uncertainties are affecting RCMs, especially when they are driven by GCMs. These uncertainties should be considered when projecting temperature over the IP along the 21st century.

4.3. Projected changes in mean seasonal precipitation

The outputs from DMI-HIRHAM5 and KNMI-RACMO2 driven by ECHAM5-r3 and HadRM3 driven by HadCM3 were used to assess the projected changes in mean seasonal precipitation in the IP for the periods 2011–2050 (*Fig. 12*) and 2051–2090 (*Fig. 13*) relative to 1961–2000 under the A1B climate change scenario.

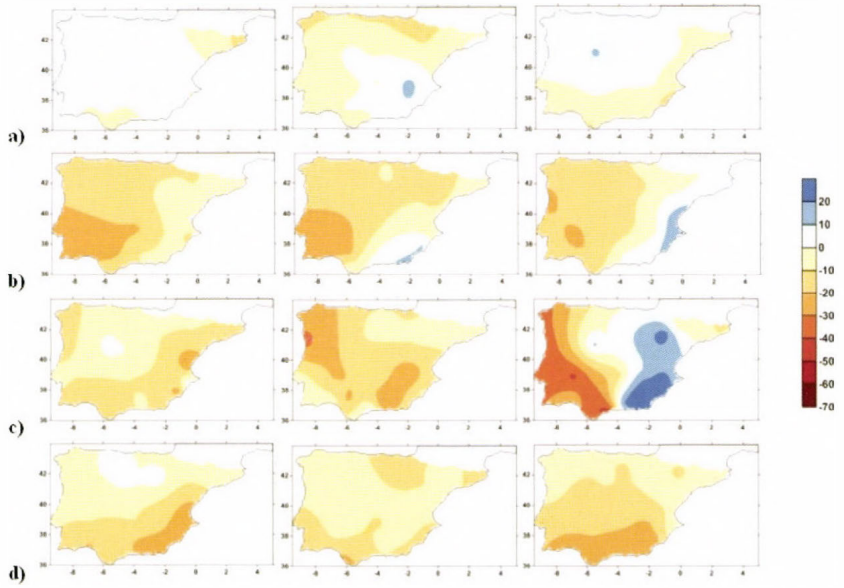

Fig. 12. Seasonal precipitation change (in %) projected for the period 2011–2050 relative to 1961–2000 in the IP for winter (DJF); **a)**, spring (MAM); **b)**, summer (JJA); **c),** and autumn (SON); **d)** using the model outputs derived from DMI-HIRHAM5 driven by ECHAM5-r3 (left), HadRM3 driven by HadCM3 (middle), and KNMI-RACMO2 driven by ECHAM5-r3 (right).

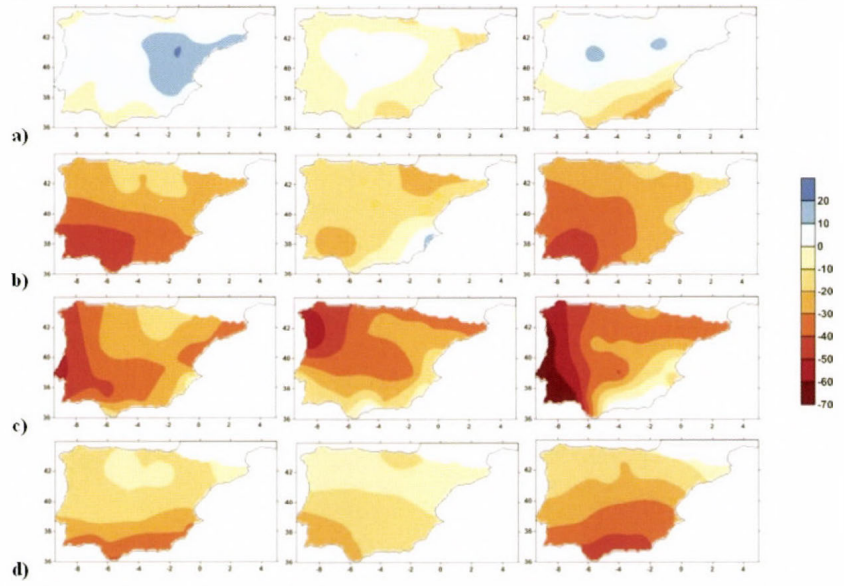

Fig. 13. Seasonal precipitation change (in %) projected for the period 2051–2090 relative to 1961–2000 in the IP for winter (DJF); **a)**, spring (MAM); **b)**, summer (JJA); **c),** and autumn (SON); **d)** using the model outputs derived from DMI-HIRHAM5 driven by ECHAM5-r3 (left), HadRM3 driven by HadCM3 (middle), and KNMI-RACMO2 driven by ECHAM5-r3 (right).

Model outputs agree on a future decrease in precipitation over most of the IP during the 21st century for spring, summer, and autumn, although no clear signal was found for winter. All RCM simulations projected a clear decrease of 10–20% in mean precipitation for spring, summer, and autumn across most of the IP for the period 2011–2050 relative to 1961–2000 (*Fig. 12*). DMI-HIRHAM5 and KNMI-RACMO2 outputs projected similar decrease in mean precipitation of 30–50% for spring and summer over most of the IP by the 2051–2090 period, while a decline of 20–30% was detected in autumn (*Fig. 13*). HadRM3 simulations showed smaller decreases in mean precipitation of 10–20% in spring and autumn, and around 20–30% increases in summer for the mid-late century. No clear signal was found in mean winter precipitation from all the RCM outputs for both time-periods (*Figs. 12* and *13*).

In particular, DMI-HIRHAM5 and KNMI-RACMO2 outputs agree on an increase in mean winter precipitation of 5–10% in central, north, and north-western IP, and a decrease of 10% in the south, south-eastern, and in the Mediterranean region for the period 2011–2050 declining by between 10–20% by the 2051–2090 period (*Figs. 12* and *13,* respectively). All RCM outputs showed a decrease in mean spring precipitation of 10–20% for most of the IP for the period 2011–2050, although HadRM3 and KNMI-RACMO2 produced precipitation increases of 10% in some areas of the Mediterranean and south-eastern coasts of the IP. An evident spring precipitation decrease of 20–40% has been projected from all RCMs for the whole IP by the 2051–2090 period being more extreme in the south and south-western areas than in the central and in the north. DMI-HIRHAM5 produced a clear decrease of 10–20% of mean summer precipitation over most of the IP for the period 2011–2050, but declining to 20–50% by the 2051–2090 period, especially in the west and south-western area. HadRM3 showed a decline of 10–30% (2011–2050) and of 20–60% in mean summer precipitation more evident in the north and north-western IP than in the south-eastern and south-western areas. KNMI-RACMO2 projected a decrease of 10–40% in summer precipitation (2011–2050) in the west and south-western area becoming 20–70% over most IP by the 2051–2090 period. Despite this, precipitation increases were found from KNMI-RACMO2 outputs in the south-eastern area of 10–60% (2011–2050) and of 5% (2051–2090). Finally, all RCM simulations showed a clear decline in mean autumn precipitation of 10–20% (2011–2050) and of 10–40% (2051–2090) for the whole IP being more extreme in the southern than in the northern area.

4.4. Projected changes in mean seasonal temperature

The model outputs associated with their GCMs were also used to assess the projected changes in mean seasonal temperature for the IP using the periods 2011–2050 (*Fig. 14*) and 2051–2090 (*Fig. 15*) relative to 1961–2000 under the A1B climate change scenario.

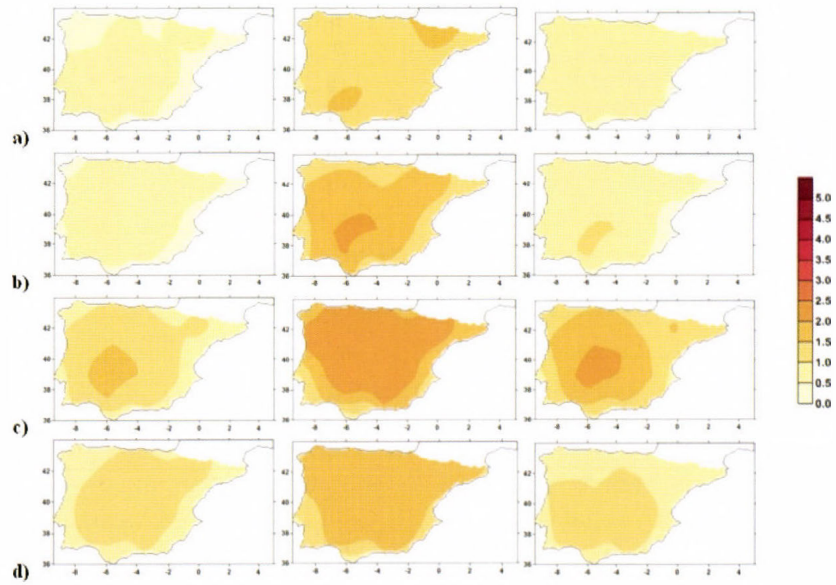

Fig. 14. Seasonal temperature change (in °C) projected for the period 2011–2050 relative to 1961-2000 in the IP for winter (DJF); **a)**, spring (MAM); **b)**, summer (JJA); **c),** and autumn (SON); **d)** using the model outputs derived from DMI-HIRHAM5 driven by ECHAM5-r3 (left), HadRM3 driven by HadCM3 (middle), and KNMI-RACMO2 driven by ECHAM5-r3 (right).

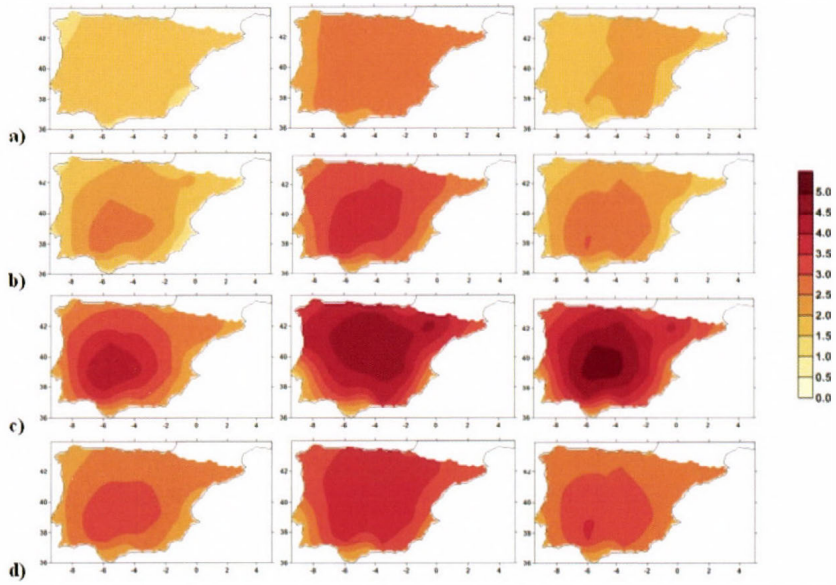

Fig. 15. Seasonal temperature change (in °C) projected for the period 2051–2090 relative to 1961-2000 in the IP for winter (DJF); **a)**, spring (MAM); **b)**, summer (JJA); **c),** and autumn (SON); **d)** using the model outputs derived from DMI-HIRHAM5 driven by ECHAM5-r3 (left), HadRM3 driven by HadCM3 (middle), and KNMI-RACMO2 driven by ECHAM5-r3 (right).

A clear increase in mean seasonal temperature has been projected from all RCM simulations over the whole IP along the year for the periods 2011–2050 and 2051–2090 relative to 1961–2000 (*Figs 14* and *15*). The highest rates were focused in summer and autumn in both time-periods, and the lowest rates were found in winter and spring. DMI-HIRHAM5 and KNMI-RACMO2 outputs showed a 0.5 ºC increase in mean temperatures for winter and spring using the period 2011–2050 with higher rates of 1.5–2 ºC by the 2051–2090 period for the whole IP. Both RCMs produced an increase of 1–1.5 ºC in summer and of 1 ºC in autumn for the period 2011–2050, while they projected an increase of 3–5 ºC in summer and of 2.5–3.5 ºC in autumn by the 2051–2090 period. HadRM3 simulations showed increases of 1.5 ºC for winter, of 1.5–2 ºC for spring and autumn, and of 2–2.5 ºC in summer for the period 2011–2050, while by the 2051–2090 period the increases reached 3 ºC in winter, 3–4 ºC in spring and autumn, and 3.5–4.5 ºC in summer.

All RCM simulations concurred in producing higher rates of change in mean temperatures over the continental IP including the Ebro basin, the Central System, the North and South Plateaus, and the south-western area for all seasons, but especially in summer and autumn. Otherwise, the smallest anomalies were found along the coastline, but especially in the north and north-western coast. In this way, RCM simulations suggested that the continental effect in temperatures will play a major role over the IP along the 21st century reaching extreme temperature increases in the interior area, especially in summer.

5. Discussion and conclusions

In this study, three regional climate models obtained from the EU-Ensembles project have been used to assess projected changes in mean seasonal precipitation and temperature over the whole IP under the A1B climate change scenario for the 21st century. These RCMs were the best-performing models for simulating precipitation and temperature for Europe according to *van der Linden* and *Mitchell* (2009), *Christensen et al.,* (2010), and *Kjellström et al.,* (2010).

The RCM outputs driven by ERA-40 reanalysis have been compared directly with observed MITPS to test the reliability of the simulations. According to the measures tested in this study, KNMI-RACMO2 is the best RCM for simulating precipitation in the IP being consistent with the results obtained by *Simpson* (2011) for UK precipitation, although some problems in summer precipitation should be appreciated. DMI-HIRHAM5 is the best regional climate model for simulation of temperature in the IP. The RCM comparisons with observed data are a necessary, but not sufficient condition to test the accuracy of the models, because current climate change can modify the original basis for a reliable simulation of past climate conditions.

Simulations of seasonal precipitation and temperature from the RCMs driven by GCMs have been used to project the mean expected changes for the periods 2011–2050 and 2051–2090 relative to 1961–2000. Large differences have been detected between RCM outputs coupled with associated GCMs and the observed MITPS. This produces large uncertainties in the results, and these have to be taken into account when assessing model outputs (*Blenkinsop et al.,* 2007; *Sheffield* and *Wood*, 2008; *Rammukainen*, 2010; *Mishra*, 2011; *IPCC,* 2012). Despite, all RCM simulations are projecting a clear decrease of 10% in mean precipitation for spring, summer, and autumn in most IP for the period 2011–2050, it is more evident in the southern than in the northern area. A significant decrease of 20–40% in mean precipitation is expected by the 2051–2090 period for the same seasons, while no clear signal was found in mean winter precipitation from all the RCM outputs and for both time-periods. Model outputs have also shown an increase in mean temperatures between 0.5–1.5 ºC for winter and spring for the period 2011–2050 with higher rates of 1.5–2.5 ºC and 1.5–3 ºC, respectively, by the 2051–2090 period. An increase of between 1–2 ºC was found in summer and 1–1.5 ºC in autumn for the period 2011–2050 being higher by the 2051–2090 period (3–4 ºC in summer and 2.5–3.5 ºC in autumn). Moreover, all RCM simulations concurred by finding higher rates of change in mean temperatures over the continental IP, and the smallest anomalies were found along the coastline, but especially in the north and north-western coasts. In this way, RCM simulations suggested that the continental effect in temperatures will be enhanced and will play a major role in producing extreme temperature increases in the interior area, especially in summer. These findings are consistent with the results obtained by *Gómez-Navarro et al.,* (2010), *Rodríguez-Puebla* and *Nieto,* (2010), and *Jerez et al.,* (2012), and *Jerez* and *Montavez* (2012) for the IP along the 21st century.

The decrease in mean precipitation and the increase in mean temperature projected from the model outputs in the IP could worse current drought conditions for the second half of the 21st century, especially in summer.

Acknowledgements: The authors acknowledge the contribution of *Mª Antonia Valente* and *Ricardo Trigo* from the Climatology and Climate Change Research Group of the Instituto *Dom Luiz*, Lisbon University, to provide us climatic data of Portugal (Porto and Lisboa time series). Original and updated Spanish daily data not included in SDATS and SDAPS were obtained from AEMET servers. Monthly simulated temperature and precipitation data from the three regional climate models driven by ERA-40 reanalysis and driven by GCMs were obtained from the EU-Ensembles project.

References

Aguilar, E., Brunet, M., Saladié, O., Sigró, J., and *López, D.,* 2002: Hacia una aplicación optima del standard normal homogeneity test para la homogeneización de series de temperatura. In (Eds.:*Cuadrat JM, Vicente SM, SAZ MA)* La Información Climática Como Herramienta de Gestión Ambiental. VII Reunión Nacional de Climatología, Grupo de Climatología de la AGE, Universidad de Zaragoza: Zaragoza, 17–33. (In Spain)

Alexandersson, H. and *Moberg, A.*,1997: Homogenisation of Swedish temperature data, Part I: Homogeneity test for linear trends, *Int. J. Climatol. 17*, 25–34.

Barrera-Escoda, A., 2008. Evolución de los extremos hídricos en Catalunya en los últimos 500 años y su modelización regional (Evolution of hydric extremes in Catalonia during the last 500 years and its regional modelling), Ph.D. Thesis, Internal Publication, University of Barcelona, Barcelona, Spain. (In Spain)

Beniston, M., Stephenson, D.B., Christensen, O.B., Ferro, C.A.T., Frei, C., Goyette, S.,Halsnaes, K., Holt, T., Jylha, K., Koffi, B., Palutikof, J., Scholl, R., Semmler, T., and *Woth, K., 2007:* Future extreme events in Eurpoean climate: an exploration of regional climate model projections. *Climatic Change 81,* 71–95.

Bosilovich, M.G., Chen, J., Robertson, F.R., Adler, R.F., 2008: Evaluation of Global Precipitation in Reanalysis. *J. Appl. Meteorol. Climatol. 47*, 2279–2299.

Blenkinsop, S. and Fowler, H.J., 2007: Changes in European drought characteristics projected by the PRUDENCE regional climate models. *Int. J. Climatol. 27,* 1595–1610.

Brunet, M., Jones, P.D., Sigró, J., Saladié, O., Aguilar, E., Moberg, A., Della-Marta, P.M., Lister D., Walther, A., and *López, D.,* 2007: Temporal and spatial temperature variability and change over Spain during 1850-2005. *J. Geophys. Res.-Atmos. 112*:D12117.

Brunet, M., Saladié, O., Jones, P.D., Sigró, J., Aguilar, E., Moberg, A., Walther, A., Lister, D., López, D., and *Almarza, C.,* 2006: The development of a new daily adjusted temperature dataset for Spain (1850–2003). . *Int. J. Climatol. 26*,1777–1802.

Christensen, J.H., Kjellström, E., Giorgi, F., Lenderink, G., and *Rammukainen, M.,* 2010: Weight assignment in regional climate models. *Climate Res. 44,* 179–194.

Christensen, J.H. and *Christensen, O.B.*, 2007: A summary of the PRUDENCE model projections of changes in European climate during this century. *Climatic Change 81*(S1), 7–30.

CLIVAR Assessment, 2010: Clima en España: Pasado presente y futuro. In (Eds. *Pérez F, Boscolo R,*) www.clivar.es (Last visit: 23-02-2013).

Collins, W.J., Bellouin, N., Doutriaux-Boucher, M., Gedney, N., Hinton, T., Jones, C.D., Liddicont, S., Martin, G., O'Connor, F., Rae, J., Senior, C., Totterdell, I., Woodward, S., Reichler, T., Kin, J., 2010: Evaluation of the HadGEM2 model. *Met Office Hadley Centre. Technical Note no. HCTN 74,* available from Met Office, FitzRoy Road, Exeter, UK. EX1 3PB.

Dai, A., 2011. Drought under global warming: A review. *Wiley Interdisciplinary Reviews:Climate Change 2*, 45–65.

Dai, A., 2012. Increasing drought under global warming in observations and models. *Nature Climate Change 3, 53–58.*

ECMWF 2004. ERA-40: ECMWF 45-year reanalysis o the global atmosphere and surface conditions 1957–2002. *ECMWF Newsletter Nº. 101.* Retrieved 5th November, 2010; http://www.mad.zmaw.de/uploads/media/e40Overwiew.pdf.

Gomez-Navarro, J.J., Montavez, J.P., Jimenez-Guerrero, P., Jerez, S., Garcia-Valero, J.A., Gonzalez-Rouco, J.F., 2010: Warming patterns in regional climate change projections over the Iberian Peninsula. *Meteorol. Z. 19,* 275–285.

IPCC climate change 2012: Managing the Risks of Extreme Events and Disasters to Advance Climate Change Adaptation. A Special Report of Working Groups I and II of the Intergovernmental Panel on Climate Change. *(Eds. Field, C.B., V. Barros, T.F. Stocker, D. Qin, D.J. Dokken, K.L. Ebi, M.D. Mastrandrea, K.J. Mach, G.-K. Plattner, S.K. Allen, M. Tignor, and P.M. Midgley),* Cambridge University Press, Cambridge, UK, and New York, NY, USA, 582.

IPCC climate change 2007: the physical science basis. In: (*Eds .Salomon S, Qin D, Manning M, Chen Z, Marquis M, Averyt KB, Tignor M, Miler HL,)* Contribution of Working Group I to the Fourth Assessment Report of the International Panel on Climate Change Program. Cambridge, UK/New York, USA: Cambridge University Press; 2007, 996.

Jerez, S., Montavez, J.P., Gomez-Navarro, J.J., Jimenez, P.A., Jimenez-Guerrero, P., Lorente-Plazas, R., Gonzalez-Rouco, J.F., 2012: The role of the land-surface model for climate change projections over the Iberian Peninsula. *J. Geophys. Res. 117*, D01,109.

Jerez, S. and *Montavez, J.P.,* 2012: A multi-physics ensemble of regional climate change projections over the Iberian Peninsula. *Clim. Dynam.* DOI: 10.1007/s00382-012-1551-5.

Kjellström, E., Boberg, F., Castro, M., Christensen, JH., Nikulin, G., and *Sanchez, E.,* 2010. Daily and monthly temperature and precipitation statistics as performance indicators for regional climate models. *Climate Res. 44*, 121–134.

van der Linden and *Mitchell, J.F.B.,* 2009: ENSEMBLES: Climate Change and its Impacts: Summary of research and results from the ENSEMBLES project. Met Office Hadley Centre, FitzRoy Road, Exeter EX1 3PB, UK.

Mariotti, A., Zeng, N., Yoon, J.H., Artale, V., Navarra, A., Alpert, P., and Li, L.Z.X., 2008: Mediterranean water cycle changes: transition to drier 21st century conditions in observations and CMIP3 simulations. *Environ. Res. Letters, 3,* 044001.

Mishra, A.K. and *Singh, V.P.,* 2011: Drought modeling-A review. *J. Hydrol. 403*, 157–175.

Rammukainen, M., 2010: State-of-the-art with regional climate models. *Wiley Interdisciplinary Reviews: Climate Change 1*, 82–96.

Rodríguez-Puebla, C. and *Nieto, S.,* 2010. Trends of precipitation over Iberian Peninsula and the North Atlantic Oscillation under climate change conditions. *Int. J. Climatol. 30*, 1807–1815.

Sánchez, E., Gaertner, M.A., Gallardo, C., 2009: Regionalización diaria de la precipitación diaria sobre la Península Ibérica: análisis de la resolución espacial en la descripción del clima actual y clima futuro. *Física de la Tierra 21*, 207–218. (In Spain)

Sheffield, J. and *Wood, E.F.,* 2008. Projected changes in drought occurrence under future global warming from multi-model, multi-scenario, IPCC AR4 simulations. *Clim. Dynam. 31*, 79–105.

Simpson, I., 2011. PhD Dissertation. Precipitation variability across the UK: Observations and model simulations. Climatic Research Unit, School of Environmental Sciences, University of East Anglia, Norwich NR47TJ, UK.

Sousa P., Trigo, R.M., Aizpurua, P., Nieto, R., Gimeno, L., Garcia-Herrera, R., 2011: Trends and extremes of drought indices throughout the 20th century in the Mediterranean, NHESS, Special Issue "*Understanding dynamics and current developments of climate extremes in the Mediterranean region", 11*, 33–51.

Van Meijgaard, E., van Ulft, L.H., van de Berg, W.J., Bosvald F., van den Hurk, B., Lenderink, G., and *Siebesma A.,* 2008*:* The KNMI regional atmospheric climate model RACMO versión 2.1. *KNMI Techn. Report TR-302,* available at: www.knmi.nl/publications/fulltexts/tr302_racmo2v1.pdf

Vicente-Serrano, S.M., Beguería, S, López-Moreno, J.I., 2011: Comment on "Characteristics and trends in various forms of the Palmer Drought Severity Index (PDSI) during 1900-2008" by Aiguo Dai, *J. Geophys. Res., 116*, D19112.

IDŐJÁRÁS

Quarterly Journal of the Hungarian Meteorological Service
Vol. 119, No. 1, January – March, 2015, pp. 23–39

Evaluation and gap filling of soil NO flux dataset measured at a Hungarian semi-arid grassland

Dóra Hidy[1], **László Horváth**[*1], and **Tamás Weidinger**[2]

[1]*MTA-SZIE Plant Ecology Research Group, Szent István University, Páter K. u. 1, 2103 Gödöllő, Hungary*

[2]*Department of Meteorology, Eötvös Loránd University, Pázmány Péter sétány 1/A, 1117 Budapest, Hungary*

[*]*Corresponding author E-mail: horvath.laszlo.dr@gmail.com*

(Manuscript received in final form February 8, 2015)

Abstract—Nitric oxide soil emission flux was measured by 2–2 parallel manual and auto dynamic chambers on hourly basis above a Hungarian semi-arid, sandy grassland between August 2012 and January 2014. The measured datasets covered 43–85% of time period depending on chambers. We applied a gap filling method based on multivariable analysis (Sigma Plot) combined with maximum likelihood method. Trend of gap filled dataset shows large peaks mostly in summer and early fall. When soil parameters are far from the optimum (dry, warm conditions), the fluxes are negligible. Application of manual chambers closed for longer period results in substantial positive bias in flux estimation compared to auto chambers as a consequence of measurement setup, different temperature, and drier soil conditions below the chamber. Mean fluxes applying permanently closed dynamic chambers are approximately three times higher compared to auto chambers: 0.176±0.489 nmol $m^{-2}s^{-1}$ and 0.058±0.130 nmol $m^{-2}s^{-1}$, respectively.

Key-words: nitric oxide, soil emission, gap filling, nitrification, grassland, dynamic chamber

1. Introduction

As it is well-known, one of the most important natural sources of atmospheric nitric oxide (NO) is the soil nitrification-denitrification process. It has been recognized earlier that soil flux of NO is similar in magnitude to fossil fuel emission of NO_x (*Davidson* and *Kingerlee*, 1997). For this reason, NO plays key role both in biosphere–atmosphere N-balance and in biogeochemical cycle of nitrogen.

Rate of soil NO flux strongly depends on soil temperature and moisture (*Smith et al.*, 1998) and on soil aeration, inorganic N content, and pH (*Bouwman*, 1996; *Cárdenas et al.*, 1993; *Pilegaard*, 2013).

There have been several research projects aiming on one hand to establish the magnitude of emission rate of nitrogen oxides from soils (e.g., NOFRETETE, *Kesik et al.*, 2005; *Pilegaard et al.*, 2006), and on the other hand to involve the soil NO emission in the N-inventory (e.g., NitroEurope, *Skiba et al.*, 2009). An Integrated Project ÉCLAIRE (http://www.eclaire-fp7.eu/) started in 2011, among others to study the effect of climate change on air pollution impacts. One of the main measurement tasks of this project was the continuous monitoring of soil NO emission at different types of land (forest, arable, grass). Among the tree European grass stations, Bugacpuszta (Hungary) was selected to monitor and report soil NO fluxes continuously for 17 months on hourly basis.

We applied parallel both so-called manual (permanently closed) and auto (closed only during short measurement period) chambers for continuous measurements. As it was established earlier (*Yao et al.*, 2009), the use of manual chamber for measuring soil fluxes has some disadvantages. One of the main disadvantages is caused by the permanently closed status of chambers preventing the surface from precipitation. On the other hand, the top of chamber is exposed to solar radiation continuously heating the chamber box inside, compared to auto chambers which are open out of measurement cycle. Lower moisture and higher temperature conditions inside the permanently closed chambers may generate systematic bias in flux calculation.

As a consequence of the malfunction and failure of sampling and monitoring equipments during our measurement period, the data covers only the 43–85% of the full time of measurement campaign for different chambers.

The aim of this paper is firstly to apply a statistical gap filling method to complete the dataset, and secondly to give a semi-quantitative estimation on the positive bias in soil NO fluxes caused by applying manual chambers.

2. Methodology

2.1. Measurement of soil NO fluxes

Measurements were carried out in Bugacpuszta, Hungary, above a grassland between August 2012 and January 2014. The climate is semi-arid temperate continental, the mean annual temperature is 10.7 °C, and the average yearly precipitation is around 550 mm. The region has sandy soil with high sand (79%) and low clay (13%) contents in the upper 10 cm soil layer. More detailed information of location and characteristics are described in *Horváth et al.* (2010); *Machon et al.* (2010; 2011; 2015). Two-two parallel manual (Chamber 1 and Chamber 2; V = 2 L, h = 5 cm) and automatic (Chamber 3 and Chamber 4; V = 6.8 L, h = 10 cm) dynamic chambers were applied. Automatic chambers (Ricambi, Milan) were settled at fix positions and were closed only for 10 minutes every hour during sampling allowing the surface to be exposed to solar radiation and precipitation out of sampling time. Two manual chambers, home made by pale grey plastic, were permanently closed. The two chambers were re-settled during bi-weekly station maintenances onto other collars among the 6 fixed ones in turn. All of four chambers were sampled for 10 minutes at a flow rate of 2 L min^{-1} in sequence every hour all together for 40 minutes; in the remaining 20 minutes, concentration gradients were measured by a mast at different heights. Soil temperature and moisture were measured a few meters apart from the chambers by 105T thermocouple probes and CS616 water content reflectometers, at –5; –30 cm and –3; –30 cm depths, respectively. A computer controlled valve system was switched the different channels in turn. The output concentrations of nitric oxide and ozone were measured by HORIBA APNA-350E and APOA-350E gas monitors through teflon tubing. Input concentrations of these gases were estimated from gradient concentration measurements at 0.5 m height, at the beginning of the one-hour long measurement cycle.

NO flux was calculated according to *Meixner et al.* (1997). Chemical correction of rapid reaction of NO with ozone ($NO+O_3 \rightarrow NO_2+O_2$) was taken into account. Under steady-state conditions, the mass balance equation for NO can be written as follows (the photolysis rate of NO_2 inside the dark chambers was estimated to be zero):

$$F_f + F_m + F_{bl} + F_{gp} = 0, \tag{1}$$

where F_f is the soil flux, F_m is the difference between fluxes entering and leaving the chamber, F_{bl} is the term for the wall effect which was negligible because of the relatively short residence time of the gas mixture in the chamber, and F_{gp} is the loss of NO due to the chemical reaction with ozone. For detailed description of flux calculations refer to *Horváth et al.* (2006) and *Machon et al.* (2015).

2.2. *Statistical gap filling method*

As soil NO flux depends on soil moisture, temperature, and soil organic nitrogen content, we have taken into account the variation of soil flux as a function of these parameters for gap filling. In the lack of regular observations we supposed that chemical characteristics of soil did not changed significantly during the observation period.

There are different gap filling methods used in micrometeorological flux measurements (*Papale*, 2012) i) empirical (e.g., look up tables), ii) interpolation (e.g., mean diurnal variation), iii) artificial neutral networks, iv) non-linear regressions, and v) process oriented models. Gap filling methodology has been applied for the long term eddy covariance dataset in most cases. A statistical–regression methodology for gap filling of the long term soil respiration measurements was constructed by *Gomez-Casanovas et al.* (2013).

Effects of soil temperature and moisture for soil NO fluxes are well investigated and described by Gaussian distributions (*Luo et al.*, 2013; *Pilegaard*, 2013). Based on these investigations and on the former analysis of soil fluxes in Bugacpuszta (*Machon et al.*, 2011), a nonlinear regression gap filling method was selected which consisted of different steps.

Firstly we analyzed the dependence of soil flux in the function of soil physical parameters. We have taken into account four parameters, namely the soil moisture measured at –3 and –30 cm and soil temperature measured at –5 and –30 cm depths as SWC1, SWC2, TS1, and TS2, respectively (*Fig. 1*). During the measurement period, a total of 4686 parallel measurements were taken when all of the 4 chambers were together in operation. The dependence of fluxes on physical parameters was tested only for these measurements ensuring the homogeneity. We supposed that shape of functions is the same for all the measuring plots (chambers).

According to the shape of these functions and on the basis of earlier observations at the same site (*Machon et al.*, 2011), we supposed a maximum shape, exponential functions for moisture (x_{SWC}) and temperature (x_{TS}) using the assumption of Gaussian distributions. Although the flux dependence on soil temperature is generally exponential, in our case the temperature often exceeded the 20 °C resulting in lower bacterial activity caused by the heat stress or by the extreme low humidity at higher temperature regimes. As the first step, Eq. (2) was used for the estimation of missing soil flux rates (F_f):

$$F_f = a_{SWC} \cdot \exp\left[-0.5 \cdot \left(\frac{x_{SWC} - x0_{SWC}}{b_{SWC}}\right)^2\right] + a_{TS} \cdot \exp\left[-0.5 \cdot \left(\frac{x_{TS} - x0_{TS}}{b_{TS}}\right)^2\right]. \quad (2)$$

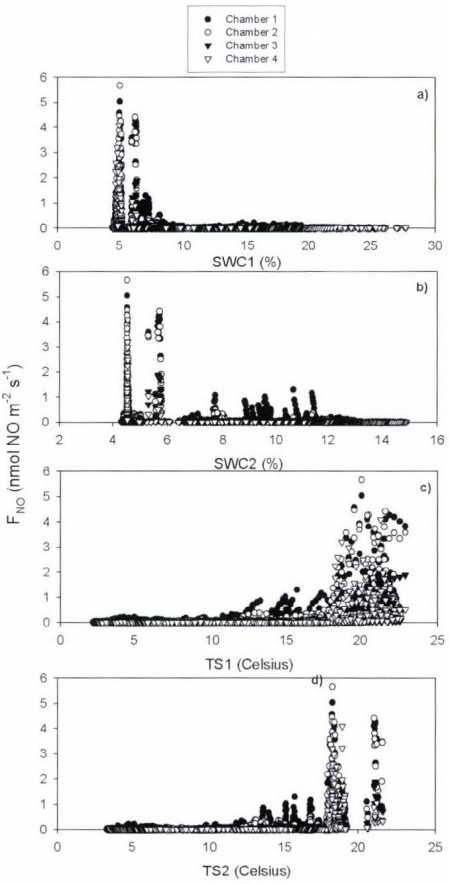

Fig. 1. NO fluxes measured by the four chambers in function of volumetric soil water content SWC1 (a), SWC2 (b) at –3 and –30 cm and soil temperature TS1 (c), TS2 (d) at –5 cm and –30 cm depths, respectively.

3. Results

3.1. Gap filling of data series

We have calculated the dependence of NO flux in 4 different combinations of SWC and TS by the SigmaPlot 8.0 (Systat Software Inc., Chicago, USA) graphing and data analyses. (The Sigma Plot curve fitter uses the Marquardt-Levenberg algorithm). The best fit was observed among soil fluxes and SWC1-TS1 (*Fig. 2*) among hourly data on the days (n=4686) when no measurement was missing (all chambers were in operation). Measured flux data

ranges within 0–6 nmol $m^{-2} s^{-1}$. The relationship is significant at the probability level of $p < 0.0001$ (except of two cases), and the calculated correlation coefficients are: $R^2_{Ch1} = 0.435$; $R^2_{Ch2} = 0.436$; $R^2_{Ch3} = 0.393$; $R^2_{Ch4} = 0.323$. The standard errors (standard deviation of differences between the measured and estimated fluxes) of estimation are: $SD_{Ch1} = 0.233$; $SD_{Ch2} = 0.233$; $SD_{Ch3} = 0.079$; $SD_{Ch4} = 0.139$ nmol $m^{-2} s^{-1}$.

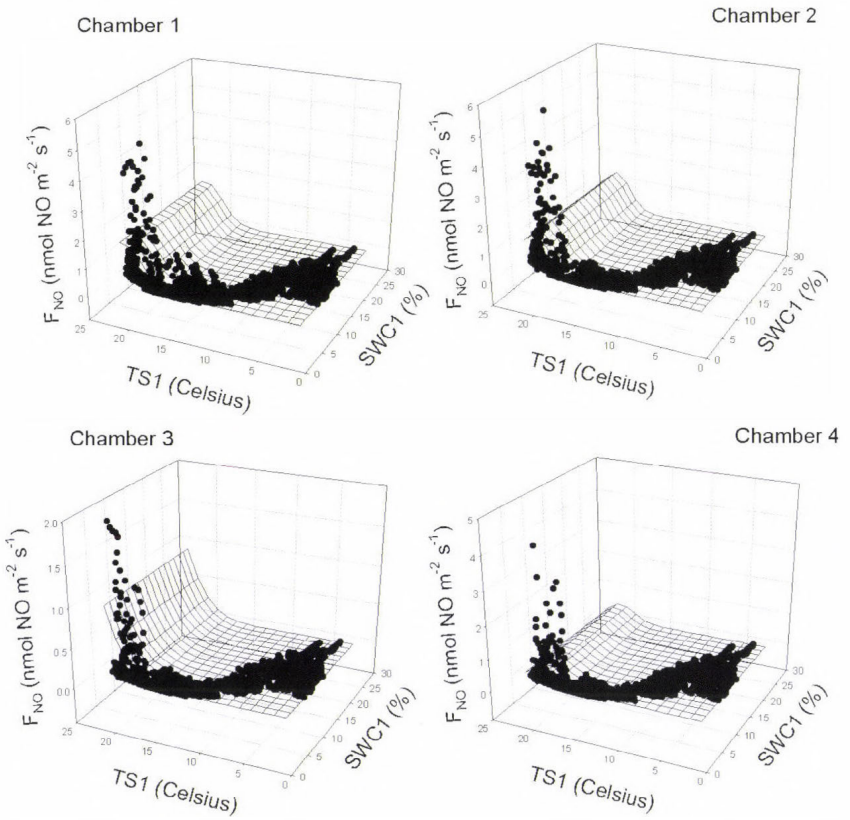

Fig. 2. Dependence of NO flux on soil properties (SWC at –3 cm depth, TS at –5 cm depth) measured by the different chambers. The fitted surface was calculated based on Eq. (2), the parameter estimation was created by Sigma Plot.

Further on, we have estimated the parameters of Eq. (2) by maximum likelihood method. There are various measures to express the distance between model and observation numerically (e.g., average, median, maximum, and normalized). It is difficult to clearly judge the significance of the different

quantitative measures, the choice of the misfit depends on the nature of the reference data (*Janssen* and *Heuberger*, 1995).

Hence, the NO flux estimation has two functions with 3–3 parameters for each chamber. In the next step, the parameter values were randomized for all chambers (Chamber 1–Chamber 4) to find the best combination of them. The measure of the goodness-of-fit is a special likelihood (Appendix Eq. A5.) taking simultaneously into account the correlation between the measured and modeled data, the average error, and the difference of the sum of measured and estimated data (see the equations in detail in the Appendix) (*Janssen* and *Heuberger*, 1995). The parameter values belonging to the maximum of the likelihood values are considered as the optimum parameter set.

After estimation for each chamber, the model was run with the optimum parameters compiled in *Table 1*. As the result of calibration, the correlation remained the same among measured and calculated data with parallel decrease of the error of estimation and the difference between measured and simulated sum (*Table 2*).

Table 1. Optimized parameters of Eq. (2)

	a_{SWC}	b_{SWC}	$x0_{SWC}$	a_{TS}	b_{TS}	$x0_{TS}$
Chamber 1	0.003	0.751	26.409	2.689	1.892	22.298
Chamber 2	0.050	0.227	48.252	2.060	1.571	21.399
Chamber 3	–1.524	–0.268	50.073	25.542	4.805	33.980
Chamber 4	2.134	0.073	3.068	1.044	1.813	21.505

Table 2. Coefficient of determination (R^2), normalized error (NE, nmol $m^{-2} s^{-1}$), and the difference between the measured and simulated sum (SE, nmol $m^{-2} s^{-1}$), before (BC, Method 1) and after (AC, Method 2) calibration (n =4686)

	Chamber 1			Chamber 2			Chamber 3			Chamber 4		
	R^2	NE	SE	R^2	NE	SE	R^2	NE	SE	R^2	NE	SE
BC	0.44	1.36	–32.8	0.44	1.27	–28.8	0.39	1.52	–55.1	0.32	1.6	–20.1
AC	0.45	1.32	–1.82	0.45	1.26	0.74	0.37	1.58	6.55	0.29	1.1	10.9

The next step of gap filling procedure was the estimation of goodness of method. We analyzed the distribution of the data gaps. Each data series (Chambers 1–4) has 12,744 rows, with 15% to 57% of data lack depending on the chamber. We found that the most frequent length of the data gaps was 1, and the maximum was 689 in hour scale (*Fig. 3*).

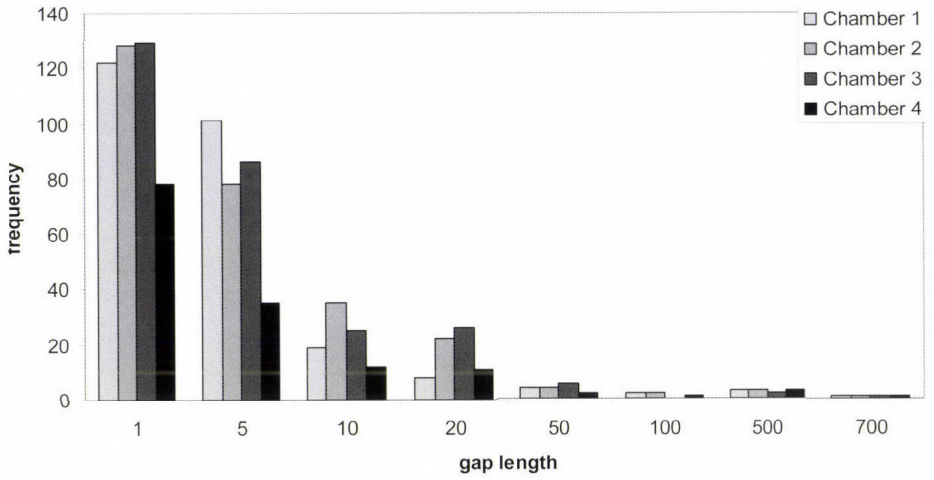

Fig. 3. Distribution of the data gaps (number of missing hourly data) regarding to the different chambers.

In order to examine the efficiency of gap filling methods, we created different numbers of data lacks in the measured data series by random number generator. *Table 3* contains the length and number of artificial gaps selected according to the original distribution of the data gaps (*Fig. 3*). The random gap creation was repeated 1000 times. The lacks were filled both by the simple method (Method 1: linear interpolation between the last data before the given gap and the first data after the given gap) and by the method described above (Method 2: using NO flux estimation based on SWC and TS data). The measured (NO flux data set without artificial gaps) and the estimated (artificial gaps are filled with estimated data) NO flux data were compared using likelihood values (function of the difference between the measured and estimated NO data defined by Eq. A5. in the Appendix) during random gap creation (1,000 random gap – 1,000 likelihood value). Hence, by the comparison of the two data series generated by the two methods (difference of the average likelihood), we found that in case of manual chambers, Method 1 gives better estimation (the difference is positive) if gap length is less than 10 hourly data and in case of automatic chambers, Method 1 is the better if gap length is less than 30. We can verify that we can use Method 2 for manual chambers in cases when gap length is longer than 10 and for automatic chambers in cases when gap length is longer than 30 (in other cases, Method 1 was used to fill the gaps) (*Fig. 4*).

Table 3. Length and number of artificial data gaps

name	length	number
G1	1	100
G5	5	100
G10	10	20
G20	20	10
G20	30	5
G50	50	5
G100	100	1
G500	500	1
G700	1000	1

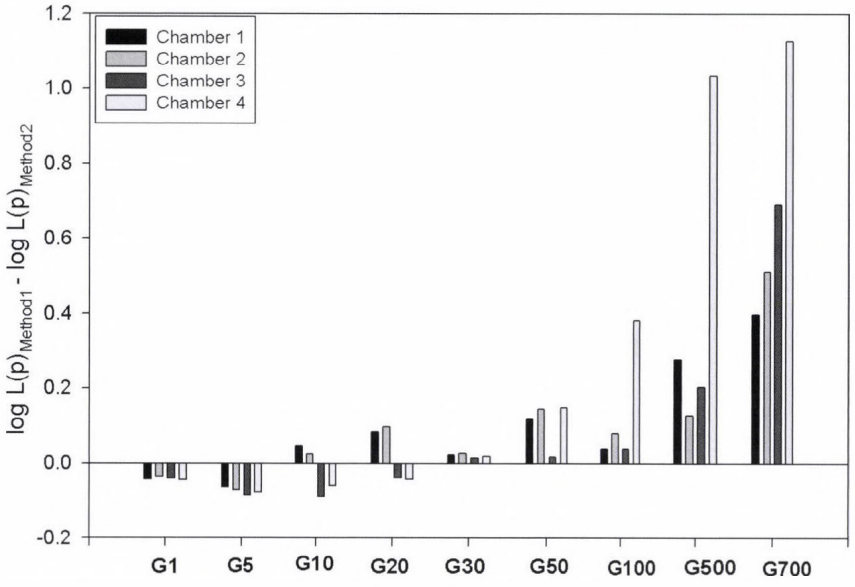

Fig. 4. The difference between the likelihood values using Method 1 and Method 2 during random gap creation in function of the gap length (G1: 1 data is missing, G5: five data are missing, etc.) for different chambers.

3.2. Evaluation of data

For evaluation, one dataset among 4 chambers was selected supposing that trend of NO flux is similar for all. The gap filled data series for Chamber 4 can be seen in *Fig. 5*. The trend of NO fluxes follows well the variation of soil wetness and temperature as it is expected. The optimum conditions for nitrification and

NO emission are in the dry and warm ranges. Two optimum periods occurred during summer/early fall during years of 2012 and 2013, when emission peaks appeared. In any other time period at either low temperature (lower than 10 °C) or high soil water content (higher than 10%), the NO production/emission are suppressed; the soil fluxes are negligible in magnitude compared to summer and early fall rates characterized by optimum soil conditions.

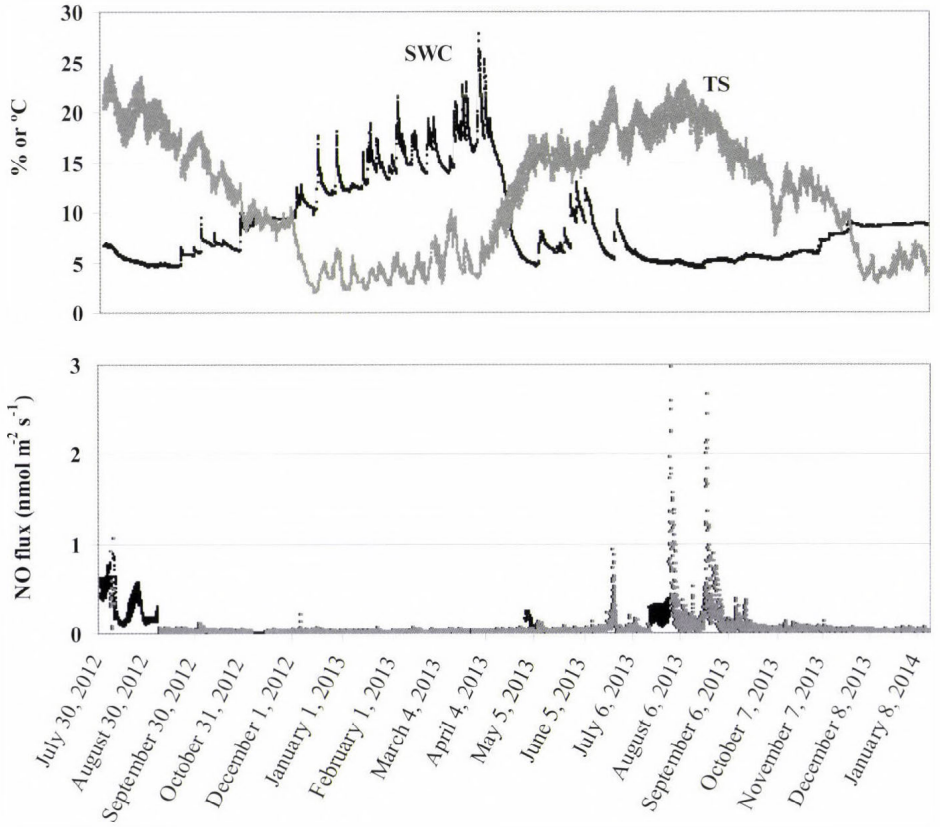

Fig. 5. Time course of soil properties, and measured (grey), and gap filled (black) NO fluxes for Chamber 4.

The statistical parameters of data series can be seen in *Table 4.* Gap filled flux data sets were compared to modeled ones for the whole period and for year 2013, separately. The agreement is acceptable for Chambers 1–3; the largest deviation

from the mean (less than 20%) appears for Chamber 4. Coefficients of variation (CV) for observed and calculated fluxes agree in magnitude for all chambers.

Table 4. Statistical parameters (mean, CV*) of measured and gap filled datasets for soil NO flux (nmol $m^{-2}s^{-1}$)

	Chamber 1	Chamber 2	Chamber 3	Chamber 4
Modeled, all				
mean	0.168	0.183	0.062	0.065
CV	3.16	2.59	2.58	2.46
n	12 747	12747	12 747	12 747
Gap-filled, all				
mean	0.171	0.181	0.061	0.055
CV	3.04	2.54	2.41	2.05
n	12 747	12 747	12 747	12 747
Modeled, 2013				
mean	0.086	0.122	0.042	0.058
CV	2.88	2.21	2.65	2.82
n	8 760	8 760	8 760	8 760
Gap-filled, 2013				
mean	0.094	0.113	0.041	0.044
CV	2.11	1.93	1.94	1.92
n	8 760	8 760	8 760	8 760

CV* (coefficient of variation): ratio of the sample standard deviation to the sample mean

3.3. Estimation of bias by using manual chambers

Mean of hourly soil NO fluxes were calculated separately for manual and auto chambers for cases when all of the 4 chambers were parallel in operation (n = 4686). The bulk daily course of ratio of fluxes measured by manual and auto chambers can be seen in *Fig. 6.* At night when solar radiation was zero, the average positive bias in fluxes measured by manual chambers (independently from the season) can be characterized by a factor of 1.6 as a consequence of drier soil conditions below the chamber. When solar radiation reached its maximum around the noon hours, the factor has increased up to 3.2. Mean flux values in *Table 4* also demonstrate a huge (around a factor of 3) increase in fluxes by applying permanently closed chambers. Because the magnitude of the

bias depends on many factors (climate, material and dimensions of chamber etc.), deeper conclusion can not be drown out of this semi-quantitative estimation.

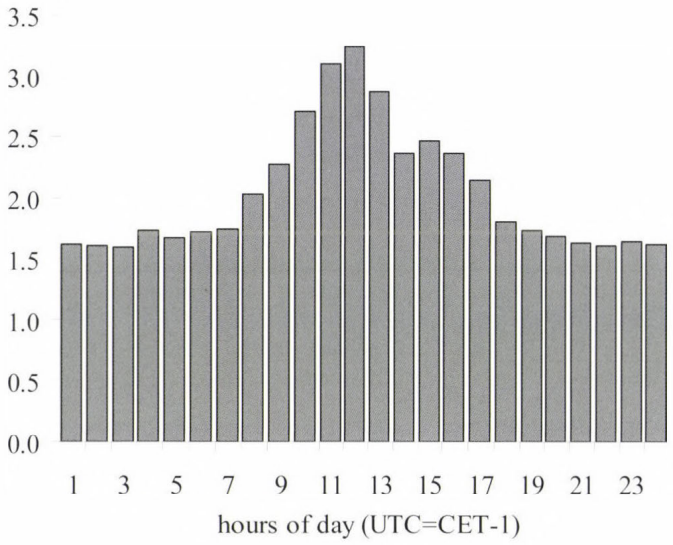

Fig. 6. Daily course of bias as ratio of measured soil NO flux by manual chambers compared to auto chambers (n=4686).

4. Conclusion

Soil nitric oxide flux over sandy grassland strongly depends on soil moisture and temperature. Using the significantly correlated functions among fluxes, soil moisture, and temperature, the missing fluxes can be predicted. Analyzing the whole dataset we can establish that significant fluxes were measured when temperature and soil wetness were near to the optimum rate. In any cases, the fluxes were practically negligible. Expecting a drier and warmer climate in our region, reduction in soil NO emission is expected in the future.

The application of manual chambers (closed for longer period) for soil flux measurement may cause significant positive bias especially through the heating effect of solar radiation. The use of white chambers may reduce this effect, but the lid of chambers is an obstruction for precipitation that can not be prevented.

Acknowledgements—Authors acknowledge the financial support of Animal Change (FP7 266018), ÉCLAIRE (FP7 282910), NitroEurope (FP6) EU projects, MTA PD 450012 project, and PIAC 13-1-2013-0141 research and development project. Special thanks to Gyula Pávó, Zoltán Istenes, and Attila Eredics for their technical help.

References

Bouwman, A.F., 1996: Direct emission of nitrous oxide from agricultural soils. *Nutr. Cycl. Agroecosys. 46*, 53–70.

Cárdenas, L., Rondón, A., Johansson, Ch., and *Sanhueza, E.*, 1993: Effects of soil moisture, temperature, and inorganic nitrogen on nitric oxide emissions from acidic tropical savannah soils. *J. Geophys. Res.: Atmos. 98*, 14783–14790.

Davidson, E.A. and *Kingerlee, W.*, 1997: A global inventory of nitric oxide emissions from soil. *Nutr. Cycl. Agroecosys. 48*, 37–50.

Gomez-Casanovas, N., Anderson-Teixeira K., Zeri, M., Bernacchi, C.J., and *DeLucia, E.H.*, 2013: Gap filling strategies and error in estimating annual soil respiration. *Glob. Change Biol. 19*, 1941–1952.

Horváth, L., Führer, E., and *Lajtha, K.*, 2006: Nitric oxide and nitrous oxide emission from Hungarian forest soils; linked with atmospheric N-deposition. *Atmos. Environ. 40,* 7786–7795.

Horváth, L., Grosz, B., Machon, A., Tuba, Z., Nagy, Z., Czóbel, Sz., Balogh, J., Péli, E., Fóti, Sz., Weidinger, T., Pintér, K., and *Führer, E.*, 2010: Estimation of nitrous oxide emission from Hungarian semi-arid sandy and loess grasslands, effect of soil parameters, grazing, irrigation and application of fertilizer. *Agric., Ecosys. Environ.139*, 255–263.

Janssen, P.H.M., and *Heuberger, P.S.C.*, 1995: Calibration of process oriented models. *Ecol. Model. 83,* 55–66.

Kesik, M., Ambus P., Baritz, R., Brüggemann, N., Butterbach-Bahl, K., Damm, M., Duyzer, J., Horváth, L., Kiese, R., Kitzler, B., Leip, A., Li, C., Pihlatie, M., Pilegaard, K., Seufert, G., Simpson, D., Skiba, U., Smiatek, G., Vesala, T., and *Zechmeister-Boltenstern, S.*, 2005: Inventory of N_2O and NO emissions from European forest soils. *Biogeosciences 2,* 353–375.

Luo, G.J., Kiese, R., Wolf, B., and *Butterbach-Bahl, K.*, 2013: Effects of soil temperature and moisture on methane uptakes and nitrous oxide emissions across three different ecosystem types. *Biogeosciences 10*, 3205–3219.

Machon, A., Horváth, L., Weidinger, T., Grosz, B., Pintér, K., Tuba, Z., and *Führer, E.*, 2010: Estimation of net nitrogen flux between the atmosphere and a semi-natural grassland ecosystem in Hungary. *Eur. J. Soil Sci. 61*, 631–639.

Machon, A., Horváth, L., Weidinger, T., Pintér, K., Grosz, B., Nagy, Z., and *Führer, E.*, 2011: Weather induced variability of N-exchange between the atmosphere and a grassland in the Hungarian Great Plain. *Időjárás 115*, 219–232.

Machon, A., Horváth, L., Weidinger, T., Grosz, B., Móring, A., and *Führer, E.*, 2015: Measurement and modeling of N-balance between the atmosphere and the biosphere over a grazed grassland (Bugacpuszta) in Hungary. *Water Air Soil Poll. 226*:27.

Meixner, F.X., Fickinger, Th., Marufu, L., Serca, D., Nathaus, F.J., Makina, E., Mukurumbira, L., and *Andreae, M.O.*, 1997: Preliminary results on nitric oxide emission from a southern African savanna ecosystem. *Nutr. Cycl. Agroecosys. 48*, 123–138.

Papale, D., 2012: Data gap filling. In (eds. *Aubinet, M., Vesala, T., and Papale, D.*), Eddy covariance. Springer, Dordrecht, Heidelberg, London, New York.159–172.

Pilegaard K., 2013: Processes regulating nitric oxide emissions from soils. *Phil. Trans. R. Soc. B 368*, 20130126.

Pilegaard, K., Skiba, U., Ambus, P., Beier, C., Brüggemann, N., Butterbach-Bahl, K., Dick, J., Dorsey, J., Duyzer, J., Gallagher, M., Gasche, R., Horvath, L., Kitzler, B., Leip, A., Pihlatie, M.K., Rosenkranz, P., Seufert, G., Vesala, T., Westrate, H., and *Zechmeister-Boltenstern, S.*, 2006: Factors controlling regional differences in forest soil emission of nitrogen oxides (NO and N_2O). *Biogeosciences 3*, 651–661.

Skiba, U., Jones, S.K., Drewer, J., Tang, Y.S., van Dijk, N., Helfter, C., Nemitz, E., Twigg, M., Famulari, D., Owen, S., Philatie, M., Vesala, T., Larsen, K.S., Carter, M.S., Ambus, P., Ibrom, A., Beier, C., Hensen, A., Frumau, A., Brüggemann, N., Gasche, R., Neftel, A., Spirig, C., Horvath, L., Freibauer, A., Cellier, P., Laville, P., Loubet, B., Magliulo, E., Bertolini, T., Seufert, G., Andersson, M., Manca, G., Laurila, T., Aurela, M., Zechmeister-Boltenstern, S., Kitzler, B., Schauffler, G., Siemens, J., Kindler, R., Flechard, C., Sutton, M.A., Erisman, J.W., Cape, J.N., and *Butterbach-Bahl, K.*, 2009: Biosphere atmosphere exchange of reactive nitrogen

and greenhouse gases at the NitroEurope core flux measurement sites: Measurement strategy and first data sets. *Agr. Ecosys. Environ.133*, 139–149.

Smith, K.A., Thomson, P.E., Clayton, H., McTaggart, I.P., and Conen, F., 1998: Effects of temperature, water content and nitrogen fertilisation on emissions of nitrous oxide by soils. *Atmos. Environ. 32*, 3301–3309.

Yao, Zh., Zheng, X., Xie,B., Liu,Ch., Mei,B., Dong, H., Butterbach-Bahl, K., and *Zhu, J.*, 2009: Comparison of manual and automated chambers for field measurements of N_2O, CH_4, CO_2 fluxes from cultivated land. *Atmos. Environ. 43*, 1888–1896.

Appendix

A1: Basic definitions

Error (E): difference between measured and simulated data on a given hour (i) using a given parameter set (p)

$$E_i = m_i(p) - d_i^{obs}$$

Normalized bias (NB): normalized difference between the sum of model predictions and observed values

$$NB = \frac{\overline{M} - \overline{O}}{\overline{O}}$$

Modeling efficiency: a measure used to assess the predictive power of models (definition is identical to coefficient of determination (R^2) in case of linear regression)

$$ME = 1 - \frac{\sum_i (E_i)^2}{\sum_i \left(d_i^{obs} - \overline{d_i^{obs}}\right)^2}$$

Log-likelihood: it is more convenient to calculate with the natural logarithm of the likelihood

$$\log L(p) = \ln[L(p)]$$

A2. Likelihood and log-likelihood from Janssen median error misfit

$$L(p)_{average} = \exp\left[-\left(\frac{1}{N}\sum_{i=1}^{N} NE_i\right)\right]$$

$$\log L(p)_{average} = -\left(\frac{1}{N}\sum_{i=1}^{N} NE_i\right)$$

A3. Likelihood and log-likelihood from Janssen modeling efficiency error misfit

$$L(p)_{efficiency} = \exp[-(ME)^{-1}]$$
$$\log L(p)_{efficiency} = -(ME)^{-1}$$

A4. Likelihood and log-likelihood from Janssen bias misfit

$$L(p)_{bias} = \exp[-NB]$$
$$\log L(p)_{bias} = -NB$$

A5. Combined Likelihood and log-likelihood form

$$L(p)_{combined} = L(p)_{average} \cdot L(p)_{bias} \cdot L(p)_{efficiency}$$
$$\log L(p)_{combined} = -\left(\frac{1}{N}\sum_{i=1}^{N} NE_i\right) + (-ME) + (-NB)$$

IDŐJÁRÁS

Quarterly Journal of the Hungarian Meteorological Service
Vol. 119, No. 1, January – March, 2015, pp. 39–51

Radar-based investigation of long-lived thunderstorms in the Carpathian Basin

Ákos Horváth[1]*, **András Tamás Seres**[2], and **Péter Németh**[3]

[1]*Hungarian Meteorological Service,*
Vitorlás u. 17, H-8600 Siófok, Hungary,
E-mail: horvath.a@met.hu

[2]*Hungarian Defence Forces Geoinformation Service,*
Szilágyi E. fasor 7–9, H-1024 Budapest, Hungary,
E-mail: seres.andrastamas@upcmail.hu

[3]*Hungarian Meteorological Service,*
Gilice tér , H-1024 Budapest, Hungary,
E-mail: nemeth.p@met.hu

**Corresponding author*

(Manuscript received in final form April 8, 2014)

Abstract – This study describes a weather-radar-based investigation of long-lived thunderstorms in Hungary in the period of 2004–2012. An objective method was developed for identifying and tracking convective cells. The cells were represented by so-called thunderstorm ellipses. In this research, intensive objects were classified into 3 categories such as severe, highly severe, and extremely severe thunderstorm ellipses. The categories were defined by radar reflectivity thresholds 45 dBZ, 50 dBZ, and 55 dBZ. Only those cells were involved in the investigation whose lifetime extended more than 1 hour. In the 9-year period, 2625 severe, 597 highly severe, and 45 extremely severe long-lived thunderstorm ellipses were found. Stronger cells moved faster and at most intensive cells, right-turning movement was more frequent. Many of these long-lived, strong objects could be supercells. The applied methods and results can be used for severe weather forecast and nowcasting in the Carpathian Basin.

Key-words: severe thunderstorm, weather radar, climatology, tracking, supercell, Hungary

1. Introduction and background

Severe thunderstorms and associated phenomena (stormy wind gusts, hailstorms, heavy rainfalls, tornadoes, intensive lightning) often occur in Hungary, mainly in late spring and summer (*Horváth* and *Geresdi,* 2003). These convective storms cause major damages mainly in the electric and transportation networks by wind gusts, in the agriculture by hail storms, and in other branches of the infrastructure by torrential rain and flash floods. A thunderstorm, developed into supercell phase, caused fatal accidents during the Constitution Day firework in Budapest in 2006 (*Horváth et al., 2007*). These events motivate the investigation to overview severe convective cells using 9-year period of observations by radar network of the Hungarian Meteorological Service. In practice, radar reflectivity data are available in that period, what explains why reflectivity based identification and tracking methods were applied for recognizing and tracking intensive thunderstorms.

Radar-based tracking of thunderstorms have been investigated in the United States since the beginning of the 1950's. *Battan* (1952) found that the storm-tops of "longer-lived" (> 20 min) cells were higher than the shorter-lived (≈10 min) ones. *Browning* (1964) defined *the supercell* term for the most organized, most severe, and longest-lived form of isolated, deep moist convection. In 1966, *Wilson* analyzed the relation of thunderstorm size and intensity (*Wilson,* 1966). In the 1970s, the development of remote sensing technique and the surface observations allowed to update the definitions of supercells (*Wilhelmson* and *Klemp*, 1978; *Lemon* and *Doswell*, 1979). Presently, the most accepted theory about supercell thunderstorms was made by *Klemp* (1987). *Henry* (1993) and *MacKeen et al.* (1999) analyzed the relationship between reflectivity–derived storm characteristics and storm longevity. In the last two decades, some radar-based algorithms were developed for tracking thunderstorms *(Lakshmanan* and *Smith*, 2010). The TITAN technique (thunderstorm identification, tracking, analysis and nowcasting) was developed by *Dixon* and *Wiener* (1993), while *Morel et al.* (1997) used a procedure of the extent of overlaps. *Johnson et al.* (1998) applied projected centroid locations and *Han et al.* (2009) combined TITAN and overlap methods.

In Hungary, first investigations of severe convection from dynamical aspects were made in the 1960s (*Bodolainé et al.*, 1967; *Götz*, 1968). Later, remote sensing data appeared in the Hungarian studies (*Horváth* and *Práger*, 1985; *Boncz et al.*, 1987). Supercell thunderstorms and formation of tornadoes were described by *Horváth* (1997). Since the 2000s, nowcasting methods (*Horváth* and *Geresdi,* 2003; *Horváth et al.,* 2007; *Csirmaz et al.*, 2013) and radar-based thunderstorm climatology (*Horváth et al.,* 2008) have appeared as well.

The aim of this study is to survey incidence and behavior of severe thunderstorms in Hungary using radar observations in the period of 2004–2012 applying radar-reflectivity based recognition and tracking methods.

2. Methodology

Hungary is covered by three weather radars operated by the Hungarian Meteorological Service. These locators work in the western part (near the western end of Lake Balaton on the hill Pogányvár), in the central region (in the southeastern district of Budapest) and in the eastern part (in Nyíregyháza-Napkor) of the country; this system covers most part of the Carpathian Basin. All of them are C-band Doppler radars (wave length=5 cm) (*Geresdi*, 2004) and have been working in operative mode since 2004. During the operative measurement, the Doppler-wind was applied for noise filtering and the results were filtered and smoothed into composite fields. From each scan the highest reflectivity data of the relevant vertical column were chosen and placed into the composite image (*Collier,* 1996). The resolution of the composite PPI (plan position indicator) images was originally 2×2 km in space and 15 minutes in time.

The first step was making a more accurate cell tracking method: the original radar image frequency had to be increased from 15 minutes to 1 minute. The TREC method (tracking radar echoes by correlation) *(Tuttle* and *Foote,* 1990; *Horváth et al.,* 2012) was applied to do the time interpolation. During TREC procedure, correlations were searching between two consecutive radar images, and motion vectors were calculated which describe displacement of radar echoes. The computed motion vector field was used for calculating series of "artificial" radar images with 1 minute frequency. A brief description of TREC is given in *Appendix A.* For further noise reducing of reflectivity, median-filter method (*Tukey*, 1977) was also applied before beginning the analysis.

The second step was the thunderstorm identification using calculated 1 minute frequency radar reflectivity images. TITAN method developed by *Dixon* and *Wiener* (1993) represents irregular shaped thunderstorms by regular, best fitting ellipses. Parameters of an ellipse can be objectively used to describe the place (by coordinates of ellipses center), the size (by area of ellipses), and even the shape (minor and major axes) of a thunderstorm. The mathematical background of TITAN is given in *Appendix B.* Ellipses calculation of TITAN method expects two types of thresholds as input data: reflectivity limit (R_{min}) and area limit (N_{min}). R_{min} shows the minimum reflectivity of radar pixels that are involved into ellipse calculation. N_{min} shows the minimum number of pixels whose reflectivity values have to be equal or larger than R_{min}, and the strong echoes must form a continuous area. For example: R_{min}= 45 dBZ and N_{min}=5 mean that the procedure orders ellipses to such thunderstorm cells which have at

least 5 pixels with higher than 45 dBZ reflectivity. These calculated ellipses were named *thunderstorm ellipses* (*Horváth et al.*, 2008). An example of cell detecting is shown on *Fig. 1,* where R_{min} is set to 45 dBZ and N_{min}=5 pixels. The results can be visualized by the Hungarian Advanced Workstation (HAWK) system (*HMS*, 2012). Note, that the applied radar resolution is 2 km in space, thus N_{min}=5 means that the size of a thunderstorm ellipse has to be equal or greater than 20 km^2. In the present study, N_{min} was assumed to 5 radar pixels, and 3 different radar reflectivity thresholds were applied: 45, 50, and 55 dBZ. These objects were named *severe*, *highly severe*, and *extremely severe thunderstorm ellipses*, respectively. Using these high reflectivity values, the detected cells could be considered as models of severe thunderstorms and the small or weak convective cells were eliminated.

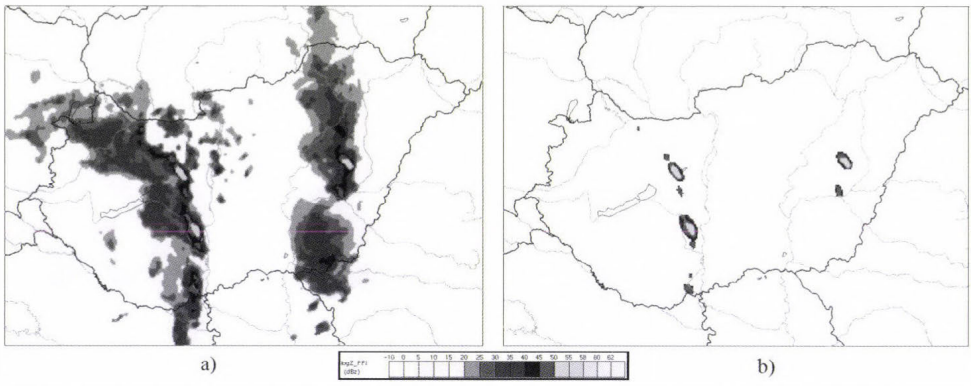

Fig. 1. Composite PPI radar images of thunderstorms observed on May 18, 2005, 16:00 UTC: a) original image b) image in which thunderstorms were represented by ellipses. For the visualization, the Hungarian Advanced Workstation (HAWK) system of the Hungarian Meteorological Service was used.

The third step was the cell tracking. For tracking thunderstorm ellipses, a special matching algorithm was applied where position of centrals and area of ellipses were considered to recognize the same cell in the next time step. The algorithm scanned the surrounding area of each ellipsis, and if one or more objects were found on the next image it chose the closest by distance and size. Also distance and size were used to recognize merging, splitting of thunderstorm ellipses. The 1 minute time steps made this procedure fairly reliable: verification on a 50-cell sample showed 98%, comparing with manually tracking. With these methods all information, i. e., size, lifetime, reflectivity, and the track of ellipses were followed and calculated from forming to dissipating and their tracks could be visualized.

The movement of severe thunderstorms, especially supercells, often shows deviation from the straight line, right or left turning of cells are important indicators of supercells (*Lemon* and *Doswell*, 1979). To describe these phenomena, the total deviation angle was introduced. This parameter was calculated in the following way: the displacement of a thunderstorm ellipse in the first 15 minutes designates a direction. Considering the direction coming from the next 15-minute interval, a deviation angle can be calculated. Summing up these angles during the lifetime of the thunderstorm ellipse, the total deviation angle was obtained *(Fig. 2.)*.

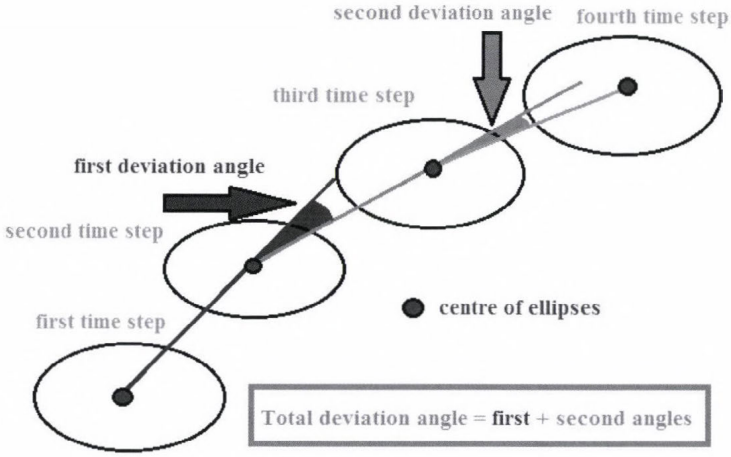

Fig. 2. Calculation method of the total deviation angle.

The present study focused on long-lived severe thunderstorms, so the investigation was applied only for severe, highly severe, and extremely severe thunderstorm ellipses with a lifetime more than 1 hour.

3. Results

In the 9-year period, 2625 severe, 597 highly severe, and 45 extremely severe long-lived ellipses were found. *Fig. 3* shows the distribution of lifetime for each type. The maximum of lifetime resolution was around 60 minutes which was followed by rather rapid than moderate decrease in number, and only few severe or highly severe cells lived more than 270 minutes. The average values were 100 minutes for severe, 95 minutes for highly severe, and 86 minutes for extremely severe ellipses.

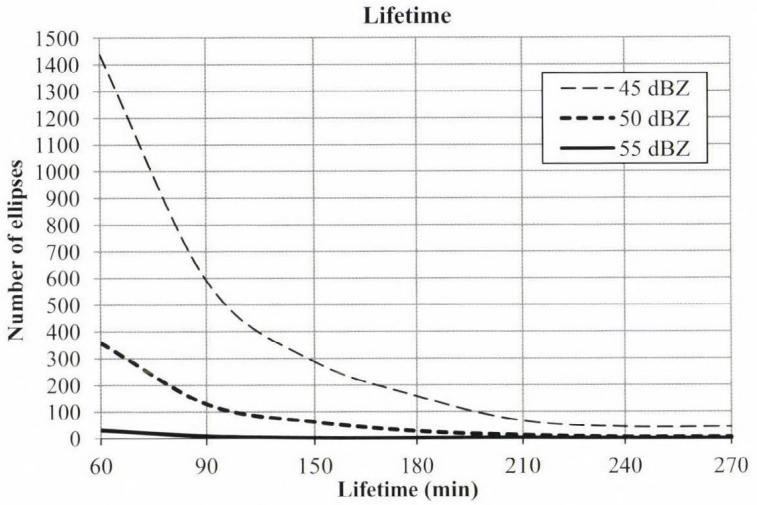

Fig. 3. Lifetime characteristics of long-lived severe (45 dBZ), highly severe (50 dBZ), and extremely severe (55 dBZ) ellipses.

The lengths of storm tracks had asymmetric distribution drawing an analogy to log-normal (*Fig. 4*). Most of investigated thunderstorms moved distance between 40 and 80 km during their lifetime and the average distance was about 70 km. There were some cells with extreme long lifetime. For example, on July 14, 2008 a strong cell crossed the whole domain (about 600 km) moving from southwest to northeast.

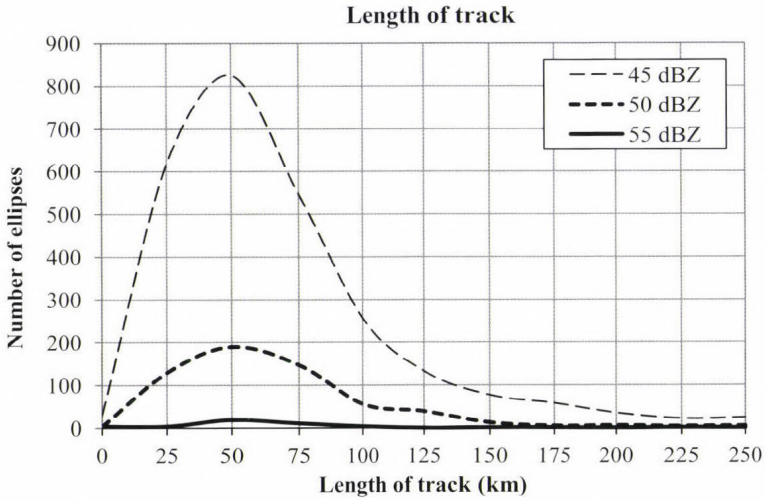

Fig. 4. Distribution of storm tracks' length for long-lived severe (45 dBZ), highly severe (50 dBZ), and extremely severe (55 dBZ) ellipses.

The total deviation angle was also investigated. The distribution of total deviation angles was mostly symmetric, especially for ellipses with 45 or 50 dBZ. The ratios between right and left directions were about 50–50% for severe, and 51–49% for highly severe thunderstorm ellipses. At extremely severe thunderstorms this rate was 58–42%, so for most intensive objects, right-turning movement occurred somewhat more often (*Fig. 5*). Considering all investigated thunderstorms, 23% have deviation angle larger than 40° and 13% have larger than 60 degrees.

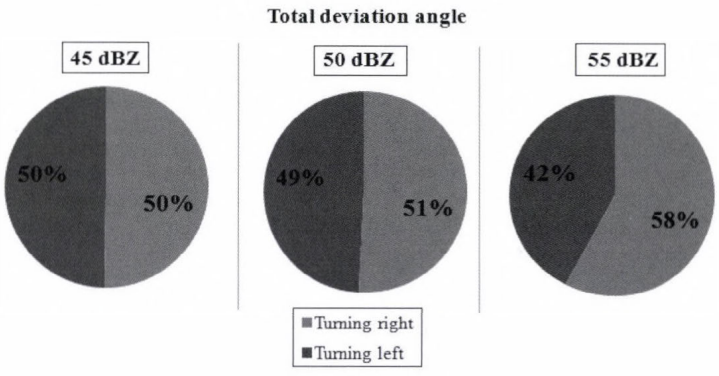

Fig. 5. Ratios between positive and negative deviation angles for severe (45 dBZ), highly severe (50 dBZ), and extremely severe (55 dBZ) ellipses.

Knowing lengths of tracks and lifetimes of thunderstorm-ellipses, their average speed could be calculated as well. The distributions of speed were asymmetric: the maximum was around 35–45 km/h (*Fig. 6*). Stronger cells moved faster. For severe thunderstorm ellipses the average speed was 42 km/h, for highly severe objects it was 45 km/h, and for extremely severe ellipses 49 km/h were calculated. Only few (8) severe objects' speed was higher than 100 km/h.

Numbers of severe thunderstorms had wide variability during 9 years. The highest values were in 2010 (with 611 severe, 146 highly severe, and 14 extremely severe ellipses). The lowest numbers were detected in 2005 (with only 95 severe, 13 highly severe, and 0 extremely severe objects).

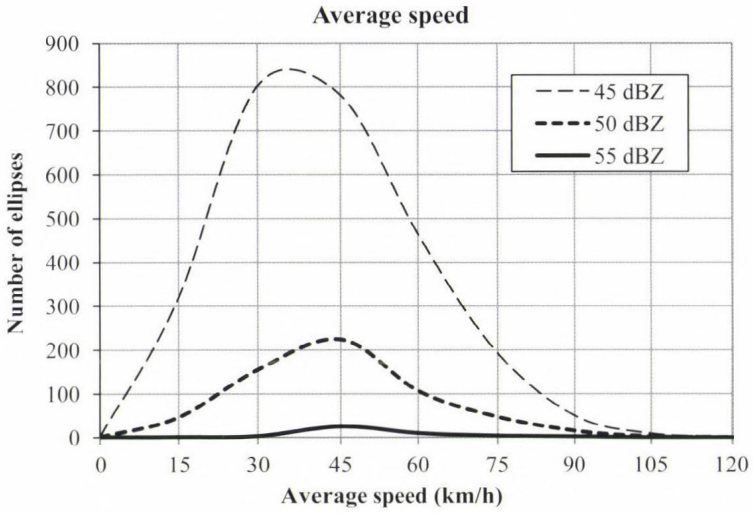

Fig. 6. Distribution of average speed for severe (45 dBZ), highly severe (50 dBZ), and extremely severe (55 dBZ) ellipses.

4. Conclusions

This study described a radar-based climatology of long-lived thunderstorms in Hungary focusing on cell motion and tracking in the period of 2004–2012. In our research, intensive thunderstorms were represented with ellipses calculated by the TITAN identification method. During the investigation, severe, highly severe and extremely severe thunderstorm ellipses were distinguished using thresholds of 45 dBZ, 50 dBZ, and 55 dBZ. The investigation was restricted only to thunderstorm ellipses with lifetime exceeded 1 hour.

In the 9-year period, 2625 severe, 597 highly severe, and 45 extremely severe long-lived ellipses were found. The time resolution of thunderstorms during this 9-year period was rather changeable showing the role of larger, synoptic-scale phenomena that determinate condition of the convection. The average values of lifetime were 100 minutes for severe, 95 minutes for highly severe, and 86 minutes for extremely severe ellipses. These values are promising from nowcasting point of view, because cell tracking is a relative easy technique, and persistent cells can be forecasted by extrapolation more than an hour ahead. Lengths of tracks were mostly between 40 and 80 km. Supposing that these storms are able to cause hail and wind damages, there is a high probability that populated places, sensitive infrastructure, or industrial areas were hit by the investigated storms. Stronger cells moved faster, the average speeds were 42 km/h for severe, 45 km/h for highly severe, and 49 km/h for

extremely severe objects. At most intensive cells, right-turning movements were more frequent. At 23% of thunderstorms, significant deviations from the straight line (>40°) were found. These deviations suggest existence of supercells. Considering the 23% of 2625 detected thunderstorms in 9 years, *the estimated number of supercells in a year is 67.*

These results are parts of the work dealing with severe storm climatology. Further researches are needed involving surface observations to obtain wind, pressure, and precipitation fields associated with thunderstorms, and more NWP case studies should be used for understanding the mechanism of severe convective storms in the Carpathian Basin.

Acknowledgement: This study is related to COST-0905 project.

References

Battan, L.J., 1952: Formation of precipitation in natural clouds indicated by radar. Preprints, Third Conference on Radar Meteorology, Montreal, PQ, Canada, Amer. Meteor. Soc., A9–A16.

Bodolainé, J.E., Bodolai, I. and *Böjti, B.,* 1967: Macrosynoptical conditions for the formation of Slovenenian squall lines and some properties of cold fronts with thunderstorm. *Időjárás 67,* 129–143.

Boncz, J., Kapovits, A., Pintér, F. and *Tänczer, T.*, 1987: A method for the complex analysis of synoptic weather radar and satellite data. *Időjárás 91*, 11–22.

Browning, K. A., 1964: Airflow and precipitation trajectories within severe local storms which travel to the right of the winds. *J. Atmos. Sci. 21*, 634–639.

Collier, C.G., 1996: Application of weather radar system: A Guide to uses of radar in meteorology and hydrology. John Wiley & Sons.

Csirmaz, K., Simon, A., Pistotnik, G., Polyánszky, Z., Neštiak, M., Nagykovácsi, Zs. and *Sokol, A.,* 2013: A study of rotation in thunderstorms in a weakly- or moderately-sheared environment. *Atmos. Res. 123,* 93–116.

Dixon, M., and *Wiener, G.,* 1993: TITAN: Thunderstorm Identification, Tracking, Analysis and Nowcasting—A radar-based methodology. *J. Atmos. Oceanic Technol. 10*, 785–797.

Doviak, R.J. and *Zrinic, D.S.*, 1993: Doppler Radar and Weather Observations. Academic Press, 335–340.

Geresdi, I., 2004: Felhőfizika. Dialóg Campus, Budapest, 153–170. (in Hungarian)

Götz, G., 1968: Hydrodynamic relationships between heavy convection and the jet stream. *Időjárás 72*, 157–165.

Han, L., S. *Fu,* L. *Zhao,* Y. *Zheng,* H. *Wang,* and *Lin, Y.*, 2009: 3D convective storm identification, tracking and forecasting–An enhanced TITAN algorithm. *J. Atmos. Oceanic Technol. 26*, 719–732.

Henry, S.G., 1993: Analysis of thunderstorm lifetime as a function of size and intensity. Preprints, 26th Conf. on Radar Meteorology, Norman, OK, Amer. Meteor. Soc., 138–140.

Horváth, Á.,1997: Tornado. *Légkör 62,* 2–9. (in Hungarian)

Horváth, Á. and *Práger, T.*, 1985: Zivatarláncok dinamikája és előrejelezhetőségét. *Időjárás 89*, 141–160. (in Hungarian)

Horváth, Á. and *Geresdi, I.,* 2003: Severe storms and nowcasting in the Carpathian Basin. *Atmos. Res. 67–68,* 319–332.

Horváth, Á., Ács, F. and *Seres, A. T.,* 2008: Thunderstorm climatology analyses in Hungary using radar observations. *Időjárás 112,* 1–13.

Horváth, Á., Seres, A.T. and *Németh, P.*, 2012: Convective systems and periods with large precipitation in Hungary. *Időjárás 116*, 77–91.

Horváth, Á., Geresdi, I., Németh, P. and *Dombai, F.*, 2007: The Constitution Day storm in Budapest: Case study of the August 20, 2006 severe storm. *Időjárás 111*, 41–65.

HMS, Hungarian Meteorological Service, 2012: HAWK-3 visualization system. http://www.met.hu/en/omsz/tevekenysegek/hawk/

Johnson, J., P. *MacKeen*, A. *Witt*, E. *Mitchell*, G. *Stumpf*, M. *Eilts*, and *Thomas, K.*, 1998: The Storm Cell Identification and Tracking algorithm: An enhanced WSR-88D algorithm. *Weather Forecast 13*, 263–276.

Klemp, J.B., 1987: Dynamics of tornadic thunderstorms. *Ann. Rev. Fluid Mech. 19*, 369–402.

Lakshmanan, V. and *Smith, T.*, 2010: An Objective Method of Evaluating and Devising Storm-Tracking Algorithms. *Weather Forecast. 25*, 701–709.

Lemon, L. R. and *Doswell III, C. A.*, 1979: Severe thunderstorm evolution and mesocyclone structure as related to tornadogenesis. *Mon. Weather Rev. 107*, 1184–1197.

MacKeen, P.L., Brooks, H.E. and *Elmore, K.L.*, 1999: Radar Reflectivity–Derived Thunderstorm Parameters Applied to Storm Longevity Forecasting. *Weather Forecast. 14*, 289–295

Morel, C., *Orain, F.*, and *Senesi, S.*, 1997: Automated detection and characterization of MCS using the Meteosat infrared channel. Proc. Meteorological Satellite Data Users Conf., Brussels, Belgium, EUMETSAT, 213–220.

Tukey, J.W., 1977: Exploratory Data Analysis. Addison-Wesley, Reading, 688. pp.

Tuttle, J.D. and *Foote, B.*, 1990: Determination of the Boundary Layer Airflow from Single Doppler Radar. *J.Atmos. Ocean. Tech. 7*, 218–232.

Wilhelmson, R.B. and *Klemp J.B.*, 1978: A numericalsStudy of storm splitting that leads to long-lived storms. *J. Atmos. Sci. 35*, 1974–1986.

Wilson, J.W., 1966: Movement and predictability of radar echoes. Tech. Memo IERTM-NSSL-28, National Severe Storms Laboratory.

Appendix A

Calculation of motion vectors using time series of radar reflectivity

(*Tuttle* and *Foote*, 1990; *Horváth et al.*, 2012)

In the period of 2004–2012, the Hungarian radar network collected data in 15-minute cycles. For a more accurate cell tracking procedure, the original radar image frequency had to be increased using the correlation tracking method TREC (tracking radar echoes by correlation; *Tuttle* and *Foote*, 1990). During the TREC procedure, the radar grid was divided into so-called macro grids, and the calculation of motion vectors was based on maximum correlations for the macro grids. After quality control to filter out noisy vectors on macro grids, fine resolution motion vectors were interpolated for all grid points of the original radar grid. Once a motion vector field – belonging to radar images at time T2 and T1 – is available, interpolation of the radar reflectivity can be done at any time between T1 and T2. Echoes from T1 are moved forward and echoes from T2 moved backward by motion vectors, and the reflectivity of a given pixel is interpolated between the forward and backward moving reflectivity values as shown in *Fig. 7.*

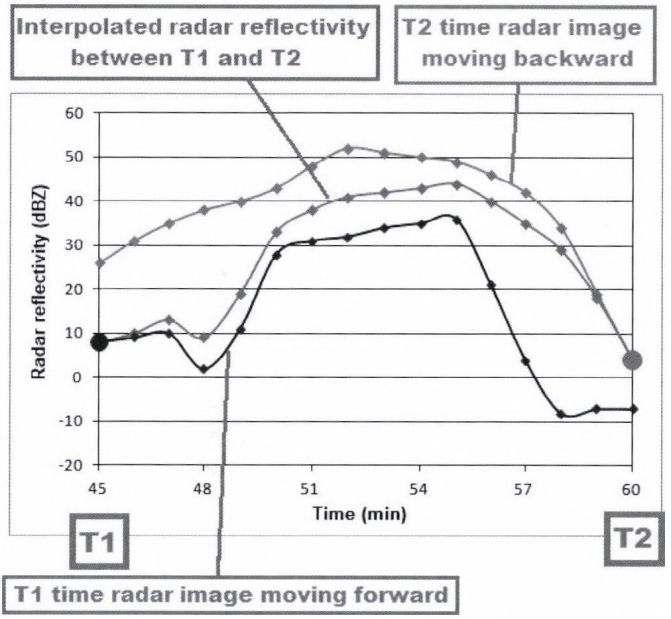

Fig. 7. Interpolation of radar reflectivity using motion vectors.

The application of the TREC method offers a more realistic and accurate cell tracking procedure. The optimal interpolation time step for calculation was found to be 1 minute.

Appendix B

Mathematical background of the identification

(*Dixon* and *Wiener*, 1993)

Suppose there is an irregular cluster on a radar image which has n detected pixels. The center of a cluster is defined by

$$\bar{x} = \frac{1}{n}\sum_{i=1}^{n} x_i , \qquad \bar{y} = \frac{1}{n}\sum_{i=1}^{n} y_i , \tag{1}$$

where x and y indicate the longitude and latitude of pixels which have reflectivity higher than a given threshold value. The covariance matrix of this cluster is

$$A = \mathrm{cov}_{xy} = \begin{bmatrix} d & e \\ e & f \end{bmatrix}, \tag{2}$$

where d is the deviation from the center by the x coordinate

$$d = \frac{1}{n-1}\sum_{i=1}^{n}(x_i - \bar{x})^2, \tag{3}$$

f is the deviation from the center by the y coordinate

$$f = \frac{1}{n-1}\sum_{i=1}^{n}(y_i - \bar{y})^2, \tag{4}$$

and e is

$$e = \frac{1}{n-1}\sum_{i=1}^{n}(x_i - \bar{x})(y_i - \bar{y}). \tag{5}$$

The eigenvalues of the covariance matrix are given by

$$\lambda_1, \lambda_2 = \frac{(d+f) \pm \left[(d+f)^2 - 4(df - e^2)\right]^{1/2}}{2}. \tag{6}$$

The normalized eigenvectors of this matrix are

$$v = \left[\frac{1}{(1+g)^2}\right]^{1/2} \qquad \mu = -gv, \tag{7}$$

where

$$g = \frac{f + e - \lambda_1}{d + e - \lambda_2}. \tag{8}$$

Then the rotation of the ellipse major axis relative to the x axis is given by these vectors

$$\theta = \tan^{-1}\left(\frac{\nu}{\mu}\right). \tag{9}$$

The eigenvalues of the covariance matrix (λ_1 and λ_2) represent the variances of the data (pixels)

$$\sigma_{major} = \lambda_1^{1/2}, \qquad \sigma_{\min or} = \lambda_2^{1/2}. \tag{10}$$

The area of the detected cluster is

$$A = ndxdy \tag{11}$$

where dx and dy are the grid spacing on the radar image. The area of an ellipse is given by

$$T = \pi ab, \tag{12}$$

where a and b represents the major and minor axes of the ellipses.
The main idea is that the area of the irregular cluster and the area of the ellipse have to be equal, therefore

$$A = T. \tag{13}$$

So the major and minor axes of the ellipses can be calculated by

$$a = \sigma_{major}\left(\frac{A}{\pi\sigma_{\min or}\sigma_{major}}\right)^{1/2}, \quad b = \sigma_{\min or}\left(\frac{A}{\pi\sigma_{\min or}\sigma_{major}}\right)^{1/2}. \tag{14}$$

With these parameters ($\bar{x}, \bar{y}$, a, b, θ), the focus points and the equation of the ellipse can be determined.

IDŐJÁRÁS

Quarterly Journal of the Hungarian Meteorological Service
Vol. 119, No. 1, January – March, 2015, pp. 53–68

Estimating spectra of unevenly spaced climatological time series

István Matyasovszky

Department of Meteorology, Eötvös Loránd University,
Pázmány Péter sétány 1/A, H-1117 Budapest, Hungary,
E-mail: matya@caesar.elte.hu

(Manuscript received in final form May 3, 2014)

Abstract—Spectral analysis is often based on a comparison of the periodogram and the spectral density of a so-called background noise. This spectral density is estimated by fitting a first order autoregressive (AR(1)) process to data, as climatological time series generally exhibit red noise spectra that can be approximated by AR(1) models. When periodogram exceeds some threshold at a frequency, the spectrum is said to differ from this background noise, and the frequency is characteristic for the time series in question. The traditional periodogram, however, must not be used without modifications for unevenly spaced data. Additionally, red noise, characterized by spectral densities monotone increasing to low frequencies, covers a much wider class of processes than the AR(1) processes. Our purpose is (1) to introduce a new periodogram (ELSP) based on a least square (LS) fit for an entire set of frequencies instead of using the well-known Lomb-Scargle periodogram (LSP) based on individual LS fits for individual frequencies; (2) to estimate the spectral density without any assumption on its analytical form using the nearly isotonic regression (NIR) method with either ELSP or LSP. As NIR allows the possibility of deviations from red noise, comparison of the periodogram with a background noise is unnecessary. Note that ELSP has never been used before as is a new concept for defining the periodogram for unevenly spaced data. NIR is more or less known for curve fitting problems but has not been applied yet to spectral density estimation. Three examples show that although ELSP does not radically differ from LSP, NIR-ELSP and NIR-LS spectra can exhibit distinct shapes.

Key-words: spectra, unevenly spaced data, Lomb-Scargle periodogram, red noise, nearly isotonic regression

1. Introduction

Literature of spectral analysis of climatological time series is extremely broad. The task of the spectral analysis is to identify sets of frequencies that essentially contribute to the behavior of time series. A common way is to calculate the

periodogram and then to fit a first order autoregressive (AR(1)) process to data in order to model the so-called background noise. When periodogram exceeds some threshold at a frequency, the spectrum is said to differ from this background noise, and the frequency is characteristic for the time series in question. The threshold depends on the AR(1) model and the significance level selected.

Let $x(t_1),...,x(t_n)$ be a stationary time series observed at $t_1,...,t_n$. Usually, the data set is evenly spaced, and $t_i = i$ can be taken. Hence, the time series can be written as $x_1,...,x_n$. The background noise is taken as red noise, and is generally described with the spectral density

$$f(\lambda) = (\sigma_e^2 / \pi)/(1 + a^2 - 2a\cos(\lambda)), \sigma_e^2 = \sigma^2(1 - a^2) \qquad (1)$$

of an AR(1) process with substituting the autoregressive parameter a and variance σ^2 with their consistent estimates $\hat{a}$ and $\hat{\sigma}^2$ obtained from $x_1,...,x_n$. As Eq. (1) provides red noise spectra under positive a, red noise and AR(1) spectra are seldom used as synonyms. But red noise, characterized by spectral densities monotone increasing to low frequencies, represents a much wider class of processes than the AR(1) processes, and the usage of AR(1) spectra can thus fail to properly detect frequencies mainly contributing to spectra. Therefore, we propose a method that ignores the comparison of periodograms with background noise models.

In some cases, time series are unevenly spaced, and hence the periodogram defined for evenly spaced data must not be used without modifications. There are two main ways to handle the problem. The first one is based on an interpolation of the data onto an equispaced time grid, and this new regularly spaced data set is analyzed with traditional techniques. Such data manipulations, however, always deform the true spectra (*Broersen*, 2006). The other way, which is addressed in this paper, produces a reformulated periodogram directly from data. Evidently, such a periodogram is always affected by temporal distributions of data spacing. Generally, the Lomb-Scargle periodogram (LSP) (*Lomb*, 1976; *Scargle*, 1982), based on a simple least squares (LS) estimation procedure, is used for the purpose. However, important statistical properties of LSP, e.g., its probability distribution are known only for white background noise. Additionally, the bias of LSP for unevenly spaced data can be substantially higher than that of the periodogram for evenly spaced data (*Vio et al.*, 2010), principally at high frequencies (*Schulz* and *Mudelsee*, 2002). Therefore, we will examine first the properties of LSP. Then we will propose a periodogram that is based on a so-called entire least squares (ELS) technique (*Matyasovszky,* 2013a). Properties of this newly introduced periodogram will also be discussed.

The methodology is described in Sections from 2 to 4. As paleoclimatological records represent a typical case of unevenly spacing, our technique is demonstrated by three paleoclimatic records in Section 5. Finally, a section for discussion and conclusions is provided.

2. Periodograms

2.1. Lomb-Scargle periodogram (LSP)

Let $x(t_1), x(t_2), ..., x(t_n)$ with $t_1 = 1, t_n = N$ be a time series coming from a stationary stochastic process with mean zero. The LSP for any frequency λ_j in the interval $(0, \pi]$ is based on an LS procedure as follows. Parameters a_j and b_j that minimize

$$\sum_{i=1}^{n} (x(t_i) - a_j \cos(\lambda_j t_i) - b_j \sin(\lambda_j t_i))^2$$

are obtained with the solution of the system of equations

$$\underline{\underline{D}}\,\underline{c} = \underline{w}, \tag{2}$$

where $\underline{\underline{D}} = \underline{\underline{Z}}^T \underline{\underline{Z}}$, and the elements of $\underline{\underline{Z}}$ are $z_{i1} = \cos(\lambda_j t_i)$, $z_{i2} = \sin(\lambda_j t_i)$, $i = 1, ..., n$, furthermore $\underline{w} = \underline{\underline{Z}}^T \underline{x}$, and $\underline{x} = (x(t_1), ..., x(t_n))^T$, $\underline{c} = (a_j, b_j)^T$ with superscript T denoting transpose. The quadratic form

$$I_{LS}(\lambda_j) = 1/(2\pi)\,\underline{c}^T \underline{\underline{D}}\,\underline{c} \tag{3}$$

defines LSP. For evenly spaced data, Eq. (3) becomes to the well-known expression

$$I(\lambda_j) = n/(4\pi)(a_j^2 + b_j^2) \tag{4}$$

with

$$a_j = 2/n \cdot \sum_{i=1}^{n} x_i \cos(\lambda_j i), \quad b_j = 2/n \cdot \sum_{i=1}^{n} x_i \sin(\lambda_j i).$$

It is known from the LS procedure that $\underline{c}$ is asymptotically normally distributed under very general conditions. Supposing that $\underline{x}$ comes from a white

noise process, the covariance matrix of $\underline{c}$ is $\sigma^2 \underline{\underline{D}}^{-1}$, where σ^2 is the variance of the process. Hence, the random variable $I_{LS}(\lambda_j)$ defined with the quadratic form in Eq. (3) follows an exponential distribution (*Scargle*, 1982). The probability distribution of LSP when $\underline{x}$ does not come from a white noise process is, however, an open question. Therefore, we will discuss this issue together with the expected value of $I_{LS}(\lambda_j)$ in Section 4. Although λ_j can be any of frequencies in an interval $[\lambda_{\min}, \lambda_{\max}]$, it is advisable to define a grid $2\pi j/(n\Delta), j = 1,..., L$, where L is the largest integer not larger than $n/2$, $\lambda_{\max} = \pi/\Delta$ is the average Nyquist frequency (*Stoica et al.*, 2009), and Δ is the average of time steps $\delta_i = t_i - t_{i-1}, i = 2,..., n$. As the frequency range of $I(\lambda)$ is $(0, \pi]$, the range $[\lambda_{\min}, \lambda_{\max}]$ of $I_{LS}(\lambda)$ is generally rescaled into $[2\pi/n, \pi]$ for convenience. $I_{LS}(\lambda)$ can thus be viewed as $I(\lambda)$ of a time series sampled evenly at time steps Δ. An important difference is, however, that elements of $I_{LS}(\lambda_j)$ are correlated in contrast to elements of $I(\lambda_j)$. Additionally, the bias of $I_{LS}(\lambda_j)$ can be higher than the bias of $I(\lambda_j)$ (*Vio et al.*, 2010). This is due to the interrelationship between unevenly spacing and the effect of the omission of frequencies different from λ_j when calculating $I_{LS}(\lambda)$ at λ_j. Furthermore, it is known that $I(\lambda)$ integrates to the sample variance $\hat{\sigma}^2$ in the sense that

$$\frac{2\pi}{n}\sum_{j=1}^{L} I(\lambda_j) = \hat{\sigma}^2 = \frac{1}{n}\sum_{i=1}^{n}(x(t_i) - \bar{x})^2,$$

while $I_{LS}(\lambda)$ does not integrate to $\hat{\sigma}^2$.

2.2. Entire least squares periodogram (ELSP)

The deficiency of LSP is that it handles the different frequencies separately. Therefore, we propose an entire least squares (ELS) procedure by calculating the constants a_j, b_j at frequencies $2\pi j/(n\Delta), j = 1,..., L$ simultaneously. This results in a system of equations Eq. (2), but with

$$z_{ij} = \begin{Bmatrix} \cos(\lambda_j t_i), j = 1,..., L \\ \sin(\lambda_j t_i), j = L+1,..., 2L \end{Bmatrix}, \quad i = 1,..., n, \quad \underline{c} = (a_1,..., a_L, b_1,..., b_L)^T.$$

It is easy to see that $\underline{c}^T \underline{\underline{D}}\underline{c} = n\hat{\sigma}^2$. As $\underline{\underline{D}}\underline{c} = \underline{w}$, hence $\underline{c}^T \underline{w} = c_1 w_1 + ... + c_{2L} w_{2L} = n\hat{\sigma}^2$. Therefore, we define ELS periodogram (ELSP) as the contribution of frequencies to the sample variance, i.e.,

$$I_{ELS}(\lambda_j) = 1/(2\pi)(c_j w_j + c_{j+L} w_{j+L}). \quad (5)$$

Although every frequency λ_j is affected by frequencies not involved in the estimation procedure, the accuracy of ELSP is expected to be higher than the accuracy of LSP. This is because ELSP is defined for the entire set of frequencies $\lambda_j, j = 1,...,L$ and not for particular frequencies separately. Properties of ELSP will be discussed in Section 4.

3. Estimating spectra

A stationary stochastic process exhibits red noise spectrum when its spectral density function satisfies $f(\lambda) \geq f(\omega), \lambda < \omega$ for every $\lambda, \omega \in (0, \pi]$. Estimation of a spectral density corresponding to this definition is now based on an LS technique. The solution of the LS problem

$$\min\left\{\sum_{j=1}^{L}\left(I_*(\lambda_j) - \hat{f}(\lambda_j)\right)^2\right\}, \quad \hat{f}(\lambda_j) \geq \hat{f}(\lambda_k),\ j < k$$

can be obtained using a procedure called isotonic regression (IR). Namely,

$$\hat{f}(\lambda_j) = \min_{i \leq j} \max_{j \leq k} \frac{I_*(\lambda_i) + ... + I_*(\lambda_k)}{k - i + 1}$$

for $j = 1,...,L$, and $\hat{f}(\lambda)$ is left-continuous otherwise (*Zhao* and *Woodroofe*, 2012), where I_* can be either I, I_{LS}, or I_{ELS}. Note that $\hat{f}(\lambda)$ is monotone decreasing and is stepwise constant over certain frequency ranges.

Behavior of periodogram elements at frequencies close to possibly existing discrete frequencies (frequencies contributing to discrete spectra) substantially differs from the behavior of the majority of periodogram elements. Thus, periodogram elements at these frequencies should be taken as outliers, and an IR, robust against outliers has to be found. *Álvarez* and *Yohai* (2011) proposed a robust IR technique that can thus be used as a method to estimate the spectral density of the red background noise without any assumption on its analytical form. A possibility to find essential frequencies is to detect significant deviations of the periodogram from this background noise utilizing the statistical properties of robust IR (*Matyasovszky*, 2013b). Another way is to give up the background noise concept and estimate the spectral density non-robustly and without monotonicity constraint. The nearly-isotonic regression (NIR) introduced by *Tibshirani et al.* (2011) permits the possibility of deviations from

monotonicity when necessary. The necessity of monotonicity violations is controlled via a parameter β that is estimated within the procedure. The task is to find $\hat{f}(\lambda_1),...,\hat{f}(\lambda_L)$ minimizing the quantity

$$\left\{\sum_{j=1}^{L}\left(I_*(\lambda_j)-\hat{f}(\lambda_j)\right)^2+\beta\sum_{j=1}^{L-1}\left(\hat{f}(\lambda_j)-\hat{f}(\lambda_{j+1})\right)_+\right\},$$

where $(u)_+ = -u$ when u is negative, and zero otherwise. When $\beta = 0$, the solution is $\hat{f}(\lambda_j) = I_*(\lambda_j)$, and letting $\beta \to \infty$, we obtain the isotonic regression. The optimal value of β, which can be estimated (*Tibshirani et al.,* 2011), gives a trade off between monotonicity and goodness-of-fit. The resulting $\hat{f}(\lambda)$ can thus correspond to red noise or colored noise with certain local peaks according to the shape of $f(\lambda)$.

4. Properties of periodograms

4.1. Lomb-Scargle periodogram (LSP)

Now we examine the probability distribution and the expected value of LSP. For this reason, take first a two-dimensional normal random vector $\underline{\xi}$ with expected value zero and covariance matrix $\underline{\underline{P}}$. Let $\underline{\underline{Q}}$ be a positive definite matrix of size (2x2), and take the random variable $q = \underline{\xi}^T \underline{\underline{Q}} \underline{\xi}$. This quadratic form can be rewritten as a linear combination of two independent chi-squared random variables with one degree of freedom, and the coefficients in this linear combination are the eigenvalues of $\underline{\underline{QP}}$. If these coefficients are identical, q is distributed exponentially, but when difference between the coefficients is not too large, the probability distribution is also closely exponential (*Yuan* and *Bentler,* 2010).

It is known from the LS theory that covariance matrix of $\underline{c}$ is $\underline{\underline{D}}^{-1}\underline{\underline{Z}}^T\underline{\underline{B}}\underline{\underline{Z}}\underline{\underline{D}}^{-1}$ (*Nielsen*, 2011), where *(i,j)*th element of $\underline{\underline{B}}$ is the covariance between $x(t_i)$ and $x(t_j)$. As $\underline{c}$ is distributed asymptotically normally, we recognize that the quadratic form Eq. (3) asymptotically corresponds to the above mentioned random variable q with $\underline{\underline{P}} = \underline{\underline{D}}^{-1}\underline{\underline{Z}}^T\underline{\underline{B}}\underline{\underline{Z}}\underline{\underline{D}}^{-1}$ and $\underline{\underline{Q}} = 1/(2\pi)\underline{\underline{D}}$. When $\underline{x}$ comes from a white noise process, the eigenvalues of $\underline{\underline{QP}} = 1/(2\pi)\underline{\underline{Z}}^T\underline{\underline{B}}\underline{\underline{Z}}\underline{\underline{D}}^{-1}$ are identical, and this is why LSP follows an exponential distribution under a white noise process. For other processes, the eigenvalues depend on length of the data set, spacing, autocovariances of the underlying process, and frequency. However, except for some degenerate cases, the difference between these eigenvalues is not too

large. Therefore, our final conclusion is that probability distribution of LSP is closely exponential even for processes different from white noise.

It can be shown (*Mathai* and *Provost*, 1992) that the expected value of q is the trace of $\underline{\underline{Q}}\underline{\underline{P}}$, and therefore, the expected value of Eq. (3) is the trace of

$$1/(2\pi)\underline{\underline{Z}}^T\underline{\underline{B}}\underline{\underline{Z}}\underline{\underline{D}}^{-1}.$$

Remember that trace of a quadratic matrix is the sum of diagonal elements of this matrix, which is identical with the sum of its eigenvalues. Utilizing basic trigonometric identities we obtain

$$E\left[I_{LS}(\lambda_j)\right]=trace\left(1/(2\pi)\sum_{k=-(N-1)}^{N-1}\underline{\underline{D}}_k\underline{\underline{D}}^{-1}B(k)\cos(\lambda_j k)\right), \tag{6}$$

where $B(k)$ is the autocovariance function of the process that generates the time series, $\underline{\underline{D}}_k=\underline{\underline{S}}_k^T\underline{\underline{S}}_k$ with *(i,j)*th element of $\underline{\underline{S}}_k$ $s_{k,ij}=\alpha_i\alpha_{i+|k|}(\cos(\lambda_j i),\sin(\lambda_j i))^T$, $i=1,...,N-|k|$, and $\alpha_i, i=1,..,N$ is an indicator series that equals with zero when no data is available at time *i*, while equals with one when data is available at time *i*. Evidently, Eq. (6) for evenly sampled data has the well-known form

$$E\left[I(\lambda_j)\right]=B(0)/\pi+2/\pi\sum_{k=1}^{n-1}(1-k/n)B(k)\cos(\lambda_j k), \text{ or} \tag{7}$$

$$E\left[I(\lambda_j)\right]=\int_{-\pi}^{\pi}g(\omega)K_n(\omega-\lambda_j)d\omega$$

with $g(\omega)=f(\omega),\omega\geq 0$, $g(\omega)=f(-\omega),\omega<0$, and

$$K_n(\omega)=1/(2\pi)\sum_{k=-(n-1)}^{n-1}u(k)\cos(\omega k),$$

where $u(k)=1-|k|/n$. Hence, $K_n(\omega)$ is the Fejér-kernel. In the frequency domain representation of

$$E\left[I_{LS}(\lambda_j)\right]=\int_{-\pi}^{\pi}g(\omega)K_n(\omega-\lambda_j)d\omega,$$

$u(k)$ corresponding to Eq. (6) is $u(k)=trace(\underline{\underline{D}}_k\underline{\underline{D}}^{-1})/2$. Note that LSP is an unbiased estimator for white noise processes (see Eq. (7)).

4.2. Entire least squares periodogram (ELSP)

As $\underline{\underline{D}}^{-1}\underline{w}=\underline{c}$, therefore $c_i w_i=(\underline{\underline{D}}^{-1}\underline{w})_i w_i$. Additionally, the covariance matrix of $\underline{w}$ is $\underline{\underline{Z}}^T\underline{\underline{B}}\underline{\underline{Z}}$. Utilizing these facts and basic trigonometric identities we obtain after *Mathai* and *Provost* (1992) that

$$E\left[I_{ELS}(\lambda_j)\right]=trace\left(1/(2\pi)\sum_{k=-(N-1)}^{N-1}\left\{\underline{\underline{D}}^{-1}\underline{\underline{D}}_k\right\}_j B(k)\cos(\lambda_j k)\right), \tag{8}$$

where $\left\{\underline{\underline{U}}\right\}_j$ denotes a matrix of size (2×2) consisting of *(j,j)*th, *(j,j+L)*th, *(j+L,j+L-1)*th *(j+L,j+L)*th elements of $\underline{\underline{U}}$. Here,

$$s_{k,ij}=\left\{\begin{matrix}\alpha_i\alpha_{i+|k|}\cos(\lambda_j i), j=1,...,L\\ \alpha_i\alpha_{i+|k|}\sin(\lambda_j i), j=L+1,...,2L\end{matrix}\right\}, i=1,...N-|k|.$$

Following *Yuan* and *Bentler* (2010) we observe that ELSP is also a linear combination of two independent chi-squared random variables with one degree of freedom, and if difference between coefficients in this linear combination is not very large, the probability distribution of ELSP is closely exponential. Eq. (8) for evenly sampled data also has the well-known form Eq. (7). In the frequency domain representation of

$$E\left[I_{ELS}(\lambda_j)\right]=\int_{-\pi}^{\pi}g(\omega)K_n(\omega-\lambda_j)d\omega,$$

$u(k)$ corresponding to Eq. (8) is $u(k)=trace\left(\left\{\underline{\underline{D}}^{-1}\underline{\underline{D}}_k\right\}_j\right)/2$. Note that for both the LSP and ELSP, $K_n(\omega)$ depends not only on n but also on data spacing and λ_j. However, ELSP is an unbiased estimator for white noise processes (see Eq. (8)).

5. Examples

5.1. Hallet Lake

The Hallet Lake temperature proxy record (*Mc Kay et al.*, 2008) from south-central Alaska available for a period of AD 492-2005 is based on biogenic silica preserved in the lacustrina sediments. Its data spacing varies from 1 to 35 years with an average spacing of 10.15 years. Data (n=150) are standardized to have zero mean and unit variance.

Fig. 1 shows no substantial differences between LSP and ELSP. However, many small differences count for much, as NIR performed with LSP (NIR-LSP) provides a red noise spectral density, while NIR with ELSP (NIR-ELSP) delivers a colored noise density. In this latter case, a moderate but wide peak of the spectral density reinforces the importance of multi-decadal oscillations shown in other Alaskan proxy records (e.g., *Wilson et al.*, 2007).

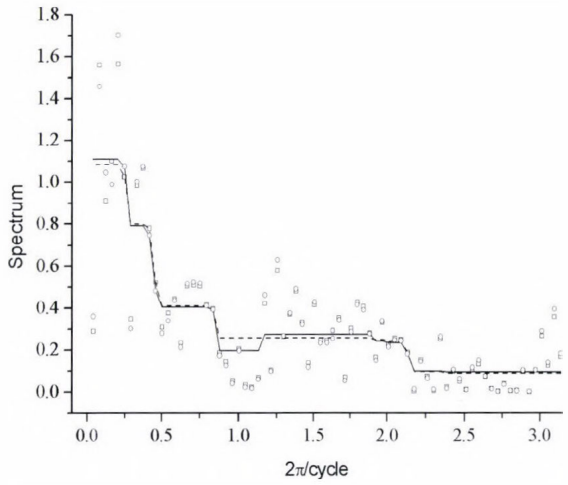

Fig. 1. ELSP (circle), LSP (square), NIR-ELSP spectral density (solid line), and NIR-LSP spectral density (dashed line) of Hallet Lake temperature proxy record AD 492-2005.

5.2. Vostok

Vostok ice core deuterium content data are available for the last 422,766 years (*Petit et al.*, 1999). Data spacing varies from 20 to 664 years with a mean spacing of 127.8 years. Data (n=3303) are standardized to have zero mean and unit variance. Not surprisingly, the highest peak of both the NIR-LSP and NIR-ELSP spectra appears at 105,500 years corresponding to the Earth eccentricity cycle (*Fig. 2*). The cycle related to obliquity can be seen at somewhat lower frequency (closer to the 41,000-year astronomical cycle) for NIR-ELSP than for NIR-LSP. More importantly, dominance of the eccentricity cycle is much clearer from NIR-ELSP, since NIR-ELSP peak at this cycle is substantially higher than the NIR-LSP peak. The ratio of the magnitude of peak at eccentricity to peak at obliquity is 1.63 for NIR-LSP, while it is 4.88 for NIR-ELSP. Peaks in an interval of 21,000-28,000 years corresponding to the precession are considerably more modest for NIR-ELSP than for NIR-LSP. The third largest peak of NIR-LSP is around a 60,000-year cycle which cannot be explained by a direct astronomical forcing but is probably a

side-effect of the aforementioned cycles (e.g., *Rial* and *Anaclerio*, 2000). Note, however, that this period is essentially missing in NIR-ELSP. *Fig. 3* shows peaks at high frequencies, too. Cycles around 270 years are substantially stronger with NIR-ELSP than with NIR-LSP. Similar fact can be mentioned for cycles corresponding to 500-525 years (almost double of the 270-year period). These cycles are clearly related to solar cycles listed in *Schove* (1983).

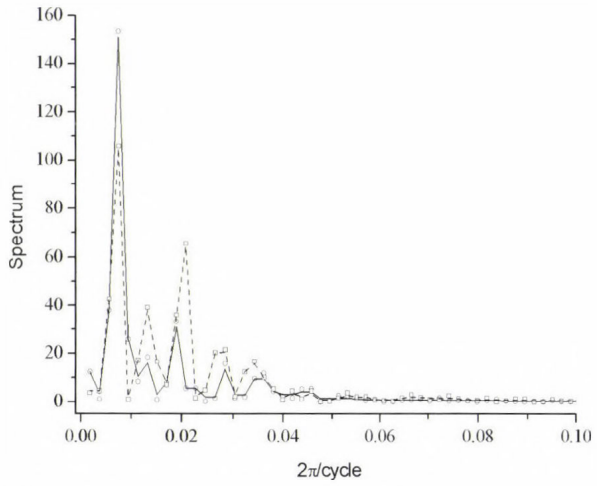

Fig. 2. ELSP (circle), LSP (square), NIR-ELSP spectral density (solid line), and NIR-LSP spectral density (dashed line) for Vostok ice core deuterium content data for the last 422,766 years at low frequencies.

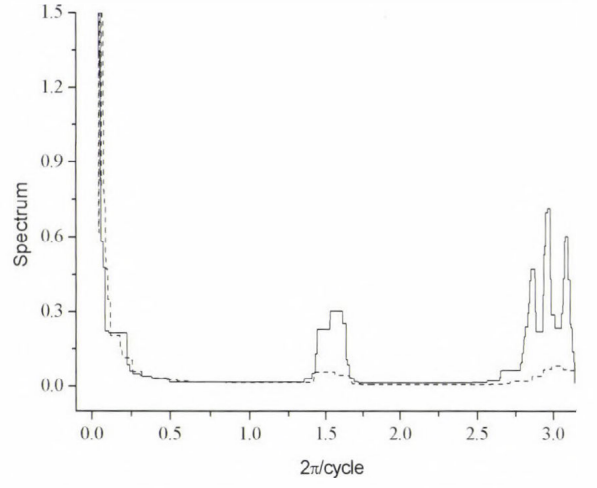

Fig. 3. NIR-ELSP spectral density (solid line) and NIR-LSP spectral density (dashed line) for Vostok ice core deuterium content data for the last 422,766 years at high frequencies.

5.3. GISP2

Oxygen-isotope data from GISP2 ice core from Greenland (*Groots* and *Stuvier*, 1997) are unevenly spaced in time, varying from 68 to 257 years with a mean spacing of Δ=125.8 years in the period between 15,000 and 60,000 BP. Data (n=358) are standardized to have zero mean and unit variance. *Schulz* and *Mudelsee* (2002) analyzed this record in order to detect a spectral peak at a 1470-year cycle corresponding to the spacing of the well-known Dansgaard-Oeschger events. Although the difference between ELSP and LSP does not seem substantial, NIR-LSP does not detect any spectral peak but does provide a red noise spectral density. In contrast, a peak at the above mentioned 1470-year cycle clearly appears when using the NIR method with ELSP (*Fig. 4*).

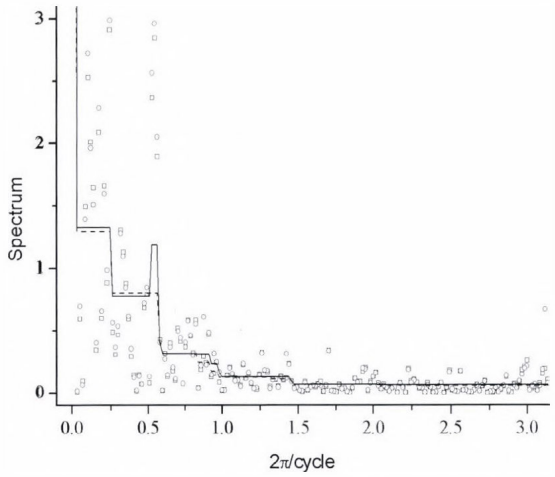

Fig. 4. ELSP (circle), LSP (square), NIR-ELSP spectral density (solid line), and NIR-LSP spectral density (dashed line) for GISP2 oxygen-isotope data for period between 15,000 and 60,000 BP. A big spectral peak around 40,000 years is not visible due to the vertical axis scale.

6. Discussion and conclusions

In order to demonstrate the ability of NIR and the drawback of AR(1) fitting, a simple example is taken by a stochastic process

$$Y_t = 0.5\cos(0.05\pi t) + X_t, \tag{9}$$

where the red background noise comes from a first order moving average (MA(1)) process $X_t = e_t - 0.5e_{t-1}$, and e_t is a white noise Gaussian process with $\sigma_e = 1$. Note that the variance corresponding to the discrete cycle $0.5\cos(0.05\pi t)$ is only 10% of the background noise variance. A time series of Y_t with n=400 is simulated and the spectrum is estimated with both the AR(1) fitting and the NIR method. The procedure is repeated 1,000 times. *Fig. 5* shows that the mean of the 1,000 NIR spectra exhibits a very sharp peak recognizing the discrete frequency at 0.05π. At the rest of frequencies, NIR spectrum reproduces well the background noise spectrum as compared to the background noise obtained with AR(1) fitting. Note that AR(1) spectral density is around two times higher than the true background spectral density at low frequencies causing difficulties in detecting the discrete frequency with traditional techniques. When omitting the discrete frequency from Eq. (9), the AR(1) spectral density is almost the same as in the previous case involving discrete frequency, while the NIR spectral density essentially coincides with the true background noise spectral density.

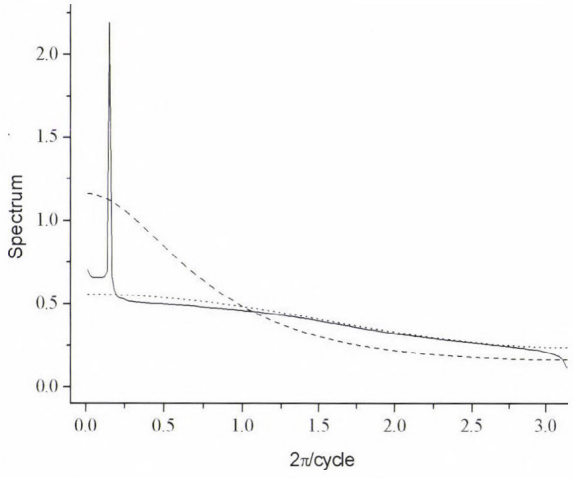

Fig. 5. Mean of NIR-ELSP spectral densities (solid line) and AR(1) spectral densities (dashed line) obtained from 1,000 simulated time series of length n=400 according to Eq. (9), and AR(1) spectral density (dotted line) of the background noise in Eq. (9).

Comparison of properties of LSP and ELSP is illustrated with the third data set in Section 5.3. As it was mentioned earlier, both the LSP and ELSP can be written as

$$I_*(\lambda_j) = h_1\xi_1 + h_2\xi_2, \tag{10}$$

where $I_*(\lambda_j)$ is either LSP or ELSP, and ξ_1 and ξ_2 are independent chi-squared random variables with one degree of freedom. For simplicity, dependence on the frequency of h_1 and h_2 is not indicated. If coefficients h_1, h_2 are identical, $I_*(\lambda_j)$ is distributed exponentially, but when the ratio $r = \max\{h_1, h_2\}/\min\{h_1, h_2\}$ is not too large, the probability distribution is closely exponential. Approximating the true probability distribution with an exponential distribution is highly accurate for ratios from r=1 to at least r=2-3 (*Yuan* and *Bentler*, 2010). Calculation of r (*Yuan* and *Bentler*, 2010) requires the autocorrelations of the underlying process. These are here substituted by autocorrelations corresponding to the AR(1) model fitted to data with a procedure described in *Schulz* and *Mudelsee* (2002). *Fig. 6* shows this ratio against frequencies. It is obvious that both periodograms can be taken as they are distributed exponentially. At very high frequencies, the distribution tends to deviate from the exponential one, but with smaller degree for ELSP than for LSP. Note that exponential approximation of the distribution of ELSP is accurate even at highest frequencies.

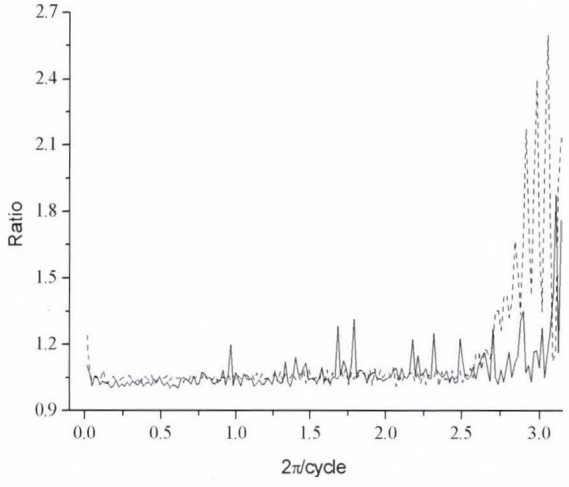

Fig. 6. Ratio $\max\{h_1, h_2\}/\min\{h_1, h_2\}$ against frequencies for ELSP (solid line) and LSP (dotted line), where coefficients h_1, h_2 are defined in Eq. (10).

Another important property of both the LSP and ELSP is that these periodogram elements at different frequencies are correlated for unevenly spaced data. *Fig. 7* shows the correlation between $I_{LS}(\lambda_j)$ and $I_{LS}(\lambda_i - \lambda_j)$ against the frequency λ_j and frequency shift $\lambda_i - \lambda_j$ for $i, j = 1,...,L$. It is apparent

that correlations are essentially zero at any frequencies and any frequency shifts except for the highest frequencies. At highest frequencies, the correlations are not negligible but only within narrow frequency shift intervals. The overall picture for ELSP (the corresponding figure is not shown) is the same but with slightly lower correlations. For instance, the largest correlation under every combination of λ_j and $\lambda_i - \lambda_j$ is 0.47 for LSP, while it is 0.43 for ELSP. These results are consistent with findings obtained for exponential approximation to the distribution of ELSP and LSP. The distribution of ELSP and LSP tends to deviate from the exponential distribution, when correlation between sinusoid and cosinusoid parts of the periodogram at a given frequency increases. Somewhat similar phenomenon can be found in *Vio et al.* (2010) but only for LSP and for time series simulated from white noise processes. It is to be mentioned that calculating the correlation between two periodogram elements utilizes that $\underline{c}$ has an asymptotic multivariate normal distribution. Hence, the mentioned correlation consists of fourth-order central moments of $\underline{c}$. These moments, due to the normality of $\underline{c}$, can be expressed via second order central moments, ie., via the covariance matrix of $\underline{c}$. Finally, this covariance matrix can be approximated using the autocorrelations corresponding to the AR(1) model fitted to data.

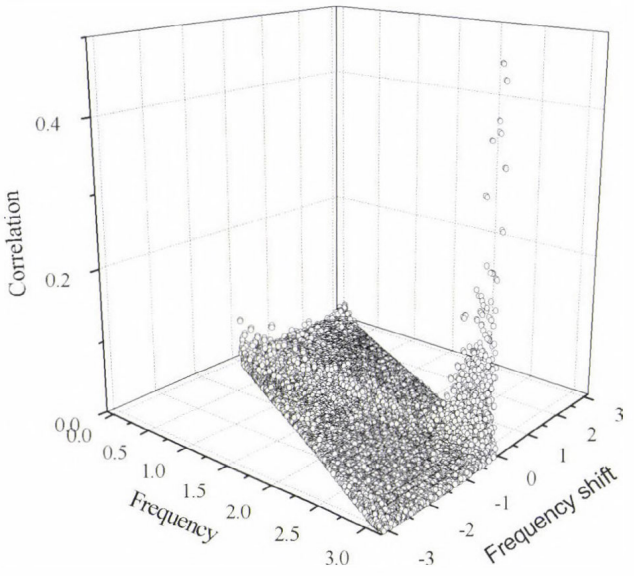

Fig. 7. Correlation between LSP elements at different frequencies and different frequency shifts.

Similar calculations shows that main conclusions discussed in the last two paragraphs are applicable for data sets of Sections 5.1 and 5.2.

Originally, LSP has been developed for time series generated by stochastic processes consisting of a certain number of periodic components plus a white noise process. Later, it has been using to estimate not only discrete spectra but spectral densities, too (e.g., *Schulz* and *Mudelsee*, 2002). Recognizing that LSP at a given frequency can be highly affected by other frequencies, *Stoica et al.* (2009) introduced a weighted least square fit at every separate frequency, where the weights are related to other LSP elements. The procedure thus necessitates an iterative technique requiring bigger computational effort than ELSP. More importantly, the weights are chosen with an approximation that holds accurately only for evenly spaced data. Such a simplification appears also in *Nygrén* and *Ulich* (2010). Here, after performing the entire least squares technique, the matrix $\underline{\underline{D}}$ is taken diagonal with elements $n/2$. Hence, their periodogram $n/(4\pi)(c_j^2 + c_{j+L}^2)$ provides a biased estimator even for white noise processes and does not integrate to $\hat{\sigma}^2$ (except for evenly spacing data) in contrast to our Eq. (5).

The matrix $\underline{\underline{D}}$ is generally close to being singular for large values of n, and solving Eq. (2) for $\underline{c}$ to form ELSP is not easy. Our experience is that traditional techniques such as Gauss-Seidel, successive over-relaxation, or conjugate gradient methods might be unsuccessful. Therefore, Eq. (2) was solved with a Monte Carlo technique (e.g., *Liu*, 2001), as this procedure is carried out numerically with a totally different scheme than the previous techniques.

References

Álvarez, E.E., and *Yohai, V.J.,* 2011: M-estimators for Isotonic Regression. arXiv: 1105.5065v1stat.ME.

Broersen, P.M.T., 2006: Autoregressive Order Selection for Irregularly Sampled Data. *IEEE Trans. Instrum. Meas. 54*, 1004–1009.

Groots, P.M. and *Stuvier, M.*, 1997: Oxygen 18/16 variability in Greenland snow and ice with 10^{-3}–10^{5}-year time resolution. J. *Geophys. Res. 102 (C12)*, 26455–26470.

Liu, J.S., 2001: Monte Carlo strategies in Scientific Computing. Springer, New York.

Lomb, N.R., 1976: Least-squares frequency analysis of unequally spaced data. *Astrophys. Space Sci. 39*, 447–462.

Mathai, A.M. and *Provost, S.B.,* 1992: Quadratic Forms in Random Variables. Taylor & Francis.

Matyasovszky, I., 2013a: Spectral analysis of unevenly spaced climatological time series. *Theor. Appl. Climatol 111*, 371–378.

Matyasovszky, I., 2013b: Estimating red noise spectra of climatological time series. *Időjárás 117*, 187–200.

Mc Kay, N.P., Kaufman, D.S., and *Michelutti, N.*, 2008: Biogenic-silica concentration as a high-resolution, quantitative temperature proxy at Hallet Lake, south-central Alaska. *Geophys. Res. Lett. 35*, LO5709.

Nielsen, A.A. ,2011: Least Squares Adjusments: Linear and Nonlinear Weighted Regression Analysis. Lecture Note, Lyngby, Denmark: IMM, DTU, http://www2.imm.dtu.dk/pubdb/views/publication_details.php?id=2804.

Nygrén, T., and *Ulich, Th.*, 2010: Calculation of signal spectrum by means of stochastic inversion. *Ann Geophys 28*, 1409–1418.

Petit, J.R., Jouzel, J., Raynaud, D., Barkov, N.I., Barnola, J.M., Basile, I., Bender, M., Chappellaz, J., Davis, J., Delaygue, G., Delmotte, M., Kotlyakov, V.M., Legrand, M., Lipenkov, V., Lorius, C., Pépin, L., Ritz, C., Saltzman, E., and *Stievenard M.*, 1999: Climate and Atmospheric History of the Past 420,000 years from the Vostok Ice Core, Antarctica. Nature 399, 429-436.

Rial, J.A., and *Anaclerio, C.A.*, 2000: Understanding nonlinear responses of the climate system to orbital forcing. *Quat. Sci. Rev. 19*: 1709–1722.

Scargle, J.D., 1982: Studies in astronomical time series analysis II: statistical aspects of spectral analysis of unevenly spaced data. *Astrophys. J. 261*, 835–853.

Schove, D.J. (Ed.), 1983: Sunspot cycles. *Benchmark Papers in Geology 68*, Hutchinson.Ross Publ.Co.

Schulz, M., and *Mudelsee, M.*, 2002: REDFIT: estimating red-noise spectra directly from unevenly spaced paleoclimatological time series. *Comput. Geosci. 28*, 421–426.

Stoica, P., Li, J., and *He, H.*, 2009: Spectral Analysis of Nonuniformly Sampled Data: A New approach Versus the Periodogram. *IEEE Trans. Signal Process. 57*, 1415–1425.

Tibshirani, R.J., Hoefling, H., and *Tibshirani, R.*, 2011: Nearly-Isotonic Regression. *Technometrics 53*, 54–61.

Vio, R., Adreani, P., and *Biggs, A.*, 2010: Unevely-sampled signals: a general formalism of the Lomb-Scargle periodogram. *Astron. Astrophys. 519*, A86, 12.

Wilson. R., Wiles, G., D'Arrigo, R., and *Zweck, C.*, 2007: Cycles and shifts: 1,300 years of multi-decadal temperature variability in the Gulf of Alaska. *Clim. Dyn. 28*, 425–440.

Yuan, K-H., and *Bentler, P.M.*, 2010: Two simple approximations to the distributions of quadratic forms. *Br J Math Stat Psychol* 63, 273–291.

Zhao, O., and *Woodroofe, M.*, 2012: Estimating a monotone trend. *Stat Sinica 22*, 359–378.

IDŐJÁRÁS

Quarterly Journal of the Hungarian Meteorological Service
Vol. 119, No. 1, January – March, 2015, pp. 69–89

Cyclic variation in the precipitation conditions of the Mátra-Bükkalja region and the development of a prognosis method

Ferenc Kovács* and **Endre Turai**

MTA-ME Research Group of Geoengineering,
Egyetem út, H-3515 Miskolc, Hungary

**Corresponding author E-mail: bgtkf@uni-miskolc.hu*

(Manuscript received in final form May 8, 2014)

Abstract—The cycle properties of the annual average, absolute maximum, and absolute minimum precipitation values have been calculated from precipitation data the Mátra and Bükk regions. The cycle parameters of annual average and annual absolute maximum precipitation values have been determined using the data of a shorter 34-year (1970–2006) and a longer 53-year (1960–2012) period (38 precipitation measurement stations) through the determination of the parameters of frequency, amplitude, and phase with an analytic version of the discrete Fourier transform (DFT), and the values obtained on the basis of the two periods have been compared. Using prognosis parameters, a prognosis until 2025 has been made. Then, the regression function of the variation in time of average and absolute maximum precipitation values has been determined on the basis of actual and prognosticated data for the whole period (1960–2025).

Key-words: Mátra-Bükkalja region, precipitation, cyclic variation, prognosis method

1. Introduction

The analysis of precipitation data in the Mátra-Bükkalja region between the years 1960 and 2012 has given the result that that both the 53-year average values of specific precipitation and the annual absolute maximum values of the measured values for the 38 precipitation measurement stations (settlements) show cylicity for both the 3–5 years and longer periods (*INNOCENTER*, 2013a; *Kovács*, 2014). Minimum and maximum 'local' values recur for both annual

average and annual maximum values. With the cyclic variation of annual precipitation values, annual average precipitation displayed constancy around the 600 mm/year value in both the Mátra and Bükkalja regions even on the basis of the combined set of data. With respect to annual absolute maximum and minimum values, regarding these parameters as indicators of extreme weather, plenty of precipitation or years of drought, the data of 53 years showed a decreasing tendency.

In the present paper, the cycle parameters of the average and absolute maximum precipitation values are calculated using the data sets reported in *INNOCENTER* (2013a) and *Kovács* (2014), analysing the precipitation data of the region investigated (Mátra-Mátraalja, Bükk-Bükkalja) and developing a calculation method of cycle parameters as a research task in the Carpathian Basin (*Szűcs*, 2012). Based on this, a prognosis is made for the period until 2025.

2. Theoretical basis of analysis and calculation, the Fourier transform

In the interpretation of frequency, amplitude. and phase, a 2π periodical $\cos(t)$ function has been taken as starting point, where $T = 2\pi$ is the period length of the function. Next, the argument of the function has been transformed (*Meskó*, 1984; *Turai*, 1983):

$$\cos(t) = \cos\left(\frac{2\pi}{2\pi}t\right) = \cos\left(\frac{2\pi}{T}t\right) = \cos\left(2\pi\frac{1}{T}t\right) = \cos(2\pi ft)$$

The rate expressing the density of periods (period density or with the commonly used term, frequency) is

$$f = \left(\frac{1}{T}\right).$$

If t stands for length in space, then frequency gives the number of periods per unit of spatial length for the given direction. Spatial frequency is called wave number.

Multiplying the $\cos(2\pi ft)$ function with factor A and shifting its maximum by Δt, after writing up

$$\cos(2\pi f[t + \Delta]), \text{ factor } A$$

is called amplitude. In the case of a monofrequency periodical signal, the amplitude equals half of the difference between the maximum (F_{max}) and minimum (F_{min}) of signal value:

$$A = \frac{F_{max} - F_{min}}{2}.$$

After a further transformation of the argument of the cosine function, the following formula can be written:

$$A\cos(2\pi f[t + \Delta t]) = A\cos(2\pi ft + 2\pi f\Delta t) = A\cos(2\pi ft + 2\pi\frac{\Delta t}{T}) = A\cos(2\pi ft + \varphi).$$

The quantity φ, thus introduced, is called phase (phase angle). the absolute phase shows the part of the phase length (phase time or wavelength) the maximum of the signal has shifted with in relation to the origin ($t = 0$). As it can be seen in *Fig. 1*, in the case of $\Delta t = 0$, the maximum shifts to the, left while in the case of $\Delta t < 0$ to the right of the origin. Absolute phase can be given in both radians and degrees:

$$\varphi = 2\pi\frac{\Delta t}{T} \quad \text{[rad]} \qquad \varphi = 360\frac{\Delta t}{T} \quad \text{[degrees]}.$$

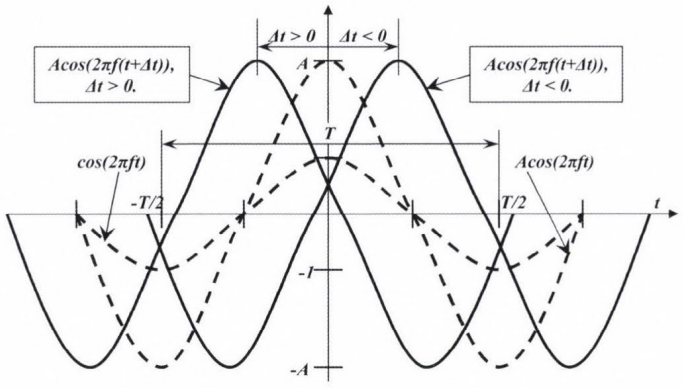

Fig. 1. The interpretation of the absolute phase.

Relative phase ($\Delta\varphi$) is interpreted between two signals and shows that in relation to the maximum of one of two signals of identical frequency, what part of the period length the maximum of the other signal has shifted with. As it can be seen in *Fig. 2*, the two signals are *x(t)* and *y(t)* while the difference of the maximums of the two signals Δt_{xy}. The relative phase between the two signals can also be calculated:

$$\Delta\varphi_{xy} = 2\pi\frac{\Delta t_{xy}}{T}\ [\text{rad}] \qquad \Delta\varphi_{xy} = 360\frac{\Delta t_{xy}}{T}\ [\text{degrees}].$$

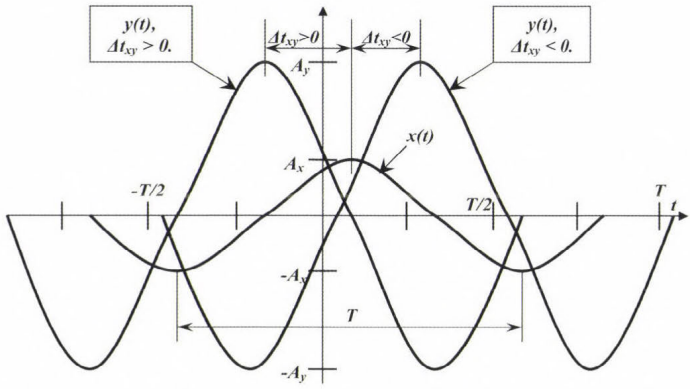

Fig. 2. The interpretation of the relative phase.

The relative phase can also be calculated as the difference of the absolute phases of the two signals:

$$\Delta\varphi_{xy} = \varphi_y - \varphi_x .$$

With the help of the Fourier transform, signals can be transferred from the space-time domain into the frequency domain. During the process, the mappings of signals in the frequency domain are called Fourier spectra.

Working with harmonic functions ($\cos(2\pi ft)$, $\sin(2\pi ft)$) in the analytic Fourier transform, a complex Fourier spectrum is obtained, which can be divided into a real and an imaginary part. The $\mathrm{Re}[F(f)]$ real part of the spectrum can be written up with a real cosine transformation

$$\mathrm{Re}[F(f)] = \int_{-\infty}^{+\infty} f(t)\cos(2\pi ft)dt , \tag{1}$$

while its imaginary part with a real sine transformation is

$$\mathrm{Im}[F(f)] = \int_{-\infty}^{+\infty} f(t)\sin(2\pi ft)dt . \tag{2}$$

The complex Fourier spectrum can be written up with two real spectra:

$$F(f) = \mathrm{Re}[F(f)] + j\,\mathrm{Im}[F(f)].$$

The real spectrum gives the weights of the cosine components falling into a frequency band unit around any f frequency, while the imaginary spectrum gives the weights of the sine components for the formation of the signal.

The $F(f)$ complex spectrum can also be defined in an exponential form by the introduction of two other real spectra:

$$F(f) = A(f)e^{j\Phi(f)}.$$

The $A(f)$ spectrum, thus introduced, is called amplitude spectrum, while the $\phi(f)$ spectrum is called phase spectrum. The amplitude spectrum gives the weight in the formation of the signal of the harmonic component falling into a frequency band unit around any f frequency, while the phase spectrum shows the part of the period length the maximum of this harmonic component shifts with in relation to the maximum of base function $\cos(2\pi ft)$, taken at point $t = 0$.

The amplitude and phase spectra are the following in the knowledge of real and imaginary spectra with the help of the correlations yielded by *Fig. 3*:

$$A(f) = \sqrt{(\mathrm{Re})^2[F(f)] + (\mathrm{Im})^2[F(f)]}$$

$$\phi(f) = arctg\frac{\mathrm{Im}[F(f)]}{\mathrm{Re}[F(f)]}$$

Real and imaginary spectrum values can also be calculated from amplitude and phase spectra:

$$\mathrm{Re}[F(f)] = A(f)\cos[\phi(f)]$$
$$\mathrm{Im}[F(f)] = A(f)\sin[\phi(f)]$$

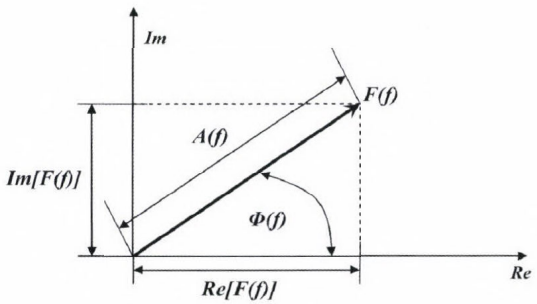

Fig. 3. Plotting of Fourier spectra in a complex plane.

3. Spectral analysis

In the search for the deterministic periodic components, the spectrum of the $\Delta y(t)$ deviations from the ($\overline{Y}$) expected values has been investigated with the following correlations:

$$\Delta y(t) = y(t) - \hat{Y},$$

$$Y(f) = \int_{-\infty}^{+\infty} \Delta y(t) e^{-j2\pi ft}\, dt.$$

The period lengths of the deterministic periodic components to be found in the stochastic signal are given by the reciprocal values of the ($f_{1,\max}$, $f_{2,\max}$, …, $f_{N,\max}$) frequencies belonging to the maximums of the $A(f)$ amplitude density spectrum of the $Y(f)$ spectrum:

$$T_1 = \frac{1}{f_{1,\max}},$$

$$T_2 = \frac{1}{f_{2,\max}},$$

…

$$T_N = \frac{1}{f_{N,\max}},$$

where N is the number of deterministic periodic components (the number of the maximums of the $A(f)$ spectrum).

It can be calculated from the $\phi(T_i)$ values of the phase-density spectrum belonging to the given period time, what $\Delta t(T_i)$ time the maximum of the given component of any T_i (i = 1, 2, …, N) period time has shifted in relation to the starting year (1973) of data registration:

$$\Delta t(T_i) = T_i \frac{\Phi(T)_i}{2\pi} \quad \text{[radian]},$$

or

$$\Delta t(T_i) = T_i \frac{\Phi(T)_i}{360} \quad \text{[degree]}.$$

The A_i amplitudes of a component of any T_i period time are given by the values of $A(f)$ amplitude density:

$$A_i = A(T_i).$$

Figure A_i gives the amplitude of the deterministic component with T_i period time.

Let $A(f)_{max}$ denote the maximum of the $A(f)$ amplitude density spectrum. The relative amplitude density spectrum normed to maximum value ($A(f)_{rel}$) as the percentage of maximum value can be calculated as follows:

$$A(f)_{rel} = \frac{A(f)}{A(f)_{max}}.100[\%].$$

Relative amplitude density spectrum values show percentage of the amplitude density of any given component of T = 1/f period time in the maximum amplitude density.

4. Spectral analysis of the variation of annual precipitation amount on the basis of Mátra Bükkalja precipitation data

In INNOCENTER (2013b) the cycle properties of the variation in time of precipitation have been investigated on the basis of the territorial average values of precipitation data in the years 1960–2012 in 23 settlements/precipitation measurement stations in the Mátra-Mátraalja region and 15 settlements/ precipitation measurement stations in the Bükk-Bükkalja region. *Table 1* shows the average annual precipitation values and the annual absolute maximum precipitation values on the basis of the data of the two regions and combined data. In order to assess the effect of the registration period on results, cycle properties have been calculated for a shorter (1973–2006, 34 years) and a longer (1960–2012, 53 years) period. (Yearbook of the Hydrographical Service of Hungary 1960–2005.)

4.1. The results of spectral analysis on the basis of precipitation data for the years 1973–2006

In the spectral analysis of the precipitation data, the registration time (T_{reg} was 33 years for end-sampling periods and the 34 years for middle-sampling periods. The sampling rate (Δt) was 1 year, while the number of samples was 34.

Analyses have been performed with an analytic version of the discrete Fourier transform (DFT) (*Turai*, 1983). The complex amplitude density spectra of the function of annual precipitation values have been determined as the function of discrete period time values. Of the four real spectra describing the complex spectrum (real spectrum, imaginary spectrum, amplitude spectrum, and phase spectrum), amplitude spectra are presented. In the plotting, logarithmic linear scale has been chosen to illustrate spectrum maximums more clearly.

Table 1. Precipitation data in the Mátra-Bükkalja region as the function of time

Number of settlements / measurement points		Years												
		1960	1961	1962	1963	1964	1965	1966	1967	1968	1969	1970	1971	1972
Mátra	Average	727	506	568	681	747	868	814	538	478	737	861	455	636
	Absolute maximum	1016	584	724	923	1012	1098	1029	610	599	899	1080	559	789
Bükk	Average	712	436	499	548	693	825	769	569	517	623	891	378	557
	Absolute maximum	811	487	535	599	769	947	956	733	563	764	971	410	674
Mátra Bükk	Average	721	476	538	624	724	849	795	551	495	688	874	422	602
	Absolute maximum	1016	584	724	923	1012	1098	1029	733	599	899	1080	559	789

Number of settlements / measurement points		Years													
		1973	1974	1975	1976	1977	1978	1979	1980	1981	1982	1983	1984	1985	1986
Mátra	Average	509	804	607	709	620	576	691	659	504	444	425	655	674	453
	Absolute maximum	712	1061	748	935	748	704	844	821	595	555	504	791	814	566
Bükk	Average	453	698	675	659	691	585	652	697	524	423	504	535	594	399
	Absolute maximum	535	735	843	747	781	708	763	740	574	506	581	648	680	438
Mátra Bükk	Average	485	759	636	688	650	580	674	676	512	435	459	604	640	430
	Absolute maximum	712	1061	843	935	781	708	844	821	595	555	581	791	814	566

Number of settlements / measurement points		Years													
		1987	1988	1989	1990	1991	1992	1993	1994	1995	1996	1997	1998	1999	2000
Mátra	Average	534	638	611	560	692	393	514	497	718	637	433	654	949	474
	Absolute maximum	654	851	729	613	774	486	603	586	874	751	519	754	1092	563
Bükk	Average	499	596	586	492	652	346	457	454	679	576	482	722	874	426
	Absolute maximum	559	613	655	523	694	418	516	509	727	609	535	774	988	474
Mátra Bükk	Average	519	620	600	531	675	373	490	479	701	611	454	683	917	453
	Absolute maximum	654	851	729	613	774	486	603	586	874	751	535	774	1092	563

Number of settlements / measurement points		Years												
		2001	2002	2003	2004	2005	2006	2007	2008	2009	2010	2011	2012	
Mátra	Average	585	639	551	647	751	651	632	657	666	1054	404	434	
	Absolute maximum	723	837	674	747	929	733	791	777	736	1195	462	486	
Bükk	Average	653	591	517	749	741	631	599	625	624	1118	447	466	
	Absolute maximum	736	669	564	828	791	711	649	701	709	1153	488	557	
Mátra Bükk	Average	614	618	536	690	746	642	619	645	658	1079	420	446	
	Absolute maximum	736	837	674	828	929	733	791	777	736	1195	488	557	

In the calculation of spectra, the spectrum of $\Delta y(t)$ deviations from ($\bar{Y}$ $\hat{Y}$) expected values has been determined:

$$\Delta y(t) = y(t) - \bar{Y}.$$

The (T_{min}) minimum period time that can theoretically be found in the signal is defined by the Nyquist frequency (f_N).

$$\Delta t = 1 \text{ year}, \qquad f_N = 0{,}5 \frac{1}{year}, \qquad T_{min} = 2 \text{ years}.$$

As in the case of all the six time series, the 'sampling' time was 1 year, the analysis can only reveal cycles of longer period time than 2 years in the changes everywhere.

In theory, maximum period time (T_{max}) is determined by the registration time (T_{reg}):

$T_{max} = T_{reg}$ – in case of end sampling,

$T_{max} = T_{reg} + \Delta t$ – in case of middle sampling.

Therefore, the maximum period time that can be revealed by analysis is 33 years in case of end-sampling and 34 years in case of middle-sampling

With the data in *Table 1*, both the amplitude spectra of the amplitude density and the relative spectra have been determined. In the latter case, spectra have been normed to maximum spectrum value. In all the six cases – annual average and annual absolute maximum precipitation, – for Mátra, Bükk, and Mátra+Bükk regions, similar amplitude and relative amplitude spectrum functions have been obtained.

The cycle properties of annual average precipitation in the Mátra region are the following on the basis of amplitude peaks, cycle time, and amplitude density:

Major cycles: 1. T_1 = 4.9 years, A_1 = 1243 mm; 2. T_2 = 3.5 years, A_2 = 1195 mm; 3. T_3 = 29.8 years, A_3 = 946 mm; 4. T_4 = 9.9 years, A_4 = 806 mm; minor cycles: 1. T_1 =7.3 years, A_1 = 476 mm; 2. T_2 = 6.3 years, A_2 = 440 mm.

Cycle properties revealed on the basis of Bükk data are, cycle time and amplitude density: major cycles: 1. T_1 = 28.7 years, A_1 = 1216 mm; 2. T_2 = 3.5 years, A_2 = 1064 mm; 3. T_3 = 4.9 years, A_3 = 1035 mm; 4. T_4 = 9.5 years, A_4= 929 mm; minor cycles: 1. T_1 = 7.3 years, A_1 = 541 mm; 2. T_2 = 6.1 years, A_2 = 308 mm.

The combined treatment of Mátra+Bükk data has also revealed 4 major and 2 minor cycles in the variation of annual precipitation values (*Figs. 4* and *5*),

cycle time and amplitude density: major cycles 1. T_1 = 5.0 years, A_1 = 1,139 mm; 2. T_2 = 3.5 years, A_2 = =1,119 mm; 3. T_3 = 29.2 years, A_3 = 1,080 mm; 4. T_4 = 9.7 years, A_4 = 860 mm; minor cycles 1. T_1 = 7.4 years, A_1 = 508 mm; 2. T_2 = 6.2 years, A_2 = 310 mm.

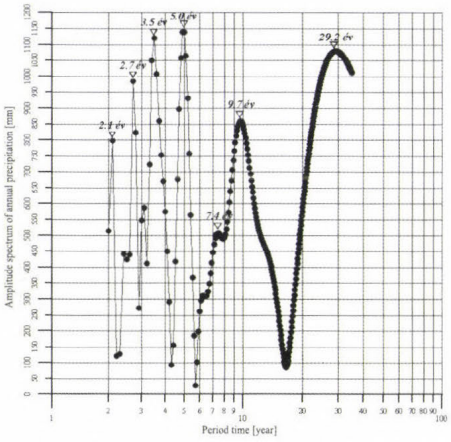

Fig. 4. Amplitude spectrum of annual precipitation int he Mátraalja and Bükkalja regions.(sampling rate = 1 year)

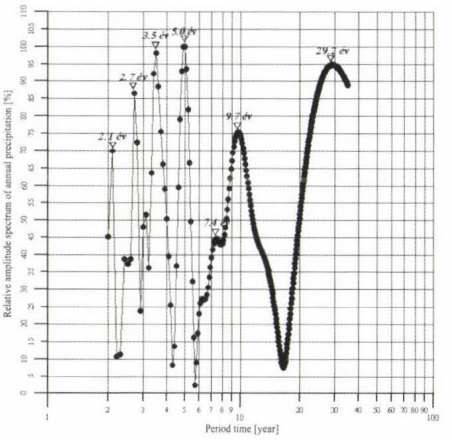

Fig. 5. Relative amplitude spectrum of annual precipitation in the Mátraalja and Bükkalja regions. (sampling rate = 1 year)

Cycle properties that can be revealed on the basis of the amplitude spectrum and relative amplitude spectrum detected in the variation of annual absolute maximum precipitation values, cycle time, and amplitude density for the Mátra region are the following: 1. T_1 = 3.5 years, A_1 = 1561 mm; 2. T_2 = 5.0 years, A_2 = 1434 mm; 3. T_3 = 10.9 years, A_3 = 1352 mm; 4. T_4 = 31.4 years, A_4 = 1262 mm; minor cycles 1. T_1 = 7.5 years, A_1 = 741 mm; 2. T_2 = 6.2 years, A_2 = 474 mm.

Cycle properties of the Bükk region are: major cycles 1. T_1 = 27.0 years, A_1 = 1408 mm; 2. T_2 = 3.4 years, A_2 = 1297 mm; 3. T_3 = 5.0 years, A_3 = 1168 mm; 4. T_4 = 9.7 years, A_4 = 973 mm; minor cycles 1. T_1 = 7.4 years, A_1 = 796 mm; 2. T_2 = 6.2 years, A_2 = 362 mm.

Cycle properties of Mátra and Bükk combined data on the basis of amplitude spectra (*Figs. 6* and *7*), cycle time, and amplitude density are the following: major cycles 1. T_1 = 3.5 years, A_1 = 1482 mm; 2. T_2 = 5.0 years, A_2 = 1413 mm; 3. T_3 = 30.3 years, A_3 = 1256 mm; 4. T_4 =11.1 years, A_4 = 1225 mm; minor cycles 1. T_1 = 7.5 years, A_1 = 734 mm; 2. T_2 = 6.2 years, A_2 = 298 mm.

On the basis of the above results, the following generalizations can be made:

— In the case of the six time series examined with respect to annual precipitation variation, cycles of approximately identical period times can be revealed.

— In the case of all the six time series, there have been found periods of 3.5 years, 5 years, 10–11 years, and 27–31 years as major cycles.
— In all the cases, 6.2-year and 7.3–7.5-year periods appear as minor cycles. (To prove the existence of 27–31-year cycles in a more reliable way, longer data series would be needed.)

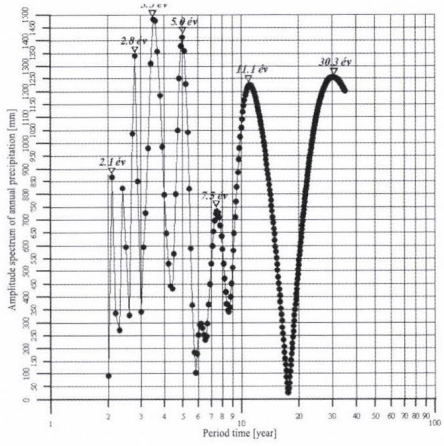

Fig. 6. Amplitude spectrum of annual precipitation in the Mátraalja and Bükkalja regions (sampling rate = 1 year).

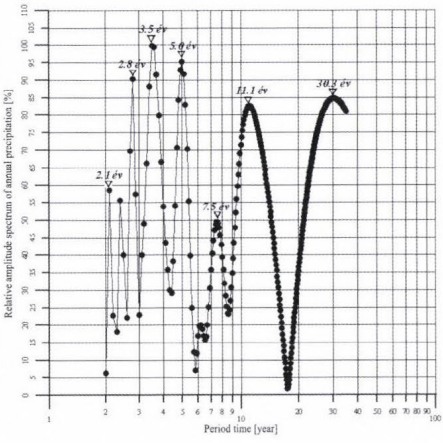

Fig. 7. Relative amplitude spectrum of the absolute maximum of annual precipitation in the Mátraalja and Bükkalja regions (sampling rate = 1 year.)

4.2. The results of spectral analysis on the basis of precipitation data in the years 1960-2012

The registration period is 1960–2012, the length of the registration period (T_{reg}) is 52 years with end sampling and 53 years with middle sampling, sampling rate (Δt) is 1 year, the number of samples is 53. The calculation process has been according to Section 4.1, the maximum period time that the analysis can reveal is T_{max} = 52 years – 53 years.

On the basis of amplitude peaks, the following precipitation cycles can be revealed for the Mátra annual precipitation values, cycle time, and amplitude density: major cycles T_1 = 5.0 years, A_1=2765 mm; 2. T_2 = 3.6 years, A_2 = 2074 mm; 3. T_3 = 41.1 years, A_3 = 1555 mm; 4. T_4 = 10.7 years, A_4 = 1494 mm; minor cycles 1. T_1 = 6.4 years, A_1 = 1101 mm; 2. T_2 = 5.7 years, A_2 = 1027 mm; 3. T_3 = 8.6 years, A_3 = 675 mm; 4. T_4 = 14.3 years, A_4 = =642 mm; 5. T_5 = 7.4 years, A_5 = 577 mm; 6. T_6 = 19.8 years, A_6 = 456 mm.

In the Bükkalja region, the following cycles can be revealed in the variation of annual precipitation values on the basis of amplitude spectrum and relative amplitude spectrum, cycle time, and amplitude density: major cycles 1. T_1 =

5.0 years, A_1 = 2567 mm; 2. T_2 = 38.6 years, A_2 = 1759 mm; 3. T_3 = 10.5 years, A_3 = 1747 mm; 4. T_4 = 3.6 years, A_4 = 1719 mm; minor cycles 1. T_1 = 5.7 years, A_1 = 1413 mm; 2. T_2 = 6.5 years, A_2 = 1220 mm; 3. T_3 = =14.2 years, A_3 = 753 mm; 4. T_4 = 7.5 years, A_4 = 552 mm; 5. T_5 = 8.4 years, A_5 = 504 mm; 6. T_6 = 19.8 years, A_6 = 323 mm.

The combined treatment of Mátra and Bükk data also reveals 4 major and 6 minor cycles on the basis of annual precipitation values (*Figs. 8* and *9*), cycle time and amplitude density: major cycles: 1. T_1 = 5.0 years, A_1 = 2685 mm; 2. T_2 = 3.6 years, A_2 = 1928 mm; 3. T_3 = 40.4 years, A_3 = 1635 mm; 4. T_4 = 10.6 years, A_4 = 1587 mm; minor cycles 1. T_1 =5.7 years, A_1 = 1188 mm; 2. T_2 = 6.4 years, A_2 = 1151 mm; 3. T_3 = 14.2 years, A_3 = 669 mm,;4. T_4 = 8.5 years, A_4 = 592 mm; 5. T_5 = 7.4 years, A_5 = 577 mm; 6. T_6 = 20.0 years, A_6 = 383 mm.

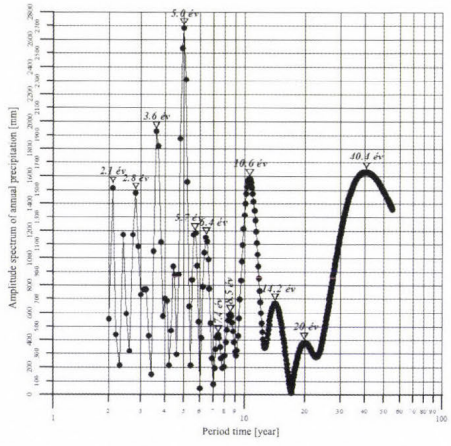

Fig. 8. Amplitude spectrum of annual precipitation in the Mátraalja and Bükkalja regions (sampling rate = 1 year).

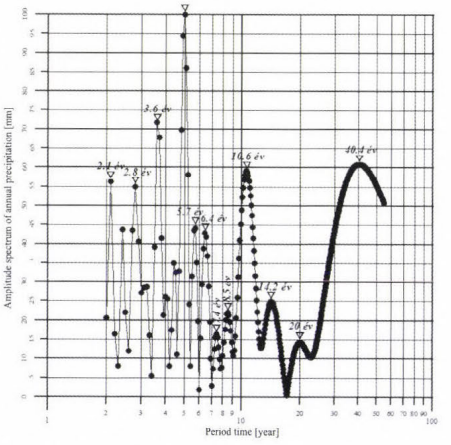

Fig. 9. Relative amplitude spectrum of annual precipitation in the Mátraalja and Bükkalja regions (sampling rate = 1 year).

The analysis of the absolute maximum values of annual precipitation reveals the following cycle properties on the basis of Mátra data, cycle time, and amplitude density: major cycles 1. T_1 = 5.0 years, A_1 = 3306 mm; 2. T_2 = 3.6 years, A_2 = 2656 mm; 3. T_3 = 45.6 years, A_3 = 2119 mm; 4. T_4 = 10.8 years, A_4 = 1806 mm; minor cycles 1. T_1 = 5.6 years, A_1 = 1319 mm; 2. T_2 = 6.4 years, A_2 = 1191 mm; 3. T_3 = 13.9 years, A_3 = 1044 mm; 4. T_4 = 7.3 years, A_4 = 1046 mm; 5. T_5 = 8.6 years, A_5 = 814 mm; 6. T_6 = 19.8 years, A_6 = 722 mm.

Similarly, 4 major and 6 minor cycles can be revealed on the basis of the Bükk-Bükkalja absolute maximum precipitation data, cycle time and amplitude density: major cycles 1. T_1 = 5.0 years, A_1 = 2646 mm; 2. T_2 = 38.6 years, A_2 = 2138 mm; 3. T_3 = 10.5 years, A_3 = 2024 mm; 4. T_4 = 3.6 years, A_4 = 1758 mm; minor cycles 1. T_1 = 5.6 years, A_1 = 1434 mm; 2. T_2 = 6.4 years, A_2 = 1351 mm;

3. T_3 = 14.0 years, A_3 = 885 mm; 4. T_4 = 8.4 years, A_4 = 883 mm; 5. T_5 = 7.3 years, A_5 = 445 mm; 6. T_6 = 19.4 years, A_6 = 454 mm.

Cycle properties of absolute maximum precipitation values cycle time, and amplitude density in the combined assessment of the Mátra+Bükk region (*Figs. 10* and *11*) are the following: major cycles 1. T_1 = 5.0 years, A_1 = 3,168 mm; 2. T_2 = 3.6 years, A_2 = 2468 mm; 3. T_3 = 46 years, A_3 = 2271 mm; 4. T_4 = 10.7 years, A_4 = 1842 mm; minor cycles 1. T_1 = 5.7 years, A_1 = 1273 mm; 2. T_2 = 6.4 years, A_2 = 1127 mm; 3. T_3 = 13.7 years, A_3 = 982 mm; 4. T_4 = 8.5 years, A_4 = 721 mm; 5. T_5 = 7.3 years, A_5 = 726 mm; 6. T_6 = 19.6 years, A_6 = 714 mm.

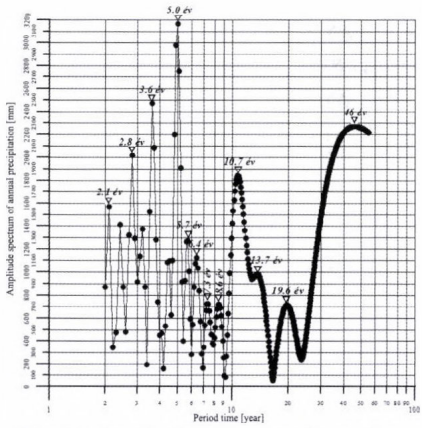

Fig. 10. Amplitude spectrum of annual precipitation in the Mátraalja and Bükkalja regions (sampling rate = 1 year) .

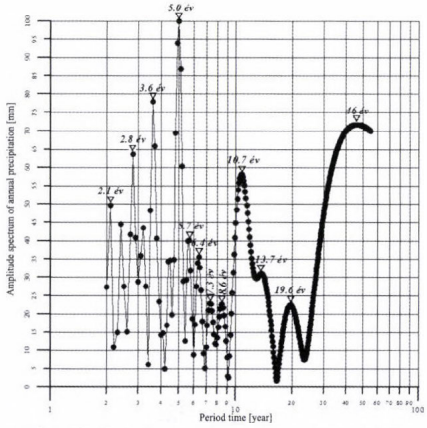

Fig. 11. Relative amplitude spectrum of the absolute maximum of annual precipitation in the Mátraalja and Bükkalja regions (sampling rate = 1 year) .

From the cycle properties determined on the basis of the data of precipitation time series of 53 years, the following generalizations can be made:

— Cycles of nearly identical period time can be revealed on the basis of the six time series investigated with respect to annual precipitation variation.

— In the case of all the six time series, the 3.6-year, the 5-year, the 10.5–10.8-year and 38.6–46-year periods appear as major cycles.

— In all the cases, the 5.6–6.7-year, 6.4-year, 7.3–7.5-year, 8.4–8.6-year, 13.7–14.3-year and 19.4–20-year periods appear as minor cycles.

The comparison of the cycle time data of the major and minor cycles revealed on the basis of the two time series of different lengths (34 years and 53 years) has yielded the following results:

— With all the three data groups, the number of major cycles that can be revealed on the basis of both time series is the same: four.

— In the case of the shorter time series, 2 minor cycles have been found for all the three data groups, while for the longer time series (53 years), 6 minor cycles have been revealed.

— With the shorter, generally maximum 10-year cycle times, practically identical/equivalent cycle time has been revealed for both the major and minor cycles, namely, in Mátra: 3.5–3.6 years, 4.9–5.0 years, 9.9–10.7 years, 6.3–6.4 years, 7.3–7.4 years,in Bükk: 3.5–3.6 years, 4.9–5.0 years, 9.5–10.5 years, in Mátra+Bükk: 3.5–3.6 years, 5.0–5.0 years, 9.7–10.6 years, 6.2–6.4 years, 7.4–7.4 years.

— In all the three areas, it has been identically found for longer cycle times (above 30 years) that on the basis of the 34-year time series, a shorter major cycle time, while on the basis of longer time series, a longer major cycle time has been revealed, namely, in Mátra: 29.8 years, 41.1 years, in Bükk: 28.7 years, 38.6 years, in Mátra+Bükk: 29.2 years, 40.4 years.

The differences found in the latter case confirm the former observation that for a long-time prognosis, a time (data) series longer than 50 years is required.

5. Determination of prognosis values

On the basis of Sections 2 and 3, including the summary of the basics of spectral data processing, the $y(t)$ time series of precipitation values can be restored through the 'use' of the $A(f)$ amplitude density and $\phi(f)$ phase density spectra, defined in the previous analyses:

$$y(t) = \overline{Y} + \int_{-f_N}^{+f_N} A(f) e^{j[2\pi ft + \phi(f)]} df ,$$

where f_N is the Nyquist frequency and it equals to 0.5 year^{-1}.

As the Fourier spectrum is even, the former equation can also be written up in the following form:

$$y(t) = \overline{Y} + \int_{o}^{+f_N} A(f) e^{j[2\pi ft + \phi(f)]} df .$$

With the use of the T_i (i = 1,2,..., N=10) period times of major and minor cycles, the A_i (i = 1,2,..., N = 10) amplitude, and the $\phi(T_i)$ (i = 1,2,..., N = 10) phase values, it is possible to define the $[y(t)^{det}]$ time series of the amount of precipitation attributable to deterministic causes:

$$y(t)^{\text{det}} = \overline{Y} + \frac{2}{T_{reg}} \sum_{i=1}^{10} A_i \cos\left[\frac{2\pi}{T_i}(t-1960) + \phi(T_i)\right].$$

Using the $\{R_e[F(T_i)]\}$ and $\{I_m[F(T)_i]\}$ values calculated for given T_i period times of real and imaginary spectra, the $\phi(T_i)$ phases of the specific components can be defined with the following correlation:

$$\phi(T_i) = arctg \frac{I_m[F(T_i)]}{R_e[F(T_i)]}.$$

The difference between the $y(t)$ actual time series and $y(t)^{det}$ represents the accidental (stochastic) impact.

If $t > 2012$ values are put in the former equation, the amount of precipitation that can be expected in the given years can be estimated (forecast) with extrapolation. It must be added, however, that this estimation would only yield a prognosis of 100% reliability by using spectra calculated from an infinitely large $y(t)$ registratum (annual data), which, of course, cannot be expected in the case of the 53 years long time series investigated.

Furthermore, there is a possibility of estimating periodicity with modern statistical methods (analysis with autocorrelation functions, factor and cluster analysis), although these tools would only give similarly precise results as the spectral analysis applied on the basis of data series of several hundred years.

Using the spectrum data in *Fig. 8*, taking into account the impact of the four deterministic major cycles (5, 3.6, 40.4, and 10.6 years) and taking into consideration the impact of the further 6 minor cycles in *Fig. 12* as well as that of the two cycles (2.1 years and 2.8 years) earlier omitted due to aliasing distortion, the prognosis values in *Figs. 13, 14* are obtained. According to *Fig. 4*, the two short cycles are present in the prognosis of annual precipitation values with a relatively high amplitude, above 55%, there has been a spectacular improvement in classic statistical indicators. Deviation (RMS) has decreased from 16.1% and 15.7% to 12.6%, while the correlation coefficient (r) has increased from 0.78 and 0.79 to 0.89.

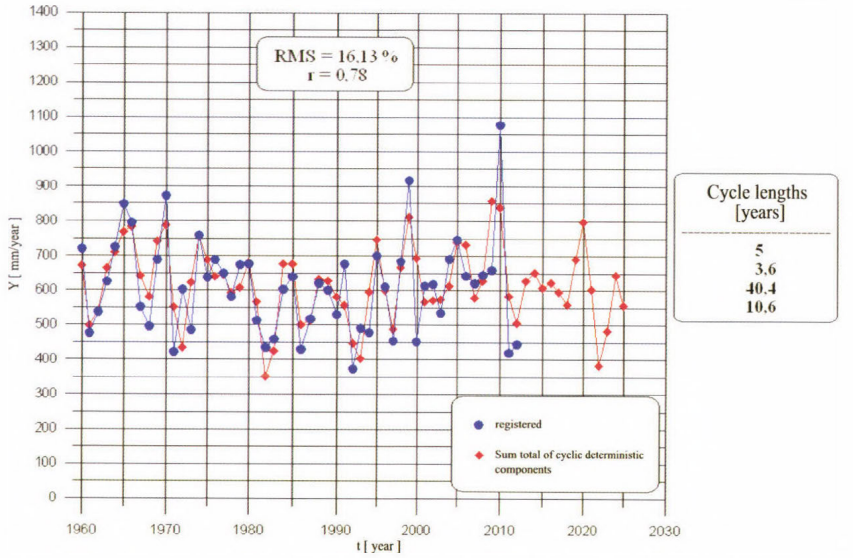

Fig. 12. Annual precipitation value in the Mátraalja and Bükkalja regions. (Prognosticated on the basis of four cyclic components.)

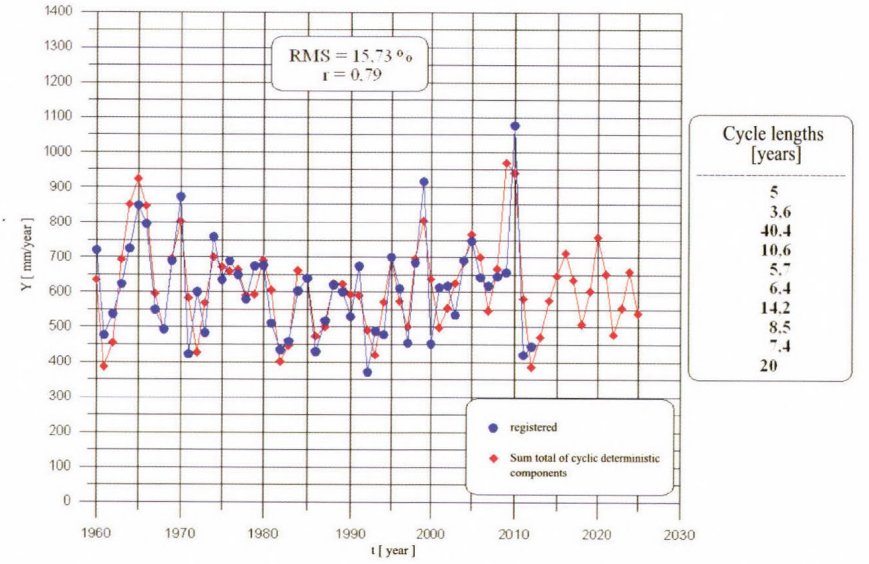

Fig. 13. Annual precipitation value in the Mátraalja and Bükkalja regions. (Prognosticated on the basis of ten cyclic components.)

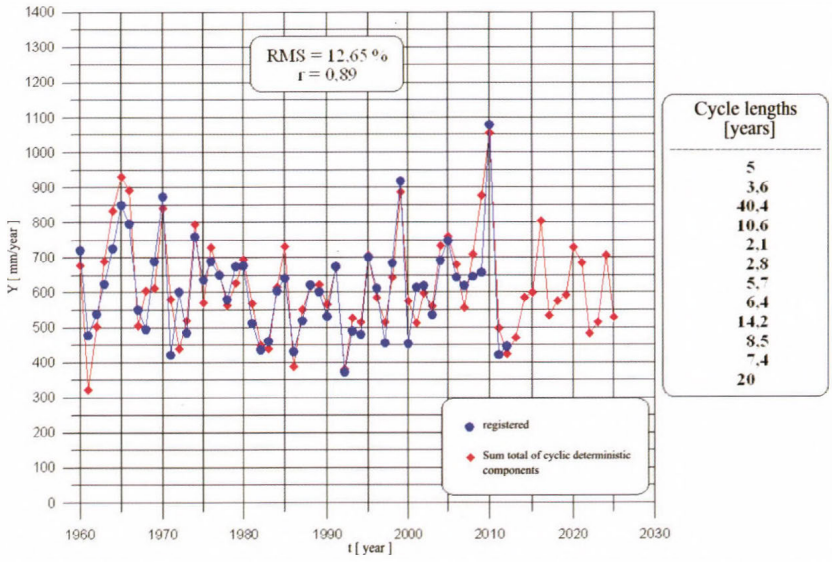

Fig. 14. Annual precipitation value in the Mátraalja and Bükkalja regions. (Prognosticated on the basis of twelve cyclic components.)

The amplitude data in *Fig. 10* and relative amplitude data in *Fig. 11* have been used in the calculation of annual absolute maximum precipitation prognosis. Taking the four deterministic and the further 6+2 cycle properties into account, the absolute maximum precipitation prognosis in *Figs. 15, 16,* and *17* has been obtained.

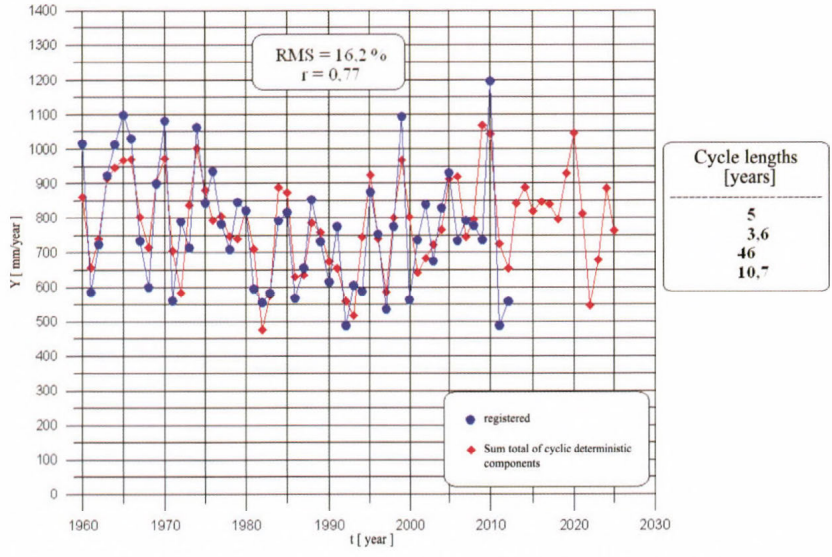

Fig. 15. Variation in the annual maximum of annual precipitation value in the Mátraalja and Bükkalja regions. (Prognosticated on the basis of four cyclic components.)

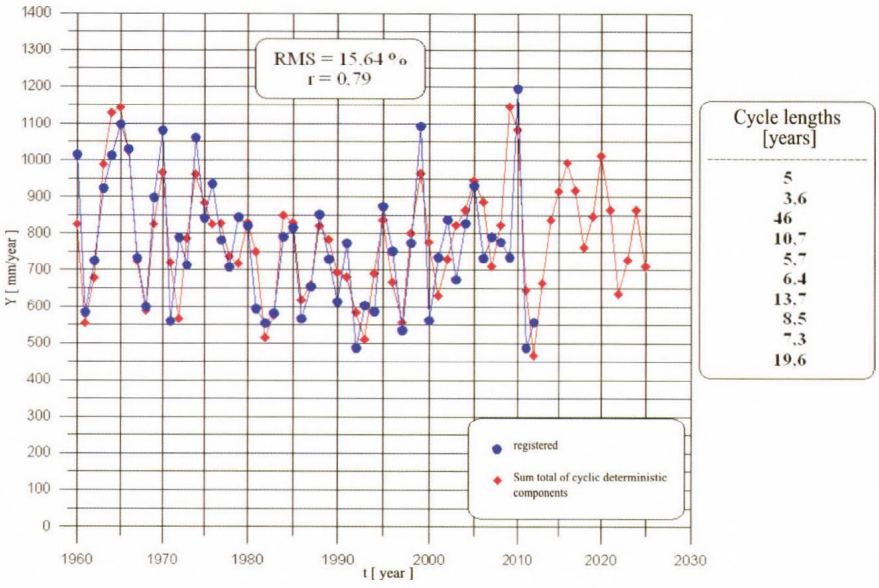

Fig. 16. Variation in the annual maximum of annual precipitation value in the Mátraalja and Bükkalja regions (Prognosticated on the basis of ten cyclic components.)

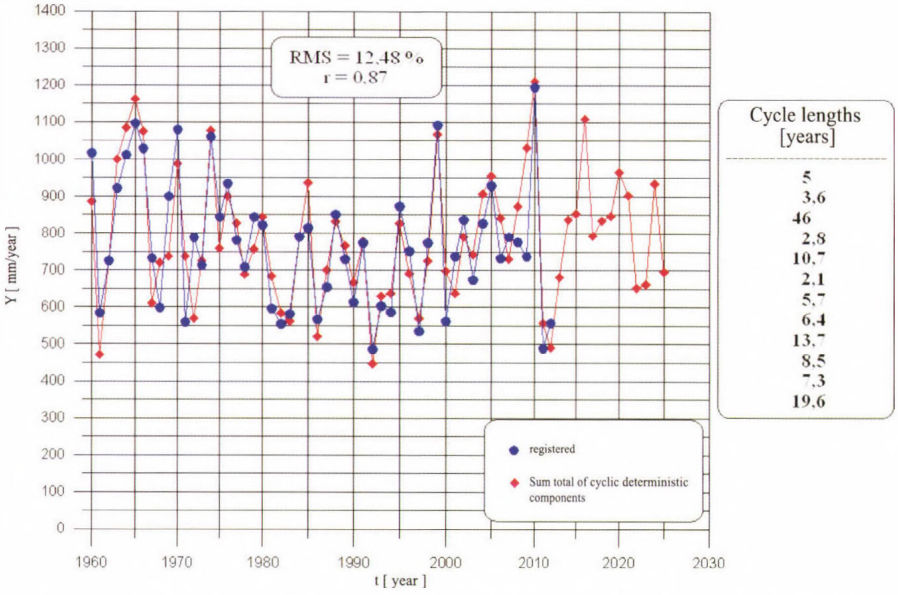

Fig. 17. Variation in the annual maximum of annual precipitation value in the Mátraalja and Bükkalja regions. (Prognosticated on the basis of twelve cyclic components.)

On the basis of the classical statistical parameters (RMS = 16.2%, r = 0.77) it can be concluded here, too, that between 1960 and 2012, the four deterministic major cycles decisively determined absolute maximums (*Fig. 15*). Taking the six minor cycles into account hardly improves classical statistical parameters (RMS = 15.6 %, r = 0.79) in this case, either, but the prognosticated sections in *Figs. 15* and *16* are significantly different here, too. Taking into account the two short cycles (2.1 years and 2.8 years), also appearing here with a high amplitude, has considerably improved classical statistical indicators (RMS = 12.5%, r = 0.87) (*Fig. 17*).

On the basis of the data in *Fig. 14*, for the purpose of practical utilisation it can be underlined in the prognosis, that the exceedingly high, 1079 mm/year amount of precipitation of 2010 – a uniquely high value in the last 53 years – will not recur in the next 12–15 years. The 850–900 mm/year annual precipitation, having occurred several times in previous years (1965, 1970, 1999) may 'probably be expected' in 2016. On the other hand, it is good news that in the coming 12–15 years, no annual precipitation below 500 mm/year, causing severe drought, may be expected.

The 1100 mm/year maximum precipitation prognosticated for 2016 (see *Fig. 17*), remains 100 mm/year below the round 1200(1195) mm/year value of 2010 but may reach the 1100 mm peak data of the years 1965, 1970, 1974, and 1999.

6. Variation in time of precipitation properties between the years 1960 and 2025

With the combined handling of the actual data for the years 1960–2012, presented in *Table 1* and *Figs. 14* and *17*, and the prognosis data in *Figs. 14* and *17* related to the Mátra+Bükk region, the time function of the variation of annual precipitation, and the absolute maximum precipitation values for the years 1960–2025 have been determined with the conventional statistical method.

The function in *Fig. 18* shows a constancy of 620–605 mm/year of annual (average) precipitation with 0.23 = 23% empirical deviation ($D_{deg}/Y_{average}$). The correlation coefficient characterizing the closeness of the function determined from the data of the 65-year time series is $r^2 = 0.00048$, which indicates the independence of the two variables of annual precipitation (average) and time (years) according to conventional statistical interpretation.

Fig. 19 shows the regression function determined on the basis of actual and prognosed annual absolute maximum precipitation data between the years 1960 and 2025. With an acceptable (reliable) 19% corrected empirical deviation and a $r^2 = 0{,}00027$ regression coefficient, the function predicts the constancy of the annual absolute maximum in the statistical sense while, for example, it predicts a 1100 mm precipitation maximum for 2016.

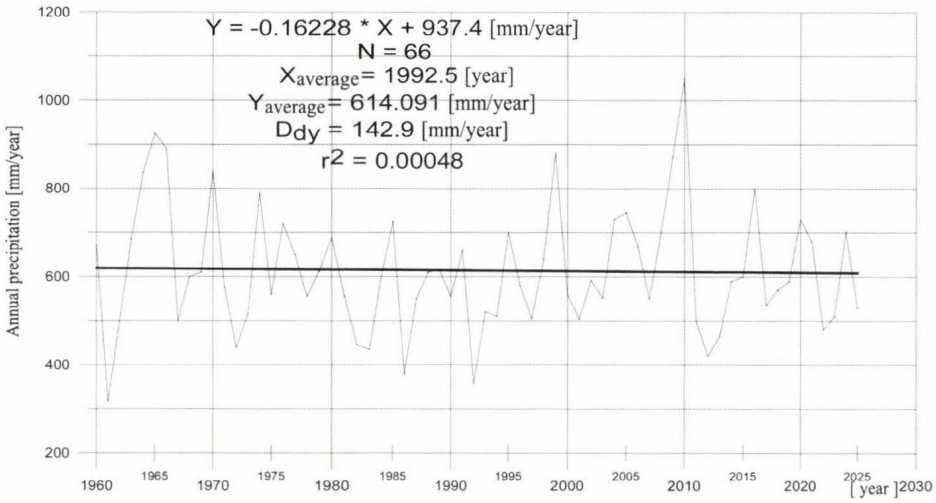

Fig. 18. Regression function of the variation in time of the annual precipitation conditions (1960-2012) and prognosis data (2013-2025) of the Mátra-Bükkalja region.

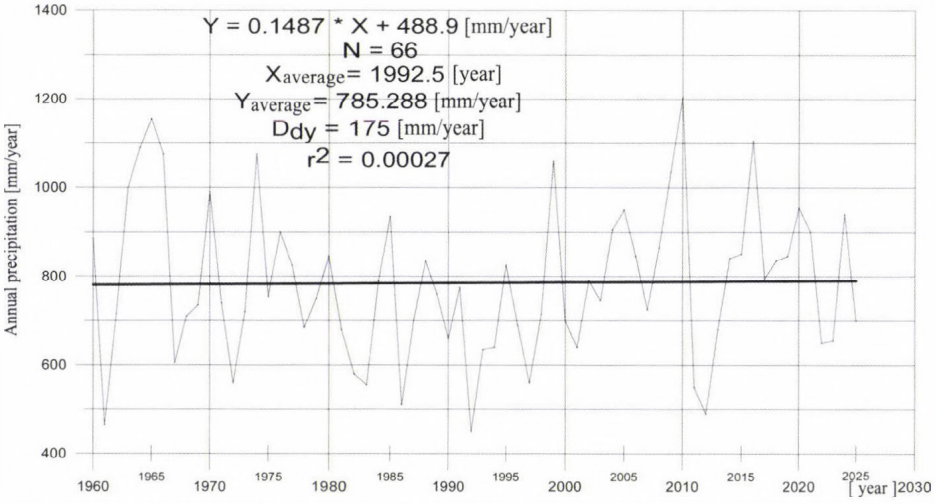

Fig. 19. Regression function of the variation in time of the annual absolute maximum precipitation properties (1960–2012) and prognosis data (2013–2025) of the Mátra-Bükkalja region.

Acknowledgements: The research was carried out in the framework of the Sustainable Resource Management Centre of Excellence at the University of Miskolc, as part of the TÁMOP-4.2.2/A-11/1-KONV-2012-0049 „WELL aHead" project in the framework of the New Széchenyi Plan, funded by the European Union and co-financed by the European Social Fund.

References

INNOCENTER, 2013a: A Mátra-Bükkalja csapadék jellemzőinek meghatározása, a csapadék jellemzők időbeli alakulása. Kutatási részjelentés a Mátrai Erőmű Zrt. részére, 2013. augusztus. (in Hungarian)

INNOCENTER, 2013b: A Mátra-Bükkalja csapadék jellemzői ciklikus változása, prognózis módszer kidolgozása. Kutatási részjelentés a Mátrai Erőmű Zrt. részére, 2013. augusztus. (in Hungarian)

Kovács, F., 2014: A Mátra-Bükk-i terület csapadék jellemzőinek alakulása az utóbbi ötven évben (1960–2012). *Bányászati és kohászati lapok. Bányászat 147*, 2–6 (in Hungarian)

Meskó, A., 1984: Digital Filtering. Akadémiai Kiadó, Budapest

Szűcs, P., 2012: Hidrogelógia a Kárpát-medencében – hogyan tovább? *Magyar Tudomány 173*, 554–565. (in Hungarian)

Turai, E., 1983: A Fourier transzformáció egy numerikus módszere és alkalmazása a GP-jelenség rendszerelemző függvénnyel történő leírásánál. *Magyar Geofizika XXIV*, 11–19.

IDŐJÁRÁS

Quarterly Journal of the Hungarian Meteorological Service
Vol. 119, No. 1, January – March, 2015, pp. 91–109

Analyzing long-term evapotranspiration of Lake Fenéki wetland (Kis-Balaton, Hungary) between 1970 and 2012

Angéla Anda[1*], Katalin Nagy[2], Gábor Soós[1], Tamás Kucserka [1]

[1]*Pannon University Georgikon Faculty,*
Department of Meteorology and Water Management
Festetics u. 7, H-8360 Keszthely, Hungary

[2]*West-transdanubian Water Inspectorate,*
Vörösmarty u. 2, H-9700 Szombathely, Hungary

**Corresponding author E-mail: anda-a@georgikon.hu; anda@keszthelynet.hu*

(Manuscript received in final form March 12, 2014)

Abstract—The aim of the study was to estimate long term evapotranspiration (ET) of Kis-Balaton wetland through the investigation of Lake Fenéki. Data set was processed using the West-transdanubian Water Inspectorate methodology. Potential evapotranspiration (PET) was calculated using Hungarian empirical models (*Antal* and *Dunay*), while Lake Fertő formula was applied evaluating the ET that includes the impacts of vegetation.

Calculated PET values of the wider (adjacent) environment of Lake Fenéki (Zalaegerszeg, Nagykanizsa, and Keszthely meteorological stations) differed significantly and further variation was observed in PET, when measured meteorological elements on Lake Fenéki were applied. PET increment, as a result of linear trend fitted to the 43-year long data (Keszthely station) was 3–4 mm year^{-1}. Relation between PET calculated from the data of Keszthely station and for Lake Fenéki was strong, so PET of Lake Fenéki can be originated from the data of Keszthely station. Calculated ET was not significantly different due to the likely similar input data in ET calculation model of Hungarian Meteorological Service (OMSZ).

43-year annual mean ET for Lake Fenéki was 809±88 mm. This ET was 84% of calculated PET. Analyzing the nine dry-warm seasons, average annual ET exceeded the long term average (874.7±37.6 mm) with 78 mm. The average ET of the remaining 34 wet-cold seasons totalled 796.6±89.4 mm.

Empirical formulas cannot be replaced, according to monthly ET comparisons, by using "A" class pan estimating the ET of aquatic habitats.

Seasonal pattern of monthly ET time series for Lake Fenéki was analyzed using autoregressive integrated moving averages (ARIMA) modeling technique. After first differencing, the transformed series was stationary and found to be governed by moving average process of order 1.

Key-words: wetland evaporation, potential evapotranspiration, seasonal ARIMA, Kis-Balaton wetland (Lake Fenéki)

1. Introduction

Kis-Balaton is a large, continuous wetland. It used to belong to Lake Balaton (Western bay). In 1863, suitable circumstances turned up to control the water level more or less separately from meteorological conditions (*Harkay*, 1983; *Virág*, 1997). Prior to the opening of the Sió-sluice in 1863, the water level of Lake Balaton was determined by the prevailing weather conditions. When the sluice gate of Channel Sió was built, the natural fluctuation of water level decreased to 0.5 m or less (earlier the fluctuation of water level could be as high as 3–5 meters). In the first part of the 19th century, the water level of Lake Balaton was lowered in several steps, therefore, the higher areas of the Kis-Balaton basin dried out. The water level turned to 2–3 m lower than the water level of the ancient lake (*Kovács et al.*, 2010; *Hatvani et al.*, 2011). The surface of Kis-Balaton wetland became smaller, water cover of higher parts disappeared, and it appeared again when River Zala flooded. In the 1920's banks were built to both sides of River Zala. As a consequence of the regulation, the Kis-Balaton and other surrounding marshes lost their function to protect the water quality of Lake Balaton. It was strengthened by the consequences of civilization, i.e., intensive agricultural chemicalization, increasing urbanization, developing and spreading of holiday resorts in the region, which altogether resulted in the significant deterioration of quality of waters entering Lake Balaton. This marsh supplied an ideal habitat for plants and animals preferring aquatic habitats. As the area became drier, the surface of the marsh got smaller (*Nguyen et al.*, 2005). At the deepest part – close to Island Diás –, two small lakes and the surrounding reed (about 1400 ha) remained behind. This area is under strict protection according to *Ramsar Convention* (1971). Because of the regulation works, the water protecting function of Kis-Balaton and the ambient groves ended.

In the 1960–70's, especially in Keszthely Basin, water quality of Lake Balaton notably decayed (*Istvánovics et al,.* 1997; *Padisak* and *Reynolds*, 2003), so a resolve was made about the artificial reconstruction of the marsh (Kis-Balaton Water Protection System, KBWPS) and the restitution of the water protecting function of Kis-Balaton (*Pomogyi et al.*, 1996; *Tátrai et al.*, 2000). Construction works began in 1981, the Stage 1, called Lake Hídvég, was constructed between 1981 and 1985 (*Korponai et al.*, 2010).

Due to economic reasons, the construction did not follow the planned timing, so in behalf of water quality of Lake Balaton a makeshift was made. In 1992, the north-northwest part of Lake Fenéki was flooded. The area was called Grove Ingói (16 km^2).

Constructions were made at the non-flooded area of Lake Fenéki as well (outer reservoir). The water of Zala-Somogy border ditch and the Marótvölgyi Channel was led to this area. One part of the effluent water from Lake Hídvégi – mostly in case of fill of water – was directed to the non-flooded area. This

caused a temporary flood and reservation. Complete construction of the Kis-Balaton Water Protection System Stage 2 is still in process (Project KEOP 2.2.1/2F/09-2009-0001). In 2015, the flood of outer reservoir is expected to happen. Coordination of water quality protection, conservation, flood and water conservation objectives and tasks is going to occur in the project.

In case of flow-through lakes (like Kis-Balaton), inflow and outflow are the most important members of the water balance. In Lake Fenéki, this value can be as high as 90% on annual basis. Although the share of evaporation is usually just under 10%, accurate estimation of evapotranspiration (*ET*) is important, because during summer – in the lack of notable flood – it can reach 30–70% of inflow and outflow. Typically, in case of low water conditions, it is problematic prescribing the water balance.

Evaporation is a major energy-consuming physical phenomenon, which can be significantly affected by climate change (*Novaky*, 2005). To refine the hydrological and climatic forecasts, it is necessary to estimate evaporation irrespectively of the other members of water balance equation.

There are only a very few studies which determine *ET* in the area of Kis-Balaton. Hungarian researchers have investigated only the *ET* of bigger lakes (*Havalda,* 1930; *Szesztay*, 1962; *Antal,* 1968; *Antal et al.,* 1977; *Varga,* 2005; *Varga et al.,* 2007).

This research aims to overview the practice of *ET* calculation used by the Inspectorate for Water Management for decades, and to produce a long time series *ET* dataset for Lake Fenéki. Time series is a collection of quantitatively measured data evenly spaced in time. Analysis of the time series is important to understand the structure and functioning of observed data. Time series analysis allows a mathematical model to be built in order to discuss the data trend (*Box et al.,* 2008; *Brockwell* and *Davis*, 2001; *Psilovikos* and *Elhag*, 2013). The autocorrelation elements of the data were extracted using ARIMA to model the underlying wetland evaporation trend more precisely.

2. Materials and methods

Our study aimed ET of Lake Fenéki (46°38'N, 17°11'E, altitude 194 m, area 54–57 km^2), which is situated in the natural valley of River Zala between Balatonhídvég and the mouth of Zala, and it is the planned reservoir of the Kis-Balaton Water Protection System Stage 2. On the northern part of the reservoir, water is kept by the southern watertight dam, on the western part by the Zalavár dam. On the east side, Zala valley is closed 3.5 km wide by the valley occlusion parallel with the railway line (*Fig. 1*).

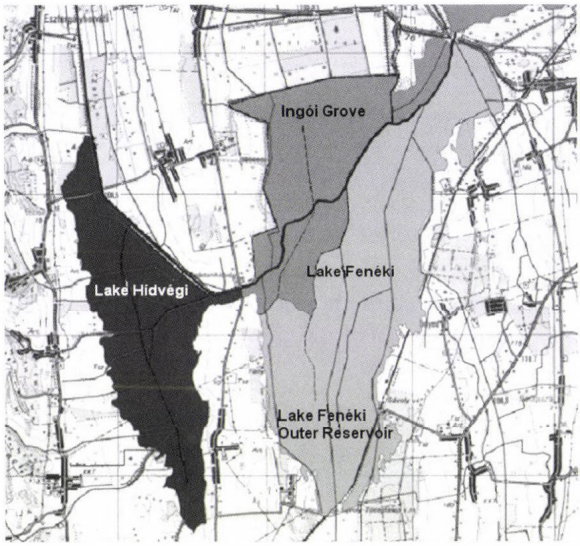

Fig. 1. The Kis-Balaton wetland including the site of the study, the Lake Fenéki (Fenéki Outer Reservoir and Grove Ingói).

When KBWPS was created, quantitative recording of its water budget has also begun with the traditional water balance equation, which includes the basic characteristics of water movements (*Zsuffa,* 1996). Members of the equation were determined from 1986 for Lake Hídvégi. In the case of Lake Fenéki, first calculations were made only after constructions have been completed, measuring points were installed, and the northwest part was flooded. Monthly water balance calculations for Grove Ingói and Lake Fenéki Outer Reservoir had started since 1993 and 2003, respectively. On the input side, the natural inflow (H), the precipitation (C), and the amount of water pumped (SZ) were taken into account, while on the output side, the outlet (L) and ET were listed. The change in water resources (ΔK) was calculated from the increase or decrease of the water level using the volume curve edited by the West-transdanubian Water Inspectorate. Subsurface water movements (inflow, leakage) are usually not quantified due to its negligible extent.

Water balance for Kis-Balaton (in the case of the three parts: Lake Hídvégi, Grove Ingói, and Lake Fenéki Outer Resevoir) is calculated separately in the following form:

$$(C + H + SZ) - (ET + L) \pm \Delta K = 0. \qquad (1)$$

In the present study, our aim was to determine the evaporation of Lake Fenéki (Grove Ingói + Lake Fenéki Outer Reservoir). Methods for calculating

ET for Hungarian areas are presented in numerous studies (*Tölgyesi*, 1993; *Kontur et al.,* 1993). When choosing a method, it is an important aspect, that data should be available from the regional meteorological parameters. The investigated period is 1970–2012, 43 years altogether. From the beginning of this period, meteorological measurements in the area of Kis-Balaton were made only at the stations in Zalaegerszeg, Keszthely, and Nagykanizsa. From these observations, air temperature and humidity data were available from 1970.

Wind speed and global radiation were available from the latter time. The West-transdanubian Water Inspectorate established automatic hydrometeorological stations (Balatonmagyaród Fekete Island, Balatonmagyaród beach 4T, Balatonmagyaród Almás Island, Keszthely-Fenékpuszta 21T) from the end of the 1990's. Air temperature, relative humidity, wind speed, and solar radiation were measured there. The data of the evaporation pan ("A" pan) at Balatonmagyaród beach 4T station are continuous from 1998.

The used data were as follows:

- Zalaegerszeg, Nagykanizsa (1986–1995): monthly potential evapotranspiration (*PET*) and *ET* based on the calculations of OMSZ (Hungarian Meteorological Service) (see later);
- Keszthely: monthly *PET* and ET (1970–1996; 2002–2012) on the basis of the OMSZ dataset;
- Keszthely: daily average temperature, relative humidity (1970–2012);
- Balatonmagyaród beach 4T, Balatonmagyaród Almás Island, Keszthely-Fenékpuszta 21T: daily average temperature, relative humidity, average wind speed (1993–2012).

Evaporation values (*PET, ET*) calculated by the operational soil moisture model (*Dunay,* 1993) developed for agrometeorological purposes was applied in this study. Data were taken from related OMSZ publications.

The long record of PET was approached in two ways. The Antal-formula which was developed for potential evapotranspiration in Hungarian climate conditions (*Antal*, 1968) was approached with the meteorological data of Keszthely for the whole period:

$$PET = 0.9(E - e)^{0.7}(1 + \alpha t)^{4.8} n \quad [mm / month], \tag{2}$$

where E is the saturation vapor pressure [hPa], e is the vapor pressure [hPa], α=1/273, t is the average air temperature [°C], and n is the number of the days in the month.

Monthly evaporation values were summarized annually. In the other method (earlier referenced as operational soil moisture model), data were taken from OMSZ agrometeorological publications for 1970–1996 on monthly basis. Data of 2002-2012 were summed from decade calculations for the water sector. For supplying the missing monthly data, we used linear regression using the

monthly values of the Antal-formula. Correlation before the supplement was 0.972.

For calculating *ET* at Kis-Balaton instead of developing a new "Kis-Balaton formula", which fits the local conditions, experts suggested using the Antal-formula for the determination of evaporation loss, although it was developed for Lake Fertő. The reason was that reed cover of both lakes was extensive. For water balance calculations, monthly *ET* was determined using the Lake Fertő formula for Grove Ingói as well:

$$ET = 0.42(E-e)^{0.9}(1+\alpha t)^{9}(1+0.015\cdot u)^{2}n \quad [mm/month], \tag{3}$$

where u is the monthly average wind speed [m/s]. To create this equation, energy balance measurements were made.

Evaporation increasing effect of wetland vegetation was taken into account with correction factors (crop coefficient) from April to October according to *Table 1*.

Table 1. Monthly average of crop coefficients for Kis-Balaton wetland

	Apr	May	Jun	Jul	Aug	Sep	Oct
Crop coefficients	1.02	1.11	1.2	1.26	1.21	1.13	1.11

For determination of local evaporation at Lake Fenéki Outer Reservoir, the method developed by *Dunay et al.* (1968) was used, which is based on "A" pan measurements:

$$ET = (100-H_{\%})(200-H_{\%})^{-1}\cdot t\cdot n \quad [mm/month], \tag{4}$$

where $H_{\%}$ is the monthly mean of relative humidity (%).

In hydrological practice, the water balance equation equals to 0, as the sum of positive and negative amounts. The expert calculating the equation needs a lot of data as many times as estimations are required. Flow rate of bigger streams is measured, some of them in every 15 minutes, but weekly or monthly measures are more common. At the most segments, water level series is created measuring the water level frequently, which is transformed into runoff time series. Integrating this series in time allows calculating the amount of inflow. Smaller streams are estimated based on hydrological analogy. At the outflow of Lake Fenéki (into Lake Balaton), some problems can temporarily occur because off

the strong upwind. In this case, an inverse circulation shows up at the surface and a kind of pulse is registered while measuring runoff. This phenomenon can be caused by the seiche of Lake Balaton. The quantification and determination of its effect on the amount of runoff should be solved in the future. In the case of precipitation over the lake, data of some precipitation gauges are considered. The precipitation of the 75 km^2 surface is calculated from the data of 3–6×200 cm^2 surfaces. Neither the surface nor the volume curves are renewed, although at some parts of Lake Hídvégi, sedimentation has begun. Curves of Lake Fenéki are sensitive; they change significantly in the error limit of water level registration. Accurate inventory of evaporation loss is not resolved, estimations containing error use of crop coefficients makes the review of vegetation rough. All of these can lead to significant errors. Experience has shown that water balance calculations are more difficult in the case of lower water level.

In a time series, within a normal data distribution, a two-tailed t-test was applied. To compare differences, when the Shapiro-Wilk normality test indicated a non-normal distribution, a non-parametric statistical hypothesis test, the Wilcoxon signed-rank test was used (SPSS Statistics v. 17.0; IBM Corp., New York, USA). To compare between daily *PET*s calculated on locally measured data observations at Keszthely, a linear regression ($y = a + bx$) was carried out, in which local *PET* was used as the dependent variable y and *PET* of Keszthely was the independent variable x. The fitness of curve was acceptable when the slope forced through the origin of the regression was close to 1 (*Alexandris* and *Kerkides*, 2003).

The purpose of the study was to develop ET prediction for Lake Fenéki. Originally the Box-Jenkins models were used for time-series analysis (*Box* and *Jenkins*, 1976) in the form of a seasonal auto-regressive integrated moving average (ARIMA(p,d,q)(P,D,Q)$_s$) model.

Box and *Jenkins* (1976) recommended the following general model:

$$\phi_p(B)\Phi_P(B)(1-B)^d\left(1-B^s\right)^D X_t = \theta_q(B)\Theta_Q\left(B^s\right)\alpha_t, \tag{5}$$

where d is the order of differencing, s is the length of the season, and D is the order of seasonal differencing.

The operator polynomials are as follows:

$$\phi_p(B) = \left(1-\phi_1 B - \ldots - \phi_p B^p\right), \tag{6}$$

$$\theta_q(B) = \left(1-\theta_1 B - \ldots - \theta_q B^q\right), \tag{7}$$

$$\Phi_p\left(B^s\right) = \left(1-\Phi_1 B^s - \ldots - \Phi_p B^{sp}\right), \tag{8}$$

$$\Theta_Q\left(B^s\right) = \left(1-\Theta_1 B^s - \ldots - \Theta_Q B^{sQ}\right), \tag{9}$$

$$(1 - B^s)X_t = X_t - X_{t-s}. \quad (10)$$

Among others, *Meshram et al.* (2011) applied seasonal ARIMA model to project evaporation for India (Solapur Station). The original *ET* time series for Lake Fenéki has not demonstrated any trend; data exhibited numerous peaks, which appeared to be equally spaced. This phenomenon suggested the presence of a periodic component to the time series, where the peak took place in the growing seasons.

To determine ARIMA model for time series analysis and produce forecasts, the SPSS 17.0 statistical program was applied. The program includes an expert modeler modul that automatically estimates the best-fitting ARIMA model, eliminating the need to identify an appropriate model through trial and error.

There are three basic terms of ARIMA models; auto-regression (AR), differencing or integration (I) and moving-average (MA) components. Although these components respond differently to a random disturbance, they are based on the concept that they may be described by ARIMA models. Since time series showed seasonality, the seasonal ARIMA $(p,d,q)(P,D,Q)_s$ orders were presented. An effective approach for isolating seasonal orders is to calculate the autocorrelation functions (ACF) and partial autocorrelation function (PACF) plots at the seasonal lags (http://www.spss.com). The number of spikes showed the order of auto-regression.

3. Results and discussion

The Kis-Balaton lake system, in which Lake Hídvégi is about 18 km^2, is typically an open water area (85%). The cover of marsh vegetation is about 15%. The area of Grove Ingói is about 16 km^2. The distribution of open water, reed, bulrush, and sedge shows a mosaic structure. Here, the share of open water is only about 15%. The Lake Fenéki Outer Reservoir – the non-flooded area – is about 41 km^2. The permanent water cover is low, about 1–2%, but temporarily it can be higher (even almost the whole area), belonging to the shallow water covered, wetland types.

A ten-year period was chosen to overview the evaporation conditions of the wider environment, which includes our study site as well. The calculated monthly values of *PET* and *ET* between 1986 and 1995 at the three sites near Lake Balaton (Keszthely, Zalaegerszeg, Nagykanizsa) matched only in respect of *ET*. *PET* values of the three stations differed significantly ($p \leq 0.0001$). The annual sums ranged between 840 and 1120 mm. The average of the ten years is the highest in Kesztely (1060 mm) as expected. This is followed by Zalaegerszeg (1025 mm) and Nagykanizsa (940 mm). Monthly maximum of *PET* occurred in August 1992 (245 mm) in Keszthely. The

maximum of *ET* (144 mm) calculated by the OMSZ operational soil moisture model occurred in July 1991, the annual sums are between 460 and 760 mm, but the differences are not significant ($p \leq 0.064$–0.502), while the average of the 10 years is about 630 mm from the values of the three stations. Even when the *ET* values from OMSZ operational soil moisture model are accepted for the wider environment, they are not applicable for Kis-Balaton because off its moist endowments. *ET* values of wider environment are surmised to be underestimated.

Data from Keszthely was included in the *PET* studies for the longer period (1970–2012), since this is the closest station to the study area (Kis-Balaton) and it is situated at the side of the prevailing wind direction.

In the first step, *PET* values for Kis-Balaton between 1970 and 2012 were determined by the Antal-method, and they were compared to the results of OMSZ operational soil moisture model. *PET* of Kis-Balaton was determinable between 1993 and 2012 by Antal-formula with locally measured data. Correlation coefficient of calculated annual *PET* between using the Antal-formula and the soil moisture model of the OMSZ was acceptable, 0.781. It should be noted that in this period in the last, shorter section (1994–2012), the correlation coefficient was much higher (0.936). The stronger correlation can be explained by changes in observation methodology (from the early 90s, the manual observation was replaced by automatic weather stations). Looking at the annual *PET* data series (*Fig. 2*) it can be stated, that the nature of changes is similar, differences among the three curves are small, but sometimes significant. The annual *PET* calculated from the data of Keszthely is 5.2% ($p \leq 0.012$) higher than the *PET* calculated from the data of Kis-Balaton. Similarly, PET calculated from the OMSZ soil moisture model is 4.1% ($p \leq 0.008$) lower, than *PET* calculated from the data of Keszthely. There was no significant difference between *PET* calculated from the local data of Kis-Balaton and the data of the OMSZ model ($p \leq 0.54$). The difference between the annual *PET* sums from the two procedures is within ±140 mm. Values calculated from the data of Kis-Balaton headed between the two other curves, close to them. Years between 2000 and 2003 should be highlighted. At this period (very hot and dry), the values calculated from the local data are much lower. *PET* values based on local data were the lowest of all; the Antal-formula and the OMSZ operational soil moisture model exceeded *PET* with 110–261 mm and 73–167 mm, respectively. The reason might be the higher humidity values in the area of Kis-Balaton (wetland).

The slope of linear trend fitted to the data of the 43 years calculated for the data of Keszthely showed 3.7 mm increment per year ($p \leq 0.004$), while according to the OMSZ model it is 2.8 mm increase per year ($p \leq 0.046$). The linear trend forecast fitted to the data of Kis-Balaton was not significant ($p \leq 0.197$).

The most important statistical indicators of *PET* data set calculated by different approaches are summed in *Table 2*.

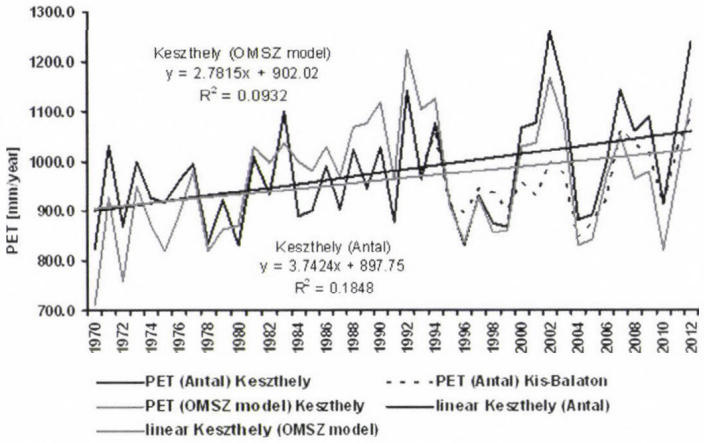

Fig. 2. Comparison of potential evapotranspiration (*PET*) calculated by using data of (i) Keszthely [*PET* (Antal) Keszthely]; (ii) the soil moisture model of the OMSZ (Hungarian Meteorological Service), and (iii) locally measured meteorological data [*PET*(Antal) Kis-Balaton]. We expressed PET after empirical equation processed by *Antal* (1968).

Table 2. Statistical parameters of potential evapotranspiration (*PET*)

	Avg.	Min.	Max.	SD	CV%
PET (Antal) Keszthely (1970–2012)	980	824	1261	109	11%
PET (Antal) Kis-Balaton (1993–2012)	963	844	1089	68	7%
PET (OMSZ model) Keszthely (1970–2012)	963	711	1224	114	12%

The monthly variation of *PET* within the year was analyzed, too (*Fig. 3*).

The maximum monthly *PET* was expected in July, the minimum in December. The difference between the two calculation methods was 7–10 mm in March, September, October, and under 6 mm in the other months. The share of the season from the annual PET was 740 mm, 75%.

Correlation among *PET* values calculated from the data of Keszthely and Kis-Balaton was very strong between 1993 and 2012, the correlation coefficient was 0.998. Thus the data of Keszthely can be converted into the data of Kis-Balaton (*Fig. 4*). There was no significant *SE* when the monthly evaporation sum was below 50 mm, however when it exceeded 100–150 mm, the *SE* was much higher weakening the accuracy of *ET* estimation.

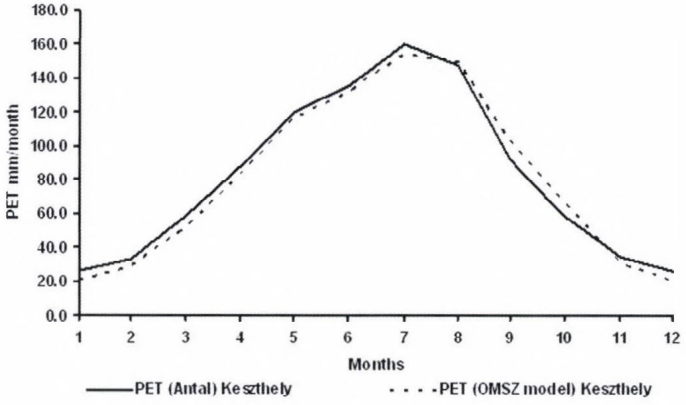

Fig. 3. Monthly means of potential evapotranspiration of Keszthely using the Antal-formula and the soil moisture model of the OMSZ between 1993 and 2012.

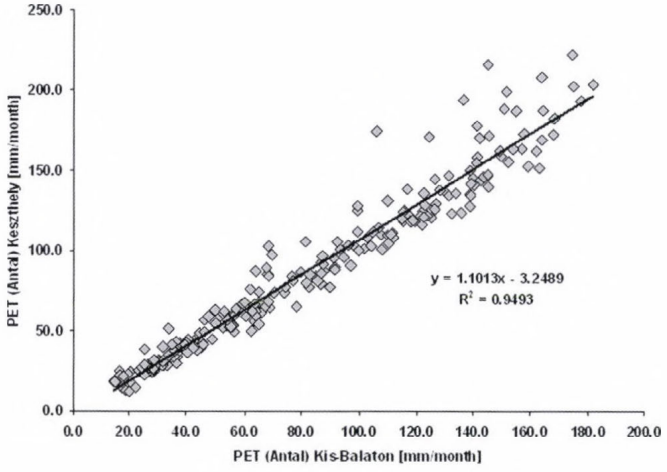

Fig. 4. Relationship between monthly calculated evapotranspiration from Keszthely meteorological data and locally measured meteorological data. To calculate *PET*, the Antal-formula was applied. The number of observed pairs was 240.

The estimation of *ET* for the area is a much more complex task, than the *PET* projection. Evaporation loss of water covered parts in the evaporation of Lake Fenéki is considered close to the potential, while at non-flooded parts, *ET* data seems to be useable. The *ET* of Lake Fenéki calculated by the OMSZ soil moisture model was not acceptable on annual basis (this model has been

developed for average soil conditions, not for quasi wet environment). Regional evaporation of Lake Fenéki was examined between 1970 and 2012. The whole area is consistent for the years 1970–1992 in determining the evaporative water loss, since this is a period before the construction (partial flood). Since 1993 two parts of the lake are distinguished: (a) the flooded Grove Ingói and (b) the non-flooded (Outer Reservoir) Lake Fenéki.

The length of *ET* time series of Grove Ingói controlled by water balance was a 20-year period (*Fig. 5*). The values of annual *ET* were between 730 and 1070 mm, with an average of 890 mm, which was 70 mm, 8% ($p \leq 0.0001$) less, than those of *PET*.

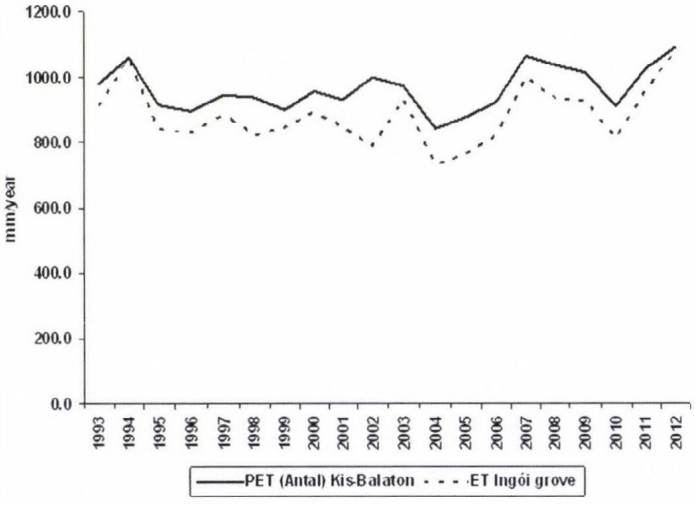

Fig. 5. The actual (*ET*) and potential (*PET*) evapotranspiration of Grove Ingói.

The estimation of evaporation for Lake Fenéki Outer Reservoir was prepared as well. Here Lake Fertő formula can not be used, since there is no permanent water cover. Water supply varying in time and space is typical for this area, which can not be followed exactly from the measured atmospheric data. Aerial photos were taken at the area (1988, 1992, 1993, 1994, 1995, 1997, 1998, 1999, 2000, 2001, 2002, 2003, 2008). According to them, the classification of the vegetation distribution (*Table 3*) was made as a starting base (*Pomogyi*, 2001; *Pomogyi et al.,* 1996). The year of 1992 is considered to be typical for the period before taking the aerial photos. 1992 was chosen in analysis, because the photos of 1988 were not detailed enough and the mapping methods were not up-to-date.

Table 3. Vegetation map data of Lake Fenéki Outer Reservoir

Lake Fenéki Outer Reservoir	Avg [ha]	%	min	max	SD	CV%
Reed	1 238	30%	1 117	1 363	74	0
Other wetland crops (marsh macrophytes)	1 753	43%	1 459	2 075	196	11
Swamp forest	177	4%	143	222	20	0
Herbaceous crops and grasses	387	9%	324	553	57	15
Wood	471	12%	309	588	114	24
Open water with seaweed	63	2%	12	99	27	42
Altogether	4 090	100%	4 064	4 107	12	0

According to the values of the table, open water surface occupies small area (2%). About 80% of the vegetation is considered to be well stocked with water similarly to wetland habitats. (In the especially dry years, lower percentage is expectable). For the characterization of the period between 1970 and 2012, precipitation data from Keszthely were used. The years were defined to be dry, when the lack of precipitation of the vegetation period exceeded the average of the period between 1970 and 2012 with 20%. These years were also warmer, than the average; their annual mean average temperature was 0.4 °C higher than the long-term average. Nine dry-warm years were found (1971, 1977, 1981, 1984, 1988, 1993, 2000, 2001, 2011), which is the fifth part of the whole period.

In the present processing, Eq. (4) was used for the estimation of *ET*. *Dunay et al.* (1968) based this method on the measurement data of "A" class evaporation pan, and suggested for the calculation of *PET*. This method was chosen, because the most of the area is a wetland well supplied with water, so a well-approximated estimation is expected. (Please note that *ET* was estimated by *Varga* (2005) for the non-flooded area, using *PET* values of the Antal-formula and the formula of *Turc* (1961) with a factor of 0.75 and 0.25.)

Application of the formula (4) was a good choice. The accuracy of calculated monthly *ET* values were checked using the monthly water balances for the period of 2003–2012. (Meteorological data used for the calculations were taken from the local measurements.) Estimation due to *PET* was quasi negated with the result that values measured with "A" class pans lag behind potential estimations. The average of the studied 10 years was 703 mm.

The evaporation of Grove Ingói and Lake Fenéki Outer Reservoir (real values, controlled with the water balance) was compared with the values of the "A" class pan at the study site (*Fig. 6*). *ET* of Grove Ingói between April and October (1998–2012) exceeded the *ET* calculated for Lake Fenéki Outer Reservoir with 14.4% ($p \leq 0.0001$). The data of "A" pan and *ET* calculated for

Grove Ingói differed with 24.1% ($p \leq 0.0001$) in the vegetation period between 1998 and 2012. The data of "A" pan and *ET* calculated for Lake Fenéki Outer Reservoir differed less, with 7.9% ($p \leq 0.0001$), as expected. *ET* is significantly underestimated in summer and autumn in the "A" pan, so its usage is not suggested for the estimation of evaporation at aquatic habitats.

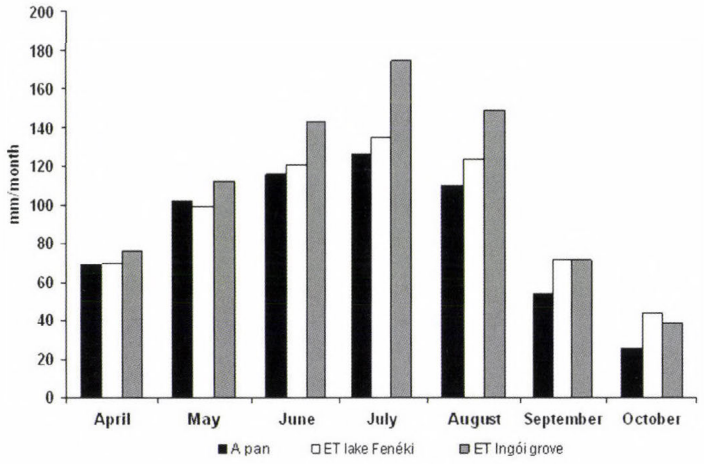

Fig. 6. Water losses calculated from water budget for Grove Ingói, Lake Fenéki Outer Reservoir and locally observed „A" pan evaporation (1998–2012).

Hereinafter, our calculations were extended to the period before the flood. The accuracy of *ET* calculated with Eq. (4) for Lake Fenéki Outer Reservoir was checked with the water balance, so this equation was adopted to the earlier period for the non-flooded area as well. Between 1970 and 2002, *ET* was calculated on a monthly basis. (The measured data of the OMSZ station in Keszthely were used.) Dataset checked with water balance was added to the values calculated with Eq. (4) for Grove Ingói before the flood (1970–1992). So a monthly data set for the period between 1970 and 2012 was made, from which annual *ET* was calculated. At Lake Fenéki Outer Reservoir for the whole period (1970–2012), *ET* was calculated with the Eq. (4). The data of the period between 1970 and 2012 were checked with the water balance. *ET* data set for the whole Lake Fenéki was made as well. Actual evaporation of Lake Fenéki for the period between 1970 and 2012 was derived from the calculated *ET* for Grove Ingói and Lake Fenéki Outer Reservoir, where the area ratio was taken into account (*Fig. 7*).

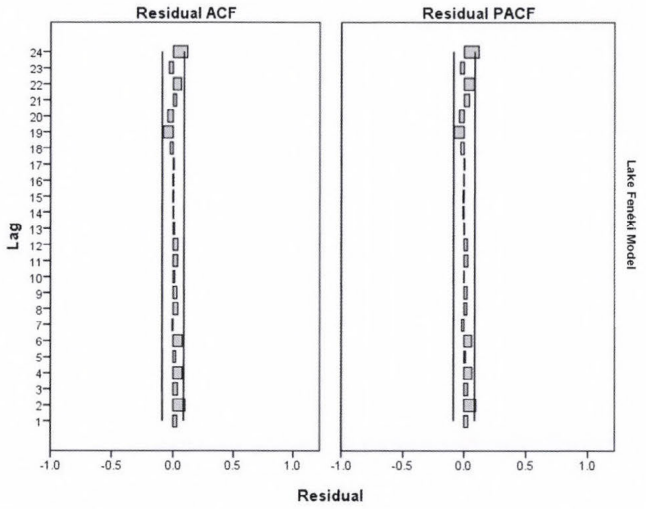

Fig. 7. Residuals (ACF and PACF) from the fitted ARIMA $(0,0,3)(0,1,1)_{12}$ for ET of Lake Fenéki.

The average annual evaporation of the whole period is 809.3±87.8 mm. If the nine dry-warm years are highlighted, their average annual evaporation exceeds the long-term average (874.7±37.6 mm) with 78 mm, with significantly lower standard deviation values. The average evaporation of the remaining wet-cold years is 796.6±89.4 mm. These years dominated (36 years), so sum of evaporation and standard deviation were close to the long-term average. None of the linear trends fitted to the two different periods (before and after the flood) were significant (1970–1992: $p \leq 0.144$; 1993–2013: $p \leq 0.366$).

In order to study *ET* time series of Lake Fenéki, an ARIMA model has been processed. We assumed that the process of *ET* was stochastic in nature. Therefore, we attempted to investigate the applicability of autoregressive integrated moving averages (ARIMA) modeling, a special time-series technique for developing forecast model for *ET*. In our study, the partial autocorrelation function (PACF) produced peak at lag 12, meaning that seasonal ARIMA $(0,0,3)(0,1,1)_{12}$ model is suggested to be the best fit for *ET* time series analysis.

To summarize *ET* seasonal variations in the present investigation, the SPSS time series modeller (http://www.spss.com) has shown that the seasonal ARIMA $(0,0,3)(0,1,1)_{12}$ model including additional seasonal term simply multiplied with the non-seasonal term has to be chosen. The reason of our choice was due to the fact that this model produced the lowest RMSE (quadratic scoring rule that measures the average magnitude of the error) and MAPE (mean absolute percentage error), equaling to 14.273 and 21.1%, respectively. The Ljung-Box-statistic (*Ljung* and *Box*, 1978) provided insignificant value of 0.398 meaning that there is no structure in the observed series, which is not accounted for by the

model. For a model to be considered as adequate at describing evaporation time series, the residuals of the model have to be correlated; both ACF and PACF have to lie within limits counted by equation (*Fig. 7*). The residuals should be without pattern. As the Kolmogorov-Smirnov-test of noise residual indicated normal distribution, the multiplicative decomposition of time series was successful ($p \leq 0.535$). The estimated model parameters for ARIMA $(0,0,3)(0,1,1)_{12}$ computed by SPSS expert modeler are presented in *Table 4*.

Table 4. Estimated model parameters for seasonal ARIMA $(0,0,3)(0,1,1)_{12}$

				Estimate	SE	t	Sig.
Lake Fenéki Model	Square Root	MA	Lag 1	–0.224	0.043	–05.161	0.000
			Lag 3	–0.177	0.043	–4.065	0.000
		Seasonal Difference		1			
		MA, Seasonal	Lag 1	0.952	0.028	33.913	0.000

Based on RMSE value, seasonal ARIMA $(0,0,3)(0,1,1)_{12}$ was selected for forecasting of monthly *ET*, at Lake Fenéki (*Fig. 8*). *Fig. 8* also includes the upper and lower (UCL, LCL) values of an estimated confidence interval at 95% for the predictions. The chosen projected time period was only three years (2013–2015).

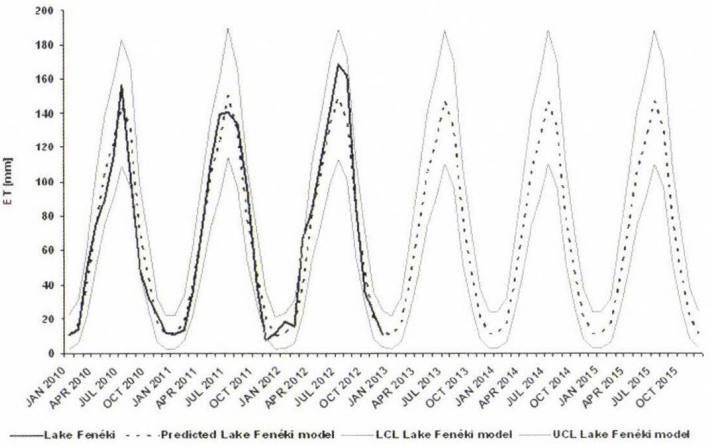

Fig. 8. The past and the future of the *ET*. Pattern of three-year actual and predicted *ET* data with three-year forecast (2013-2015) for monthly *ET* sums of Lake Fenéki by using the ARIMA $(0,0,3)(0,1,1)_{12}$ model. The LCL and UCL are the lower and upper limits of the confidence interval (95%), respectively.

The ARIMA $(0,0,3)(0,1,1)_{12}$ model parameters finalized for *ET* forecasting were as follows: $\theta_1 = -0.224$, $\theta_3 = -0.177$, $\Theta_1 = 0.952$. In our case $D=1$ (the order of seasonal differencing), $s=12$ (number of month per year). Seasonal pattern of *ET* series was also maintained in the projected values (see also *Table 4*).

4. Conclusions

Investigations were carried out on evaporation of Lake Fenéki (Kis-Balaton wetland) in the time period between 1970 and 2012. *PET* for the lake was generated using meteorological data of different stations. This study revealed that the locally measured meteorological values or regression equation derived from meteorological data of Keszthely would be appropriate in Lake Fenéki's *PET* calculation.

One part of the lake's observation site (Grove Ingói) has been artificially flooded in 1993. Irrespective to human intervention, the whole lake's spatial *ET* was statistically the same during the two time periods with modified watering levels (unflooded and flooded Grove Ingói). The long-term yearly *ET* averages of Lake Fenéki were 813 and 805 mm/year between 1970–1992 and 1993–2012, respectively. On the basis of fitted curves (*ET*), no significant trend has been confirmed either for the whole time period or after/before artificial intervention. Using trend analysis, we might conclude that in spite of flooding of Grove Ingói, there was no significant difference in long-term yearly *ET* sum of Lake Fenéki between 1972 and 2012. The probable reason might be the shortage of the used models. These formulas could not distinguish the various kinds of crop covers and their different evapotranspiration.

ET values of Lake Fenéki showed seasonal cycle, therefore, monthly data were used for generating a stochastic model. Investigation indicated that the seasonal ARIMA $(0,0,3)(0,1,1)_{12}$ model is a viable tool for studying long-term monthly *ET* data for Lake Fenéki. The generated *ET* values kept the earlier observed seasonal pattern, probably due to special wetland circumstances. The seasonal ARIMA $(0,0,3)(0,1,1)_{12}$ with lowest RMSE may also be selected for forecasting of monthly *ET* sums at Lake Fenéki (part of Kis-Balaton wetland, Hungary) using the following equation:

$$\left(1-B^{12}\right)X_t = \left(1-0.224B\right)\left(1-0.177B\right)\left(1+0.952B^{12}\right)\alpha_t, \qquad (11)$$

where X_t represents the time series data at period t. α_t represents a Gaussian white noise process (random shock) at period *t*. *B* represents a backward shift operator (*Box* and *Jenkins*, 1976).

Future research should be addressed to extend our results on other regions of Kis-Balaton wetland.

Acknowledgements: Present article was published in the frame of the project TÁMOP-4.2.2.A-11/1/KONV-2012-0064. The project is realized with the support of the European Union, with the co-funding of the European Social Fund.

References

Alexandris, S., Kerkides P., 2003: New empirical formula for hourly estimations of reference evapotranspiration. *Agr. Water Manage. 60,* 157–180.

Antal, E., 1968: Új módszer a potenciális evapotranspiráció számítására. *Beszámolók 1968*, Országos Meteorológiai Szolgálat Hivatalos Kiadványai, Budapest. (In Hungarian)

Antal, E., Baranyi, S., and *Kozmáné Tóth, E.*, 1977: A Balaton hőháztartása és párolgása. *Hidrológiai Közlöny 57*, 182–190. (In Hungarian)

Box, G.E.P. and *Jenkins, G.M.*, 1976: Time series analysis, forecasting and control. Holden Day, San Francisco.

Box, G.E.P., Jenkis, G.M., and *Reinsel, G.C.*, 2008: Time series analysis, Forecasting and Control. 4th edn. John Wiley and Sons, Inc, New Jersey.

Box, G.E.P., and *Jenkins, G.M.*, 1976: Time series analysis, forecasting and control. Holden Day, San Francisco.

Brockwell, P.J. and *Davis, R.A.*, 2001: Introduction to Time Series and Forecasting. Springer Verlag, New York.

Dunay, S., 1993: A termőhely vízháztartásának modellezése. In (Ed.: Szalay) Éghajlati és agrometeorológiai tanulmányok 1) Országos Meteorológiai Szolgálat Hivatalos Kiadványai, Budapest. (In Hungarian)

Dunay, S., Posza, I., and *Varga Haszonits, Z.*, 1968: Egyszerű módszer a tényleges evapotranspiráció és a talaj vízkészletének meghatározására. I. A párolgás meteorológiája. *Öntözéses gazdálkodás 6*, 39–48. (In Hungarian)

Harkay, M. 1983: A Kis-Balaton rekonstrukció és környezeti hatásai. Évezredek üzenete a láp világából. Régészeti kutatások a Kis-Balaton területén, Kaposvár-Zalaegerszeg, 7–10.(In Hungarian)

Hatvani, I.G., Kovács, J., Székely Kovács, I., Jakusch, P., Korponai, J. 2011: Analysis of long-term water quality changes in the Kis-Balaton Water Protection System with time series-, cluster analysis and Wilks'lambda distribution. *Ecol.Eng.* 37, 629–635.

Havalda, E., 1930: A Balaton párolgása *Vízügyi Közlemények 1,* 87–97. (In Hungarian)

Istvánovics, V., Kovács, A., Vörös, L., Heródek, S., and *Pomogyi, P.*, 1997: Phosphoruscycling in a large, reconstructed wetland, the lower Kis-Balaton Reservoir (Hungary). *Int.Ver.Theor. Ang.Limn.26,* 323–329.

Ljung, G.M. and Box, G.E.P., 1978: On a Measure of a Lack of Fit in Time Series Models. *Biometrika 65*, 2, 297–303.

Kontur, I., Koris, K., and *Winter, J.*, 1993: Hidrológiai számítások. Akadémiai Kiadó, Budapest. (In Hungarian)

Korponai, J., Braun, M., Buczkó, K., Gyulai, I., Forró, L., Nedli, J., and *Papp, I.*, 2010: Transition from shallow lake to a wetland: a multi-proxy case study in Zalavari Pond, Lake Balaton, Hungary. *Hydrobiologia 641*, 225–244.

Kovács, J., Hatvani, I.G., Korponai, J., and *Kovácsné, Sz.I.*, 2010: Morlet wavelet and autocorrelation analysis of long term data series of the Kis-Balaton Water Protection System (KBWPS). *Ecol. Eng. 36,* 1469–1477.

Meshram, D.T., Gorantiwar, S.D., and *Lohakare, A.S.*, 2011: ARIMA model for forecasting of evaporation of Solapur station of Maharashtra, India. *Mausham 63*, 573–580.

Nguyen, H.L., Leermakers M., Kurunczi, S., Bozó, L., Baeyens, W., 2005: Mercury distribution and speciation in Lake Balaton, Hungary. *Sci. Total Environ. 340,* 231–246.

Nováky, B., 2005: A Balaton vízpótlása és éghajlata. *Vízügyi Közlemények 87,* 1, 114–123.(In Hungarian)

*Padisak, J.*and *Reynolds, C.S.*, 2003: Shallow lakes: the absolute, the relative, the functional and the pragmatic. *Hydrobiologia 506–509*, 1–11.

Pomogyi, P., 2001: Az Ingói berek vegetáció térképezése 1998 és 2000 között. Nyugat-dunántúli Vízügyi Igazgatóság: Szombathely. (In Hungarian)

Pomogyi, P., Szeglet, P., and *Csato, E.,* 1996: The change in the reed community of the KBWPS, Feneki pond, based on vegetation-mapping results. In (Ed.: *Pomogyi, P.*) 2. Kis-Balaton Conference: Summary of the Research Result on the KBWPS between 1991–1995. University of Pannonia Georgikon, Faculty of Agriculture, Keszthely, 206–207.

Psilovikos, A. and *Elhag, M.,* 2013: Forecasting of Remotely Sensed Daily Evapotranspiration Data Over Nile Delta Region, Egypt. *Water Res. Manage 27,* 4115–4130.

Ramsar Convention, 1971: *Convention on Wetlands of International Importance especially as Waterfowl Habitat.* Ramsar (Iran), February 2, 1971. UN Treaty Series No. 14583. As amended by the Paris Protocol, December 3, 1982, and Regina Amendments, May 28, 1987.

Szesztay, K., 1962: A Balaton vízháztartása. *VITUKI Tanulmányok és eredmények 9,* 299–310. (In Hungarian)

Tátrai, I. Mátyás K., Korponai J., Paulovits G., and *Pomogyi P.,* 2000: The role of the Kis-Balaton Water Protection System in the control of water quality of Lake Balaton. *Ecol. Eng. 16,* 73–78.

Tölgyesi, L., 1993: Az éghajlat változékonyságának hatása a talajnedvességre. In (ed.:*Szalay S.*) Éghajlati és agrometeorológiai tanulmányok 1. Országos Meteorológiai Szolgálat Hivatalos Kiadványai, Budapest. (In Hungarian)

*Turc, L.,*1961: Evaluation des besoins en eau d'irrigation, evapotranspiration potentielle, formuleclimatique simplifee et mise a jour.*Annal Agronomy 12,* 1, 13–49. (In French)

Varga, Gy., 2005: A Balaton vízháztartási viszonyainak vizsgálata. *Vízügyi Közlemények 87,* 100–101. (In Hungarian)

Varga, Gy., Pappné, U.J., and *Bálint, G.*, 2007: Recent extremes in the water budget of Lake Balaton. *Georgikon for Agric. 10,* 1, 25-44.

Virág, Á., 1997: A Balaton múltja és jelene. Eger Nyomda Kft., Eger. (In Hungarian)

Zsuffa, I., 1996: Műszaki hidrológia. Műegyetemi Kiadó, Budapest. (In Hungarian)

URL addresses:

http://www.spss.com

IDŐJÁRÁS

Quarterly Journal of the Hungarian Meteorological Service
Vol. 119, No. 1, January – March, 2015, pp. 111–126

Evaluation of the cold drops based on ERA-Interim reanalysis and ECMWF ensemble model forecasts over Europe

Nikolett Gaál[1] and **István Ihász**[2]

[1]*Department of Meteorology, Eötvös Loránd University*
P. O. Box 32, H-1518 Budapest, Hungary
E-mail: gaalnikki@gmail.com

[2]*Hungarian Meteorological Service,*
P.O. Box 38, H-1525 Budapest, Hungary
E-mail: ihasz.i@met.hu

(Manuscript received in final form February 19, 2014)

Abstract—In our work, we planned deeper understanding of cold drops, closed air masses separated from the main western stream, by using ECMWF ERA-Interim reanalysis and ensemble forecasts. Upper level low (ULL) recognition algorithms were used to study 70 independent cold drop occurrences from the last decade in the middle and eastern European region. This led to the ascertainment of the usual location of ULLs in relation to Hungary, their core temperature, axis lean, horizontal temperature change, and identification on „plum" diagrams. Our studies included the usage of the potential temperature of the 2PVU (2 potential vorticity unit) surface, potential vorticity field related to 315 K, and 300 hPa wind speed These recommended new variables are available from operational deterministic and ensemble forecasts, and their usage is highly effective, hence making the identification of cold drops a lot easier than before.

Key-words: cold drops, upper level lows, reanalyses, ensemble model, statistical studies, 2PVU, isentropic potential vorticity, jet stream, visualization, case studies

1. Introduction

Synoptical studies of the cold drops got less attention in the past decades (both in domestic and international literature) than their significance would suggest. Therefore, we have a slice of all the information about their formation points, development conditions, synoptical and dynamical backgrounds. We find that the importance of their study lies in their ability to inflict natural disasters, such as massive thunderstorms that can lead to flooding, or in rare cases, even

tornadoes. Furthermore, upper level lows, or ULLs also have a negative impact on human health. At first, the expression of cold drop, ("der Kaltufttropfen") was likely used by *Scherhag* (1948). His article contained case studies, including winter and summer weather situations influenced by cold drops above the territory of Germany.

A cold crop (also called upper level low or ULL) is a closed air mass separated from the main western stream. Isolated from the cooler air of higher latitudes, it carries air substantially colder than its surroundings, to the warm regions of lower latitudes. In practice, its analysis is done at heights of about 5500 m, and a pressure level of 500 hPa, in the middle troposphere. ULLs being elliptically shaped with a diameter of hundreds kilometres, they resemble miniature cyclones on satellite images. A cold drop can determine the weather of the region for a couple of days, often bringing high amounts of intensive rain, especially in summer. They can occur at any time of the year. The unstable nature of ULLs provides perfect conditions for the forming of hails and thunderstorms in summer, and for intensive snowing winter. One of the main characteristics of a cold crop is that the air inside its higher regions is a lot colder than that of the area outside the cold drop. ULLs are sometimes referred to as "eddies", because of their counter-clockwise cyclone-like motion.

Peltonen (1963) investigated an intensive upper air low occurred in late autumn above Northern Europe. He found that the direction of the transition was parallel to surface wind direction, but the typical transition wind speed was only about 60–70% of the surface wind speed.

In Hungary, the first comprehensive study was made by *Bodalainé* (1983). She created subjective classification system based on synoptical patterns caused heavy floods in the Carpathian Basin.

A quite complex study was made by *Kurz* (1990) for the territory of Germany. Kurz investigated the life cycle of the cold drops and studied the relationship between the cold drops and cut off cyclones. He found that this phenomenon mainly occurred in winter the season. He stated that two main mechanisms could cause cold drops. The first one is the consequence of the cut off procedure, and the second one is the consequence of the cyclogenesis in the case when, due to dissipation near to the surface upper level, low becomes dominant.

It is important to note that cold drops could occur in Mediterranean areas too, and they are even mentioned in studies in central and northern Europe. Impacts of the cold drops are important in the Iberian Peninsula, too (*León*, 2003). In the Iberian Peninsula, especially in the southeastern part of Spain it occurs when a large size polar air mass slowly moves to that region in the middle and upper troposhere. It causes high impact weather including heavy rains or snowing (up to 500 mm/day) and extremely strong wind (between 100 and 200 km/h), when cold air mass mixes with warm Mediterranean air mass.

Complex climatological study based on a 41 years long NCEP reanalysis was made by *Nieto et al.* (2005). An objective recognition system using three meteorological variables was applied. The three meteorological variables were the following: cold core at 200 hPa, circulation pattern at 200 hPa, and thermal front parameter field. In contrast to the former studies, it was found that cold drops occurred more often in the winter season than in summer. Authors also found a connection between jet streams and upper level lows.

2. Life cycle of the ULL and relationship between blocking and upper level lows

A classic cold crop has four development phases, starting with the ULL isolating from the main stream and ending with dissolving or fusing with another stream (*Nieto et al.*, 2005). The four phases are

— ULL,
— tear-off,
— cut-off, and
— final stage.

2.1. Upper level low phase

In order for a cold drop to form, there have to be unstable waves inside the main stream, where the temperature wave is behind the geopotential wave (*Fig. 1a*). This is the phase where the ULL is still behind the frontal cloud mass, so it shows as a clearly visible cloud trail on satellite images.

2.2. Tear-off phase

The main meteorological process of this phase is the trough tearing off from the main stream (*Fig. 1b*). The waves amplitude gets higher ("the wave gets deeper"), followed by cold air detaching from the stream in its southern regions. The bottom part of the ULL slowly isolates from the main stream, leading to a closed circulation in the upper troposphere.

2.3. Cut-off phase

Contrary to the earlier phases, the isolation is completely finished in this phase, and the ULL is at its prime. The wind field shows the most advanced closed circulation at 500 hPa (*Fig. 1c*).

2.4. *Final phase*

Convection begins to develop in the cold drop (except for its coldest parts). As the air on the surface gets warmer, the eddies' circulations get slowed down by friction. The upper air mass gets warmer by the conviction and friction starts to take effect in this region as well. This causes the ULL to decay slowly (*Fig. 1d*). In most cases, the ULL reattaches to the main western stream before dissolving completely (*ZAMG*, 2007).

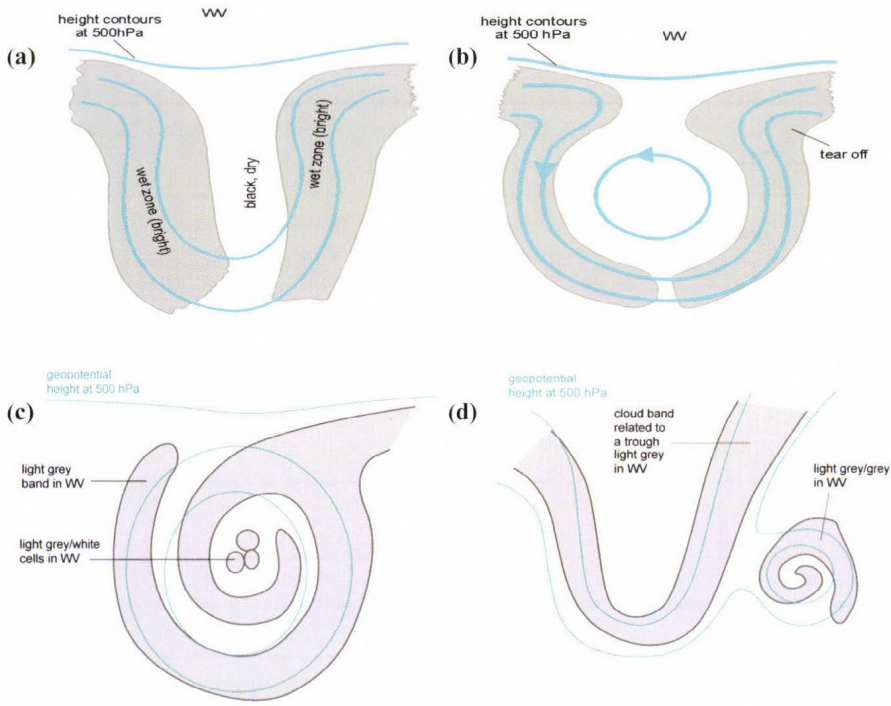

Fig. 1. Phases of the ULL: upper level low phase (a), tear-off phase (b), cut-off phase (c), final phase (d) (*ZAMG*, 2007)

The development of ULL usually takes 3–10 days. There are two kinds of ULLs, based on size and lifetime, "small eddies" which last 2–4 days, and "big eddies" which can last up to 14 days. Larger eddies are usually more common than smaller ones.

When studying cold drops, the phenomenon of blocking has a very high synoptic significance. First comprehensive studies of the blocking were made by *Rex* (1950a, 1950b). At the middle latitudes, two main patterns of the flow are typical: zonal flow and meridional flow (blocking). Life cycle of the blocking can extend from a few days up to two weeks. In the typing of the blocking

situations, we can see characteristic flow images that can be analyzed well at 500 hPa pressure level during the occurrence of blocking events. By analyzing the blocking anticyclones at 500 hPa, the following types can be distinguished: Rex-type blocking, Omega-situation, "fire ring" or detaching anticyclone, detaching low-pressure system, and splitting flow field. For our studies, Omega-type blocking is the one of important, because this event often leads to the detachment of cold drops (*Pelly* and *Hoskins*, 2003).

3. Former studies on cold drops in Hungary

ULLs are mentioned only in a few pieces of Hungarian literature. A synoptic classification system for the Carpathian Basin was invented by *Bodolainé* (1983). This classification system listed situations only that caused floods in the area of the rivers Danube and Tisza. She specified 7 classes: western, "western boundary disturbance", zonal, passing Mediterranean, central, cold air drop, and western cyclone-type. *Bodolainé* was a pioneer (both in Hungary and Europe in general) in studying the relation between dangerous weather conditions and cold air drops. She found that cold air drops occur quite rarely and mainly in the summer season.

Their occurrence often forms mezo-scale convective weather-systems (*Horváth*, 2007), and in some cases they have strong effect on the flooding of the river Tisza (*Bodolainé*, 1983; *Bonta et al.*, 1989; *Szépszó*, 2003).

The distinction between upper level lows and upper level cold vortexes is typical. Due to this distinction, the characteristic size of the upper cold drops is up to thousand kilometers, while the characteristic size of the cold vortexes varies between 1000 and 3000 kilometers. Due to the meteorological terminology phrase, "cold drop" is used if around cold core there are isolated isolines in geopotential field in the middle troposhere and the characteristic size is only several hundred kilometers (*Fig. 2*).

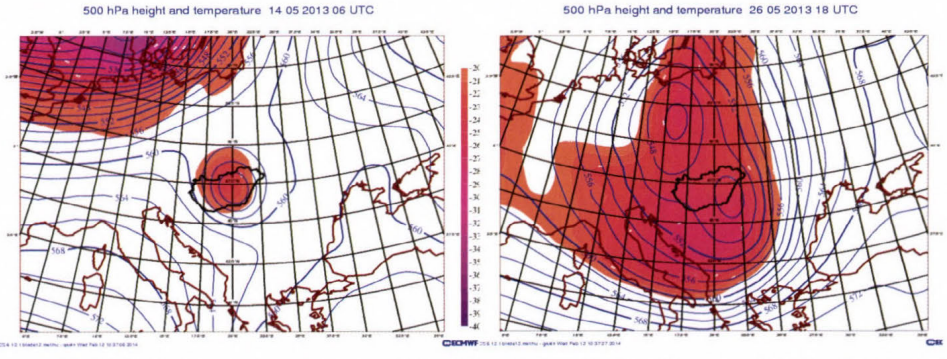

Fig. 2. Cold drop: May 14, 2013, 06 UTC (left), upper level cold vortex: May 26, 2013, 18 UTC (right).

4. ERA-Interim reanalysis of the European Centre for Medium-range Weather Forecasts

Due to the fact that there is a continuous development in the numerical weather prediction models, the use of operational models is not the most straightforward way to go if we would like to intend to study climatological characteristics of any atmospheric phenomena. To solve this problem, several reanalysis projects started applying a frozen version of the model to provide homogeneous quality of the analysis and forecasts.

The European Centre for Medium-Range Weather Forecast (ECMWF) was established in 1975, with the collaboration of 18 European countries (*Woods*, 2006). The ECMWF was among the first centers which create reanalysis database of a longer time period (from 1979 to 1993), it was ERA-15 project in the mid '90s (*Gibson et al.*, 1997). In 2003, ECMWF produced a new longer reanalysis, ERA-40 for the period between 1958 and 2002, with improved spatial resolution and state-of-the-art 3D data-assimilation (*Uppala et al.*, 2005).

The ERA-Interim reanalysis project started in the middle of the first decade of the 21st century. At first, the starting year of this reanalysis was 1989, but it was extended to 1979 (*Dee et al.*, 2011). The ERA-Interim database gets updated each month, with a 2 months delay. Using even more advanced spatial resolution (0.75*0.75 degrees) and the newest 4D-var dataassimilation techniques (as opposed to ERA-40s 3D-var technology) led to a significant increase in the quality of ERA-Interim.

As it was shortly summarized above, the currently available datasets provide state-of-the-art tools for studying cold drops in our region. In addition to model and pressure level fields, several selected predefined isentropic fields are also available from ERA-Interim. It widely supports to extend the potential tools and methods for recognition and investigation of the cold drops.

Beside the importance of the reanalysis datasets, we have to shortly summarize the main characteristics of the current operational models, too. Since June 25, 2013, the deterministic model has contained 137 levels in the vertical and its horizontal resolution is 16×16 kms. Ensemble model contains 62 levels in the vertical and its horizontal resolution is 32×32 kms. In the autumn 2013 vertical resolution of the ensemble model will be increased to 91 levels. The above-mentioned developments have positive impacts on forecasting of the ULLs too. Forecasted meteorological fields are available at standard pressure levels, all model levels, and selected isentropic levels from deterministic and ensemble models.

5. Developments of new methods for statistical and meteorological studies of cold drops

5.1. The horizontal and vertical structure of cold drops

Due to the fact that cold drops relatively rarely occur at any geographical locations, it is not an easy task to get a quite large sample if we plan to study and summarize the typical characteristics of cold drops. For solving the above mentioned problem, we planned to collect cold drops from a larger area, so we needed to develop an objective method for recognition of cold drops. Firstly, several occurrences were collected when cold drops was determined by forecasters in the last ten years. Secondly, the general characteristics of cold drops were determined by applying our newly developed methods. Finally, we plan to extend the sample to investigate cold crops by applying objective recognition algorithm for a 30-year period.

At first, we gathered 70 cases from those submitted by synoptical meteorologists as ULL situations between 2002 and 2011 (*Gaál*, 2012a). These 70 cases were studied daily in 6-hour intervals, so this led us to have 280 different states. At first, a few meteorological parameters as temperature, geopotential, relative humidity, and winds were commonly used at standard pressure levels (850, 700, 500, and 400 hPa), so this approach supported our examination of 3D structure in the atmosphere. Since cold crops have characteristically small horizontal extension, and they rarely occur at each geographical location, we had to choose an area which is large enough for our examinations. The northwestern counterpoint of the area was at latitude N 60° and longitude E 10°, while its southeastern counterpoint was at latitude N 40° and longitude E 40° (*Fig. 3*). *Fig. 3* shows the core positions of the 280 ULLs studied between 2002 and 2011. As we can see, the minimum temperature spots of the cold drops are located mostly west, northwest, and north from Hungary. The purple spots mark the center of the ULLs, and they mostly appear west, north, and northeast from Hungary. All the data used came from the ECMWF MARS database (*Raoult*, 2001).

In the period between 1979 and 2008, we calculated the monthly average temperatures at 500 hPa. We looked at the 30-year average, the minimum and maximum monthly-mean temperatures for each month (*Fig. 4*). Based on the timeline of these 30 years, the amplitude is smaller at 500 hPa (15 °C) than at the surface (22–25 °C). The annual thermal values of the mid-troposphere follow those of the surface with about a month delay. This is in accordance with the fact that the atmosphere gets heated mainly from the direction of the ground, and the effects of the minimum and maximum levels of irradiation show up with an offset in the mid-troposphere. The temperature is clearly lower on days with cold drops than the monthly averages of the 30 years. *Fig. 4* shows the monthly average temperatures (at 500 hPa) from the last 30 years (1979–2008). This is marked by the brown line on the picture, and it stands out quite well that the

temperature of the cold drops (marked in purple) resides below the average monthly data in every case. We can also see that ULLs do not have an absolute temperature threshold.

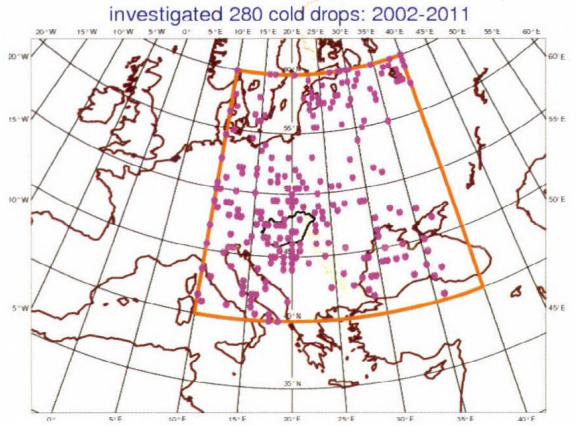

Fig. 3. Centers (local minimums) of the investigated 280 cold drops between 2002 and 2011.

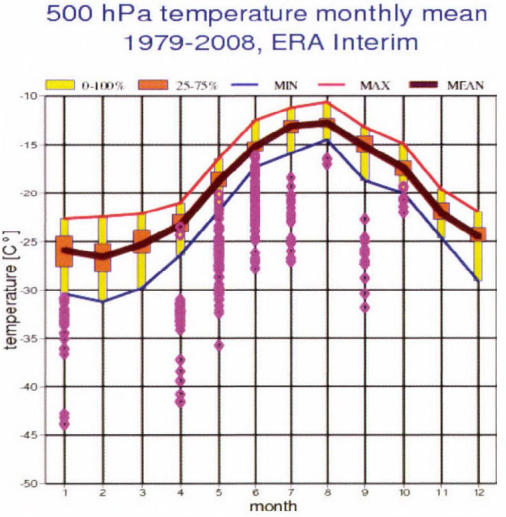

Fig. 4. Monthly means of the 500 hPa temperature (brown line), the coldest monthly means (blue lines), and the warmest monthly means (red lines) in the last 30 years. Purple dots show the investigated minimums of 280 cold drops.

As it has been mentioned, in order to have enough samples for statistical analysis, we have set a goal of generating an algorithm that recognizes ULLs (*Gaál*, 2012a, *Gaál*, 2012b). Firstly, local minima of the temperature fields are

determined at 400, 500, 700, and 850 hPa standard pressure levels. Secondly, we calculated horizontal gradients with several radius around the minima. Lastly, we calculated the axis inclination of cold drops at a few layers in the vertical. In the next few paragraphs, the results are briefly summarized.

Around the local minima, horizontal gradients were calculated within a circle determined by radius, which was changed between 100 and 750 km. Histograms were made from the 280 elements sample for each selected radius and pressure. Typical characteristics of the horizontal structure of ULLs were studied by the investigation of these histograms.

Our results match up with the anticipated structure, which means that gradients are getting lower as we get further away from the core. The unique horizontal temperature structure of cold drops gives us a good way of distinction from the cyclones of temperate zones, which are characterized by a much larger extension and thermal dissymmetry (except for their occluded phase). Another unique trait of cold drops is that their inner core is only clear in the upper troposphere, while in the lower troposphere, it is barely visible (as opposed to those of temperate cyclones). The horizontal thermal gradients are calculated around the core at 100, 250, 500, and 700 km. We also made a histogram of the aforementioned 400, 500, 700, and 850 hPa pressure levels with a gradient frequency of 0.5 °C/100 km (*Fig. 5*).

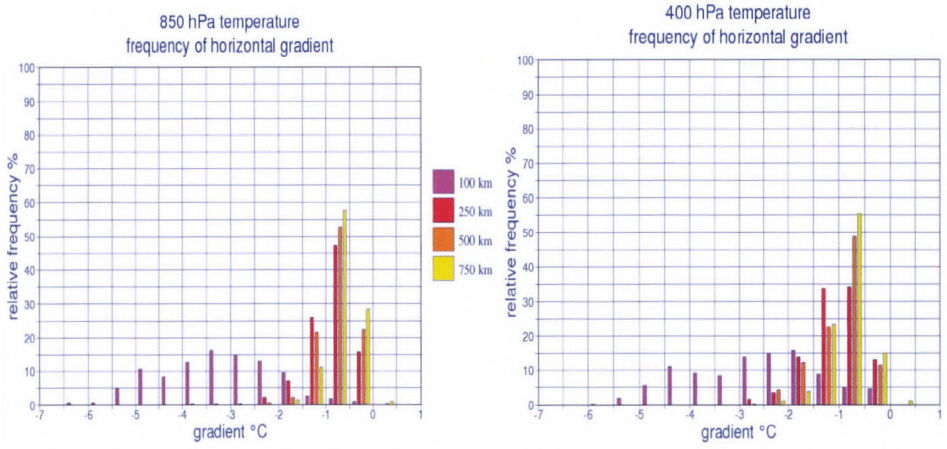

Fig. 5. Histograms of the gradient around the center of cold drops from 100 to 750 km circles at 850 hPa (up) and 400 hPa (down).

Gradients studied at 100 km are usually much larger than those studied at larger areas, and the values of the gradients get lower as the studied area gets larger, since ULLs have a characteristically small horizontal extension. We also made a cross chart showing the gradients calculated at the main isobaric-pairs.

Our calculation of the gradient pairs of 750/100 km, 500/100 km, and 250/100 km allowed us to establish that the gradients calculated on a larger area are always lower than those calculated on a smaller area (*Fig. 6*).

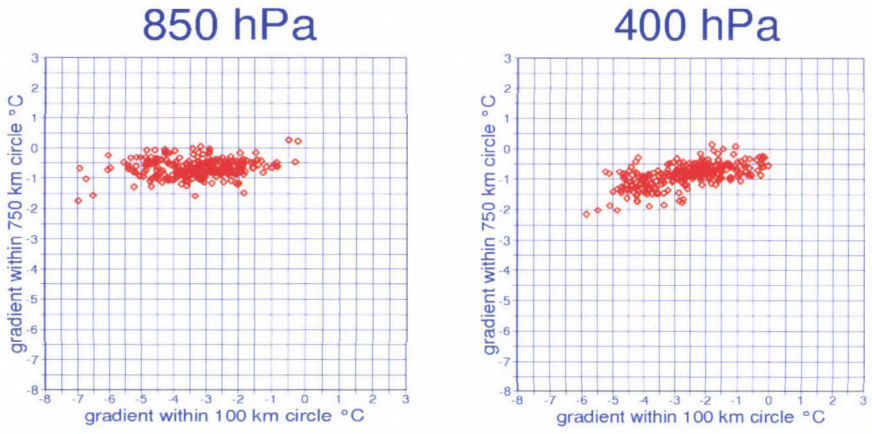

Fig.6. 750/100 km gradient pairs at 850 hPa (left) and 400 hPa (right) pressure levels

We also studied the relative spatial displacement of the cold drops on the mentioned pressure levels, or in other words, the axis inclination of the ULLs. *Fig. 7* shows the axis inclinations at the 400/500 hPa and 400/850 hPa layers. As we can see, the inclination is much lower at 400/500 hPa than at the higher-difference layers, with the axis usually being straight, or leaning towards the east of southeast (which also allows a clear study of the orientations towards different directions).

5.2. Relationship between meteorological fields in cold drops

In this part of the work, we aimed to extensively extend the number of the applied meteorological variables for studying cold drops. Additional variables are 300 hPa wind speed, potential temperature of the 2 potential vorticity unit (2PVU), isentropic potential vorticity at 315 K, horizontal temperature advection at 500 hPa, and wind shear between 850 and 300 hPa. In this paragraph, considering the technical limitations of this paper, only two new meteorological variables are briefly mentioned below.

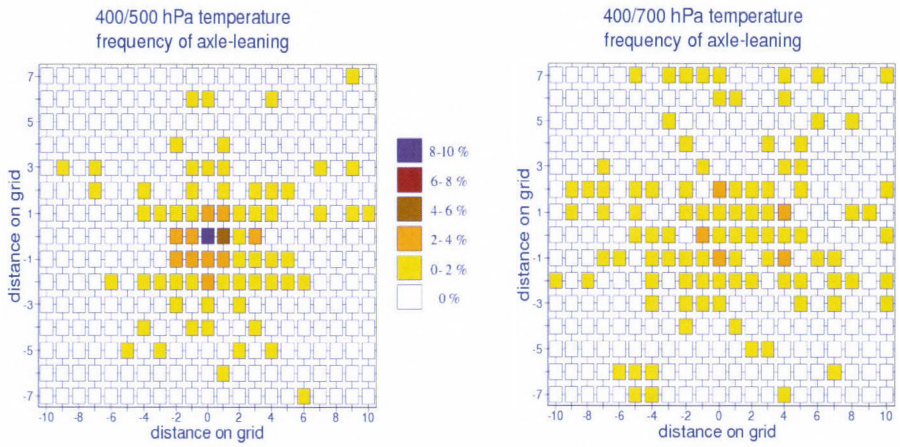

Fig. 7. Frequency of axis leaning at the 400/500 hPa layer (left) and 400/700 hPa layer (right).

Studying connection between cold drops and jet streams we found, that there is a very strong relationship between the position of the cold core and the structure of the jet stream (*Fig. 8*). Before the tear-off phase, the area of the most intensive part of the jet stream quickly moves to south at most part of the wave. At the next step it moves toward to northeast, this change causes a tearing of the drop. In most cases due to further rotation of the cold drop, two intensive parts of the wind shear are visible. One of them appears to the left and the other one appears to the right of the core. In cases of larger cold vortexes, 3 or 4 separated intensive parts of the jet streams can be found quite often. At the final stage of the lifecycle, when the cold drop joins to the main stream, an intensive part of the jet is always found at the eastern part. When the cold drop does not join the main stream it becomes stationary, increased warming at the core is typical, and the intensity of the jet stream decreases.

Besides studying cold drops on standard pressure levels, the investigation could benefit by applying "pv-thinking". The potential vorticity (pv) was introduced by *Ertel* (1942), it was not commonly used until the middle 1980s (*Hoskins et al.*, 1985; *Hoskins*, 1991; *Hoskins*, 1997). The potential vorticity theory is based on the structure of the potential vorticity field. Potential vorticity is the absolute circulation of the air mass between two isentropic surfaces. In the troposphere, its value is usually low. Approaching the tropopause, it sharply rises in the vertical (from 1 PVU to 4 PVU, 1 PVU=10^{-6} $m^2s^{-1}Kkg^{-1}$) with 2PVU being the dynamic tropopause, the subject of our studies.

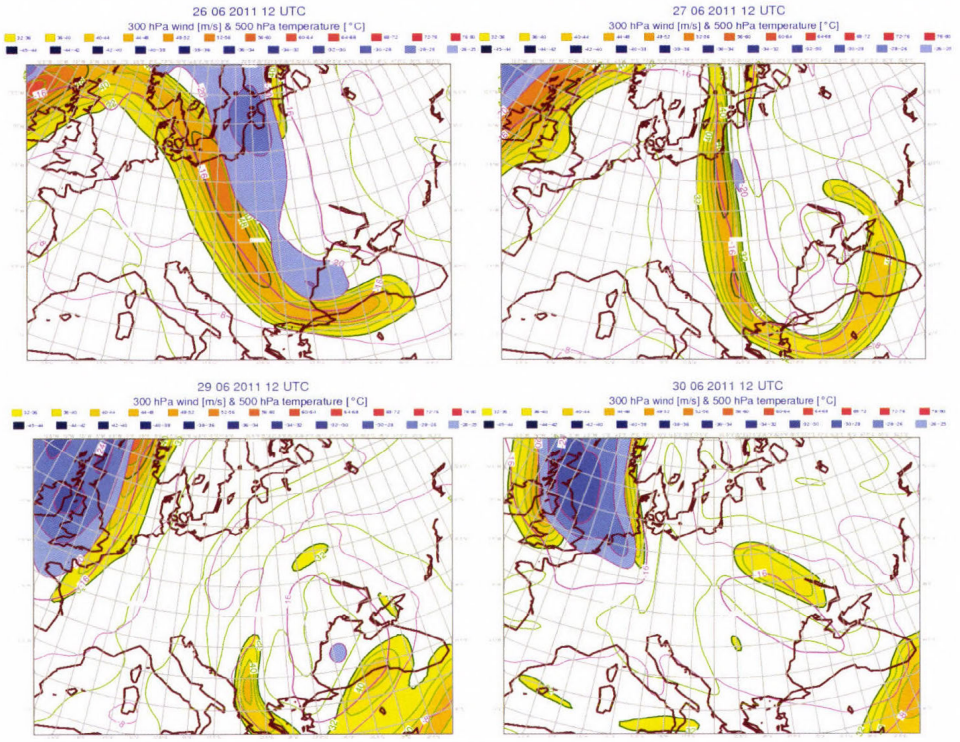

Fig. 8. 300 hPa wind stream and 500 hPa temperature at 12 UTC, June 26, 27, 29, and 30, 2011.

Studying the relationship between the local minimum of the isentropic level of the 2PVU and the position of the cold drops at 500 hPa we found, that these two minimums are typically very close to each other (*Fig. 9*). If there are more than one cold cores, there are consequently more minimums on the 2PVU fields too. We found that in tearing phase there was always a short delay (6–18 h) of the 2PVU field with tailing shape comparing to cold core at 500 hPa.

5.3. New ensemble based graphical products for supporting the recognition of cold drops

Predictability of cold drops of the numerical weather prediction models is not an easy task. It is highly recommended to use ensemble forecasts besides deterministic forecasts. At the Hungarian Meteorological Service, wide range of the ensemble based graphical products, among them EPS plumes, meteograms, spagetthy and probability maps are available in the operational forecasting practice. As a result of our former investigation of the cold drops, it would have

been useful to develop new tools for supporting better recognition and forecast of the cold drops. As in Section 4.1 it was clearly stated, additional meteorological fields besides the 500 hPa temperature can provide very valuable information as far as cold drops are concerned. We developed two new types of ensemble plume diagrams. First one contains three variables: 500 hPa temperature, isentropic potential vorticity at 315 K isentropic level, and potential temperature of the 2PVU surface. The second one contains four variables: in addition to previous three variables, 300 hPa wind speed is also part of the graph.

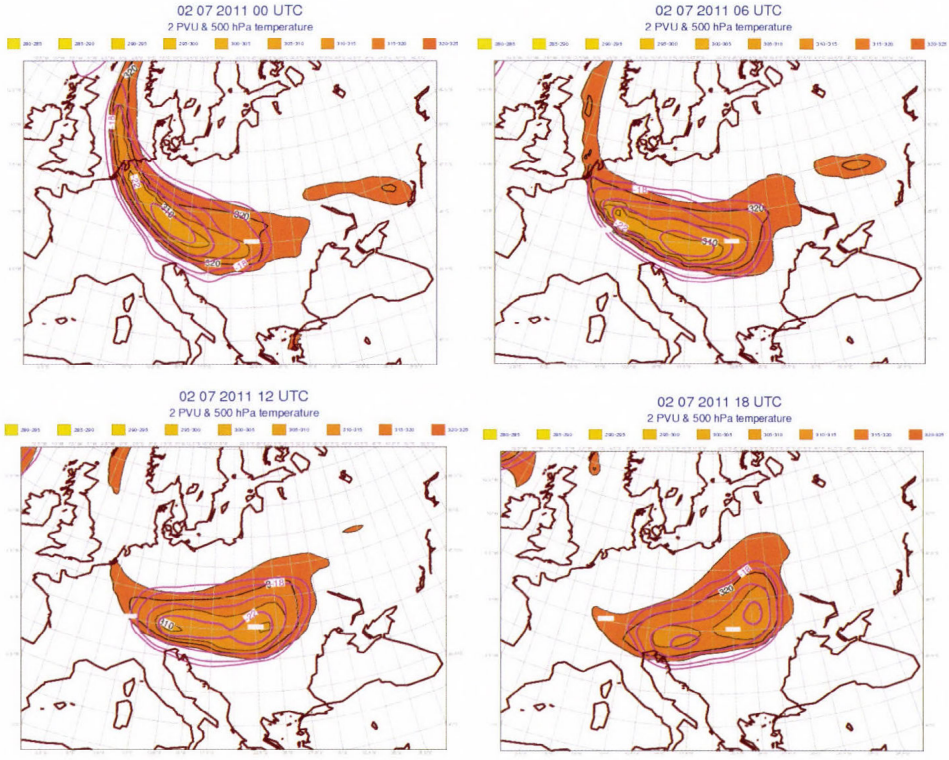

Fig. 9. Potential temperature of the 2PVU surface and the 500 hPa temperature between 00 and 18 UTC, July 2, 2011.

Usefulness of these new tools is demonstrated in a case study. On June 30, 2011, a cold drop pathed across Hungary. *Fig. 10* shows new ensemble plume diagram, ULL occurred on June 30, 2011. We can see the strong U-shape on the second forecast day at 500 hPa, showing a high chance of about 8 degrees drop in temperature in 24 hours and the same amount of rising temperature after the

cold drops passing. *Fig. 10* displays the uncertainty of ULL core forecasting and intensity perfectly.

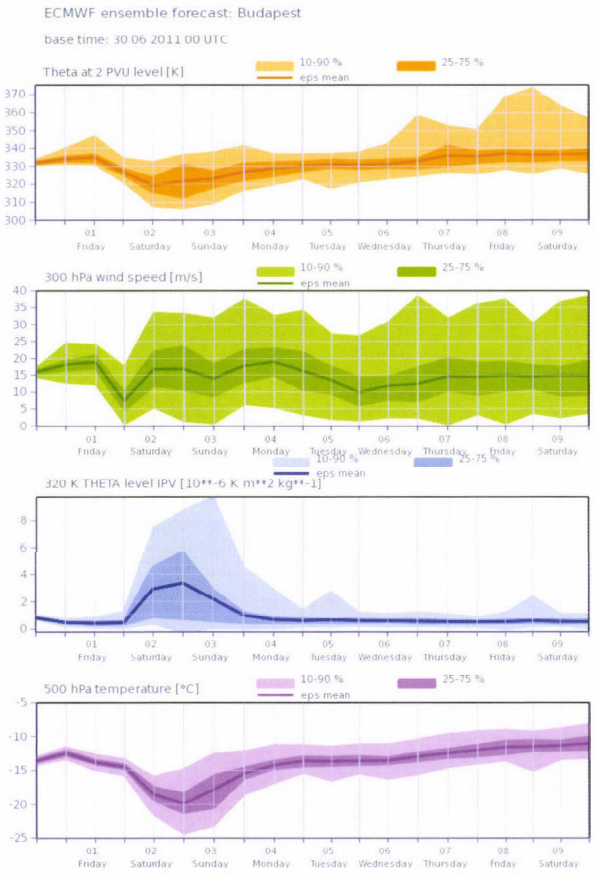

Fig. 10. New ensemble plume diagram, containing potential temperature of the 2PVU surface, isentropic potential vorticity at 315 K isentropic level, wind speed at 300 hPa, and temperature at 500 hPa, for Budapest, model started at 00 UTC, June 30, 2011.

6. Summary, conclusions

Due to the fact that cold drops relatively rarely occur at any geographical locations, it is not an easy task to get quite a large sample if we plan to study and summarize the typical characteristics of cold drops. For solving the above-

mentioned problem, we collected cold drops from a larger area and developed an objective method for recognizing cold drops. Firstly, several situations were collected when cold drops were determined by forecasters in the last ten years. Secondly, the general characteristics of the cold drops were determined by applying our newly developed methods.

Besides determining the general characteristics of the horizontal and vertical structure of cold drops, several new methods were developed for studying and providing guidance for forecasting cold drops. The two most important aspects are the usage of the ensemble forecasts and model forecasts on isentropic levels. At the operational practice, using ensemble forecasts besides the deterministic model can provide very valuable additional information due to the fact that the intensity and position of the cold drops are quite often uncertain. In addition to applying standard pressure level fields, potential temperature of the 2PVU and isentropic vorticity fields are also useful, they could provide more realistic features of the cold drops than we can see from pressure levels. The objective ULL-recognition is required to be able to reliably distinguish cold drops from cyclones. Our results so far make this a very real and reachable goal. One of our plans is to designate the areas with a potential for the formation of cold drops based on ensemble forecasts. In the future, we would like to run further tests with our ULL-recognition algorithm to study the last 30 years of cold drops, and we would also like to experiment more with ULL forecasting.

Acknowledgements: Authors would like to thank *Zoltán Fodor* and *Ákos Horváth* for their motivating suggestions and comments on work. Thanks for anonym reviewers for comments on improving this article.

References

Bodolainé, J.E: 1983: Árhullámok szinoptikai feltételei a Duna és a Tisza vízgyűjtő területén. *OMSZ Hivatalos Kiadványai 56*, Budapest. (In Hungarian)

Bonta, I., Molnár K., and *Vadkerti, F.*, 1989: Zöldár a Tiszán. *Légkör 34(3)*, 8–12. (In Hungarian)

Dee D.P, Uppala S.M., Simmons A.J., Berrisfordm P., Poli P., Kobayshi S., Andrae U., Balmaseda, M.A., Balsamo, G., Bauer P., Bechtold P. Beljaars A.C.M., Van de Ber L., Bidlot J., Bormann N., Delsol C., Dragani R., Fuentes M., Geer A.J., Matricardi M., McNally A.P. Monge-Sanz B.M., Morcrette J.J., Park B.K., Puebey C., Rosnay P., Tavolato C., Thépaut J.N., and *Vitart* F., 2011: The ERA-Interim reanalysis: configuration and performance of the data assimilation system. *Q. J. R. Meteorol. Soc. 137*, 553–597.

Ertel, H., 1942: Ein neuer hydrodynamischer Wirbelsatz. *Meteorol. Z. 59*, 277–281.

Gaál, N., 2012a*:* Study of cold drops based on ECMWF ERA Interim over Europe *BSc thesis.* Budapest.

Gaál, N., 2012b*:* Study of cold drops based on ECMWF ERA Interim over Europe *Proceedings of the Scientific Student Conference on Environment, 5-7 April 2012*, Veszprém, Hungary.

Gibson, J.K., Kallberg, P., Uppala, S., Hernandez, A., Nomura, A. and *Serrano, E.*, 1997: ERA-15 description, *ERA-15 Project series 1.* ECMWF.

Hoskins, B.J., McIntyre, M. E., and *Robertson, A. W.*, 1985: On the use and significance of isentropic potential vorticity maps *Q. J. R. Meteorol. Soc. 111*, 877–946.

Hoskins, B.J., 1991: Towards a PV - Theta view of the general circulation; *Tellus 43 AB*, 27–35.

Hoskins, B.J., 1997: A potential vorticity view of synoptic development. *Meteorol. Appl. 4*, 325–347.

Isaksen, L., Haseler, J., Buizza, R., and *Leutbecher, M.,* 2010: The new ensemble of Data Assimilations, *ECMWF Newsletter 123*, 17–21.

Horváth, Á., 2007: Components of the convection in the atmosphere (in Hungarian). In (ed. *Horváth, Á.*) Atmosheric convection, *Hungarian Meteorological Service*. Budapest. 4–17.

Kurz, M., 1990: Synoptische Meteorologie. *Verlag Deutscher Wetterdienst*, Offenbach.

León F.M., 2003: Las gotas frías / DANAS: Ideas y conceptos básicos. Servicio de Técnicas de Análisis y Predicción, INM. Instituto Nacional de Meteorología. (In Spain)

Nieto, R., Gimeno, L., Torpe, L, Ribera P., Gallego, P., Garcia-Herrera, R., Garcia, J.A, Nunez, M., Redano, A., and *Lorente, J.,* 2005: Climatological features of cutoff low systems in the Northern Hemisphere. *J. Climate 18,* 3085–3012.

Pelly, J.L. and *Hoskins, B.J.,* 2003: A New Perspective on Blocking. *J. Atmos. Sci. 60*, 743–755.

Peltonen, T., 1963: A Case Study of an Intense Upper Cyclone over Eastern and Northern Europe in November 1959. *Geophisica 8*, Helsinki, 225–251.

Raoult, B., 2001: MARS on the web: a virtual tour. *ECMWF Newsletter 90*, 9–17.

Rex, D.F., 1950a: Blocking action in the middle troposphere and its effect upon regional climate. Part I. An aerological study of blocking action. *Tellus 2*, 196–211.

Rex, D.F., 1950b: Blocking action in the middle troposphere and its effect upon regional climate. Part II. The climatology of blocking action. *Tellus 2*, 275–301.

Scherhag, .R, 1948: Neue Methoden der Wetteranalyse und Wetterprognose. Springer, Berlin.

Simmons, A., Uppala, S., Dee, D., and *Kobayashi, S.,* 2007: ERA-Interim: New ECMWF reanalysis products from 1989 onwards. *ECMWF Newsletter 110*, 25–35.

Szépszó, G., 2003: A 80-as és 90-es évek árhullámainak szinoptikus-klimatológiai értékelése. Master thesis. Eötvös Loránd University, Budapest. (In Hungarian)

Uppala, S.M., Kallberg, P.W., Simmons, A.J., Andrae, U., Bechtold, V.D., Fiorino, M., Gibson, J.K., Haseler, J., Hernandez, A., Kelly, G.A., Li, X., Onogi, K., Saarinen, S., Sokka, N., Allan, R.P., Andersson, E., Arpe, K., Balmaseda, M.A., Beljaars, A.C.M., Van De Berg, L., Bidlot, J., Bormann, N., Caires, S., Chevallier, F., Dethof, A., Dragosavac, M., Fisher, M., Fuentes, M., Hagemann, S., Holm, E., Hoskins, B.J., Isaksen, L., Janssen, P.A.E.M., Jenne, R., McNally, A.P., Mahfouf, J.F., Morcrette, J.J., Rayner, N.A., Saunders, R.W., Simon, P., Sterl, A., Trenberth, K.E., Untch, A., Vasiljevic, D., Viterbo, P., and *Woollen, J.,* 2005: The ERA-40 Reanalysis. *Quart. J. Roy. Met. Soc. 131*, 2961–3013.

ZAMG, 2007: Manual of synoptical and satellite meteorology: Conceptual models and cases studies. http://www.zamg.ac.at/docu/Manual/

Woods, A., 2006: Medium-Range Weather Prediction The European Approach. Springer.

NEWS

IN MEMORIAM JEAN-FRANÇOIS GELEYN (1950-2015)

Jean-François Geleyn passed away on January 8, 2015. We knew that Jean-François was struggling with his health in the last years, but still the incoming news was devastating for everybody in the Numerical Weather Prediction (NWP) community. We lost a leader in NWP in general and our leader in the ALADIN cooperation in particular. Jean-François had enormous influence on the progress of NWP in Central and Eastern Europe certainly including also Hungary. He had special ties with Hungary as honorary member of the Hungarian Meteorological Society (since 2000) and a member of the Editorial Board of "Időjárás". He paid 12 visits to Hungary between 1992 and 2011 (his last talk in Hungary can be seen at http://www.mettars.hu/wp-content/uploads/2015/01/Eloadas110328.pdf).

Jean-François Geleyn was the main initiator of the ALADIN international cooperation in 1990 with the proposal of the support programme of Météo France towards several Central and Eastern European countries. Hungary joined the cooperation among the first countries and already took part (by Dezső Dévényi) in the feasibility study of the project in March, 1991 in Paris. The development work of the ALADIN limited-area model started in Toulouse in September, 1991. Jean-François was leading the group in charge of the development of the ALADIN model. He was not only our scientific supervisor. He was also very supportive to help the newly arriving Météo France "stagiaires" (the French word for students) from Prague, Budapest, Vienna or Bucharest to find their way into their new lives in Toulouse. We remember very well, he was waiting for us at "Gare Matabiau" at our first arrival to Toulouse. He helped us to settle down in our new temporary home in France, he was showing us around in Toulouse and at Météo France, he was jogging with us, when we prepared for our marathon along the Canal du Midi and he was keen to join our "stagiaire" parties at the Météo France campus. His attitude and helpfulness made possible to "cement together" the "students" in Toulouse inside and outside work. This strong cohesion among the ALADIN developers was one of the secrets of the success of the ALADIN project. This made possible that the researchers working together on ALADIN was not simply forming a scientific team, but also a friendly and supportive company, which is spanning much farther than work on Numerical Weather Prediction. Based on all these scientific and personal achievements it was not accidental that the HIRLAM cooperation decided (around 10 years ago) to join forces with the ALADIN partners and further develop the ALADIN system together (they refer to it as HARMONIE). Now the ALADIN and HIRLAM communities together are forming the strongest NWP limited-area consortium in Europe.

Jean-François's main area of interest was physical parameterisations of the NWP models, but he was extremely knowledgeable at every aspect of numerical modelling. He had an excellent overview of the entire NWP and he was a very fast thinker making it almost impossible to follow him real time. He had a firm long-term vision on NWP, he was stubbornly insisting on his views and he was tirelessly working on its realisation. Basically, he had never had a rest, he devoted his entire life to NWP and to the ALADIN cooperation.

We all know that the landscape of numerical weather forecasting modelling in Europe would be very different without the contributions of Jean-François. We owe him enormous professional and personal gratitude for all what he had done for meteorology. We will always remember him as a scientist and friend who was always supporting us and our meteorological community. We will miss Jean-François with sorrow, but we will preserve his memory and put forward his legacy in Numerical Weather Prediction.

András Horányi and *Gábor Radnóti*

INSTRUCTIONS TO AUTHORS OF *IDŐJÁRÁS*

The purpose of the journal is to publish papers in any field of meteorology and atmosphere related scientific areas. These may be

- research papers on new results of scientific investigations,
- critical review articles summarizing the current state of art of a certain topic,
- short contributions dealing with a particular question.

Some issues contain "News" and "Book review", therefore, such contributions are also welcome. The papers must be in American English and should be checked by a native speaker if necessary.

Authors are requested to send their manuscripts to

Editor-in Chief of IDŐJÁRÁS
P.O. Box 38, H-1525 Budapest, Hungary
E-mail: journal.idojaras@met.hu

including all illustrations. MS Word format is preferred in electronic submission. Papers will then be reviewed normally by two independent referees, who remain unidentified for the author(s). The Editor-in-Chief will inform the author(s) whether or not the paper is acceptable for publication, and what modifications, if any, are necessary.

Please, follow the order given below when typing manuscripts.

Title page: should consist of the title, the name(s) of the author(s), their affiliation(s) including full postal and e-mail address(es). In case of more than one author, the corresponding author must be identified.

Abstract: should contain the purpose, the applied data and methods as well as the basic conclusion(s) of the paper.

Key-words: must be included (from 5 to 10) to help to classify the topic.

Text: has to be typed in single spacing on an A4 size paper using 14 pt Times New Roman font if possible. Use of S.I. units are expected, and the use of negative exponent is preferred to fractional sign. Mathematical formulae are expected to be as simple as possible and numbered in parentheses at the right margin.

All publications cited in the text should be presented in the *list of references*, arranged in alphabetical order. For an article: name(s) of author(s) in Italics, year, title of article, name of journal, volume, number (the latter two in Italics) and pages. E.g., *Nathan, K.K.,* 1986: A note on the relationship between photosynthetically active radiation and cloud amount. *Időjárás 90,* 10-13. For a book: name(s) of author(s), year, title of the book (all in Italics except the year), publisher and place of publication. E.g., *Junge, C.E.,* 1963: *Air Chemistry and Radioactivity.* Academic Press, New York and London. Reference in the text should contain the name(s) of the author(s) in Italics and year of publication. E.g., in the case of one author: *Miller* (1989); in the case of two authors: *Gamov* and *Cleveland* (1973); and if there are more than two authors: *Smith et al.* (1990). If the name of the author cannot be fitted into the text: *(Miller,* 1989); etc. When referring papers published in the same year by the same author, letters a, b, c, etc. should follow the year of publication.

Tables should be marked by Arabic numbers and printed in separate sheets with their numbers and legends given below them. Avoid too lengthy or complicated tables, or tables duplicating results given in other form in the manuscript (e.g., graphs).

Figures should also be marked with Arabic numbers and printed in black and white or color (under special arrangement) in separate sheets with their numbers and captions given below them. JPG, TIF, GIF, BMP or PNG formats should be used for electronic artwork submission.

More information for authors is available:
journal.idojaras@met.hu

Published by the Hungarian Meteorological Service

Budapest, Hungary

INDEX 26 361

HU ISSN 0324-6329

IDŐJÁRÁS

QUARTERLY JOURNAL
OF THE HUNGARIAN METEOROLOGICAL SERVICE

Special Issue: Severe weather events and their impact on society

Guest Editors: **Balázs Szintai** and **Tamás Weidinger**

CONTENTS

VOL. 119 * NO. 2 * APRIL – JUNE 2015

IDŐJÁRÁS

Quarterly Journal of the Hungarian Meteorological Service

Editorial Office: Kitaibel P.u. 1, H-1024 Budapest, Hungary
P.O. Box 38, H-1525 Budapest, Hungary
E-mail: journal.idojaras@met.hu
Fax: (36-1) 346-4669

Indexed and abstracted in Science Citation Index Expanded™ and Journal Citation Reports/Science Edition
Covered in the abstract and citation database SCOPUS®

Subscription by mail:
IDŐJÁRÁS, P.O. Box 38, H-1525 Budapest, Hungary
E-mail: journal.idojaras@met.hu

Editorial

Special Issue: Severe weather events and their impact on society

According to the latest reports of the Intergovernmental Panel on Climate Change (IPCC), it is expected that the occurrence of severe weather events like long heatwaves or strong thunderstorms will significantly increase by the end of the 21st century in Europe. Consequently, it is getting more and more important to study the underlying scientific basics and to develop such forecasting systems which are able to accurately predict these events. Noting the increasing relevance of this topic, the theme of the 39th Meteorological Scientific Days was chosen to be severe weather events and their impact on society. The Scientific Days were organized during autumn 2013 at the Hungarian Academy of Sciences by the Subcommittee for Atmospheric Dynamics and Synoptic Meteorology of the Meteorological Scientific Committee. The program consisted of 21 oral presentations, and as a new and successful initiative, a poster session was also organized with 7 posters (see at www.met.hu/omsz/rendezvenyek). The large number of presentations allowed to give an extensive overview on the topic of severe weather events and present several applications. Similarly to previous years, the opening presentation was a foreign invited speaker, who presented the nowcasting systems applied at European national meteorological services. This was followed by an overview talk about the evolution of nowcasting systems in Hungary. The next couple of presentations investigated severe weather events on large time and spatial scales. Furthermore, a presentation highlighted the actual challenges of hydrology. The following speakers presented the numerical modeling aspects of the forecasting of severe weather events. The first day was closed with three presentations showing interesting examples of research connected to severe precipitation events. The second day was devoted to the applications presenting different areas in society (e.g., aviation, defense, transportation) where severe weather could have a large impact, and accurate forecasting of such events is essential.

Similarly to previous years, the present special issue of IDŐJÁRÁS devoted to papers based on the presentations of the Meteorological Scientific Days. A high number of 11 papers were accepted, which well reflects the increasing interest in the topic of severe weather events from both scientific and application oriented communities. The organization of the papers follows the structure of the Scientific Days itself. The first two papers deal with severe weather events on large time and spatial scales, followed by two studies about the climatology cyclones and thunderstorms. Three papers are dedicated to the numerical modeling systems predicting severe weather events. The last four papers are dealing with applications like weather warnings at the Hungarian Defense Forces, forecasting of blowing snow, usage of unmanned meteorological aircrafts, and urban human comfort. It is important to note that due to the high number of papers, the last two presentations dealing with aviation and urban meteorology – are going to be included in the next issue of IDŐJÁRÁS.

Finally, we would like to thank the Editor-in-Chief of IDŐJÁRÁS for making it possible to publish the present special issue, and all the authors who contributed to the 39th Meteorological Scientific Days. Careful work of the Executive Editor of the journal by compiling the present issue is also appreciated.

Balázs Szintai and *Tamás Weidinger*
Guest Editors

IDŐJÁRÁS

Quarterly Journal of the Hungarian Meteorological Service
Vol. 119, No. 2, April–June, 2015, pp. 129–142

Projected changes of extreme precipitation using multi-model approach

Judit Bartholy, **Rita Pongrácz**, and **Anna Kis**

Department of Meteorology, Eötvös Loránd University,
Pázmány Péter sétány 1/A, H-1117 Budapest, Hungary

E-mail: bartholy@caesar.elte.hu, prita@nimbus.elte.hu,
kisanna@nimbus.elte.hu

(Manuscript received in final form October 6, 2014)

Abstract—Excessive precipitation may result in different environmental and socio-economical damages. In order to mitigate or avoid the potential losses associated to these, it is essential to provide estimations of precipitation tendencies for the future, which facilitate to build appropriate adaptation strategies in time. In this paper we used bias-corrected daily precipitation outputs of 11 regional climate model (RCM) simulations to determine the projected precipitation trends for the Carpathian Basin. According to the results of the analysis of precipitation indices, frequency of extreme precipitation will generally increase in the entire Central/Eastern European domain, except in summer, when decreasing trend is very likely in Hungary as well as in the southern regions.

Key-words: regional climate change, heavy precipitation, precipitation intensity, percentile values, climate index

1. Introduction

In the recent years, extreme precipitation events have become more frequent as well as more intense in many regions of Europe, e.g., in the western part of Central Europe since 1961 (*Kyselý*, 2009; *Seneviratne et al.*, 2012). This is especially valid for winter. In other seasons and other regions, including the

Carpathian Basin, the observed trends are not significant and inconsistent for the past (e.g., *Klein Tank* and *Können*, 2003; *Bartholy* and *Pongrácz*, 2005; 2007). In order to be prepared for the coming changes and make appropriate plans in various socio-economic sectors, it is essential to provide future estimates of mean precipitation trends and extreme events. Different sectors, different activities consider extreme precipitation very differently. Therefore, several types of extreme indices can be defined for describing these events (*Zhang et al.*, 2011). One of the most widely used types is based on exceeding various threshold values, which can be an absolute value (e.g., 10 mm, 20 mm, etc.) or a given (e.g., 90th, 95th, etc.) percentile of long climatological time series. Other more complex indices consider duration, intensity, and/or persistence of the events. Extreme indices usually focus on daily scale using daily precipitation totals. Despite the huge demand of sub-daily scale extreme analysis, there is a lack of such studies due to reliable data availability.

Climate model simulations for the future suggest that number of heavy precipitation days is likely to increase in the northern mid-latitudes in the 21st century, especially in winter (*IPCC*, 2012). Furthermore, in some regions more heavy precipitation days are likely to occur despite of the projected decrease in total precipitation amount. For instance, in Europe, more frequent extreme precipitation events are likely to occur in the coming decades (e.g., *Kyselý et al.*, 2011; 2012; *Rajczak et al.*, 2013). For Hungary, PRUDENCE (*Christensen et al.*, 2007) simulation results suggest that extreme precipitation events are projected to increase in winter, whereas a general decrease is estimated in summer (*Bartholy et al.*, 2008).

Intense precipitation may lead to a severe flood event, which is considered one of the major possible natural hazards on society. Specifically, in Central Europe, river flood risk and vulnerability are likely to have grown in many areas in the recent years (*Kundzewicz et al.*, 2005). As Working Group II of the Intergovernmental Panel on Climate Change (IPCC) pointed out in the Fifth Assessment Report (*IPCC*, 2014), river management is the main factor determining the flood trends of the past. Although the detected regional flood trends in Europe are inconsistent and statistically not significant for the past (*Renard et al.*, 2008, *Stahl et al.*, 2010), it is important to estimate the future change of precipitation, especially extremes, in order to develop appropriate river management strategies. According to the results of *Dankers* and *Feyen* (2008), extreme discharge levels are projected to occur in many European rivers.

In this paper, extreme precipitation is analyzed for Hungary using climate model simulations output. For this purpose, precipitation-related climate indices calculated from bias-corrected time series serve as main indicators for future climate change. First, the data and the applied indices are described. Results are discussed for indices based on (i) absolute value thresholds, (ii) percentile-based thresholds, and for intensity-based indices.

2. *Data and methods*

In order to estimate the future extreme precipitation trends, outputs from 11 regional climate models (RCMs) embedded in global climate models (GCMs) are analyzed taken into account the intermediate SRES A1B emission scenario (*Nakicenovic* and *Swart*, 2000). According to this scenario, the population is estimated to increase up to 8.7 billions and decline after the middle of the 21st century. The energy demand is assumed to be covered from both fossil fuels and renewable/nuclear energy sources. Thus, global mean CO_2 concentration level is estimated to reach 717 ppm by 2100. Simulation datasets are available with 25 km horizontal resolution on daily scale for 1951–2100 from the ENSEMBLES project (*van der Linden* and *Mitchell*, 2009). Due to the general underestimation of summer precipitation and overestimation of winter precipitation (*Pongrácz et al.*, 2011), raw data have to be bias-corrected prior to the detailed analysis. The applied correction (*Pongrácz et al.*, 2014) is based on a quantile matching technique (*Formayer* and *Haas*, 2010) for which E-OBS datasets (*Haylock et al.*, 2008) serve as reference for the 1951–2000 time period. The 25 km horizontal resolution gridded daily E-OBS data were created in the framework of the ENSEMBLES project by interpolating measured datasets of meteorological stations from all over Europe. For the area focused in this analysis, data from about 400 stations were used (note that the spatial coverage is not homogeneous).

After the correction, several precipitation-related climate indices are calculated. This paper focuses on excessive precipitation, whereas analysis of the lack of precipitation, i.e., drought-related indices can be found in *Pongrácz et al.* (2014). Among the indices connected to extreme precipitation (*Table 1*), two indices are defined by using different absolute threshold values (RR10, RR20), two indices indicate precipitation intensity (RX1, RX5) for different durations, and six indices are based on percentiles of daily precipitation amount (R90p, R95p, R99p, R90pGT, R95pGT, R99pGT). The grid cell values of all the 10 indices are calculated from the 11 bias-corrected RCM simulations for Central/Eastern Europe (covering the area of 43.625°–50.625°N, 13.875°–26.375°E) for the whole 1951–2100 simulation period. In this analysis, mean seasonal changes for the 2021–2050 and 2071–2100 periods are determined relative to the 1961–1990 reference period. Moreover, nine subregions are defined in the selected domain (Southeastern Czech Republic, Eastern Austria, Slovakia, Southwestern Ukraine, Slovenia, Hungary, Romania, Croatia, and Northern Serbia), for which the spatial average of annual and seasonal mean changes are calculated.

Table 1. Name, definition, and unit of the analyzed precipitation-related climate indices

Index	Definition	Unit
RR10	Number of heavy precipitation days ($R_{day} \geq 10$ mm)	day
RR20	Number of very heavy precipitation days ($R_{day} \geq 20$ mm)	day
RX1	Highest 1-day precipitation amount ($R_{max,1day}$)	mm
RX5	Highest 5-day precipitation amount ($R_{max,5day}$)	mm
R90p	The 90th percentile of daily precipitation time series	mm
R95p	The 95th percentile of daily precipitation time series	mm
R99p	The 99th percentile of daily precipitation time series	mm
R90pGT	Fraction of total precipitation above the base period's 90th percentile ($\sum(R_{2071-2100} > R90p_{1961-1990})/\sum R_{2071-2100}$)	%
R95pGT	Fraction of total precipitation above the base period's 95th percentile ($\sum(R_{2071-2100} > R95p_{1961-1990})/\sum R_{2071-2100}$)	%
R99pGT	Fraction of total precipitation above the base period's 99th percentile ($\sum(R_{2071-2100} > R99p_{1961-1990})/\sum R_{2071-2100}$)	%

3. Results and discussion

First, analysis of exceeding absolute daily precipitation threshold values is presented for the mid- and late-century compared to the reference period 1961–1990. Then, the projected changes of percentile-based indices are evaluated. Finally, intensity-type precipitation indices are analyzed.

3.1. Estimated future changes of precipitation indices using absolute threshold values

On a daily scale, 10 mm and 20 mm precipitation amounts are usually considered as heavy and very heavy precipitation days, respectively. Due to the different processes resulting in rainfall or snowfall, these days occur generally more often in summer than in winter, i.e., more precipitation occur from convective systems in the summer months. Two indices (RR10 and RR20) are analyzed in this paper and compared seasonally for the three selected time slices (1961–1990, 2021–2050, and 2071–2100). The average numbers of days are very different for the two indices, therefore, different scales and units are used in *Fig. 1*, i.e., RR10 and RR20 are shown as the mean frequency in 10 and 30 years, respectively. In July and August both indices are projected to decrease relative to the reference period 1961–1990, moreover, in May and June, RR10 is likely to decrease by the end of the 21st century. In all the other months, indices are projected to increase on average.

If we consider the estimated changes between the middle and late 21st century, the two indices differ in the three autumn months, namely, RR10 is projected to increase in September and October, whereas RR20 is likely to decrease in these two months. In November, the opposite is projected: RR10 tends to decrease and RR20 tends to increase.

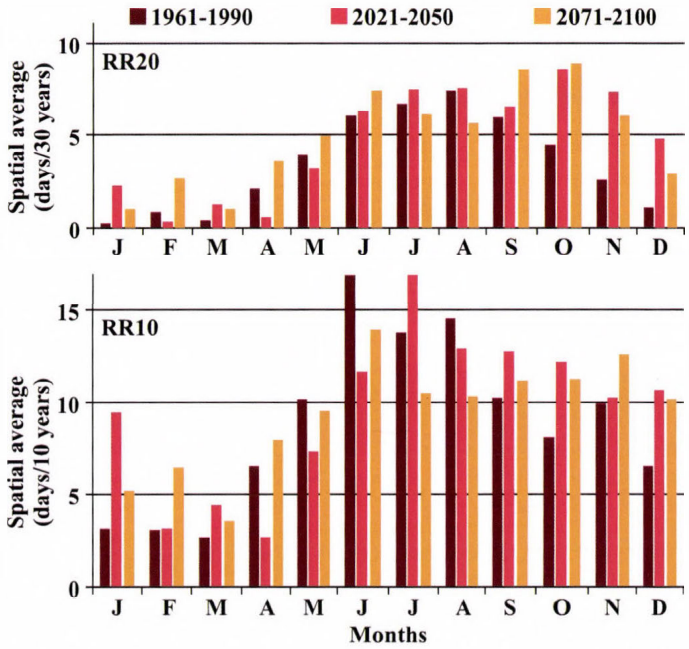

Fig. 1. Multi-model monthly average values of RR20 (upper panel) and RR10 (lower panel) for Hungary in 1961–1990, 2021–2050, and 2071–2100. Original units from Table 1 are modified to show simulated occurrence frequencies in longer time periods, 30 and 10 years, respectively.

Higher values are projected for 2021–2050 relative to 1961–1990 for both RR10 and RR20 in January, March, July, and December (which implies dominantly the winter half-year). This is followed by the decrease of average index values in the second half of the century. On the contrary, in April and May, both RR10 and RR20 are projected to decrease first, and then, increase by the last few decades of the century (in case of RR10, the estimated mean changes are similar also for June).

3.2. Estimated future changes of percentile-based precipitation indices

From the aspect of excessive precipitation, this paper focuses on large percentiles, i.e., the 90th, 95th, and 99th percentile values themselves, and the precipitation totals above these percentile thresholds relative to the entire precipitation totals. The seasonal mean changes of these percentile-based precipitation indices by the end of the 21st century compared to the reference period are summarized in *Fig. 2* for Hungary.

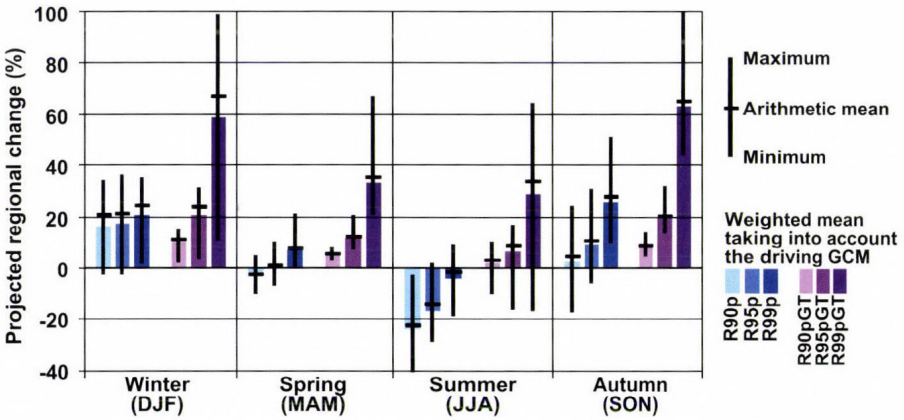

Fig. 2. Projected seasonal mean changes (%) of the percentile-based precipitation indices for Hungary by 2071–2100 relative to the reference period 1961–1990. The thicker bars indicate the average changes on the basis of RCM projections using equal weights to the driving GCMs. The thinner bars indicate the total ranges of RCM projections.

The fractions of the extreme daily precipitation totals from the entire precipitation totals are dominantly projected to increase, only two RCM (HIRHAM/ARPEGE and HadRM/HadCM3) simulations estimate decrease of summer index values. RCM simulations suggest quite similar changes of R90pGT, the entire multi-model uncertainty is less than 15%. Estimated spatial average changes of R95pGT are less similar compared to those of R90pGT, however, the uncertainty due to the different RCM use does not exceed 33%. The largest multi-model uncertainty in relative changes is projected in case of R99pGT exceeding 45% in all the seasons, moreover, it is 88.5% in winter. Similarly to the uncertainty ranges of multi-model estimations, the projected increases of the fractions of the higher extreme daily precipitation totals are also larger than those of the smaller extremes, i.e., estimated seasonal changes of R90pGT (2–10% on average) are smaller than changes of R95pGT (6–21% on average), which are considerably smaller than changes of R99pGT (33–63% on average). For all the

three indices, the largest increase is projected generally in winter and autumn, and the smallest increases are likely to occur in summer and spring.

The spatial structures of the projected seasonal mean changes for the entire domain are shown in *Fig. 3*. The composite maps clearly suggest that the estimated increases are larger in the northern part of the domain than in Hungary, and generally smaller in the southern regions. In summer, overall slight decreases are projected for all the three indices in the southwestern regions. Within Hungary, the projected average changes of all the three indices are generally larger in the eastern lowlands than in the western Transdanubian part of the country. However, in spring, the smallest increases are estimated in the middle subregions of the country.

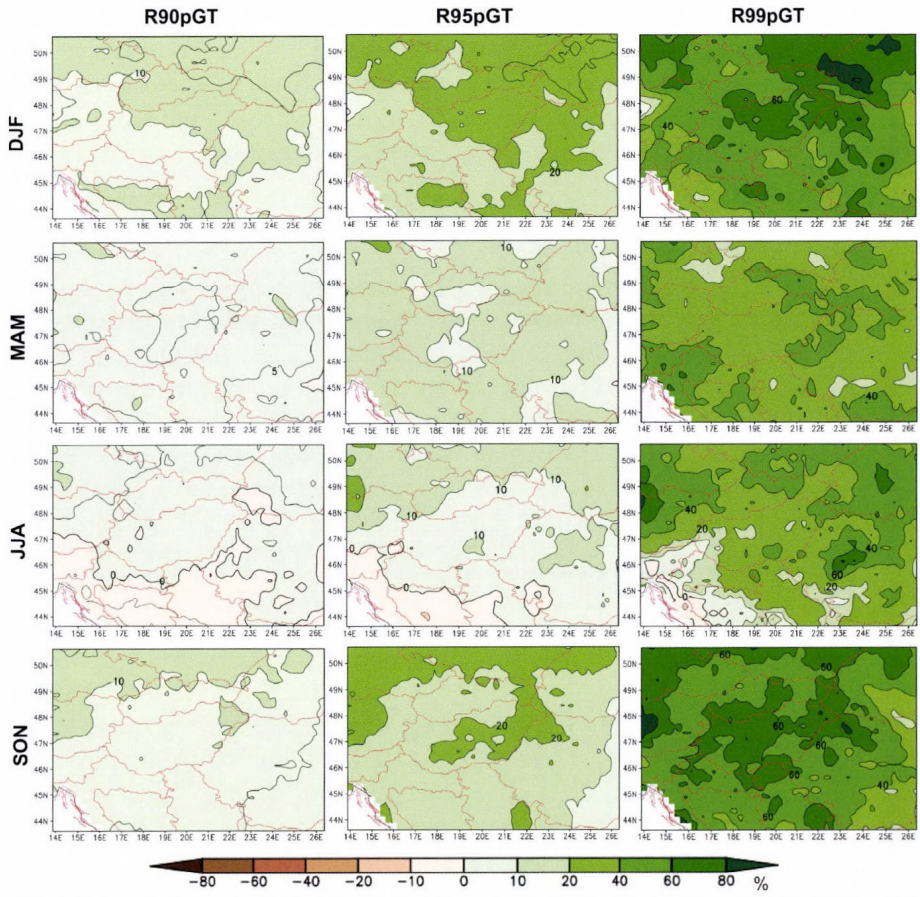

Fig. 3. Projected multi-model mean changes (%) of the fraction of total precipitation greater than the 90th, 95th, and 99th percentiles of daily precipitation in the four seasons (from top to bottom: winter, spring, summer, autumn) for 2071–2100 relative to the reference period 1961–1990.

The entire ranges of the estimated changes of high percentile values of daily precipitation are relatively large, mostly exceeding 25%, except in spring when they are 15–20% (*Fig. 2*). These large ranges suggest quite large uncertainty within the multi-model ensemble, when even the signs of the projected trends can be different (i.e., both increasing and decreasing). However, in winter, all the three percentile values in Hungary are very likely to increase, the estimated multi-model mean changes are 21%, 21%, and 24% for R90p, R95p, and R99p, respectively. In autumn, the higher the extreme percentile, the larger the projected increase. For instance, R99p is projected to increase by about 26% by the end of the 21st century relative to the reference period. In summer, the multi-model ensemble projects clear decrease of R90p (by 23% on average) in Hungary, mainly decrease of R95p (by 15% on average), whereas higher uncertainty is associated to the estimation of changes in R99p: the majority of the RCMs project slight increase (not exceeding 9%), nevertheless, some of the RCMs project relatively high decrease (10–19%), resulting in an overall slight decrease of R99p. Finally, in spring, slight changes are projected in general, which do not exceed 10%. However, note that R99p is estimated to clearly increase (by 7% on average), since all the RCMs project positive changes by 2071–2100 compared to 1961–1990.

The spatial structures of the projected seasonal mean changes are shown in *Fig. 4*. The estimated summer decreases show clear zonal differences, the largest decrease in percentile values of daily precipitation exceeds 40% and 20% in the southern part of the entire domain in case of R90p and R95p, respectively. The summer values of R99p tend to increase in the northern (and especially the northwestern) part of the domain, and decreases of R99p values are projected only in the southern part (the largest average decreases exceed 10%). Within Hungary, the quasi-zonal structure can be recognized as well, as in the entire domain. All the three indices are projected to decrease in summer in the whole country, the largest decreases are likely to occur along the southern border of Hungary. In winter, increases of the indices are estimated in the entire domain, the largest changes are likely to occur in the northern part, especially in the mountainous subregions. Percentile values in the northern part of Hungary are also projected to increase more than in the southern subregions. R99p – representing the very high extreme daily precipitation – is projected to increase in the entire domain also in spring and autumn, however, the projected seasonal average changes are generally smaller than in winter. In the equinox seasons, R90p values are projected to increase in the northern part and decrease in the southern part of the domain, whereas R95p is estimated to increase dominantly (except in small regions in the southern part).

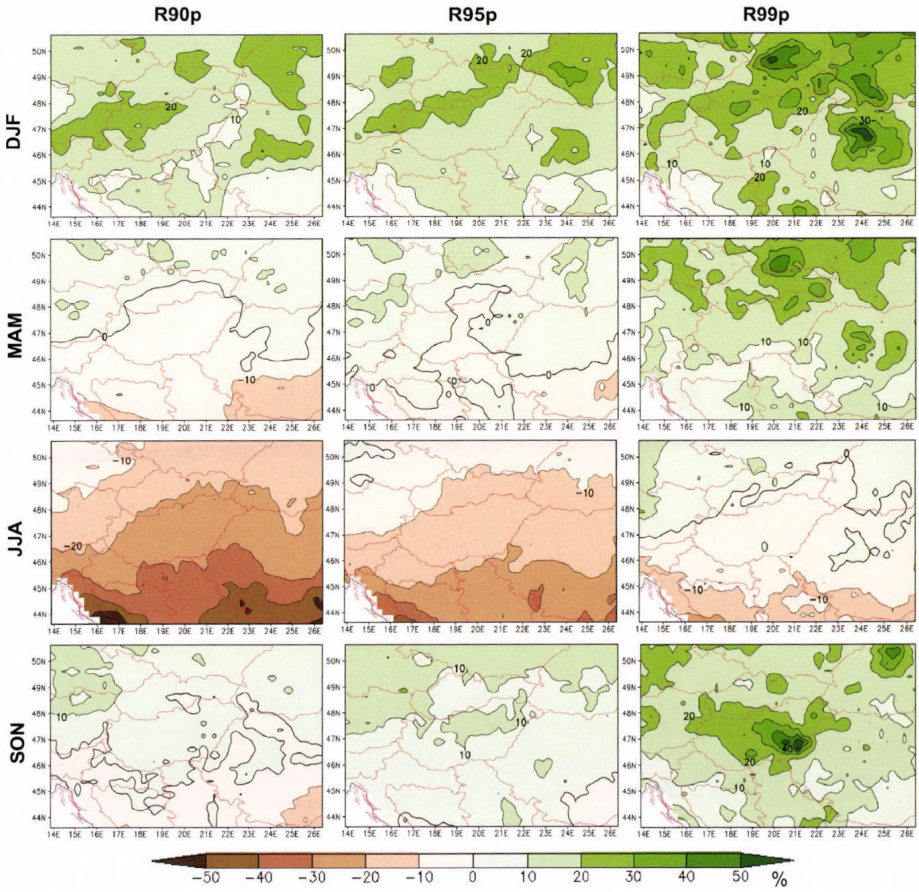

Fig. 4. Projected multi-model mean changes (%) of the 90th, 95th, and 99th percentiles of daily precipitation in the four seasons (from top to bottom: winter, spring, summer, autumn) for 2071–2100 relative to the reference period 1961–1990.

3.3. Estimated future trends of precipitation intensity indices

The precipitation intensity is represented in this paper by the highest precipitation totals during 1 day and 5 days (i.e., RX1 and RX5, respectively). The summary of multi-model monthly estimations of spatial average for Hungary is shown in *Fig. 5* for RX5 (similar changes are projected for RX1). These results clearly suggest that the maximum 5-day precipitation totals are projected to increase in the 21st century in all months, except August. The inter-model variability of the estimated RX5 values is much higher in July, August, and September than in the rest of the year (the entire RX5 ranges of RCM-estimations for the winter months do not exceed 20 mm). In general, the inter-

model variability of RX5 is projected to increase in the 21st century compared to the reference period.

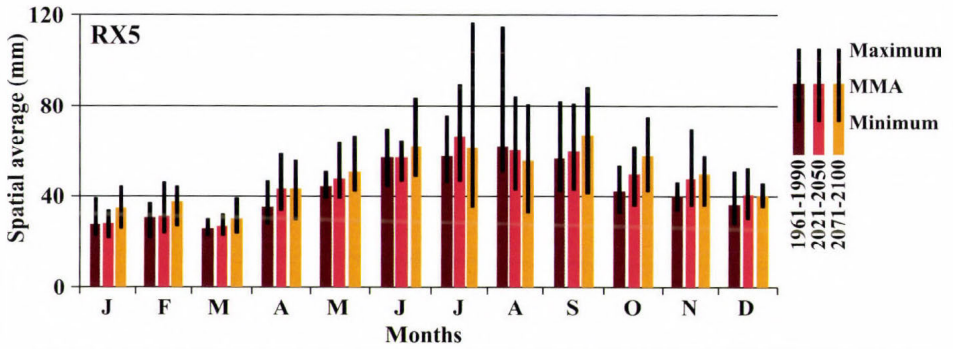

Fig. 5. Comparison of estimated monthly average values of RX5 for Hungary in 1961–1990, 2021–2050, and 2071–2100 using 11 RCM simulation outputs. MMA indicates the multi-model average.

Composite maps of the projected seasonal mean changes of RX1 show the spatial structures of the estimated changes by 2071–2100 relative to 1961–1990 (*Fig. 6*). Increasing trends are projected for all seasons, except in summer in the southern part of the domain, where the estimated negative changes on average imply decreasing trends for the future. The estimated spatial average changes of RX1 for the whole domain are 20%, 11%, 2%, and 23% in winter, spring, summer, and autumn, respectively. In summer, a zonal structure similarly to the changes of the summer percentile values can be recognized: in the northern part of the selected domain RX1 is projected to increase, whereas in the southern subregions it is projected to decrease. Specifically, the estimated multi-model average changes by the late 21st century in summer are +11% and –8% in the southeastern Czech Republic and in Croatia, respectively. In Hungary, the largest increase is estimated in autumn (+23%), when projected changes calculated from 9 individual RCM simulations (out of 11 total experiments studied in this paper) are statistically significant.

Since the largest increases are likely to occur in winter and autumn, more detailed temporal analysis is presented for these two seasons in *Fig. 7* showing the average decadal values of RX1 from the 1950s to the 2090s for Hungary. The ensemble of the individual RCM simulations clearly suggest increasing trends in the multi-model mean as well as in the 1st, 2nd, and 3rd maximum and minimum decadal values of RX1. All these trend coefficients are statistically significant at 0.05 level. The estimated overall change of the multi-model mean between the 1950s and 2090s is 30% in winter, and 33% in autumn, when the

decadal average of the highest daily precipitation amount is very likely to exceed 24 mm in the 2090s (and it was about 18 mm in the 1950s according to the RCM simulations).

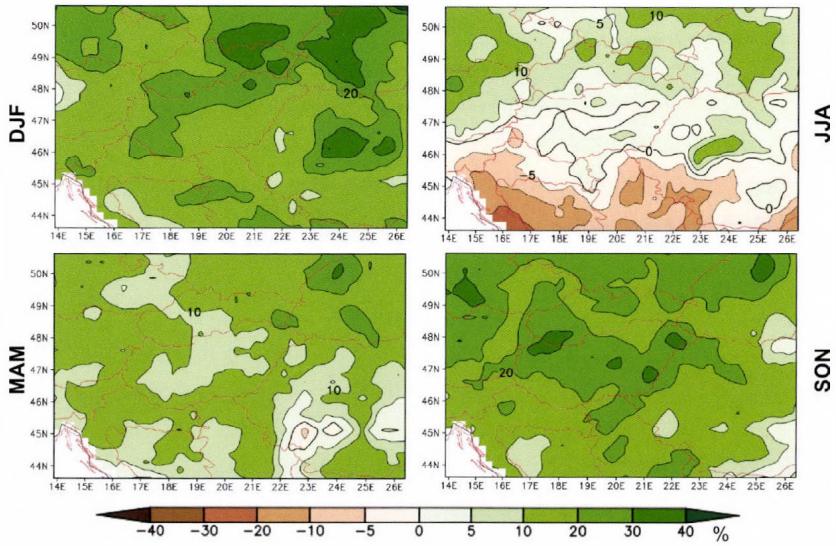

Fig. 6. Composite maps of the projected seasonal mean changes (%) of RX1 by 2071–2100 relative to the reference period 1961–1990. Average changes are calculated on the basis of RCM projections using equal weights to the driving GCMs.

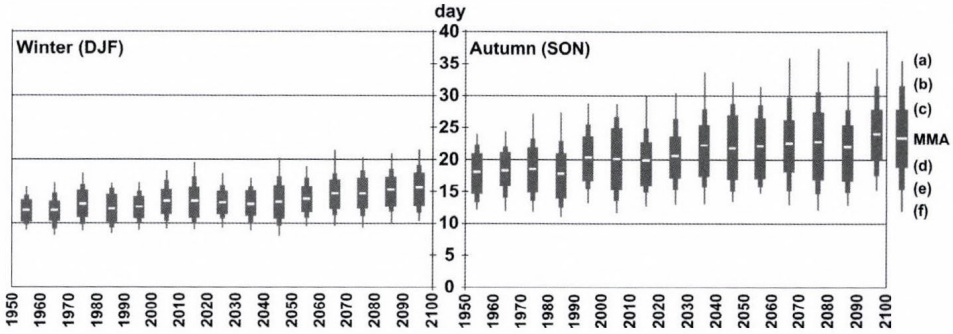

Fig. 7. Average decadal values of RX1 for Hungary in winter (left panel) and autumn (right panel), 1951–2100. MMA indicates the multi-model average. (a) and (f) indicate the maximum and minimum RX1 values, respectively. (b) and (e) indicate the second largest and smallest RX1 values, respectively. (c) and (d) indicate the third largest and smallest RX1 values, respectively.

4. Conclusions

Estimated changes of extreme precipitation conditions in Central/Eastern Europe (with special focus on Hungary) have been analyzed in this paper using bias-corrected daily precipitation outputs of 11 RCM simulations from the ENSEMBLES project considering the intermediate A1B scenario. Based on the results, the following conclusions can be drawn for the late 21st century relative to the reference period.

(i) Excessive precipitation (R90p, R95p, R99p) is mostly estimated to increase, except in summer, when decrease is projected both in Hungary and in the southern regions of the entire domain.

(ii) The fraction of the excessive precipitation relative to the total amount (R90pGT, R95pGT, R99pGT) is projected to increase in general. Only a few RCMs estimate slight decrease in summer for Hungary, and the multi-model average change in summer is slightly negative in the southwestern part of the entire domain.

(iii) Frequency of heavy precipitation (RR10, RR20) is projected to decrease in summer, and increase in the rest of the year.

(iv) Precipitation intensity (RX1, RX5) is likely to increase overall. However, in summer decreasing trend is estimated in the southern parts of the selected domain.

Overall, remarkable increasing trends of precipitation extremes are projected for Central/Eastern Europe by 2071–2100 relative to the 1961–1990 reference period. These changes may result in more frequent and more severe river flooding, therefore, in order to mitigate the vulnerability of the region, it is highly suggested to develop appropriate flood protection and management strategies in time considering these estimated changes.

Acknowledgements–Research leading to this paper has been supported by the following sources: the Hungarian Scientific Research Fund under grants K-78125 and K109109, the European Union and the European Social Fund through project FuturICT.hu (TÁMOP-4.2.2.C-11/1/KONV-2012-0013), and the AGRÁRKLIMA2 project (VKSZ_12-1-2013-0001). The ENSEMBLES data used in this work was funded by the EU FP6 Integrated Project ENSEMBLES (Contract number 505539), whose support is gratefully acknowledged. Furthermore, we acknowledge the E-OBS dataset from the EU-FP6 project ENSEMBLES (http://ensembles-eu.metoffice.com), and the data providers in the ECA&D project (http://eca.knmi.nl).

References

Bartholy, J. and *Pongrácz, R.*, 2005: Tendencies of extreme climate indices based on daily precipitation in the Carpathian Basin for the 20th century. *Időjárás 109*, 1–20.

Bartholy, J. and *Pongrácz, R.*, 2007: Regional analysis of extreme temperature and precipitation indices for the Carpathian Basin from 1946 to 2001. *Global Planet. Change 57*, 83–95.

Bartholy, J., Pongrácz, R., Gelybó, Gy., and *Szabó, P.,* 2008: Analysis of expected climate change in the Carpathian Basin using the PRUDENCE results. *Időjárás 112*, 249–264.

Christensen, J.H., Carter, T.R., Rummukainen, M., and *Amanatidis, G.,* 2007: Evaluating the performance and utility of regional climate models: The PRUDENCE project. *Climatic Change 81*, 1–6.

Dankers, R. and *Feyen, L.*, 2008: Climate change impact on flood hazard in Europe: An assessment based on high resolution climate simulations. *J. Geophys. Res. 113*, D19105, 17.

Formayer, H. and *Haas, P.*, 2010: Correction of RegCM3 model output data using a rank matching approach applied on various meteorological parameters. Deliverable D3.2 RCM output localization methods (BOKU-contribution of the FP 6 CECILIA project). http://www.cecilia-eu.org/

Haylock, M.R., Hofstra, N., Klein Tank, A.M.G., Klok, E.J., Jones, P.D., and *New, M.*, 2008: A European daily high-resolution gridded dataset of surface temperature and precipitation for 1950–2006. *J. Geophys. Res (Atmospheres) 113*, D20119,

IPCC, 2012: Managing the Risks of Extreme Events and Disasters to Advance Climate Change Adaptation. A Special Report of Working Groups I and II of the Intergovernmental Panel on Climate Change. (Eds. *Field, C. B., Barros, V., Stocker, T. F., Dahe, Q., Dokken, D. J., Plattner, G-K., Ebi, K. L., Allen, S. K., Mastandrea, M. D., Tignor, M., Mach, K. J., Midgley, P. M.*), Cambridge University Press, Cambridge, UK and New York, NY, USA,

IPCC, 2014: Climate Change 2014: Impacts, Adaptation, and Vulnerability. Part A: Global and Sectoral Aspects. Contribution of Working Group II to the Fifth Assessment Report of the Intergovernmental Panel on Climate Change (Eds. *Field, C.B., Barros, V.R., Dokken, D.J., Mach, K.J., Mastrandrea, M.D., Bilir, T.E., Chatterjee, M., Ebi, K.L., Estrada, Y.O., Genova, R.C., Girma, B., Kissel, E.S., Levy, A.N., MacCracken, S., Mastrandrea, P.R., White, L.L.*) Cambridge University Press, Cambridge, United Kingdom and New York, NY, USA,

Klein Tank, A.M.G. and *Können, G.P.,* 2003: Trends in indices of daily temperature and precipitation extremes in Europe, 1946-1999. *J. Climate 16*, 3665–3680.

Kundzewicz, Z.W., Ulbrich, U., Brücher, T., Graczyk, D., Krüger, A., Leckebusch, G.C., Menzel, L., Pinskwar, I., Radziejewski, M., and *Szwed, M.,* 2005: Summer floods in Central Europe – Climate change track? *Nat. Hazards 36*, 165–189.

Kyselý, J., 2009: Trends in heavy precipitation in the Czech Republic over 1961–2005. *Int. J. Climatol. 29*, 1745–1758.

Kyselý, J., Gaál, L., Beranová, R., and *Plavcová, E.,* 2011: Climate change scenarios of precipitation extremes in Central Europe from ENSEMBLES regional climate models. *Theor. Appl. Climatol. 104*, 529–542.

Kyselý, J., Santiago, B., Beranová, R., Gaál, L., and *Lopez-Moreno, H.I.,* 2012: Different patterns of climate change scenarios for short-term and multi-day precipitation extremes in the Mediterranean. *Global Planet. Change 98–99*, 63–72.

van der Linden, P. and *Mitchell, J.F.B.*, (Eds.), 2009: ENSEMBLES: Climate Change and Its Impacts: Summary of research and results from the ENSEMBLES project. UK Met Office Hadley Centre, Exeter, UK.

Nakicenovic, N. and *Swart, R.*, (Eds.) 2000: Emissions Scenarios. A special report of IPCC Working Group III. Cambridge University Press, UK, 570p.

Pongrácz, R., Bartholy, J., and *Miklós, E.*, 2011: Analysis of projected climate change for Hungary using ENSEMBLES simulations. *Appl. Ecol. Environ. Res. 9*, 387–398.

Pongrácz, R., Bartholy, J., and *Kis, A.*, 2014: Estimation of future precipitation conditions for Hungary with special focus on dry periods. *Időjárás 118*, 305–321.

Rajczak, J., Pall, P., and *Schar, C.,* 2013: Projections of extreme precipitation events in regional climate simulations for Europe and the Alpine Region. *J. Geophys. Res. Atmos. 118*, 3610–3626.

Renard, B., Lang, M., Bois, P., Dupeyrat, A., Mestre, O., Niel, H., Sauquet, E., Prudhomme, C., Parey, S., Paquet, E., Neppel, L., and *Gailhard, J.,* 2008: Regional methods for trend detection: Assessing field significance and regional consistency. *Water Resour. Res. 44*, W08419.

Seneviratne, S.I., Nicholls, N., Easterling, D., Goodess, C.M., Kanae, S., Kossin, J., Luo, Y., Marengo, J., McInnes, K., Rahimi, M., Reichstein, M., Sorteberg, A., Vera, C., and *Zhang, X.,* 2012: Changes in climate extremes and their impacts on the natural physical environment. In: (Eds. *Field, C.B., Barros, V., Stocker, T.F., Dahe, Q., Dokken, D.J., Plattner, G-K., Ebi, K.L., Allen,*

S.K., Mastandrea, M.D., Tignor, M., Mach, K.J., Midgley, P.M.) Managing the Risks of Extreme Events and Disasters to Advance Climate Change Adaptation A Special Report of Working Groups I and II of the Intergovernmental Panel on Climate Change (IPCC). Cambridge University Press, Cambridge, UK, and New York, NY, USA, 109–230.

Stahl, K., Hisdal, H., Hannaford, J., Tallaksen, L.M., van Lanen, H.A.J., Sauquet, E., Demuth, S., Fendekova, M., and *Jódar, J.,* 2010: Streamflow trends in Europe: Evidence from a dataset of nearnatural catchments. *Hydrol. Earth Syst. Sci. 14*, 2367–2382.

Zhang, X., Alexander, L., Hegerl, G.C., Jones, P., Klein Tank, A., Peterson, T.C., Trewin, B., and *Zwiers, F.W.,* 2011: Indices for monitoring changes in extremes based on daily temperature and precipitation data. *Wiley Interdis. Rev. Clim. Change 2*, 851–870.

IDŐJÁRÁS

Quarterly Journal of the Hungarian Meteorological Service
Vol. 119, No. 2, April– June, 2015, pp. 143–158

Assessment of heat-related mortality in Budapest from 2000 to 2010 by different indicators

János Bobvos*, Balázs Fazekas, and **Anna Páldy**

National Institute of Environmental Health, Budapest, Hungary
Albert Flórián u. 2-6, H-1097 Budapest, Hungary
E-mails: bobvos.janos@oki.antsz.hu;
fazekasbalazshu@gmail.com; paldy.anna@oki.antsz.hu

**Corresponding author*

(Manuscript received in final form April 17, 2014)

Abstract—The increase of the temperature and frequency of extreme weather events are predicted as the most visible effects of expected climate change. The number of publications dealing with heat-related mortality has been increasing for the last 20 years. They concluded that no formal definition of a heat wave existed, so the definition of such events would be very important. A more consistent methodology for calculating excess mortality would enhance comparisons between studies.

It is a growing demand to elaborate and use indicators which can provide comparable information of the impact of heat on mortality in different geographic and climatic regions. Therefore, the World Health Organization developed a set of climate change related health indicators in the CEHAPIS (Climate, Environment and Health Action Plan Information System) project. The authors aimed to assess heat related excess mortality by using this methodology, in addition to indicators used in the Hungarian Heat Alert System, in order to provide a recommendation for a more precise detection of health effects in Budapest.

In this paper, the heat wave related daily excess mortality is analyzed for the summer periods of 2000–2010 in Budapest. Mortality is characterized by the daily total mortality and that of the age group 65 years and over. Meteorological variables of the Pestszentlőrinc station, regarded as an urban background meteorological station, were used. Daily temperature was characterized by four indicators: mean and maximum daily temperatures, and mean and maximum daily apparent temperatures. The impact on mortality was compared in relation to the different temperature indicators and threshold values. A method was developed to define the optimal threshold range where the excess mortality could be identified effectively.

The recommended method is capable to detect the changes of temperature and to assess the impact of heat waves on daily mortality. The results are in accordance with previous studies. Concerning the indicators, the application of daily mean temperature values seems to be optimal for Budapest. Further analyses are required to answer the question to what extent the Budapest findings can be used in other cities.

Key-words: heat indicators, heat-related mortality, heat-health warning system, climate change, health effects of climate change

1. Introduction

The number of publications dealing with heat related mortality has been increasing for the last 20 years. These studies have been reviewed from different points of view. In a review article, *Basu* (2009) analyzed the epidemiological studies dealing with the association of ambient temperature and mortality published in the period of 2001–2008. The majority of the studies used time series analysis or case-crossover methods and proved the impact of heat on mortality. Several studies identified cause- or age-specific vulnerable subgroups. In their critical review, *Hajat* and *Kosatsky* (2010) identified the comparable multicenter studies in order to explore the heterogeneity of the effects. Heat-related mortality could be detected in the majority of cities, the older age groups were more vulnerable, and the bigger heat effect was associated with higher population density. A higher threshold value was found in cities with higher summer temperatures.

The majority of studies call attention to the negative impacts of predicted climate change. According to the latest report of IPCC (Intergovernmental Panel on Climate Change, AR5 Fifth Assessment Report), the global mean surface temperature change for the period 2016–2035 relative to 1986–2005 will likely be in the range of 0.3 °C to 0.7 °C. The increase of global mean surface temperatures for 2081–2100 relative to 1986–2005 is projected to likely be in the ranges 0.3 °C to 4.8 °C (*IPCC,* 2013). A greater likelihood of injury, disease, and death due to more intense heat waves and fires is expected (*IPCC,* 2014). In his critical review, *Gosling et al.* (2009a) examined present temperature-mortality relationships and discussed climate change issues. He concluded that no formal definition of a heat wave existed, so the definition of such events would be very important. A more consistent methodology for calculating excess mortality would enhance comparisons between studies. There is evidence that climate change will affect temperature-related mortality heterogeneously, so there is a need for inter-regional comparisons that account for changes in the mean and variance of temperature.

Several studies analyzed the Budapest data as well. *Paldy et al.* (2005) investigated the effect of weather on daily mortality in Budapest, 1970–2000. *Hajat et al.* (2006) and *Gosling et al.* (2007) analyzed the same period by different methods. The data from the nineties were evaluated by *Ishigami et al.* (2008) and *Baccini et al.* (2008); a cause- and age-specific analysis was carried out by *D'Ippoliti et al.* (2010). Besides the Budapest data, a comparison of heat related mortality was carried out between the urban and rural populations in Hungary (*Bobvos* and *Paldy,* 2009). The excess mortality due to the strongest heat wave ever recorded in 2007 was analyzed at regional (*Paldy* and *Bobvos,* 2009) and small area levels (*Paldy et al.,* 2011). The predicted heat related excess mortality due to climate change was assessed by *Gosling et al.* (2009b), *Baccini et al.* (2011), and *Bobvos et al.* (2011) using a regional climate model.

Based on the studies, the proven impact of heat on mortality is a great burden on society. In order to decrease the negative effects, heat-health warning systems have been developed by public health services all around the world. These systems are based on meteorological forecasts and include different measures during warnings. *Kovats* and *Ebi* (2006) reviewed the public health aspects of heat waves and evaluated the relative effectiveness of public health responses. *Kovats* and *Hajat* (2008) emphasize the important differences in vulnerability existing between populations, depending on climate, culture, infrastructure (housing), and other factors. Based on the forecasts of the Hungarian Meteorological Service, the Hungarian Heat Alert System was introduced in Hungary in 2005. The system has three levels: a 1st warning, a 2nd alert, and a 3rd alarm level. The threshold temperature of the alert is 25 °C daily mean temperature. A heat wave is defined as three or more consecutive days with temperatures above this threshold. During the heat waves, the health care services and the local authorities launch previously prepared measures.

The above cited studies used a great variety of heat-related indices. It is a growing demand to develop and use indicators which can provide comparable information of the impact of heat on mortality in different geographic and climatic regions. Therefore, the WHO – in collaboration with WHO Member States – developed a set of climate change related health indicators (categorized into exposure, effect, and action) within the frame of the CEHAPIS project (*WHO*, 2011). This project recommends using two types of temperature indicators for heat exposure. The authors aimed to assess heat-related excess mortality by using the CEHAPIS methodology in addition to indicators used in the Hungarian Heat Alert System in order to provide a recommendation for a more precise detection of the health effects in Budapest.

2. Data and methods

In this paper, the heat wave-related daily excess mortality was analyzed for the summer period (May 16–Sept 15) of 2000–2010 for Budapest. Daily mortality data were gained from the Central Statistical Office of 1995–2010 for Budapest. All natural cause mortality (International Classification of Diseases codes ICD-9: 1–799) was characterized by the daily total mortality (M 0-X) and that of the age group 65 years and above (M 65+). Meteorological variables of the Pestszentlőrinc measuring station were retrieved from the Global Surface Summary of the Day Data (*GSOD,* 2010) archived in the National Climatic Data Centre (NCDC) at National Oceanic and Atmospheric Administration (NOAA) for 1990–2010. The Pestszentlőrinc monitoring station was regarded as an urban background meteorological station of Budapest. Daily temperature was characterized by four indicators: mean (T) and maximum daily temperatures

(Tx), and mean (AT) and maximum (ATx) daily apparent temperatures in °C. Apparent mean and maximum temperatures (*Kalkstein* and *Valimont,* 1986) were used as indices of thermal discomfort based on air temperature (T) and dew point temperature (T_{dp}) according to the following formula:

$$AT = -2.653 + 0.994(T) + 0.0153\left(T_{dp}\right)^2. \quad (1)$$

To follow the changes in the temperature, a 10-year fixed reference period of 1990–1999 was chosen. The hot days were identified by the 90th percentile of the frequency distribution of temperature indicators, where the daily mean temperature value was 25 °C, being a threshold of the Hungarian Heat Alert System. A heat wave was defined as three or more consecutive days with temperatures above this threshold.

After the initial description of the data, linear trend analyses were carried out to detect the changes in time. An assessment was done to compare the number of heat waves identified by the different temperature indicators in relation to the threshold. The number of heat waves and the number of days of heat waves corresponding to the 90th percentile threshold were defined by year, respectively for the whole period.

The effect of heat waves on daily mortality – absolute excess mortality (EM, in case number) – was defined as the difference of the mortality during heat waves (observed mortality: M_o) and the expected mortality (M_e) computed form the daily mortality of the previous five years (reference periods of mortality) excluding the daily mortality of days of heat waves in the given years:

$$EM = \sum(M_0 - M_e). \quad (2)$$

The relative excess mortality was also computed in a similar way, defining the percent increase of mortality during the heat waves of a given summer period. The mean relative excess mortality ($EM\%$, in percent) of the heat wave days (L) of a summer period can be computed by the following formula:

$$EM\% = 100\sum(M_0 - M_e)L^{-1}. \quad (3)$$

To characterize the whole period, the sum and mean of excess mortality due to heat wave days were calculated above different percentiles in case of each indicator. To define the optimal threshold ranges, the product of the two data was used.

3. Results

3.1. Characteristics of mortality data and temperature indicators

Mortality data of the investigated period are shown in *Table 1*. The summer mean daily mortality of the whole period was 60.8 of the total population and 44.7 of the age group 65 years and over. Maximum daily mortalities were recorded in both age groups in 2007. The standard deviation (SD) was also the highest in that year. Total mortality showed a significant decreasing tendency by 0.33 cases per year in the total population and by 0.21 cases in the older age group.

Table 1. Yearly descriptive statistics of daily mortality of the total population and age group 65 and over years in the summer (cases), periods of 2000–2010 in Budapest

	2000	**2001**	**2002**	**2003**	**2004**	**2005**	**2006**	**2007**	**2008**	**2009**	**2010**	**mean**
M 0-X min	43	46	38	38	40	39	36	35	35	39	36	38.6
M 0-X mean	62.9	62.9	61.3	58.8	61.3	60.8	62.6	61.2	58.2	57.5	60.8	60.8
M 0-X max	106	93	97	89	83	93	99	113	80	82	107	94.7
M 0-X SD	10.5	8.5	10.0	9.7	9.0	9.2	10.9	12.7	9.4	7.7	10.7	9.8
M 65+ min	29	33	28	26	28	29	25	22	22	26	25	26.6
M 65+ mean	46.1	46.7	45.2	43.1	44.9	44.4	45.1	44.9	42.3	42.7	45.8	44.7
M 65+ max	77	72	77	67	65	68	77	95	61	64	78	72.8
M 65+ SD	8.6	7.5	8.4	8.1	6.9	7.3	8.3	10.8	7.2	6.6	8.9	8.0

Table 2 contains the temperature data of the period. The mean of the daily mean temperatures were between 20 °C and 21 °C, the mean of the maximum daily temperatures was around 25–26 °C. Based on the daily mean temperature, the hottest year was 2003, while the daily maximum value was the highest in 2007, when the daily mean temperature was over 32 °C and the daily maximum was over 40 °C. The strongest heat wave was recorded in 2007, when several new record temperature values were measured.

3.2. Associations between the threshold values of temperature indicators and the number of defined heat wave days.

Fig 1 shows the values of the four temperature indicators in relation to different percentiles (p%) of the reference period – between 1990 and 1999 – of the study.

The shapes of the curves of the corresponding indicator pairs were similar in the range of p50–p80. The values of apparent temperature were lower in the cooler periods; the difference reached 2 °C in relation to the values of simple temperature indicators. The threshold values of the apparent temperature were somewhat greater, by 0.2–0.3 °C, in the hottest range. The value of the 90th percentile corresponded to the threshold temperature of the Hungarian Heat Alert System (mean daily temperature, T=25 °C), the exact threshold values were T=25.1 °C, AT=25.5°C, Tx=32.8 °C, and ATx=32.0°C.

Table 2. Yearly descriptive statistics of temperature indicators (°C) in the summer, periods of 2000–2010 in Budapest

	2000	**2001**	**2002**	**2003**	**2004**	**2005**	**2006**	**2007**	**2008**	**2009**	**2010**	**mean**
T min	11.8	10.4	12.9	13.2	10.7	9.9	11.2	9.3	11.7	10.1	8.8	10.9
T mean	20.8	20.2	21.5	22.3	19.7	20.2	20.4	21.7	21.0	21.1	20.0	20.8
T max	29.6	28.8	28.7	29.5	28.2	28.6	28.5	32.3	27.1	27.7	28.7	28.9
Tx min	14.7	14.5	16.1	16.1	14.0	11.7	13.1	11.1	14.6	12.7	10.1	13.5
Tx mean	26.9	25.6	27.0	28.5	25.4	25.2	26.0	27.8	27.0	26.9	24.9	26.5
Tx max	38.0	36.0	35.4	38.3	34.4	35.2	35.9	40.6	36.1	35.0	35.2	36.4
AT min	10.3	8.4	10.7	10.6	8.0	8.0	9.6	7.5	9.1	8.3	6.6	8.8
AT mean	19.8	19.7	21.4	21.8	19.0	20.0	20.5	21.3	20.6	20.4	20.5	20.5
AT max	29.9	30.0	29.1	28.9	28.6	31.5	31.8	32.6	28.4	29.1	31.9	30.2
ATx min	13.2	12.7	13.9	15.2	11.3	10.3	11.5	9.3	12.0	10.9	7.9	11.6
ATx mean	25.9	25.1	26.9	27.9	24.7	25.1	26.1	27.4	26.5	26.2	25.4	26.1
ATx max	37.0	37.2	36.8	37.7	34.8	37.6	37.5	40.7	37.4	35.7	38.3	37.3

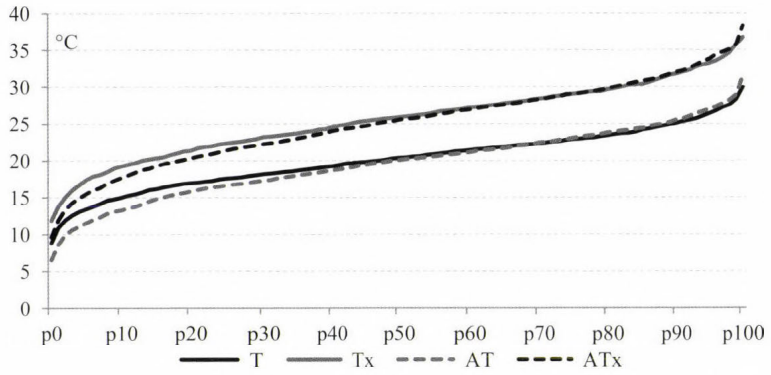

Fig. 1. Values of the four temperature indicators (°C) in relation to the percentiles between 1990 and 1999 in Budapest.

The temperature indicators identified different numbers of heat wave days in the period of 2000–2010. *Fig. 2* demonstrates the numbers of heat wave days by different threshold values in the warmer intervals. It can be observed that apparent temperature indicators defined more heat wave days. This means that the different indicators identified the same number of heat waves by different percentiles. The curves of the *T-Tx* and *AT-ATx* indicator pairs crossed each other several times in relation to threshold values.

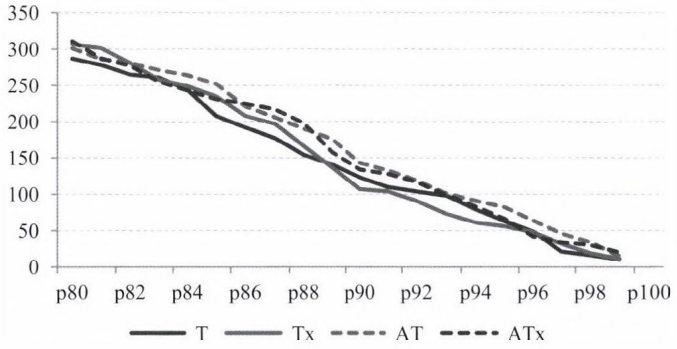

Fig. 2. Number of heat wave days defined by the four indicators in relation to percentiles between 2000 and 2010 in Budapest.

Fig. 3 represents the number of heat waves lasting for three or more days defined by the 90th percentile by different indicators. In some years, the number of heat waves defined by different indicators was the same (2001, 2005); however, the number of heat waves was different in most of the years. In the period from 2006 to 2010, the differences in the number of heat waves became bigger and more frequent. The yearly mean numbers of heat waves were 1.9–2.5 events.

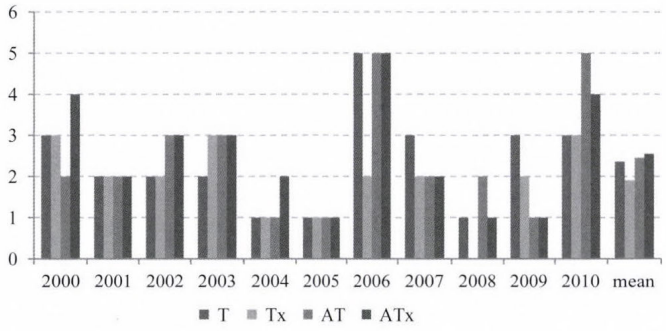

Fig. 3. The number of heat waves defined by the 90th percentile of indicators between 2000 and 2010 in Budapest.

Fig. 4 represents the number of heat wave days defined by the 90th percentile by different indicators. The numbers of heat wave days were different in each year. The differences became greater and more frequent in the last five years. The yearly mean numbers of heat wave days were between 10 and 13 days.

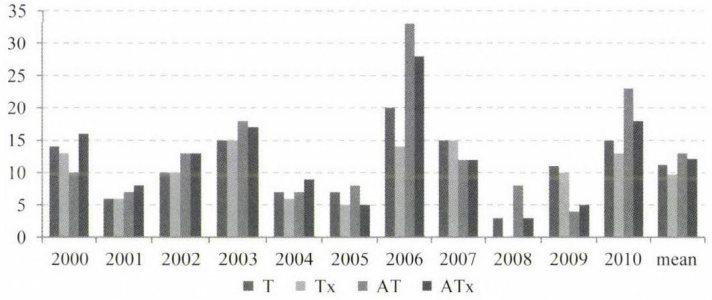

Fig. 4. The number of heat wave days defined by the 90th percentile of indicators between 2000 and 2010 in Budapest.

Based on the previous results, we can state that different heat wave days were identified by the different indicators. It was necessary to test to what extent the heat wave days were defined by the indicators as identical. *Fig. 5* shows the number of heat wave days defined by the indicator pairs, furthermore, the number of identical heat wave days defined by both indicators for the whole study period. The most heat wave days were identified by the indicator pairs *AT* and *ATx* (143 and 134 days, respsctively), while 123 and 107 days were identified by *T* and *Tx*. The number of identical heat wave days was between 88 and 129 days, meaning a correspondence of a range of 66–87% by indicators.

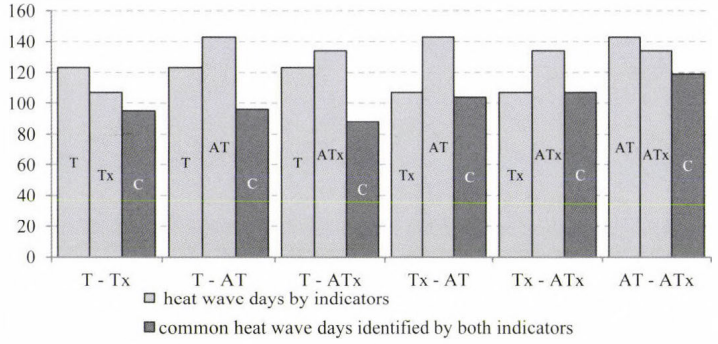

Fig. 5. The number of heat wave days identified by indicator pairs at the 90th percentile threshold value and the number of common heat wave days identified by both indicators between 2000 and 2010 in Budapest.

3.3. *Associations of heat and mortality*

The association between daily mortality and temperature has a U or J shape in general. In case of Budapest, the curve has a typical J shape. *Fig. 6* shows the difference of the daily mortality from the mean mortality in relation to daily mean temperature in the total population and in the group over 65 years. The approximate curve was produced by a cubic spline function having 4 degrees of freedom. The shape of the curves were similar, however, the effect of the temperature was somewhat bigger in the older age group. There was a higher mortality on cooler (<10 °C mean temperature), and warmer days (>23 °C mean temperature). The daily mortality significantly increased on days with higher mean temperature; the difference was greater than 40% on the hottest days. Concerning daily mortality, the optimal temperature range was between 17–20 °C. The shapes of the curves of the other indicators were similar.

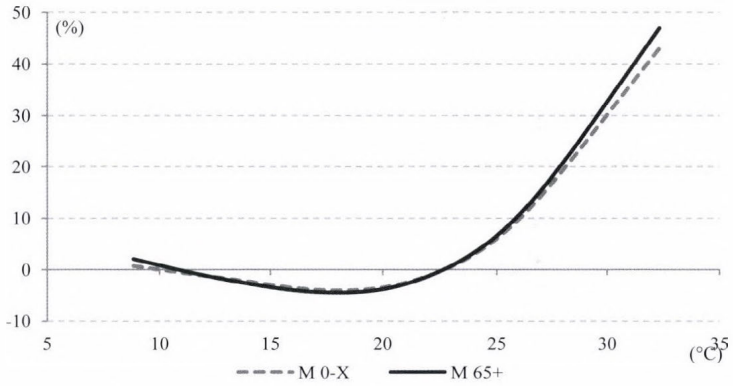

Fig. 6. Characteristics of association of daily mortality (percent differences from mean mortality) and daily mean temperature between 2000 and 2010 in Budapest.

3.4. *Effect of heat waves on mortality*

Fig. 7 shows the calculated daily expected total mortality (M_e) during the studied period and the total observed mortality (M_o) of the heat wave days by years. The expected daily mortality calculated on the basis of a 5-year moving reference period showed a decreasing tendency in relation to time. An excess mortality could be observed on the heat wave days in each year. In 2008, no heat wave was defined by the *Tx* indicator; therefore, no excess mortality was shown. The observed mortality was higher than expected mortality in every year. The association was similar in the older age group as well (not shown).

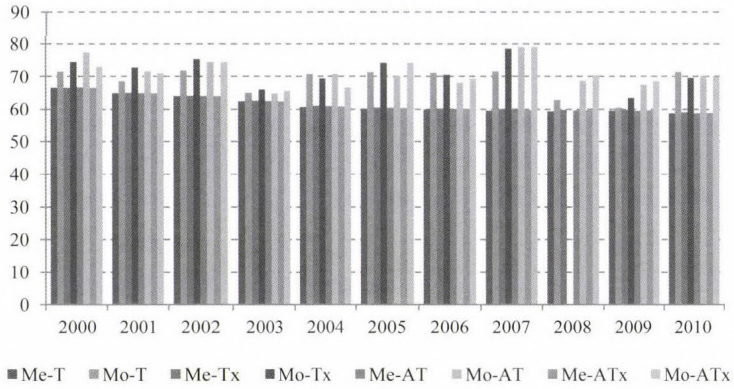

Fig. 7. The expected daily total mortality (M_e) and the observed total mortality (M_o) during the heat wave days defined by the four indicators between 2000 and 2010 in Budapest.

Fig. 8 shows the difference between observed and expected mortality: the excess mortality by years. The yearly numbers of excess mortality due to heat waves showed great variability. The lowest excess mortality was observed in 2008, and it was also very low in 2009 and 2001. The highest excess mortality was recorded in 2007, due to the strongest heat wave ever recorded. In that year, the number of excess death cases was 230–270 in the total population and 202–240 cases in the older age group during the 15 heat wave days by the different indicators. Similarly high excess mortality was observed in 2006 and 2010. There were great differences in the number of excess death cases in those years, when the indicators identified considerably different numbers of heat wave days (in 2006, 2008, and 2010). An average of 102–122 excess mortality cases could be attributed to heat waves in the total population, whereas there were 86–96 cases in the older age group defined by the different indicators. The mean percent excess mortality was between 15–18%; however, it surpassed 30% in 2007.

3.5. The relationship of excess mortality and different threshold values

The sum of death cases decreased by the increase of temperature threshold values as the number of identified heat wave days decreased. On the other hand, excess mortality increased on days with increasing temperature, while the mean excess mortality on identified heat wave days increased in relation to threshold values. To define the proper threshold, the product of the corresponding values of the two curves can be used. At the maximum range of the product curve, the two opposite processes were equally considered. *Fig. 9* represents the sum of total excess mortality, the mean excess mortality above different percentiles, as well as the product of the two datasets in case of daily mean temperature

indicator. The shapes of the curves of the sum of total excess mortality and the mean excess mortality changed more steeply over the 80th percentile, the value of their product started to increase over this percentile. Above the 95th percentile, the total excess mortality started to decrease significantly, while the excess mortality on heat wave days changed in the opposite direction. The range between the 85th and 95th percentiles met the criteria of the threshold value the best. The chosen threshold of daily mean temperature is 25 °C, which is the national alert threshold, corresponding to the 90th percentile seemed to be a suitable cut-off point. The shapes of the curves of the other indicators were similar (not shown).

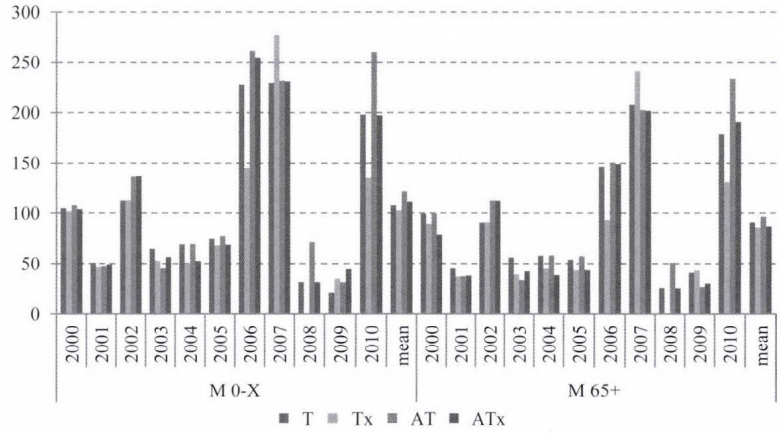

Fig. 8. The difference between expected and observed mortality in the total population and in the older age group between 2000 and 2010 in Budapest.

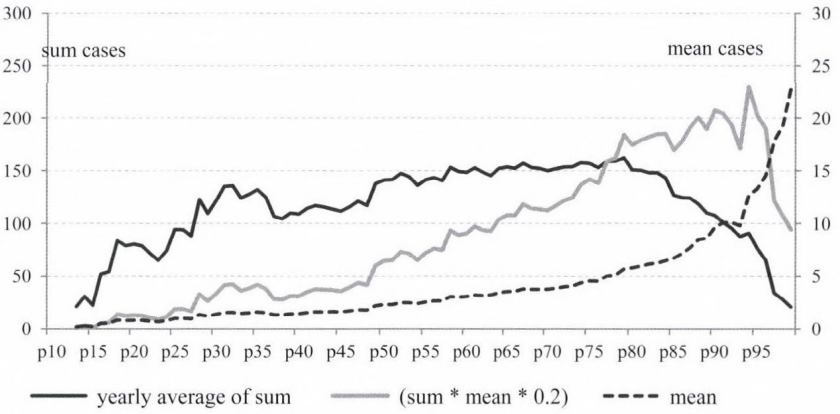

Fig. 9. The sum of total excess mortality, the mean excess mortality of heat wave days above thresholds, as well as their product in case of daily mean temperature indicator between 2000 and 2010 in Budapest.

The increase of the mean excess mortality on heat wave days in relation to the threshold values differed by the different temperature indicators (*Fig 10*). Similar values of excess mortality could be observed within the range of 85th–92nd percentiles of temperature indicators. In the range of higher temperatures, the differences between the shapes of the curves were bigger, the highest excess mortality could be observed when using the daily mean temperature indicator. In case of the other three indictors, considerably lower increase of excess mortality was related to the increase of threshold values. Excess mortality increased only over the threshold value corresponding to the 99th percentile.

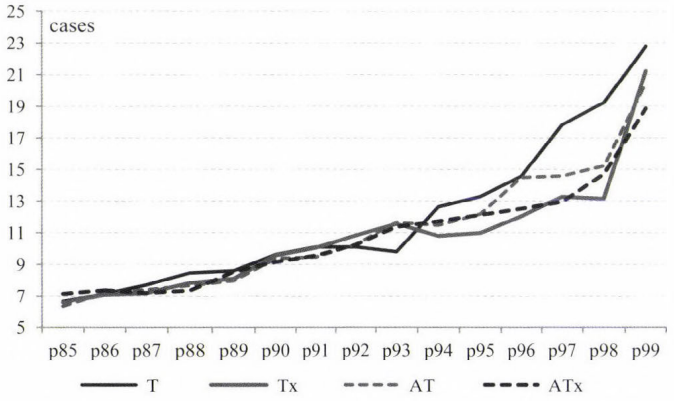

Fig. 10. The mean excess mortality on days above threshold by different indicators between 2000 and 2010 in Budapest.

4. Discussion

Heat related mortality was studied very intensively in the last two decades all around the world. The adverse impact was shown with great certainty. Several methods were used to characterize heat waves; different indicators were elaborated and applied.

The majority of studies used simple temperature parameters to characterize the impact of heat, while others applied more complex thermal indices based on different meteorological factors like humidity, radiation, wind speed, etc. Many papers tested several indicators in order to find the most suitable temperature predictor to detect heat-related excess mortality (*Barnett et al.,* 2010; *Kim et al.,* 2011; *Vaneckova et al.,* 2011; *Yu et al.,* 2011; *Morabito et al.,* 2014). The results could not identify the best indicator, the use of complex indices did not prove to be more efficient in determining the impact. Furthermore, the computation of complex indices is troublesome, their forecast is more ambiguous.

There is no universal definition of heat waves; the threshold values also show great variability. Health endpoints also vary, different age and cause-specific mortalities, as well as different groups (sex, race, socio-economic state, etc.) are studied. The results within multicenter studies can be compared due to the applied common methodology.

There is an increasing need to have comparable results in the public health system. The CEHAPIS methodology aims to monitor the change of heat related mortality in relation to climate change in the long run. The major concept was to develop simple indicators and computation for wide range use and comparability. Similarly to climate models, a 10-year reference period of the temperature indicators (daily maximum and daily apparent maximum temperature) is used in order to follow the future changes. The methodology describes heat waves as days with at least three consecutive days above the threshold value of temperature indicators defined as the 95th percentile of the reference temperature. The methodology recommends assessing the impact on cities with more than 500,000 inhabitants. Mortality, excluding external causes of the total and the 65 years and older population, is used to characterize vulnerability. A moving reference period (five years prior to the year of study year) of mortality is chosen to follow the changes of sensitivity (aging, adaptation, etc.). The expected (baseline) mortality, i.e., the average daily number of deaths is calculated using daily mortality in the reference period excluding the daily number of deaths on heat wave days. In the present paper, two simple temperature indices (T, Tx) and two other ones including humidity (AT, ATx) were used. The calculations did not need sophisticated statistical methods.

The mortality data of Budapest showed a significantly decreasing tendency. The use of a moving reference period could handle this tendency when calculating the expected values, i.e., the baseline decreased from year to year. No trend could be observed in the temperature data, as well as in the number of heat waves or heat wave days. It can be supposed that the increasing tendency of temperature due to heat waves will be detectable by these indicators using longer time series.

The different indicators identified different numbers of heat wave days by different threshold values in the warmer intervals. Using the same percentiles, the number of heat waves and the number of heat wave days were different in most of the years. Furthermore, the number of identical heat wave days defined by the indicator pairs showed great variability. This meant that the chosen temperature indicator considerably defined the length and number of heat waves and consequently, influenced the number of excess death cases of the given year. This phenomenon was detected in case of defined threshold as the result of calculated excess mortality showed. It should always be taken into consideration; however, this is a general feature of each other methodology as well.

The product function provides help to determine the optimal indicator and threshold. The range between the 85th and 95th percentiles was found to meet the criteria of the threshold values the best. This range is wide enough to make a choice based on several criteria. If we would like to detect the most cases of excess mortality, then we should choose a lower threshold value that can identify more heat waves. If we would like to identify heat waves with bigger numbers of excess death cases, then we have to choose a threshold of a higher percentile. When we would like to compare the impact of heat in several cities, we should choose a common threshold suitable for each city. Further analyses are necessary to test the applicability of the method in multicenter studies.

The mean excess mortality on days above threshold by different indicators can provide further assistance to choose the suitable indicator. Similar values of excess mortality can be observed within the range of the 85th – 92nd percentiles of temperature indicators. Within this range, the indicators are similarly sensitive and effective. In the range of higher temperatures above the 92nd percentile, the differences of the shapes of curves are bigger. The highest excess mortality can be observed when using the daily mean temperature indicator, therefore, it is more effective. On the other hand, the other three indicators are less sensitive in the range of the 94th–98th percentiles; they can effectively identify excess mortality on very hot days. Further analyses are required to answer the question, to what extent the Budapest findings can be used in other cities.

The threshold in this study – the national alert threshold, which is the 25 °C daily mean temperature, corresponding to the 90th percentile – seems to be a suitable cut-off point. This threshold, lower than the one recommended by the CEHAPIS methodology, was chosen, while an excess death rate of 7% was detected at this cut off point of the sensitivity curve. This increase of mortality already requires actions according to the public health authorities.

5. Conclusion

The aim of the study was to develop a simpler method than time series analysis to identify excess mortality attributable to heat. The methodology is suitable to assess the changes of weather and climatic conditions to follow the impact of heat on daily mortality. The results are in accordance with the findings of previous studies.

At the chosen threshold value of 90th percentile, the mean excess mortality of the whole period computed by using the four indicators did not differed considerably, although the identified heat wave days varied to some extent. The use of apparent temperature indicators is not more advantageous and their prediction is more complicated. The apparent temperatures as well as the maximum temperature indicator are able to identify high excess mortality mainly on very hot days, while the daily mean temperature indicator is effective

in a wider threshold range. Based on these results, the use of daily mean temperature is recommended.

The thorough analysis of threshold values is desirable using longer time series of the data of different cities. By this comparative analysis, we can get an answer to whether the system based on the daily mean temperature can be generalized.

References

Baccini, M., Biggeri, A., Accetta, G., Kosatsky, T., Katsouyanni, K., Analitis, A., Anderson, H. R., Bisanti, L., D'Ippoliti, D., Danova, J., Forsberg, B., Medina, S., Paldy, A., Rabczenko, D., Schindler, C., and *Michelozzi, P.,* 2008: Heat effects on mortality in 15 European cities. *Epidemiology 19,* 711–719.

Baccini M., Kosatsky T., Analitis A., Anderson H. R., D'Ovidio M., Menne B., Michelozzi P., and *Biggeri, A.,* 2011: PHEWE Collaborative Group. Impact of heat on mortality in 15 European cities: attributable deaths under different weather scenarios. *J Epidemiol. Commun. Health 65,* 64–70.

Barnett, A.G., Tong, S., and *Clements, A.C.A.,* 2010: What measure of temperature is the best predictor of mortality? *Environ. Res. 110,* 604–611.

Basu, R., 2009: High ambient temperature and mortality: a review of epidemiologic studies from 2001 to 2008. *Environ. Health 8,* 40.

Bobvos, J. and *Paldy, A.,* 2009: Impact of Heat on the Urban and Rural Population in Hungary. *Epidemiology 20, S127.*

Bobvos, J., Solymosi, N., and *Paldy, A.,* 2011: Climate change and heat-related mortality in Budapest - comparative methods of impact estimation of temperature change. *Environ. Health Perspect.* Available at: http://ehp.niehs.nih.gov/isee/, accessed 15 April 2014.

D'Ippoliti, D., Michelozzi, P., Marino, C., de'Donato, F., Menne, B., Katsouyanni, K., Kirchmayer, K., Analitis, A., Medina-Ramón, M., Paldy, A., Atkinson, R., Kovats, R.S., Bisanti, L., Schneider, A., Lefranc, A., Iñigue. C., and *Perucci, C.A.,* 2010: The impact of heat waves on mortality in 9 European cities: results from the EuroHEAT project. *Environ. Health 9,* 37.

Gosling, S.N., McGregor, G.R., and *Paldy, A.,* 2007: Climate change and heat-related mortality in six cities Part 1: model construction and validation. *Int. J. Biometeorol. 51,* 525–540.

Gosling, S.N., Lowe, J.A., McGregor, G.R., Pelling, M., and *Malamud, B.D.,* 2009a: Associations between elevated atmospheric temperature and human mortality: a critical review of the literature. *Climatic Change 92,* 299–341.

Gosling, S N., McGregor, G.R., and *Lowe, J.A.,* 2009b: Climate change and heat-related mortality in six cities Part 2: climate model evaluation and projected impacts from changes in the mean and variability of temperature with climate change. *Int. J. Biometeorol. 53,* 31–51.

GSOD, 2010: Global surface summary of the day data Version 7. At National Climatic Data Centre (NCDC). Available at: ftp://ftp.ncdc.noaa.gov/pub/data/gsod/, accessed 15 April 2014.

Hajat, S., Armstrong, B., Baccini, M., Biggeri, A., Bisanti, L., Russo, A., Paldy, A., Menne, B., and *Kosatsky, T.,* 2006: Impact of high temperatures on mortality: is there an added heat wave effect? *Epidemiology 17,* 632–638.

Hajat, S., Kosatky, T., 2010: Heat-related mortality: a review and exploration of heterogeneity. *J. Epidemiol. Commun. Health 64,* 753–760.

IPCC, 2013: Climate Change 2013: The Physical Science Basis. Summary for Policymakers. In: (Eds.: *Stocker, T.F., Qin, D., Plattner, G.K., Tignor, M., Allen, S.K., Boschung, J., Nauels, A., Xia, Y., Bex, V., Midgley, P.M.*) Contribution of Working Group I to the Fifth Assessment Report of the Intergovernmental Panel on Climate Change. Cambridge University Press, Cambridge, United Kingdom and New York, NY, USA.

IPCC, 2014: Climate Change 2014: Impacts, Adaptation, and Vulnerability. Summary for Policymakers. In: (Eds. *Aldunce, P., Ometto, J.P., Raholijao, N., Yasuhara, K.*) Final draft of Working Group II to the Fifth Assessment Report of the Intergovernmental Panel on Climate Change. Available at: http://ipcc-wg2.gov/AR5/images/uploads/IPCC_WG2AR5_SPM_Approved.pdf, accessed 15 April 2014.

Ishigami, Ai., Hajat, S., Kovats, R. S., Bisanti, L., Rognoni, M., Russo, A., Paldy, A., 2008: An ecological time-series study of heat-related mortality in three European cities. *Environ. Health . 7,* 5.

Kalkstein, L.S. and *Valimont, K.M.,* 1986: An evaluation of summer discomfort in the United States using a relative climatological index. *Bull. Am. Meteorol. Soc. 67,* 842–848.

Kim, Y.M., Kim, S., Cheong, H.K., Kim, E.H., 2011: Comparison of temperature indexes for the impact assessment of heat stress on heat-related mortality. *Environ. Health Toxicol. 26,* Available at: http://dx.doi.org/10.5620/eht.2011.26.e2011009, accessed 15 April 2014.

Kovats, R S. and *Ebi, K.L.,* 2006: Heatwaves and public health in Europe. *Eur. J. Publ.Health 16,* 592–599.

Kovats, R.S. and *Hajat, S.,* 2008: Heat stress and public health: a critical review. *Ann. Rev. Publ. Health 29,* 41–55.

Morabito, M., Crisci, A., Messeri, A., Capecchi, V., Modesti, P. A., Gensini, G. F., and *Orlandini, S.,* 2014: Environmental Temperature and Thermal Indices: What Is the Most Effective Predictor of Heat-Related Mortality in Different Geographical Contexts? *Sci. World J.* Available at: http://dx.doi.org/10.1155/2014/961750 , accessed 15 April 2014.

Paldy, A., Bobvos, J., Vamos, A., Kovats, R.S., and *Hajat, S.,* 2005: The effect of temperature and heat waves on daily mortality in Budapest, Hungary, 1970–2000. In: (Eds. *Kirch, W., Menne, B., Bertollini, R.*) Extreme weather events and public health responses. Springer, New York, 99–107.

Paldy, A. and *Bobvos, J.,* 2009: Impact of the Unusual Heatwave of 2007 on Mortality in Hungary . *Epidemiology 20(6),* S126–S127.

Paldy, A., Juhasz, A., Bobvos, J., and *Nagy, CS.,* 2011: Modelling of the association of health impacts of exposure to 2007-heatwave and the effect modifiers at small area level in Hungary . *Environ. Health Perspect.* Available at: http://ehp.niehs.nih.gov/isee/, accessed 15 April 2014.

Vaneckova, P., Neville, G., Tippett, V., Aitken, P., Fitzgerald, G., Tong, S., 2011: Do biometeorological indices improve modeling outcomes of heat-related mortality? *J. Appl. Meteorol. Climatol. 50,* 1165–1176.

WHO, 2011: Tools for the monitoring of Parma Conference commitments. Report of the meeting 25–26 November 2010. Available at:http://www.euro.who.int/data/assets/pdf_file /0019/134380/e94788.pdf, accessed 15 April 2014.

Yu, W., Guo, Y., Ye, X., Wang, X., Huang, C., Pan, X., and *Tong, S.,* 2011: The effect of various temperature indicators on different mortality categories in a subtropical city of Brisbane, Australia. *Sci.Total Environ. 409,* 3431–3437.

IDŐJÁRÁS

Quarterly Journal of the Hungarian Meteorological Service
Vol. 119, No. 2, April – June, 2015, pp. 159–184

Multivariable cyclone analysis in the Mediterranean region

Fanni Dóra Kelemen*, **Judit Bartholy**, and **Rita Pongrácz**

Eötvös Loránd University, Department of Meteorology
Pázmány P. sétány 1/A, 1117 Budapest, Hungary

**Corresponding author E-mail: kelemenf@nimbus.elte.hu*

(Manuscript received in final form September 22, 2014)

Abstract—This paper analyzes midlatitude cyclones identified and tracked in the Mediterranean region for the recent past, between 1981 and 2010. The Mediterranean region is especially interesting since the complex land orography favors lee cyclogenesis, and the warm sea area provides latent heat for the developing cyclones. These cyclones may result in heavy precipitation, even flood events affecting southern and central Europe, including Hungary.

Cyclones are identified using two different reanalyses, the ERA Interim reanalysis from ECMWF at 0.75° horizontal resolution and the NCEP-DOE R2 reanalysis at 2.5° horizontal resolution. For the identification, a multivariable approach is used to eliminate and assess the uncertainties rising from the choice of a specific variable, which is particularly important in the Mediterranean, where the systems are tend to be weak and shallow. Mean sea level pressure (MSLP), geopotential heights of the 1000 hPa, and the 850 hPa isobaric levels are used as main variables, and relative vorticity at 850 hPa isobaric level serves, an additional variable. The applied algorithm has uni- and bivariate modes. In the bivariate mode, relative vorticity at 850 hPa is added to the main variable.

The results suggest that time series of annual number of cyclones using the two reanalyses correlate significantly, however, using the higher resolution dataset, more cyclones can be identified. The largest and the smallest frequency of cyclones over the entire domain occur in spring and summer, respectively. The largest spread of the multivariable ensemble is in summer, probably caused by non-frontal thermal lows. Furthermore, summer is mostly dominated by short-lived cyclones. The main cyclogenesis regions are the Gulf of Genoa and the Cyprus region, with some minor centers at the Adriatic Sea, the northern part of the Black Sea, and the Iberian Peninsula. The cyclone frequency trend is slightly increasing in most parts of the region, especially over the Adriatic Sea and near Cyprus. Hungary is affected annually by approximately 30 cyclones from the Mediterranean area, most frequently in spring.

Key-words: cyclone identification, cyclone tracking, cyclone climatology, Mediterranean region, reanalysis, MSLP, geopotential height, relative vorticity

1. Introduction

Mid-latitude cyclones play a major role in the general circulation of the atmosphere, they largely contribute to the energy transfer between the equatorial and the polar regions. The potential energy derived from the temperature differences of air masses along the frontal surface is transformed by cyclones into kinetic energy. Cyclones are basically large vortices, in which warm and moist air mixes with cold and dry air. Through this process, energy is transformed and released.

In the Mediterranean region, the presence of large warm sea surface almost completely surrounded by land (the Mediterranean sea is connected to the ocean only through narrow straits) and the orography both induce the evolution of cyclones. The cyclones occurring in this region transfer moist and warm air over the continental regions, then, as mixing with colder air, the embedded moisture condensates, often resulting in intensive precipitation. *Jansa et al.* (2001) showed that the majority of heavy rain events in the Mediterranean occurred in the vicinity of a cyclone center. Thus, these cyclones determine substantially the local weather and climate.

The cyclones associated with intensive precipitation can cause floods, or other severe weather events, like on March 15th, 2013 when a snowstorm hit Hungary. The snow even caused power-cut in some regions of the country. In large areas of Hungary snowdrift occurred, which resulted in chaotic traffic conditions, especially due to the coincidence of the storm with a national holiday. Also in 2013, severe flood occurred in Central Europe, which was mainly caused by the precipitation of three consecutive cyclones triggered by a cut-off at the upper level of the atmosphere (*Grams et al.*, 2014). The relationship between Mediterranean cyclones and Central European floods is often mentioned, i.e., the Vb cyclone track from the *van Bebber* (1891) categories is usually associated with flood events (*Hofstätter et al.*, 2012), for example the Danube flood in Central Europe in 2002 (*Ulbrich et al.*, 2003).

The aim of this study is (i) to analyze objectively the cyclones in the Mediterranean region with particular focus on the Genoa lows, (ii) to investigate the performance of the multivariable cyclone identification method, and (iii) to overview the climatology of those cyclones coming from the Mediterranean region, which directly affect Hungary.

The exact identification of a mid-latitude cyclone is difficult since there are no generally accepted criteria. Cyclone identification and tracking can be done by manually analyzing meteorological fields, however, for comprehensive analyses, objective methods must be used. The most commonly used method for cyclone identification is to search local extremes in a selected variable field, and connect the successive centers according to some constraints.

One of the most commonly used variable for cyclone identification is the mean sea level pressure (MSLP) (*Serezze*, 1995; *Lionello et al.*, 2002; *Hanson et*

al., 2004; *Bartholy et al.*, 2008), which refers to the pressure information at a specific surface reduced from the geographic surface by using a temperature profile. This reduction estimates the pressure at sea level sometimes below the actual surface level. Since temperature profiles affect the MSLP values and they can be unusual at high elevations, the fields can produce anomalous patterns in the area of mountains. In addition to MSLP, some detecting algorithms calculate the gradient of MSLP as well, to find a cyclone center (*Picornell et al.*, 2001; *Jansa et al.,* 2001). Others investigate the Laplacian of MSLP (*Murray* and *Simmonds,* 1991), which can be interpreted as the quasi-geostrophic relative vorticity (*Pinto et al.,* 2005). Besides quasi-geostrophic relative vorticity, relative vorticity at 850 hPa can also be used to identify cyclones (*Hodges et al.*, 2011*; Catto et al.,* 2010; *Woollings et al.,* 2010). 850 hPa isobaric level can be considered as the lowermost level of the free atmosphere. Relative vorticity has an advantage over MSLP, namely, it is more independent from the direct effects of topography. *Hoskins* and *Hodges* (2002) compared several cyclone climatology results using different fields, and they showed that relative vorticity is especially good when describing smaller-scale systems, which are typical in the Mediterranean region. On the other hand, the disadvantage of using relative vorticity is that at high resolution it becomes a very noisy field (*Hodges et al.,* 2011). Hence, a truncation of the field is necessary if relative vorticity field is the key element of the identification algorithm. Besides MSLP and relative vorticity, geopotential height of the 1000 hPa is also used to identify cyclones (*Trigo et al.,* 1999, 2000; *Alpert et al.*, 1990).

Most of the studies considered only one specific variable to identify cyclones, sometimes including its derivatives, too. An exception is found in *König et al.* (1993), who used both the 850 hPa relative vorticity and 1000 hPa geopotential height, however, their algorithm considered these fields separately and later combined the information from the two fields along the lifecycle of a specific cyclone.

All Lagrangian cyclone identification methods are based on a search for local extremes in a selected gridded field. The most common approach is to investigate the neighboring points of a grid point. In many cases, only the 8 nearest neighboring points are analyzed (*Alpert et al.,* 1990; *Trigo et al.*, 1999; *Hanson et al.,* 2004; *Maheras et al.*, 2001) whether the values are larger or smaller than in the central point. Sometimes the evaluated area covers a larger region, i.e., 5×5 grid points or even more (*Bartholy et al.*, 2008). Obviously, the investigated region size depends on the grid's horizontal resolution. For a 2.5° horizontal resolution grid, the investigation of the 8 neighboring points is adequate for cyclone center identification. In case of higher resolution grid, the investigated area should cover the same sized region, which evidently includes more grid points. Another way to find local minima in a gridded field is used by *Lionello et al.* (2002). They identified at each time step the sets of the steepest decreasing paths, which led to the same MSLP minimum by comparing the

neighboring point values. *Picornell et al.* (2001) and *Jansa et al.* (2001) used MSLP for their studies, where the search of MSLP minimum was extended with the analysis of pressure gradients around the already found minimum points along eight major directions (E, NE, N, NW, W, SW, S, SE). If the gradient exceeds a threshold along at least six directions then the system is considered to an open cyclone, whereas if the gradients are sufficiently large along all the eight directions then the system is considered to be a closed cyclone. Open and closed systems have been distinguished at other studies, too (e.g., *Sinclair*, 1994; *Murray* and *Simmonds*, 1991; *Picornell et al.*, 2001). *Sinclair* (1994) analyzed the geostrophic relative vorticity (calculated from 1000 hPa geopotential height) and used MSLP to decide whether a system is closed or not. He considered a system to be closed in the Southern Hemisphere if its vorticity minimum was closer than 5° latitude to a pressure minimum.

To get a more comprehensive picture about cyclones, the identified centers are usually tracked by a criterion to follow the center along the lifecycle of the cyclone. In some studies the tracking is not included (e.g., *Jansa et al.*, 2001; *Finnis et al.*, 2007). The most common tracking technique is the nearest neighbor concept, where the continuation of one specific cyclone is that center in the following time step, which is located the nearest to the center of the preceeding step. The search for the nearest neighbor is sometimes specified in an area often asymmetric to the center, taking into account the typical eastward movement of the mid-latitude cyclones. For example, when a rectangular area around the center is evaluated, its west-east axis is longer than the north-south axis (*König et al.*, 1993). *Trigo et al.* (1999) used a method, which searches for the next cyclone center within an area determined by the maximum cyclone velocity (33 km/h westward and 90 km/h in any other direction). Another tracking approach (i.e., *Murray* and *Simmonds*,1991; *Sinclair,* 1994; *Pinto et al.*, 2005; *Wernli* and *Schwierz*, 2006) pre-estimates the new position of a cyclone, evaluates all the cyclone centers being close to this first guess location, and selects the most likely candidate. This technique is a good solution when the available time steps are not too frequent, so the cyclones' separation and displacement should be considered together. Tracking method of *Muskulus* and *Jacob* (2005) uses the Kalman filter approach, in which the matching is carried out by minimizing a weighted prediction error function. This technique has several advantages: (i) besides one previous time step, it can consider the whole lifetime of the cyclone, and (ii) estimating the error, which predicts the maximum distance for the next match.

Depending on the identification technique and the aim of a particular study, additional filtering of the identified cyclones is possible. The most common filtering is to use thresholds for the cyclones' lifetime and/or for the MSLP of their centers. For instance, the lifetime of accepted cyclones should last longer than 12 hours (*Trigo et al.*, 1999), and the pressure of the cyclone center should be lower than 1000 hPa (*Gulev et al.*, 2001; *Muskulus* and *Jacob*, 2005).

Bartholy et al. (2008) considered different lifetime thresholds for Atlantic-European and Mediterranean cyclones (3 days and 1 day, respectively).

For some special applications, the extension of the cyclone must be calculated, e.g., *Hanson et al.* (2004) and *Trigo et al.* (1999) applied the definition from *Nielsen* and *Dole* (1992), according to which the cyclone radius is the distance between the center and the outermost closed isobar. *Muskulus* and *Jacob* (2005) used a watershed segmentation method for cyclone identification, and also for determining the area of the cyclones. *Piocornell et al.* (2001) defined the cyclone area as the positive geostrophic vorticity area around the center. The zero vorticity line is determined along the four main directions (N, E, S, W), and these points form an ellipse, which is the final cyclone area.

Due to the lack of exact identification of cyclone tracks, several cyclone tracking methods are available, and they can be used for cross-validation. The manual analyses are highly influenced by the subjective choices made by the analyst. The Intercomparison of Mid Latitude Storm Diagnostics (IMILAST) project (*Neu et al.*, 2013) made an effort to investigate the method-related uncertainties of cyclone identifications, and concluded that the results can be sensitive to several aspects of the applied method. They found important differences in the interannual variability and geographical distribution of cyclones in the Mediterranean. That is why we use a multivariable cyclone identification ensemble in this study for this region. In our identifying system, the same algorithm forms several individual methods with different variables used to identify cyclone centers. This way the uncertainties arising from the variable choice are assessed and taken into account in the final conclusions.

The paper briefly presents the used two reanalyses in Section 2. Then, in Section 3, the methodology and composition of the multivariable ensemble are described. In Section 4, the results of the cyclone time series based on the two reanalyses are compared, then, the ERA Interim results are analyzed in detail. The features of the ensemble are investigated, then the annual variability and trends of cyclones are analyzed. The section is closing with a short analysis of the cyclones passing over Hungary. The study ends with the discussions (Section 5) followed by the conclusions (Section 6).

2. Data

The present cyclone analysis is based on reanalysis data forming a spatially and temporally appropriate resolution, regular database, which is needed for the objective. Here, two available reanalyses are selected, the European Centre for Medium-Range Weather Forecasts (ECMWF) Reanalysis (ERA Interim) (*Dee et al.*, 2011) and the reanalysis data from the National Centers for Environmental Prediction (NCEP) and the National Energy Research Supercomputing Center (NERSC) of the Department of Energy (DOE) (*Kanamitsu et al.*, 2002) (NCEP-

DOE R2), which is the updated NCEP/NCAR (National Center for Atmospheric Research) reanalysis. Both datasets are available from 1979 up to the recent past, and we use the data for the 30-year period between 1981 and 2010. Both of the reanalyses are widely used for cyclone climatology studies. Preceding reanalyses of ECMWF (i.e., ERA-15, ERA-40) were earlier used by *Alpert et al.* (1990), *Sinclair* (1994), *Trigo et al.* (1999), *Hoskins* and *Hodges* (2002), *Hanson et al.* (2004), *Wernli* and *Schwierz* (2006), *Bartholy et al.* (2008), *Catto et al.* (2010). Some of these studies, e.g., *Trigo et al.* (1999), *Alpert et al.* (1990) and *Bartholy et al.* (2008) investigated the Mediterranean region. NCEP reanalyses were also used for cyclone analysis in general (e.g., *Hanson et al.*, 2004; *Pinto et al.*, 2005; *Hodges et al.*, 2011), and for the Mediterranean region, too (e.g., *Maheras et al.*, 2001).

ERA Interim is constructed with a use of a spectral model, whose horizontal resolution is expressed by its truncation number T255 indicating the number of waves used to represent the data. This horizontal resolution corresponds with a lat-lon 0.75°×0.75° regular grid, and the data can be downloaded in this interpolated form.

The NCEP-DOE R2 dataset is available on a 2.5°×2.5° horizontal resolution lat-lon grid, which we interpolated to a 0.75°×0.75° grid to achieve the same grid resolution as ERA Interim. The interpolation was made by a bicubic spline method. *Pinto et al.* (2005) showed that the use of spline interpolation improves the localization of cyclones. The improvement is mainly due to the better spatial representation of cyclone centers, however, this method does not add any extra information to the original data. The bicubic spline interpolation produces a smooth field from the original data, since it utilizes both the first and the second derivatives of the original data. The interpolation formula is smooth in the first derivative and continuous in the second derivative.

Both ERA Interim and NCEP-DOE R2 are used with a 6-hour temporal resolution.

The area investigated in this study is the Mediterranean region from 29.25°N to 55.5°N and from 11.25°W to 42.75°E, which is approximately the Med-CORDEX region (*Ruti et al.*, 2015), and thus, it eases future comparison of our reanalysis results to the climate simulations interpolated on the Med-CORDEX domain.

Pressure and geopotential fields are directly available from both database. The relative vorticity field is available only in case of the ERA Interim reanalysis. In order to use similar methodology and ensure consistency in the analysis, we calculate vorticity from the wind fields both from ERA Interim and NCEP-DOE R2.

3. Method

A multivariable ensemble approach is used in this study to assess uncertainties due to the selection of specific cyclone identification method. Several objective methods exist for identifying mid-latitude cyclones using more or less similar (however, not exactly identical) criteria. The advantages of objective methods are shown in *Jansa et al.* (2001), where more cyclones were found with using an objective analysis of high resolution model data than with the human-based subjective analysis. The objective analysis has special advantages in the areas with less measurements and meteorological experiences. Furthermore, the assessment of differences in objective methods is studied in the framework of the IMILAST project (*Neu et al.*, 2013), which is an explicit community effort to intercompare extratropical cyclone detection and tracking algorithms.

The definition of a mid-latitude cyclone is not entirely exact, it is commonly characterized as a low pressure system, which rotates in positive direction (in the Northern Hemisphere). Consequently, the identification of an extratropical cyclone is not standardized either. The different tracking methods capture different aspects of these mid-latitude low pressure systems.

For this presented analysis, we developed our own cyclone identification and tracking method based on previous studies and experiences found in the literature. The uni- and bivariate versions of our method search for extremes in gridded fields. The univariate version uses one specific variable field, which is selected from different variables related to pressure or geopotential height. The bivariate version consists of a combination of two fields, where the second field is always the relative vorticity at 850 hPa isobaric level, whose maxima are located. The relative vorticity is selected on the basis of *Hoskins* and *Hodges* (2002) who showed its importance in case of the Mediterranean small scale systems. The minima of the basis variable field are searched successively in regions of 15×15 grid points corresponding to 11.25°×11.25° area (when using 0.75° horizontal resolution data), which is approximately the typical size of a Mediterranean cyclone. In the relative vorticity field, the maxima are located in regions of 11×11 grid points, which is more appropriate due to the smaller scale structures of this field.

For the univariate version, three variables are selected to find their minima: in addition to the most commonly used MSLP, 1000 hPa and 850 hPa geopotential heights are also considered. The 1000 hPa geopotential height has already been successfully used in the Mediterranean region (e.g., *Trigo et al.*, 1999). The 850 hPa geopotential height is selected, since its tracking statistical characteristics are similar to MSLP's (*Hoskins* and *Hodges*, 2002), and moreover, it represents the same level as the relative vorticity, which might help in the identification of extremes.

The cyclone tracking algorithm is based on a nearest neighbor search procedure, which uses specific search regions to find the sequential steps of a

trajectory. Around each cyclone center a rectangular search region is defined (*König et al.*, 1993), where the continuation of the trajectory is searched in the next time step. The rectangular area extends more in the west-east direction than in the north-south taking into account the mainly eastward propagation of cyclones. If two possible next locations are found within the search region, the nearest one will be selected. The analysis considers only the cyclone tracks exceeding 1 day lifetime threshold similarly to other studies (*Neu et al.*, 2013; *Hanson et al.*, 2004; *Wernli* and *Schwierz*, 2006).

The use of three basic variables, and the uni- and bivariate versions of the method (*Table 1.*) results in six different cyclone track time series, from which an ensemble is formed and analyzed together instead of the difficult decision to identify the one and only ideal method.

Table 1. The set up of the multivariable ensemble for cyclone identification

Univariate	**Bivariate**
U1 Mean sea level pressure (MSLP)	B1 Mean sea level pressure (MSLP) + Relative vorticity at 850 hPa level (RV850)
U2 Geopotential height of the 1000 hPa level (Z1000)	B2 Geopotential height of the 1000 hPa level (Z1000) + Relative vorticity at 850 hPa level (RV850)
U3 Geopotential height of the 850 hPa level (Z850)	B3 Geopotential height of the 850 hPa level (Z850) + Relative vorticity at 850 hPa level (RV850)

For further analysis, the cyclone area for each identified cyclone center is determined. Cyclone domain is defined in a 11.25°×11.25° lat-lon area centered on the cyclone center and located where the relative vorticity is positive. This definition is sufficient for detecting the effect of a passing cyclone, however, it is insufficient for detailed analysis of weather fronts or other smaller scale phenomena.

The cyclones are investigated seasonally, for this purpose their genesis date determines the seasonal membership. We consider December, January, and February as winter, from March until May as spring, June, July, and August as summer, and finally from September till November as autumn.

For the analysis, cyclone track density maps are calculated. Cyclone track density values denote the number of cyclone tracks crossings per 0.75°×0.75° cells in each season during the investigated entire 30 years. Since unequal-area grid is used for the counting of cyclones per grid cells, the effect of changing area per latitude is calculated. However, the difference is negligible considering the scales used in this study. Furthermore, cyclone genesis density maps are calculated similarly to the track densities, except that only the starting points of the trajectories are considered.

In the 30-year time series of track density maps trends are detected in each grid cell. To find the trend coefficient, linear regression is used where the explanatory variable is the year and the dependent variable is the number of cyclones per year. For the trend analysis, the second coefficient of the linear regression is used, which is the slope of the fitted regression line. In each grid point and in case of all ensemble members, the trend coefficients are evaluated whether or not they are statistically significant, and only the significant values are used.

4. Results

4.1. Reanalysis comparison

The above described methodology is applied to construct six cyclone track time series using the ERA Interim and six time series using the NCEP-DOE R2 reanalysis. In our study, first, the differences of the results using the two datasets are evaluated. Overall, more cyclones are found using the ERA Interim reanalysis (around 75 cyclones annually) than the NCEP-DOE R2 (around 64 cyclones annually), which has lower horizontal resolution. Nevertheless, the courses of the time series of the annual numbers of identified cyclones are quite similar (*Fig. 1*), the correlation coefficient is 0.86, which is statistically significant at the 0.05 level. The spreads of both ensembles are 20 in average. In the first half of the time period, the peaks of the lines (i.e., the large cyclone numbers) are in the same years (1984, 1988, 1991, and 1996). In the second half of the period, the peaks are somewhat shifted relative to each other. The results of using the two reanalyses agree on the general growing trend, which is statistically not significant.

The empirical distributions of the cyclone lifetimes are shown in *Fig. 2.* Evidently, less cyclones are found with longer trajectory, this is valid for the identified cyclones using both reanalyses. The largest difference (21%) between the frequencies of cyclones is in case of the shortest living cyclones. These results suggest that more weak and small cyclones can be identified using the ERA Interim reanalysis that typically occur in the Mediterranean region. This can be explained partially by the higher resolution of ERA Interim reanalysis, which affects the representation of orography as well as other small scale physical processes, and these affect the development and appearance of cyclones in the reanalysis.

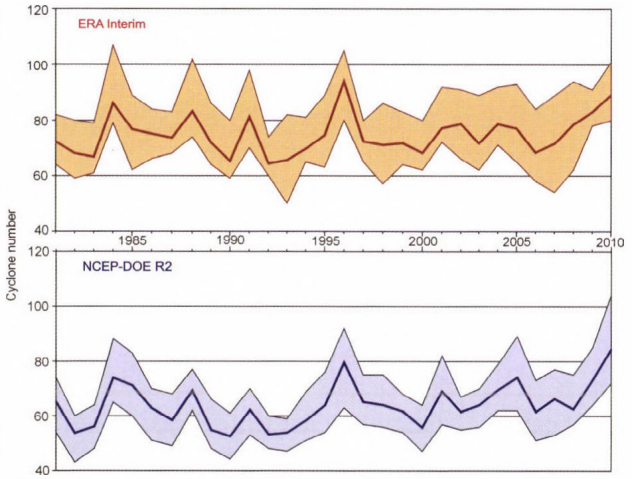

Fig. 1. Time series of the multivariate cyclone identification ensemble from the two reanalyses, ERA Interim (top) and NCEP DOE R2 (bottom). The solid line presents the mean of the ensemble (the average cyclone numbers in each year), and the light colored band presents the spread of the ensemble (the maximum and minimum cyclone numbers in each year).

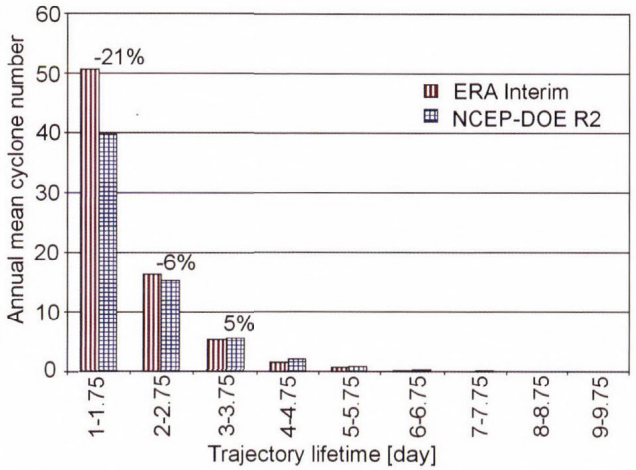

Fig. 2. Histogram of the cyclone lifetime using the two reanalyses. The values above the columns indicate the differences in percentages compared to the results using ERA Interim data.

The results of the comparison suggest, that the higher resolution ECMWF reanalysis is more appropriate for identifying cyclones in the Mediterranean region. Therefore, in the further analyses of cyclones, we use only the ERA Interim based cyclone identification.

4.2. Investigation of the ensemble

The evaluation of the ensemble members are shown through the members' cyclone track density maps and a cyclone lifetime histogram. The comparison presents the features of the different variables, which contributes to the quality of the ensemble mean.

30 years seasonal cyclone track densities are mapped for all the four seasons and all the six members of the multivariable ensemble. Here only the maps for summer (when the ensemble spread is the largest) are shown in *Fig. 3*. The large spread between the ensemble members is most likely caused by the occurrences of thermal lows, which are non-frontal low pressure areas and can not be detected at all levels, neither in the vorticity field. The mean of the ensemble, nevertheless, compensates the effect of using different variables (shown later in *Fig. 7c*). The overall patterns are very similar, the largest cyclone density values occur in the Gulf of Genoa and the southwestern coasts of Turkey, additionally, intense cyclone activity is present over the Iberian Peninsula and the northern part of the Black Sea. The differences between the maps are mainly in the cyclone density values, and not in the spatial patterns, which are basically very similar. The methods using MSLP or geopotential height at 1000 hPa level (i.e., information close to the surface) result in more cyclones, and thus, larger cyclone track density values, which might be the influence of the orography. Furthermore, the limiting effect of the relative vorticity as a second variable is noticeable. The standard deviation of the ensemble mean cyclone track density field in summer is around 2.45 cyclones per 30 years on average over the domain, with the maximum of 87.1 occurring near Cyprus. This means that the largest difference between the two extremes of the entire ensemble is approximately 3 cyclones per grid cell annually, which occurs during the summer months.

After the cyclone track density analysis, the multivariable ensemble is also evaluated in terms of cyclone lifetime. Identified tracks lasting at least 1 day are considered in this analysis. The histogram (*Fig. 4*) clearly shows decreasing numbers for longer-lived cyclones in case of all the six members of the ensemble. In general, the identified numbers of cyclones with 1, 2, 3, ... days lifetime are similar in all members of the ensemble. The only exception is member U2, where considerably more cyclones are identified with less than 2 days lifetime. Furthermore, using relative vorticity at 850 hPa geopotential level as a second variable, B1, B2, B3 identify somewhat less cyclones in each category than the corresponding U1, U2, U3. On higher levels the effects of orography are smaller and the meteorological fields are smoother, therefore, relatively more longer-lived cyclones can be identified in case of U3 and B3 than using the other variables closer to the surface. The difference between U3 and B3 are so small that it cannot be detected on the scale of the histogram, but the limiting effect of using the relative vorticity together with the basic variable

can be detected in this case, too. The small difference might be due to the fact that in both cases the used variables are from the 850 hPa level, which is less sensitive to the orography and does not show the thermal lows. Furthermore, in case of B3, the tilt of the cyclone axis does not complicate the identification of the cyclone centers, unlike in case of B1 and B2, where two different levels are considered and two slightly biased extremes have to be connected to find a cyclone center.

For the further analysis, the mean of the ensemble is used, which incorporates the different characteristics of the ensemble members. Therefore, it gives a more reliable picture about the features of the identified cyclones.

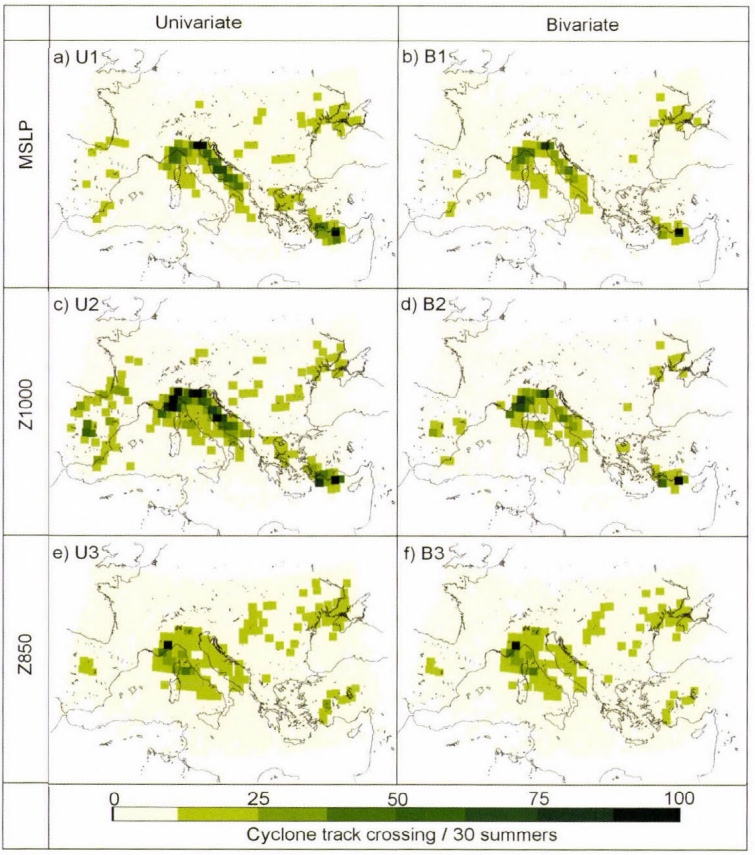

Fig. 3. Cyclone track density maps for summer (1981–2010) from the six members of the multivariable ensemble.

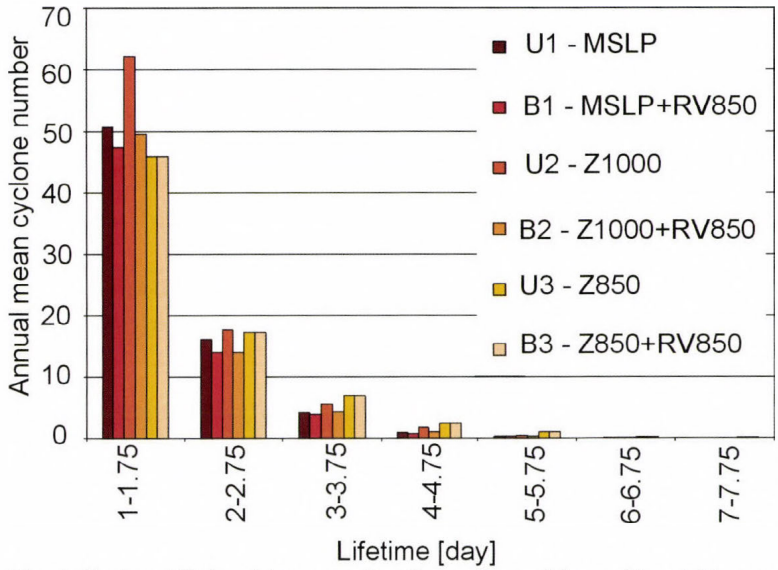

Fig. 4. Cyclone lifetime histogram for all members of the multivariable ensemble.

4.3. Annual cyclone distribution

The annual distribution of cyclones for the whole area is presented in *Fig. 5*. Geographical location and extension of the investigated area highly influence the cyclone frequency and its seasonal distribution. In our study we mainly focused on cyclogenesis areas of the Genoa region, the Aegean Sea, and Cyprus. Other low pressure areas (e.g., over the Iberian Peninsula, the Black Sea) might be also important, however, they are not completely covered here, since their locations are at the border of our domain. Cyclogenesis centers outside Europe (e.g., Saharan lows, Middle East cyclones) are not considered, either. The frequency analysis within the year suggests that the least number of cyclones is in summer. The only exception can be found when the univariate identification is applied using the 1000 hPa geopotential U2 field, in this case the minimum occurred in autumn. The largest and the smallest differences between frequency results of the various identifications occur in summer and winter, respectively. The cyclone identification methods result the maximum cyclone frequency in either spring or winter. Nevertheless, the maximum of the ensemble mean is in spring. Our findings are in a good agreement with those of *Hofstatter* and *Chimani* (2012), who analyzed *van Bebber*'s (1891) track V types between 1961 and 2002, and found their maximum frequency in April and minimum in July.

Cyclogenesis points are counted in every grid cell during the 30 years for every season and for every ensemble member. The results of the members are averaged seasonally, the ensemble means per season are presented in *Fig. 6*. The most active cyclogenesis area is certainly the Gulf of Genoa, which is basically permanent throughout the year. The absolute maximum of genesis event per $0.75°\times0.75°$ grid cell is in the summer near Cyprus (25 cyclogenesis in one particular grid cell per 30 years). Nevertheless, the spatial extensions of genesis centers are small in summer compared to the rest of the year, so the maximum genesis per grid cell is reached by having many genesis episodes in the same relatively small area, and not by having many cyclogenesis overall in the entire domain. The overall seasonal numbers of genesis in the whole area are higher in any other season than summer. The maximum number of cyclogenesis in the whole investigated area occurs in spring. The genesis area near Cyprus is also present throughout the year, but extends less than in the Gulf of Genoa. In both areas, the cyclones are mainly formed over the lee side of the mountains. In winter the Adriatic Sea appears as an additional genesis center, whereas in spring some genesis occur over the Aegean Sea, too. Finally, in summer the Iberian center becomes more prominent. Our findings strengthen the results of *Trigo et al.* (1999).

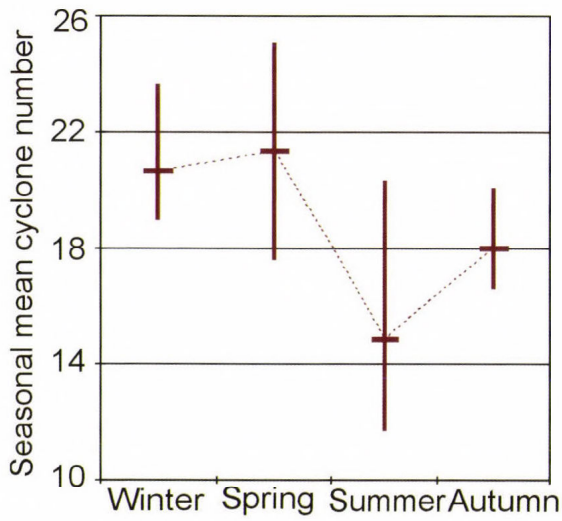

Fig. 5. Mean seasonal frequency of identified cyclone tracks using the 6 time series (horizontal line: ensemble mean, vertical line: ensemble spread).

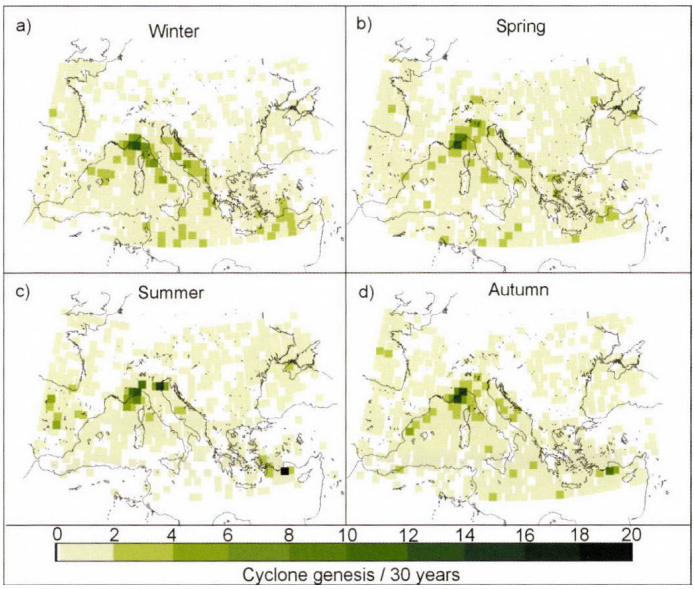

Fig. 6. Seasonal cyclogenesis center numbers from the mean of the multivariable ensemble (1981–2010).

The seasonal track density maps (*Fig. 7*) indicate seasonally the number of cyclone centers crossing each grid cell during the entire 30 years, averaged for the 6 ensemble members. (Note that the whole cyclone areas are not fully represented here, since we focus on the cyclone centers and their close vicinity only.) In general, the most frequent cyclone tracks are the Vd tracks from van Bebber's cyclone track classification (*van Bebber,* 1891), which typically turns south after Gulf of Genoa along the Adriatic Sea. The patterns in the equinox seasons are similar, the main differences listed as follows: (i) in spring the Black Sea cyclone pathway region is more extended and shows its largest activity, (ii) in autumn the region near Cyprus is more active with larger number of cyclones. This can be explained by the temporal extension of the high summer cyclone activity in the Cyprus area. The high track density regions concentrate around the genesis regions, i.e., the Gulf of Genoa, Cyprus, and the northern part of the Black Sea. The spatial extension of the cyclone track density is the largest in winter, whereas the maximum cyclone crossing per grid cell occurs in summer in an isolated point. This implies that the overall cyclone activity in the investigated area is the most intense in winter. The summer cyclones isolated maximum is due to that they tend to follow the same tracks, live shorter, and thus, they affect only the vicinities of their genesis region. This is highlighted in *Fig. 8,* which indicates that the ratio of short trajectories is the largest in summer. In *Fig. 5*, the annual number of spring cyclones is the highest of all season, but this cannot be seen in *Fig. 7*, where winter cyclones are spatially

more extent. This is explained by the fact that in spring the absolute value of short cyclones is maximal (*Fig. 9*). So the difference between the numbers of spring and winter cyclones is compensated by the length of the cyclone lifetime.

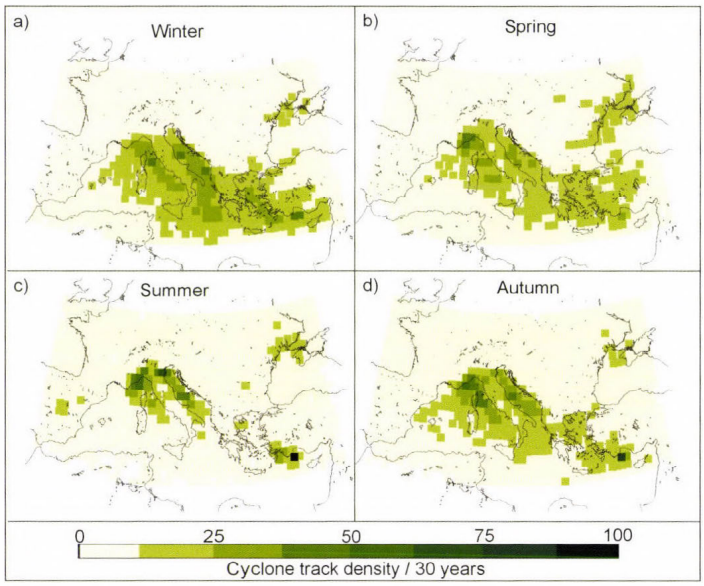

Fig. 7. Seasonal cyclone track density maps from the mean of the multivariable ensemble (1981–2010).

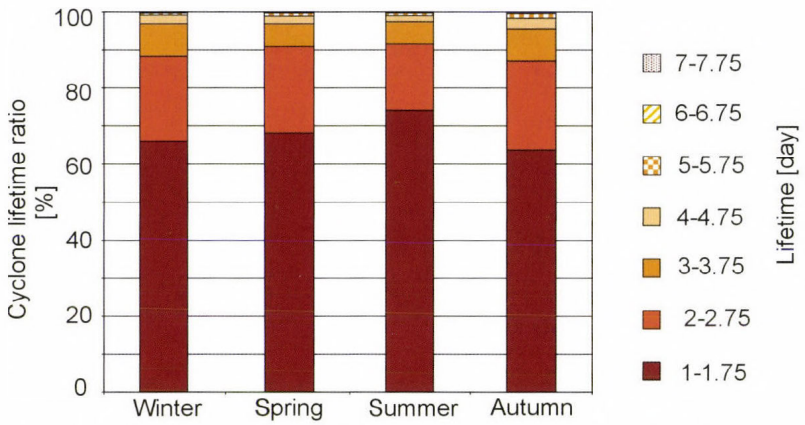

Fig. 8. Seasonal distribution of average cyclone lifetime frequency from the multivariable ensemble.

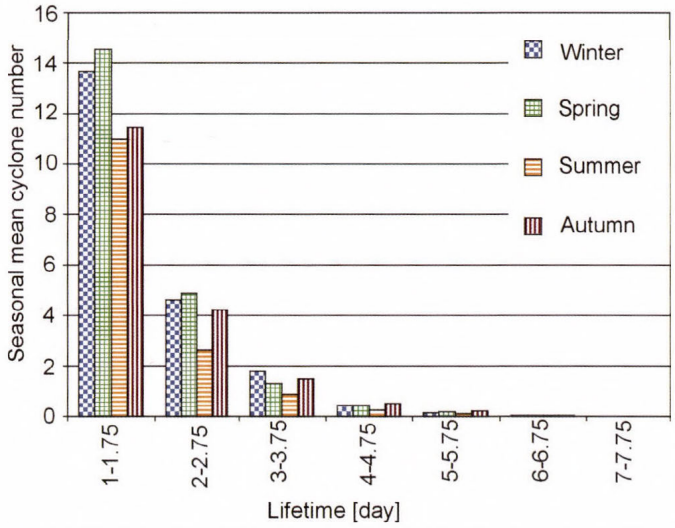

Fig. 9. Histogram of ensemble mean cyclone lifetimes for all seasons.

4.4. Trends

In the investigated 30 years, the changes in annual cyclone numbers are analyzed by calculating the linear trend coefficient of all ensemble members in each grid point. Then, the average value of the individual ensemble members is evaluated. *Fig. 10* shows the significantly positive (top) and negative (bottom) trend coefficients as well as the standard deviation (middle) of the ensemble coefficients. The majority of the significant trend coefficients are positive, located mainly along the Adriatic Sea and southwestern Turkey. Moreover, increasing cyclone numbers are present around the Balearic Island and Sardinia, the Pyrenees, Transylvania, Bulgaria, the Bosporus, and along the coasts of Tunisia. Decreasing tendencies are smaller and more dispersed, they are found at some parts of southern Italy, the region eastward from Malta, the middle part of France, and the northern part of the Black Sea along the Crimean Peninsula. The standard deviation of the ensemble members' trend coefficients shows that the difference between the ensemble members is larger where the detected change is larger.

4.5. Cyclones passing over Hungary

In our study, besides the full domain-based analysis, we also aim to evaluate the comprehensive role of the Mediterranean cyclones on the climate of the Carpathian Basin. For this purpose, those cyclones are selected, whose domain passed over Hungary.

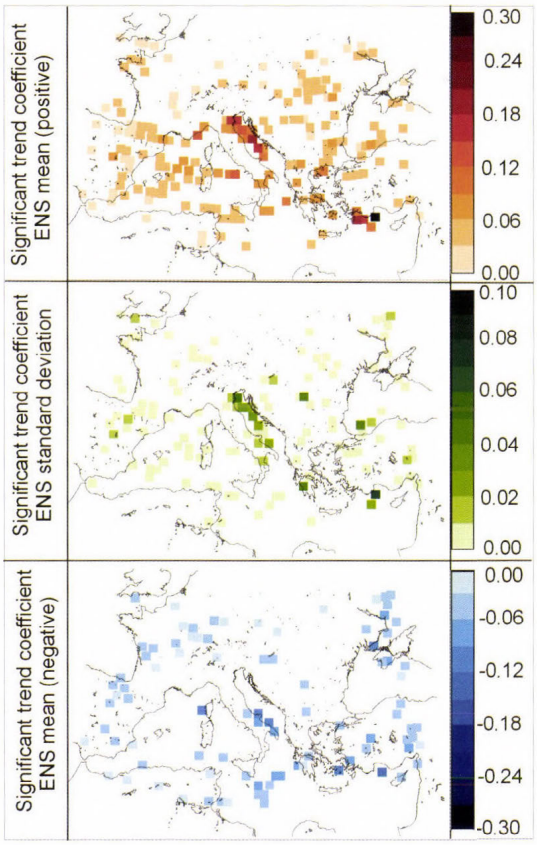

Fig. 10. Spatial distribution of significant trend coefficients (top and bottom: positive and negative coefficients of the ensemble mean, respectively, middle: standard deviation of the significant trend coefficients).

As a result of our analysis, we found that in an average year, roughly 30 cyclones influence the weather in Hungary. This does not include all cyclones affecting Hungary, but mostly the cyclones from the Genoa genesis area, since in our domain we focus on cyclones from the Mediterranean (*Fig. 7*). The time series (*Fig. 11*) correlate strongly with the time series of the whole area (upper part of *Fig. 1*), the correlation coefficient is 0.62, and it is statistically significant at the 0.05 level. The average spread of the ensemble is 11 cyclones/year, which is naturally less than the spread for the whole domain (23 cyclones/year). The local maxima of the cyclones passing over Hungary and the local maxima of all the identified cyclones are not always in the same years. The coincidence of the two maxima is more frequent towards the end of the period (e.g., in 1996, 2001, 2005, and 2010).

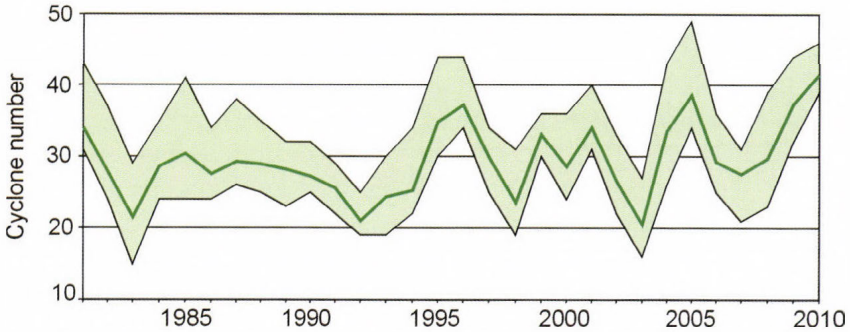

Fig. 11. Time series of the cyclones effecting Hungary from the multivariate cyclone identification ensemble. The solid line presents the mean of the ensembles (the average cyclone numbers in each year), and the light colored band presents the spread of the ensemble (the maximum and minimum cyclone numbers in each year).

The annual distributions of cyclone frequency over Hungary (*Fig. 12*) and the whole domain (*Fig. 5*) are somewhat different. Most of the cyclones occur in spring in both cases, however, the maximum is more robust for the Carpathian Basin, all members of the ensemble have their maximum occurrences in spring, and the relative difference between spring and the other seasons is larger than for the whole domain. Thus, the analysis suggests that the Mediterranean cyclones affect largely the spring weather of the Carpathian Basin. Furthermore, the largest spreads of the ensembles are in summer implying larger uncertainties in this season probably due to thermal lows.

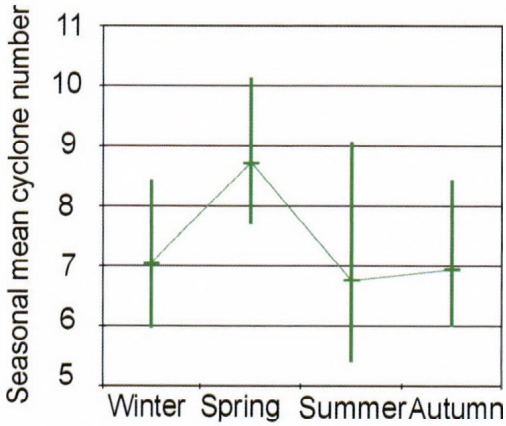

Fig. 12. Mean seasonal frequency of cyclone tracks passing Hungary from the 6 time series (horizontal line: ensemble mean, vertical line: ensemble spread).

5. Discussion

One of the main aims of the study is to develop an adequate cyclone identification method. The evaluation of the method starts by applying it on two different reanalyses, ERA Interim and NCEP-DOE R2, and comparing the results. This comparison provides useful information about the method itself, and also about the datasets. If the pattern or the general features of the results are similar then it can be concluded that the method is not sensitive to the small differences in the reanalyses. However, the differences of the cyclone numbers in the two reanalyses are probably due to general differences of the datasets. These are caused by the different systems used for the production, e.g., data assimilation, physical parameterizations, or the higher/lower resolution of the reanalyses. We found that the correlation is high between the results from the two reanalyses, and ERA Interim datasets include more cyclones. This clearly suggests that the method is adaptable for different datasets. The more cyclones in ERA Interim is probably due to the higher resolution, which better represents the orography, the physical processes, and also their effects. Thus, the primarily orographic cyclogenesis in the Mediterranean is identified more properly in ERA Interim.

Other studies also evaluated the differences between the cyclone climatologies using different reanalyses. For instance, *Hanson et al.* (2004) investigated North Atlantic cyclones between 1979 and 2001, identifying them through MSLP data from NCEP reanalysis (2.5°×2.5°) and from ECMWF ERA-15 reanalysis (1.125°×1.125°) (ERA-15 was extended using operational analyses for the end of the examined period). They concluded that the cyclone climatology from ECMWF data was more comprehensive at all scales. In addition, more very weak and more very strong cyclones were found using the ECMWF data than the NCEP data. *Trigo* (2006) compared storm-tracks using ERA-40 (T159 interpolated to a 1.125°×1.125° regular grid) and NCEP/NCAR (T62 interpolated to a 2.5°×2.5° regular grid) data in the December-March season between 1958 and 2000. It was shown that the main characteristics of genesis and lysis areas in the results of two reanalyses are similar, however, the numbers of storms differ appreciably. Similarly to *Hanson et al.* (2004), the higher resolution ECMWF reanalysis produced more cyclones than the NCEP/NCAR reanalysis. Furthermore, ERA-40 favored the detection of small (sometimes even subsynoptic) scale systems, which are present in the Mediterranean region (*Trigo et al.*, 1999). *Hodges et al.* (2011) compared four reanalyses, i.e., the ERA-Interim (T255), NASA-MERRA (2/3° longitude, 1/2° latitude), NCEP-CFSR (T382), and the JRA25 (T106), focusing on the winter cyclones in both hemispheres between 1989 and 2009. The number, spatial distribution, intensity distribution, track, and lifecycle of cyclones were all compared for the four reanalyses. The conclusions suggest that from a simple intercomparison it is not possible to decide which reanalysis represents the

reality better, only the disagreement between the results can be seen. They found that the spatial differences are small and not significant between the reanalyses, however, there are some orographic regions (e.g., the Mediterranean storm track) where the differences are relatively large. These differences might be the result of the different representation of orography in the reanalyses. Overall, the cyclone numbers and spatial distribution in the new, higher resolution reanalyses are similar, and more realistic than using the lower resolution reanalysis (i.e., JRA25).

According to the previous studies and our own experiences, cyclone identification in the Mediterranean region is difficult due to the frequent occurrence of small and weak systems. The comparisons of reanalyses suggest that (i) the high resolution reanalyses are more appropriate to recognize these systems, and (ii) ECMWF reanalysis is successful in identifying them.

Through the development of the objective cyclone identification method, several variables were tested but no clear distinction could have been made. Different variables have different advantages, so their ensemble are kept and analyzed. MSLP and 1000 hPa geopotential height are both close to the surface, which can be considered as a clear advantage, since a surface-based system is the object of the identification. On the other hand, they are more influenced by the orography, which is a disadvantage. Cyclones are defined as low pressure systems, this is why MSLP is one of the basic variables, but it is a derived field which can cause errors. Cyclones are also rotating systems, this is why relative vorticity at the 850 hPa level is included as a second variable. The advantage of using a second variable, next to the low level values is that only realistic, vertically extent formations are identified. The disadvantage of using the 850 hPa relative vorticity is that it might not be present through the whole lifetime of the cyclone, or it cannot be found in the vicinity of the first level extreme because of the tilt of the cyclone. Thus, the usage of two variables together limits the identified centers. These effects are less obstructive if both variables are from the same level, this is why geopotential height at 850 hPa level is also included. The disadvantage of this configuration is that the shallow, early, or occluding systems are not always detectable. The analysis of the results from the different ensemble members shows the potentials of the multivariable method. In the near-surface variables (Z1000 and MSLP), higher cyclone track densities are present than in the higher level (Z850). It does not necessarily entail that from the near-surface variables more cyclones are identified, just that the cyclones tend to use the same path more frequently. This can be due to the orography, which influences the variable fields, and thus, the tracking too. On the other hand, on the 850 hPa level more numerous longer trajectories are detected, the tracking is more successful than in the lower levels. Besides these differences between the basic variables, in general the use of an additional variable, i.e., relative vorticity, decreases the cyclone

number, but it affects less the longer trajectories. Thus, it serves mainly to omit the weak, short-lived cyclones.

The cyclones in the domain identified by the multivariable ensemble are dominantly the cyclones originated from the Gulf of Genoa, and also include some other genesis areas as southwestern Turkey, the Adriatic Sea and the Iberian Peninsula. The minimum cyclonic activity throughout the year is in summer, when the spread of the ensemble is the largest. The explanation for this probably is the appearance of thermal lows, which are not captured in all variables. They are not aimed to be captured anyway, since they are non-frontal pressure depressions. The most active period is the winter-spring half year. In spring there are more cyclones in our ensemble, but the track density maps show more spatially extent cyclone activity in winter. Although it seems to be a contradiction, winter cyclones have longer lifetimes so they contribute more to the track density maps than spring cyclones. Despite of the largest track density extension in winter, the isolated per grid maximum value is in summer. This means that the summer cyclones' paths more overlap, and produce extreme high track density in a cell than the winter cyclones'. The major cyclone pathway on the track density maps is van Bebber's Vd class, furthermore, Vb and Vc tracks are rare but sometimes occur.

Cyclones transport moisture, heat, and energy, that is why they have an important role in the local weather events of the area hit by their path. Both increase and decrease in their frequency can cause extreme events such as floods or droughts (e.g., *Grams et al.*, 2014). The investigation of trend coefficients in our analysis suggests that in the 30-year period, increasing linear trend is present in larger area than decreasing trend (almost twice as many grid cells). Also, the average of the positive trend coefficients is higher than the negative coefficients'. There are some more pronounced areas where the coefficients are higher, and in many neighboring grid cells the trends are statistically significant, e.g., over the Adriatic Sea. Nevertheless, there is no detectable sign of any north-south or west-east shift in the cyclone track densities.

The average radius of Mediterranean cyclones is between 300 km and 500 km (*Trigo et al.* 1999), their effects on local weather can certainly be observed in the whole area inside their domain not only focusing on their center regions. Therefore to select the cyclones affecting the weather of Hungary, the area where the domain of a cyclone swept through were calculated. The annual variability of these cyclones is a bit different from the general analysis. Namely, the most active season is clearly spring. The difference between spring and winter is almost as large as between spring and summer unlike in case of the entire domain. This implies that among the cyclones originated from the Gulf of Genoa, more cyclones follow northerly paths in spring than in winter.

6. Conclusions

Detailed cyclone analysis covering the time period between 1981 and 2010 was presented in this paper for the Mediterranean region. The spatial focus has been selected on the basis of the importance in influencing local weather throughout Southern and Central Europe, since these cyclones transfer moist air from the sea to the land and are often associated with heavy precipitation and/or flood events. On the basis of the discussed results, the following conclusions can be drawn.

(1) A multivariable cyclone identification and tracking process system was developed, which consists of uni- and bivariate modes of a general method with three basic variables (MSLP, geopotential height at 1000 hPa and 850 hPa), and one additional variable (relative vorticity at 850 hPa) in case of the bivariate mode. Evaluation of the individual ensemble members showed that the use of relative vorticity as a second field has a limiting effect. Furthermore, it was found that the methods using the 850 hPa level geopotential height and/or relative vorticity result in more long-lived cyclone tracks than the others. Overall, our results are in good agreement with previous analyses, highlighting that our developed method is appropriate to use for the identification of cyclones in the Mediterranean region.

(2) Data for the cyclone identification was derived from two reanalyses, i.e., ERA Interim and NCEP DOE R2 to evaluate both the method and the datasets. More cyclones were found using the ERA Interim data, mainly because of more numerous short-lived cyclones, which is probably due to the higher resolution of ERA Interim compared to NCEP DOE R2. Nevertheless, the time series of the two ensemble means from the two reanalyses correlate strongly with each other, therefore, we conclude that the method is not sensitive to small differences in the dataset. Due to the mentioned conclusions detailed analysis was presented only on the basis of cyclone tracks using ERA Interim datasets.

(3) The largest spread of the individual ensemble members occurred in summer possibly because of the presence of thermal lows. However, the spatial distribution of cyclone track density maps of the six ensemble members did not show large differences.

(4) The main cyclogenesis areas in the investigated domain are the Gulf of Genoa and the region around Cyprus, both located on the lee side of a mountain, which enhances cyclogenesis. Moreover, other minor cyclogenesis centrums can be identified over the Iberian Peninsula in summer and the Adriatic Sea in winter.

(5) The largest cyclone number occurred in spring, whereas the analysis of cyclone track density resulted in that the area affected by the cyclones is

the largest in winter, the circulation is more intense in winter. The cyclone lifetime analysis showed that although the number of cyclones is larger in spring than in winter, there are more short cyclones in spring, thus, they do not affect as large areas as winter cyclones. This implies that the cyclonic activity in the Mediterranean is mostly in the winter-spring period. The lowest cyclone activity was found in summer, also the total extension of cyclone passes is the least in summer, although the maximum value of cyclone tracks crossing a grid point occurs in summer. This means that although the number of cyclones is the lowest in summer, they are typically short-lived and they do not get too far from their genesis areas.

(6) The long-term tendencies of cyclone track density for the entire 30-year period are evaluated on the basis of the linear trend coefficients. Considering the whole domain, we found more grid points with statistically significant increasing trends than decreasing, and the absolute mean value of the trend coefficients is slightly higher in case of the positive trends than the negative trends. The most intense growing occurred along the Adriatic Sea and near Cyprus.

(7) In order to investigate the cyclones directly affecting the local weather in Hungary, the cyclone area is defined around the identified cyclone centers, and the cyclones whose domain affects the country are selected. The time series of the cyclones passing over Hungary correlate strongly with the cyclone number time series of the whole domain. The average frequency of Mediterranean cyclones passing over Hungary is 29.5 per year, most of them occurred in spring, similarly to the overall cyclone number in the whole investigated domain.

(8) Our presented results can serve as an adequate reference for further studies using global and regional climate model outputs for the identification of mid-latitude cyclones, which are key elements of the future climatological conditions, especially in Europe. For a complex region like the Mediterranean, the use of regional climate models is especially essential, since they are more appropriate to reconstruct and describe local features compared to the global climate models.

Acknowledgments: Research leading to this paper has been supported by the following sources: the Hungarian Scientific Research Fund under grant K-78125, the European Union and the European Social Fund through project FuturICT.hu (TÁMOP-4.2.2.C-11/1/KONV-2012-0013), also the AGRARKLIMA2 project (VKSZ_12-1-2013-0001).
The NCEP DOE Reanalysis 2 data for this study was provided by the NOAA/OAR/ESRL PSD, Boulder, Colorado, USA, from their website at http://www.esrl.noaa.gov/psd/. The ERA Interim data for this study was downloaded from the website of the European Centre for Medium-Range Weather Forecasts (ECMWF), http://data-portal.ecmwf.int/data/d/interim_full_daily/. We would like to acknowledge the organisations for their efforts to prepare these databases.

References

Alpert, P., Neeman, B.U., and *Shay-El, Y.,* 1990: Climatological analysis of Mediterranean cyclones using ECMWF data. *Tellus, 42,* 65–77.

Bartholy, J., Pongrácz, R., and *Pattantyús-Ábrahám, M.,* 2008: Analyzing the genesis, intensity, and tracks of western Mediterranean cyclones. *Theor. Appl. Climatol. 96,* 133–144.

van Bebber, W.J., 1891: Die Zugstrassen der barometrischen Minima nach den Bahnenkarten der Deutschen Seewarte für den Zeitraum von 1870–1890. *Meteorol. Z. 8,* 361–366.

Catto, J.L., Shaffrey, L.C., and *Hodges, K.I.,* 2010: Can Climate Models Capture the Structure of Extratropical Cyclones? *J. Climate 23,* 1621–1635.

Dee, D.P., Uppala, S.M., Simmons, A.J., Berridford, P., Polis, P., Kobayashi, S., Andrae, U., Balmaseda, M.A., Balsamo, G., Bauer, P., Bechtold, P., Beljaars, A.C.M., van de Berg, L., Bidlot, J., Bormann, N., Delsol, C., Dragani, R., Fuentes, M., Geer, A.J., Haimberger, L., Healy, S.B., Hersbach, H., Holm, E.V., Isaksen, L., Kallberg, P., Kohler, M., Matricardi, M., McNally, A.P., M.Monge-Sanz, B., Morcrette, J.J., Park, B.K., Peubey, C., de Rosnay, P., Tavolato, C., Thepaut, J.N., and *Vitart, F.,* 2011: The ERA-Interim reanalysis: configuration and performance of the data assimilation system. *Q. J. Roy. Meteor. Soc. 137,* 553–597.

Finnis, J., Holland, M.M., Serreze, M C., and *Cassano, J J.,* 2007: Response of Northern Hemisphere extratropical cyclone activity and associated precipitation to climate change, as represented by the Community Climate System Model. *J. Geophys. Res. 112(G4),* G04S42.

Grams, C.M., Binder, H., Pfahl, S., Piaget, N., and *Wernli, H.,* 2014: Atmospheric processes triggering the Central European floods in June 2013. *Nat. Hazard. Earth Sys. Discussions, 2,* 427–458.

Gulev, S.K., Zolina, O., and Grigoriev, S., 2001: Extratropical cyclone variability in the Northern Hemisphere winter from the NCEP/NCAR reanalysis data. *Climate Dynamics 17,* 795–809.

Hanson, C.E., Palutikof, J.P., and *Davies, T.D.,* 2004: Objective cyclone climatologies of the North Atlantic? A comparison between the ECMWF and NCEP Reanalyses. *Climate Dynamics 22,* 757–769.

Hodges, K.I., Lee, R. and *Bengtsson, L.,* 2011: A Comparison of Extra-tropical Cyclones in Recent Re-analyses; ERA-INTERIM, NASA-MERRA, NCEP-CFSR and JRA25. *J. Climate, 24,* 4888–4906.

Hofstätter, M. and *Chimani, B.,* 2012: Van Bebber's cyclone tracks at 700 hPa in the Eastern Alps for 1961–2002 and their comparison to Circulation Type Classifications. *Meteorol. Z. 21,* 459–473.

Hoskins, B.J. and *Hodges, K.I.,* 2002: New Perspectives on the Northern Hemisphere Winter Storm Tracks. *J. Atmos. Sci. 59,* 1041–1061.

Jansa, A., Genoves, A., Picornell, M.A., Campins, J., Riosalido, R., and *Carretero, O.,* 2001: Western Mediterranean cyclones and heavy rain. Part 2: Statistical approach. *Meteorol. Appl. 8,* 43–56.

Kanamitsu, M., Ebisuzaki, W., Woollen, J., Yang, S.-K., Hnilo, J.J., Fiorino, M., and *Potter, G.L.,* 2002: NCEP–DOE AMIP-II Reanalysis (R-2). *Bull. Amer. Meteorol. Soc. 83,* 1631–1643.

König, W., Sausen, R., and *Sielmann, F.,* 1993: Objective Identification of Cyclones in GCM Simulations. *J. Climate 6,* 2217–2231.

Lionello, P., Dalan, F., and *Elvini, E.,* 2002: Cyclones in the Mediterranean region: the present and the doubled CO 2 climate scenarios. *Climate Res. 22,* 147–159.

Maheras, P., Flocas, H.A., Patrikas, I., and *Anagnostopoulou, C.,* 2001: A 40 year objective climatology of surface cyclones in the Mediterranean region: spatial and temporal distribution. *Int. J. Climatol. 21,* 109–130.

Murray, R.J. and *Simmonds, I.,* 1991: A numerical scheme for tracking cyclone centers from digital data Part I: development and operation of the scheme. *Australian Meteorol. Mag. 39,* 155–166.

Muskulus, M., and *Jacob, D.,* 2005: Tracking cyclones in regional model data : the future of Mediterranean storms. *Adv. Geosci. 2,* 13–19.

Neu, U., Akperov, M.G., Bellenbaum, N., Benestad, R., Blender, R., Caballero, R., Cocozza, A., Darce, H.F., Feng, Y., Fraedrich, K., Grieger, J., Gulev, S., Hanley,J., Hewson, T., Inatsu, M., Keay,K., Kew, S.F., Kindem, I., Leckebusch, G.C., Liberato, M.L.R., Lionello, P., Mokhov, I.I., Pinto, J.G., Raible, C.C., Reale, M., Rudeva, I., Schuster, M., Simmonds, I., Sinclair, M., Sprenger, M., Tilinina, N.D., Trigo, I.F., Ulbrich, S.,Ulbrich, U., Wang, X.L., Wernli, H., 2013: IMILAST: A

Community Effort to Intercompare Extratropical Cyclone Detection and Tracking Algorithms. *Bull. Amer. Meteorol. Soc. 94,* 529–547.

Nielsen, J.W. and *Dole, R.M.,* 1992: A survey of extratropical cyclone characteristics during GALE. *Mon Weather Rev 120,* 1156–1167

Picornell, M.A., Jansá, A., Genovés, A., and *Campins, J.,* 2001: Automated database of mesocyclones from the HIRLAM(INM)-0.5° analyses in the western Mediterranean. *Int. J. Climatol. 21,* 335–354.

Pinto, J.G., Spangehl, T., Ulbrich, U., and *Speth, P.,* 2005: Sensitivities of a cyclone detection and tracking algorithm: individual tracks and climatology. *Meteorol. Z. 14, 823–838.*

Ruti, P.M., Somot, S., Giorgi, F., Dubois, C., Flaounas, E., Obermann, A., Dell'Aquila, A., Pisacane, G., Harzallah, A., Lombardi, E., Ahrens, B., Akhtar, N., Alias, A., Arsouze, T., Aznar, R., Bastin, S., Bartholy, J., Béranger, K., Beuvier, J., Bouffies-Cloché, S., Brauch, J., Cabos, W., Calmanti, S., Calvet. J-C., Carillo, A., Conte, D., Coppola, E., Dell'Aquila, A., Djurdjevic, V., Drobinski, P., Elizalde-Arellano, A., Gaertner, M., Galàn, P., Gallardo, C., Gualdi, S., Goncalves, M., Jorba, O., Jordà, G., L'Heveder, B., Lebeaupin-Brossier, C., Li, L., Liguori, G., Lionello, P., Maciàs, D., Nabat, P., Onol, B., Raikovic, B., Ramage, K., Sevault, F., Sannino, G., MV Struglia, Sanna, A., Torma, C., Vervatis, V., 2015: MED-CORDEX initiative for Mediterranean Climate studies *(submitted to BAMS, October 2011, resubmitted in August 2014, resubmitted in March 2015)*

Serreze, M.C., 1995: Climatological aspects of cyclone development and decay in the Arctic. *Atmosphere-Ocean, 33,* 1–23.

Sinclair, M.R., 1994: An objective Cyclone Climatology for Southern Hemisphere. *Month. Weather Rev. 122,* 2239–2256.

Ulbrich, U., Brücher, T., Fink, A.H., Leckebusch, G.C., Krüger, A., and *Pinto, J.G.,* 2003: The central European floods of August 2002: Part 2 –Synoptic causes and considerations with respect to climatic change. *Weather, 58,* 466–471.

Trigo, I.F., Davies, T.D., and *Bigg, G.R.,* 1999: Objective Climatology of Cyclones in the Mediterranean Region. *J. Climate 12,* 1685–1696.

Trigo, I.F., Davies, T.D., and *Bigg, G.R.,* 2000: Decline in Mediterranean rainfall by weakening of Mediterranean cyclones. *Geophys. Res. Lett. 27,* 2913–2916.

Trigo, I.F., 2006: Climatology and interannual variability of storm-tracks in the Euro-Atlantic sector: a comparison between ERA-40 and NCEP/NCAR reanalyses. *Climate Dynamics 26,* 127–143.

Wernli, H. and *Schwierz, C.,* 2006: Surface Cyclones in the ERA-40 Dataset (1958 – 2001). Part I: Novel Identification Method and Global Climatology. *J. Atmos. Sci. 63,* 2486–2507.

Woollings, T., Hoskins, B., Blackburn, M., Hassell, D., and *Hodges, K.,* 2010: Storm track sensitivity to sea surface temperature resolution in a regional atmosphere model. *Climate Dynamics 35,* 341–353.

IDŐJÁRÁS

Quarterly Journal of the Hungarian Meteorological Service
Vol. 119, No. 2, April – June, 2015, pp. 185–196

Thunderstorm climatology in Hungary using Doppler radar data

András Tamás Seres[1]* and **Ákos Horváth**[2]

[1]*Hungarian Defence Forces Geoinformation Service,*
Szilágyi E. fasor 7–9, H-1024 Budapest, Hungary
E-mail: seres.andrastamas@upcmail.hu

[2]*Hungarian Meteorological Service,*
Vitorlás u. 17, H-8600 Siófok, Hungary,
E-mail: horvath.a@met.hu

**Corresponding author*

(Manuscript received in final form June 20, 2014)

Abstract—This paper presents the results of an objective analysis on thunderstorm climatology in Hungary. The examination was based on composite PPI (plan position indicator) images made by Doppler radars of the Hungarian Meteorological Service between 2004 and 2012. In our research, thunderstorms were represented with so-called thunderstorm ellipses, and their time and spatial distribution were examined. Three types of thunderstorm ellipses and stormy days were defined with radar reflectivity set to 45, 50, or 55 dBZ. Most stormy days and ellipses happened in late spring and summer of 2007 and 2010. The daily frequency of these objects peaked in the late afternoon period. The detected ellipses had maxima in the north-eastern, north-central, and south-western parts of Hungary. Beyond information and characteristics from the past, these methods and results can be useful for forecasting severe thunderstorms.

Key-words: severe thunderstorm, Doppler radar, climatology, TITAN method, Hungary.

1. Introduction

Radar-based thunderstorm climatology has a long history in the United States. The first studies appeared in 1950s (*Braham*, 1958), followed by many other researches for different parts of the country (for example: *Myers,* 1964; *Henz,* 1974; *Falconer*, 1984; *Croft* and *Shulman,* 1989; *Mohee* and *Miller*, 2010). In the last two decades, some works have been carried out in this field in Europe (*Höller*, 1994; *Jaeneke*, 2001; *Rigo* and *Liasat*, 2002; *Weckwerth et al.*, 2010; *Rudolph et al.*, 2011; *Davini et al.,* 2012), South America (*Paiva Pereira* and

Rutledge, 2003), Canada (*Brimelow et al.*, 2004), and Australia (*Steiner* and *Houze*, 1996) as well.

The first Hungarian study on thunderstorm climatology was made by *Héjas* (1898), followed by *Raum* (1910). Some studies dealing with different aspects of thunderstorm climatology appeared in the 1960s (*Ozorai*, 1965; *Götz* and *Pápainé*, 1966; 1967). All these works were based on visual observations. Later, radar and satellite data (*Boncz et al.*, 1987; *Bodolainé* and *Tänczer*, 1991), then nowcasting methods (*Horváth* and *Geresdi*, 2003; *Horváth et al.*, 2007) appeared in the Hungarian studies. However, these works considered thunderstorms from mainly dynamical and synoptical aspects, so our work is the first attempt to examine thunderstorm climatology in Hungary using Doppler radar data. The first results of this research were presented by *Horváth et al.* (2008) but only for a shorter period.

The aim of this paper is to briefly describe the time and spatial distribution of severe thunderstorms detected by HMS's radars in the period of 2004 to 2012.

2. Methodology

2.1. Radar measurements

The first weather radar in Hungary was introduced in 1967. In the next decades, other locators were set in the country and the Hungarian Meteorological Service (HMS) built up its radar network system. By 2004, HMS's Soviet-made MRL-5 locators were replaced by modern Doppler radars.

Hungary is covered by three weather radars: (the western, the central, and the eastern locators, and they all operate on C-band (wave length = 5 cm) (*Geresdi*, 2004). During the measurement, the Doppler-wind was applied for noise filtering and the results were upgraded, filtered, and smoothened into composite fields. From each scan column, the highest reflectivity values were taken (*Collier*, 1996). The resolution of the composite PPI (plan position indicator) images was 2 km × 2 km in space and 15 minutes in time. To further reduce noises of reflectivity, median-filter method (*Tukey*, 1977) was also used before beginning the analysis.

2.2. Core of the methodology: the TITAN method

The TITAN (Thunderstorm Identification, Tracking, Analysis and Nowcasting) method was developed by *Dixon* and *Wiener* (1993). Using the identification part of this method the irregular-shaped thunderstorms detected by radar could be characterized by regular ellipses. The main point of identification is as follows: the parameters of the ellipses are determined by the covariance matrix of the isolated, irregular-shaped cluster on the image using the condition that the area of the cluster and the ellipse has to be equal. With this method, the focus

points and the equation of the ellipses could easily be determined and the objects were visualized by the Hungarian Advanced WorKstation (HAWK) system developed by HMS (*HMS*, 2012). These calculated ellipses were called thunderstorm ellipses (*Horváth et al.*, 2008). The detailed background of the identification method is given in the *Appendix*.

Two types of thresholds: the area limit ($N_{minlimit}$) and the reflectivity limit ($R_{minlimit}$) were defined. The area threshold determined the minimum area of a cluster. In our examination $N_{minlimit}$ was set to 5 radar pixels (which equals to 20 km^2). The reflectivity threshold specified that each pixel of the cluster (in our case 5 pixels) had to reach this limit. $R_{minlimit}$ was set to 45 dBZ, 50 dBZ, and 55 dBZ and these objects were named severe, highly severe, and extremely severe thunderstorm ellipses, respectively. Using these high reflectivity values, the detected cells could be considered as severe thunderstorms and the small or weak objects could be eliminated. The original radar image is presented in *Fig. 1a* for May 18, 2005 at 16:00 UTC, while ellipses with $N_{minlimit} = 5$ pixels and $R_{minlimit} = 45$ dBZ are visualized in *Fig. 1b*.

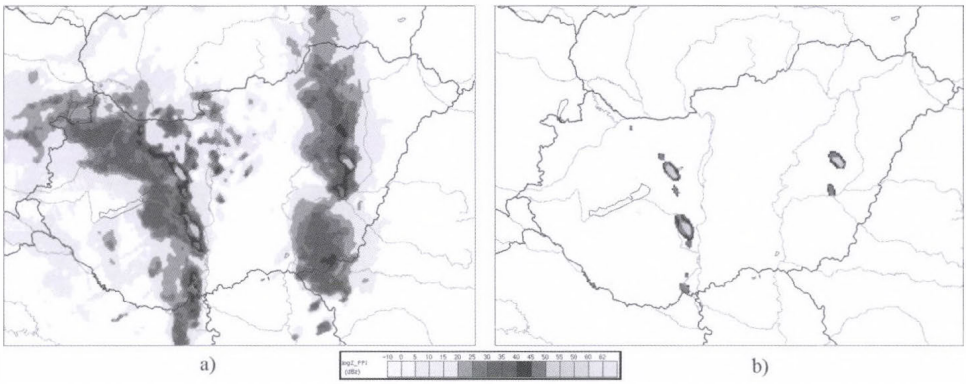

Fig. 1. Composite PPI radar images of thunderstorms observed on May 18, 2005, 16:00 UTC. Left: original image, right: image where thunderstorms were represented by ellipses.

3. Results

3.1. Time distribution of thunderstorm ellipses and stormy days

A day was called severe, highly severe, or extremely severe stormy day when at least one detected severe, highly severe, or extremely severe thunderstorm ellipse could be found on radar images. Using these data, the number of stormy days could be counted for a given time period.

The highest number of stormy days was counted in 2007 for all categories. The lowest values were detected in 2005 for extremely severe days and in 2012 for the other two types (*Table 1*). About 80 to 95% of stormy days and 97 to 98% of thunderstorm ellipses were detected between April and September, therefore this period was called thunderstorm season. The stormiest month was July followed by June, August, and May. Other months had much lower values (*Fig. 2*). On average, 118 severe, 82 highly severe, and 20 extremely severe ellipses were detected on a stormy day in the thunderstorm season. Note that these calculated values are not equal to the number of thunderstorms, because a severe thunderstorm may appear on subsequent radar images. *Table 2* shows the time distribution of days with at least 50 or 100 objects. The maxima were in 2007 and 2010, while 2004, 2005, and 2012 had the lowest values. The highest number of severe thunderstorm ellipses (1,115 objects) were detected on August 20, 2007, while for the other two types, June 14, 2010 had the highest values (527 and 139 ellipses). According to ECMWF (European Centre for Medium-Range Weather Forecast) analysis, on these days a cold front of a northern cyclone reached the country.

The daily cycle of these ellipses was also investigated (*Fig. 3*). Only results for the thunderstorm season are shown in this paper. The minima of appearance were detected at 8:30 and 9:15 for severe, 8:30 for highly severe, and 7:00 for extremely severe ellipses. The time distribution of the objects was asymmetric and the maxima were at 16:45 for severe, 16:30 for highly severe, and 16:30 and 17:30 for extremely severe ellipses.

Table 1. Annual distribution of severe, highly severe, and extremely severe stormy days in the period of 2004 to 2012.

Year	Severe stormy days	Highly severe stormy days	Extremely severe stormy days
2004	189	116	44
2005	188	101	26
2006	169	107	38
2007	190	121	69
2008	142	94	40
2009	142	102	45
2010	141	93	53
2011	136	99	52
2012	122	90	43
Average	*158*	*103*	*46*

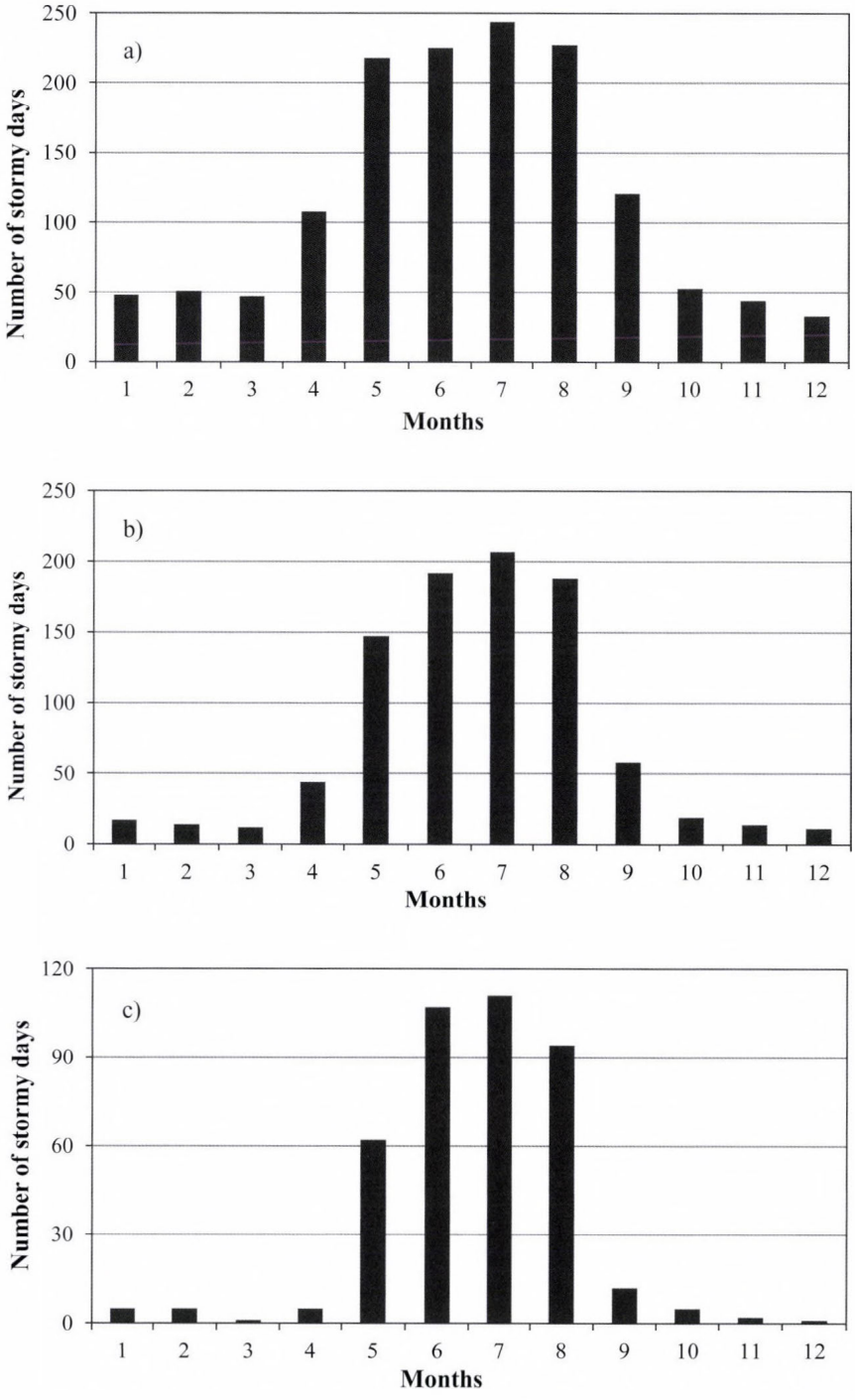

Fig. 2. Annual course of a) severe, b) highly severe, and c) extremely severe stormy days in the period of 2004 to 2012.

Table. 2. Annual distribution of days with 50 or 100 severe, highly severe, or extremely severe ellipses in the period of April to September between 2004 and 2012.

Year	Days with at least 50			Days with at least 100		
	severe	highly severe	extremely severe	severe	highly severe	extremely severe
	ellipses			ellipses		
2004	57	12	1	34	6	0
2005	45	10	0	30	2	0
2006	61	18	1	39	13	0
2007	75	40	1	59	19	0
2008	65	20	2	42	12	0
2009	62	15	1	42	4	0
2010	67	35	2	54	20	1
2011	72	32	3	53	16	0
2012	54	23	0	36	8	0
Average	*62*	*23*	*1*	*43*	*11*	*0*

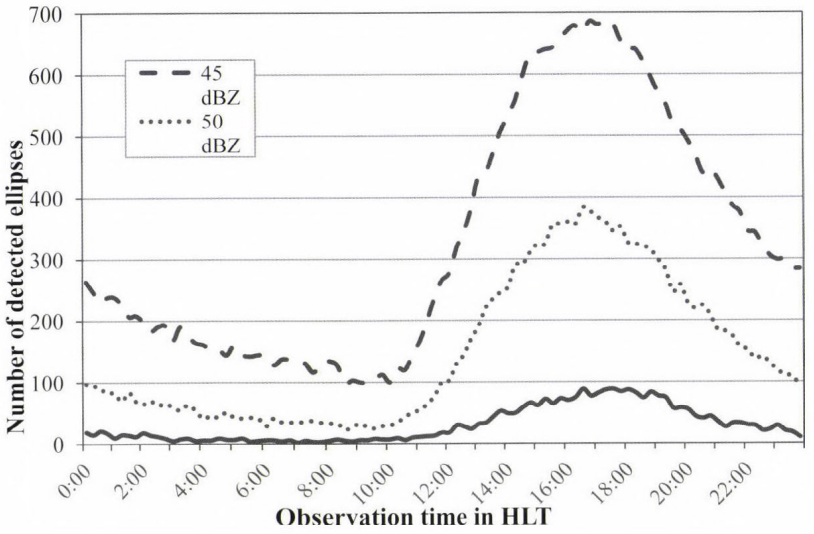

Fig. 3. Daily cycle of the detected severe (45 dBZ), highly severe (50 dBZ), and extremely severe (55 dBZ) thunderstorm ellipses in the period of April to September between 2004 and 2012. The time resolution is 15 minutes. Times are given in Hungarian Local Time (HLT = UTC + 2 hours).

3.2. Spatial distribution of thunderstorm ellipses

The spatial distribution of thunderstorm ellipses was analyzed by constructing thunderstorm statistic maps. The area resolution was set to 18 km×18 km.

Thunderstorm statistic maps were created for the entire year in the period of 2004 to 2012, but only results for the thunderstorm season are represented in this paper. Between October and March, there was only a few objects detected, while the measurement noises were high, especially in the early years. During the nine-year period, the maxima of severe, highly severe, and extremely severe thunderstorm ellipses were detected mostly in the north-eastern, north-central, and south-western parts of Hungary. Fewer objects appeared in the north-western and south-eastern parts of the country. Note that minima were mostly far from radars; these lower values could be originated to detecting problems (*Fig. 4*).

4. Summary and conclusions

This paper presents the results of an objective, radar-based analysis on thunderstorm climatology in Hungary for the nine-year period of 2004 to 2012. Most stormy days and ellipses were detected in late spring, summer and in 2007, 2010. The daily frequency of these objects peaked in the late afternoon period. The detected ellipses had maxima in the north-eastern, north-central, and south-western parts of Hungary. Beyond information and characteristics from the past, these methods and results can be useful for forecasting severe thunderstorms. The cell-detection algorithm should be more integrated into automatic warning systems or can be used in researches on supercells. In the future, this objective examination can be carried out for previous years but better noise-filtering methods should be developed. Furthermore, satellite and lightning data can be combined with these results as well.

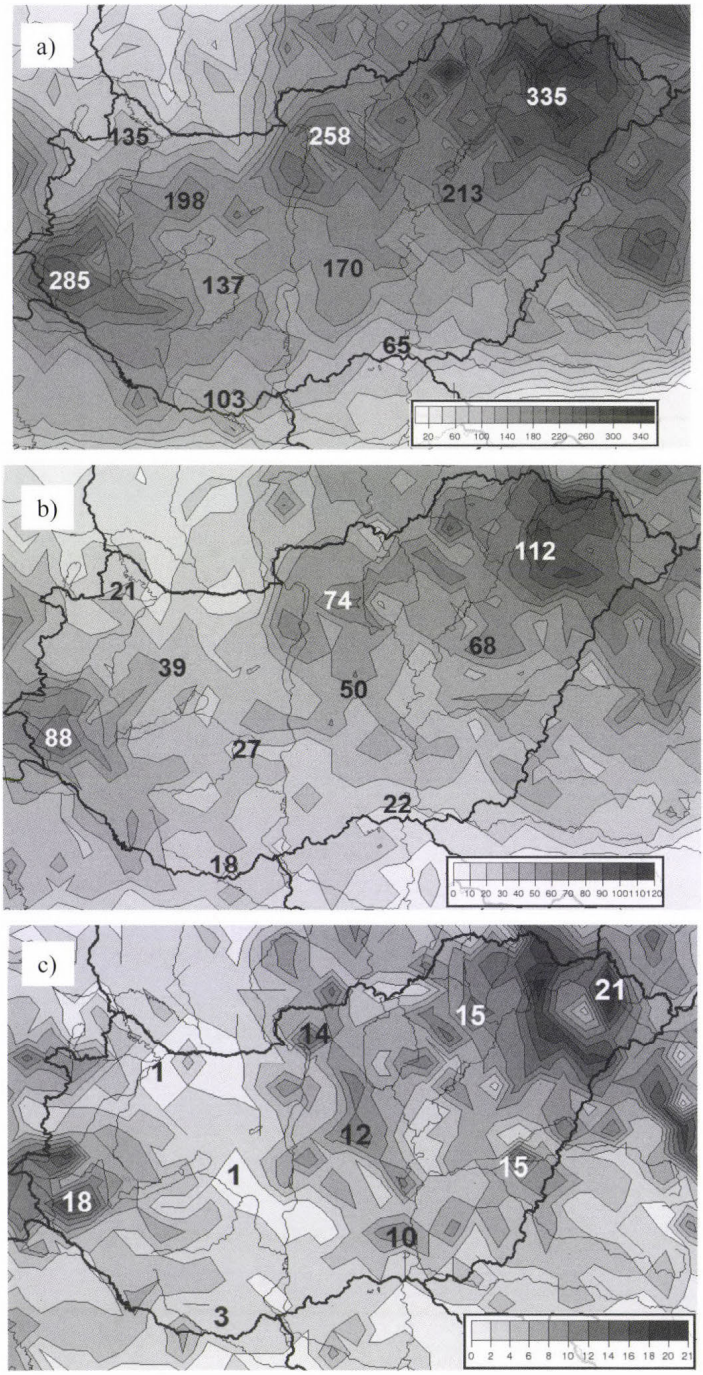

Fig. 4. Spatial distribution of a) severe, b) highly severe, and c) extremely severe thunderstorm ellipses in the period of April to September between 2004 and 2012. The area resolution is 18 km×18 km. These images were visualized by the Hungarian Advanced WorKstation (HAWK) system developed by the Hungarian Meteorological Service.

Appendix

Mathematical background of the identification

The method of calculating ellipses is as follows (*Dixon* and *Wiener*, 1993): Suppose there is an irregular cluster on a radar image which has n detected pixels. The center of a cluster is defined by

$$\bar{x} = \frac{1}{n}\sum_{i=1}^{n} x_i , \quad \bar{y} = \frac{1}{n}\sum_{i=1}^{n} y_i , \tag{1}$$

where x and y indicate the longitude and latitude of pixels which have reflectivity higher than a given threshold value. The covariance matrix of this cluster is

$$A = \mathrm{cov}_{xy} = \begin{bmatrix} d & e \\ e & f \end{bmatrix}, \tag{2}$$

where d is the deviation from the center by the x coordinate

$$d = \frac{1}{n-1}\sum_{i=1}^{n} (x_i - \bar{x})^2 , \tag{3}$$

f is deviation from the center by the y coordinate

$$f = \frac{1}{n-1}\sum_{i=1}^{n} (y_i - \bar{y})^2 , \tag{4}$$

and e is

$$e = \frac{1}{n-1}\sum_{i=1}^{n} (x_i - \bar{x})(y_i - \bar{y}) . \tag{5}$$

The eigenvalues of the covariance matrix are given by

$$\lambda_1, \lambda_2 = \frac{(d+f) \pm \left[(d+f)^2 - 4(df - e^2)\right]^{1/2}}{2} \tag{6}$$

The normalized eigenvectors of this matrix are

$$v = \left[\frac{1}{(1+g)^2}\right]^{1/2}, \qquad \mu = -gv, \tag{7}$$

where

$$g = \frac{f + e - \lambda_1}{d + e - \lambda_2}. \tag{8}$$

Then the rotation of the ellipse major axis relative to the x axis is given by these vectors

$$\theta = \tan^{-1}\left(\frac{v}{\mu}\right). \tag{9}$$

The eigenvalues of the covariance matrix (λ_1 és λ_2) represent the variances of the data (pixels)

$$\sigma_{major} = \lambda_1^{1/2}, \qquad \sigma_{minor} = \lambda_2^{1/2}. \tag{10}$$

The area of the detected cluster is

$$A = ndxdy, \tag{11}$$

where dx and dy are the grid spacing on the radar image.
The area of an ellipse is given by

$$T = \pi ab, \tag{12}$$

where a and b represents the major and minor axes of the ellipses.
The main idea is that the area of the irregular cluster and the area of the ellipse have to be equal, therefore

$$A = T . \tag{13}$$

So the major and minor axes of the ellipses can be calculated by

$$a = \sigma_{major} \left(\frac{A}{\pi \sigma_{\min or} \sigma_{major}} \right)^{1/2}, \qquad b = \sigma_{\min or} \left(\frac{A}{\pi \sigma_{\min or} \sigma_{major}} \right)^{1/2}. \tag{14}$$

With these parameters $(\bar{x}, \bar{y}, a, b, \theta)$, the focus points and the equation of the ellipse can be determined.

References

Bodolainé, J. E. és *Tänczer, T.*, 1991: Instabilitási vonal regionális ciklonban. *Időjárás 95,* 178–195.

Bodolainé, J.E. és *Tänczer T.*, 2007: Mezoskálájú konvektív komplexumok (szerk.: Horváth, Á.) A légköri konvekció, Országos Meteorológiai Szolgálat, Budapest, 35–45.

Boncz, J., Kapovits, A., Pintér, F. and *Tänczer, T.*, 1987: A method for the complex analysis of synoptic weather radar and satellite data. *Időjárás 91*, 11–22.

Braham, R.R., 1958: Cumulus cloud precipitation as revealed by radar- Arizona 1955. *J. Meteor. 15*, 75–83.

Brimelow, J.C., Reuter, W.G., Bellon, A. and *Hudak, D.*, 2004: A Radar-Based Methodology for Preparing a Severe Thunderstorm Climatology in Central Alberta. *Atmosphere-Ocean 42,* 13–22.

Collier, C.G., 1996: Application of weather radar system: A Guide to uses of radar in meteorology and hydrology. John Wiley & Sons,

Croft, P.J. and *Shulman, M.D.*, 1989: A five-year radar climatology of convective precipitation for New Jersey. *Int. J. Climatol. 9,* 581–600.

Davini, P., Bechini, R., Cremonini R. and *Cassardo, C.*, 2012: Radar-Based Analysis of Convective Storms over Northwestern Italy. *Atmosphere 3*, 33–58.

Dixon M. and *Wiener, G.*, 1993: TITAN: Thunderstorm Identification, Tracking, Analysis and Nowcasting – A radar-based methodology. *J. Atmos. Ocean. Tech. 10,* 785–797.

Falconer, P.D., 1984: A Radar-Based Climatology of Thunderstorm Days across New York State. *J. Appl. Meteorol. 23,* 1115–1120.

Geresdi, I., 2004: Felhőfizika. Dialog Campus, Budapest, 153–170.

Götz, G. és *Pápainé, Sz. G.*, 1966: Zivatartevékenység a nyári félévben Magyarországon. *Időjárás 70,* 106–116.

Götz, G. és *Pápainé, Sz. G.*, 1967: Zivatartevékenység a téli félévben Magyarországon. *Időjárás 71,* 302–309.

Henz, J., 1974: Colorado High Plains thunderstorm systems - a radar synoptic climatology. Colorado St. Univ., M.S. thesis.

Héjas, E., 1898: Zivatarok Magyarországon az 1871-től 1895-ig terjedő megfigyelések alapján. Királyi Magyar Természet Tudományi Társulat, Budapest, 174 pp.

Höller, H., 1994: Mesoscale organization and hailfall characteristics of deep convection in Southern Germany. *Beitr. Phys. Atmosph. 67,* 219–234.

Horváth, Á. and *Geresdi, I.*, 2003: Severe storms and nowcasting in the Carpathian Basin. *Atmos. Res. 67–68,* 319–332.

Horváth, Á., Ács, F. and *Seres, A. T.*, 2008: Thunderstorm climatology analyses in Hungary using radar observations. *Időjárás 112,* 1–13.

Horváth, Á., Geresdi, I., Németh, P. and *Dombai, F.*, 2007: The Constitution Day storm in Budapest: Case study of the August 20, 2006 severe storm. *Időjárás 111,* 41–65.

Hungarian Meteorological Service, 2012: HAWK-3 visualization system. http://www.met.hu/en/omsz/tevekenysegek/hawk/

Jaeneke, M., 2001: Radar Based Climatological Studies of the Influence of Orography of Thunderstorms Activity in Central Europe. In: Proceedings of the 30th International Conference on Radar Meteorology, Session 12A, Munich, Germany, 19-24 July 2001; p. 12A5.

Mohee, F.M. and *Miller, C.,* 2010: Climatology of Thunderstorms for North Dakota, 2002–06. *J. Appl. Meteorol. Climatol. 49,* 1881–1890.

Myers, J., 1964: Preliminary radar climatology of central Pennsylvania. *J. Appl. Meteor. 3,* 421–429.

Paiva Pereira, L.G. and *Rutledge, S.A.,* 2003: Convective Characteristics over the East Pacific and Southwest Amazon Regions: A Radar Perspective. EPIC 2001 Workshop, Boulder, CO, 15-16 September 2003.

Ozorai, Z., 1965: A zivatarok gyakorisága Budapest-Ferihegy repülőtéren. *Időjárás 69,* 375–377.

Raum, O., 1910: A Magyarországon észlelt 15 évi zivatarok megfigyelések eredményei az 1896–1910 időszakban. *Királyi Magyar Természettudományi Társulat Évkönyve 40, 2.*

Rigo, T. and *Liasat, M.C.,* 2002: Analysis of convective structures that produce heavy rainfall events in Catalonia (NE of Spain), using meteorological radar. Proc. ERAD, 45–48.

Rudolph, J.V., Friedrich, K. and *Germann, U.,* 2011: Relationship between Radar-Estimated Precipitation and Synoptic Weather Patterns in the European Alps. *J. Appl. Meteor. Climatol. 50,* 944–957.

Steiner, M. and *Houze, R.,* 1996: Sensitivity of the Estimated Monthly Convective Rain Fraction to the Choice of Z–R Relation. *J. Appl. Meteorol. 36,* 452–462.

Tukey, J.W., 1977: Exploratory Data Analysis. Addison-Wesley, Reading.

Weckwerth, T.M., Wilson, J.W., Hagen, M., Emerson, T.J., Pinto, J.O., Rife, D.L. and *Grebe, L.,* 2010: Radar climatology of the COPS region. *Q. J. Roy. Meteorol. Soc. 137,* 31–41.

IDŐJÁRÁS

Quarterly Journal of the Hungarian Meteorological Service
Vol. 119, No. 2, April – June, 2015, pp. 197–213

MEANDER: The objective nowcasting system of the Hungarian Meteorological Service

Ákos Horváth[1*], **Attila Nagy**[1], **André Simon**[2], and **Péter Németh**[2]

[1]*Hungarian Meteorological Service Storm Warning Observatory*
Vitorlás u. 17. H-8600 Siófok

[2]*Hungarian Meteorological Service,*
Kitaibel Pál u. 1., H-1024 Budapest, Hungary

**Corresponding author E-mail:horvath.a@met.hu*

(Manuscript received in final form March 3, 2015)

Abstract—In this paper, an overview of the complex nowcasting system of the Hungarian Meteorological Service is presented. The system named MEANDER started to work as a linear extrapolation process to provide warnings on convective storms. The role of the numerical weather prediction (NWP) models have been increased by involving the Weather Research and Forecasting (WRF) Model into nowcasting procedures. In the current state, MEANDER system consists of 2 main segments: NWP and linear parts.

In the NWP segment, WRF model is used in two steps: in the first step, WRF (WRF-ALPHA) is run at a 2.5×2.5 km horizontal resolution grid, using non-hydrostatic dynamics and ECMWF model data as initial and boundary conditions. The second step is a higher resolution (1.2×1.2 km) WRF model run – named WRF-BETA –, that uses lateral conditions and first guess data coming from WRF-ALPHA outputs and assimilates radar reflectivity, satellite and surface observation data. The domain of WRF-BETA is included in the domain of WRF-ALPHA. The applied nowcasting-specific assimilation helps the model to develop significant precipitating weather systems on the right location in the right time. WRF-BETA outputs provides such background information for the nowcasting system that makes the forecast of the linear segment more exact.

In the linear part, the actual objective analysis is considered at the beginning and the NWP prediction at the end of the nowcasting period. In the meantime, linear interpolation is applied. Radar data has key role in the nowcasting procedures in the linear segment, too. There are several derived parameters that are used for calculating the SYNOP-type present weather parameter for all grid points in the analysis and for the entire forecast time.

The MEANDER system has a warning process that is able to create weather warnings for all districts of Hungary, helping decisions of forecasters.

Key-words: nowcasting, nowcasting-systems, Weather Research and Forecasting Model (WRF), storm warning

1. Introduction

The term nowcasting is related to detailed analysis of the present state of the weather and to its very short-range (only few hours)[1] forecasts. Objective methods were developed for such purposes already in the 70-s and early 80-s of the previous century (*Browning*, 1982). Originally, the nowcasting techniques focused on the forecast of thunderstorms and on the extrapolation of radar or satellite images. Mathematical methods (e.g., fuzzy-logic techniques) or conceptual models have been developed to refine the analyses of the storms motion and to assess the development of precipitation bands (*Conway* and *Labrousse*, 1997). The extrapolation-based nowcasting systems can be cell-oriented, like the system TITAN (Thunderstorm Identification, Tracking, Analysis and Nowcasting, described by *Dixon* and *Wiener*, 1993) or can use object-tracking algorithms as the system COTREC (*Li et al.*, 1995; *Mecklenburg et al.*, 2000) or the system TREC (*Horváth et al.*, 2012). The extrapolation of radar echoes can be combined with several other kinds of observation data, parameterizations, conceptual models, thus, striving to emulate the approach of a human forecaster. An example of such (sometimes called expert) system is the NCAR Auto-Nowcaster (*Mueller et al.*, 2003). Some systems have been based on stochastic approaches to decompose the precipitation field in order to create an ensemble of nowcasts for several spatial scales – e.g., the system STEPS (*Bowler et al.*, 2006; *Foresti et al.*, 2014).

Several studies and demonstration cases showed that the performance of extrapolation methods is strongly limited. The predictability depends on the scale and intensity of the extrapolated precipitation (e.g., *Germann* and *Zawadzki*, 2002). Refinement of the extrapolation techniques (e.g., filtering of nonpredictable scales of precipitation described by *Turner et al.*, 2004) can increase the forecast lead time, but for higher intensities (occurring typically in convective environment), the forecast skills usually decrease very rapidly with time (shown e.g., by *Lee et al.*, 2009). This also motivated the use of forecasts of numerical weather prediction (NWP) models in nowcasting systems, already in the 90-s of the 20th century. NWP inputs have sometimes only support role in estimating the speed and direction of the motion of precipitation cells and their development (for example, in the GANDOLF system, described by *Pierce et al.*, 2000). Several nowcasting systems provide blending of the extrapolation methods with NWP data. This approach was used in the system NIMROD (Nowcasting and Initialization for Modeling Using Regional Observation Data System, described by *Golding*, 1998). Blending with NWP data is important for systems, which forecasts of temperature, wind, or other meteorological parameters generate besides

[1] At the beginning, the 0–1 or 0–2-hour period was denoted as nowcasting-range, but (perhaps as a consequence of increasing influence and use of numerical weather prediction models for nowcasting purposes) the 0–6-hour period is mentioned more often now.

precipitation nowcasts. For example, tendencies from NWP models are used in the nowcasting system INCA (Integrated Nowcasting through Comprehensive Analyses, described by *Haiden et al.*, 2011).

Current efforts to improve the forecasts (mainly beyond the 0–1 h forecast range) are closely related to assimilation of all available observational data (surface, radar, satellite observations, etc.) and preparation of a three-dimensional objective analysis, which can be used as initial condition in a high-resolution NWP model run. This is the basic approach for systems such as LAPS (Local Analysis and Prediction System, introduced in *Albers et al.*, 1996). The advance of the computational technology enabled frequent updates of the NWP models (so-called rapid update cycles), which can be either directly used for nowcasting purposes or for blending with extrapolation systems. Several assimilation techniques have been applied in order to improve the very short range NWP forecasts, e.g., nudging, 3DVAR, or ensemble Kalman Filter technique (an overview of these methods was given by *Sun et al.*, 2014).

Despite of advances in NWP techniques, it is recognized that the role of the conceptual models and forecasters in nowcasting is still important as shown during the WMO demonstration projects for Sidney and Beijing Olympic games (*Ebert et al.* 2004, *Wilson et al.*, 2010).

At the Hungarian Meteorological Service (OMSZ), subjective methods to forecast thunderstorm activities have been developed since the 1960-s based on surface and sounding data (*Bodolai*, 1954; *Götz* and *Bodolainé*, 1963a, 1963b, *Bodolainé et al.,* 1967). These studies were concentrating on prefrontal squall lines and severe thunderstorms. Methods were developed and applied to evaluate remote sensing data and introduce that information into weather warning (*Bodolainé*, 1980*; Boncz et al.,* 1987; *Bodolainé* and *Tänczer,* 1991; *Putsay et al.*, 2009). Because of the geographical environment, the Carpathian Basin is inherently susceptible to floods, and conceptual models were created to understand and recognize weather patterns responsible for local and regional scale floods (*Bodolainé* and *Homokiné*, 1984; *Bonta* and *Takács,* 1988; *Bodolainé* and *Tänczer*, 2003). Appearance of more accurate radar data and increasing number of automated weather stations created the need for developing objective nowcasting system MEANDER (mesoscale analysis, nowcasting and decision routines) that was introduced to operational service in the year of 2003 (*Horváth* and *Geresdi*, 2003). The first version of MEANDER was based on simple extrapolation of radar data. Later, using blending technique with NWP data, MM5 (*Dudhia*, 1993) model was applied as the background NWP tool. The analyses of MEANDER were also tested as input for the MM5 model (*Horváth*, 2005). In the last few years, several modifications and upgrades were done on the MEANDER system. In this paper the recent state of the nowcasting system of the Hungarian Meteorological Service is presented.

2. *Development of the MEANDER system*

Earlier versions of the nowcasting system used by the Hungarian Meteorological Service were linear extrapolation based procedures, and they focused on severe thunderstorms nowcast. For this reason, MEANDER considered radar-measured heavy precipitation echoes and these echoes were extrapolated using a constant motion vector field. Motion vectors were calculated from a background hydrostatic numerical model, taken the closest forecast time step to the actual time. For the motion vector calculation, density and wind component values of vertical model levels were applied. The calculation based on the idea, that thunderstorm cells are massive objects and their movement is determined by conditions in the surrounding vertical layers of the atmosphere (*Fig. 1*). The speed of the cloud is $\vec{V}^c$ and the mass of the cloud is represented by the sum of **n** vertical layers with each layer with ρ_i. The ***I*** momentum of the cloud can be written as

$$\boldsymbol{I} = \sum_{i=1}^{n} \rho_i \vec{V}^c \quad .$$

The momentum of the cloud supposed to be equal to the sum of its environment momentum, thus

$$\sum_{i=1}^{n} \rho_i \vec{V}^c = \sum_{i=1}^{n} \rho_i \vec{v}_i^e \quad ,$$

where $\vec{v}_i^e$ represents the environment wind on the ith vertical level (taken from NWP). The above equation provides the cloud motion vector:

$$\vec{V}^c = \frac{\sum_{i=1}^{n} \rho_i \vec{v}_i^e}{\sum_{i=1}^{n} \rho_i} \quad .$$

The above calculated motion vector is useful for thunderstorms, but for stratiform precipitation it didn't work properly (*Horváth* and *Geresdi*, 2003).

Objective analysis of earlier MEANDER versions was based mainly on observations. The spatial and temporal resolution of available NWP was not high enough for effective use in meso-scale. Increase in density of surface observations enabled production of higher resolution surface analyses, but that was not physically consistent with higher level model data.

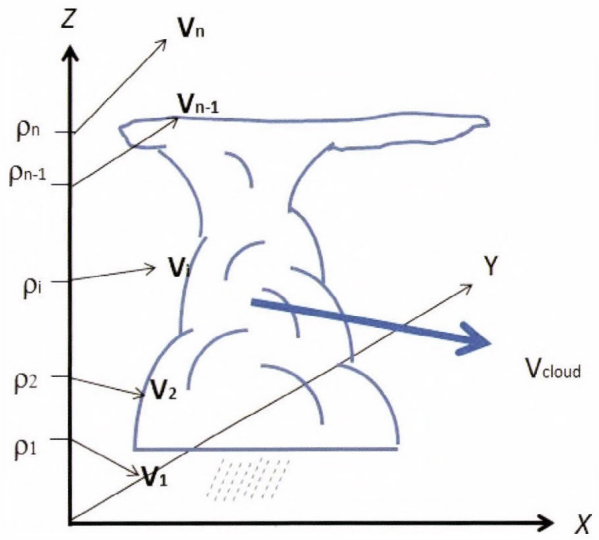

Fig. 1. Calculation of motion vectors for convective clouds. On the vertical axis ρi and Vi represents the vertical profiles of density and wind of the environment, $Vcloud$ represents the cloud motion vector.

Installation of non-hydrostatic MM5 model allowed to use the blending technique for nowcasting: linear interpolation was applied instead of linear extrapolation. The system interpolated between the objective analysis at the beginning and the numerical forecast at the end of a nowcasting period (*Horváth*, 2005). The objective analysis used not only observation but, in addition, MM5 outputs as first guess information, and four dimensional data assimilation technique were applied to enhance the analysis (*Stauffer* and *Seaman*, 1990).

Motion vectors for radar echo replacement were also calculated from MM5 upper level wind data. Operational usage of high resolution satellite data also helped to improve the nowcasting, especially the cloud type and overcast part (*Putsay et al.*, 2010). Later versions of MEANDER considered not only convective but stratiform precipitation, too. A decision procedure determined that a precipitating system was stratiform or convective. For startiform systems, the average wind vector between 1000–4000 m proved to be the best parameter as motion vector.

The third generation of the MEANDER system is more NWP-based. The initial conditions provided by background NWP model are modified with

respect to certain significant, observed meteorological objects, using conceptual models. For example: radar detected thunderstorms are included in the initial model field in such a way, that convergence and divergence in the wind field and anomaly in the temperature and humidity field are placed to the appropriate location. These impacts allow the model (or at least give it a chance) to develop significant objects on the right location in the right time. The presently applied WRF model (*Skamarock et al.*, 2005) is able to manage these dynamically not balanced modification of first guess fields and, as it is shown later, WRF is able to provide corrected background data for the nowcasting system. Below, the currently used 3rd generation MEANDER system is presented.

3. Two-layer NWP background of the nowcasting system

The basic input data for the NWP segment of nowcasting are ECMWF deterministic model forecasts. Model level ECMWF data provide boundary conditions and first guess information for the non-hydrostatic WRF model. The WRF domain covers the Carpathian Basin with a 2.5×2.5 km horizontal resolution grid. This model version named WRF-ALPHA runs with 6-hour frequency and has 36-hour forecasting range. In addition to ECMWF data, surface and upper air measurements are also involved into initial conditions using WRF data assimilation tools (*Skamarock et al.*, 2005). WRF-ALPHA also uses special input coming from a stand-alone soil model that calculates soil humidity and soil temperatures on 4 soil layers. The soil model is based on the NOAH model (*Chen* and *Dudhia*, 2001), and it receives meteorological input data from MEANDER analysis (for example precipitation) and from previous WRF model run (surface fluxes, etc.). Calculated soil data are updated 4 times a day. The sensitivity of deep convection to soil condition of the Carpathian Basin was described by *Ács et al.*, 2010, and this sensitivity justifies special care of soil input data.

The second part of the NWP segment is based on a higher resolution WRF model run (1.2×1.2 km). In this model, named WRF-BETA, measured data have got higher role. First guess data originating from WRF-ALPHA input, observed temperature, humidity and wind data are assimilated using nudging facility of WRF. Two hours of nudging period are applied, i.e., the –2, –1, and 0-hour analyses are used (0 hours means the last time when analysis is available). Not only weather station data, but remote sensing information are also involved in the analyses. Especially at cases of thunderstorms, radar reflectivity can be involved into the analyses using conceptual models.

Thunderstorms can be identified by radar reflectivity in such a way, that ellipses are assigned to locations where radar reflectivity is higher than a threshold value (45 dBz). The ellipses procedure was developed in the TITAN method (*Dixon* and *Wiener*, 1993) and was applied – among of others – for

nowcasting related research (*Horváth at al.*, 2008; 2012). On locations where thunderstorms are detected, the analysis field is modified by the conceptual model as described below.

The model is based on the idea that a thunderstorm has an updraft and a downdraft channel. In the updraft channel, there is a positive temperature and humidity anomaly and there is significant convergence of the wind field at lower layers. The other pole of the thunderstorm is the downdraft channel where deficit in the absolute humidity (mixing ratio of water vapor) and divergence at lower layers can be found. The fuel of this "two-pole engine" is the humidity. Normally, the moisture is available from the basic analysis field, but the objective analysis is not necessary exact concerning the humidity analysis. To supply the thunderstorm with humidity in its initial phase, a humidity reservoir is added to the model with positive humidity anomaly and slight convergence at the lower layers (*Fig. 2*). The temperature profile of the updraft channel is calculated in such a way that equivalent potential temperature (EPT) is considered to be constant (*Fig. 3*), and EPT is calculated from the near surface layers supposing saturated air. In this way, the updraft channel of the thunderstorm appears as wet and warm bubbles in the analysis field (*Horváth*, 2006). The wind field is modified in lower layers (~lower 1000 m) to be convergent with respect to the center of the updraft channel. On the bottom of the downdraft channel the wind is divergent, blowing out of the center of the downdraft channel, and there is a weak depression in the field of absolute humidity. In the humidity reservoir, there is a weak horizontal flow in the direction of dual channels. The modification made by the conceptual model is added to the field of the objective analysis. Several numerical experiments were made to set parameters for the conceptual models. Experiments show that relatively little perturbation of humidity and wind values are enough for the conceptual model for triggering thunderstorms (*Fig. 4*). WRF model is tolerant of conceptual model made perturbations, and this triggering procedure helps to develop thunderstorms on proper place in proper time. The life time of triggered thunderstorm is more than 2 hours at about 70% of investigated cases. Sometimes the initial thunderstorms dissipated, but they made neighboring groups of incorrectly forecasted thunderstorms weaker or disappear.

Satellite data also can be used for WRF-BETA initial data by EUMETSAT provided SAFNWC information (*Derrien* and *Le Gléau*, 2005). Cloud mask and cloud type information allow to recognize opaque and thick cloudiness. Considering the mean value of cloud water mixing ratio (CLW) coming from WRF-ALPHA, it is possible to assign CLW values for cloudy areas. WRF-BETA accepts CLW as initial data and involving CLW does not increase numerical instability during the model run (numerical experiments were made to involve rain water into initial condition, but this input parameter increased the instability). Case studies showed that involving CLW has some positive influence on cloudiness, but improvement of this procedure is still under way.

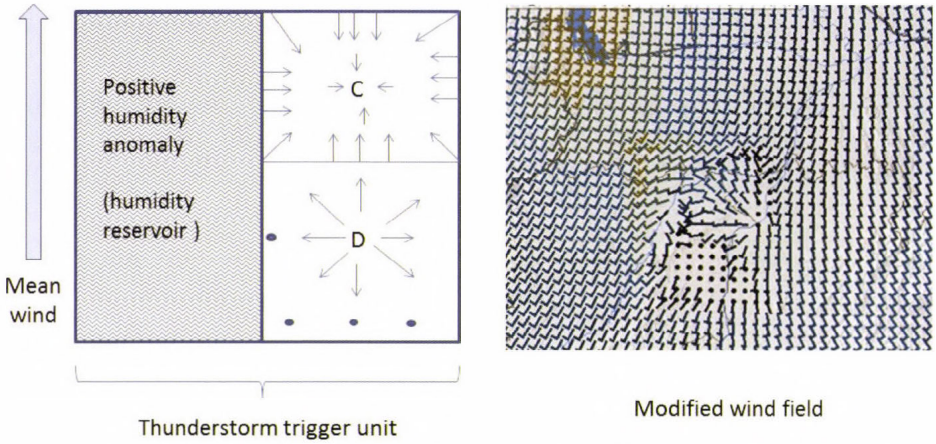

Fig. 2. The structure of a convective trigger unit (left) and the perturbed low level wind field (right). In the trigger unit, the square denoted by C represents the convergence in the updraft channel and letter D represents the divergence in downdraft channel. The right rectangle represents the humidity reservoir where is extra humidity added relative to the first guess to supply convection.

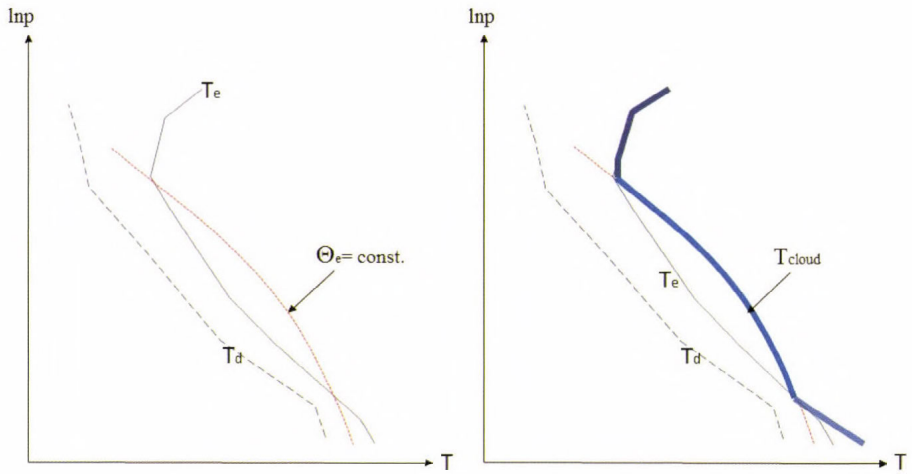

Fig. 3. Modification of the vertical temperature profile in the updraft channel of the triggering unit. In the original profile (left): T_e and T_d represents the temperature and dew point profiles of the first guess and θ_e shows the constant equivalent potential temperature (EPT) calculated from the lower 1000 m. The modified profile (right) is represented by the thick line.

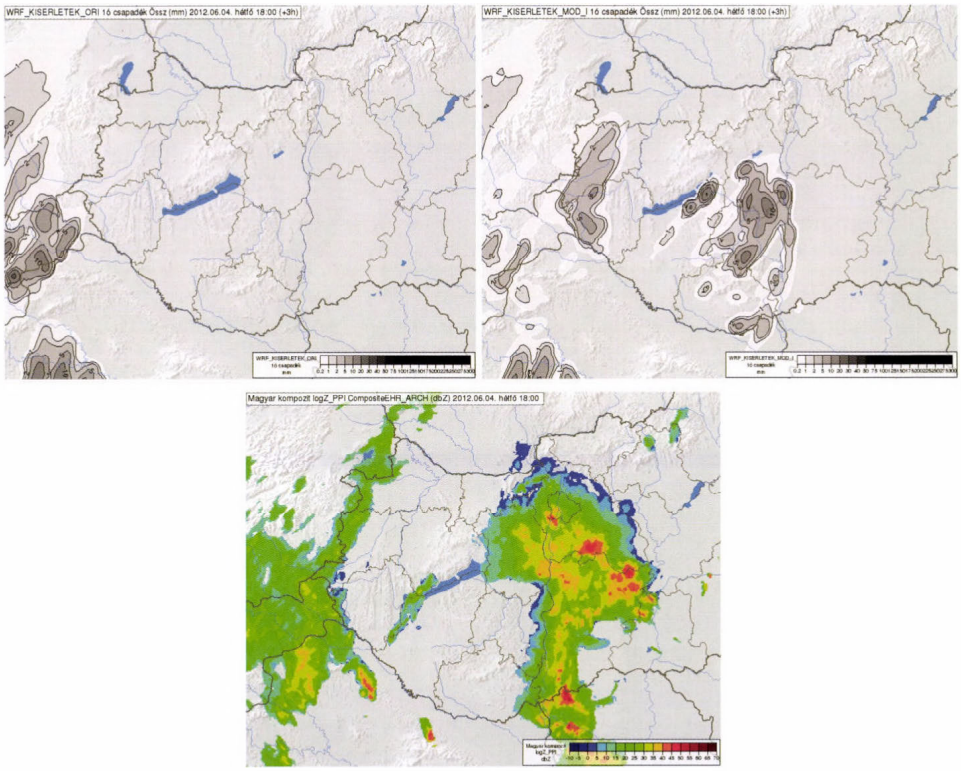

Fig. 4. 1-hour accumulated precipitation of +3-hour forecast of the WRF model at reference (upper left) and triggered forecasts (upper right) and the measured radar reflectivity (lower image). The model start time is 15:00 UTC June 4, 2012, the radar reflectivity image time is 18:00 UTC June 4, 2012. The triggered model run produced more realistic result than the reference run.

There are some derived parameters calculated as first guess data for nowcasting applications. The visibility for all grid points is computed from the lowest model level using mixing ratio of water vapor, cloud water, rain water, cloud ice, and snow (*Kunkel*, 1984). Radar motion vectors are calculated separately for convective and stratiform precipitating systems as described above.

In an ideal case, WRF-BETA should always be run when new observations are available. Because of limited computer power, WRF-BETA runs in every third hours providing NWP output for the nowcasting system for the next 8 hours with 15 minutes output frequency.

4. The linear segment of the nowcasting system

The linear segment of the MEANDER system consists of two parts: an objective analysis and a linear forecast. The objective analysis uses the coincidental WRF-BETA forecast, measured surface data, radar data, and satellite information. The grid of the objective analyses is the same as the WRF-BETA grid (1.2×1.2 km). During the objective analysis, derived parameters are also calculated, and finally, for all grid points, synoptic-type present weather code values (snow, rain, thunderstorm, etc.) are assigned. The frequency of the objective analysis is 10 minutes. From all objective analyses, a linear forecast is made for 3 hours ahead and updated in every 10 minutes.

The analysis segment uses WRF-BETA outputs as first guess data. For basic parameters, differences between observed and first guess values are calculated at all observation points. These differences are interpolated to all grid points using biharmonic spline procedure (BHS). Input for BHS are (1) coordinates of observation points, (2) coordinates of grid points of the objective analysis, (3) difference values between grid point and observation point data at the observation point. Outputs of BHS are interpolated differences at all grid points of the objective analysis. Finally, first guess data are corrected by the interpolated values at grid points.

In order to decrease representation error, grid points of first guess data are considered in the circle of radius R around an observation point. Differences between observation value and first guess values are calculated, and that grid point is chosen where the difference is the smallest. This minimum value is considered as the difference between first guess and observation as input (3) for BHS at the given observation. Coordinates of the observation point are taken to be equivalent to the coordinate of the chosen grid point as input (1) for BHS. This "wobbling observation" procedure proved to be useful on those locations, where the gradient of the considered parameter is large, for example at lake or sea side observation points or hilly regions. In practice, R is chosen 4 km for flat regions, and 5 km for hilly regions and lake side stations.

Radar data for the nowcasting system are from the Hungarian composite radar images that are created from 3 Doppler radars of the Hungarian Meteorological Service in every 5 minutes. The spatial resolution of radar information has the same order than the nowcasting grid has, so transformation of radar reflectivity data to the nowcasting grid does not cause distortion or data loss. Satellite data can also be projected to the nowcasting grid. Applied satellite data are NWCSAF products such as cloud cover, cloud type, cloud top temperature (*Derrien* and *Le Gléau*, 2013). When radar and satellite data are on the common platform of the nowcasting grid, a process compares them and eliminates large radar errors. This procedure (not detailed here) is important because of large number of commercial electromagnetic devices (for example WIFI devices) that make artificial noise and sometimes

remain in the reflectivity field despite filtering procedures of the radar facility.

The linear forecasting segment of the nowcasting system is based on the blending technique for basic parameters such as pressure, humidity, wind, and temperature. At the beginning of the 3-hour-long nowcasting period, the objective analysis is considered, and at the end there is an actual WRF-BETA forecasted data field. In the meantime, linear interpolation is applied (*Fig. 5*). Radar echoes can be advected using motion vector fields. (Motion vector fields, coming from WRF-BETA, are not permanent fields, but they are changing during the forecast time, so forecasted radar echoes are moving along fractionally linear paths.) The forecast of precipitating clouds allows the calculation of integrated precipitation using Marshal-Palmer form between radar reflectivity and rain intensity (*Marshal* and *Palmer*, 1948). In this procedure, the amount of precipitation is computed up to 3 hours, using 1 minute time step.

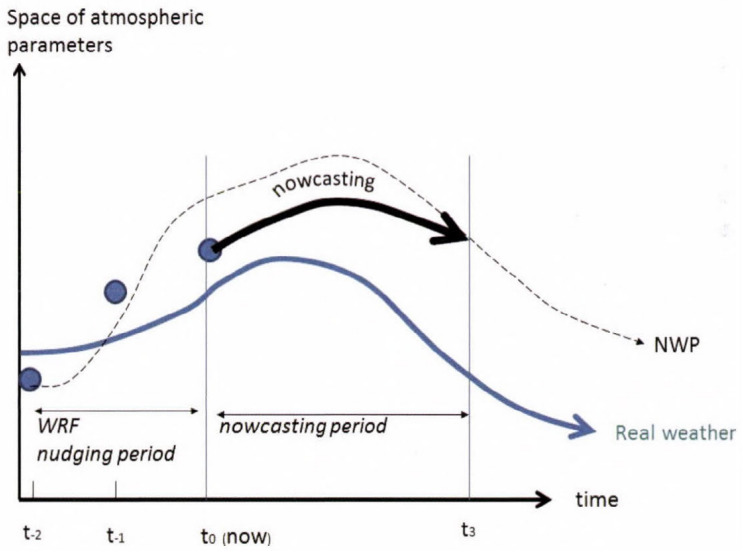

Fig. 5. Theoretical background of MEANDER system. Along the vertical axis the atmospheric parameters, on the horizontal axis the time are labeled. The continuous line represents the trajectory of the real weather, dashed line shows NWP forecast, circles represents objective analysis. The thicker solid line shows the nowcasting.

Derived parameters can be calculated at any time step of the nowcasting period. Among these parameters the precipitation phase, which frequently changes in wintertime, is especially important in the Carpathian Basin. There is a method developed by Geresdi (*Geresdi* and *Horváth*, 2000) to calculate the phase of precipitation applying cloud physics. The 1D cloud model is applied to calculate the cloud top, maximum updraft, and hailstone size of a potential thunderstorm (*Geresdi et al.*, 2004). The TREC method that was developed by the remote sensing division of the Hungarian Meteorological Service is also applied for the nowcasting system for 1 hour accumulated precipitation estimation (*Horváth et al.*, 2012). The radar based process considers previous radar reflectivity images and calculates a motion vector field taking correlations between two images. Motion vectors are applied to interpolate radar images with 1 minute temporal resolution in such a way, that radar echoes are replaced by motion vectors. Using these interpolated reflectivity images (and calculated precipitation intensity from that), the accumulated precipitation can be computed. A procedure calculates thunderstorm-associated maximum wind gust using the maximum radar reflectivity and the maximum cloud top height of cumulonimbus cells (*Bartha*, 1994). The convective wind field of a stormy day is shown in *Fig. 6*. Non-convective wind gusts are also computed from WRF-BETA, and this parameter is included in the objective analysis. During the forecast, it is blended with NWP data similarly to other basic parameters. The final result of derived parameters calculating procedure is "present weather" code values for all grid points. This parameter is depicted in similar way as the observed present weather parameters from WMO-SYNOP code.

Warning segment of the nowcasting system is designed to issue weather warning for the next 3 hours using the actual analysis and nowcasted present weather parameters. There are 3 warning levels, and the actual level is clearly defined by the previously calculated present weather code. (For example, there are three kinds of present weather code for thunderstorm in MEANDER: thunderstorm – first level; severe thunderstorm – second level; extreme thunderstorm – third warning level). There are 175 districts in Hungary, and the warning system generates individual weather warnings for those districts where it is justified by calculated present weather parameters. In the practice the forecaster on duty receives automatically generated warning maps on a special graphical user interface, and he or she can accept or interactively modify proposed information. Actual weather warnings appear on the warning page of the Hungarian Meteorological Service (http://met.hu/idojaras/veszelyjelzes/riasztas/). The flow chart of the nowcasting system is presented in *Fig. 7*.

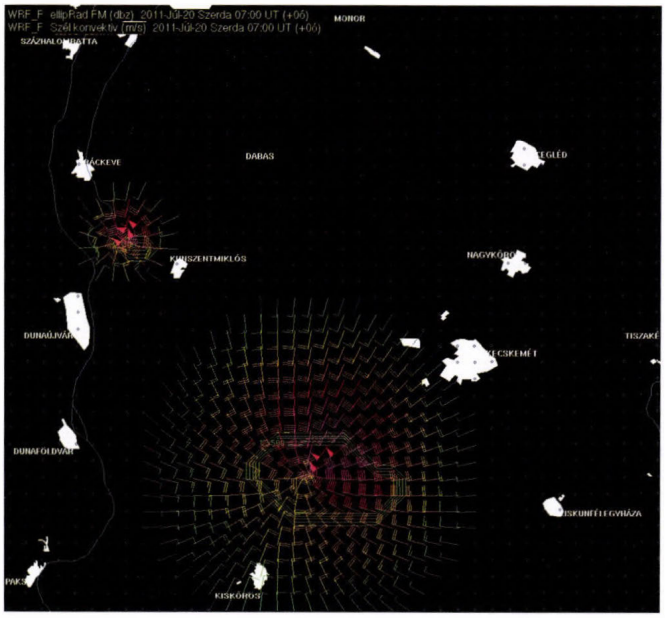

Fig. 6. Calculated convective wind field and thunderstorm contour lines on east of Danube at 07:00 UTC, July 20, 2011. That was a severe convective storm case caused serious damages near Kecskemét.

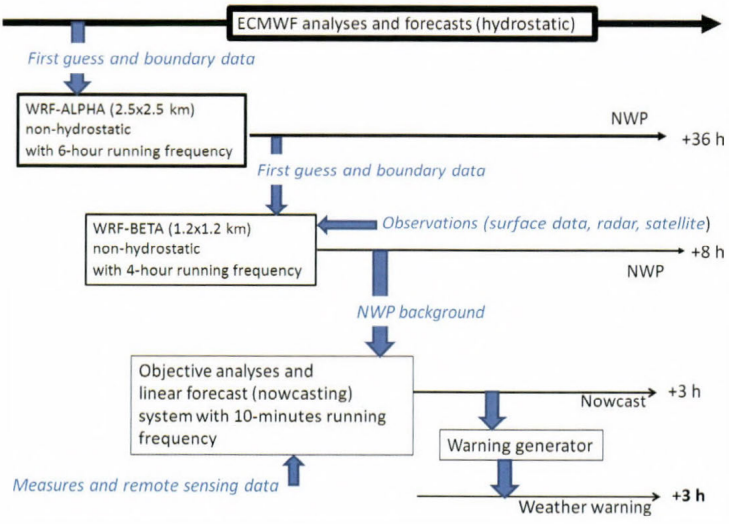

Fig. 7. Flow chart of the MEANDER system.

5. Evaluation and experiences

Concerning NWP (WRF-BETA) background, many case studies have been done to analyze the impact of radar assimilation made by the conceptual thunderstorm model. In about 70% of cases, the conceptual model has unambiguous positive impact up to 5 hours forecast. This way of introducing thunderstorm is safe, no significant gravity waves or other side effects were experienced. The limitation of the conceptual model is that it cannot be applied before first radar signs of thunderstorms appear. Currently used computer resources do not allow to run numerical models exactly in the same time when thunderstorms appear. The ideal solution would be a flexible NWP model run: WRF-BETA should run any time when the weather condition justifies that.

The nowcasting of the linear segment for basic parameters is verified by comparison of the analyses with earlier issued nowcasting at all grid points. Verification shows that basic parameters have relative small errors for the first 2 hours. The RMSE for temperature is above 0.5 °C, for pressure 0.1 hPa, for relative humidity 10%, and for wind speed 1.6 m/s. The precipitation forecast is highly dependent on the precipitation type. The forecast of stratiform precipitation is significantly better than forecast of convective precipitation (93% vs. 72%). There are problems with the verification of the derived parameters. For parameters like present weather, it is problematic to compare analysis fields with forecasts, because present weather itself is a derived parameter at the analysis time, too. Therefore, present weathers like freezing rain, severe thunderstorms can be verified via case studies, where inherently subjective visual observations are collected posteriorly. Case studies show that the most sensitive parameter is the precipitation phase and phase related present weather, especially freezing rain. Also, there is high spatial variability concerning visibility parameters. Most "nowcastable" significant present weathers are associated with stratiform precipitation like summer rain or winter snow. Severe convective storms and multicell thunderstorms can also be relative properly forecasted, especially when they are in developing phase and the advection is more decisive than developing. In the linear segment, the thunderstorm development has not been solved yet, the blending technique of radar observed cell transition to NWP simulated cell is still under development. The precipitation-associated parameters show significantly growing errors after 2 hours, hence in operational public usage only this forecast range is considered.

Evaluation of the warning segment shows better results than point-to-point comparison above. A district contains several grid points and the chance that weather objects hits at least a grid point in a district is definitely larger. Considering significant weather events, there is overestimation of weather warning for freezing rain and slight overestimation of severe convective events for 2 hours.

6. Summary

The MEANDER nowcasting system takes advantages of high resolution numerical modeling and very short range linear extrapolation. The hydrostatic ECMWF data are downscaled (in both time and space) to the resolution of the nowcasting system in two steps. During the first phase, the applied WRF (WRF-ALPHA) creates high resolution non-hydrostatic forecast 4 times a day. The WRF-ALPHA outputs are first guess and lateral condition data for a higher resolution WRF-BETA that produces forecast for the nowcasting domain with 1.2×1.2 km horizontal resolution. WRF-BETA uses nearly all available remote sensing and measured data and provides first guess information for the linear segment.

The linear segment uses observations for making analysis, which is the first pillar of the linear nowcasting. The second pillar is the WRF-BETA forecast that is considered at the end of the 3-hour-long nowcasting period. Radar located precipitating systems are moved in the linear segment using motion vector fields, calculated from WRF-BETA forecast. Derived parameters are computed during the linear segment, and finally, present weather values are assigned to all grid points. Finally, the warning segments are used to issue weather warnings for 175 districts of Hungary. The linear segment runs every 10 minutes, 24 hours a day.

Verifications and experiments show that the MEANDER system in the present stage provides usable forecast and warnings for the next 2 hours. Developing nowcasting-oriented assimilation techniques and more frequent model runs may help to extend this range in the near future.

References

Ács, F., Horváth, Á., Breuer, H., and *Rubel, F.*, 2010. Effect of soil hydraulic parameters on the local convective precipitation. *Met. Z.* 19,143–153.

Albers, S.C., McGinley, J.A., Birkenheuer, D.A., and *Smart, J.R.*, 1996: The local analysis and prediction system (LAPS): Analysis of clouds, precipitation and temperature. *Weather Forecast. 11*, 273–287.

Bartha, I., 1994: Development of a decision procedure for forecasting maximum wind gusts associated with thunderstorms. *Meteorol. Appl. 1*, 103–107.

Bodolai, I., 1954: A konvektív zivatarok aerológiai-szinoptikai feltételeiről. OMI Kisebb Kiadványai 27, OMSZ, Budapest. (in Hungarian)

Bodolainé, J.E, 1980: Radarral végzett csapadékmérések a csapadék rövidtávú előrejelzésben OMSZ Kisebb Kiadványai 48, OMSZ, Budapest. (in Hungarian)

Bodolainé, J.E, Bodolai, I. and *Böjti, B.*, 1967: Macrosynoptical conditions for the formation of Slovenian squall lines and some properties of cold fronts with thunderstorm. *Időjárás 71*, 129–143.

Bodolainé, J.E. and *Homokiné, U.K.*, 1984: A csapadékmennyiség előrejelzése az orografikus többlet figyelembevételével. *Az OMSZ Kisebb Kiadványai 57, OMSZ, Budapest.* (in Hungarian)

Bodolainé, J.E. and *Tänczer, T.*, 1991: Instabilitási vonal regionális ciklonban. *Időjárás 95*, 178–195. (in Hungarian)

Bodolainé, J.E. and *Tänczer, T.*, 2003: Mezoléptékű konvektív komplexumok. OMSZ, Budapest. (in Hungarian)

Boncz, J., Kapovits, A., Pintér, F. and *Tänczer, T.*, 1987: MÓdszer a szinoptikus-, radar- és műholdadatok complex analízisére. *Időjárás 91*, 11–22. (in Hungarian)

Bonta, I. and *Takács, Á.*, 1988: Heves esőzés veszélyét jelző rendszer kiépítése Magyarországon. OMSZ Kisebb Kiadványai 63, OMSZ, Budapest. (in Hungarian)

Bowler, N.E., Pierce, C.E., and *Seed, A.W.*, 2006: STEPS: A probabilistic Precipitation forecasting scheme which merges an extrapolated nowcast with downscaled NWP, *Q. J. Roy. Meteorol. Soc. 132*, 2127–2155.

Browning, K.A., (Ed.), 1982: Nowcasting. Academic Press.

Chen, F. and *Dudhia, J.*, 2001: Coupling an advanced land-surface/ hydrology model with the Penn State/ NCAR MM5 modeling system. Part I: Model description and implementation. *Mon. Weather Rev. 129*, 569–585.

Conway, B., and *Labrousse, J.*, 1997: Improvement of nowcasting techniques. Offices of Official Publication of the European Communities ISBN 9282787435.

Derrien, M. and *Le Gléau, H.*, 2005: MSG/SEVIRI cloud mask and type from SAFNWC. *Int. J. Remote Sens. 26*, 4707–4732.

Derrien, M. and *Le Gléau, H.*, 2013: Algorithm Theoretical Basis Document for "Cloud Products" (CMa-PGE01 v3.2, CT-PGE02 v2.2 & CTTH-PGE03 v2.2), SAFNWC documentation, available on-line: http://www.nwcsaf.org

Dixon, M., and *Wiener, G.*, 1993: TITAN: Thunderstorm Identification, Tracking, Analysis and Nowcasting – A Radar-based Methodology. *J. Atmos. Ocean. Tech. 10*, 785–797.

Dudhia, J., 1993: A non-hydrostatic version of the Penn State NCAR Mesoscale Model: validation tests and simulation of an atlantic cyclone and cold front. *Mon. Weather Rev. 121*, 1493–1513.

Ebert, E.E., Wilson, L.J., Brown, B.G., Nurmi, P., Brooks, H.E., Bally, J., and *Jaeneke, M.*, 2004: Verification of Nowcasts from the WWRP Sydney 2000 Forecast Demonstration Project. *Wea. Forecast. 19*, 73–96.

Foresti, L., Reyniers, M., and *Delobbe, L.*, 2014: Probabilistic Precipitation Nowcasting with the Short-Term Ensemble Prediction System in Belgium. Presented at the European Nowcasting Conference, Vienna, 29–30 April 2014.

Geresdi, I. and *Horváth, A.*, 2000: Nowcasting of precipitation type. Part I : Winter precipitation. *Időjárás 104*, 241–252.

Geresdi, I., Horváth, A., and *Mátyus, Á.*, 2004: Nowcasting of the precipitation type. Part II: Forecast of thunderstorms and hailstone size. *Időjárás 108*, 33–49.

Germann, U., and *Zawadzki, I.*, 2002: Scale-dependence of the predictability of precipitation from continental radar images. Part I: Description of the methodology. *Mon. Weather Rev. 130*, 2859-2873.

Golding, B.W., 1998: Nimrod: A system for generating automated very short range forecasts. *Meterorol. Appl. 5*, 1–16.

Götz, G. and *Bodolainé, J.E.*, 1963a: A mezoszinoptikus képződményekről. *Időjárás 67*, 46–53. (in Hungarian)

Götz, G. and *Bodolainé, J.E.*, 1963b: Structures and analyses of instability lines. OMI Kisebb Kiadványai 33, OMSZ, Budapest, (in Hungarian).

Haiden, T., Kann, A., Wittmann, C., Pistotnik, G., Bica, B., and *Gruber, C.*, 2011: The Integrated Nowcasting through Comprehensive Analysis (INCA) System and Its Validation over the Eastern Alpine Region. *Weather Forecast. 26*, 166–183.

Horváth, Á. and *Geresdi, I.*, 2003: Severe Storms and Nowcasting in the Carpathian Basin. *Atmos. Res. 67–68*, 319–332.

Horváth, Á., 2005: Nowcasting System of the Hungarian Meteorological Service. Proceedings. Abstracts, WWRP International Symposium on Nowcasting and Very Short range Forecasting. Toulouse, France, 5–9 September 2005

Horváth, Á., 2006: Numerical studies of severe convective phenomena using robust radar impact method. Proceedings of ERAD 2006. Barcelona, 19-22 September, 557-558.

Horváth, Á., Ács, F., and *Seres, T.*, 2008: Thunderstorm climatology analyses in Hungary using radar observations. *Időjárás 112*, 1–13.

Horváth, Á., Seres,T., and *Németh,P.*, 2012: Convective systems and periods with large precipitation in Hungary. *Időjárás 116,* 77–91.

Kunkel, A.B., 1984: Parameterization of Droplet Terminal Velocity and Extinction Coefficient in Fog Models. *J. Climate Appl. Meteor. 23*, 34–41.

Lee, H.C., Bellon, A., Zawadzki, I., and *Kilambi, A.*, 2009: McGill Algorithm for Precipitation Nowcasting by Lagrangian Extrapolation (MAPLE) applied to the South Korean to the South Korean radar network. Part 1: Sensitivity studies of the Variational Echo Tracking (VET) technique, Proceedings of the 34th Radar Conference, American Meteorological Society, 5–9 October 2009, Williamsburg, VA.

Li, L., Schmid, W., and *Joss, J.* 1995: Nowcasting of motion and growth of precipitation with radar over a complex orography. *J. Appl. Meteorol. 34*, 1286–1300.

Marshall, J.S. and *Palmer, W.M.*, 1948: The distribution of raindrops with size. *J. Meteorol. 5*, 165–166.

Mecklenburg, S., Joss, J., and *Schmid, W.*, 2000: Improving the nowcasting of precipitation in an Alpine region with an enhanced radar echo tracking algorithm, *J. Hydrol. 239*, 46–68.

Mueller, C., Saxen, T., Roberts, R., Wilson, J., Betancourt, T., Dettling, S., Oien, N., and *Yee, J.*, 2003: The NCAR Auto-Nowcast System. *Weather Forecast. 18, 545–561.*

Pierce, C.E., Hardaker, P.J., Collier, C.G., and *Haggett, C.M.*, 2000: GANDOLF: a system for generating automated nowcasts of convective precipitation. *Met. Apps.* 7, 341–360.

Putsay, M., Szenyán, I., and *Simon, A.,* 2009: Case study of Mesoscale Convective Systems over Hungary on 29 June 2006 with satellite, radar and lightning data. *Atmos. Res.* 93, 82–92.

Putsay, M.,Kocsis,Zs., and *Szenyán,I.*, 2010: Use of Satellite information in Hungarian Nowcasting System. EUMETSAT Meteorological Satellite Conference, 20–24 September 2010, Córdoba, Spain

Skamarock, W.C., Klemp, J.B., Dudhia, J., Gill, D.O., Baker, D.M., Wang, W., and *Powers, J.G.*, 2005: A description of the advanced research WRF version 2. NCAR Tech Note NCAR, TN-4681STR.

Stauffer, D.R. and *Seaman, N.L.*, 1990: Use of Four-Dimensional Data Assimilation in a Limited-Area Mesoscale Model. *Mon. Weather Rev. 118*, 1250–1277.

Sun, J., Xue, M., Wilson, J.W., Zawadzki, I., Ballard, S.P., Onvlee-Hooimeyer, J., Joe, P., Barker, D., Li, P-W., Golding, B., Xu, M., and *Pinto, J.*, 2014: Use of NWP for Nowcasting Convective Precipitation: Recent Progress and Challenges, *Bull. Amer. Meteor. Soc. 95*, 409–426.

Turner, B. J., Zawadzki, I., and *Germann, U.* 2004: Predictability of precipitation from continental radar images. Part III: Operational nowcasting implementation (MAPLE), *J. Appl. Meteorol. 43*, 231–248

Wilson, J.W., Feng, Y., Chen, M., and *Roberts, R.D.*, 2010: Nowcasting challenges during the Beijing Olympics: successes, failures, and implications for future nowcasting systems. *Weather. Forecast. 25,* 1691–1714.

IDŐJÁRÁS

Quarterly Journal of the Hungarian Meteorological Service
Vol. 119, No. 2, April – June, 2015, pp. 215–239

Overview of mesoscale data assimilation developments at the Hungarian Meteorological Service

Máté Mile[1*], **Gergely Bölöni**[1], **Roger Randriamampianina**[2], **Roland Steib**[1], and **Ersin Kucukkaraca**[3]

[1]*Hungarian Meteorological Service*
P.O. Box 38, H-1525 Budapest, Hungary

[2]*Norwegian Meteorological Institute*
P.O. Box 43, Blindern, N-0313 Oslo, Norway

[3]*Turkish State Meteorological Service*
P.O. Box 401, Ankara, Turkey

[*]*Corresponding authors E-mail: mile.m@met.hu*

(Manuscript received in final form June 03, 2014)

Abstract—The operational AROME (Applications of Research for Operations at MEsoscales) mesoscale numerical weather prediction (NWP) model has been run using interpolated analyses of the ALADIN (Aire Limitée Adaptation Dynamique Développement International) NWP model for its initialization since the end of 2010 at the Hungarian Meteorological Service (HMS). In order to improve the initial conditions, a local three-dimensional variational (3DVAR) data assimilation system was developed for the Hungarian version of AROME (AROME-Hungary). Regarding the data assimilation cycling strategy, it was shown that 3 hourly rapid update cycling (RUC), which was implemented operationally in March 2013 using conventional observations, outperforms 6 hourly cycling method. This paper describes at length the main characteristics of this local data assimilation system and its impact on the model short-range forecasts. Although the forecasts of AROME-Hungary based on a local data assimilation were already improved compared to the previous implementation (initialization via interpolated analyses of the ALADIN model), there is still a way to go to exploit the full benefit of the local 3DVAR assimilation cycle. Current development works aim at improving the system through exploitation of remote sensing observations (radar, GPS, satellite AMVs), with a special emphasis on humidity information. All tested observations showed promising performance on both the analyses and forecasts of the AROME-Hungary model, which should lead to their respective operational implementation in the near future.

Key-words: operational numerical weather prediction, mesoscale data assimilation, rapid update cycle, remote sensing observations

1. *Introduction*

State of the art mesoscale numerical weather prediction (NWP) models, such as ALADIN (*Horányi et al.,* 1996) and AROME (*Seity et al.,* 2010), describe the time evolution of small scale processes in the atmosphere (e.g., convection, sea breeze, fog), through the applied prognostic microphysical parametrization schemes and the non-hydrostatic dynamics. Advanced model dynamics and physics are, however, in vain, if the initial state does not contain appropriate information regarding the small-scale weather systems we aim to describe. The simplistic approach for the initialization of limited area models (LAMs) is to interpolate the analysis or the forecast of the driving model (i.e., a global model or another LAM) to the mesoscale grid. This approach, often referred to as spin-up initialization, is computationally cheap (i.e., there is no need to run expensive data assimilation schemes), nevertheless it implies several drawbacks, which will be demonstrated in this section. The sophisticated and scientifically sound alternative of the spin-up initialization is to run a local data assimilation system in the LAM, combining the high-resolution first guess of the mesoscale model with the available high-density observations.

Data assimilation is achieved by solving the BLUE (Best Linear Unbiased Estimation) analysis equation, which shows that the two main information used for estimating the initial state (x_a) are the background (x_b) and the actual observation set (y) (see e.g., *Kalnay*, 2003; *Lorenc*, 1986; *Evensen,* 2009):

$$x_a = x_b + K\left(y - H\left(x_b\right)\right) \tag{1}$$

In Eq.(1), K stands for the Kalman gain determining the weight of the background and the observations in each gridpoint in an optimal way, i.e., based on their reliability in a statistical sense. H denotes the observation operator, which enables the comparison of the observations with the background through a projection from the model space to the observation space.

In practice local data assimilation is substantially more expensive to implement than spin-up initialization (both computationally and regarding manpower), but in turn, it enables a more accurate representation of small-scale phenomena in the initial state. In order to demonstrate this, the kinetic energy spectra for a spin-up analysis (ALADIN analysis interpolated to the AROME-Hungary grid) and the local 3DVAR analysis of AROME-Hungary are plotted in *Fig. 1*. It can be seen that the energy spectra for the AROME analysis follows rather close the theoretical slope of energy cascade, i.e., k^{-3} for small k wavenumbers (large scales) and $k^{-5/3}$ for high k wavenumbers (small scales). In contrast, the energy spectra of the spin-up analysis is far from the theoretical slopes, especially at mesoscales (above wavenumber 50, which corresponds to spatial scales smaller than 25 km), where the energy curve is rather noisy. The mesoscale noise in the spin-up analysis is introduced by the interpolation, and it

reflects that the ALADIN analysis with its 8 km grid-length (30–45 km effective resolution) do not hold physical information on the mesoscales resolved by the AROME model with its 2.5 km grid-length. Among others, this diagnostic comparison gave a great motivation for implementing a local 3DVAR data assimilation system for the AROME-Hungary, which finally became operational in March 2013 due to approved ability to improve the forecast performance compared to the spin-up initialization approach. Similar positive impact of mesoscale data assimilation implementations have been reported by *Benjamin et al.,* (2004), *Fischer et al.,* (2005), *Bölöni* (2006), *Randriamampianina* (2006a), *Brousseau et al.* (2011).

The structure of the article is as follows: In the next section, the operational DA system will be described, with special emphasis on rapid update cycling, and also, the added value and the impact of the AROME-Hungary data assimilation system will be detailed. In Section 3, we briefly review experimental data assimilation studies with non-conventional observations added to the existing operational system. Finally, the last section gives a summary of the presented work and provides corresponding conclusions.

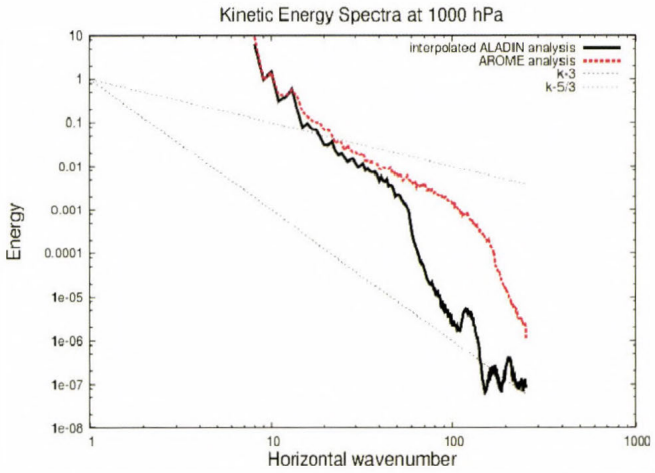

Fig. 1. Wind energy spectra (kg m^2 s^{-2}) at 1000 hPa for the AROME (dx = 2.5 km) analysis (red) and for an interpolated ALADIN (dx = 8 km) analysis (black). Dotted straight lines correspond to the theoretical slopes of kinetic energy at large- (k^{-3}) and mesoscales ($k^{-5/3}$) if using a log-log scale.

2. *Operational data assimilation system of the AROME mesoscale model*

2.1. The assimilation system

The local data assimilation system of AROME-Hungary is based on a 3 hourly rapid update cycle (RUC). The organization of one particular assimilation step at 00 UTC is shown schematically in *Fig. 2*, where the lateral boundary conditions in the assimilation cycle are provided by the global ECMWF/IFS (European Centre for Medium-Range Weather Forecasts / Integrated Forecast System) model, and surface parameters are initialized either using the surface analysis of the operational ALADIN model where available (at synoptic times, i.e., 00, 06, 12, and 18 UTC) or using the previous AROME/SURFEX (SURFace Externalized) forecast (at sub-synoptic times i.e., 03, 09, 15, and 21 UTC).

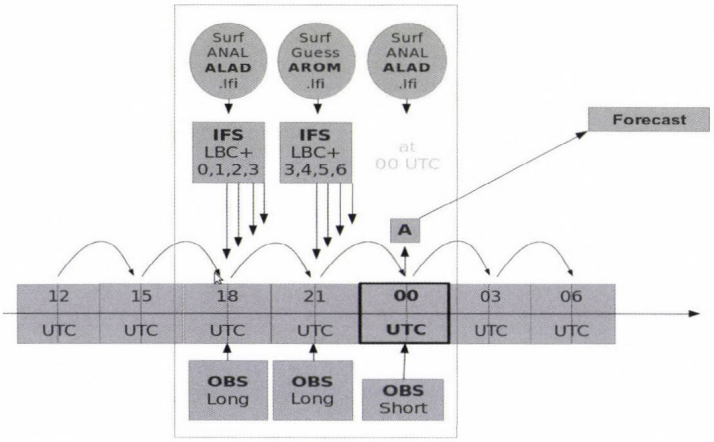

Fig. 2. Schematic figure of the data assimilation cycle applied for AROME showing the elements of a 00 UTC assimilation run.

The core of AROME-Hungary data assimilation system is an incremental 3DVAR method, where the basic mathematical formulation and its corresponding implementation is very similar to the one used in the IFS, ARPEGE, and ALADIN models (*Courtier et al.*, 1998; *Fischer et al.*, 2005; *Vasiliu* and *Horányi*, 2005; *Bölöni* 2006). An important component of the 3DVAR is the representation of background error statistics which plays a key role in filtering the information coming from observations and spreading it out to the model grid (see e.g., *Berre* 2000; *Brousseau et al.*, 2011). In the current operational system, the background error covariance matrix was sampled from

the downscaling of an ALADIN Ensemble Data Assimilation (EDA) experiment, run for a summer period using 3-hour forecast ranges and 5 EDA members to get sufficient statistical sample (*Bölöni et al.,* 2014). Input observations for the AROME-Hungary 3DVAR suite are provided by the OPLACE (Observation Preprocessing for LACE (Limited Area modeling for Central Europe)) system, which includes both conventional and non-conventional observations. Although the currently operational AROME-Hungary data assimilation system uses only conventional observations, the system is able to assimilate non-conventional observations, as described in Section 3.

Delivering the mesoscale NWP forecasts as early as possible is of high priority for every operational forecasting centre. In order to find the optimal observation cut-off time (waiting time after the nominal analysis time) of the operational AROME-Hungary data assimilation system, the timeliness of the incoming observations was diagnosed for the area of interest. In *Fig. 3*, the availability of conventional observations at 00 UTC is shown, based on the amount of data received by the OPLACE system. After gaining this result, the observation (short) cut-off time has been set to one hour, which brings the fastest possible production of AROME forecast with an almost complete input observation set. This rather early cut-off enables a faster AROME forecast production compared to the former operational version of AROME-Hungary, which was based on a spin-up initialization from the 3DVAR analysis of the ALADIN model, because the ALADIN data assimilation system uses longer cut-off.

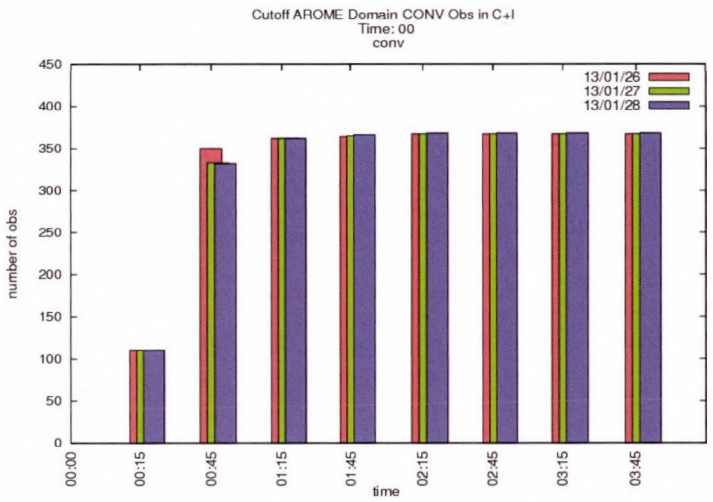

Fig. 3. Estimation of the optimal short cut-off time (considering AROME integration domain at 00 UTC) on January 26 (red columns), 27 (green columns) and 28 (blue columns) 2013.

2.2. *The Rapid Update Cycle*

In mesoscale NWP models, the accuracy of initial conditions is getting more and more crucial with an increasing resolution, hence small scale processes of the atmosphere have less and less predictability (*Fabry* and *Sun*, 2009). The rapid update cycling approach with increased analysis frequency in the assimilation cycle aims to involve more observations with reduced representativity error in time. It is assumed that the more observations we consider for the update of the model state, the better initial conditions we will get when starting a forecast from an analysis of the assimilation cycle. Considering conventional observations for instance, the different amount of used observations between a 6 hourly data assimilation cycle and a 3 hourly RUC is plotted in *Fig. 4* for a short period. At sub-synoptic times, mainly aircraft and SYNOP reports provide almost a double amount of data per day, due to the 4 extra analyses. To further emphasize the benefits of a RUC, it should be mentioned that many remote sensing observations are available with high temporal frequency, which are potentially beneficial in a data assimilation system with high frequency cycling. Also, many of the remote sensing observations are available in a very timely manner, almost immediately after analysis time, which allows to keep the operational observation cut-off time rather short, and thus to provide the forecasts with an early delivery.

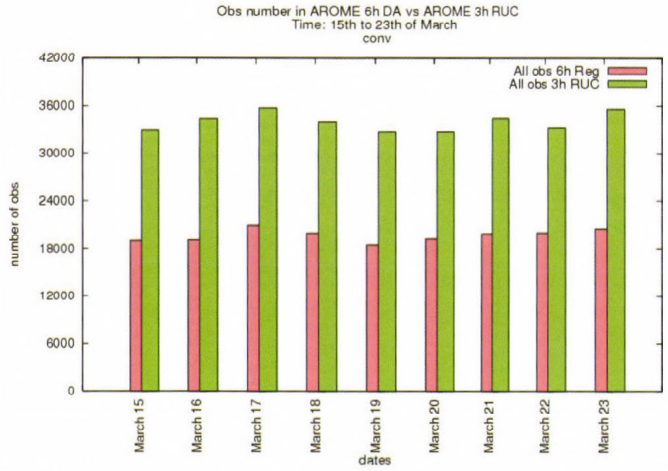

Fig. 4. The number of conventional observations used in a day in the RUC implementation (green) and in a 6 hourly cycling (red). The amount of data was counted in the period of March 15-23, 2014.

Beside these attractive features of the RUC system, there are some issues which have to be treated carefully in case of using a frequent assimilation cycle,

and thus, shorter background forecast lengths. The forecast model integration may imply spin-up effects (noise due to spurious gravity waves or imbalances between dynamics, atmospheric and soil physics) at the very short ranges, which can be accumulated in the assimilation cycle through the background forecasts, and thus, lead to degradation in the analyses and the forecasts. A usual practice in NWP, and in the Hungarian version of the ALADIN model as well, is the use of initialization techniques e.g., digital filter initialization (DFI) (*Daley*, 1991; *Lynch et al*, 1997), which is a low-pass spectral filter removing high-frequency components of the initial conditions. In case of AROME-Hungary, no DFI is applied because such filtering is assumed to be too strong in case of a mesoscale non-hydrostatic model, where gravity waves are described by the dynamics. To diagnose spin-up effects in AROME-Hungary, surface pressure tendencies have been examined for very short-range forecasts (+2 hours) for an arbitrarily chosen case. In *Fig. 5*, time evolution of the surface pressure tendency provided by three different forecasts is shown for a particular gridpoint over orography. The red curve corresponds to a forecast, which was started from an AROME 3DVAR analysis, using a time-consistent coupling scheme, i.e., when the lateral boundary condition (LBC) at initial time is the interpolated global IFS forecast. The blue curve stands for a similar run with the only difference of using a space-consistent coupling scheme, i.e., when the lateral boundary condition (LBC) at initial time is the AROME 3DVAR analysis itself. As an additional reference, the tendency from an AROME forecast using a spin-up initialization is added (green curve), i.e., where both the initial condition and the LBC at initial time is the interpolated global IFS forecasts. As the high amplitude oscillation in the time evolution of surface pressure tendency is an indicator of noise, it has been concluded based on *Fig. 5*, that AROME forecasts using a RUC assimilation with a space-consistent coupling scheme imply less noise than a RUC with a time-consistent coupling approach or the spin-up initialization. Supposedly, the higher amplitude oscillation in case of the spin-up initialization is caused by the interpolation noise which is more emphasized over orography. It should be also mentioned that plotting the evolution of surface pressure tendency on a horizontal map (not shown) supports the choice for the space-consistent coupling scheme. Namely, in the time-consistent case, noise patterns (indicated by large tendencies) penetrate from the domain borders towards the middle of the domain in a rectangular shape. In *Fig. 5*, this is captured by the red curve at integration steps 40–45 as an outstanding wave. An explanation for this structured noise might be that imbalances between the local 3DVAR analysis and the LBC at initial time arise, due to the inconsistent model states of the AROME and IFS models near the boundaries. The final decision on implementing a 3 hourly RUC instead of a traditional 6 hourly cycling was based on a comparison study over a 1 month period during summer 2012, where the skill of these two cycling options was measured. Verification results – which will be studied in the next section – reflected a better performance of the 3 hourly RUC, leading to its operational implementation.

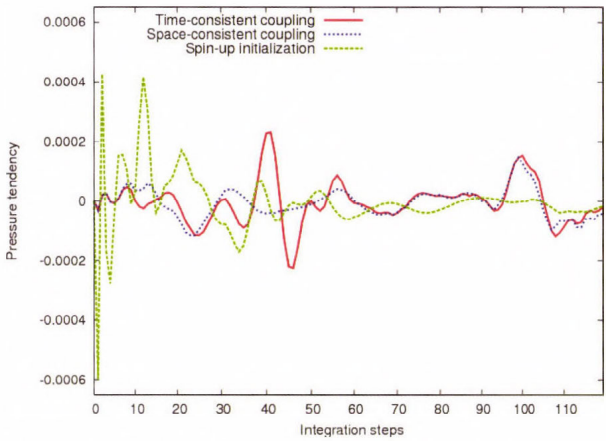

Fig. 5. Temporal evolution of surface pressure tendency (Pa/min) over orography during the first 2 hours of a forecast concerning spin-up initialization (green dashed line), time-consistent coupling approach (red line), and space-consistent coupling approach (blue dashed line).

2.3. The impact of local data assimilation scheme on the analysis and forecast

For measuring the impact of the local data assimilation scheme, three experiments with AROME-Hungary have been run and compared for several periods based on objective verification scores primarily. The three experiments are an AROME suite based on spin-up initialization (called DYNA), and two AROME suites based on local 3DVAR data assimilation, one of them using a 6 hourly cycling (called CONV6H) and another one using a 3 hourly rapid update cycling (called CONV). Forecasts have been run up to +36 hours starting at 00 UTC network times. Concerning the verification, both point-based and object-based scores have been computed. In the point-based verification, surface and radiosonde observations have been used as reference. The applied object-based method calculates average precipitation of forecasted weather objects (or alternatively the full domain average), and compares with calibrated radar precipitation measurements as reference. In *Figs. 6a* and *6b*, 10 m wind and mean sea level pressure scores are shown for the period between June 25 and July 25, 2012. It is rather clear from these figures that both the 6 hourly and the 3 hourly RUC 3DVAR provide an added value compared to the spin-up initialization with respect to both RMSE and BIAS. Moreover, the 3 hourly RUC provides slightly better scores than the 6 hourly cycling during daytime, while during the night, scores show a rather low sensitivity to the cycling frequency. To demonstrate the impact on precipitation, object-based verification score (domain average precipitation) is shown in *Fig. 7*. It can be seen, that in comparison with the spin-up initialization, both the 6 hourly 3DVAR cycling

and the 3 hourly RUC could reduce the overestimation of the precipitation maximum linked to convective activity in the afternoon. It is also clear from *Fig. 7*, that the 3 hourly RUC provides slightly better precipitation forecasts than the 6 hourly cycling, by reducing the overestimation further.

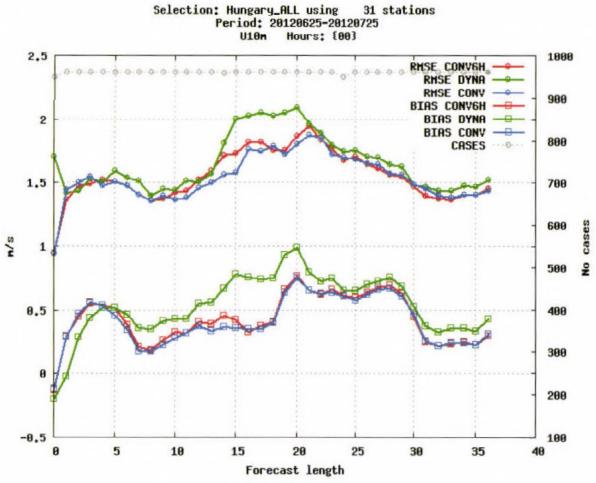

Fig. 6a. RMSE and BIAS scores corresponding to the spin-up initialization scheme (green), 3 hourly RUC (blue), and 6 hourly cycling (red) for 10 m wind speed (m/s).

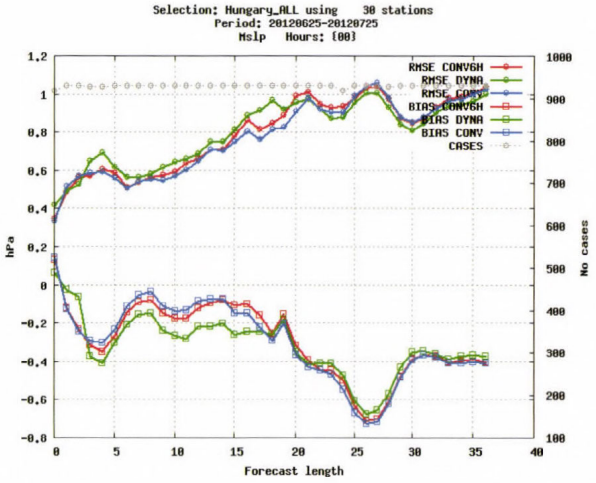

Fig. 6b. RMSE and BIAS scores corresponding to the spin-up initialization scheme (green), 3 hourly RUC (blue), and 6 hourly cycling (red) for mean sea level pressure (hPa).

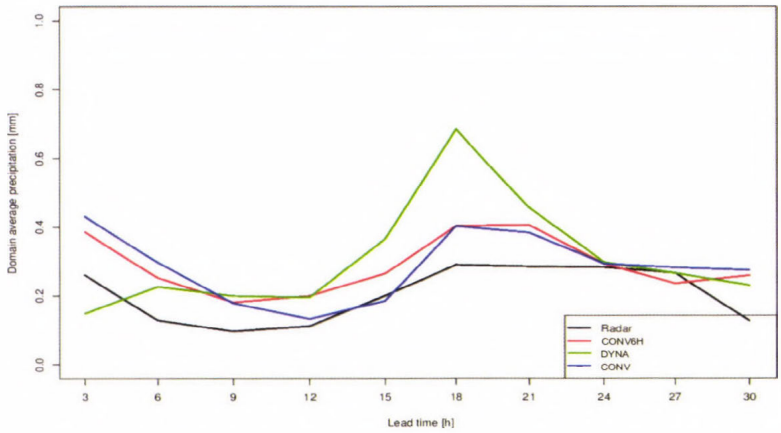

Fig. 7. Comparison of 3h RUC (blue), 6 hourly cycling (red) and the spin-up initialization scheme (green) regarding domain average precipitation (mm/h). The reference is the calibrated radar measurement (black).

Based on the success of the RUC approach (*Figs. 6a, 6b,* and *7*), a parallel suite with a 3 hourly RUC data assimilation system was compared with the former operational AROME-Hungary system (based on spin-up initialization) over the period from February 20 to March 12, 2013. This parallel suite was set up in a fully operational environment, providing real time outputs for the forecasters of the Hungarian Meteorological Service (this time both for 00 and 12 UTC base times), with the main aim to make a final decision about the operational implementation of the RUC system, in case of preferable scores and positive feedbacks from the forecasters. Based on the verification results, the RUC system clearly outperformed the forecasts of the former operational AROME-Hungary suite with spin-up initialization, which is demonstrated in *Figs. 8a, 8b* for 2 m temperature and in *Fig. 9* for precipitation. Feedbacks of the forecasters also confirmed the slight but consistent improvements implied by the RUC system, and this led to its operational implementation on March 17, 2013.

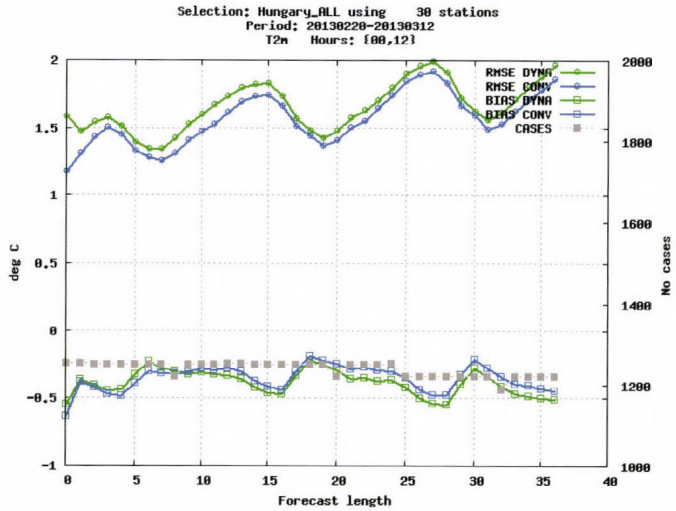

Fig. 8a. RMSE and BIAS scores of AROME forecasts according to the spin-up initialization (DYNA – green), and the 3 hourly rapid update cycle (CONV – blue) for 2 m temperature (°C).

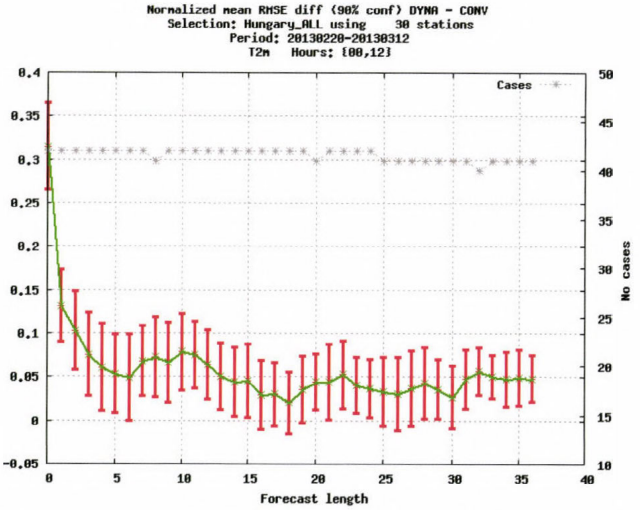

Fig. 8b. Normalized RMSE differences according to the spin-up initialization (DYNA – green), and the 3 hourly rapid update cycle (CONV – blue) for 2 m temperature (°C).

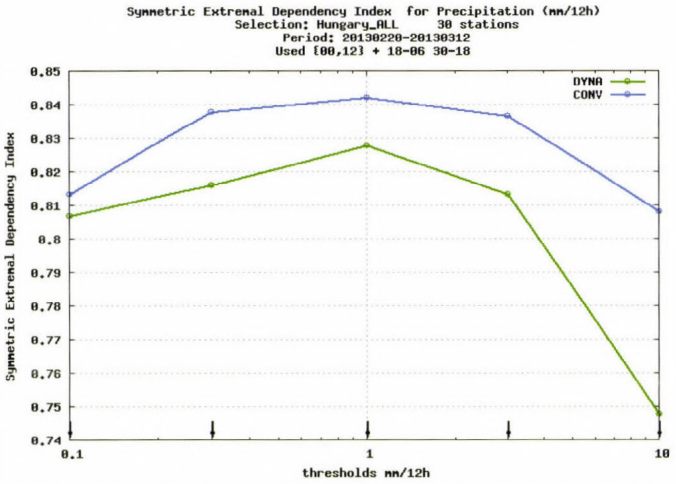

Fig. 9. Symmetric Extremal Dependency Index (SEDI) for precipitation according to the spin-up initialization (DYNA – green), and the 3 hourly rapid update cycle (CONV – blue) for precipitation (mm/12h).

2.4. Diagnosing analysis sensitivity to observations

An obvious way for the further development of the operational RUC is to bring non-conventional observations to its analysis system. In order to figure out, which observations would contribute the most to the analysis, the DFS (Degrees of Freedom for Signal) diagnostic tool (*Chapnik et al.,* 2006; *Cardinali et al.*, 2004) has been adapted and applied at the Hungarian Meteorological Service. The DFS tool diagnoses the observation influence on the analysis, thus, if applied for the available observation types, it provides an indication on their relative contribution. The DFS diagnostic is computed as the trace of the Kalman gain matrix projected to observation space:

$$DFS = Tr(HK) \tag{2}$$

where K and H denote respectively the Kalman gain matrix and the observation operator introduced in Eq. (1). In practice, this trace cannot be computed, because the gain matrix K is not known explicitly. *Girard* (1987) suggested a solution which enables to evaluate the above mentioned trace with the following approximation:

$$Tr(HK) \approx \left(y^{'} - y\right)^{T} R^{-1}\left(H\left(x_{a}^{'}\right) - H\left(x_{a}\right)\right) \tag{3}$$

where $H(x_a)$ gives the analysis state at observation locations using a background and the observations (y), and $H(x'_a)$ stands similarly for the analysis at observation space but using the perturbed observations (y') (and the same background). In Eq. (3), R stands for the observation error covariance matrix.

Therefore, DFS can be calculated through a random perturbation of the observations, and the method is flexible in a sense that DFS values can be computed for any subset of the available observational data. For a given date, the DFS was computed with conventional and some experimentally used non-conventional observations. In order to verify the influence of the available observations, both the absolute and the relative DFS diagnostics were computed (*Fig. 10*). Absolute DFS stands for what have been explained above in Eqs. (2) and (3), while relative DFS is the absolute DFS normalized by the number of observations within the given observation subset. The first conclusion based on the absolute DFS is that the largest contribution to the analysis is provided by wind observations, i.e., the largest amount of information is extracted from these observations in the current data assimilation system. On the other hand, relative DFS reflects the importance of humidity (from surface SYNOP stations and TEMP radiosondes), RADAR reflectivity (RADAR-Z), and GNSS (global navigation satellite system) ZTD (zenith total delay) observations. In conclusion, DFS diagnostics show that radar reflectivity and GNSS ZTD observations are promising candidates for assimilation in the future version of the RUC system. It should be mentioned that DFS provides a theoretical measure of the information content projected from the observations to the analysis and it does not provide any indications on the impact attributed to the forecasts. Another point to be added here is that no radiance observations have been considered and diagnosed in the recent RUC system.

3. *Use of non-conventional observations in the AROME 3DVAR system*

In the following section, we present the latest developments of the RUC system since its operational implementation. The need of using more observations, especially non-conventional ones, was already mentioned. Specifically, the observations measuring humidity are potentially good candidates based on the results of the DFS analysis sensitivity study shown in the previous section. At the same time, to gain advantage of the RUC system, early accessible observations with high frequency and high density are also required. Taken into account these objectives, the atmospheric motion vectors (AMV) from Meteosat Second Generation (MSG) geostationary satellite, RADAR measurements as reflectivity and radial wind, and GNSS ZTD observations have been investigated in the operational data assimilation system of AROME-Hungary.

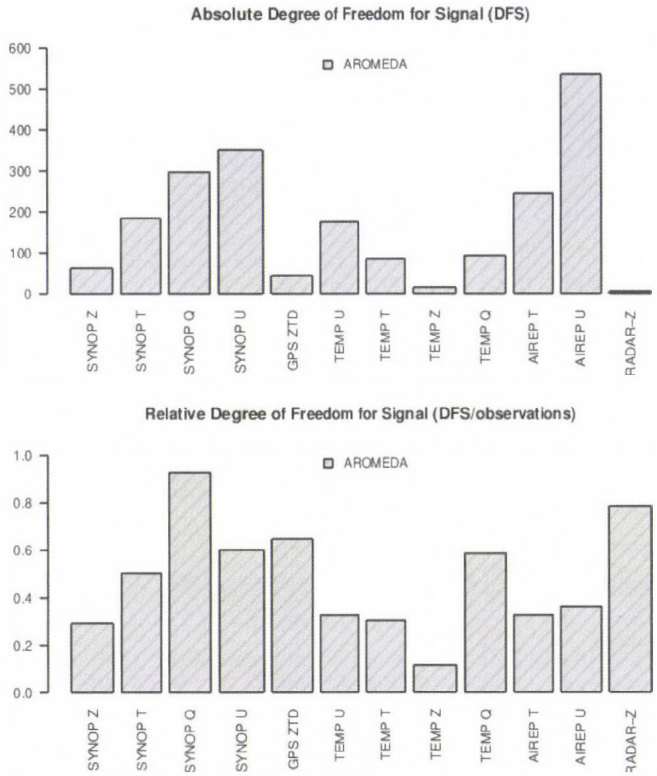

Fig. 10. Absolute and relative degrees of freedom for signal (DFS) for experimental data assimilation of AROME-Hungary at 12 UTC, January 3, 2014.

3.1. The impact of the Atmospheric Motion Vectors

EUMETSAT (European Organization for the Utilization of Meteorological Satellites) MSG provides sets of satellite winds (AMVs) extracted from sequences of well-navigated and calibrated images produced by the SEVIRI (Spinning Enhanced Visible and Infrared Imager) instrument. Accordingly, AMVs are derived from SEVIRI infrared, water vapor, and visible channels. At the HMS MSG AMV date is received through the EUMETCast broadcasting service of EUMETSAT with hourly frequency and processed in OPLACE for data assimilation purposes.

MSG AMV data is proved to be beneficial in nowcasting applications and in data assimilation systems (*Randriamampianina*, 2006b). Furthermore, numerous examples exist (*Forsythe et al.*, 2014), where AMVs are operationally assimilated in a similar way like the adopted technique used in the ALADIN

model in Hungary. As MSG AMV observations possess many advantages needed for a RUC data assimilation, a summertime impact study has been run with AROME-Hungary, where MSG AMV observations were added to the conventional observations. The implementation of the AMV data in AROME-Hungary was done according to *Randriamampianina* (2006b). To assess the impact of AMVs two experiments were conducted during the period of June 25 – July 25 in 2012. The AROME-Hungary forecasts initialized at 00 and 12 UTC were verified against SYNOP and radiosonde observations. Regarding the impact of MSG AMV observations, in *Figs. 11a* and *11c* RMSE and BIAS scores are plotted with the corresponding (*Figs. 11b* and *11d*) normalized RMSE differences for 10 m wind speed and 2 m dew point temperature forecasts. In these figures, CONV stands for the operational AROME-Hungary and GEOW denotes the experimental run, where MSG AMV was assimilated as well. In case of 10 m wind speed forecasts, the AMV experiment provides better skill for the shorter range forecasts up to 15 hours. Concerning the 2 m dew point temperature verification scores, the overall decrease of the error is perceptible and it is even statistically significant for some longer ranges. To conclude, AMV data in AROME-Hungary provides small contribution with respect to the amount of assimilated data, but with positive signal on the short-range forecasts.

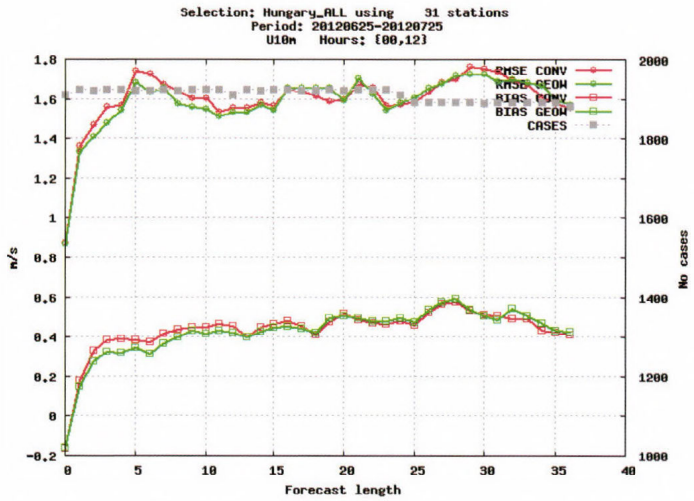

Fig. 11a. Experimental assimilation study of AROME-Hungary for the period between June 25 and July 25, 2013. RMSE and BIAS scores of AROME forecasts corresponding operational AROME with conventional observations (CONV – red) and AROME with conventional plus AMV observations (GEOW – green) are plotted for 10 m wind speed (m/s).

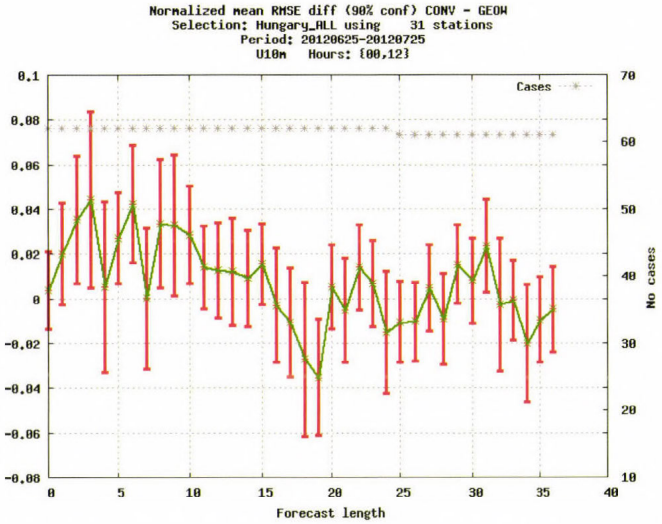

Fig. 11b. Experimental assimilation study of AROME-Hungary for the period between June 25 and July 25, 2013. Normalized RMSE differences between operational AROME with conventional observations (CONV – red) and AROME with conventional plus AMV observations (GEOW – green) are plotted for 10 m wind speed (m/s).

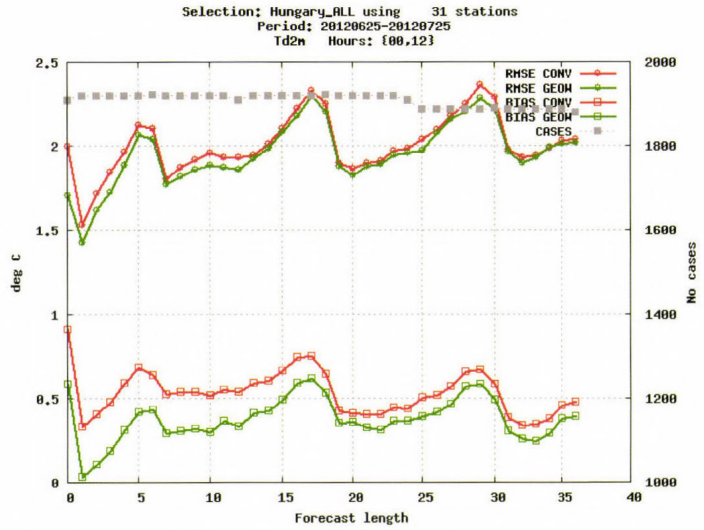

Fig. 11c. Experimental assimilation study of AROME-Hungary for the period between June 25 and July 25, 2013. RMSE and BIAS scores of AROME forecasts corresponding operational AROME with conventional observations (CONV – red) and AROME with conventional plus AMV observations (GEOW – green) are plotted for 2 m dew point temperature (°C).

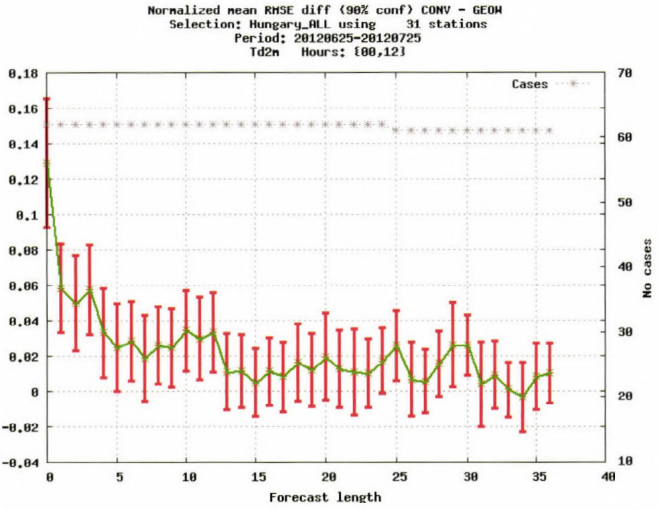

Fig. 11d. Experimental assimilation study of AROME-Hungary for the period between June 25 and July 25, 2013. Normalized RMSE differences between operational AROME with conventional observations (CONV – red) and AROME with conventional plus AMV observations (GEOW – green) are plotted for 2 m dew point temperature (^{0}C).

3.2. The impact of the radar reflectivity and radial wind observations

Radar measurements play an important role in nowcasting, and nowadays they also contribute to the initial conditions of mesoscale NWP models. The weather RADAR instrument receives emitted electromagnetic signal to measure the reflectivity of the atmosphere's elements along the emitted ray's path. From the backscattered radiation one can estimate the reflectivity, i.e., the precipitation intensity, and from the phase shift of the backscattered signals the radial wind can be measured using Doppler's law.

Focusing on data assimilation, the utility of radar observations has been already demonstrated by different studies (see, e.g., *Lindskog et al,* 2004; *Snyder* and *Zhang,* 2003; *Montmerle* and *Faccani,* 2008). However, assimilating the observed quantities of the radar is not straightforward since the relationship between the measured quantities and the control variables of the data assimilation scheme is complex and non-linear. This relation in case of radial wind observation is less complex than that with reflectivity, where the radar equation gives the direct relationship between the observed hydrometeors and the 3DVAR control variables. Instead of extending the control variables to account also for hydrometeors, an alternative solution was worked out by *Caumont et al.* (2010) and *Wattrelot et al.* (2014) using 1D+3DVAR method, which enables to retrieve columns of relative humidity and temperature from reflectivity profiles as pseudo-observations. This approach is based on a 1D Bayesian estimate, which uses the assumption that a

well-chosen linear combination of model simulated reflectivities in the neighborhood of the observation provides comparable quantities to what is observed (see *Wattrelot et al.* (2014) for more details).

In the observing system of the Hungarian Meteorological Service dual-polarized Doppler radars are used which provide reflectivity and radial wind observations with 240 km and 120 km range, respectively. Raw radar data requires specific pre-processing in consideration of data assimilation which consists of the elimination of non-meteorological and noisy signals. Due to this quality control, for instance, reflectivity data under 7 dBz is filtered to avoid clear-sky echo and also unwanted RLAN (Radio Location Area Network) signals are rejected. After a thorough pre-processing with quality control, RADAR data is presented in Cartesian coordinates and in BUFR, which is one of the accepted format of the current 3DVAR system.

An observing system experiment with AROME-Hungary was made for an early, but convective summer period of May 15 – June 18, 2012. Point- and object-based verifications were computed to evaluate the performance of the operational AROME-Hungary and experimental runs including a combination of radar reflectivity and radial wind. In the first experiment with assimilation of both the radar Doppler wind and reflectivity, skill scores showed positive impact on forecasts of precipitation, but we observed also a cold and wet bias for surface parameters (not shown). A possible explanation of the observed bias might be that the assimilation of reflectivity data over-saturates the planetary boundary layers (PBL), which degrades the forecast of surface parameters through physical process along the model integration. To verify this assumption, another experiment was run avoiding the use of reflectivity observations below 1000 m from all 3 used radar stations. As a result, no degradation on surface parameters was observed, but on the other hand, the impact on precipitation forecasts was also reduced. The average intensity of the precipitation objects was verified against objects measured by the radar (*Fig. 12*). The four curves are respectively the operational AROME-Hungary (AromeCONV), the experimental AROME with complete set of radar data (AromeFULL), AROME runs with blacklisted reflectivity (AromeBLACK), and radar observations (RADAR). In *Fig. 12*, one can see that AromeBLACK provides the closest estimation to radar, however, the diurnal cycle of the maximum precipitation is still slightly shifted with delay in time. Additionally, a case study is shown in *Fig. 13*, where 3 hourly accumulated precipitation forecasts are plotted for all the three tested runs. One can see that the AromeFULL run predicts more realistic precipitation over north-eastern Hungary than AromeCONV, but it overestimates slightly in the mid-western part of the country. AromeBLACK is able to correct this overestimation, but the positive signal is also suppressed by filtering reflectivity. To conclude, the assimilation of radar data has major impact on forecasts of precipitation, but the quality control has to be further investigated and improved for better accounting of all potential measurements.

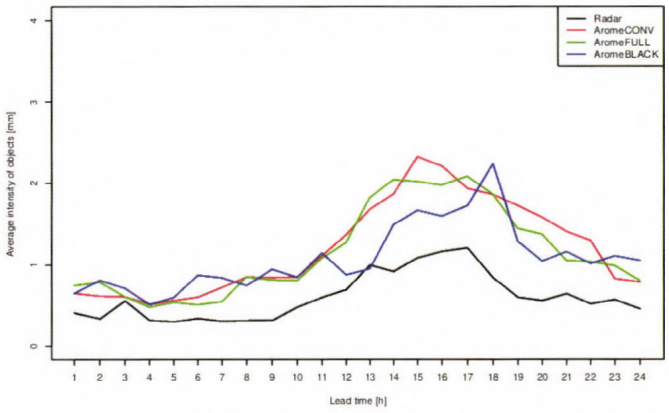

Fig. 12. Object-based verification of radar data assimilation experiments where average intensity of precipitation (mm/h) objects is verified against radar measurements for the period June 7 – June 18, 2012. AromeCONV: Operational AROME-Hungary (red line), AromeFULL: experimental AROME with RADAR reflectivity and radial wind observations added to conventional ones (green line), AromeBLACK: experimental AROME with same set of observations except reflectivity which was blacklisted below 1000 m elevation (blue line).

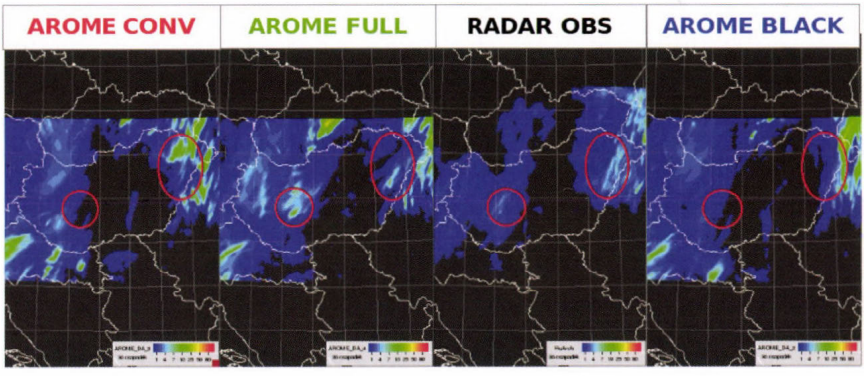

Fig. 13. A case study at 03 UTC, June 5, 2012 for 3 hourly accumulated precipitation forecast according to AROME model with operational configuration (AROME CONV), experimental AROME with radar reflectivity and radial wind (AROME FULL), experimental AROME with blacklisted low level reflectivity (AROME BLACK), and radar composite image (RADAR OBS).

3.3. The impact of the GNSS ZTD observations

Signal delay originating from different constituents of the troposphere and stratosphere can be extracted from satellite constellations of GNSS. The zenith tropospheric delay (ZTD), which is the converted-to-distance time delay,

provides valuable information on atmospheric water vapor content expressed in length units along the zenithal direction above the ground-based GPS receiver station. *Bevis et al.*, (1992) describes at length the principle of such measurement. The number of ground-based GPS stations over Europe has been increasing during the last years, and their use for meteorological purposes is coordinated by EUMETNET GNSS Water Vapour Programme (E-GVAP). E-GVAP also provides a data hub allowing the assimilation of GNSS ZTD observations with high spatial and temporal resolution. The Hungarian GNSS network (so called SGOB) operated by the Satellite Geodetic Observatory of Hungary was added to E-GVAP officially at the end of 2013, which provides access to a dense station network of ground-based GPS over the Carpathian Basin. This was a good motivation for us to assimilate the GNSS ZTD data.

The impact of GPS ZTD observations in data assimilation systems has been already investigated in the ARPEGE/ALADIN/AROME model family (see e.g., *Yan et al,* 2008; *Poli et al,* 2007; *Storto* and *Randriamampianina,* 2010). For the assimilation of E-GVAP ZTD data, a whitelist approach is used containing only stations with good-quality measurements. The whitelist is created according to the following criteria evaluated during a passive assimilation for a period of 15 days: i) the availablility of data is more than 40%, ii) observation minus background departures have Gaussian distribution, the absolute bias and also the standard deviation are both less than 40 mm, iii) the difference between station altitude and corresponding model orography height is less than 250 meter. We were able to choose 67 active stations inside our area of interest. The computed bias at each selected station is used as static bias correction in the assimilation scheme.

The impact of ground-based GNSS ZTD was investigated with AROME-Hungary over a winter period of 2014, namely January 5 to 27. The operational AROME-Hungary forecasts and the experimental AROME run with GNSS ZTD were compared with verification against SYNOP and radiosonde observations. In *Fig. 14a*, RMSE and BIAS scores are plotted for 2 m dew point temperature forecasts and the corresponding (*Fig. 14b*) normalized RMSE differences with significance test check. It can be seen that the experimental run (marked PGPS) has better skill scores on forecast of surface dew point temperature than the operational one (marked CONV), however, it is not statistically significant. In addition, one case study is presented in *Fig. 15*, showing the accumulated precipitation during the first 3 hours of the forecasts. In this case, the operational AROME-Hungary (CONV) provided a strong overestimation of precipitation as compared to the measured SYNOP observations plotted with numbers, probably due to spin-up effects. By assimilating ZTD observations (PGPS), the AROME forecast became more realistic with a reduction in the amount of predicted precipitation. This example showed, that the assimilation of GNSS ZTD observations is advantageous for improving short-range model forecasts, particularly regarding humidity, which is very promising to further improve the current operational AROME system.

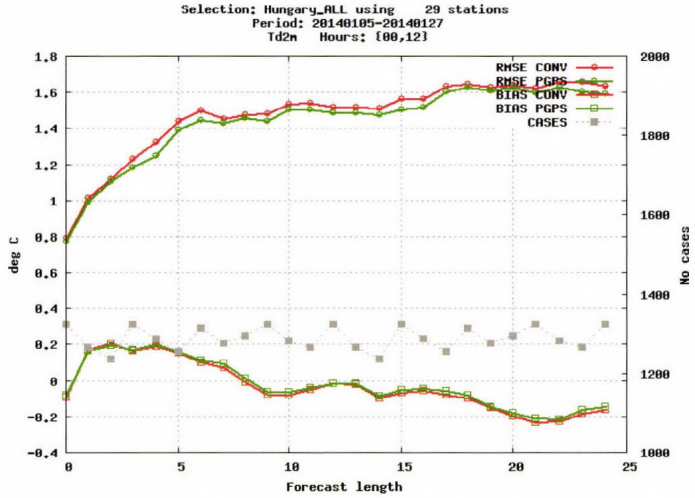

Fig. 14a. RMSE and BIAS scores of AROME forecasts corresponding to the operational AROME with conventional observations (CONV – red) and AROME with conventional plus GNSS ZTD observations (PGPS – green) for 2 m dew point temperature (°C).

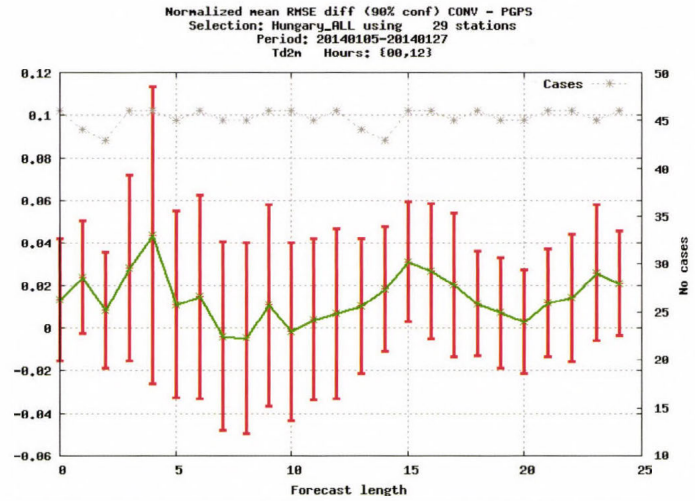

Fig. 14b. Normalized RMSE differences between operational AROME with conventional observations (CONV – red) and AROME with conventional plus GNSS ZTD observations (PGPS – green) for 2 m dew point temperature (°C).

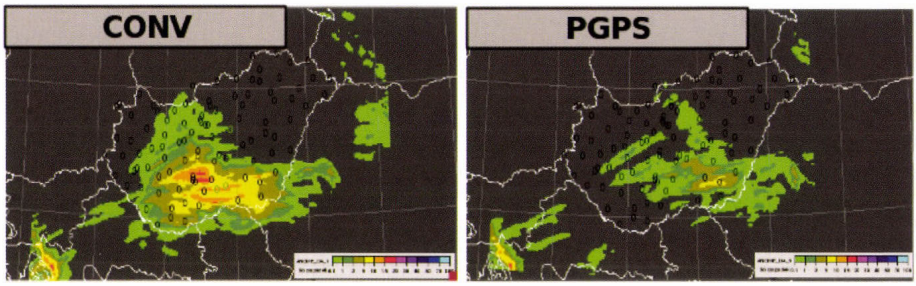

Fig. 15. A case study at 15 UTC, January 3, 2014 for 3 hourly accumulated precipitation forecast, AROME model with operational configuration (CONV), experimental AROME with GNSS ZTD (PGPS) and SYNOP precipitation (in numbers) are plotted.

4. ***Summary and conclusions***

The current operational RUC data assimilation system of the AROME-Hungary mesoscale model has been described with a special emphasis on the design of the assimilation cycle and the use of observations. It has been demonstrated, that the RUC system using conventional observations (surface, radiosonde, and aircraft measurements) improves the reliability of short-range forecasts compared to the spin-up initialization technique (former operational configuration) and also compared to the use of a 6 hourly data assimilation cycle.

The most important attempts for improving the current operational RUC system so far consisted of impact studies using remote sensing observations, such as MSG AMV, radar reflectivity, radial wind, and GNSS ZTD. The impact of AMV data assimilation was found to be significantly positive on the forecast of surface parameters, up to a forecast range of 15 hours. These results imply an operational use of MSG AMV data in the near future. The assimilation of radar data has been found to be useful in ameliorating precipitation forecasts, however, as a side effect of radar data assimilation, a bias have been found in surface parameters. The cause of these systematic errors has to be understood in order to achieve an operational implementation of radar data assimilation. The impact of GNSS ZTD data assimilation has been found to be slightly positive regarding the forecasts of surface parameters. Given that GNSS ZTD data provide information on atmospheric humidity also in clear-sky conditions, their importance is high in mesoscale data assimilation. This is reflected in some of our case studies through the preferable feature that ZTD data assimilation allows to reduce possible humidity and precipitation overestimations originating from the model first guess. Based on the overall impact of ZTD data, they are anticipated for an operational implementation in the near future.

Apart from the observation impact studies, an overview has been given about the relative importance of observing networks and observed variables based on the DFS method. The main message to be extracted out of these analysis sensitivity studies is that humidity observations are really important in mesoscale data assimilation, as they have relatively large influence on the analysis as compared to other observed variables. This indicates that the density of humidity observations have to be increased in the coming years either by using cloudy information from satellites or by implementing humidity sensors on board European aircrafts, similarly to the practice applied at the USA.

The paper gives an indication, that by increasing the resolution of mesoscale models, it becomes highly important to implement local data assimilation at the full resolution of the model, using high-resolution observations. It is shown that doing so, the spin-up initialization scheme can be outperformed both in terms of verification scores and case studies. This experience justifies that data assimilation will remain one of the major directions for improving mesoscale forecasts at the Hungarian Meteorological Service, with a special emphasis on remote sensing data. Besides the implementation of new observations to the RUC system, attention will have to be paid to the development of the background error covariance representation, which is responsible for the efficient filtering and spreading of observed information to the model space. It is foreseen that the background error covariance matrix for AROME-Hungary will be recalculated based on AROME ensembles of data assimilations similarly to the work of *Brousseau et al.* (2011).

Acknowledgements: The authors would like to thank *András Horányi, Edit Adamcsek, Helga Tóth* for their earlier work on data assimilation developments at the Hungarian Meteorological Service. Also we are grateful to *Balázs Szintai* for providing the object-based verification for RADAR assimilation experiments, *Ulf Andrae* for installing the Harmonie verification package at HMS, *Szabolcs Rózsa* to preparing test ZTD data for the assimilation study, and to *Xin Yan* who provided useful advices for ZTD pre-processing. We would like to thank also *László Kullmann* for the great support of AROME configurations and *István Sebők* for the important development of RADAR BUFR converter. Last but not least we are grateful to the organizers of the 39th Meteorological Scientific Days to found the possibility of this IDŐJÁRÁS special issue.

References

Benjamin, S.G., Dévényi D., Weygandt S.S., Brundage K.J., Brown J.M., Grell G.A., Kim D., Schwartz B.E., Smirnova T.G. and *Smith T.L.*, 2004: An hourly assimilation-forecast cycle: The RUC. *Mon. Weather Rev. 132,* 495–518.

Berre, L., 2000: Estimation of synoptic and mesoscale forecast error covariances in a limited area model. *Mon. Wea. Rev. 128*, 644-667.

Bevis, M., Businger, S., Herring, T., Rocken, C., Anthes, R., and *Ware, R.H.*, 1992: GPS meteorology: Remote sensing of atmospheric water vapor using the global positioning system. *J. Geophys. Res. 97,* 15787–15801.

Bölöni, G., 2006: Development of a variational data assimilation system for a limited area model at the Hungarian Meteorological Service. *Időjárás 110*, 309–327.

Bölöni, G., Berre, L., and *Adamcsek, E.*, 2014: Comparison of static mesoscale background error covariances estimated by three different ensemble data assimilation techniques. *Q. J. Roy. Meteor. Soc., 141*, 413-425.

Brousseau, P., Berre, L., Bouttier, F., and *Desroziers, G.*, 2011: Background-error covariances for a convective-scale data-assimilation system: AROME–France 3D-Var, *Q. J. Roy. Meteor. Soc., 137*, 409–422.

Cardinali, C., Pezzuli, S. and *Andersson, E.* 2004: Influence matrix diagnostic of data assimilation system. *Q. J. Roy. Meteor. Soc. 130*, 2767–2786.

Chapnik, B., Desroziers, G., Rabier, F., and *Talagrand, O.*, 2006: Diagnosis and tuning of observational error in a quasi-operational data ssimilation setting, *Q. J. Roy. Meteor. Soc. 132*, 543–565.

Caumont, O., Ducroq, V., Watterlot, E., Jaubert, G., and *Pradier-Varbe, S.*, 2010: 1D+3DVar assimilation of radar reflectivity data: a proof of concept, *Tellus A 62*, 173–187.

Courtier, P., Andersson, E., Heckley, W., Pailleux, J., Vasiljevic. D., Hamrud, M., Hollingsworth, A., Rabier, F., and *Fisher, M.*, 1998: The ECMWF implementation of three dimensional variational assimilation (3D-Var). Part I: Formulation. *Q. J. Roy. Meteor. Soc., 124*, 1783–1808.

Daley, R., 1991: Atmospheric Data Analysis. Atmospheric and Space Science Series, Cambridge.

Evensen, 2009: Data Assimilation, The Ensemble Kalman Filter, Springer.

Fabry, F. and *Sun, J.*, 2009: For How Long Should What Data Be Assimilated for the Mesoscale Forecasting of Convection and Why? Part I. *Mon. Weather Rev. 138*, 244–255.

Fischer, C., Montmerle, T., Berre, L., Auger, L., and *Stefanescu, S.* 2005: An overview of the variational assimilation in the Aladin/France numerical weather prediction system, *Q. J. Roy. Meteor. Soc. 131*, 3477–3492.

Forsythe M, C Peubey, C Lupu and *J Cotton*, 2014: Assimilation of wind information from radiances: AMVs and 4D-Var tracing, *ECMWF Annual Seminar*, September 2014, available in-line at: http://www.ecmwf.int/sites/default/files/ecmwf_sep14.pdf.

Girard, D., 1987: A fast Monte-Carlo cross-validation procedure for large least-squares problems with noisy data. *Technical Report 687-M, IMAG, Grenoble, France*

Horányi, A., Ihász, I. and *Radnóti, G.*, 1996: ARPEGE/ALADIN: a numerical weather prediction model for Central-Europe with the participation of the Hungarian Meteorological Service. *Időjárás 100*, 277–301.

Kalnay, E., 2003: Atmospheric Modeling, Data Assimilation and Predictability. Cambridge University Press.

Lindskog, M., Salonen, K., Järvinen, H.,Michelson, D., B., 2004: Doppler Radar Wind Assimilation with HIRLAM 3DVAR. *Mon Wea. Rev., 132*, 1081-1092.

Lorenc, A., 1986: Analysis methods for numerical weather prediction. *Q. J. Roy. Meteor. Soc. 112*, 1177–1194.

Lynch, P., D. Giard, and *V. Ivanovici*, 1997: Improving an efficiency of Digital Filtering Scheme for Diabatic Initialization. *Mon. Wea. Rev. 125*, 1976–1982.

Montmerle T. and *Faccani, C.*, 2008: Assimilation of Doppler wind into the French mesoscale model AROME. Proceedings of the ERAD 2008 conference (http://erad2008.fmi.fi/proceedings/index/session_wednesday.html)

Poli, P., Moll, P., Rabier, F., Desroziers, G., Chapnik, B., Berre, L., Healy, S. B., Andersson, E., and *El Guelai, F.-Z.* 2007: Forecast impact studies of zenith total delay data from European near realtime GPS stations in Meteo France 4DVAR, *J. Geophys. Res. 112*, D06114.

Randriamampianina, R., 2006a: Impact of high resolution observations in the ALADIN/HU model. *Időjárás 110*, 329–349.

Randriamampianina, R., 2006b: Investigation of the AMV data derived from Meteosat-8 in the ALADIN/HU data assimilation system. Eighth International Winds Workshop. 24-28 April 2006 Bejing, China, Available from: http://www.eumetsat.int/website/wcm/idc/idcplg?IdcService=GET_FILE&dDocName=PDF_CONF_P47_S2_06_RANDRIAMA_V&RevisionSelectionMethod=LatestReleased&Rendition=Web

Seity, Y., Brousseau, P., Malardel, S., Hello, G., Bénard, P., Bouttier, F. Lac, C., and *Masson, V.,* 2010: The AROME-France Convective-Scale Operational Model, *Mon. Weather Rev. 139,* 976–991.

Snyder, C. and *Zhang, F.,* 2003: Assimilation of Simulated Doppler Radar Observations with an Ensemble Kalman Filter, *Mon. Weather Rev. 131,* 1663–1677.

Storto, A. and *Randriamampianina, R.,* 2010: A new bias correction scheme for assimilating GPS zenith tropospheric delay estimates, *Időjárás 114,* 237–250.

Vasiliu S. and *Horányi A.,* 2005: An evaluation of the performance of the three-dimensional variational data assimilation scheme for the ALADIN/HU spectral limited area model, *Időjárás 109,* 233–257.

Wattrelot, E, O Caumont, and *J-F Mahfouf,* 2014: Operational Implementation of the 1D+3D-Var Assimilation Method of Radar Reflectivity Data in the AROME Model. *Mon. Weather Rev. 142,* 1852–1873.

Yan, X., Ducrocq, V., Poli, P., Jaubert, G., and *Walpersdor,f A.,* 2008: Mesoscale GPS Zenith Delay assimilation during a Mediterranean heavy precipitation event, *Adv. Geosci.* 17, 71–77.

IDŐJÁRÁS

Quarterly Journal of the Hungarian Meteorological Service
Vol. 119, No. 2, April – June, 2015, pp. 241–265

Application of the AROME non-hydrostatic model at the Hungarian Meteorological Service: physical parameterizations and ensemble forecasting

Balázs Szintai[1]*, **Mihály Szűcs**[1], **Roger Randriamampianina**[2], and **László Kullmann**[1]

[1]*Hungarian Meteorological Service,*
Kitaibel Pál u. 1., H-1024 Budapest, Hungary

[2]*Norwegian Meteorological Institute*
P.O. Box 43, Blindern, N-0313 Oslo, Norway

**Corresponding author E-mail:szintai.b@met.hu*

(Manuscript received in final form November26, 2014)

Abstract—At the Hungarian Meteorological Service (HMS), the AROME non-hydrostatic numerical weather prediction model has been running operationally since the end of 2010. The horizontal resolution is 2.5 km, thus it is assumed that deep convection is explicitly resolved. To achieve this, apart from increasing the horizontal and vertical resolution of the model, advanced physical parameterizations have to be applied. In this paper, some recent developments in connection with dynamics and physical parameterizations performed at the HMS are described. Model sensitivities related to horizontal diffusion, microphysics, turbulence, and shallow convection are discussed. Main features of the applied surface scheme "SURFEX" are highlighted as well as developments in connection with the prognostic treatment of vegetation. Recent work focusing on high resolution probabilistic forecasting with the AROME model is also summarized. It is shown that the AROME model is able to adequately predict severe weather events, however, as resolution increases, the importance of a probabilistic forecasting approach increases. An initial condition perturbation method and a model error representation scheme are described and their impact in an AROME-EPS test configuration is also presented.

Key-words: numerical weather prediction, physical parameterization, semi-Lagrangian horizontal diffusion, convection permitting ensemble system

1. Introduction

Thanks to the fast evolution in computing technology, more national numerical weather prediction centers can run models with increased resolutions. Using high-resolution models is very important in predicting fast-developing and intense atmospheric events. Good prediction of such hazardous events can protect lives and properties. Hence, investing in development of such models is very important for environmental and societal protection.

Hungary, together with several other European countries, has been participating in the ALADIN (Aire Limitée Adaptation Dynamique Développement International) consortium since 1991. The ALADIN consortium was initiated by France. The aim of this consortium is to develop a short-range limited-area numerical weather prediction (NWP) model. As a result of this collaboration, the ALADIN/AROME model family has emerged and is constantly being developed in the participating countries.

At the beginning of the ALADIN collaboration, the ALADIN model was a hydrostatic NWP model and was designed to run at relatively coarse horizontal resolutions (i.e., not higher resolution than 8 km), where the hydrostatic approximation (vertical acceleration of air is neglected) is valid. By the beginning of the new millennium, it became possible to run operational non-hydrostatic models at a horizontal resolution of 2–3 km. At Météo-France, the AROME (Application of Research to Operations at Mesoscale) project was initiated in 2002 with the aim to develop a non-hydrostatic NWP model running at 2.5 km horizontal resolution (*Seity et al.*, 2011). The AROME model has three main components: the non-hydrostatic ALADIN dynamical core (*Bubnová et al.*, 1995; *Benard et al.*, 2010), the atmospheric physical parameterizations, which are taken from the French Meso-NH research model (*Lafore et al.*, 1998), and the SURFEX surface model (*Le Moigne et al.*, 2009). A mesoscale data assimilation system with a three-dimensional variational (3D-VAR; *Fischer et al.*, 2005) scheme for the upper-air and an optimum interpolation (OI) technique for the surface analysis provides reliable initial condition for the AROME model.

The AROME model is now used in several countries of the ALADIN and HIRLAM (HIgh Resolution Limited Area Model) consortia. At the Hungarian Meteorological Service (HMS), work related to the AROME model started in 2006. After five years of scientific and technical development, the AROME model became operational in December 2010. In the beginning of the operational implementation, the model ran four times a day (at 00, 06, 12, and 18 UTC) at a horizontal resolution of 2.5 km, and provided forecasts up to 48 hours for a domain covering the Carpatian Basin (*Fig. 1*). The initial conditions were provided by the ALADIN/Hungary (Hereafter ALADIN/HU) limited area model (LAM) (*Horányi et al.*, 1996), while lateral boundary conditions are obtained from the ECMWF/IFS (European Centre for Medium-

Range Weather Forecasts / Integrated Forecast System) model. The ALADIN/HU model has its own three-dimensional variational (3DVAR) data assimilation system (*Bölöni*, 2006, *Randriamampianina,* 2006), which is partly inherited by the AROME model. The AROME assimilation system, using only conventional observations, was operationally implemented in March 2013 (*Mile et al.*, 2014). The short-range forecasts of AROME are mainly used by the forecasters of HMS to produce early warnings of severe weather events. Furthermore, products derived from AROME are utilized by wind energy farms to plan their production.

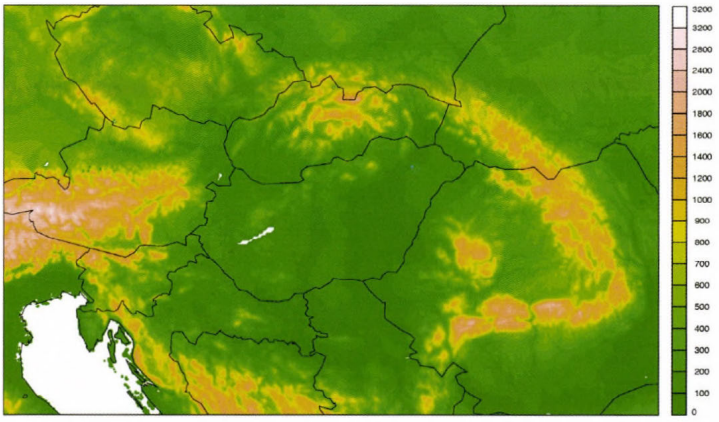

Fig. 1. Domain and orography of the AROME model as run operationally at the Hungarian Meteorological Service.

The aim of this paper is to present recent developments of the AROME model performed at HMS regarding dynamics, physical parameterizations, and ensemble prediction. In Section 2, the dynamical core of the model is briefly described and developments related to horizontal diffusion are presented. In Section 3, an overview of the physical parameterizations applied in AROME is given, together with the description of certain developments related to the turbulence parameterization and surface processes. Section 4 presents new developments regarding non-hydrostatic probabilistic forecasting. Finally, results are summarized in Section 5.

2. Dynamics

At horizontal mesh sizes at or below two kilometers, vertical accelerations could be of the order of the gravitational acceleration (g) and cannot be neglected any more, thus the hydrostatic approach is not recommended. Consequently, a new

equation has to be carried for the vertical momentum in the non-hydrostatic dynamical cores. The advantage of this approach is that certain atmospheric phenomena (like deep convection or orographic gravity waves) are resolved explicitly by the model, therefore no parameterization of these processes is required. The AROME model uses the non-hydrostatic dynamical core which was developed by the ALADIN consortium (*Bubnová et al.*, 1995).

The application of high resolution atmospheric models is a computationally demanding task, due to the increased number of grid points, the additional equation for vertical momentum in the dynamical core, and the increased complexity of certain parameterization schemes (e.g., microphysics). These requirements are only partly compensated by the fact that the deep convection scheme could be switched off in the model. In the case of the AROME model, this high computational demand is tackled by the application of advanced and efficient numerical schemes. AROME is a spectral model, which means that in the dynamical part of the model, the prognostic equations are handled in spectral space, which enables a fast computation of horizontal derivatives. Regarding the time integration, a very efficient semi-implicit, semi-Lagrangian time integration scheme is applied in AROME. This scheme permits a rather long time step even at fine horizontal resolutions. In the current operational version at the HMS, a time step of 60 s is used in AROME at 2.5 km horizontal resolution. This is approximately five times larger than the time step applied in other widely used non-hydrostatic models.

2.1. Horizontal diffusion

In current mesoscale NWP models, one dimensional physical parameterizations are applied. The reason for this is that above 1 km horizontal resolution, vertical gradients of meteorological variables are much larger than the horizontal gradients. However, due to numerical stability constraints, it is necessary to ensure a horizontal communication of grid cells. Apart from advection, this can be realized by the application of a numerical horizontal diffusion filter operator. In the case of the ALADIN/AROME model family, there are two main options for numerical horizontal diffusion. The first one is the spectral diffusion which is calculated in spectral space and consequently acts on the full model domain. The second option is the semi-Lagrangian horizontal diffusion (SLHD, *Váňa et al.*, 2008), which is calculated in grid point space as a function of wind deformation, hence it has a physically based and more local effect. It is important to note that in the AROME model, SLHD is used in combination with the spectral diffusion. In fact, next to SLHD, two other spectral diffusion operators are used: a fourth order spectral diffusion which acts mainly at the upper part of the model domain to prevent the reflection of gravity waves from the model top and a sixth order spectral diffusion to filter noise due to orography.

At HMS, several experiments have been done in connection with SLHD. The main goal of these experiments was to tackle some known deficiencies of

the AROME model during convective conditions (e.g., too strong updrafts, too high precipitation peaks in the cells, too strong gust fronts). In the original configuration, SLHD is applied to all (falling and non-falling) hydrometeors. The experiment presented here is based on the work of *Bengtsson et al.* (2010). SLHD is applied only to non-falling hydrometeors, and additionally it is also applied to the dynamical fields (wind, temperature, and humidity) and turbulent kinetic energy (TKE). Characteristics of the fourth order spectral diffusion have also been changed: while in the original configuration spectral diffusion acts on all levels (although with increasing intensity upwards), in the experiments spectral diffusion was only applied above 100 hPa. *Fig. 2* presents the impact of SLHD changes on a convective event. With the new SLHD configuration, the AROME simulation is closer to observations: the intensity of convective precipitation is reduced, convective wind gusts are weaker and the number of convective cells is decreasing. Apart from case studies, the new SLHD settings were tested on longer summer and winter periods, and the forecasts were compared against the surface (SYNOP) observations and radar-based precipitation data. Verification scores against SYNOP data show a clear improvement in the wind speed, wind gust, and cloudiness forecast, while the impact on temperature and humidity is neutral (*Fig. 3*). The diurnal cycle of convective precipitation is also improved, as the overestimation in the late afternoon is decreased (*Fig. 4*).

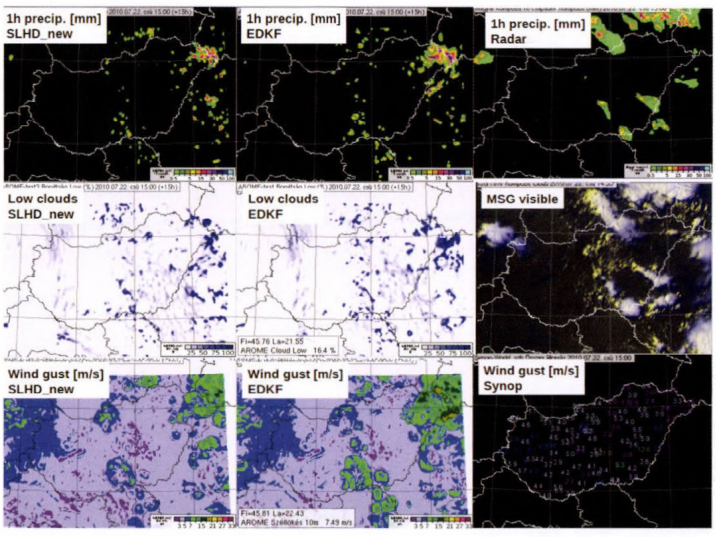

Fig. 2. Forecasted fields of two AROME experiments and measurements for July 22, 2010, at 15 UTC (+15 h forecasts). Left column: AROME with new SLHD settings, middle column: AROME with original SLHD settings, right column: measurements. First row: hourly precipitation, second row: low cloud cover, third row: hourly maximum wind gust.

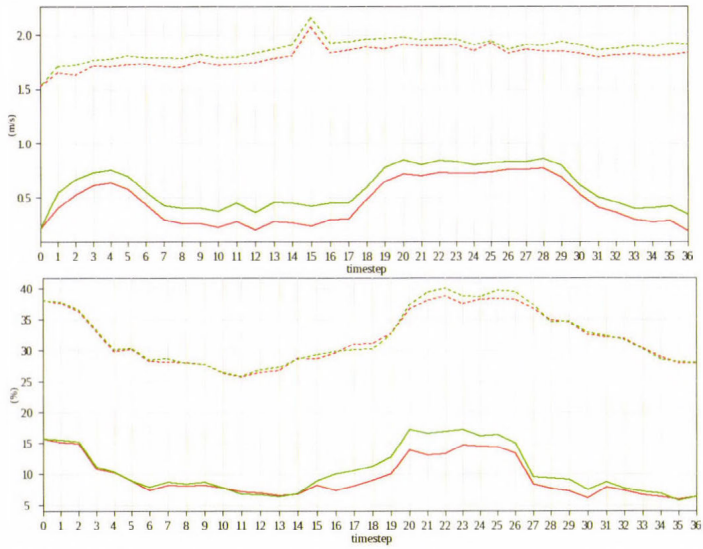

Fig. 3. Verification scores for the period between May 1, and June 1, 2013 as a function of lead time (in hours). Upper panel: 10-meter wind speed, lower panel: cloudiness. Green line: original SLHD settings, red line: new SLHD settings. Dashed line: root mean square error, solid line: bias. Always the 00 UTC forecasts were verified against low-altitude (station altitude below 400 m) SYNOP observations above sea level on the operational AROME domain.

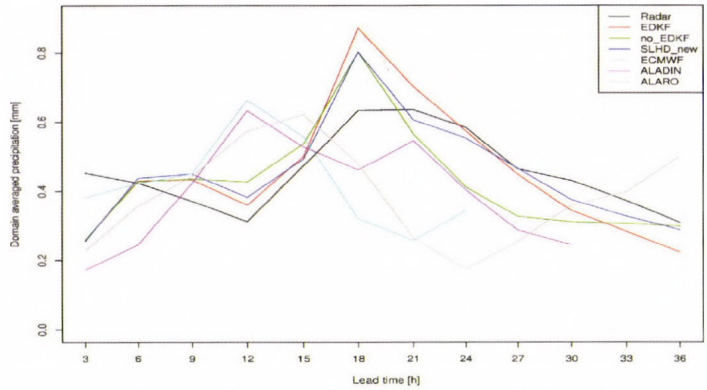

Fig. 4. Observed (radar) and predicted diurnal cycle of convective precipitation (area averaged precipitation on the AROME domain) for the period between July 17 and August 17, 2010. AROME experiments mentioned in the text: green: without EDKF parameterization and original SLHD settings; red: with EDKF parameterization and original SLHD settings; blue: with EDKF parameterization and new SLHD settings. Forecasts of the 8 km resolution limited area regional model run at the Hungarian Meteorological Service with two different physical parameterizations (ALADIN and ALARO) and of the ECMWF model are also indicated.

3. Physical parameterizations

Numerical weather prediction models are not able to resolve explicitly those processes which are smaller than the grid scale of the model, thus these processes have to be parameterized. Parameterization means the description of the overall effect of a given subgrid scale process on the grid scale values, using the given grid scale variables. The AROME model uses the physical parameterizations of the Meso-NH French research model. In the following, an overview is given on the components of this physical parameterization package, and the corresponding developments performed at HMS are described.

3.1. Microphysics

Phase changes occurring in clouds are described by the microphysical parameterization. In convection permitting NWP models, the choice of the microphysical scheme is of great importance. As these models do not apply a deep convection parameterization, the convective cloud should explicitly be simulated by the model, and thus the non-hydrostatic dynamical core and the microphysical parameterization play a crucial role. Consequently, the microphysical scheme has to be rather sophisticated to be able to simulate all the relevant processes during a lifetime of a convective cloud.

In AROME, the so-called ICE3 scheme (*Pinty* and *Jabouille*, 1998) is used, which carries six prognostic microphysical variables (vapor, cloud water, cloud ice, rain, snow, graupel), and describes the phase change processes among these variables. In the AROME model this means 35 processes: warm-cloud and mixed-phase processes are distinguished. Warm-cloud processes are autoconversion, accretion, evaporation, sedimentation, while mixed-phase processes are nucleation, ice-crystal autoconversion, aggregation, raindrop contact freezing, riming, melting, deposition, Bergeron-Findeisen effect, and ice-crystal sedimentation. The ICE3 scheme is a bulk one-moment scheme. This means that the mixing ratio of each hydrometeor is written as the third momentum of the size distribution of the given hydrometeor. The advantage of this approach is that the microphysical processes become analytically resolved processes. It has to be noted that a new two-moment microphysical scheme is currently under development in Meso-NH and is planned to be available in AROME soon. Next to the mixing ratios, this scheme handles the number concentration of hydrometeors prognostically as well.

Several tests were performed in connection with the initialization of the hydrometeor fields in the microphysics parameterization at the Hungarian Meteorological Service. The problem regarding hydrometeors is that these variables are not measured regularly, thus it is not possible to initialize these model fields based on measurements in an operational setting. In the early years of AROME development, it was considered that the formation of hydrometeors

is a relatively fast process, and consequently, it is possible to initialize these fields with zero. It was assumed that if the initial temperature and humidity fields are correct, then the hydrometeors would form within a couple of time steps. As a contrary to this assumption, case studies showed that if the hydrometeors are initialized with zero, then precipitation events could be missed by AROME in the early hours of the forecast. To overcome this problem, the following procedure was applied: the hydrometeors are "cycled" from the previous run, so, e.g., the initial hydrometeor fields of an AROME forecast starting at 06 UTC are the +6 h forecasted hydrometeor fields of the 00 UTC AROME forecast. With this approach, several previously missed precipitation objects could be well simulated by AROME (*Fig. 5*).

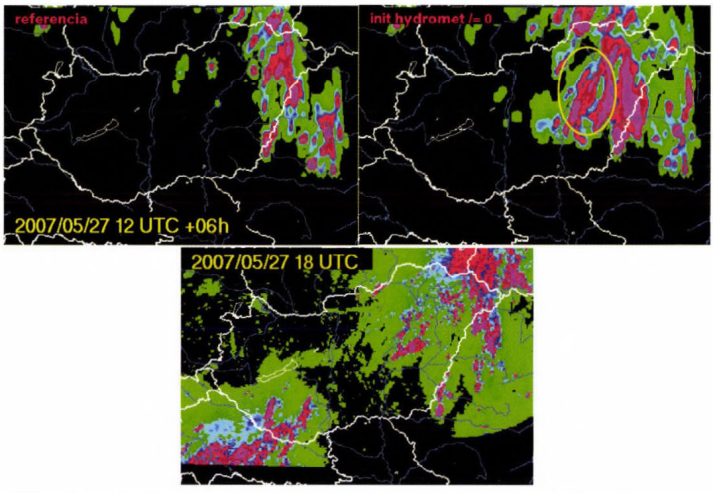

Fig. 5. Impact of hydrometeor initialization on the AROME forecast. Left: hydrometeors are initialized with zero; middle: hydrometeors are initialized from the 6 hour forecast of the previous run; right: hourly accumulated radar precipitation. A +6 h forecast of hourly precipitation is shown valid for 12 UTC, May 27, 2007.

3.2. Turbulence and shallow convection

Shallow convection refers to the warm updrafts (thermals) which originate from the surface and reach the top of the planetary boundary layer (PBL). These thermals are usually indicated by small non-precipitating clouds (Cumulus humilis). Boundary layer turbulence refers to those eddies which are generated either by wind shear (mechanical turbulence generation) or buoyancy, with a characteristic size much smaller than the depth of the PBL. Until recently, shallow convection was parameterized separately from boundary layer turbulence in NWP models, however, nowadays these two processes are handled in a unified way in several schemes.

In the AROME model, the eddy diffusivity – mass flux (EDMF) approach is followed to parameterize turbulence and shallow convection. The eddy diffusivity part of the parameterization uses the CBR scheme (*Cuxart et al.*, 2000) to describe the effect of boundary layer turbulence. This is a 1.5 order closure which carries a prognostic equation for the turbulent kinetic energy. The diffusion coefficients are then calculated based on TKE, a turbulent length scale and stability functions. In the AROME model, the length scale formulation after *Bougeault* and *Lacarrere* (1989) is applied. Originally, the CBR scheme has both one and three dimensional versions, however, currently the one dimensional version is applied in AROME. Based on recent experiments, it is assumed that a three dimensional turbulence scheme is not necessary above 1 km horizontal resolution (*Yann Seity* and *Rachel Honnert*, personal communication). The main drawback of the CBR scheme is that it is a local scheme, which means that turbulent fluxes at a given vertical level are determined by the local vertical gradients of wind and temperature at that level. Consequently, with a local turbulence scheme, it is not possible to reproduce the correct behavior of the convective boundary layer, which has a strong non-local nature: thermals originating at the surface result in considerable vertical transport in the middle part of the PBL, where the local vertical gradients are very close to zero. To resolve this problem, in the EDMF framework a mass flux parameterization is applied next to the CBR scheme.

In the AROME model, the mass flux parameterization of a shallow convection thermal is divided to two parts (*Pergaud et al.*, 2009). On vertical levels below the shallow convective cloud base, the parameterization of *Lappen* and *Randall* (2001) is used. This scheme is closed with the surface sensible heat flux, consequently, the entire mass flux part of the EDMF parameterization is inactive if the surface sensible heat flux is negative (stable conditions). Above the cloud base, the *Kain* and *Fritsch* (1990) parameterization is applied (this is why the EDMF parameterization is mentioned as EDKF in connection with the AROME model). The closure of this scheme is performed by taking the mass flux at cloud base from the parameterization of the non-cloudy part of the thermal. The cloudy part uses a diagnostic cloud scheme where the cloud fraction at a given level is proportional to the area fraction of the updraft.

At the Hungarian Meteorological Service, the impact of the EDKF parameterization on the overall performance of the AROME model has been investigated before the operational introduction of the scheme. As the scheme is only active during unstable conditions, largest impact was expected for summer convective events. *Fig. 6* shows the impact of EDKF on a summer convective case. Here, two AROME simulations are compared; one with EDKF, and a second one which parameterized turbulence and shallow convection separately (with the CBR and Kain-Fritsch schemes, respectively). The run without EDKF significantly overestimates the number of convective cells during early afternoon, while during the evening it fails to simulate the heavy thunderstorms

(not shown here). Also, convection itself is initiated too early (around 8 UTC) in this experiment (see also in *Fig. 4*), and consequently, convective wind gusts are overestimated until the early afternoon hours.

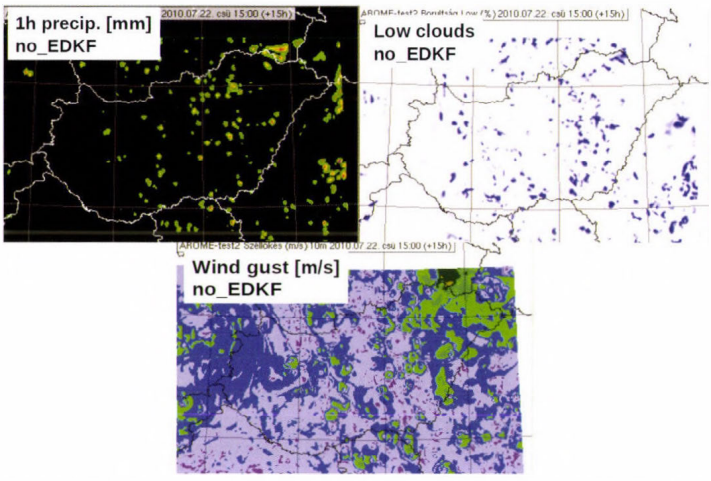

Fig. 6. Same AROME forecast of hourly precipitation, low clouds and wind gusts as in *Fig. 2*, but the EDKF parameterization is switched off, thus turbulence and shallow convection is parameterized separately (CBR scheme for turbulence and Kain-Fritsch scheme for shallow convection). Colour scales are the same as in *Fig. 2*.

3.3. Surface

Surface processes are calculated using the SURFEX (SURFace EXternalisée, *Le Moigne*, 2012) platform.

SURFEX uses the tiling approach: each grid point is divided into 4 different surface types (tiles): sea, inland water, town, and vegetated land. Each tile uses the same atmospheric forcing (air temperature, humidity, wind speed, long and shortwave radiation, pressure, precipitation), but the parameterizations are different and independent of each other. The resulting surface fluxes (momentum, sensible- and latent heat) are averaged according to the area fraction of the tiles and returned to the atmosphere. Surface parameters are determined by physiographic databases: GTOPO30 for orography, ECOCLIMAP for surface covers, and FAO for soil texture.

In the current operational version, over sea and inland water (lakes) SURFEX uses simple schemes: surface temperatures are kept constant, roughness length and fluxes are computed with the Charnock's approach. However, there is a more advanced scheme for lakes, FLAKE (Freshwater lake, *Mironov et al.*, 2010), in which lake temperature is a prognostic variable.

Over artificial surfaces, the TEB scheme (Town Energy Budget, *Masson,* 2000) is used. Towns are represented by the canyon concept: there is a single road with two buildings and a canyon between them. Each surface (road, wall, roof) consists of 3 layers and has a different temperature , while the temperature inside the buildingsis constant. The time evolution of the temperatures are calculated by heat conduction equations. In the radiative forcing, trapping and shadowing effects are also taken into account. The scheme also accounts for anthropogenic heat and water fluxes (traffic and industry).

Vegetated land surfaces are parameterized with the ISBA scheme (*Noilhan* and *Planton*, 1989; *Noilhan* and *Mahfouf,* 1996). The current operational version uses a 3-layer (surface, root zone, and deep soil) force-restore scheme. Over snow mantel, a one layer snow scheme (*Douville et al.* 1995) is used in which snow albedo and density are prognostic variables.

The 2 m temperature and 10 m wind are calculated by the Canopy scheme (*Masson* and *Seity*, 2009) ,which is a one dimensional vertical turbulence scheme in the surface boundary layer.

Vegetation is constant and determined from climatology databases. However, a more advanced version of the ISBA scheme, called ISBA-A-gs (*Calvet et al.* 1998), uses a simplified photosynthesis model which is able to describe the evolution of vegetation. In this model version, biomass is a prognostic variable. Growing of the active biomass is due to assimilation of CO_2 (photosynthesis), while the decline (or mortality) can be due to soil moisture stress, senescence, or transport of organic molecules from active biomass to structural one. Since the photosynthesis process depends on the vegetation type, the vegetated land tile in SURFEX is further divided into 12 patches according to the vegetation or surface type, like grass, crops, trees, etc. Beside the prognostic treatment of the vegetation, the scheme also calculates the carbon fluxes (assimilation and soil respiration).

In the framework of the Geoland2 EU-FP7 project, the task of the Hungarian Meteorological Service was to simulate the natural carbon fluxes and the evolution of vegetation over Hungary. SURFEX was used in offline mode (no influence on the atmosphere) with the ISBA-A-gs photosynthesis model. To improve the accuracy of the initial soil moisture and biomass fields, assimilation of satellite observations (surface wetness index and leaf area index) was developed and used. Results have shown that the model is able to describe the seasonal cycle of the vegetation and the natural carbon fluxes, and that assimilation of the above mentioned satellite observations (SWI and LAI) gives some improvement in spring (*Fig. 7*).

The Hungarian Meteorological Service also takes part in the IMAGINES EU-FP7 project. Our task – besides the simulation of vegetation and carbon fluxes – is the development of the model to be able to assimilate surface albedo from new generation Proba-V satellite observations and to calculate agricultural indicators like drought indices.

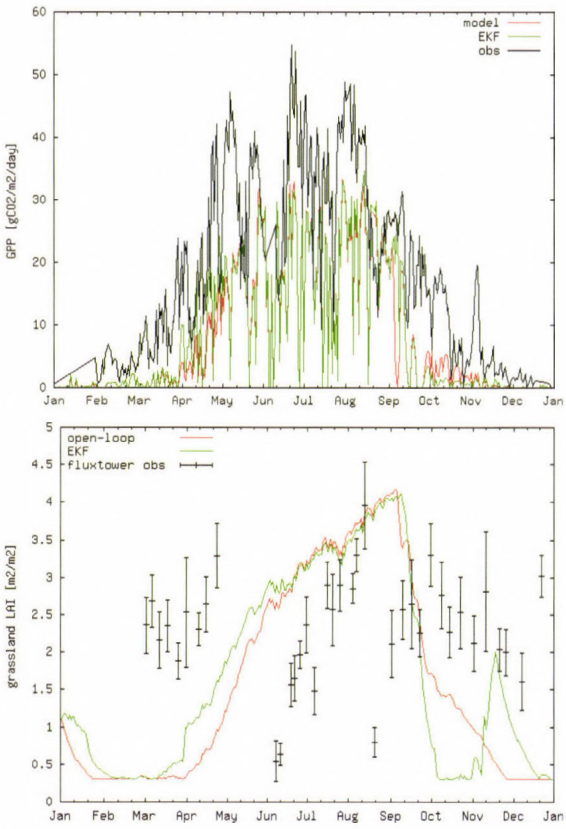

Fig. 7. Simulated and measured carbon flux (up) and leaf area index, LAI (down). Black line is observation, red line is without and green line is with assimilation.

3.4. General performance of the AROME model

As a result of the developments described in the previous sections, the AROME model has become a robust and reliable operational NWP model at HMS. The quality of AROME forecasts is comparable to that of other operational models used at HMS. In this section we show verification scores of a longer period, where the performance of AROME is compared to two operational hydrostatic models: the IFS global model run at ECMWF at 16 km horizontal resolution and the ALADIN regional model run at HMS at 8 km resolution.

The time period for the comparison was chosen in a way that no major changes should be applied in any of the three models. According to this criteria the period between September 16, 2013 and July 2, 2014 was selected. In this period, AROME was running with the model cycle 36, and the 3DVAR data assimilation system was operational using conventional upper air observations.

In the following, verification scores for screen and surface level variables (using SYNOP stations) as well as upper level variables (using radiosounding stations) are presented. Only forecasts with 00 UTC initial time were verified, and the verification scores were investigated as a function of lead time.

Regarding temperature and dew point at 2 meters, performance of AROME is comparable with the ECMWF model, while these two models outperform the ALADIN model for these variables (*Figs. 8a* and *8b*). The model bias has a diurnal dependency, daytime temperatures are underestimated, while nighttime temperatures are overestimated in AROME. Wind speed and wind gusts at 10 meters are generally overestimated by all three models (*Figs. 9a* and *9b*). For wind speed, ECMWF gives the best forecasts followed by AROME and ALADIN. Wind gusts are best captured by AROME, while ALADIN and ECMWF have similar performance for this variable.

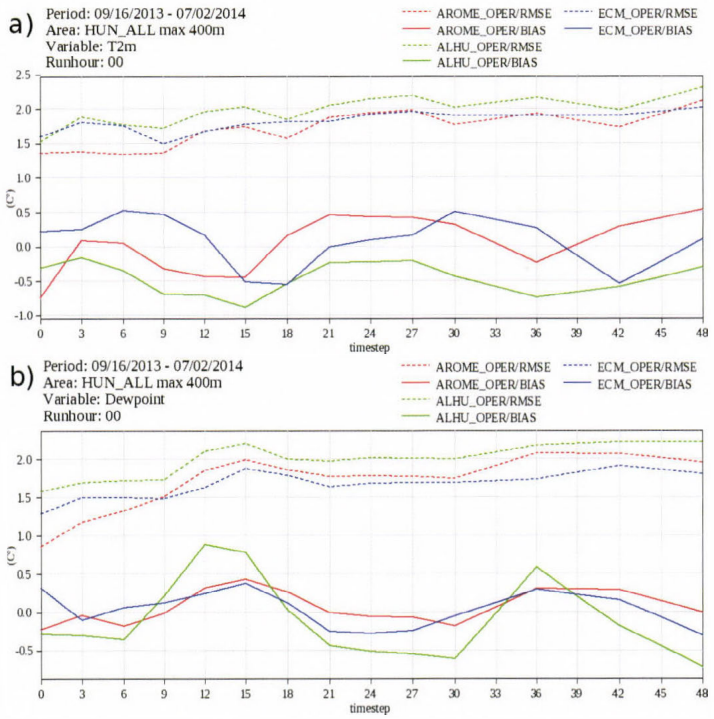

Fig. 8. Verification scores as a function of forecast lead time for temperature (a) and dew point (b) at 2 meters for operational NWP models at HMS between September 16, 2013 and July 2, 2014. Red: AROME, green: ALADIN, blue: IFS; dashed line: root mean square error, solid line: bias.

High resolution non-hydrostatic models are mainly applied for the forecasting of severe weather events, thus it is important to assess the quality of forecast performance for heavy precipitation. *Fig. 10* presents the symmetric extremal dependence index (SEDI), which is often used to verify high threshold events and the frequency bias for forecasted 12 hourly precipitation amounts. The SEDI score shows that for higher thresholds, the AROME model gives the best precipitation forecasts out of the three operational models. However, the frequency bias score points out a serious problem of AROME, namely that the model tends to forecast intensive convective cells more often than in reality. This erroneous model behavior is currently investigated at HMS.

Model performance at upper levels is mainly important for aviation forecasting. Based on the investigation of geopotential, temperature, wind, and humidity at several vertical levels, it can be concluded that the three models have similar performance, and the AROME model has usually a low bias but somewhat higher RMSE scores than the other two models (*Figs. 11a* and *11b*).

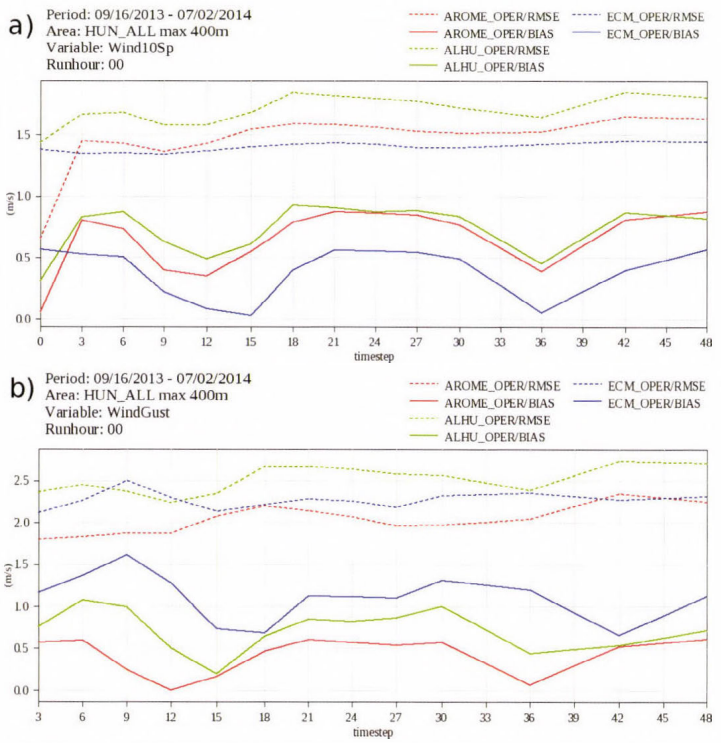

Fig. 9. Same as *Fig. 8* but for wind speed (a) and wind gusts (b) at 10 meters.

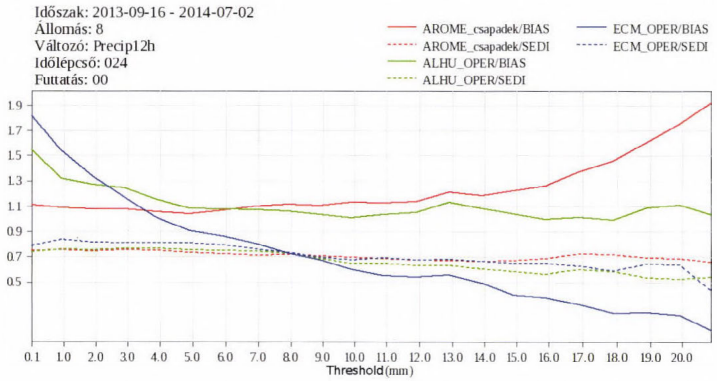

Fig. 10. Verification scores for 12 hourly accumulated precipitation for operational NWP models at HMS between September 16, 2013 and July 2, 2014. Red: AROME, green: ALADIN, blue: IFS; dashed line: SEDI, solid line: frequency bias.

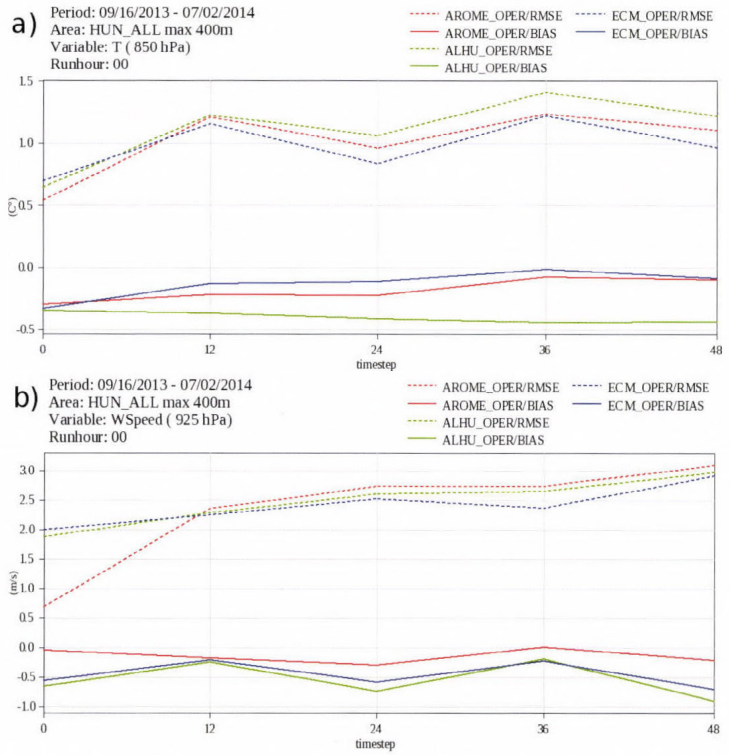

Fig. 11. Same as *Fig. 8* but for temperature at 850 hPa (a) and wind speed at 925 hPa (b).

4. Ensemble prediction system with AROME model

4.1. Motivation for a convection-permitting EPS

The uncertainty of numerical weather predictions is usually thought to originate from two main sources (*Palmer* and *Tibaldi*, 1988):
– Initial condition (IC) errors which evolve with time in the models due to the chaotic nature of the non-linear atmospheric system;
– Model errors which are based on limited human knowledge about atmospheric processes and finite resolution and representation possibilities of our models.
In reality, these errors can not be absolutely separated and they evolve together with time in the numerical models. Instead of giving a single-value as a forecast of a meteorological variable, it is more correct to give a probability density function (PDF) of it which contains information about forecast uncertainty. Until now, ensemble prediction systems (EPS) have been the only feasible and widely used tools to estimate such PDF. The main idea behind EPS is to run not only a single-forecast but an ensemble of numerical integrations where members can differ from each other in various aspects. These differences are defined by the perturbation generation methods which are designed to address different sources of error, so basically IC perturbation methods and model error representation can be separated.

The first ensemble prediction systems (EPS) were implemented in the early 90's with global models of ECMWF and NCEP (*Buizza et al.*, 1993; *Toth* and *Kalnay*, 1997). These global systems described synoptic-scale motions on medium-range. Consequently, their error is dominated by the chaotic growth of IC error, and that is why early methods focused on IC perturbations (singular vector and breeding methods). Later it was realized that classic methods can not always ensure sufficient spread at the early stage of the forecast, so new methods were implemented, which aim is usually to identify the most uncertain parts of analysis fields where bigger initial spread is needed. One possible way is to run an ensemble of data assimilation cycles (EDA) with perturbed observations. This method has been successfully used for example in ECMWF's EPS or in Meteo-France's global ensemble, called PEARP (*Desroziers et al.*, 2009; *Vié et al.*, 2011).

In the improving ensemble systems, it was recognized that the representation of model error is also a very important challenge, so the perturbation of the model formulations is also necessary. Generally, it is assumed that model physics is more uncertain than dynamics because of the fluctuation of sub-grid scale processes and the bigger error of the parametrization methods. For that purpose, ensemble members can run with different parametrization schemes (multi-physics approach, used e.g., in PEARP) or with slightly different parameter settings in physics (parameter

perturbations). Another possible way of representing model error is the stochastic perturbation of the total tendencies coming from the physics. Such a method is the so-called stochastically perturbed parameterized tendencies (SPPT) which was first implemented at ECMWF (*Buizza et.al.*, 1999).

Limited area ensemble prediction systems (LAMEPS) have become also popular tools to refine global probabilistic forecasts on a shorter time range and for a smaller domain. LAMEPS have to be coupled to global EPS, which results in some additional challenges. Global perturbations have to be taken into account through the interpolated lateral boundary conditions (LBC) of the perturbed members. The potential benefit of LAMEPS motivated the HMS to start its own researches on that field and established an operational system in 2008. This EPS uses the hydrostatic ALADIN model and runs with 8 km horizontal resolution. It has 11 members which are the simple dynamical downscaling of the control and the first 10 perturbed members of the 18 UTC run of the Prevision Ensemble ARPege (PEARP). While no local perturbation or data assimilation have been implemented yet, its quality depends highly on PEARP, and the impact of the changes in global system can be also measured in the LAMEPS. The slightly positive impact of a simple EDA implementation was shown, where only near-surface observations were perturbed in an ensemble of surface optimal interpolations (*Horanyi et al.*, 2011).

The quality of numerical weather prediction has been improving for the previous decades because of the better model formulations and the finer resolution which was enabled by the growing computer capacity. As it has been already mentioned in Section 2, at around 2 km resolution, models become non-hydrostatic and they can resolve such small-scale phenomena like deep convection. This way, finer structures can be produced and more realistic fields can appear. Unfortunately, this type of improvement is not necessarily associated with better scores, because resolving smaller scales can cause more uncertainty in model results (e.g., localization problems can lead to double-penalty effect). To overcome this problem, more and more national meteorological services in Europe started to develop non-hydrostatic model based ensemble systems. This new generation of EPS is also referred to as convection-permitting EPS. The introduction of such systems has already happened at Deutscher Wetterdienst (DWD) with COSMO-DE which has 20 members and runs with 2.8 km resolution (*Gebhardt et.al.*, 2008). Met Office has also started its operational convection-permitting EPS based on the 1.5 km resolution version of Unified Model (*Migliorini et.al.*, 2011). Météo-France has also joined the bigger services and runs its 12-member EPS with AROME model (*Vié et al.*, 2011).

HMS started its own research around convection-permitting EPS in 2012, and many tests have been run since then. Some of the results will be presented in this chapter. In this paper, an 11-member test configuration is called as a reference, which is, similarly to the operational LAMEPS, the simple dynamical downscaling of the first 11 PEARP member. AROME model runs with very

similar settings to what was detailed in previous parts for single-forecasts. The only notable difference was that the SLHD settings were not changed (cf. Section 2.1). In the following parts, the impact of two perturbation methods will be presented, which have been already mentioned as successfully used approaches in global EPS. The EDA method is addressed to IC error (see Section 4.2), while the SPPT method represents the model error (see Section 4.3).

4.2. Impact of Ensemble Data Assimilation Method

Modern data assimilation methods are based on complex algorithms which usually combine model forecasts as background fields and different types of observations. Similarly to the atmospheric models, these algorithms also have their limitations, while background fields and observations are also sources of additional errors. As a result of the above mentioned weaknesses, it has to be admitted that analysis fields are imperfect. A plausible way for handling this imperfection is to define the most uncertain areas of the analysis, which is possible with generating not only a single analysis field but running an ensemble of data assimilation cycles. This ensemble can provide flow dependent information about the accuracy of the background fields which is very useful to the data assimilation itself (*Brousseau et al.*, 2006; *Desroziers et al.*, 2009). From the aspect of an ensemble, it is even more important that more analysis fields are generated in EDA which can be the initial conditions of different ensemble members in an EPS.

The differences between the members of EDA originate usually from the perturbations which are added to the observations:

$$y'_j = y + \sigma(y) r_j \tag{1}$$

where it is assumed that observations y are imperfect but they are not biased and their uncertainty can be described by σ, which is estimation of the accuracy of the instrument. There is an r random number for the jth member, picked from a Gaussian-distribution, which has 0 mean, unit variance, and bounded in a [–3;3] interval. Observation perturbations can evolve in assimilation cycles, so in new steps there are always uncertainty information in the system which comes from the background fields. Additionally, LBCs are needed in LAM EDA during the model integration when background fields are generated. These LBCs are usually interpolated from different members of a global EPS, so they can be also sources of perturbations inside an EDA system.An EDA was implemented to construct better perturbed initial conditions for our test AROME-EPS compared to those obtained by simple downscaling of the global EPS. In this implementation of EDA (very similar to the EPS itself), different members were coupled to the different members of PEARP. The data assimilation methods are very similar to the operational AROME system of

HMS (*Mile et al.*, 2014). Conventional data (SYNOP, radiosonde, aircraft measurements) were used in a 3D-VAR data assimilation which generated atmospheric fields. Surface fields were simply interpolated from HMS's operational ALADIN model, where an optimal interpolation method is used to improve surface variables with observations.

In comparison with the reference, it is expected from the EDA based configuration that the quality of all members can be improved simply because of the positive impact of data assimilation itself. It is also expected that additional perturbations can increase the spread of the system. These two effects can result in a better relationship between the root mean square error (RMSE) of the ensemble mean and the system's spread. These expectations are verified on spread-skill relationship plots (*Figs. 12a, 12b, 12c, 12d*), where RMSE is smaller and spread is bigger in the early stage of the forecast. Later the difference between reference and EDA based version are smaller, because on such a small domain, the effect of LBC's become dominant quite fast. For total cloudiness scores, *Fig. 12c* underlines another advantage of EDA which is valid in AROME-EPS framework: hydrometeors can be initialized from background, which importance have been already mentioned in Section 3.1. In this paper, mainly near-surface scores are presented because of the big number and high frequency of independent SYNOP observations (*Figs. 12a. 12b, 12c*). ECMWF analysis was chosen as a reference for upper-air verification (*Fig. 12d*). It has to be noted that the remarkable resolution difference between AROME model (2.5 km) and reference analysis (16 km) can be questionable. Unfortunately, the short test period and the small domain resulted a very limited number of radiosonde measurements, what has not permitted to calculate atmospheric scores on higher level with observations.

a)

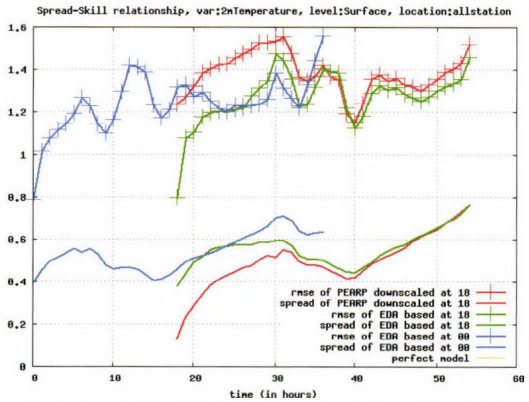

Fig. 12 a. Spread-skill relationship of 2 meter temperature. Red is a simple PEARP downscaling as a reference; blue and green are the test versions where IC is generated in an EDA system. Scores are calculated for the period between December 26, 2011 and January 8, 2012.

b)

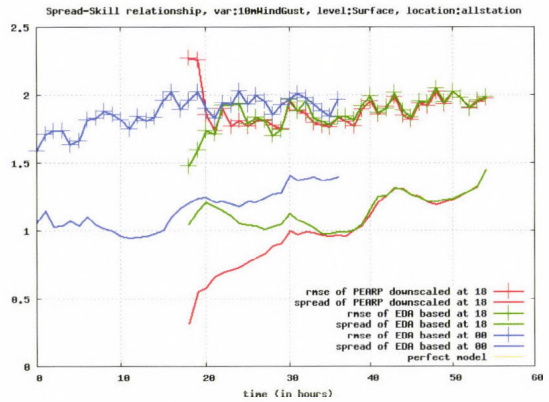

c)

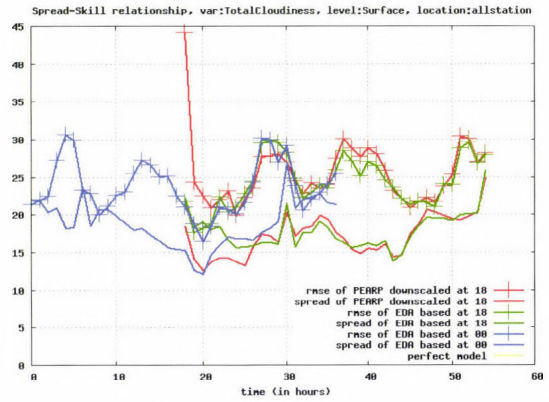

d)

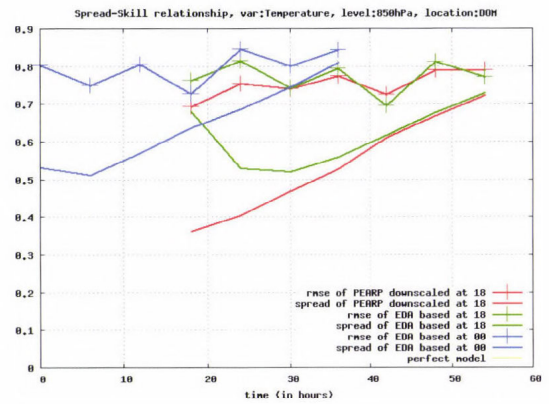

Fig. 12 b-d. Spread-skill relationship of 10 meter wind gust values (b), and total cloudiness (c), temperature on 850hPa pressure level Red is a simple PEARP downscaling as a reference; blue and green are the test versions where IC is generated in an EDA system. Scores are calculated for the period between December 26, 2011 and January 8, 2012.

4.3. Impact of Stochastically Perturbed Parametrized Tendencies

The original version of Stochastically Perturbed Parameterized Tendencies (SPPT) scheme was developed at ECMWF and called just as stochastic physics or BMP (*Buizza et al.*, 1999). Later it has been revised (*Palmer et al.*, 2009) and used as a successful tool to increase ensemble spread during the whole range of the forecast. It had positive impact even on the quality of single-model runs, especially in the tropical region.The concept can be expressed by the following equation:

$$e_j(T) = \int \{A(e_j;t) + P'(e_j;t)\} dt \,, \tag{2}$$

where e is the model state of the jth member at time T, which can be simply evolved from the integration of two processes: A is the contribution of the resolved scales (model dynamics) and P is the total tendency coming from the parametrized processes (model physics). While model physics is assumed to be a more uncertain part, in SPPT (as in other methods representing model error), this term is perturbed and P' is calculated from the original P :

$$P'(e_j;t) = (1 + \alpha r_j) P_j(e_j;t) \,, \tag{3}$$

where r is random number.

In the revised SPPT scheme, a spectral pattern generator is introduced, which provide horizontally smooth fields of r. Its horizontal structure is defined by an L horizontal correlation length parameter. The scheme has been implemented in AROME model (*Bouttier et al.,* 2012), where r is represented by biFourier functions and r' spectral coefficients are defined as first order auto-regressive processes:

$$(r')_{mn}(t + \Delta t) = \Phi (r')_{mn}(t) + \sigma_n \mu_{nm}(t) \,, \tag{4}$$

where σ sets the size of the perturbation and μ is a random number picked from a Gaussian-distribution, which has 0 mean, 1 variance, bounded in interval [–2;2], and it is a white process in time. The correlation between time-steps is determined via a τ decorrelation time parameter:

$$\Phi = \exp(-\Delta t / \tau) \,. \tag{5}$$

In Eq. (4) α is an attitude dependent number which varies on [0;1] interval and it has 0 value at the highest and the lowest model levels because of numerical stability reasons, and it is set to 1 in middle-troposphere.

In our AROME-EPS tests, SPPT was active in the case of perturbed members and inactive in the case of the control forecast. σ=0.5 and τ=2 hours

settings were used and two different L parameters were applied: in the so-called 'SpptLong' test L=500 km and in the so-called 'SpptShort' test L=125 km. As it was in EDA related experiments, simple dynamical downscaling of PEARP is referred to as reference forecast. The impact of SPPT scheme is represented also via spread-skill relationship. This impact was found quite limited in this research: neither the RMSE of the ensemble mean has improved, nor the spread of the ensemble members has increased for the examined variables (*Fig. 13a*). The most sensitive parameter was the total cloudiness, but unfortunately, some model quality degradation in connection with the growth of the system's spread (*Fig. 13b*) was observed.Further examination is needed for better understanding of this limited impact. More tests are needed on summer periods, when a 'more active' atmosphere is expected to behave differently. The importance of control parameters (σ, τ, and L) also needs some additional clarification in our AROME model.

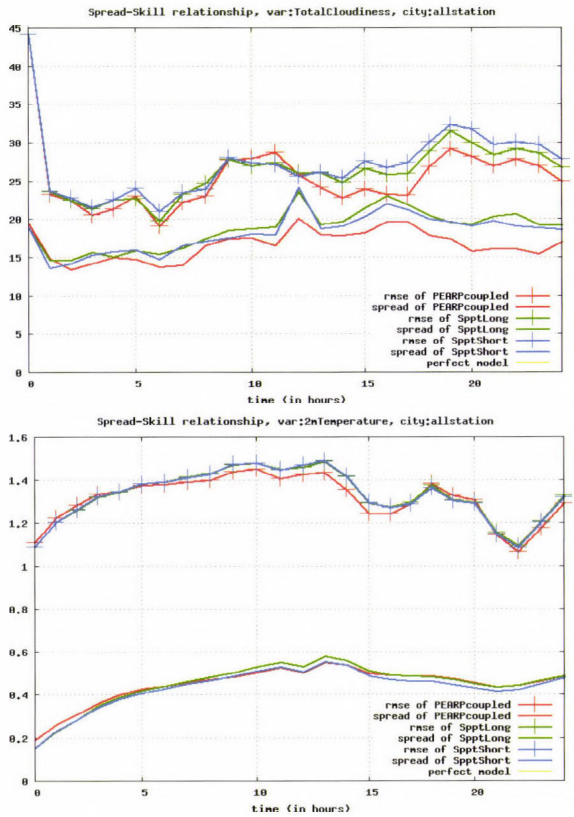

Fig. 13. Spread-skill relationship of 2 meter temperature (a) and total cloudiness (b). Red is a simple PEARP downscaling as a reference; blue and green are the test versions where SPPT scheme has been activated. Scores are calculated for the period between December 26, 2011 and January 8, 2012.

5. Summary and conclusions

In this paper, the AROME non-hydrostatic numerical weather prediction model as implemented at the Hungarian Meteorological Service was described with a focus on physical parameterizations and ensemble prediction. It was shown that high resolution NWP models are capable of predicting severe weather events. To achieve this, apart from increasing the horizontal and vertical resolution of the model, a non-hydrostatic dynamical core and advanced physical parameterizations have to be applied.

In connection with the dynamical core, aspects of horizontal diffusion in AROME were discussed. Recent developments regarding the semi Lagrangian horizontal diffusion scheme (SLHD) were described. It was shown that if SLHD is applied to all dynamical fields and not to falling hydrometeors then model performance – especially convective precipitation and wind gusts – could be improved.

The AROME model uses a state-of-the-art physical parameterization package, which was originally developed for the Meso-NH French research model. In this paper, some recent developments in connection with physical parameterizations performed at the Hungarian Meteorological Service were described. Regarding microphysics, the importance of the correct initialization of hydrometeor fields was highlighted. In connection with turbulence and shallow convection, the main ideas behind the eddy diffusivity – mass flux (EDMF) approach were discussed, and the positive impact of this parameterization on the resolved deep convection in the AROME model was shown. As the horizontal resolution of NWP models increases, surface processes are getting more and more important. In AROME, the SURFEX externalized surface model is utilized. Basic features of SURFEX were summarized as well as a recent development in connection with the prognostic treatment of vegetation.

To conclude the description of the deterministic AROME model, some verification scores were presented both for surface variables and upper levels. The performance of AROME was compared to other operational NWP models used at HMS. It was found that AROME has good performance for those meteorological variables (wind gusts and high precipitation amounts) which are linked to severe weather events.

As the horizontal resolution of NWP models is increasing, models are getting able to resolve even finer scales atmospheric phenomena. However, this not necessarily lead to better forecasts if forecast skill is measured locally (which is the case for most model applications). This is mainly related to localization problems in space and time. The application of the probabilistic approach could be a path to overcome this problem and handle the chaotic error growth in the model. In this paper, certain aspects of convection-permitting ensemble forecasts were highlighted and their impact was demonstrated using ensemble forecasts based on the AROME model. First, the ensemble data assimilation (EDA) method was

described, which aims at the correct determination of perturbed initial conditions for ensemble members. Secondly, one possible solution for the representation of model errors, namely, the stochastically perturbed parametrized tendencies (SPPT) approach was described. Based on the experiments performed with the AROME-EPS, it can be concluded that the EDA approach could significantly improve the high resolution ensemble forecasts, while the SPPT scheme has limited impact in its current configuration.

Acknowledgements: Useful discussions in the framework of the COST ES0905 project ('Basic concepts for convection parameterization in weather forecast and climate models') which contributed to the sections about dynamics and physics are greatly acknowledged. The authors are thankful to *Filip Vana* and *Lisa Bengtsson* for discussions about the SLHD scheme. The work about prognostic vegetation with the SURFEX model was carried out in the frameworks of the Geoland2 and ImagineS EU FP7 projects. AROME-EPS related tests were realized in the framework of an ECMWF's special project, called 'Continental winter weather prediction with the AROME ensemble prediction system', where HMS participate together with Météo France. We are really grateful to the project partners, and personally to *Francois Bouttier*. Remarks of the anonymous reviewer which lead to an improvement of the manuscript are greatly acknowledged.

References

Benard, P., Vivoda, J., Masek, J., Smolikova, P., Yessad, K., Smith, C., Brozkova , R., and *Geleyn, J.-F.,* 2010: Dynamical kernel of the Aladin-NH spectral limited-area model: Revised formulation and sensitivity experiments. *Q. J. Roy. Meteor. Soc., 136*, 155–169.

Bengtsson, L., Tijm, S., Váňa, F., and *Svensson, G.,* 2012: Impact of Flow-Dependent Horizontal Diffusion on Resolved Convection in AROME. *J. Appl. Meteor. Climatol. 51*, 54–67.

Bougeault, P. and *Lacarrere, P.,* 1989: Parameterization of orography-induced turbulence in a meso-beta-scale model. *Mon. Weather Rev. 117*, 1870–1888.

Bouttier, F., Vié, B., Nuissier, O., and *Raynaud, L.,* 2012: Impact of Stochastic Physics in a Convection-Permitting Ensemble. *Mon. Weather Rev., 140*, 3706–3721.

Bölöni, G., 2006: Development of a variational data assimilation system for a limited area model at the Hungarian Meteorological Service. *Időjárás 110*, 309–327.

Brousseau, P., Berre, L., Bouttier, F., and *Desroziers, G.,* 2011: Background-error covariances for a convective scale data-assimilation system: Arome-France 3D-Var. *Q. J. Roy. Meteor. Soc. 137*, 409–422.

Bubnová, R., Hello, G., Bénard, P., and *Geleyn, J.-F.,* 1995: Integration of the fully elastic equations cast in the hydrostatic pressure terrain-following in the framework of the ARPEGE/ALADIN NWP system. *Mon. Weather Rev. 123*, 515–535.

Buizza, R., Tribbia, J., Molteni, F., and *Palmer, T.,* 1993: Computation of optimal unstable structures for a numerical weather prediction model. *Tellus 45A*, 388–407.

Buizza, R.,. Miller, M., and *Palmer, T.N.,* 1999: Stochastic representation of model uncertainties in the ECMWF Ensemble Prediction System, *Q. J. Roy. Meteorol. Soc. 125*, 2887–2908.

Calvet, J.C., Noilhan, J., Roujean, J.L., Bessemoulin, P., Cabelguenne, M., Olioso, A., and *Wigneron, J.P.,* 1998: An interactive vegetation svat model tested against data from six contrasting sites. *Agr. Forest Meteorol. 92*, 73–95.

Cuxart, J., Bougeault, P., and *Redelsberger, J.-L.,* 2000: A turbulence scheme allowing for mesoscale and large-eddy simulations. *Q. J. Roy. Meteor. Soc. 126*, 1–30.

Desroziers, G., Berre, L., Chabot, V., and *Chapnik, B.,* 2009: A posteriori diagnostics in an ensemble of perturbed analyses. *Mon. Weather Rev. 137*, 3420–3436

Douville, H., Royer, J.-F., and *Mahfouf, J.-F.,* 1995: A new snow parameterization for the French community climate model. Part I: Validation in stand-alone experiments, *Clim. Dynam., 12*, 21–35.

Fischer, C., Montmerle, T., Berre, L., Auger, L., and *Stefanescu, S.E.,* 2005: An overview of the variational

assimilation in the Aladin/FranceNWP system. *Q. J. Roy. Meteor. Soc. 131,* 3477–3492.

Gebhardt, C., Theis, S., Krahe, P. and *Renner, V.,* 2008: Experimental ensemble forecasts of precipitation based on a convection-resolving model. *Atmos. Sci. Lett. 9,* 67–72.

Horányi A., Ihász I. and *Radnóti G.,* 1996: ARPEGE/ALADIN: A numerical weather prediction model for Central-Europe with the participation of the HMS. *Időjárás 100,* 277–301.

Horányi A., Mile M., and *Szűcs M.,* 2011: Latest developments around the ALADIN operational short-range ensemble prediction system in Hungary, *Tellus 63A,* 642–651.

Kain, J.S., and Fritsch, J.M., 1990: A one-dimensional entraining/detraining plume model and its application in convective parameterizations. *J. Atmos. Sci.* 47, 2784–2802.

Lafore, J.-P., Stein, J., Asencio, N., Bougeault, P., Ducrocq, V., Duron, J., Fischer, C., Héreil, P., Mascart, P., Masson, V., Pinty, J. P. , Redelsperger, J. L. , Richard, E. and Vilà-Guerau de Arellano J., 1998: The Meso-NH atmospheric simulation system. Part I: Adiabatic formulation and control simulations. *Ann. Geophys., 16,* 90–109.

Lappen, C.L. and *Randall, D. A.,* 2001: Toward a unified parameterization of the boundary layer and moist convection, Part 2: lateral mass exchanges and subplume-scale fluxes. *J. Atmos. Sci. 58,* 2037–2051.

Masson, V., 2000: A physically-based scheme for the urban energy budget in atmospheric models, *Bound.-Lay. Meteorol. 94,* 357–397.

Masson, V. and *Seity, Y.,* 2009: Including atmospheric layers in vegetation and urban offline surface schemes, *J. Appl. Meteorol. Clim. 48,* 1377–1397.

Migliorini, S., Dixon, M., Bannister, R., and *Ballard, S.,* 2011: Ensemble prediction for nowcasting with a convection-permitting model. I: Description of the system and the impact of radar-derived surface precipitation rates. *Tellus 63A,* 468–496.

Mile, M., Bölöni, G., Randriamampianina, R., Steib, R., and *Kucukkaraca, E.,* 2015: Overview of mesoscale data assimilation developments at the Hungarian Meteorological Service. *Időjárás 119,* 215–239.

Mironov, D., Heise, E., Kourzeneva, E., Ritter, B., Schneider, N., and *Terzhevik, A.,* 2010: Implementation of the lake parameterisation scheme flake into the numerical weather prediction model COSMO. *Boreal Env. Res. 15,* 218–230.

Le Moigne, P., 2012: SURFEX scientific documentation. Note de centre du Groupe de Météorologie a Moyenne Echelle, 87, Météo-France, CNRM, Toulouse, France, on-line available at: http://www.cnrm.meteo.fr/surfex/

Noilhan, J., and *Planton, S.,* 1989: A simple parameterization of land surface processes for meteorological models, *Mon. Weather Rev. 117,* 536–549.

Noilhan, J., and *Mahfouf, J.-F.,* 1996: The ISBA land parameterization scheme, *Global Planet. Change 13,* 145–159.

Pergaud, J., Masson, V., Malardel, S., and *Couvreux, F.,*2009: A parameterization of dry thermals and shallow cumuli for mesoscale numerical weather prediction, *Bound.-Lay. Meteor., 132,* 83–106.

Randriamampianina, R., 2006: Impact of high resolution observations in the ALADIN/HU model, *Időjárás 110,* 329–349.

Palmer, T.N., and *Tibaldi, S.,* 1988: On the prediction of forecast skill, *Mon. Weather Rev. 166,* 245.

Palmer, T., Buizza, R., Doblas-Reyes, F., Jung, T., Leutbecher, M., Shutts, G., Steinheimer, M., and *Weisheimer, A.,* 2009: Stochastic parametrization and model uncertainty. *Tech. Rep., ECMWF Tech. Memo. 598.* Available online at http://www.ecmwf.int/publications/.

Pinty, J.-P., and *Jabouille, P.,* 1998: A mixed-phased cloud parameterization for use in a mesoscale non-hydrostatic model: Simulations of a squall line and of orographic precipitation. *Preprints, Conf. on Cloud Physics, Everett, WA, Amer. Meteor. Soc.,* 217–220.

Seity, Y., Brousseau, P., Malardel, S., Hello, G., Bénard, P., Bouttier, F., Lac, C., and *Masson, V.,* 2011: The AROME-France Convective-Scale Operational Model. *Mon. Weather Rev. 139,* 976–991.

Toth, Z. and *Kalnay, E.,* 1997: Ensemble forecasting at NCEP and the breeding method. *Mon. Weather Rev. 127,* 3297–3318.

Vána, F., Bénard, P., Geleyn, J.-F., Simon, A., and *Seity, Y.,* 2008: Semi-Lagrangian advection scheme with controlled damping: An alternative to nonlinear horizontal diffusion in a numerical weather prediction model. *Q. J. Roy. Meteor. Soc. 134,* 523–537.

Vié, B., Nuissier, O., and *Ducrocq, V.,* 2011: Cloud-resolving ensemble simulations of Mediterranean heavy precipitating events: Uncertainty on initial conditions and lateral boundary conditions. *Mon. Weather Rev. 139,* 403–423.

IDŐJÁRÁS

Quarterly Journal of the Hungarian Meteorological Service
Vol. 119, No. 2, April – June, 2015, pp. 267–275

Meteorological support, weather warnings and advisories in the Hungarian Defence Forces

Richárd Büki[1]* and **Kornélia Radics**[2]

[1]*Geoinformation Service of the Hungarian Defence Forces*
Szilágyi Erzsébet fasor 7–9., H-1024 Budapest, Hungary

[2]*Hungarian Meteorological Service,*
Kitaibel Pál u. 1., H-1024 Budapest, Hungary

**Corresponding author E-mail: buki.richard@mhtehi.gov.hu*

(Manuscript received in final form April 25, 2014)

Abstract—During the history, it has been proved several times that ignoring the quickly changing meteorological circumstances and atmospheric phenomana or their insufficient assessement can result in catastrophic impacts on military operations. Weather plays a very significant role in flight operations, and it can be vital even for planning and executing operations of land forces and for any other open air activities involving armed forces (e.g., disaster relief activities, industrial and natural catastrophes, and in assessement of chemical, biological, radiological, and nuclear events). The possible course of weather and the range of the climatological factors should be taken into consideration for protecting life, property and infrastucture.

In the Hungarian Defence Forces, the focus of the meteorological support is on providing the necessary meteorological information for decision makers supporting the planning and executing certain military activities, and enhancing efficiency. This is a very complex task and that is the reason for having specialized meteorological service and capability within the Hungarian Defence Forces which can meet these requirements.

The military weather warnings and advisories ("military weather warnings") are specialized type of forecasts. They alert the military users on the possible or expectable severe weather, which can significantly impact life and property in order to mitigate the unfavorable effects of the severe weather. For avoiding misinformation in the meteorological support in our daily routine, the military weather warnings should be in harmony with the weather warnings issued by the Hungarian Meteorological Service for civilian users, which is enabled by the strong and efficient cooperation between the two services.

This paper describes some effects of weather on military activities in general and military weather warnings within the Hungarian Defence Forces.

Key-words: weather impact, warning, advisory, severe weather, military

1. Introduction

In order to deeply understand how civilian and military meteorology differ, firstly it is needed to be defined. By definition, the military meteorology is the science concerned with the collection and analysis of the understandings of the physical characteristics of the past, current, and predicted states of the atmosphere, including space, and the ability to exploit this information for the planning and conduct of military activities.

This paper highlights those weather elements that affect the different branches of the Hungarian Defence Forces.

2. Impacts of different meteorological elements on military activities

2.1. Barometric pressure

The weight of the air affects gunnery computations and ballistic preformance in armour operations.

The air pressure affects artillery operations due to projectile trajectory, barofuzing, and fire control calculations. Moreover, the vertical pressure profiles are essential in both baroarming and barofuzing as they are required for calculating densities for ballistic firing data (*METOC Effects Smart Book, (http://www.fas.org)* – Homepage of the Federation of American Scientist, 2002).

Aviation is one of the main user of barometric pressure data. Densitiy altitude, which is in strong connection with the barometric pressure, determines if an aircraft has enough lift capabilities and performance to get off the ground. Too much densitiy altitude limits fuel, weapons, and passenger loads.

2.2. Clouds and sky cover

Low overcast clouds limit the effectiveness of aerial illumination devices. Overcast clouds tend to limit heating of inactive targets and lower target detection ranges for thermal sights. NVG (night vision googles) are limited by clouds blocking natural light from the moon and stars. Close air support and aerial resupply missions are degraded by low clouds. Low ceilings affect target acquisition systems and terminally guided munitions. Low overcast clouds will limit the effectiveness of aerial illumination devices (*METOC Effects Smart Book, (http://www.fas.org)* – Homepage of the Federation of American Scientist, 2002).

Clouds are always a major consideration for aviation operations. Low overcast clouds will limit the effectiveness of aerial illumination devices. Overcasts tend to limit heating of inactive targets and lower target detection range for thermal sights. NVG are limited by clouds blocking natural illumination from the moon or the stars. Best use of most NVG requires about a

quarter of the moon, 30 degrees above the horizon, scattered clouds, and the sun more than 5 degrees below the horizon. Close air support and aerial resupply missions are degraded by low clouds.

From a CBRN (chemical biological radiological and nuclear) point of view, persistent overcast low clouds usually indicate a neutral condition for the hazardous materials, while broken low clouds indicate an unstable condition during the day and a moderately stable condition at night.

Overcast skies with low cloud bases reduce the effectiveness of infrared and photographic collection systems, and may restrict the use of UAVs (unmanned aerial vehicle).

2.3. Humidity

Coupled with high temperatures, high humidity decreases crew effectiveness in closed vehicles. The humidity should be taken into consideration in artillery operations due to its use to compute virtual temperatures for ballistic firing data.

High humidity destroys some chemical agents such as lewisite and phosgene because of rapid hydrolysis. High humidity increases the effectiveness of HC and phosphorous smokes, some chemical agents, and both wet and dry forms of biological agents. High humidity improves the effectiveness of wet aerosols by reducing evaporation, while low humidity assists agent aerosols (*METOC Effects Smart Book, (http://www.fas.org)* – Homepage of the Federation of American Scientist, 2002).

Extreme humidities affect handling, storage, and use of building materials. When coupled with high temperatures, humidity affects personnel and significantly increases the time to perform physical work.

2.4. Precipitation and icing

Rain and snow degrade trafficability and limit visibility. They also degrade target acquisition and NVG. Rain and snow affect visibility and the safety of both crew and airframe.

Rain and snow will effect the persistence of chemical agents and may produce radioactive rainout and hot spots. Snow may cover and neutralize certain liquid agents. Rain may even work as a decontaminate. On the other hand, some agents may be very persistent on snow (*METOC Effects Smart Book, (http://www.fas.org)* – Homepage of the Federation of American Scientist, 2002).

High rainfall rates influence river currents, water depth, and bridging operations. It complicates other construction or maintenance jobs, affects flooding, rivercrossings, soil bearing strength, and explosives.

Ice on lifting surfaces affects the aerodynamics of the aircraft. Even a little ice is a big problem.

Even moderate amounts of rain and snow will obstruct vision and degrade photographic and infrared data collection systems (*METOC Effects Smart Book, (http://www.fas.org)* – Homepage of the Federation of American Scientist, 2002).

2.5. Wind and turbulence

Trajectory projections and first round hit capability can be affected by high crosswinds. Winds affect the accuracy of rocket fire and firefinder radar trajectory computations (*METOC Effects Smart Book, (http://www.fas.org)* – Homepage of the Federation of American Scientist, 2002).

Strong winds aloft impact all ballistic projectile aiming calculations. Accurate and timely meteorological data can compensate for the problem. Wind profiles play a major role in ballistic wind compensations for artillery firing.

Strong winds, especially cross-winds, affect aircraft control near the ground during take-off and landings. Turbulence is a critical condition affecting all aviation assets and missions. It may cause aircraft structural damage or even crashes during take-offs and landings. Severe turbulence may cancel all operations.

Winds play a significant role in CB (chemical and biological) agent dispersion, chemical agent persistence, and aerial delivery methods. Very light and strong winds degrade effectiveness of smoke and CBRN operations. Wind direction is considered for fallout pattern determination.

Ground level winds affect river crossings, port management, and all watercraft. Construction projects in chronic wind areas may need to recalculate structural strength figures. Strong winds may damage or prevent installing antennas.

2.6. State of the ground

Frozen ground improves mobility and significantly increases the time available to prepare fighting positions. Deep snow slows movement of tracked vehicles. Frozen ground and mud affects munitions, sensors, and indirect fire.

Soil conditions impact the effectiveness of chemical agents. Bare, hard ground favors short-term effectiveness and high-vapor concentrations. If the surface is porous, such as sand, the liquid agent quickly soaks in. Vegetative cover reduces exposure to ultraviolet light and favors the survival of wet aerosols (*METOC Effects Smart Book, (http://www.fas.org)* – Homepage of the Federation of American Scientist, 2002). Wet soil degrades the effectiveness of smoke munitions.

Ground conditions impact mining operations, trenching, and any excavation job. Snow cover can impact the emplacement of scatterable mines.

Ground state affects trafficability and movement rates. Frozen ground improves mobility and will increase the time available for preparing fighting positions.

Wet grounds can affect trafficability and movement rates. Frozen ground improves mobility and significantly increases time available for preparing fighting positions. Deep snow slows movement of tracked vehicles. Frozen ground affects systems such as mines, sensors, and indirect fire.

2.7. Temperature, frost line, and thaw depth

High and low temperatures influence the type of lubricants to be used, engine warm-up periods, and sustained rates of fire for weapons.

High temperatures decrease the time personnel can remain in vehicles. High temperatures cause gun tube droop, shimmering, mirages, and vehicle exteriors to be too hot to touch. Extremely high temperatures increase water consumption.

Low temperatures degrade the ballistics of main guns, require frequent starting of engines, and may increase maintenance problems and possible detection by the enemy. Extremely low temperatures reduce personnel effectiveness and decrease the availability of water because of freezing.

Temperature profile affects calculations of ballistic artillery firing. The profile is used to compute virtual temperatures for artillery firing. Extreme cold affects gun accuracy and fuse functioning.

High temperatures reduce lift capability. Cold temperatures increase maintenance requirements and the time needed to accomplish each task. The number of personnel that can be carried on a flight is reduced due to the weight of cold-weather gear.

Some agents are more persistent at low temperatures. Vaporization may be a problem with higher temperatures. Normal atmospheric temperatures have little direct effect on a biological agent aerosol. Sub-freezing temperatures make water-based decontamination methods ineffective.

High temperatures impact trafficability, influence flood control, and dictate the use of certain construction materials. Cold weather influences ice thickness and river crossings, while ice flow problems affect bridges. For example, armored vehicle launched bridges are affected by warming if they were set up on frozen ground. Alternating freezing and thawing (frost heaves) may destroy the effectiveness of emplaced mines.

Frozen soil increases the difficulty of grounding equipment. At extreme cold temperatures, cables snap and wire is unmanageable. Extreme cold also shortens battery life and may put systems requiring a good source of battery power out of service.

Too cold or too hot conditions dictate the type of lubricants to be used, engine warm-up periods, and sustained rate of fire for weapons. Extreme low temperatures reduce personnel effectiveness, and decrease the availability of water because of freezing. Temperatures changing from above to below freezing can freeze stationary tracks into the mud. High temperatures cause gun tube "droop," shimmering, mirages, and vehicle exteriors to be too hot to touch.

The frost line impacts site selection, construction, excavation, and trafficability.

2.8. Visibility

Visibility affects visual target acquisition, fire adjustment, and electro-optical (E-O) target designation. Reduced visibility affects the placement of forward observers and fire support teams (*METOC Effects Smart Book, (http://www.fas.org)* – Homepage of the Federation of American Scientist, 2002).

The lack of good visibility affects landings and take-offs, terminally guided munitions, and the ability to distribute scatterable mines.

Low visibility decreases the effectiveness of visual, photographic, infrared, and E-O collection systems.

Poor visibility increases the survivability of infantry units.

2.9. Thunderstorms and lightning

Electrical storms restrict the use of and handling some munitions and fuse types because of safety.

Extreme weather that includes thunderstorms and lightning is very hazardous to inflight operations, refueling, and rearming operations.

Electrical storms, and the associated rain and wind, affect electronic systems in general and antennas, shelters, and mobility in particular.

3. Weather warnings and advisories

Certain weather conditions endanger life and/or property, pose a safety hazard, or adversely impact operations. Weather units should monitor these phenomena and provide products and services to support the possbily affected services and units when these conditions are observed or forecasted. These items include weather advisories and warnings.

A weather warning (WW) is a special notice provided to supported customers that alerts them to very likely weather conditions of such intensity that could pose a hazard to life or property.

A weather advisory (WA) is a special notice provided to supported customer that alerts them the likely potential of weather conditions that could affect their operations.

Within the Hungarian Defence Forces (HDF), the meteorological support is clearly defined in a Manual on Supporting Military Activities signed by the Chief of General Staff. This manual is the highest level document, and it is a framework for the main principles, duties ans goals in the field of military meteorological support.

Each unit involved in military meteorological support has its Standard Operating Procedure (SOP). This SOP deals with the aspects of military meteorolgical support at a certain unit in detail (including range of product, duties and responsibilities, order of reporting, threshold values for different weather elements if they apply). The SOPs are completed by the respective meteorological unit and approved by the Geoinformation Service of the HDF (GEOS).

GEOS is the supervising unit in the field of military meteorology in Hungary. There is a Weather Forecast and Training Department within the GEOS providing the personnel for the continuous meteorological support and professional supervision over the meteorolgical support acitivities carried out in the HDF.

As the leading professional meteorological unit of the HDF, GEOS is entitled to issue WWs and WAs for the whole activity spectrum of the HDF and MoD including excercises, troop movement, tansport, and any other open air activities.

There are three types of WAs and WWs isued by GEOS:

- Preliminary General WA is a forecast in plain text format for general military users with 24–72 hours lead time.
- General WA is a forecast in plain text format for general military users with 3–24 hours lead time.
- WW is a forecast in plain text for general military users with 1–3 hours lead time (*Fig. 1*).
- In every case when a WA or WW has been issued, its receipton is verified by phone call and sent via electronically as well.

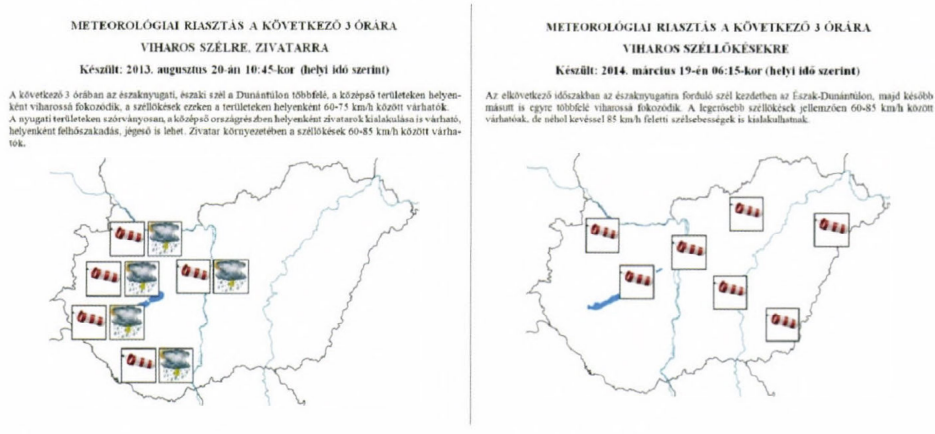

Fig. 1. Two examples for weather warnings issued by GEOS.

The Meteorological Center of the Air Command and Control Center of HDF (ACCC) provides meteorological support for the military aviation in Hungary and entitled to issue aviational WWs in harmony with the WWs and WAs issued by GEOS. The WWs are in a text and map combination format with an abbreviated form of text explanation (*Fig. 2*). The issued WWs are sent to GEOS and the MSUs at the airfields.

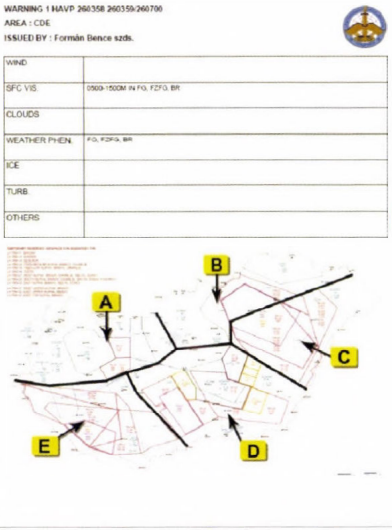

Fig. 2. An example for weather warning issued by ACCC.

Different weather warnings and advisories by Hungarian military MSUs are summarized in *Table 1*.

Table 1. WAs and WWs

No.	Station	Airbase	Lon [° E]	Lat [° N]	Altitude [m]	To
1	Kecskemét	59. Szentgyörgyi Dezső Air Base	19.75	46.91	114.0	designated local users GEOS ACCC
2	Szolnok	86. Szolnok Helicopter Base	20.13	47.17	90.0	designated local users SARS GEOS ACCC
3	Pápa	Pápa Airbase	17.50	47.37	146.6	designated local users Heavy Airlift Wing Search and Rescue Service GEOS ACCC

4. Conclusions

The weather and its effect can pose significant threat to life and property. This is valid to a wide range of military activities; therefore, it is vital to operate a capable, well structured, and regulated system of meteorological support. In order to fulfil its mission, every level of the military meteorological support in Hungary provides in-time weather warnings and weather advisories to mitigate the possible negative effects of weather.

References

METOC Effects Smart Book, (http://www.fas.org) – Homepage of the Federation of American Scientist, 2002

IDŐJÁRÁS

Quarterly Journal of the Hungarian Meteorological Service
Vol. 119, No. 2, April – June, 2015, pp. 277–306

Forecasting of wet- and blowing snow in Hungary

Katalin Somfalvi-Tóth[1], **János Tordai**[2], **André Simon**[1*], **Kornél Kolláth**[1], and **Zsuzsanna Dezső**[2]

[1]*Hungarian Meteorological Service,*
Kitaibel Pál u. 1., H-1024 Budapest, Hungary

[2] *Department of Meteorology, Eötvös Loránd University,*
Pázmány Péter sétány 1/a, 1117 Budapest, Hungary

**Corresponding author E-mail:simon.a@met.hu*

(Manuscript received in final form September 8, 2014)

Abstract—Deep cyclones, originating in the Mediterranean area, are frequently the cause of heavy precipitation and environments characterized by large temperature gradients and strong wind. In winter period, several types of precipitation can be observed in such situations, including freezing rain and wet snow, which can cause serious damage on the electricity power lines or other infrastructure. On March 14–15, 2013, deep snowdrifts resulted in blocking of thousands of vehicles on Hungarian highways. Similar cases motivated the research of these phenomena in Hungary, using and adapting empirical approaches to calculate wet snow loads on wires or to calculate the blowing snow index (BSI) to assess the intensity of the snowdrifts development. Forecasting of these parameters is possible by using inputs from global and limited numerical weather prediction models (ECMWF, WRF). The paper describes methods for wet- and blowing snow diagnostics and classification of their intensity. The results are demonstrated on case studies and supported by observations and available damage reports. The possibility of further refinement of the diagnostics and its operational application is also discussed.

Key-words: wet snow, blowing snow, forecasting, winter weather, numerical models, WRF, diagnostics

1. Introduction

Wet snow is defined as "deposited snow that contains a great deal of liquid water" (*Glickman et al.*, 2000). It typically occurs during snowfall within the temperature range between 0 and +3 °C (*ISO*, 2001), though, snow accretion on structures have sometimes been observed also by temperatures below zero

(*Sakamoto*, 2000). The liquid water content of the accreted wet snow is usually between 5 and 40% (*Admirat*, 2008). Heavy and long-lasting snowfall in such conditions can develop considerable snow loads on wires, sometimes in order of several tens of N/m (*Makkonen* and *Wichura*, 2010). Serious problems with electricity failures caused by wet snow are frequently reported in cold regions or in mountains (*Eliasson et al.*, 2013; *Bonelli et al.*, 2011).

The study of wet snow occurrence in Hungary started in 2009, and it was related to situation with heavy snowfall and large damage on electricity power lines in the southwest part of Hungary on January 27–28, 2009 (*Tóth et al.*, 2009). Methods of *Sundin* and *Makkonen* (1998), *Poots* (1996), and *Admirat* (2008) were tested with use of both observational data and analysis and forecasts of the WRF (Weather Research and Forecasting) model (*Skamarock et al.*, 2008). The method of Admirat has recently been refined and adapted with respect to long- term observations (*Nygaard et al.*, 2013). In Hungary, in some years, up to 35 wet snow events can occur (*Gulyás et al.*, 2012) a substantial portion of these events is related to intense cyclogenesis in the Mediterranean area and frequent passages of cyclones over or near Hungary. These are characterized by widespread and high amount of often mixed-phase precipitation, including wet snow. Adjusted diagnostics of wet snow accretion and estimation of the snow sleeve mass and diameter was tested in these types of situations and the analyses and forecasts obtained from the WRF model run at relatively high (2.7 km) resolution were investigated and compared with available observations and reports. Drifting or blowing snow occurrence in Hungary can be sometimes related to intense cyclogenesis over the Mediterranean as well (it usually develops on the northwestern flanks of propagating cyclones). Similarly to wet snow, combination of several meteorological parameters (snowfall, wind, snow density, snow depth, surface temperature) must be taken into account during forecasting of blowing snow. Over the past years, several methods were elaborated in order to study and forecast its development (*Baggaley* and *Hanesiak*, 2005). There were attempts to parameterize the blowing snow as function of wind, temperature, and state of the snow surface (*Li* and *Pomeroy*, 1997). These studies motivated the development of a comprehensive index (blowing snow index or BSI) for forecasting blowing snow in Hungary. The index was proposed with a purpose of easier evaluation of blowing snow conditions and more precise determination of areas eventually threaten by snow drifts. The method was developed upon several case studies and recently tested during severe wind- and snowstorms of January 18 and March 14–15, 2013, which hit the western part of Hungary. Above all, the usefulness of the short-range (mainly 24h) forecasts of the BSI distribution in the forecasting praxis was evaluated and compared with available observations.

This paper is divided in five sections. In the next one, we describe the methods of the wet- and blowing snow diagnostics, in Section 3 we explain the synoptic background of some major (or interesting) weather events, and we

present the corresponding results (forecasts compared with observations) in Section 4. Conclusions are given in Section 5.

2. Methodology

2.1. Method of wet snow diagnostics

Admirat (2008) proposed a formula for calculation of the diameter Φ (m) of the snow sleeve accumulated on the wire. He expected that the snow sleeve has nearly cylindrical shape and started from the relationship between the variation of Φ and the mass M (kg/m), supposing that the density of the accreted snow ρ_s (kg/m^3) is constant:

$$\Phi \frac{d\Phi}{dt} = \frac{2}{\pi \rho_S} \frac{dM}{dt}. \tag{1}$$

The time variation of the mass is proportional to flow R of the snow, which passes a rectangle surface S (of unitary length and of width equal to Φ). It is expected that the airflow in front of the wire is perpendicular with respect to this surface. The basic formula for the flow (similar to the formula for accretion intensity in *Nygaard et al.*, 2013) yields:

$$R = c \sqrt{u^2 + w^2}\, S, \tag{2}$$

where u is the horizontal wind speed, w is the terminal velocity of snowflakes (both in m/s), and c is the mass concentration of wet snow in the air. Because c is usually not directly measured, it is often parameterized from water equivalent precipitation intensity at the ground P (mm/h):

$$c = \frac{P}{3600 w}. \tag{3}$$

Thus, the time variation of the mass can be expressed as:

$$\frac{dM}{dt} = \beta R = \frac{\beta P}{3600} \sqrt{1 + \frac{u^2}{w^2}}\, \Phi. \tag{4}$$

In Eq. (4), the parameter β is the collection coefficient (sometimes named also as coefficient of sticking efficiency). It expresses that only a part of the snowflakes crossing the area of the wire is accreted (some snowflakes will not accrete due to curvature of the flow around the wire or some snowflakes break up).

The final formula of *Admirat* (2008) for the diameter variation can be obtained from the combination of Eqs. (1) and (4):

$$\frac{d\Phi}{dt}=\frac{2K}{\pi\rho_S}, \tag{5}$$

where $K=\frac{\beta P}{3600}\sqrt{1+\frac{u^2}{w^2}}$.

Neither β nor ρ_S are measured or calculated in the used numerical models and these variables had to be parameterized. It is often expected that β is indirectly proportional to wind speed (*Admirat*, 2008), however, it was shown that such approach significantly decreases the role of wind in the snow accretion model described by Eq. (5). *Nygaard et al.* (2013) proposed a computation of beta, denoted BETA_U, in which beta is indirectly proportional to the square root of the wind speed u ($\beta=1/\sqrt{u}$), which has been used in this study. The density of the accreted snow can vary between 100 and 800 kg/m^3 (including extreme cases), and laboratory studies indicate that it is also dependent on the wind speed. One of the suggested empirical formulas (*Admirat*, 2008) used in the presented wet snow calculations yields:

$$\rho_S = 200 + 20u. \tag{6}$$

Because w is usually also not observed at synoptic stations, it is supposed to be constant in many wet snow studies. Here a value of 1.5 m/s was used, which is in the middle between $w=1$ m/s proposed by *Admirat* (2008) and the average fall velocities of wet snow ($w=2$ m/s) reported by *Yuter* (2006).

For diagnostics, based on data from synoptic stations with direct observation of the weather type, wet snow was considered if the 2 m temperature was between 0 and +3 °C and if snowfall, corresponding to 70–75 codes of the SYNOP report (*WMO*, 1995), was present at the same time. Because there were no reports of the liquid water content, we used the assumption that there must be a positive heat flux from the environment to the snowflakes, so that the snow surface can melt and accrete. It can be shown that this is equivalent to condition that the environmental wet-bulb temperature t_w is positive (*Makkonen*, 1989):

$$t_w > 0 \tag{7}$$

For NWP data, the same temperature conditions for wet snow were used as in case of observed data. It was supposed that the fraction of frozen precipitation (FR)

had to be between 0.7 and 0.98 as used in the BETA_U model (denoted as FR method in this paper). We also tested a method, where snowfall was distinguished from liquid precipitation upon the 850/1000 hPa relative topography – $RT_{850/1000}$ (*Cantin* and *Bachand*, 1993). *Hirsch* (2006) showed that in the area of Hungary snowfall might be usually expected by $RT_{850/1000} \leq 1300\ gpm$. This method was chosen because it is often used in the operational forecasting, and it could be very simply applicable on basic model fields or sounding data. Because the $RT_{850/1000}$ method does not provide any information about the liquid water content of the precipitation, we used the condition Eq. (7) to distinguish between wet- and dry snow. The FR and the $RT_{850/1000}$ criterions calculated from model forecasts were also applied on wet snow diagnostics at synoptic stations, where no direct observation of the precipitation type was available.

Eq. (5) has been integrated for a 24-hour period with 1-hour timesteps, during which P and u were considered to be constant (u was equal to the average of the wind at the start and end of the step). As final output, we visualized the difference ($\Delta\Phi$) between the diameter of the snow sleeve and the diameter of the wire without snow d, which is taken equal to 0.031 m (typical diameter of transmission wires). The advantage of calculating $\Delta\Phi$ is that it can be relatively easily measured or even visually estimated (e.g., upon photographs).

The estimation of the snow mass on the wire was based on combination of Eqs. (4) and (5):

$$\frac{dM}{dt} = K\Phi. \tag{8}$$

If the wind is assumed to be constant for the whole wet snow period, the diameter can be converted to snow mass with use of a simple geometrical relationship (expecting nearly cylindrical shape of the snow accumulation):

$$M = \frac{\rho_S \pi}{4}\left(\Phi^2 - d^2\right). \tag{9}$$

Upon several cases and damage reports in Hungary, it was proposed to issue warning in cases where certain threshold of calculated snow mass or increase in the diameter would be exceeded (*Table 1*). However, alertness in some situations can be recommended already by lower values (2–3 cm diameters of snow accumulation), especially if higher snow density can be expected or if the wet snow event is combined with strong wind (so-called wind-on-ice load).

Melting of snow is not yet included in the presented wet snow diagnostics. This can eventually cause overestimation, especially when the wet snow parameters are integrated for a long period, during which the character of the weather significantly changes (but this was not typical for the evaluated cases).

Table 1. Proposal on wet snow warning thresholds upon calculated mass and diameter of snow accumulation on wires (*Somfalvi-Tóth*, 2014). The values of $\rho_S = 300$ kg/m^3 and d=0.031 m were chosen for this conversion, based on Eq. (9)

Wet snow mass M [kg/m]	Increase of the snow-sleeve diameter $\Delta\Phi$ [cm]	Proposed level of warning
1.5	5.5	1
3	8.6	2
5	11.8	3

2.2. *Method of blowing snow diagnostics*

In situations with blowing snow we evaluated the so-called blowing snow index (BSI) parameter (*Tordai*, 2012). The index evaluates six meteorological parameters, which can influence the development of snowdrifts. This influence is represented by weighting functions *f*. These can be negative – thus, one term itself can counteract positive contributions of other terms (e.g., snowdrifts are improbable by very low windspeed, even if other conditions would be optimal). The maximum values of the weighting functions are 1. The final formula for BSI sustains from the sum of the functions:

$$BSI = f(T)+f(T_s)+f(U)+f(G)+f(H)+f(\rho_H)\,, \tag{10}$$

where $f(T)$ represents temperature at 2 m, T_s is the surface (skin) temperature, U is the wind speed at 10 m, G is the wind gust at 10 m, H is the snow depth, and ρ_H is the snow density. The criteria and formulas for determination of each weighting function (given in *Table 2*) were based on the work of *Tordai* (2012), and it was only slightly modified for mathematical reasons. The thresholds in the weighting function calculations were determined upon observations and several case studies of blowing snow. The BSI can acquire negative values (if impact of certain components would strongly inhibit the development of blowing snow). The maximum possible value is 6 (very high probability of snowdrift development). Although BSI is rather related to probability of blowing (or drifting) snow occurrence, higher values of BSI usually also indicate higher intensity of snowdrift production. It has been observed that blowing snow is probable by BSI exceeding 2, values exceeding 3.5 are already significant and are usually accompanied by light or moderate development of snowdrifts.

Table 2. Determination of respective weight functions (f) in the calculation of the BSI index

State determinating parameter	Interval	Weight function
T [°C] (2 m temperature)	$T \leq -6.5$	$f(T)=1$
	$-6.5 < T \leq 0.5$	$f(T)=-0.0087T^2-0.1727T+0.2447$
	$T > 0.5$	$f(T)=-(0.0181T)^2-0.139T+0.2257$
T_S [°C] (Surface temperature)	$T_S \leq -3.0$	$f(T_S)=1$
	$-3.0 < T_S \leq -0.5$	$f(T_S)=-0.0406T_S^2-0.2436T_S+0.6342$
	$-0.5 < T_S \leq 2.0$	$f(T_S)=0.3397\exp(-1.5717\,T_S)$
	$T_S > 2.0$	$f(T_S)=-0.1264T_S^2+0.5056T_S-0.4915$
U [m/s] (10m wind)	$U < 4.0$	$f(U)=1.014U-4.014$
	$4.0 \leq U < 15.0$	$f(U)=-0.0076U^2+0.2314U-0.7616$
	$U \geq 15.0$	$f(U)=1$
G [m/s] (10m wind gust)	$G < 6.0$	$f(G)=-0.075G^2+1.1192G-3.9657$
	$6.0 \leq G \leq 21.0$	$f(G)=-0.0029G^2+0.1416G-0.6952$
	$G > 21.0$	$f(G)=1$
H [cm] (snow depth)	$H < 5.0$	$f(H)=0.0732H^2+0.6711H-4.9321$
	$5.0 \leq H < 31.0$	$f(H)=-0.0007H^2+0.0538H+0.0022$
	$H \geq 31.0$	$f(H)=1$
ρ_H [kg/m^3] (snow density)	$\rho_H < 100.0$	$f(\rho_H)=1$
	$100.0 \leq \rho_H < 240.0$	$f(\rho_H)=-1.83\times10^{-5}\rho_H^2+0.0019\rho_H+0.9912$
	$\rho_H \geq 240.0$	$f(\rho_H)=-0.0534\rho_H+13.207$

At the Hungarian Meteorological Service, warnings on blowing snow have already been issued prior to development of BSI, although the criteria for it were arbitrary. Upon these criteria, we developed a simple warning decision index (WDI) in order to compare the original formulation (*Table 3*) with a warning system proposed upon BSI thresholds (*Tordai*, 2012). When using BSI, it was recommended to issue first level (yellow) warning on blowing snow for values higher than 3.5. Strong development and second level (orange) warnings can be expected by BSI exceeding 4, and very severe blowing snow and third level of warnings (red) can occur by BSI equal to 4.5 or higher.

Both BSI and WDI were estimated upon data from synoptic station observations (and compared with forecasts of these parameters from numerical models). We considered only stations, where measurements of snow depth and density were available, or where it was possible to assess them using spatial and temporal interpolations. Instead of the skin surface temperature (which can eventually be the temperature of the snow surface, and it is usually not measured at the stations), we used the near-surface temperature measured 5 cm above the terrain. We also checked the reports on drifting- and blowing snow, which are

coded at certain synoptic stations (*WMO*, 1995). We assumed that the code on slight or moderate drifting snow (36) would nearly correspond to current yellow warning, the codes 37 (heavy drifting snow), 38 (slight or moderate blowing snow) to orange and the 39 code (heavy blowing snow) to red warning. Though, the original definitions of drifting and blowing snow are rather related to visibility conditions as to height or intensity of snowdrift production.

Table 3. Blowing snow warning criteria of the Hungarian Meteorological Service and corresponding WDI codes and algorithms. The meaning of parameters is the same as in Table 2, except for R_{24} (snow precipitation of past 24 hours, in mm) and R_{03} (snow precipitation of past 3 hours, in mm)

HMS warning criteria	Level of warning	WDI algorithm	WDI code
The wind produces snowdrifts of low depth occurring on territories covered by fresh snow	Yellow 1	$U \geq 4 m/s \quad H \geq 5 cm$	1
The wind accompanied by strong gusts (> 60 km/h) produces deep (depth locally > 0.5 m) snowdrifts on territories covered by fresh snow	Orange 2	$U \geq 4 m/s \quad H \geq 5 cm$ $G \geq 16.7 m/s \quad R_{24} \geq 1 mm$	2
The wind accompanied by strong gusts (> 60 km/h) produces deep (depth > 0.5 m at many places) snowdrifts on territories covered by fresh snow. Besides, snowfall can be still expected (several cm of fresh snow).	Red 3	$U \geq 4 m/s \quad H \geq 5 cm$ $G \geq 16.7 m/s \quad R_{24} \geq 1 mm$ $R_{03} \geq 0.1 mm$	3

2.3. Description of numerical models and their setup used in the study

Blowing snow parameters were calculated from operational forecasts of the deterministic ECMWF global numerical model (*Persson*, 2011), which outputs were available in a regular latitude-longitude grid of 0.125 degree (nearly 16 km) horizontal resolution. The wet snow has been diagnosed upon outputs of non-hydrostatic limited area model WRF (*Skamarock et al.*, 2008). The WRF model, implemented and computed at the Hungarian Meteorological Service (HMS), provides data at nearly 2.7 km horizontal resolution and 37 vertical levels. In the HMS implementation, WRF is using the microphysics scheme of Thompson (*Thompson et al.*, 2004) and the YSU PBL scheme (*Hong et al.*, 2006) for the parameterization of planetary boundary layer processes. The higher horizontal resolution (compared to global models) and advanced physical parameterizations are important to obtain finer, mesoscale structures in the precipitation, temperature, and wind fields and the estimates of the precipitation type (fraction of frozen precipitation, *FR*). This seems to be currently more important by wet snow, which occurrence fits a relatively narrow temperature interval and which parameters (snow sleeve diameter and mass) are more sensitive on the precision and exact quantity of input parameters than in the BSI case.

3. Selected synoptic situations

3.1. Blowing snow on January 18, 2013

On January 18, 2013, the weather over Hungary was largely influenced by a deep cyclone, which centre was over the Adriatic Sea (*Fig. 1*). The cyclone had initially developed over the Bay of Genoa (on January 15) and became deeper as a result of interaction with an upper air potential vorticity (PV) anomaly, which centre was situated over the southwest flank of the surface low. The cyclone later moved toward east-northeast. The drop of the pressure over the Balkan Peninsula and increase of the pressure gradient in the north-south direction induced a low-level jet and cold-air advection over the western part of Hungary (*Fig. 2*). This was the primary reason for strong wind and gusts observed at several places in northwestern Hungary (the maximum wind gust, 21.4 m/s was reported at Sármellék at 09:40 UTC). The depth of the snow cover over western Hungary had already been high (20–50cm at many places) as a result of previous snowfalls. In the same region, moderate snowfall (up to 10 mm of precipitation) occurred on January 18 as well (*Fig. 3*). Although, at several stations, where blowing snow was observed, only light precipitation was measured (or estimated from radar measurements) during the event.

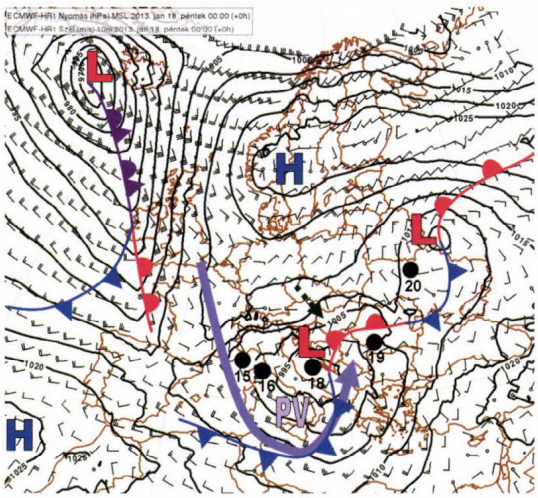

Fig. 1. ECMWF analysis of mean sea level pressure (lines, by 5 hPa), 10 m wind (barbs), and fronts valid for January 18, 2013, 00:00 UTC. The letters L and H represent lows and highs, respectively. The letter "PV" marks the position of the center of the upper-air PV anomaly; the arrow-headed line shows the segment of the upper-air jet surrounding the anomaly (at nearly 250 hPa height). The dots show the positions of the centre of the studied Mediterranean cyclone on January 15, 16 (and 17), 18, 19, and 20, 2013. The dashed line points toward northwestern Hungary, where the blowing snow event occurred.

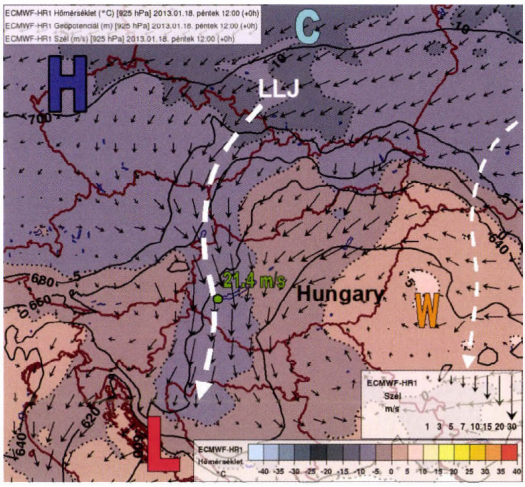

Fig. 2. ECMWF analysis of 925 hPa geopotential (lines, by 20 gpm), temperature (°C, shaded), and 925 hPa wind (arrows, m/s) valid for January 18, 2013, 12:00 UTC. The letters L, H represent low and high pressure, respectively; C, W the cold (warm) airmasses. The dashed line approximately shows the axis of the low level jet (LLJ). A point is placed on the area of the station Sármellék, where the maximum wind gust (21.4 m/s) was recorded on January 18, 2013, 09:40 UTC.

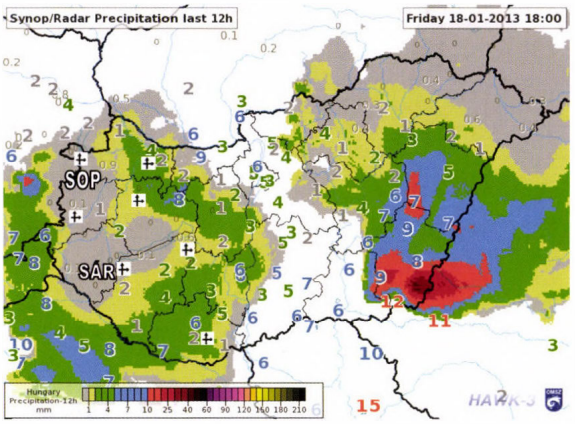

Fig. 3. 12 h precipitation amounts valid for January 18, 2013, 18:00 UTC from stationary measurements (numbers) and radar estimates (shaded). Stations, where drifting or blowing snow was coded in the past weather (–01 h) section are emphasized by square and symbol of blowing snow. Meteorological stations Sopron Kuruc-domb and Sármellék are denoted by abbreviations SOP and SÁR.

3.2. Wet snow on February 6–7, 2013

The weather in central Europe was governed by large area of low pressure (exhibiting several centres) and by a frontal system, which evolved in the Mediterranean region. On February 6–7, 2013, one of the centers of the low pressure was situated over Hungary and east Slovakia (*Fig. 4*). The eastern part of the countries was located in the warm zone of the system, while the colder air propagated around the low-pressure center and forced the mild air toward the mountainous region in northeast Hungary and east Slovakia (*Fig. 5. a–b*). There was an intensive positive temperature advection and high (almost 100%) mean relative humidity between 925–600 hPa (not shown), especially in east Slovakia, where heavy snowfall occurred. Vertical cross-sections of temperature show that across Hungary and Slovakia, over the localities, where wet snow was reported/diagnosed, there was a 200–300 meters deep layer of 0–2 °C temperature (*Fig. 6. a–b*). This layer was well expressed over the northern part of Hungary and the central-eastern part of Slovakia, where 10–20 mm precipitation occurred (*Fig. 7*). Upon precipitation estimates from radars and temperature profiles, favorable wet snow conditions could have developed on the southern slopes of the mountains in the central part of Slovakia, but surface observations were sparse in this region. Damage reports and photographs (*Railpage.net,* 2013) indicate that wet snow occurred also in the valley of the river Hornád (on the railway between Krompachy and Margecany). There was no positive temperature layer on the vertical cross-sections in this region, probably because the valley is not yet resolved by the ECMWF model orography by current resolution (nearly 16 km). The cross-sections also show that the area of the positive temperature layer reduced in time as the cold-air advection was progressing (marked by the decrease of the near-surface equivalent potential temperature).

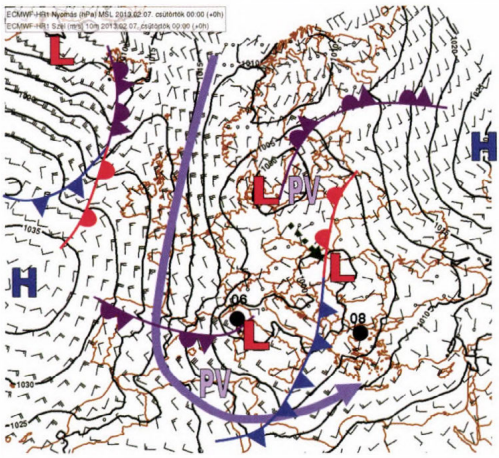

Fig. 4. As in *Fig. 1* but for February 7, 2013, 00:00 UTC. The dots show the positions of the (deepest) centre of the Mediterranean cyclone on 6, 7, and 8 February, 2013. The dashed line points toward the border region of northeastern Hungary and southeastern Slovakia, where the wet snow event occurred.

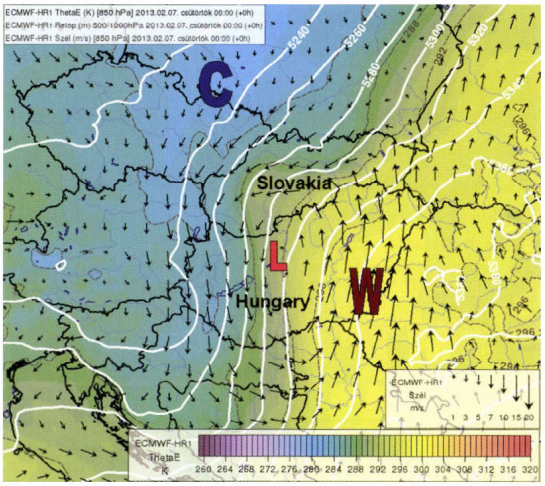

Fig. 5a. ECMWF analysis of the 850 hPa equivalent potential temperature (color shades and dashed lines, K), wind field (arrows, m/s), and the 500/1000 hPa relative topography (white lines, m) valid for February 7, 2013, 00:00 UTC. The letter L denotes the center of the cyclonic circulation over Hungary, letters W, C show the warm and cold air-masses.

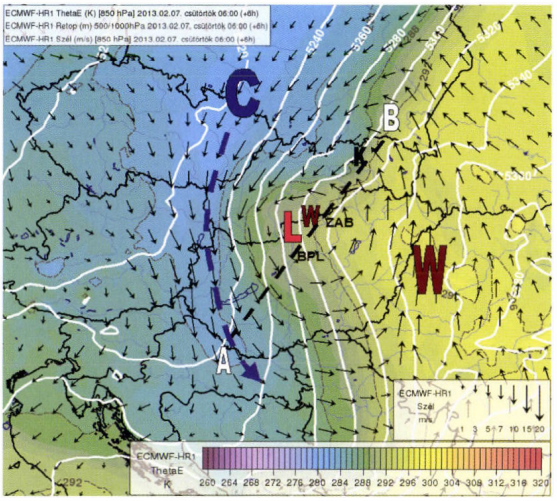

Fig. 5b. As in *Fig. 5a* except for the 6h ECMWF forecast valid for February 7, 2013, 06:00 UTC. The dashed, arrow-headed line schematically shows the flow of the colder airmass, which started to surround and force the warmer air away. The AB line shows the direction of the cross-section in *Fig. 6a-b*. The abbreviations BPL, ZAB emphasize the positions of the weather stations at Budapest Lőrinc and Zabar, respectively (mentioned also later in the text). The letter K denotes the town Krompachy in Slovakia (wet snow caused damages were reported in its neighborhood).

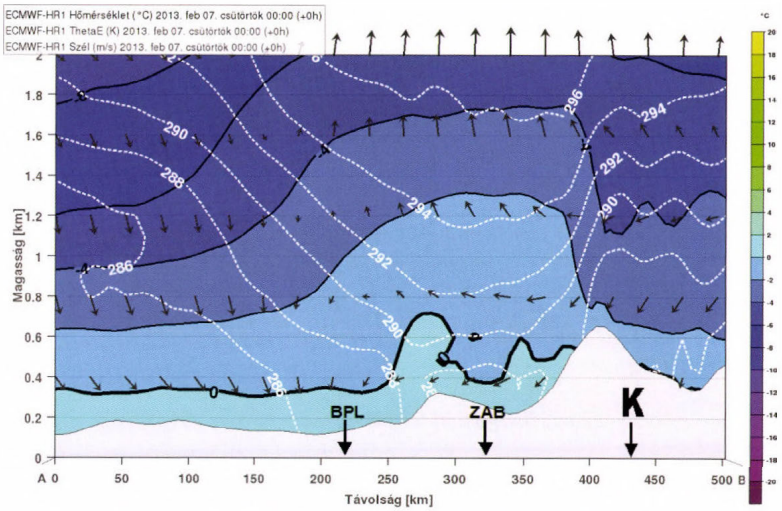

Fig. 6a. ECMWF analysis of temperature (shades and solid lines by 2 °C), equivalent potential temperature (dashed lines, by 2 K) and wind (arrows, m/s) valid for February 7, 2013, 00:00 UTC in a vertical cross-section, which direction is shown in *Fig. 5b*. The abbreviations and arrows mark places, where wet snow was diagnosed/reported (see also *Figs. 5b* and *14a-b*).

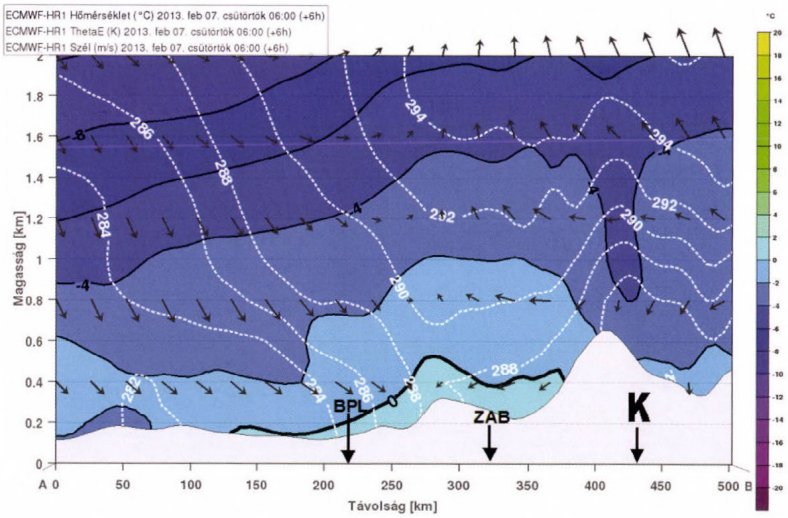

Fig. 6b. As in *Fig. 6a* but for the ECMWF forecast of temperature valid for February 7, 2013, 06:00 UTC.

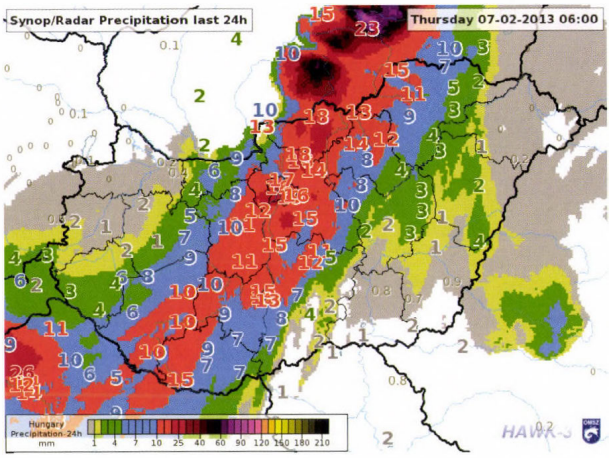

Fig. 7. As in *Fig. 3* but for 24 h precipitation amounts valid for February 7, 2013, 06:00 UTC.

3.3. Wet- and blowing snow on January 24–25, 2014

On January 25, 2014, a cyclone with centre over southern Italy and the Adriatic Sea was moving eastwards (*Fig. 8.*). Its frontal system affected several countries of southern and central Europe causing extraordinary heavy snowfall (Slovenia, Croatia, Serbia, Bulgaria). The northern flank of the warm frontal precipitation band also reached the southern part of Hungary (already on January 24, 2014). At 850 hPa level ECMWF analyses (*Fig. 9*), it was possible to observe that while the cold-air advection already started over large part of western Hungary, there was still a "tongue" of warmer and moist air overturning toward the southwest part of Hungary, where the intense snowfall occurred. This is likely a signature of an occlusion process (in rather mesosynoptic scale), similar to the one observed in the February 6–7, 2013 wet snow situation. The maximum of 20 mm precipitation in Hungary was also reported close to this area (*Fig. 10*).

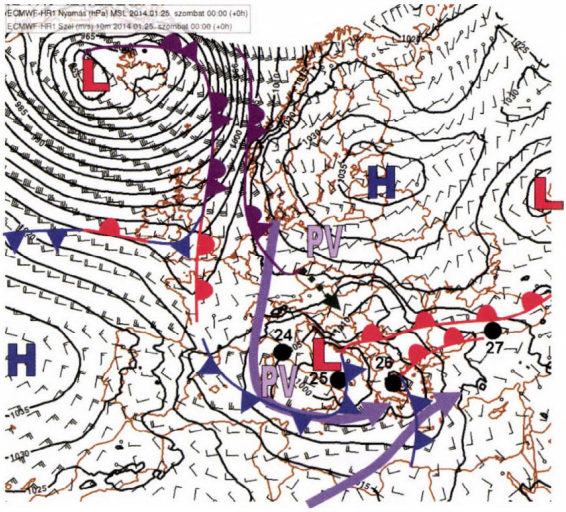

Fig. 8. As in Fig. 1 but for January 25, 2014, 00:00 UTC. The dots show the positions of the (deepest) centre of the Mediterranean cyclone on January 24–27, 2014. The dashed line points toward southwestern Hungary, where both wet snow and blowing snow were observed.

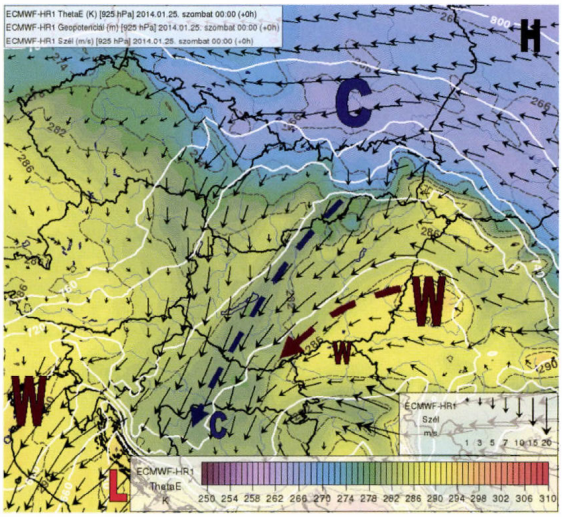

Fig. 9. ECMWF analysis of the 925 hPa equivalent potential temperature (color shades and dashed lines, K), wind field (arrows, m/s), and geopotential (solid lines, m) valid for January 25, 2014, 00:00 UTC. The letters L, H represent low and high geopotential, respectively; C and W represent the cold (warm) regions. The dashed lines schematically show the flow of colder/warmer air over Hungary.

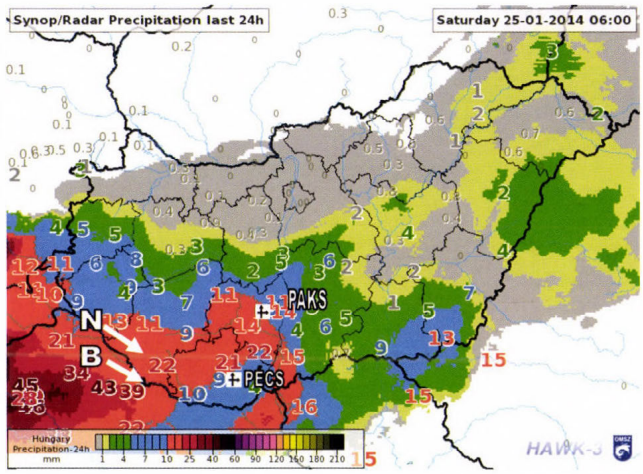

Fig. 10. As in *Fig. 3* but for 24 h precipitation amounts valid for January 25, 2014 06:00 UTC. Meteorological stations Pécs-Pogány and Paks, which reported blowing snow on January 24, 2014, are displayed. Arrows denoted by letters B and N point toward the position of settlements Barcs and Nagyatád, respectively. Damage due to wet snow was reported in their surroundings on January 24–25, 2014.

4. Results for wet- and blowing snow diagnostics

4.1. Blowing snow on January 18, 2013

The January 18, 2013 weather situation was one of the most serious blowing-snow events of the past ten years in Hungary. The blowing snow developed at a large area (almost entire western Hungary), causing serious problems in transport and requiring numerous actions of the disaster management (*Fig. 11*). Such cases are relatively rare – for example, between 2007 and 2012 there was only one case that the highest, third-level warning was issued on blowing snow (18 second- and 60 first-level warnings were issued during the same period). Only light-to-moderate snowfall (few mm of precipitation) had been expected upon available NWP forecasts a day before this event, hence, the intensity of the snowdrift developments had been debated in the HMS forecasters team. The 24h forecast of BSI from the January 17, 2013, 12:00 UTC ECMWF run indicated a possibility of very intense blowing snow for the area northwest of the Lake Balaton (*Fig. 12a*). This area was also emphasized in the WDI outputs (*Fig. 12b*). Though, there would hardly be any transition between the yellow and red warning in WDI (the red warning is distinguished from the orange one only upon the presence of precipitation, which had been forecast by the ECMWF

model for the entire area with strong wind). The analysis of respective weighting functions present in Eq. (10) reveals that all of them positively contributed to BSI in the model forecast for the localities (meteorological stations Sopron Kuruc-domb and Sármellék), where snowdrifts were expected (*Table 4*).

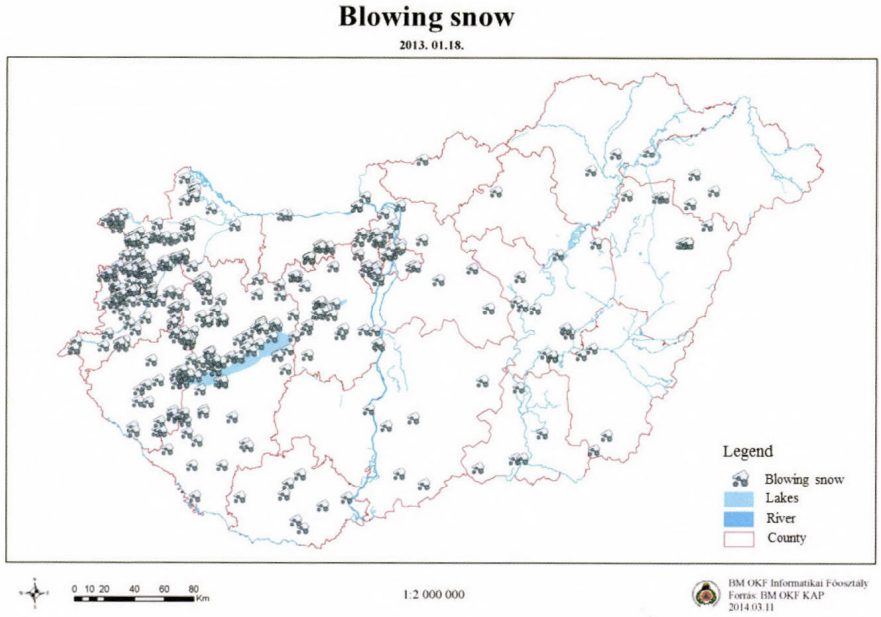

Fig. 11. Actions of the disaster management on January 18, 2013. (source: National Disaster Management Directorate General, with permission)

Table 4. Weighting functions, BSI, and WDI for Sopron Kuruc-domb and Sármellék, derived from the ECMWF 24h forecast valid for January 18, 2013, 12:00 UTC.

Station	$f(T)$	$f(T_S)$	$f(U)$	$f(G)$	$f(H)$	$f(\rho_H)$	***BSI***	***WDI***
Sopron	0.77	1	0.83	0.97	1	0.81	5.4	3
Sármellék	0.84	1	0.71	0.91	1	0.78	5.2	3

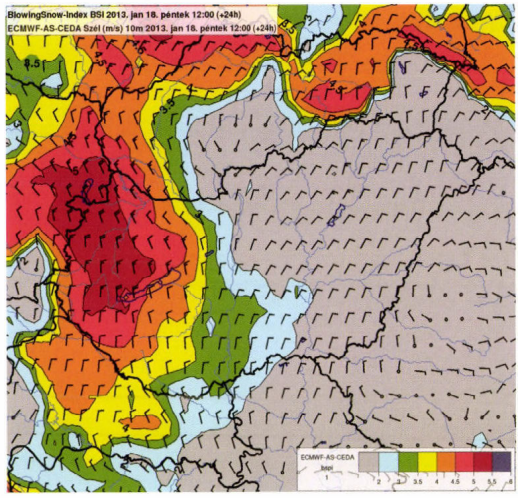

Fig. 12a. ECMWF 24 h forecasts of BSI (shades and solid lines) and 10 m wind (barbs, m/s) valid for January 18, 2013, 12:00 UTC.

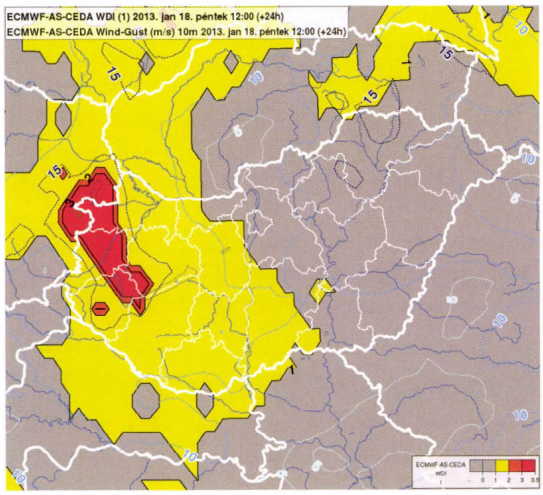

Fig. 12b. ECMWF 24 h forecasts of WDI (shades and solid lines, by 1) and of wind gusts (dotted lines, by 5 m/s) valid for January 18, 2013, 12:00 UTC.

Available observations, close to the time of the forecast validity (January 18, 11:40 UTC), show that drifting or moderately blowing snow was really coded at several stations in western Hungary (*Fig. 13*). Though, heavy blowing snow (code 39) was not observed and BSI estimated from the measurements did not exceed 5. This could have been caused by the use of temperature measured

close to terrain surface, instead of the skin surface temperature (of the snow cover), because the weights of surface temperature are significantly lower in the observations (*Table 5*) than in the forecasts. Interestingly, WDI would suggest only 1st level of warning for the evaluated stations. The main reason for it is that only low precipitation amounts were reported at stations concerned (although light or moderate snowfall had been coded at some observation dates). One possible explanation is that the strong wind blew the snow off the measuring devices. The radar-estimated precipitation indicates that the real snow precipitation could have been somewhat bigger compared to surface observations, though this was not typical in the area of highest gust and snowdrift occurrences (refer to *Fig. 3*).

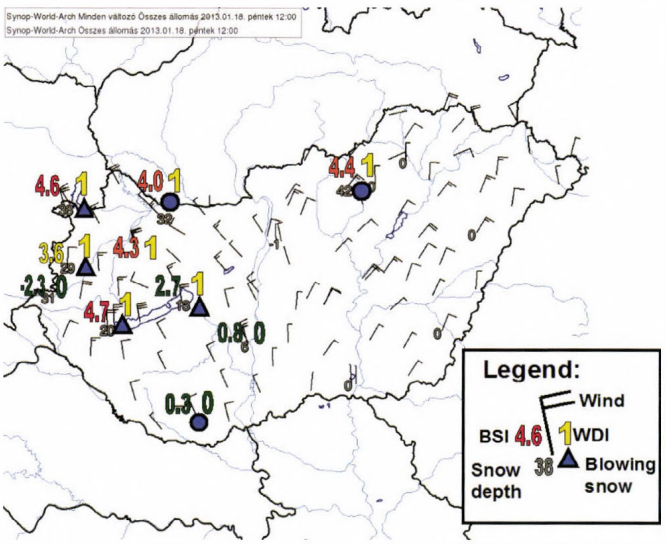

Fig. 13. Observations of 10m wind (barbs, m/s) and snow depth (numbers, cm) from Hungarian meteorological stations on January 18, 2013, 12:00 UTC. Further numbers (see the description in the legend) denote the estimated value of BSI and WDI valid for 11:40 UTC. The circles are drawn at stations, where drifting snow (code 36) was reported on January 18, 2013, triangles are for blowing snow (code 38).

Table 5. As in *Table 4* but derived from observations at Sopron Kuruc-domb and Sármellék, on January 18, 2013, 11:40 UTC.

Station	$f(T)$	$f(T_S)$	$f(U)$	$f(G)$	$f(H)$	$f(\rho_H)$	***BSI***	***WDI***
Sopron	0.68	0.18	0.85	0.91	1	0.96	4.6	1
Sármellék	0.73	0.84	0.78	0.86	0.8	0.74	4.7	1

4.2. Wet snow on February 6–7, 2013

Wet snow calculations were provided upon WRF model run based on February 6, 2013, 12:00 UTC. In the first calculation, the FR criterion was chosen for wet snow diagnostics (*Fig. 14a*).

Wet snow was detected at several places in Hungary and Slovakia (mostly in the southern part of central Slovakia and in the valley between the towns Košice and Prešov), though, the values of $\Delta\Phi$ were mostly below the proposed warning thresholds (maximum detected values were 5–6 cm). When using the $RT_{850/1000}$ criterion, the area of potential wet snow occurrence became considerably bigger (*Fig. 14b*), and the condition for first-level warning according to *Table 1* would be fulfilled on several places. The maximum detected $\Delta\Phi$ was about 8 cm. If we assume, that the density of the wet snow on wires was between 250 and 300 kg/m^3 (according to mean wind speed in this area), this diameter would be equivalent to 2.2–2.7 kg/m snow-mass, which can potentially cause damage on the overhead lines, particularly if the wind speed is strong. The comparison of the diagnostics on observations (*Table 6a*) and on the corresponding model outputs (*Table 6b*) showed that the FR-criterion largely reduced the precipitation, which potentially occurred in wet snow form. This is the main cause of the differences between the forecast diameters (wet snow loads) and the ones diagnosed upon observations, because forecasts of other parameters (wind-speed, temperature) were relatively close to the observed ones. Examination of the course of FR (e.g., for station Košice, *Fig. 15*) showed that this parameter was rather low when the temperature was higher than 1 °C, although, in the reality, snowfall was reported in such conditions. The low *FR* could have been partially also influenced by somewhat higher (by 0.5–1 °C) temperature in the model compared to observations. The $RT_{850/1000}$ criterion seemed to be more successful in detection of wet snow occurrence, but it is possible that the diagnosed values of the snow sleeve diameter were too high when using this method (especially in the area of Budapest, where wet snow accretion on wires corresponding to $\Delta\Phi$ of 5 cm or bigger probably did not occur).

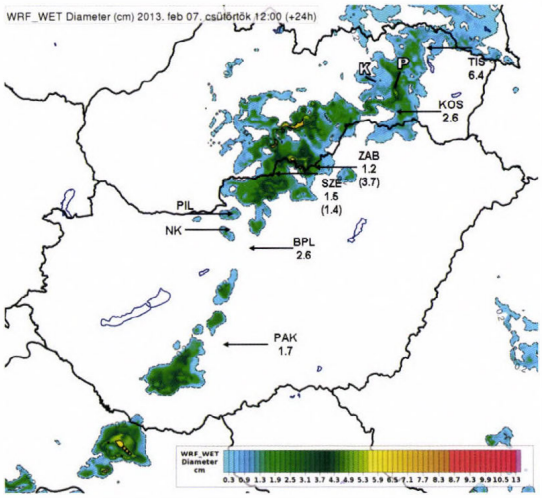

Fig. 14a. WRF 24 h forecast of the snow sleeve diameter increase (shades, in cm) valid for February 7, 2013, 12:00 UTC calculated using the FR method. The solid lines denote the diameters of 5.5 and 8.6 cm corresponding to warning thresholds. The arrows and abbreviations denote the positions of weather stations and localities, where wet snow was reported/diagnosed (PAK-Paks, BPL-Budapest Lőrinc, SZE-Szécsény, ZAB-Zabar, KOS-Košice, TIS-Tisinec, NK- Nagy-Kevély, PIL-Pilis). The numbers show the increase of the snow sleeve diameter (cm) assessed from the observations (as in *Table 6a*). The thick line denoted K (P) shows the direction of the railway between Krompachy and Margecany (Prešov and Kysak), where damage due to wet snow was reported.

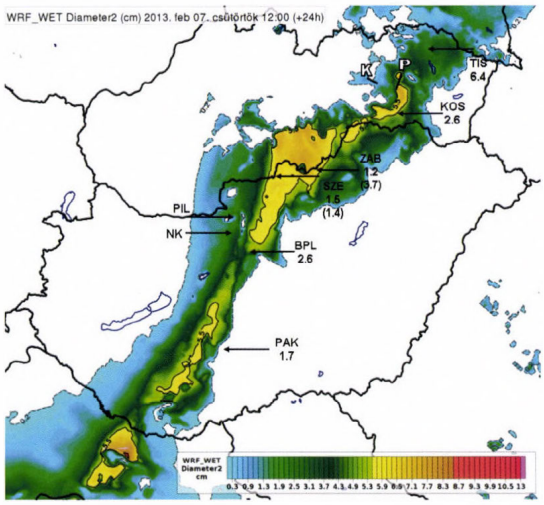

Fig. 14b. As in *Fig. 14a* but for the $RT_{850/1000}$ method.

Table 6a. Parameters of wet snow precipitation observed or derived from observations of several synoptic stations in Hungary and Slovakia during the period of February 6, 2013, 12:00 UTC – February 7, 2013, 12:00 UTC. There were no weather-type observations on the star-marked stations (Szécsény and Zabar), the wet snow period was assessed from the WRF model data (upper record using the FR, lower record in parenthesis the $RT_{850/1000}$ method). At the station Tisinec (marked by two stars), weather-type observations were not available between 20:00 and 05:00 UTC, but from the amounts and course of other parameters (snow-depth, temperature, wet-bulb temperature) it is probable that all the precipitation in this period was in wet snow form.

Synoptic station: / **Parameter:**	**Paks (PAK)**	**Budapest Lőrinc (BPL)**	**Szécsény (SZE)***	**Zabar (ZAB)***	**Košice Letisko (KOS)**	**Tisinec (TIS)****
Station height (*ASL*) [m]	97	139	153	226	230	216
P [mm] Total precipitation	7.9	12.1	15.8	11.6	19.0	26.0
Pw [mm] Wet snow precipit.	5.15	8.3	4.35 (4.3)	3.7 (11.6)	8.08	20.5
U [m/s] Average wind	1.66	1.93	0.97 (0.73)	1.18 (0.99)	5.34	1.98
Δϕ [cm] Snow-sleeve diameter increase	1.68	2.60	1.50 (1.43)	1.18 (3.72)	2.64	6.41
M [kg/m] Wet snow mass	0.236	0.436	0.199 (0.185)	0.157 (0.639)	0.528	1.526

Table 6b. Parameters of wet snow precipitation derived from the WRF model forecasts valid for the period of February 06, 2013 12:00 UTC – February 07, 2013 12:00 UTC and for the grid-points nearest to observations listed in the *Table 6a*. The upper (lower) values are for the *FR* ($RT_{850/100}$) method of snowfall determination. The abbreviation NR (Not Relevant) means that wet snow was not detected.

Synoptic station: / **Parameter:**	**Paks (PKS)**	**Budapest Lőrinc (BPL)**	**Szécsény (SZE)**	**Zabar (ZAB)**	**Košice Letisko (KOS)**	**Tisinec (TIS)**
Grid-point height (*ASL*) [m]	87.7	124.1	161.2	301.2	250.2	258.7
P [mm] Total Precipitation	10.86	17.63	19.37	18.49	17.83	8.06
Pw [mm] Wet snow precipitation	0 (0)	0 (16.81)	5.22 (19.37)	5.77 (18.49)	3.03 (17.24)	0 (6.7314)
U [m/s] Wet snow period average wind	NR (NR)	NR (2.19)	2.83 (2.26)	2.74 (2.12)	4.15 (3.33)	NR (2.64)
Δϕ [cm] Snow sleeve diameter increase	NR (NR)	NR (5.26)	1.64 (6.09)	1.83 (5.85)	0.98 (5.56)	NR (2.11)
M [kg/m] Wet snow mass	NR (NR)	NR (1.153)	0.26 (1.475)	0.297 (1.368)	0.157 (1.420)	NR (0.342)

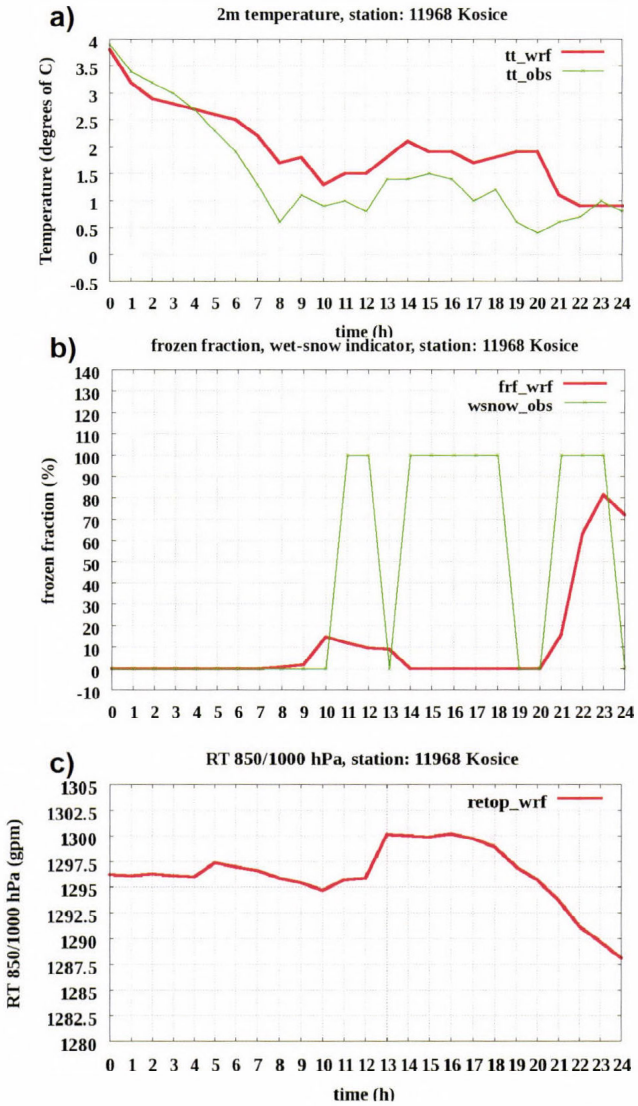

Fig. 15. Course of observed/diagnosed (thinner lines) and forecasted (thicker lines) meteorological parameters valid for the station Košice and for the period of February 6, 2013, 12:00 UTC –February 7, 2013, 12:00 UTC. The February 6, 2013, 12:00 UTC WRF run outputs were used for this visualization. The horizontal axis shows the time (h) from the start of this run. Evolution of the 2 m temperature is shown in a), figure b) shows the change of the model-computed fraction of frozen precipitation (FR). This is depicted together with an index showing detection of wet snow upon observed precipitation type, temperature, and wet-bulb temperature (0 – no wet snow, 100-wet snow). Figure c) shows the evolution of the $RT_{850/1000}$ parameter forecast by WRF.

Available reports (*Pilis parkerdő,* 2013) mentioned damage in the forest due to high snow loads in Pilis mountains, and there is also photographic evidence (*Kolláth*, 2013) of wet snow accumulated on wires in this region (e.g., in the area of the Nagy-Kevély mountain). Although, this region seemed to be only marginally affected by wet snow in the WRF forecasts (see *Figs. 14a–b*). In Slovakia, wet snow was reported on the railway electric power lines between the railway stations Margecany and Krompachy and also between stations Kysak and Prešov. Though, the damage on the power lines was probably not only direct, due to high loads on the wires, but it was also caused by trees, which broke under the weight of heavy, accumulated wet snow (*Railpage.net*, 2013). Wet snow was forecast for the surrounding of both above-mentioned railways. A local maximum of $\Delta\Phi$, close to the Kysak-Prešov railway, appeared in the diagnostic outputs, using both FR and $RT_{850/1000}$ methods.

4.3. Wet- and blowing snow on January 24–25, 2014

Most reports of the wet snow occurrence in Hungary and associated damage (electric power failures) were concentrated to the southwestern border of Hungary (region of Barcs and Nagyatád), yet, several thousands of inhabitants were concerned (*E.O.N. Hungária Zrt.*, 2014, data on power failures, photographs, and personal communication). The wet snow was diagnosed using both FR and $RT_{850/1000}$ criterions in this territory.

In case of *FR*, the forecast diameters of snow-sleeve mostly did not reach the proposed warning thresholds (5.5 cm, not shown). In the second diagnostics, significant, up to 8–9 cm diameters were predicted during the 24-hour accretion period, until January 25, 06:00 UTC (*Fig. 16*). Very high accumulation of wet snow was also forecast for the region close to the synoptic station Paks. However, here the development of wet snow was questionable: though the forecast 2 m temperature fitted the wet snow criterions (between 0 and 3 °C), in the reality, it was probably well below 0 °C during most of the investigated period, as indicated by observations of the Pécs and Paks stations.

During this situation, blowing snow was reported at synoptic stations Pécs and Paks. Its intensity was probably highest in the evening of January 24, 2014 (at around 21:00 UTC), when wind gusts of 12–15 m/s were observed. Upon available observations, the BSI was estimated to be 3.54 for Pécs and 3.49 for Paks. There were no snow density measurements in this case, thus, a mid-value of 170 kg/m^3 between the two thresholds mentioned in *Table 2* was used in this calculation. But, because of the uncertainty in both skin-surface temperature and snow density, it is probable that the true BSI values were bigger (e.g., in case of fresh snow, these parameters could have been lower and their weight functions higher). The more simple WDI index also indicated the possibility of blowing snow, corresponding to the first level warning at the two evaluated locations (*Fig. 17*).

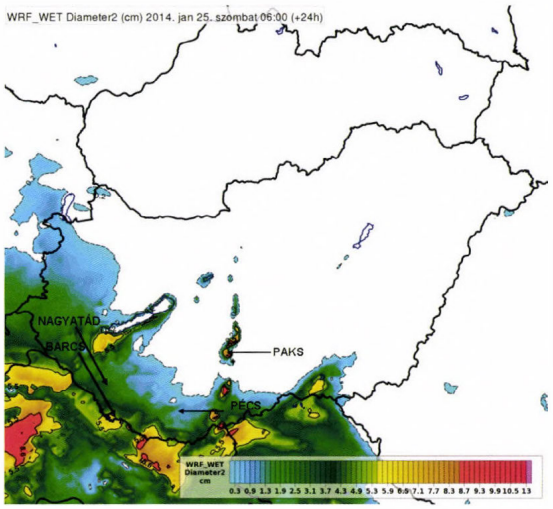

Fig. 16. As in *Fig. 14b* but for the 24 h forecast valid for January 25, 2014, 06:00 UTC. The arrows point toward Nagyatád and Barcs, where wet snow damages were reported and toward meteorological stations Pécs and Paks (mentioned in the text).

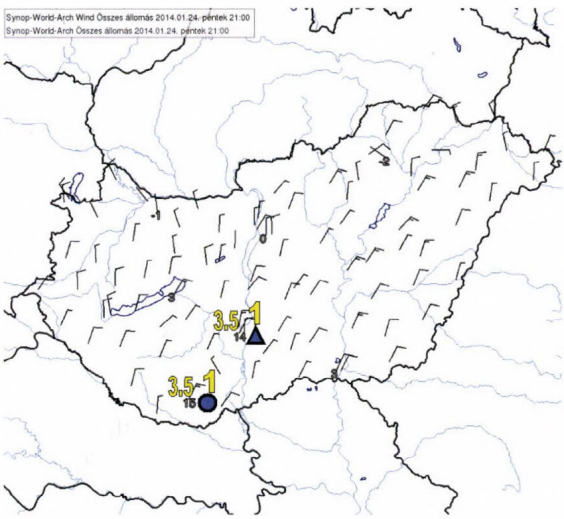

Fig. 17. As in *Fig. 13* except for January 24, 2014, 21:00 UTC. The BSI/WDI indices are valid for 20:40 UTC, the observations of drifting/blowing snow for 21:00 UTC (note that the station Pécs-Pogány reported blowing snow as well but only until 20:20 UTC).

The short-range ECMWF-based BSI forecasts showed maximum values exceeding 4 between Pécs and Paks but 3 hours later, on January 25, 2014, 00:00 UTC (*Fig. 18*). Evaluation of the BSI contributions showed that the temperature and snow-surface state were of at least same importance for snow-drift generation than wind, because the wind- and windgust speed were not as high as in the January 18, 2013 case (*Table 7*).

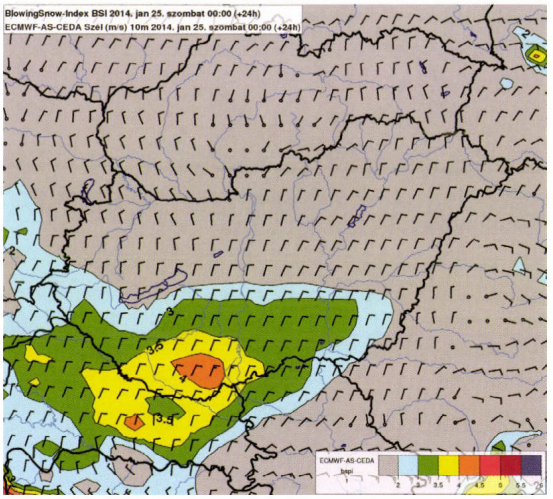

Fig. 18. As in *Fig. 12a* except for the 24-hour ECMWF forecast valid for January 25, 2014, 00:00 UTC.

Table 7. As in Table 4 but for the stations Pécs-Pogány and Paks, derived from the ECMWF 24 h forecast valid for January 25, 2014, 00:00 UTC.

Station	$f(T)$	$f(T_S)$	$f(U)$	$f(G)$	$f(H)$	$f(\rho_H)$	***BSI***	***WDI***
Pécs	0.63	1.0	0.44	0.70	0.5	0.83	4.1	1
Paks	0.56	0.97	0.17	0.38	0.3	0.83	3.2	1

5. Conclusion

The previous examples showed that the wet- and blowing snow occurrence is influenced by several factors (precipitation, wind, temperature) at once. Thus, foreseeing of such events only upon basic model outputs is not easy, and it requires a lot of forecasting experience and continuous study of typical synoptic

and mesosynoptic situations favorable for wet- or blowing snow. There could be, for example, cases with one dominant factor (e.g., very strong wind), when significant snowdrifts can develop even in areas, where there is currently no or only very weak snowfall. Or, there are limit cases, where existence of blowing snow is determined by reaching of some sufficient (but not extreme) intensity for all contributing parameters, including skin-surface temperature and snow density (which are generally rarely studied in forecasting practice). Thus, indices like BSI or snow sleeve diameter can help the forecaster to immediately turn attention to areas, where such conditions could appear providing guidance for further analysis of the potential causes of the event. Another advantage of these methods is that they are relatively simple from computational point of view (extraordinary computational time and power are not required) and can be easily applied on outputs of various NWP models.

The deficiency of the above-described diagnostic methods is that they can be interpreted or verified rather in qualitative sense. At Hungarian Meteorological Service, there is no parameter for blowing snow, which would forecast a directly measurable quantity (e.g., the height of the snowdrift), and such parameters are also not measured. Though, the statistically based BSI seems to be somewhat better in specifying the intensity of the event than indices based on arbitrary criterions (WDI). The BSI forecasts were also more consistent with the observed values than the simple WDI index in the evaluated cases. For future, it could be recommended to develop and test a "cumulative" form of BSI as well (e.g., a simple time-integral of this index), which could help to distinguish between short- and long-period blowing snow events, which can eventually cause especially high snowdrifts.

In contrary to blowing snow parameters, the algorithms for calculation of the wet snow mass on wires and diameter of snow accumulation give measurable quantities on outputs (although at the cost of several assumptions and simplifications). However, there are rarely precise reports based on such measurements in Hungary – generally no wet snow accumulation measurements are provided at the meteorological stations, estimates of the significance of wet snow loads can be currently done rather upon damage reports (e.g., from electricity companies) or upon photographs. The verification of the forecasts of wet snow or blowing snow parameters is further complicated by the fact that even observations of some "basic" input parameters (like precipitation type, snow depth, or snow density) are relatively sparse. These could be partially replaced by using interpolations or calculated from outputs of numerical models or nowcasting systems analyses – which is not an optimal solution, but even partial use of observations would still give better estimates of the real intensity of such events as if we would use only NWP model forecasts.

The determination of the type of precipitation and of the fraction of solid precipitation is very important for both blowing- and wet snow forecasting (essential for the latter one). It seems that numerical forecast of snowfall by

positive temperature is still difficult, even in LAM models which use parameterization of microphysical processes. Although, we tested only the scheme of Thompson, which is currently operationally used, and which was suggested in other winter precipitation studies (e.g., *Nygaard et al.*, 2011, *Podolskiy et al.*, 2012, *Liu et al.*, 2011). The inaccuracy of some forecast parameters (e.g. temperature) and of the model parameterizations can be one of the reasons, why relatively simple, empirical approaches (e.g., the $RT_{850/1000hPa}$ method) can be still more successful than criterions, based on the direct outputs of the model microphysics or precipitation schemes. Improved parameterization of the type of precipitation and of other characteristics (terminal velocity of snowflakes, collection coefficient, accreted snow density, etc.) is necessary to get quantitatively useful results. The accretion models (e.g., of the one described by Eq. 5) are often tested under laboratory conditions with nearly constant wind or density of the accreted snow. But even in such cases, it is difficult to directly measure some input characteristics, e.g., the collection coefficient. Although it was shown that the evaporation/condensation processes do not have substantial effect on the accreted snow diameter or snow mass (*Admirat*, 2008), it can be expected that (especially for long accretion periods) the changes of the snow density or fall speed of snowflakes can have a non-negligible impact on the forecast wet snow characteristics.

The analyses of the pressure, geopotential, and temperature fields in Section 3 indicate that there are some similarities in the macro- or mesosynoptic situations, in which the wet- or blowing snow appears in Hungary. The most typical feature is a deep cyclone with center over Italy or the Adriatic Sea moving (extending) toward east-northeast; a deep upper-air trough (eventually a cut-off low) surrounded by a jet and situated on the west-southwest flank of the surface cyclone (indicating a strongly meridional type of circulation). The blowing snow can develop in presence of a mesoscale, low-level jet, which was observed in other cases as well, e.g., during the March 14–15, 2013 blowing snow event in western Hungary (*Simon et al.,* 2013). Wet snow often appears at or behind the warm frontal boundaries characterized by large temperature gradients but sometimes also in the neighborhood of stationary occlusions at the rear side of the cyclone. Although the BSI and wet snow parameters were developed in order to make the recognition of wet- and blowing snow conditions easier, we are convinced that the knowledge of typical types of synoptic situations, favorable for such events, is also important for their successful forecasting and should be further studied.

Acknowledgements: The authors are indebted to *Attila Nagy* and *Kornél Locher* (HMS) for their support and for providing the NWP data. We are also grateful to *Jozef Csaplár* (SHMÚ) for additional information and for sending us useful materials. The study has been prepared in the frame of the COST Action ES1002 WIRE and INCA-CE (2CE120P3) CENTRAL EUROPE projects, with the support of the European Regional Development Fund.

References

Admirat, P., 2008: Wet Snow Accretion on Overhead lines. In: Atmospheric Icing of Power Networks. Springer Netherlands, 119-169.

Baggaley, D.G. and *Hanesiak, J.M.*, 2005: An Empirical Blowing Snow Forecast Technique for the Canadian Arctic and the Prairie Provinces. *Weather Forecast. 20*, 51–62.

Bonelli, P., Lacavalla, M., Marcacci, P., Mariani G., and *Stella, G.*, 2011: Wet snow hazard for power lines: a forecast and alert system applied in Italy. *Nat. Hazard. Earth Sys. 11*, 2419–2431.

Cantin, A. and *Bachand, D.*, 1993: Synoptic pattern recognition and partial thickness techniques as a tool for precipitation types forecasting associated with a winter storm. Centre Meteorologique du Quebec Tech. Note 93N-002.

Elíasson, Á.J., Ágústsson, H., and *Hannesson, G.M.*, 2013: Wet-Snow accumulation - A study of two severe events in complex terrain in Iceland. 15th IWAIS conference. St. John's, Newfoundland and Labrador, Canada.

E.O.N. Hungária Zrt., 2014: Összesített üzemzavari adatok 2014.01.24. 15:00 - 2014.01.26. 15:00 (in Hungarian)

Glickman, T.S. (ed.), 2000: Glossary of Meteorology, 2d. ed., American Meteorological Society, Boston.

Gulyás, K., Somfalvi-Tóth, K., and *Kolláth, K.*, 2012: A tapadó hó statisztikus-klimatológiai viszonyai hazánkban. *Légkör 57*, 49–54. (in Hungarian)

Hirsch, T., 2006: Téli magyarországi nagy csapadékos helyzetek vizsgálata és előrejelzése. PhD thesis. ELTE, Budapest. (in Hungarian)

Hong, S.Y., Noh Y., and *Dudhia J.*, 2006: A new vertical diffusion package with an explicit treatment of entrainment processes. *Month. Weather Rev. 134*, 2318–2341.

ISO, 2001: Atmospheric icing of structures. International Standardization Organisation (ISO) International Standard 12494, Geneva, Switzerland.

Kolláth, K., 2013: 2013.02.07. Tapadó hó. Website http://mrstratus.blogspot.hu/2013/02/20130207-tapado-ho.html (in Hungarian).

Li, L. and *Pomeroy, J.W.*, 1997: Probability of occurrence of blowing snow. *J. Geophys. Res. 102*, 21955–21964.

Liu, C., Ikeda, K., Thompson, G., Rasmussen, R., and *Dudhia, J.*, 2011: High-Resolution Simulations of Wintertime Precipitation in the Colorado Headwaters Region: Sensitivity to Physics Parameterizations. *Month. Weather Rev. 139*, 3533–3553.

Makkonen, L., 1989: Estimation of wet snow accretion on structures. *Cold Reg. Sci. Technol. 17*, 83–88.

Makkonen, L. and *Wichura, B.* 2010: Simulating wet snow loads on power line cables by a simple model. *Cold Reg. Sci. Technol. 61*, 73–81.

Nygaard, K., Egil, B., Kristjánsson, J.E., and *Makkonen, L.*, 2011: Prediction of In-Cloud Icing Conditions at Ground Level Using the WRF Model. *J. Appl. Meteorol. Climatol. 50*, 2445–2459.

Nygaard, K., Egil, B., Ágústsson H., and *Somfalvi-Tóth K.*, 2013: Modeling Wet Snow Accretion on Power Lines: Improvements to Previous Methods Using 50 Years of Observations. *J. Appl. Meteorol. Climatol. 52*, 2189–2203.

Persson, A., 2011: User guide to ECMWF forecast products. Meteorological Bulletin M3.2, ECMWF.

Pilis parkerdő, 2013: Hótörés a Pilisben – balesetveszélyes az erdő Website, http://www.parkerdo.hu/index.php?pg=news_1_667. (in Hugarian)

Podolskiy, E.A., Nygaard, B.E.K., Nishimura, K., Makkonen, L., and *Lozowski, E.P.*, 2012: Study of unusual atmospheric icing at Mount Zao, Japan, using the Weather Research and Forecasting model, *J. Geophys. Res.: Atmospheres, 117(D12)*, 1984–2012.

Poots, G., 1996: Ice and snow accretion on structures. Research Studies Press Ltd. – Wiley, Taunton, England.

Railpage.net, 2013: Sneh opäť ochromil železničnú dopravu. Website http://www.railpage.-net/modules/news/article.php?storyid=2560. (in Slovak)

Sakamoto, Y., 2000: Snow accretion on overhead wires. *Philos. T. R. Soc. Lon. A 358(1776)*, 2941–2970.

Simon, A., Kolláth, K., Somfalvi-Tóth, K., Dezső, Zs., and *Tordai, J.*, 2013: A 2013-as év veszélyes időjárási jelenségei. Presentation. *39. Meteorológiai Tudományos Napok*, 2013. November 21–22. http://www.met.hu/doc/rendezvenyek/metnapok-2013/21_Simon.pdf. (in Hungarian)

Skamarock, W.C., Klemp, J.B., Dudhia, J., Gill, D.O., Barker, D.M., Duda, M.G., Huang, X.-Y., Wang, W., and *Powers, J.G.*, 2008: A description of the Advanced Research WRF version 3. *NCAR Technical Note NCAR/TN-475+STR.*

Somfalvi-Tóth, K., 2014: *Tapadó hó számolása HAWK3-ban.* Technical report, OMSZ. (in Hungarian),

Sundin, E. and *Makkonen, L.*, 1998: Ice Loads on a Lattice Tower Estimated by Weather Station Data. *J. Appl. Meteorol. 37*, 523–529.

Thompson, G., Rasmussen, R.M., and *Manning, K.*, 2004: Explicit forecasts of winter precipitation using an improved bulk microphysics scheme. Part-I: Description and sensitivity analysis. *Mont.Weather Rev. 132*, 519–542.

Tordai, J., 2012: A hófúvás előrejelzése Magyarország térségére. MSc thesis, ELTE, Budapest. (In Hungarian)

Tóth, K., Lakatos M., Kolláth K., Fülöp R., and *Simon A.*, 2009: Climatology and forecasting of severe wet-snow icing in Hungary. In: Proceedings of the 13th International Workshop on Atmospheric Icing of Structures, IWAIS 2009 and the Final Workshop of the COST Action 727 "Measuring and Forecasting Atmospheric Icing on Structures". Andermatt, Switzerland, 8–11 September 2009.

WMO, 1995: *WMO* Manual on codes. International Codes VOLUME I. 1 Part A — Alphanumeric Codes. WMO–No. 306.

Yuter, S.E., Kingsmill, D.E., Nance, L.B., and *Löffler-Mang, M.*, 2006: Observations of precipitation size and fall speed characteristics within coexisting rain and wet snow. *J. Appl. Meteorol. Climatol. 45*, 1450–1464.

INSTRUCTIONS TO AUTHORS OF *IDŐJÁRÁS*

The purpose of the journal is to publish papers in any field of meteorology and atmosphere related scientific areas. These may be

- research papers on new results of scientific investigations,
- critical review articles summarizing the current state of art of a certain topic,
- short contributions dealing with a particular question.

Some issues contain "News" and "Book review", therefore, such contributions are also welcome. The papers must be in American English and should be checked by a native speaker if necessary.

Authors are requested to send their manuscripts to

Editor-in Chief of IDŐJÁRÁS
P.O. Box 38, H-1525 Budapest, Hungary
E-mail: journal.idojaras@met.hu

including all illustrations. MS Word format is preferred in electronic submission. Papers will then be reviewed normally by two independent referees, who remain unidentified for the author(s). The Editor-in-Chief will inform the author(s) whether or not the paper is acceptable for publication, and what modifications, if any, are necessary.

Please, follow the order given below when typing manuscripts.

Title page: should consist of the title, the name(s) of the author(s), their affiliation(s) including full postal and e-mail address(es). In case of more than one author, the corresponding author must be identified.

Abstract: should contain the purpose, the applied data and methods as well as the basic conclusion(s) of the paper.

Key-words: must be included (from 5 to 10) to help to classify the topic.

Text: has to be typed in single spacing on an A4 size paper using 14 pt Times New Roman font if possible. Use of S.I. units are expected, and the use of negative exponent is preferred to fractional sign. Mathematical formulae are expected to be as simple as possible and numbered in parentheses at the right margin.

All publications cited in the text should be presented in the *list of references*, arranged in alphabetical order. For an article: name(s) of author(s) in Italics, year, title of article, name of journal, volume, number (the latter two in Italics) and pages. E.g., *Nathan, K.K.,* 1986: A note on the relationship between photosynthetically active radiation and cloud amount. *Időjárás 90,* 10-13. For a book: name(s) of author(s), year, title of the book (all in Italics except the year), publisher and place of publication. E.g., *Junge, C.E.,* 1963: *Air Chemistry and Radioactivity.* Academic Press, New York and London. Reference in the text should contain the name(s) of the author(s) in Italics and year of publication. E.g., in the case of one author: *Miller* (1989); in the case of two authors: *Gamov* and *Cleveland* (1973); and if there are more than two authors: *Smith et al.* (1990). If the name of the author cannot be fitted into the text: *(Miller,* 1989); etc. When referring papers published in the same year by the same author, letters a, b, c, etc. should follow the year of publication.

Tables should be marked by Arabic numbers and printed in separate sheets with their numbers and legends given below them. Avoid too lengthy or complicated tables, or tables duplicating results given in other form in the manuscript (e.g., graphs).

Figures should also be marked with Arabic numbers and printed in black and white or color (under special arrangement) in separate sheets with their numbers and captions given below them. JPG, TIF, GIF, BMP or PNG formats should be used for electronic artwork submission.

More information for authors is available: journal.idojaras@met.hu

Published by the Hungarian Meteorological Service

Budapest, Hungary

INDEX 26 361

HU ISSN 0324-6329

IDŐJÁRÁS

QUARTERLY JOURNAL
OF THE HUNGARIAN METEOROLOGICAL SERVICE

CONTENTS

VOL. 119 * NO. 3 * JULY – SEPTEMBER 2015

IDŐJÁRÁS

Quarterly Journal of the Hungarian Meteorological Service

Editorial Office: Kitaibel P.u. 1, H-1024 Budapest, Hungary
P.O. Box 38, H-1525 Budapest, Hungary
E-mail: journal.idojaras@met.hu
Fax: (36-1) 346-4669

Indexed and abstracted in Science Citation Index Expanded™ and Journal Citation Reports/Science Edition
Covered in the abstract and citation database SCOPUS®

Subscription by mail:
IDŐJÁRÁS, P.O. Box 38, H-1525 Budapest, Hungary
E-mail: journal.idojaras@met.hu

IDŐJÁRÁS

Quarterly Journal of the Hungarian Meteorological Service
Vol. 119, No. 3, July – September, 2015, pp. 307–335

Measuring and modeling of hazardous weather phenomena to aviation using the Hungarian Unmanned Meteorological Aircraft System (HUMAS)

Zsolt Bottyán[1*], **András Zénó Gyöngyösi**[2], **Ferenc Wantuch**[3], **Zoltán Tuba**[1], **Rita Kurunczi**[4], **Péter Kardos**[5], **Zoltán Istenes**[6], **Tamás Weidinger**[2], **Katalin Hadobács**[7], **Zoltán Szabó**[2], **Márton Balczó**[8], **Árpád Varga**[8], **Andrea Bíróné Kircsi**[9], and **Gyula Horváth**[10]

[1]*Department of Military Aviation, National University of Public Service, P. O. Box. 1,H-5008 Szolnok, Hungary*

[2]*Department of Meteorology, Eötvös Loránd University, Pázmány Péter sétány 1/A., H-1117 Budapest, Hungary*

[3]*Aviation Authority, National Transport Authority, Lincoln u. 1., H-2220 Vecsés, Hungary*

[4]*Időkep Ltd., Bartók B. út 65/b., H-1224 Budapest, Hungary*

[5]*HungaroControl, Hungarian Air Navigation Plc, Iglo u. 33–35, H-1185 Budapest, Hungary*

[6]*Department of Software Technology and Methodology, Eötvös Loránd University, Pázmány Péter sétány 1/C., H-1117 Budapest, Hungary*

[7]*Geoinformation Service, Hungarian Defence Forces, H-1524 Budapest, Hungary*

[8]*Department of Fluid Mechanics, Budapest University of Technology and Economics, Budafoki út 8, H-1111 Budapest, Hungary*

[9]*Department of Meteorology, University of Debrecen, H-4032 Debrecen, Egyetem tér 1., Hungary*

[10]*Hungarian Meteorological Service, Gilice tér 39, 1181 Budapest, Hungary*

**Corresponding author E-mail: bottyan.zsolt@uni-nke.hu*

(Manuscript received in final form November18, 2014)

Abstract—At present, Unmanned Aircraft Systems (UAS) are playing more and more significant role in military and civil operations in Hungary. A well-used meteorological support system is essential during the planning and executing phases of different UAS

missions. In the present work, the structure of an applied analog statistical and a WRF-based numerical forecast system is to be introduced with special regards to aviation meteorological factors, such as visibility, ceiling, turbulence, icing, etc. Within such a system, it is very important to generate an accurate short-time visibility prediction. In order to develop such forecasts, we combined an analogy based statistical approach to a high-resolution numerical model for visibility prediction, which are currently available as a hybrid visibility prediction for the regions of four main airports in Hungary. On the other hand, we also present the first Hungarian Unmanned Meteorological Aircraft System (HUMAS). In our case study, the HUMAS measurements are compared to dynamical weather prediction data during the international planetary boundary layer (PBL) campaign in Szeged, Hungary.

Key-words: aviation meteorology, Unmanned Aircraft Systems, integrated forecast system, fuzzy logic, WRF model, visibility, cloud ceiling

1. Introduction

Application of Unmanned Aircraft Systems (UAS) for both civilian and military purposes spreads very rapidly worldwide because of its low operational costs that are expected to even more decrease significantly in the near future (*Gertler*, 2012; *Watts*, 2012). Unmanned systems are playing more and more significant role in military and civil operations also in Hungary (*Fekete* and *Palik*, 2012; *Somlyai et al.*, 2012; *Restás*, 2013). Aerial support for natural or industrial disaster management, monitoring (earthquakes, floods and forest fire etc.), government and private survey (cartography, agriculture, wild life monitoring, border control, security and maintenance control for industrial companies, electricity cords or oil and gas pipeline networks, etc.) and the defense of critical infrastructures may benefit from the onboard instruments that might be the payload of such UASs (*Adams* and *Friedland*, 2011; *Gyöngyösi et al.*, 2013; *Restás* and *Dudás*, 2013). Unmanned aviation, on the other hand, is even more sensitive to the actual weather situation than manned flights. Due to their smaller dimensions compared to manned vehicles, the areodynamic processes during flight that highly depend on the present state of the atmosphere are affecting the reliability of flight in a manner more sensitive than for larger sized aircrafts. In addition, the weather itself is able to modify not only the (aero)dynamic aspects of aviation processes but the navigation and execution of a given mission (reconnaissance, observation, etc.), too. The mentioned atmospheric influence on the aviation is more important in the case of unmanned flights which are controlled by autonomous onboard robotic systems or remote pilots (*Williams*, 2004; *Drury et al.*, 2006). These airplanes usually have relatively large wings with a slim airfoil and significant surface area, thus, they are especially sensitive to gusts, turbulence, and airframe icing as well. Beyond that – similarly to manned ones –, they are also sensitive to heavy precipitation, low cloud, and poor visibility condition during their flights (*Østbø et al.*, 2004; *Hadobács et al.*, 2013).

In spite of the relative ease of controlling of most UAS, weather hazards may be extremely dangerous to their flights. Numerous UAS crashes and accidents were reported that were principally caused by hazardous weather factors. Despite of the mentioned sensitivity of UASs to weather – at present –, the number of systems that are specially developed for the meteorological support of UAS operators is relatively low (*Garcia et al.*, 2013; *Sun et al.*, 2014).

In order to decrease the weather-related risks during UAS flights, we had developed a complex meteorological support system for UAS users, mission specialists, and decision makers. This system is based on an integrated weather prediction software, the Integrated Forecasting System (IFS). Calibration and verification have been carried out using a special meteorological UAS, called the Hungarian Unmanned Meteorological Aircraft System (HUMAS). Finally, it is important to point out that this meteorological support system can easily be adopted for any location at all over the world, because the applied meteorological data and numerical model system are mainly open-access.

2. The Integrated Forecast System (IFS)

Prediction of key aviation meteorological parameters such as visibility and ceiling is one of the greatest challenges for an operational forecaster. These variables are usually the Achilles' heel of numerical weather prediction (NWP) models, too (*Jacobs* and *Maat, 2005*; *Souders* and *Showalter,* 2008; *Hirardelli* and *Glahn*, 2010). Unfortunately, most of the phenomena which are affecting flight operations are not predicted directly even by high resolution NWP models. Visibility and ceiling are playing clearly a key role in the success of UAS missions, (*Bankert* and *Hadjimichael,* 2007). Usually, the operational minima of UAS flights are below the limits of special mission execution. For example, for reconnaissance or surveillance tasks, poor visibility and low ceiling can eliminate the mission but yield no restrictions to the UAS flight itself.

Accordingly, high resolution NWP model output data should be processed parallel to a statistical analysis of archive database for a given weather situation to produce the best combination forecast in a certain occasion. To solve the challenge of visibility and ceiling prediction, we developed the Integrated Forecast System (IFS) which consists of i) a suitable, specially tuned NWP model, ii) a statistical climatological prediction component, which all together are capable to generate iii) a reliable and appropriate hybrid (combined statistical and numerical) aviation meteorological forecasts for UAS operations.

The construction of the experimental complex meteorological IFS is based on the following parts:

- statistical modeling subsystem (SMS),
- numerical modeling subsystem (NMS),
- hybrid modeling subsystem (HMS),
- post processing subsystem (PPS),
- UAS measurements (UM).

The main components of the UAS meteorological support system and the relations of its different components are shown in *Fig. 1.* The Integrated Forecast System is a modeling and post-processing unit using both statistical and numerical outputs of its subsystems to produce hybrid visibility and ceiling forecasts. IFS uses climatological data of mentioned parameters from the statistical modeling subsystem and actual weather forecast data (basic meteorological variables) from the numerical modeling subsystem. Based on these parts, IFS is able to produce the hybrid (combined) short-time predictions with respect to both visibility and ceiling. On the other hand, IFS has a coupled UAS measurement (UM) component to verify and test the IFS predictions during the development time. The applied Hungarian Unmanned Meteorological Aircraft System (HUMAS) was equipped by meteorological sensors to measure the atmosphere with special regard to the state of the planetary boundary layer (PBL).

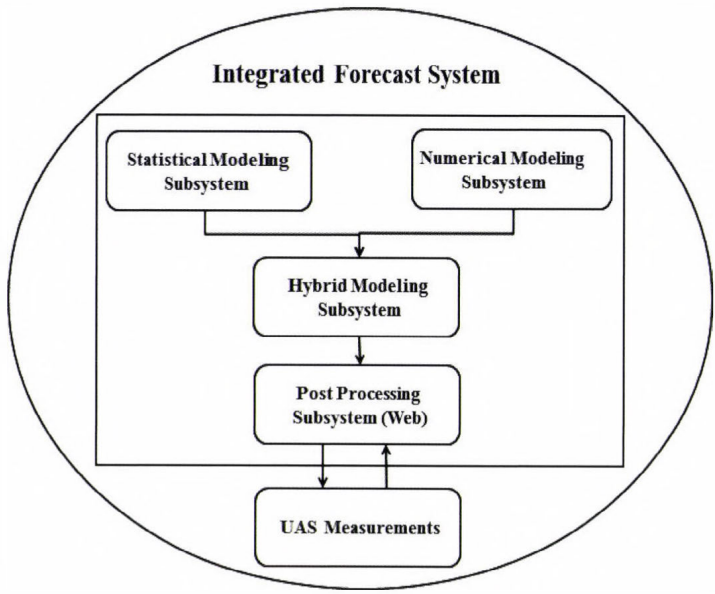

Fig. 1. The structure of the Integrated Forecast System (IFS) for UAS missions.

3. Statistical approach in the IFS

Fuzzy logic based analog forecasting is a quiet new and effective tool of ultra-short term weather forecasting (*Hansen,* 2007).

The basic principle of analog forecasting is well known (from *Toth*, 1989) as to find similar weather situations in the past to the current and recent conditions and rank them according to the degree of their similarity in the interest of giving relevant information for weather forecasts. The term *weather situation* hereafter is meant as a couple-of-hour continuous observation. Therefore, analog forecasting does not work without a relevant climatic database which contains the meteorological parameters planned to forecast in the future. We had set up an appropriate database for Hungarian military airbases (LHKE, LHPA, and LHSN) and for the largest Hungarian international airport (LHBP), based on routine aviation weather reports (METARs) (*Bottyán et al.*, 2012; *Wantuch et al.*, 2013). *Fig. 2* presents the location of airports. The applied database contains the meteorological variables for every half hour from 2006. More than 30 variables have been introduced, including the parameters both in raw and derived formats (e.g., year, month, day, hour, minute vs. day of the year). The records are more than 99% complete, and the whole database is reproducible from raw METAR reports in short time with our script (*Bottyán et al., 2012*).

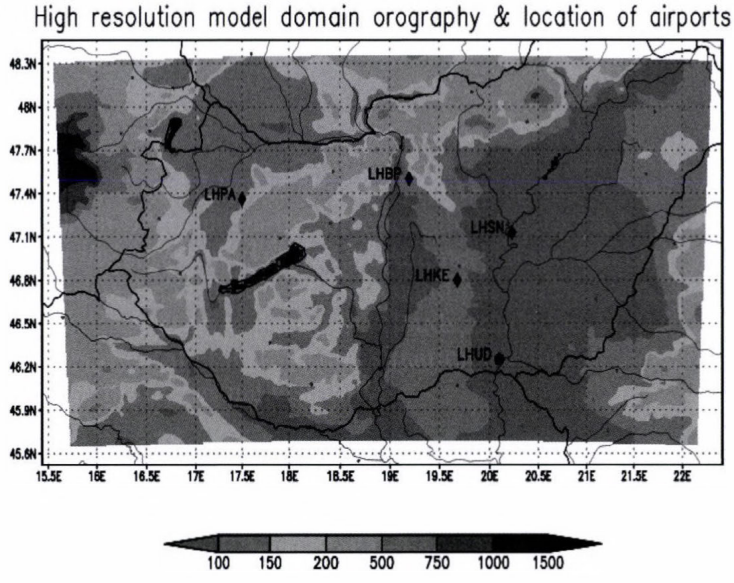

Fig. 2. Locations of four Hungarian airports inside the highest resolution, innermost (d03) model domain that were examined in the present study (black diamonds). LHKE: Kecskemét; LHSN: Szolnok; LHBP: Budapest; LHPA: Pápa. LHUD is the Szeged aerodrome (black dot), the location of field experiments.

The applied fuzzy logic based algorithm is measuring the similarity between the most recent conditions and the appropriate elements of the database. During the examination of every single weather situation, the model uses the current and the eleven previous METARs' content. The algorithm compares the meteorological variables of every examined time step using fuzzy sets *(Tuba et al.*, 2013b; *Wantuch et al.*, 2013).

The fuzzy sets – composed to describe the degree of similarity – were determined by experts (in this case by operational meteorologists), which is a common method in the development of fuzzy systems (*Meyer et al.*, 2002). These functions are applied for all compared parameters, to output the measure of similarity ranging from 0 to 1. The individual parameters at a given weather situation are examined one by one, and the overall measure of similarity for that situation is constructed from the weighted average of the individual measures of similarity of the parameters (*Tuba et al.*, 2013b).

Obviously, the initial values (or situation) of a given meteorological parameter from the most similar cases have determinative role in the forecast process. The higher the difference between initial values, the higher the risk of an inaccurate forecast of the selected element.

This led to our assumption: we could improve the accuracy of the forecast of individual elements by using appropriate weights highlighting the importance of them during the fuzzy logic based forecasting process (*Tuba et al.*, 2013b). As we have shown in our mentioned study: there are two different ways to highlight meteorological parameters which help to give more similar initial values for the parameters selected as more important. The first method is the suitable designation of fuzzy sets. Unfortunately, this approach is very difficult, because the expert judgments are hardly applicable on indirect way. In this case, they have to define the potential modification of the chosen fuzzy set in order to give a better prediction of the selected element. In another approach, we assign weights to the meteorological variables. The higher the importance of the parameter, the larger the applied weight. Because of the large number of variables, the direct determination of weights was excluded.

We applied the Analytic Hierarchy Process (AHP) introduced by *Saaty* (1977), which is a widely used technique in different fields of life except meteorology. This method is mainly used in multi-criteria decision making, especially in solving complex problems from most different fields (*Bardossy et al., 1993*; *Al-Harbi*, 2001; *Tuba et al.*, 2013a). Its main idea is to model the problem as a hierarchy. It is needed to define decision makers' goal, the applied criteria in decision making, which evaluates the possible alternatives and the alternatives to be chosen. In our case, the goal is to find the most similar situations in the database. Actually, it means the decision making. The conclusion of the lines above is that the alternatives are the single weather situations which are evaluated by the criteria: the different meteorological and time parameters. The meteorological problem to be solved has seven-seven

different criteria and sub-criteria, and more than 100,000 different alternatives. The large number of alternatives makes impossible to apply the whole analytic hierarchy process for finding the most similar situations, but for this we have the fuzzy logic based algorithm described above.

AHP was used only for determining the applicable weights for the different parameters as criteria. It was implemented by the first steps of AHP technique. Firstly, it is necessary to apply pairwise comparison on criteria which is based on general definition. In our case, these experts' judgments were assigned by operational forecasters' joint opinion. The ratios of pairwise comparisons can give the elements of a matrix. The best choice for the weight vector is the eigenvector belonging to the maximal eigenvalue of this matrix (see *Saaty*, 1977). To determine the eigenvector, we used the standard power iteration method. The received weights will be shown at the verification results. Obviously, the matrix might be inconsistent due to the subjective comparisons. We found an inconsistency of 2.5% which is less than the tolerable 10%, so the results are significantly reliable (*Saaty*, 1991).

Knowing the calculated weights we can determine the similarity of the individual time steps under investigation by weighted averaging of the single parameters' similarity. Finally, we calculate the overall similarity ($S_{overall}$) of the examined case from weighted averaging of the similarity of time steps. The current observation ($t-0$th time step) gets the largest weight, and this weight decreases rapidly as we go through time steps. It provides that the most similar cases probably contain the dynamic changes and guarantee the convergence in similarity during the examined time period. General description of the weighted averaging is the following:

$$S_{overall} = \frac{\sum_{n=1}^{k} \left(2^{n-1} \cdot S_{t-(n-1)}\right)}{2^{k}-1}, \qquad (1)$$

where k is the number of the time steps applied in comparisons and $S_{t-(n-1)}$ is the similarity value of the $(t-(n-1))$th time step.

After finding the most similar weather situations, we can compose a deterministic prediction from the consecutive observations of the chosen cases with an appropriate method. The model collects the 30 most similar situations which are used for producing deterministic forecast. In the semi-operational phase, we used the 30th percentile value of the chosen parameter as prediction following *Hansen* (2007). We found that the percentile value is not independent from the examined parameter and the category limit of dichotomous forecast. We plan to investigate, if the verification results could be improved by dynamically changing percentile value in the function of category limits.

4. Numerical modeling in the IFS

The Weather Research and Forecasting (WRF) model from the UCAR (*Skamarock et al.*, 2008) with the Advanced Research WRF (ARW) core, version 3.5 (release April 18, 2013) has been applied to generate numerical input for our NWP system.

WRF is a well-established, tested, and documented, non-hydrostatic, meso-scale meteorological model, applicable for both atmospheric research and weather forecasting purposes ranging from micro to global scales. Its modularity and flexibility together with its detailed documentation suited well for the needs of our purposes (*Passner et al.*, 2009). The modular structure of our development provides the possibility to swap one limited area model with another – e.g., ALADIN/AROME (*Hágel*, 2009; *Balogh et al.*, 2011; *Horányi et al.*, 2011, *Seity, et al.*, 2011) –to be used as a dynamical driver for the numerical unit of the system.

Input geographical dataset have been generated from two different sources. Landcover/land-use information were taken from the Corine 2000 (Coordinate information on the environment) database (*Büttner et al.*, 2002) adapted and modified for the applications in WRF by *Drüszler et al.* (2011). The main advantage of this database with respect to the USGS (United States Geological Survey) dataset (originally used by WRF) is the much more realistic and detailed representation of land characteristic features (e.g., much better and more specified representation of various types of forests and scrubland; in addition to more than 3 times larger area specified as urban land). These characteristics are essential in surface-atmosphere interactions and boundary layer processes, the most valuable input for aviation meteorology parameters.

Similarly, the original FAO (Food and Agriculture Organization) soil texture dataset has also been replaced by the DKSIS (Digital Kreybig Soil Information System), produced by the Center for Agricultural Research, Hungarian Academy of Sciences (see *Pásztor et al.*, 2010 for more details). The false over-representation of clay and loam type soils within the FAO data has been removed from the input data, and sand (absent from the original database) and sandy clay have been introduced in an additional extent covering more than 12% of the area of the country. The spatial distribution of the difference between the two different input data with respect to landuse (USGS vs. Corine 2000) and soil texture (FAO vs. DKSIS) geographical data fields are depicted in *Fig 3.* The most significant differences are the representation of urban area, water bodies and the under representation of evergreen forests in mountainous area, while with respect to soil texture. Contrarily to the Corine 2000 database, which covers whole Europe and can be applied to all model domains, DKSIS covers only the area of Hungary, inside the political boundaries of the country and is usable only for the best resolution (d03) domain (*Fig. 4*).

In addition, soil hydraulic parameters used by the WRF model were modified according to Hungarian soil sample data (MARTHA and HUNSODA), giving more realistic values for the soil structure in Central Europe (*Ács et al.*, 2010). Sensitivity tests showed that even during a sunny summer day, model results featured significant differences in terms of planetary boundary layer heights with respect to the soil hydraulic parameters that have been applied (*Breuer et al.*, 2012; *Ács, et al.*, 2014).

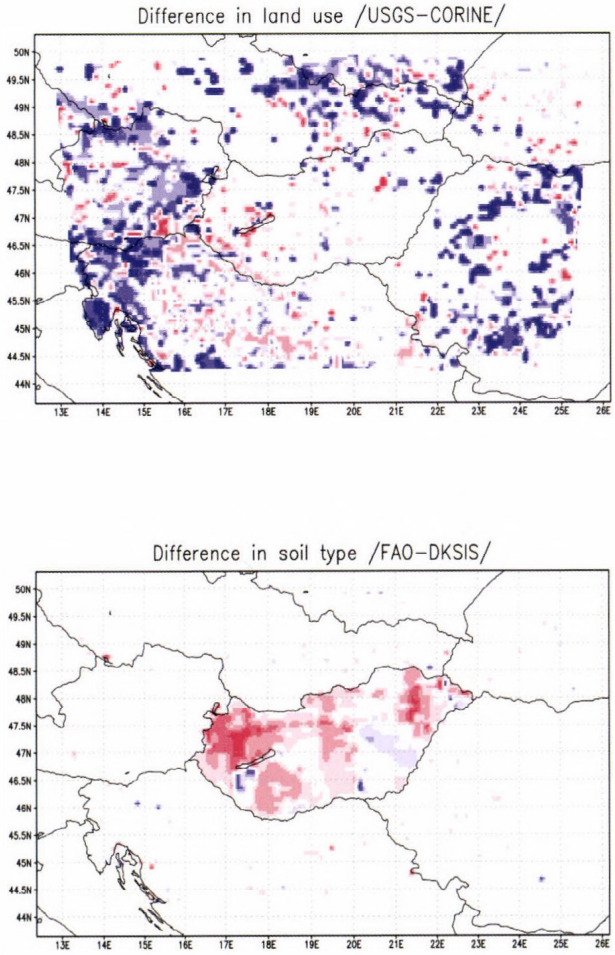

Fig. 3. Differences between the original and replaced geographical data with respect to land use (top) and soil texture (down) databases, applied for the integration of the WRF numerical weather model. Red (blue) shades indicate areas where the land use index has been increased (decreased), and white areas were not changed. It can be seen, that for soil texture, only the area inside the political boundaries of Hungary was modified.

The model setup in the newly developed IFS is the following. The number of vertical levels is 44, from which 24 levels are below 2 km. The vertical layers depth is ranging from 25–250m in the lower portion of the domain through 500 m layer in the middle levels up to 780 m in the upper portion of the model domain (see *Fig. 4*, left panel). Three level telescopic nesting is applied ranging from 22.5 km in the coarsest (d01) domain through 7.5 km in the intermediate (d02) domain to 2.5 km horizontal resolution in the high resolution lowest (d03) nested domain that is located in the Carpathian Basin (centered N47.43; E019.18) and covers Hungary with 202 × 121 grid cells (*Fig. 3.*, see also *Gyöngyösi et al.*, 2013 and *Fig. 4*, right panel).

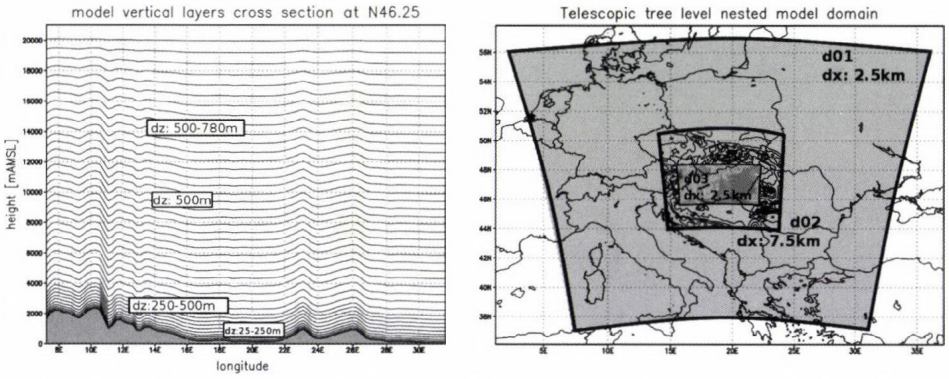

Fig. 4. Vertical levels with higher resolution in the lower levels and deeper layers in the upper portion (right panel) and the three level telescopic nested domain setup for high resolution modeling of the Carpathian Basin in the IFS system (left panel). Horizontal resolution is 22.5 km, 7.5 km and 2.5 km, grid size is 97 × 97, 97 × 97, and 202 × 121, respectively.

In order to apply a setup tuned for the special requirements of the designated purpose, extensive tests were performed: 30 different combination of parameterization setups (*Gyöngyösi et al.*, 2013) – including 8 types of micro-physics (types 3–9 and 13), 6 types of land surface models (types 1, 2, 4, 5, 7 and 10), and 8 types of PBL (1, 2, 4, 5, 7–10) schemes (see WRF-ARW Version 3 user's manual, *Wang et al.*, 2009) – have been tested. Tests have been performed for 9 selected weather situations, all having aviation weather relevancies (*Table 1*). Similar investigation has been made by *Hu et al.* (2010) for the optimization of the modeling of PBL processes with the comparison of three different parameterization schemes. An extensive test with a physical ensemble, using different parameterization setup (e.g., *Evans et al.*, 2012) requires enormous computational capacity, while in the current project we were focusing only to the study of a limited number of typical weather situations.

The test case studies investigated in the current test were chosen according to their aviation meteorology relevance, all of them are typical in the Carpathian Basin, including heavy icing, deep convection, abrupt wind direction change, etc. The list of the cases is detailed in *Table 1.*

Table 1. Test cases (date and short description) of weather situations for the evaluation of the numerical weather prediction unit

No.	Date	Description
1.	10.27.2012.	Widespread precipitation from a Mediterranean low pressure system
2.	09.20.2012.	High horizontal pressure gradient situation with strong winds, with a special wind pattern
3.	01.19.2012.	Significant low-level inversion during winter period
4.	09.08.2012.	High pressure ridge transition resulting in significant and rapid change in wind direction
5.	07.29.2012.	Deep convection resulting in local and heavy showers that were not well resolved by most operational models
6.	05.12.2012.	Significant change in wind direction following a cold front
7.	01.22.2012.	Well documented severe icing case weather situation
8.	02.16.2012.	Convective precipitation from a high level cold vortex, temperature in the mid-troposphere is less than –25 °C
9.	12.06.2012.	UAS test flight case for direct verification purpose

Model output have been compared to synoptic surface observations at 31 ground stations in Hungary located in the high resolution (d03) domain, and operational radiosonde data of 4 stations located in the medium resolution (d02) domain. Temperature, dew point, and wind data have been compared using RMS error and a wind score derived with respect to wind speed and wind direction differences. Results showed that in the surface data there is a wide variation in humidity and temperature, while in the upper level only wind speed and direction are significantly affected by the choice of the parameterization schemes.
From the analysis of the results the Bretherton and Park (2009) moist turbulence PBL scheme, the WRF Single Moment Scheme with 3 micro-physics class

(*Hong et al.*, 2004) and the Noah scheme (joint development of the National Centers for Environmental Prediction, Oregon State University, Air Force and Hydrologic Research Lab) for land-surface processes (*Chen* and *Dudhia*, 2001) performed the best. For parameterization the RRTM (Rapid Radiative Transfer Model) for longwave radiation (*Mlawer et al.*, 1997), the *Dudhia*'s (1989) scheme for shortwave radiation and a modified version of the Kain-Fritsch scheme (*Kain*, 2004) for cumulus convection parameterization have been applied.

GFS data with $0.5^{\circ} \times 0.5^{\circ}$ resolution was applied as initial and boundary conditions for the limited area integration of the outermost domain in every 3 hours, with no additional data assimilation. Soil temperature and humidity data were taken from GFS model as initial data only and were handled separately from meteorological data as boundary conditions, i.e., it is not updated from the large scale model during the integration. Appropriate adjustment of the lower boundary conditions to the physics of the model was achieved during the spin-up period in the beginning of the model integration. Input data was prepared with WPS, the vendor preprocessor of the WRF system.

This model setup has been considered as the best choice for the current purpose and it has been kept for operational integrations that are being run for 96 hours lead time, performed two times a day, initialized from 00 and 12:00 UTC, and 04:00 and 16:00 UTC, respectively. Data download of 1.5 GB input data from NOAA server takes 40 minutes, model preprocessing and integration on 24 cores for about half an hour, and post-processing for another 40 minutes. Model products are delivered to the users through the web interface of the integration server itself 6 hours after initialization time.

For the need of UAS forecasts, two different post-processors (ARWpost and the Universal Post-processor, UPP) are used. Output data is interpolated to both pressure levels (with UPP) and height levels (with ARWpost). Times series of predicted values at selected locations for (QNH) pressure; wind speed, direction (barbs), and wind gust; temperature, dew point, trigger temperatures for 1000 m and 1500 m deep thermal convection; grid scale and convective precipitation (both accumulated and intensity); and different level cloud amount, low-level cloud base (ceiling), and visibility forecasts are also published operatively (*Fig. 5a*).

In order to support UAS operation in the lower troposphere (from surface up to 3000 mAMSL) and above (up to 7000 mAMSL), evolution of vertical profiles (time-altitude cross-sections) of wind, temperature, lapse rate, and humidity are also plotted using shading and contouring at certain height levels (instead of pressure levels), that are easily interpretable by the user (*Fig. 5b*). Model prediction is presented in the usual form for the days of the intensive PBL observation period at Szeged, from in November 27–30, 2013 (*Cuxart et al.*, 2014; *Weidinger et al.*, 2014).

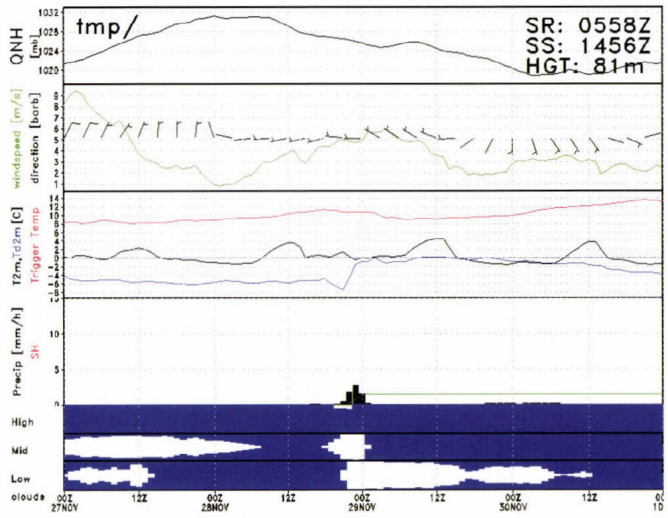

Fig. 5a. Meteogram graphical output of the predicted time variation of surface meteorological variables. Description of variables depicted on each panel, from top to bottom: sea level pressure (QNH), wind speed (green line, m s^{-1}) and direction (barbs), 2 m temperature (black line), dew point (blue line), and the calculated trigger temperature for a 1500 m mixed convective layer (red line), precipitation intensity (black bars), accumulated precipitation (green line), and low-, medium-, and high level cloud amount (white shaded area in the respective blue strips) with respect to time (UTC, horizontal axis), in the form as delivered to the users through the web based interface. Calculated sunrise and sunset times (UTC) are printed on the top right corner together with surface elevation.

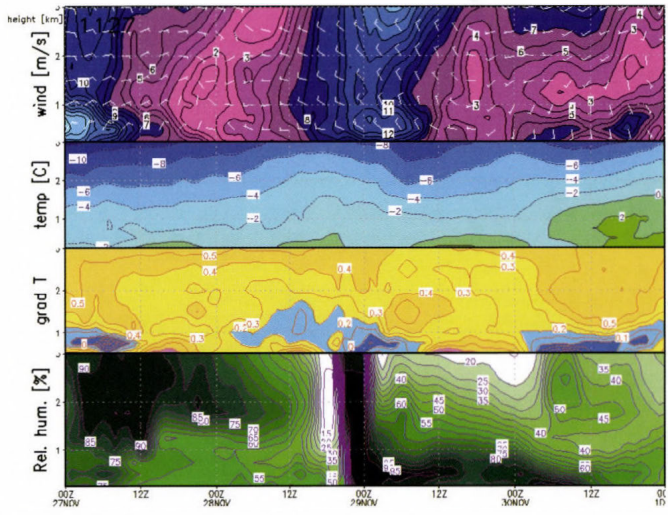

Fig. 5b. Same as *Fig 5a.* but for vertical profiles of atmospheric variables: wind speed and direction (barb), temperature, vertical temperature gradient (lapse rate, blue shades for absolute stable, yellow shades for conditionally unstable, and red shades for unstable stratification), and relative humidity.

In addition to basic model forecasts, time series of derived aeronautical weather parameters are also given (*Gyöngyösi et al.*, 2013). For example, predicted thermal characteristics (temperature advection, condensation level convective layer height, thermal index profile, and expected convective vertical velocity) can also be seen on a separate page for all locations. Visibility is computed using both the built-in scheme of UPP and the decision-tree based algorithm developed by *Wantuch* (2001), including FogSSI as a function of predicted temperature at the surface and 850 hPa level dew points (T_d) and the wind speed at 850 hPa.

Derived icing and turbulence forecasts are plotted on time-vertical cross-sections using different methods for the estimation of the intensity of processes (*Mireles et al.*, 2003; *Sousounis*, 2005; *Fövényi*, 2010).

5. Hybrid visibility forecasting in the IFS

Applicability of statistical (i.e., analogy based) and numerical forecasting of visibility is limited. Analog forecasting is based on a special database and on the measured information of the actual ($t + 0$) weather and a short period before. Its efficiency (accuracy or reliability) decreases over time. On the other hand, the performance of NWP model is basically constant over the examined short forecasting period (nine hours time interval). The correlation coefficients between category differences – which are based on the difference of numerically predicted and observed visibilities (*Bottyan et al.*, 2013; *Wantuch et al.*, 2013) – at the initial ($t + 0$) and latter time steps show also gradual and significant decrease over time (*Fig. 6*). Five visibility categories are used within the 0 – 800 m, 800 – 1500 m, 1500 – 3000 m, 3000 – 5000 m, and above 5000 m intervals initially, the possible absolute category differences are 0, ±1, ±2, ±3, and ±4, respectively.

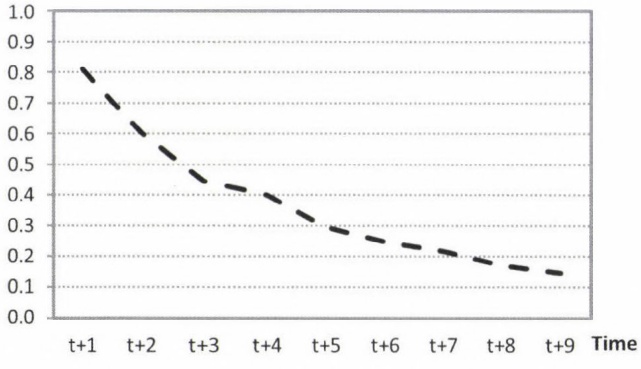

Fig. 6. Correlation coefficients of category differences between numerically predicted and observed visibility at the initial ($t + 0$) and latter time steps.

Preliminary results showed that the error of the initial time step is in close correlation with the latter inaccuracy of forecast from the same model run, but only for an ultra-short time period. This gave us the idea to combine the different methods during this period keeping their advantages and eliminating their disadvantages at the same time. This kind of models run only every 6 to 24 hours, thus the incorrect forecasts can be amended after the next model run which means the same loss of time. In contrast, the refresh rate of statistical forecasts fits the observation frequency which is not more than 1 hour. In consideration of the above, we created this hybrid model, which is from the simple linear combination of the statistical and numerical model outputs (*Tuba, 2014*):

$$Visibility_{HYBRID} = a \cdot Visibility_{STAT} + b \cdot Visibility_{NUM} , \quad (2)$$

where $a + b = 1$ and $a, b \in [0; 1]$. We specified that the statistical prediction weights should decrease

- with increasing category difference, because it corrects the potential initial inaccuracy of numerical model, and
- monotonically over time to provide the gradual transition between the statistical and numerical methods (*Bottyan et al.*, 2013).

On the basis of the above mentioned things, we can compose a weight matrix, with rows for the absolute category differences and columns for the time steps. *Table 2* gives an example for this kind of matrix with statistical model weights. Weights are optimized by verification parameters as absolute and root mean square error.

Table 2. The potential weights of statistical model are based on an experimental experts' first guess was examined on the LHSN data in the August 2013 and February 2014 period

		t+1	t+2	t+3	t+4	t+5	t+6	t+7	t+8	t+9
Absolute category difference	**4**	1.00	1.00	1.00	0.90	0.80	0.65	0.50	0.35	0.20
	3	1.00	1.00	0.90	0.80	0.70	0.55	0.45	0.30	0.20
	2	1.00	0.90	0.85	0.75	0.65	0.50	0.40	0.25	0.15
	1	0.90	0.85	0.80	0.70	0.60	0.45	0.35	0.20	0.10
	0	0.90	0.80	0.70	0.60	0.50	0.40	0.30	0.20	0.10

6. The Hungarian Unmanned Meteorological Aircraft System (HUMAS)

In the Hungarian Unmanned Meteorological Aircraft System (*Mikó et al.*, 2009; *Szabó et al.*, 2013) for meteorological UAS measurements the BHE Bonn UAS has been mounted with the meteorological system as described below. The main features of the aircraft are the following: 16 kg total weight with 3 kg maximum payload, electrical propulsion that provides around 60–90 km/h IAS cruising speed, approximately 60–90 minutes duration, and more than 3000 mAGL flight altitude. The aircraft is equipped with a two-way microwave data communication system with a range of 15–20 km. The meteorological system is autonomous, independent of the UAS flight system, with its own power, GPS, IMU, and other sensors. It can be easily mounted on any other platform such as multi-copters or balloons.

The meteorological system is composed of a central unit and sensor units. The central unit (CU) is responsible for collection of the sensor unit (SU) data, pre-processing, and logging as well. The CU contains the power supply for the system, the onboard computer, and an UAS key for the data storage as shown below (*Table 3*).

Table 3. The structure of the central unit (CU)

Device	Application
BeagleBone A6 single-board-computer	Pre-processing and logging. Features: 700MHz ARM Cortes-A8, Linux OS on micro SD card, 256MB DDR2
Replaceable USB-key storage	Collecting of SU data
Power supply	Power supply for the independent meteorological measurement system. 7.4V, 3300mAh Li-Po with 2 cells providing > 6 hours duration depending on SU setup

The SU contains all those instruments that necessary for collecting data usually provided by radiosondes. Because of the fast climbing and sinking rate during airborne measurements, it is necessary to sampling in a high frequency, particularly in temperature and relative humidity measurements (*Martin et al.*, 2011). According to this expectation, two sensors were placed on the HUMAS: a Vaisala HMP 45 (slow sampling) and a Texas Instruments TMP102 with a high frequency sampling rate (*Table 4.*). The sensors were mounted on the top part of the HUMAS's nose in a well perfused box (*Fig. 7*). The Vaisala probe was shielded with a white PVC tube with holes. The high sampling rate gave us an opportunity to measure not only vertical profile but temperature and relative humidity anomalies in up- and downdrafts during horizontal flight path (*Reuder et al.*, 2009).

Table 4. The structure of the sensor Unit (SU)

Device	Measured variables	Derived variables	Sampling frequency (Hz)	Accuracy	Resolution
TMP102	Temperature		10	0.5°C	0.0625°C
HIH-4030	Relative humidity		10	±3.5%	0.5%
BMP085	Pressure	Barometric altitude	10	±1.0hPa	±0.2hPa
GPS uBlox 6 SPK-GPS-GS407A 50 Channel	φ, λ	Ground speed, Track	4		Horiz. <2.5m
3-Axis MEMS accelerometer, 9-Axis MotionFusion	Euler angles (Θ, φ, ψ)		100	16384 LSB/g	±16384 LSB/g
HMC5883L 3-Axis digital compass with Atmega328 microcontroller	Magnetic direction (MagX, MagY, MagZ)	Heading	100	1370LBS /gauss	1°
Vaisala HMP50	T		1	±4.0%	1%
Vaisala HMP50	RH		1	±0.6°C	0.1°C
Prandtl-tube with HCLA 12X5EU and HCA-BARO pressure sensor	Pdin, Pstat	IAS, Barometric altitude	100	±6Pa, ±5mbar (baro.)	
5HP with HCLA 02X5EB and HCLA 12X5EU pressure sensor	Pdin, Pstat	IAS, Barometric altitude, Angles of attack: α, β	100	±2.5Pa	

The system included GPS, accelerometer, digital compass, and the Prandtl-tube or the 5HP five holes probe that allowed us to apply several wind estimation methods, however, new methods were developed for wind measurements which have a lower instrumentation demand (*Szabó et al. 2013*). With the five holes probe (5HP) developed by the Technical University of Budapest (*Varga* and *Balczó*, 2013), high frequency 3D flow data became available (*Fig. 7*). With the combination of the measured 3D flow field and the temperature and humidity data, sensible and latent heat flow, could be investigated (*Bonin et al., 2013*).

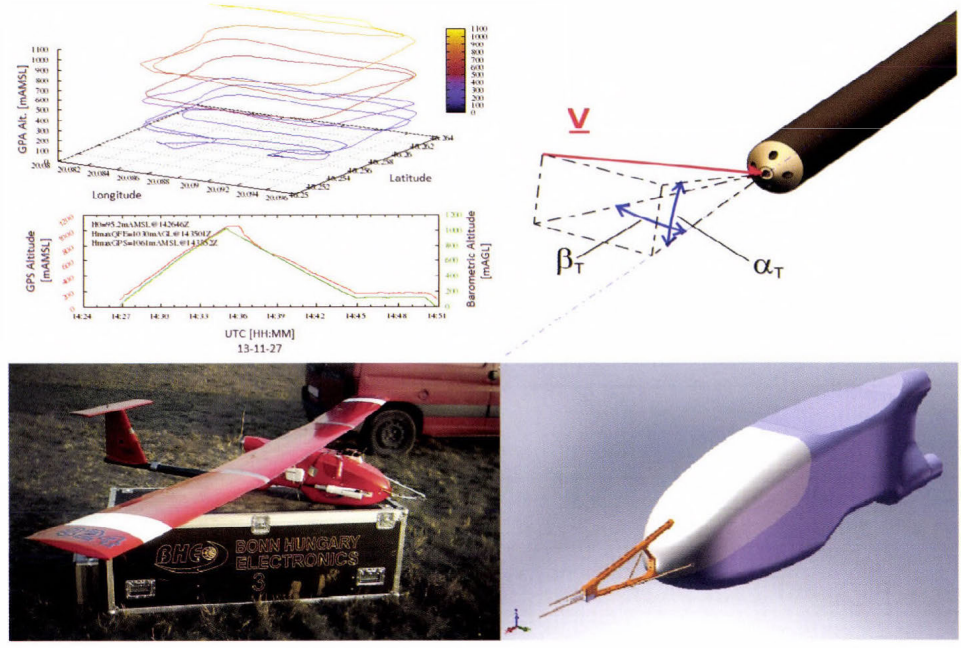

Fig. 7. Track of flight No. 4, Szeged, November 28, 2013 during the PABLS-2013 international measurement campaign (upper left), picture of the HUMAS (bottom left) and the 5HP pressure sensor (upper right) and its mounting on the nose of the HUMAS (bottom right).

7. Preliminary results and discussion

After the description of the statistical, dynamical, and hybrid forecast system, followed by the presentation of the UAS based meteorological aircraft system, hereafter the applicability of the development will be demonstrated. In the following section the evaluation of the visibility forecast of a longer period of case is followed by the presentation of the preliminary results of an international atmospheric boundary layer observation campaign, where the system has been tested and performed suitable.

7.1. Visibility forecast

In order to show the efficiencies of developed analog visibility forecasting model, the whole climatic database was divided into two different and

independent parts. The first one is for searching analog weather situations using fuzzy logic to the selected reports which are from the second dataset and they represent its every third hour. This control dataset contains the available and selected weather information of 2012. Nine-hour-long categorical forecast was examined (*Bottyán et al.*, 2013). The number and interval of categories are easily changeable in the verification template, so we can control the dependency of the results due to the different values.

Doswell et al. (1990) showed that there is no omnipotent verification method. For comprehensive verification of forecasts, it is advised to use several skill scores and verification parameters (α, *BIAS*, *POD*, *POFD*, *FAR*, *HIT*, *CSI*, *TSS*, *HSS*, etc – see *Nurmi*, 2003). To the calculations we used a 2×2 contingency table of different categories of the parameter under verification (*Table 5*). As described in *Bankert* and *Hadjimichael* (2007): "Heidke skill score (*HSS*) is computed to measure the performance of each algorithm relative to random chance". Positive, zero, or negative *HSS* value indicates better, no better, or worse forecast performance than random chance, respectively. It is very important to note, that HSS values remain correct with verification of rare events, which is typical in case of low visibilities. According to the reasons, we present mainly the *HSS* values of visibility forecasts of the different prediction methods.

Table 5. Contingency table for categorical forecasts of binary events

		Event observed	
		YES	**NO**
Event forecasted	**YES**	**a** (hit)	**b** (false alarm)
	NO	**c** (missed)	**d** (correct rejection)

Some naive forecasts (e.g., persistence) can be a standard of reference *Murphy* (1992), or in other words, a competitive benchmark in the field of short term forecast verification. Thus, we show the verification results of persistence forecast on every figure for the comparability of outcomes. As it can be shown in *Fig. 8,* analog statistical forecast was generated for every third hour of the control period applying two different methods. Firstly, we did not use weights for highlighting the importance of the forecast element; secondly, we applied the calculated AHP weights. Each of them means almost 3000 model runs per examined airports (LHSN, LHPA, LHKE, and LHBP) in 2012.

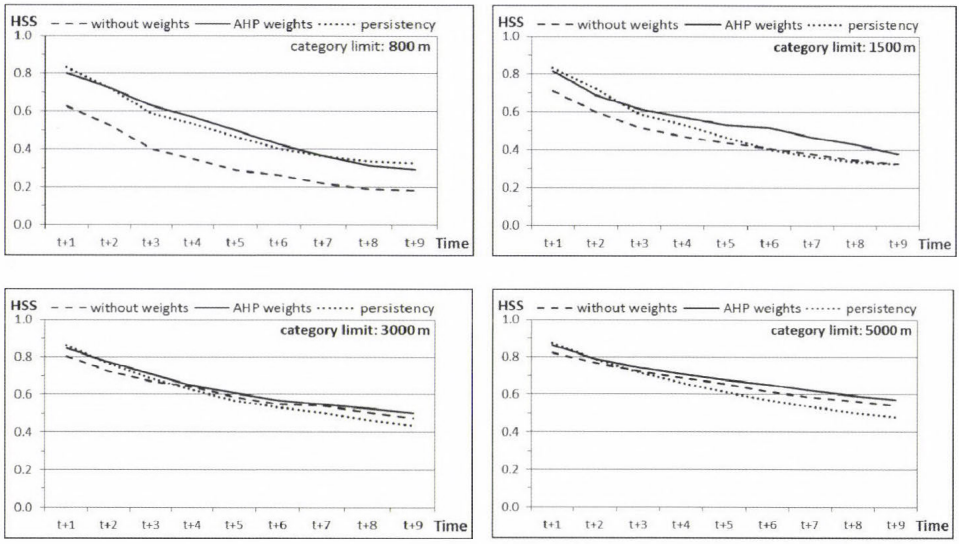

Fig 8. Average *HSS* of examined Hungarian airports (see *Fig. 2*) for predictions of different category limits and for the applied forecast methods for the year of 2012

Then we calculated the *HSS* values for both the methods and all of the examined category limits (800 m, 1500 m, 3000 m, and 5000 m), as well as the persistence forecast.

We found that application of AHP weights improved significantly the performance of analog forecasting during the whole nine-hour forecasting period. It is especially true in case of lower visibility ($\leq$ 1500 m). The applied AHP weights make analog forecasting highly competitive with persistence forecast in these categories.

In the following we show a case study, which represents how the hybrid model can correct the different visibility forecasts. On December 23, 2013, the synoptic situation over Central Europe was determined by anticyclonic effects. In Hungary, the weather was misty and foggy in several places day long. Only weak cold front touched the northern part of the country, and it caused some changes later. In Szolnok Airport (LHSN, 12860) there was broken or overcast ceiling at 4000 m during the previous night. Due to the clouds, the visibility decreased only to 3000 m. The clouds did not help the improvement of visibility during daytime. In the early evening hours the clouds became scattered, and due to the radiation, the visibility started to decrease rapidly, and finally dense fog formed by 21 UTC.

The most important part of this situation for us is the forecast period which starts at 15 UTC. The nine-hour time period covered the formation of fog. The

numerical forecasts were from the 12 UTC model run, and the statistical model used data from the 14:45 UTC and the previous observations. This case study intentionally uses the situation described aboave, when the numerical forecast is significantly different from the observation at the initial time step ($t + 0$). *Fig. 9* shows the observed and forecasted visibility values calculated by the different models.

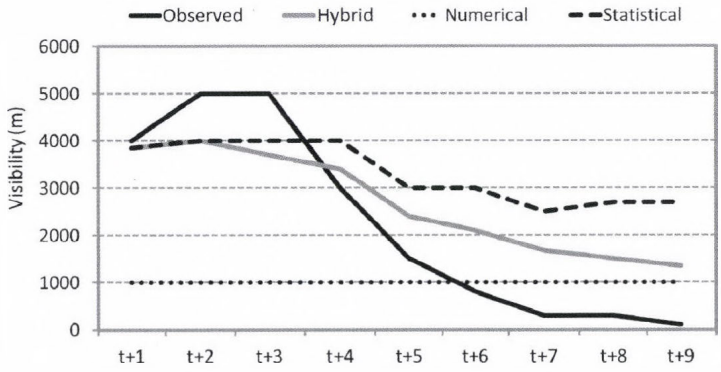

Fig. 9. The observed and different predicted visibility values for Szolnok Airport (LHSN, 12860) on December 23, 2013 ($t + 0 = 15$ UTC).

The lowest output value of the out-processing method of the numerical forecast is 1000 m. It means in the practice, that fog formed at the location. In the first part of the forecasting period, the numerical model significantly missed to correctly predict the visibility. In the second part, the statistical model missed to forecast the decreasing amount of clouds, and due to this, its visibility forecast was incorrect after that. In this situation, the hybrid model provides the best performance in forecasting visibility.

7.2. PBL profiles from HUMAS measurements and model forecasts

In the following part of this section, the preliminary results of an international measurement campaign in late November, 2013 at Szeged, Hungary is discussed, on which the HUMAS has been deployed and performed suitable.

In the first iIntensive operation periods (IOP), on November 27 and 28, 2013, during the Pannonian Atmospheric Boundary Layer Experiment (PABLS-2013, in November 25–30, 2013), Szeged was located between a high pressure system over Central Europe and a low one over the Balkans. Airflow was from E-

NE to W-SW, and layer clouds between 800 m and 3000 m could be observed. Not far from the site, to the North of latitude N45.5°, the sky cleared up and remained clear during the whole night, but stayed overcast with occasional snow falls over Szeged. After 2300Z, precipitation stopped and cloud cover decreased from OVC to BKN, and finally to FEW clearing up until sunrise (0558Z). Altogether five different HUMAS measurement flights were performed before sunset and after sunrise. The main characteristics of the flights are summarized in *Table 6.* In this section, the WRF model results of the high resolution (d03) domain will be compared to UAS measurements, and also to other data from different sources with respect to temperature, humidity, and wind features.

Table 6. Main characteristics of the HUMAS flights during the PABLS-2013 measurement IOP1 on November 27–28, 2013. T/O time is the take-off time in UTC, Flt time is the flight time seconds, Hmax is the maximum height above ground level, achieved during the flight, T range, Rh range, and p range: temperature, relative humidity, and pressure maxima and minima, respectively

No.	T/O time [day UTC]	Flt time [sec]	Hmax [m]	T range [°C]	Rh range [%]	p range [hPa]
1	27. 10 29:19	847	530	–3.4/2.5	66.8/88.1	955/1014
2	27. 12 49:37	674	483	–2.4/2.9	66.4/81.9	961/1015
3	27. 14 26:46	1444	1030	–5.9/5.9	62.4/93.9	901/1016
4	28. 06 04:28	2813	1979	–6.3/-0.2	63.3/91.9	806/1020
5	28. 09 34:41	3166	2178	–5.9/0.2	48.1/84.6	800/1021

Flight patterns have been selected to ensure maximum measurement accuracy with respect to meteorological variables, especially the calculation of wind components from GPS ground speed, (Prandtl-tube) IAS (indicated airspeed), and magnetic data. The flight path followed vertically staggered, quadratic path, keeping altitude for 3 legs and ascending/descending to the next level on the 4th leg, respectively (*Fig. 7*). Wind component speeds have been calculated from the ground speed differences on counter direction legs, and corrected with airspeed and magnetic data (*Cho et al.*, 2011; *Szabó*, 2014). In addition to onboard thermometers and humidity sensors, the UAS carried an additional Vaisala RS92-SGP radiosonde measuring unit for calibration purpose. During the IOP, the vertical flow structure of the site has been monitored with a SODAR equipment (METEK PCS.2000–24) in the lower 400 to 500 m layer.

From the comparisons, only for flight No. 4 will be presented here (*Figs. 10–11*). This flight has been carried out during the morning transition on the dawn after the night of 28 of November 2013.

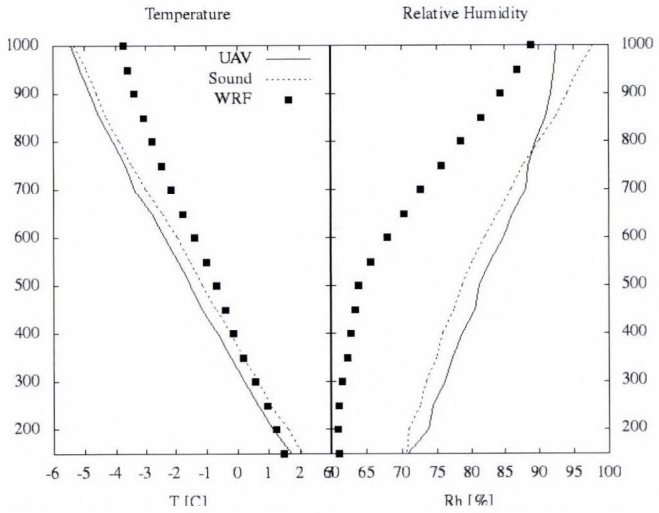

*Fig. 10.*Temperature and relative humidity data comparison. Measured data (HUMAS – solid line) is compared to measurements by operational Vaisala radiosonde device onboard of HUMAS (dotted line) and to the predicted data of the numerical weather model (high resolution, (d03) nested WRF domain – black squares). Flight No. 4, Szeged, November 28, 2013.

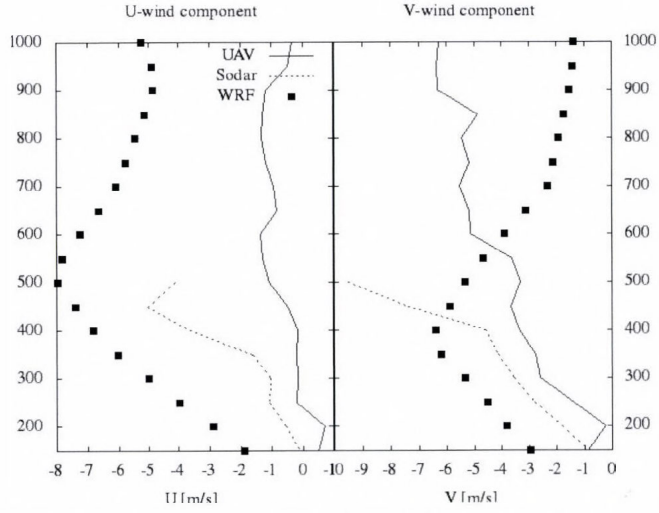

Fig. 11. Wind speed components *U* (zonal) and *V* (meridional) data comparison. Measured data (solid line) is compared to measurements by METEK PCS.2000-24 SODAR (dotted line) and to the predicted data of the numerical weather model (high resolution, (d03) WRF nested domain – black squares). Flight No. 4, Szeged, November 28, 2013.

In order to verify the measurements to standard meteorological sensors, temperature and relative humidity data were compared to a normal Vaisala RS92-SGP radiosonde unit that was carried onboard. From the qualitative comparison of *Fig. 10* it can be seen, that the temperature measurements were a little bit underestimated (negative bias), while humidity data provided by the HUMAS were a little higher than the reference, yielding an overestimation in the measurements. Comparing the measurements to modeled data shows that the model predicted more stability in the lower layer than the real temperature lapse rate, that might be a result of the under prediction of layer clouds and humidity (and of radiative cooling near surface) compared to realistic conditions in the lower layers. This sort of under-prediction in terms of humidity is clearly visible on the right panel as well, where the modeled relative humidity curve differs significantly from both measurements, especially in the lower 800 m layer. In *Fig. 11* data are presented in a manner same as in *Fig. 10* but for U and V wind components. Here the measured data has been compared to SODAR detection in the lower 500 m layer.

From the comparison of SODAR data to HUMAS measured wind data it can be seen, that there is a significant difference between the data over 300 m AGL. It should be noted however, that other wind measurements during this campaign yielded much better agreement to SODAR data than in this case, and the SODAR measurements over 300 m in certain meteorological conditions are slightly unreliable. Provided that the SODAR data are unreliable in this case over 300 m and if we consider the wind measurements of HUMAS as accurate, we can verify our model results to UAS measurement. It should be pointed out that the model predicted wind direction relatively precisely, but performed poorly in terms of wind speed, yielding in significant overestimation for wind speeds.

According to the preliminary results above, it should be pointed out that HUMAS proved to be a suitable platform for micro-meteorological in-situ measurement of the atmospheric boundary layer. Its operational costs and flexibility are much more suitable to the possibilities and needs of PBL measurements. As pointed out by *Passner et al.* (2009), *Marius et al.* (2012), *Stenmark et al.* (2014), for example, UAS measurements can yield valuable atmospheric data not only for experimental research but it may become an operational source of data for regional model calculations in the near future.

8. Conclusions

Proper, detailed, and significant meteorological support is essential during the planning and executing phases of civilian and military UAS missions. For the smooth operation of such systems, it is very important to generate accurate, high-resolution, short-time predictions of ceiling, visibility, turbulence, icing, and other aviation meteorological factors.

The meteorological support system for UAS missions described in the current paper is based on the followings parts:

- an adequate data base of four Hungarian airports derived from freely accessible METAR data,
- application of statistical, dynamical, and special hybrid methods that can help the forecaster to give prognostic information for the UAS pilots and specialists,
- specially tuned and set-up numerical weather prediction model which can provide high resolution weather prediction over the Carpathian-basin,
- special post-processing system which is based on model products for the prediction of some hazardous weather phenomena such as low visibility and ceiling, turbulence, wind shear, icing etc.,
- a special web site to deliver adequate meteorological information in graphical, text and other formats via (mobile) web connection, and
- the first Hungarian meteorological UAS (HUMAS) specially equipped for the purpose of boundary layer measurements, which has been developed and successfully used during the mentioned project.

In the future, we can give the flight path optimization based on our predicted weather situation, and also we continue the development and testing of our UAS-based airborne meteorological measurement system.

Acknowledgement: The authors thank *Károly Kazi* for using of Bonn Hungary Ltd's UAS system and *Péter Szalóky* for the AIRMET data set. Great thanks for providing the dataset during Pannonian Atmospheric Boundary Layer Experiment Szeged (PABLS-2013) to *Joan Cuxart Rodamilans*, *Gemma Simó Diego*, *Burkhard Wrenger*, *Dávid Tátrai*, *István Aszalos*, *Szabolcs Rózsa*, *Árpád Bordás*, *János Unger*, *János Józsa*, and *Melinda Kiss*. This research supported by the European Social Fund (TÁMOP-4.2.1.B-11/2/KMR-2011-0001 and TÁMOP-4.2.2.C-11/1/KONV-2012-0010 projects). Financial support by the Hungarian Scientific Research Foundation (OTKA, project no. K83909 and no. NN109679) is also gratefully acknowledged.

References

Ács, F., Horváth, Á., Breuer, H., and *Rubel, F.*, 2010: Effect of soil hydraulic parameters on the local convective precipitation. *Meteorol. Z. 19,* 143–153.

Ács, F., Gyöngyösi, A.Z., Breuer, H., Horváth, Á., Mona, T., and *Rajkai, K.*, 2014: Sensitivity of WRF-simulated planetary boundary layer height to land cover and soil changes. *Meteorol. Z. 23*, 279–293

Adams, S.M. and *Friedland, C.J.*, 2011: A survey of unmanned aerial vehicle (UAS) usage for imagery collection in disaster research and management." 9th International Workshop on Remote Sensing for Disaster Response.

Al-Harbi, K.M., 2001: Application of the AHP in project management. *Int. J. Proj. Manag. 19*, 19–27.

Balogh, M., Horányi, A., Gyöngyösi, A.Z., André, K., Mile, M, Weidinger, T., and *Tasnádi P.* 2011: The ALADIN/CHAPEAU model as a new tool for education and inter-comparison purposes at the Eötvös Loránd University in Budapest. *HIRLAM Newsletter 58*, November 2011.

Bankert, R. L. and *Hadjimichael, M.*, 2007: Data Mining Numerical Model Output for Single-Station Cloud-Ceiling Forecast Algorithms. *Weather Forecast. 22,* 1123–1131.

Bardossy A., Duckstein, L. and *Bogardi, I.*, 1993: Combination of fuzzy numbers representing expert opinions. *Fuzzy Set. Syst. 57*, 173–181.

Bonin, T., Chilson, P., Zielke, B. and *Fedorovich, E.*, 2013: Observations of the Early Evening Boundary-Layer Transition Using a Small Unmanned Aerial System. *Bound.-Lay. Meteorol. 146*,119–132.

Bottyán, Z., Wantuch, F., Tuba, Z., Hadobács, K., and *Jámbor, K.*, 2012: Repülésmeteorológiai klíma adatbázis kialakítása az UAV–k komplex meteorológiai támogató rendszeréhez. *Repüléstudományi Közlemények 24*, 11–18. (In Hungarian.)

Bottyán, Z., Wantuch, F., Gyöngyösi, A.Z., Tuba, Z., Hadobács, K., Kardos, P., and *Kurunczi, R.*, 2013: Development of a Complex Meteorological Support System for UASs. *World Academy of Science, Engin. Technol. 7*, 648–653.

Breuer, H., Ács, F., Laza, B., Horváth, Á., Matyasovszky, I. and *Rajkai, K.*, 2005: Sensitivity of MM5-simulated planetary boundary layer height to soil dataset: comparison of soil and atmospheric effects. *Theor. Appl. Climatol. 109*, 577–590.

Bretherton, C.S. and *Park, S.*, 2009: A new moist turbulence parameterization in the Community Atmosphere Model. *J. Climate 22*, 3422–3448.

Büttner, G., Feranec, J., Jaffrain, G., Steenmans, C., Gheorghe, A., and *Lima, V.*, 2002: Corine land cover update 2000. Technical guidelines. Copenhagen, Denmark: European Environment Agency.

Chen, F. and *Dudhia, J.*, 2001: Coupling an advanced land-surface/hydrology model with the Penn State-NCAR MM5 modeling system, part I, Model implementation and sensitivity. *Month. Weather Rev. 129*, 569–585.

Cho, A., Kim, J., Lee, S. and *Kee, C.*, 2011:, Wind Estimation and Airspeed Calibration using a UAS with a Single-Antenna GPS Receiver and Pitot Tube. *Aerospace Electronic sys. 47*, 109–117.

Cuxart, J., Weidinger, T., Wrenger, B., Jimenez, M. A., Simo, G., Gomila, G., Warmers, H., Gyongyosi, A. Z., Istenes, Z., Bottyan, Z., Tatrai, D., Kiss, M., and *Jozsa, J.*, 2014: Joint Surface Budget Station, Tethered Balloon and RPAS Campaign SEABREEZE13 and PABLS13. ISARRA 2014 is held at Hans Christian Andersen Airport in Odense, Denmark, on May 26 to 28., http://www.isarra.org/isarra2014.html

Doswell III, C. A., Davies-Jones, R., and *Keller, D. L.*, 1990: On summary measures of skill in rare event forecasting based on contingency tables. *Weather Forecast. 5*, 576–585.

Drury, J.L., Riek, L. and *Rackliffe, N.*, 2006: A decomposition of UAS-related situation awareness. In proceedings of the 1st ACM SIGCHI/SIGART conference on Human-robot interaction, New York, NY, USA, 88–94.

Drüszler, Á; Vig, P. and *Csirmaz, K.*, 2011: Impacts of Hungarian Land Cover Changes on the Regional Climate during the 20th Century. In: XXVth Conference of the Danubian Countries, Budapest, Hungary.

Dudhia, J., 1989: Numerical study of convection observed during the Winter Monsoon Experiment using a mesoscale two-dimensional model. *J. Atmos. Sci. 46*, 3077–3107.

Evans, J.P., Ekström, M. and *Ji, F.*, 2012: Evaluating the performance of a WRF physics ensemble over South-East Australia. *Clim. Dynam. 39*, 1241–1258.

Fekete, Cs., and *Palik, M.*, 2012: Introduction of the Hungarian unmanned aerial vehicle operator's training course. *Def. Res. Manage. 21st Cent. 1*, 55–68.

Fövényi, A., 2010: Meteorológiai előrejelzések készítése sportrepülők részére numerikus modelladatok felhasználásával – régi és új módszerek adaptálása és automatizálása. *Repüléstudományi Közlemények 22* (Special Issue). (In Hungarian)

Garcia, M., Viguria, A., and *Ollero, A.*, 2013: Dynamic Graph-Search Algorithm for Global Path Planning in Presence of Hazardous Weather. Dynamic Graph-Search Algorithm for Global Path Planning in Presence of Hazardous Weather. *J. Intelligent Robotic Sys. 69*, 285–295.

Gertler, J., 2012: U.S. Unmanned Aerial Systems. Congressional Research Service. https://www.fas.org/sgp/crs/natsec/R42136.pdf.

Gyöngyösi, A.Z., Kardos, P., Kurunczi, R., and *Bottyán, Z.,* 2013: Development of a complex dynamical modeling system for the meteorological support of unmanned aerial operation in Hungary. Proceedings of International Conference on 28 – 31 May 2013, Atlanta, GA, USA.

Hansen, B., 2007: A Fuzzy Logic–Based Analog Forecasting System for Ceiling and Visibility. *Weather Forecast. 22*, 1319–1330

Hadobács, K., Tuba, Z., Wantuch, F., Bottyán, Z., and *Vidnyánszky, Z.*, 2013: A pilóta nélküli légijárművek meteorológiai támogató rendszerének kialakítása és alkalmazhatóságának bemutatása esettanulmányokon keresztül. *Repüléstudományi Közlemények 25*, 405–421. (in Hungarian)

Hágel, E., 2009: Development and operational application of a short-range ensemble prediction system based on the ALADIN limited area model. Ph.D. Thesis, Eötvös Loránd University, Faculty of Science.

Hirardelli, J.E.G., and *Glahn, B.*, 2010: The Meteorological Development Laboratory's Aviation Weather Prediction System. *Weather Forecast. 25*, 1027–1051.

Hong, S.-Y., Dudhia, J., and *Chen, S.-H.*, 2004: A Revised Approach to Ice Microphysical Processes for the Bulk Parameterization of Clouds and Precipitation. *Month. Weather Rev. 132*, 103–120.

Horányi, A., Mile, M., and *Szűcs, M.*, 2011: Latest developments around the ALADIN operational short-range ensemble prediction system in Hungary. *Tellus A 63*, 642–651.

Hu, X.-M., Nielsen-Gammon, J.W., and *Zhang, F.*, 2010: Evaluation of three planetary boundary layer schemes in the WRF model. *J. Appl. Meteorol. Climatol. 49*, 1831–1844.

Jacobs, A.J.M. and *Maat, N.*, 2005: Numerical guidance methods for decision support in aviation meteorological forecasting. *Weather Forecast. 20*, 82–100.

Kain, J. S., 2004: The Kain–Fritsch Convective Parameterization: An Update. *J. Appl. Meteorol. 43*, 170–181.

Marius, O.J, Ólafsson, H., Ágústsson, H., Rögnvaldsson, Ó., and *Reuder, J.*, 2012: Improving High-Resolution Numerical Weather Simulations by Assimilating Data from an Unmanned Aerial System. *Month. Weather Rev.140*, 3734–3756.

Martin, S., Bange, J. and *Beyrich, F.*, 2011: Meteorological profiling of the lower troposphere using the research UAS "M2AV Carolo". *Atmos. Measure. Tech. 4*, 705–716.

Meyer, M.A., Butterfield, K.B., Murray, W.S., Smith, R.E. and *Booker, J.M.*, 2002: Guidelines for eliciting expert judgment as probabilities or fuzzy logic. In (Eds.: *Ross, T.J., Booker, J.M.* and *Parkinson, W.J.*) Fuzzy Logic and Probability Applications: Bridging the gap. Society for Industrial and Applied Mathematics, 105–123.

Mikó, G., Kazi, K., Solymosi, J. and *Földes, J.*, 2009: UAS Development at BHE Bonn Hungary Ltd. 10th International Symposium of Hungarian Researchers on Computational Intelligence and Informatics, Proceedings. 2009, November 12-14, Budapest, Budapesti Műszaki Főiskola, 803–820.

Mireles, M., Kirth, R., Pederson, L. and *Elford, C. H.*, 2003: Meteorological Techniques (Revision 26 April 2006). No. AFWA/TN-98/002-REV. Air Force Weather Agency Offutt AFB NE.

Mlawer, E.J., Taubman, S.J., Brown, P.D., Iacono, M.J., and *Clough, S.A.*, 1997: Radiative transfer for inhomogeneous atmospheres: RRTM, a validated correlated k-model for the longwave. *J. Geophys. Res.: Atmos. 102(D14)*, 16663–16682.

Murphy, A., H., 1992: Climatology, persistence, and their linear combination as standards of reference in skill scores. *Weather Forecast. 7*, 692–698.

Nurmi, P., 2003: Recommendations on the verification of local weather forecasts. The Library ECMWF Shinfield Park Reading, Berks RG2 9AX, 21 p.

Østbø, M., Osen P., Rokseth, G., Homleid O. V. and *Sevaldrud T.*, 2004: Exploiting meteorology toenhance the efficiency and safety of UAS operations. Forsvarets Forskningsinstitutt, Norwegian Defence Research Establishment FFI/RAPPORT-2004/00981, 50 p.

Passner, J.E., Dumais, R.E., Flanigan, Jr. R. and *Kirby, S.*, 2009: Using the Advanced Research Version of the Weather Research and Forecast Model in Support of ScanEagle Unmanned Aircraft System Test Flights. No. ARL-TR-4746, Computational and Information Sciences Directorate, ARL, 49 p.

Pásztor, L., Szabó, J. and *Bakacsi, Zs.*, 2010: Digital processing and upgrading of legacy data collected during the 1:25.000 scale Kreybig soil survey. *Acta Geodaetica et Geophysica Hungarica 45*, 127–136.

Restás, Á., 2013: On Half Way between the Military and Civil Use - Disaster Management Supported by UAS Applications. In (Eds. *Bale, P., Alderson, R.)* AUVSI 2013 Exhibition and Conference, Washington, USA, 2013. August 12-*15*, 1–10.

Restás, A. and *Dudás, Z.*, 2013: Some aspect of human features of the use of Unmanned Aerial Systems in a disaster-specific division International Conference on Unmanned Aircraft Systems. (ICUAS), 2013_28-31 May 2013 in Atlanta, GA, USA, DOI: 10.1109/ICUAS.2013.6564791.

Reuder, J., Brisset, P., Jonassen, M., Müller, M. and *Mayer, S.*, 2009: The Small Unmanned Meteorological Observer SUMO: A new tool for atmospheric boundary layer research. *Meteorol. Zeit.18,* 141–147.

Saaty, T.L., 1977: A scaling method for priorities in hierarchical structures. *J. Math.Psychol.15*, 234–281.

Saaty, T.L., 1991: Some mathematical concepts of analytic hierarchy process. *Behaviormetrika 29*, 1–9.

Seity Y., Brousseau P., Malardel S., Hello G., Bénard P., Bouttier F., Lac C., and *Masson V.*, 2011: The AROME-France Convective-Scale Operational Model. *Mon. Weather Rev. 139*, 976–999.

Skamarock, W.C., Klemp, J.B., Dudhia, J., Gill, D.O., Barker, D.M., Duda, M.G., Huang, X-Y., Wang, W. and *Powers, J.G.*, 2008: A description of the Advanced Research WRF Version 3. NCAR/TN-475 + STR NCAR Technical Note.

Somlyai, L., Turóczi, A. and *Molnár, A.*, 2012: Atmospheric analyser for mobile robots. *Computational* Intelligence and Informatics (CINTI), 2012 IEEE 13th International Symposium on Date 20–22 November, 2012 Budapest.

Souders, C.G. and *Showalter, R.C.*, 2008: Transformation of NAS to NEXTGEN and FAA's weather architecture impacts: an update. Aerospace Meteorology, AMS 88th Annual Meeting.

Sousounis, P.J., 2005: Short term turbulence forecasts over the Atlantic Ocean using WRF. Preprints, World Weather Research Program Symposium on Nowcasting and Very Short Range Forecasting, September 5-9 2005. Toulouse, France.

Stenmark, A., Hole, L.R., Voss, P., Reuder, J. and *Jonassen, . M.O.*, 2014: The Influence of Nunataks on Atmospheric Boundary Layer Convection During Summer in Dronning Maud Land, Antarctica." *J. Geophys.Res. Atmospheres 119* (11) 6537–6548.

Sun, X., Cai, C. and *Shen, X.*, 2014: A New Cloud Model Based Human-Machine Cooperative Path Planning Method. *J. Intelligent Robotic Sys.*

Szabó, Z. A., 2014: Pilóta nélküli repülőgépeken alkalmazható szondázási módszerek vizsgálata és fejlesztése. MSc Thesis, Department of Meteorology Eötvös Loránd University (In Hungarian).

Szabó, Z.A., Istenes, Z., Gyöngyösi, A.Z., Bottyán, Zs., Weidinger, T. and *Balczó, M.*, 2013: Sounding the planetary boundary layer with Unmanned Aerial Vehicles (UAS). *Repüléstudományi Közlemények 25,* 422–434. (In Hungarian.)

Toth, Z., 1989: Long-Range Weather Forecasting Using an Analog Approach. *J.Climate 2*, 594–607.

Tuba, Z., Bottyán Z., Wantuch, F. Vidnyánszky, Z. and *Hadobács K.*, 2013a: Meteorological support model for meteorological support in military mission planning. *Hadmérnök 8*, 294–304. (in Hungarian)

Tuba, Z., Vidnyánszky, Z., Bottyán, Z., Wantuch, F. and *Hadobács, K.*, 2013b: Application of Analytic Hierarchy Process (AHP) in fuzzy logic-based meteorological support system of unmanned aerial vehicles. *Acad. Appl. Res. Military Sci. 12*, 221–228.

Tuba, Z., 2014: Selected questions of Unmanned Aerial Vehicles (UASs) and visibility. *Repüléstudományi Közlemények 26*, 94–105. (in Hungarian)

Varga, Á. and *Balczó, M.*, 2013: Development of a multi-hole probe for atmospheric boundary layer Measurements. PHYSMOD 2013 – International Workshop on Physical Modeling of Flow and Dispersion Phenomena EnFlo Laboratory, University of Surrey, UK, 16th – 18 th September 2013. http://www.dapple.org.uk/Physmod.html

Wang, W., Bruyère, C., Duda, M. G., Dudhia, J., Gill, D., Lin, H. C., Michalakes, J., Rizvi, S. and *Zhang, X.*, 2009: WRF-ARW Version 3 Modeling System User's Guide, July 2009, Mesoscale & Microscale Meteorology Division, National Center for Atmospheric Research, Boulder, USA Tech. Note.

Wantuch, F., 2001: Visibility and fog forecasting based on decision tree method. *Időjárás 105*, 29–38.

Wantuch, F., Bottyán, Z., Tuba, Z. and *Hadobács, K.*, 2013: Statistical Methods and Weather Based Decision Making in Meteorological Support for Unmanned Aerial Vehicles (UASs). Proceedings of International Conference on 28 – 31 May 2013, Atlanta, GA, USA.

Watts, A.C., Ambrosia, W.G. and *Hinkley, E.A.*, 2012: Unmanned Aircraft Systems in Remote Sensing and Scientific Research: Classification and Considerations of Use. *Remote Sensing 4*, 1671–1692.

Weidinger, T., Cuxart, J., Gyongyosi, A.Z., Wrenger, B., Istenes, Z., Bottyan, Z., Simó, G., Tatrai, D., Jericevic, A., Matjacic, B., Kiss, M. and *Jozsa, J.*, 2014: An experimental and numerical study of the ABL structure in the Pannonian plain (PABLS13). AMS, 21st Symposium on Boundary Layers and Turbulence. June 09 - 13, 2014, Leeds, United Kingdom. ams.confex.com/ams/21BLT/webprogram/21BLT.html

Williams, K.W., 2004: A Summary of Unmanned Aircraft Accident/Incident Data: Human Factors Implications. Final report, Federal Aviation Administration Oklahoma City Ok Civil Aeromedical Inst., ADA460102, 17 p.

IDŐJÁRÁS

Quarterly Journal of the Hungarian Meteorological Service
Vol. 119, No. 3, July – September, 2015, pp. 337–354

Development, data processing and preliminary results of an urban human comfort monitoring and information system

János Unger*, Tamás Gál, Zoltán Csépe, Enikő Lelovics, Ágnes Gulyás

Department of Climatology and Landscape Ecology, University of Szeged
P.O.Box 653, 6701 Szeged, Hungary

**Corresponding author E-mail:* unger@geo.u-szeged.hu

(Manuscript received in final form April 22, 2014)

Abstract—In this study, the infrastructure development and operation of an urban human comfort monitoring network and information system in Szeged and the related preliminary research results are discussed. The selection of the representative sites of the network is based primarily on the pattern of the local climate zones in and around the city. After the processing of the incoming data (air temperature and relative humidity, as well as global radiation and wind speed), a human comfort index (PET) is calculated from the four meteorological parameters are with a neural network method (MLP), then the measured and calculated parameters interpolated linearly into a regular grid with 500 m resolution. As public information, maps and graphs about the thermal and human comfort conditions appear in 10-minute time steps as a real-time visualisation on the internet. As the preliminary case studies show, the largest intra-urban thermal differences between the LCZ areas in a two-day period occurred in the nocturnal hours reaching even 5 °C in early spring. In the spatial distribution of human comfort conditions, there are distinct differences in the strength of the loading or favorable environmental conditions between the neighborhoods during the daytime. Finally, the utilization possibilities of the results in the future are detailed.

Key-words: local climate zones (LCZ), representative measurement sites, monitoring network, psychologically equivalent temperature (PET), multilayer perceptron, thermal and human comfort maps, real-time visualization, Szeged, Hungary

1. Introduction

Examination taking place in the field of urban environmental changes due to the large number of people affected is considered as an important task. The urban environments are specific – compared to the natural ones – because of the alteration in land cover and surface geometry characteristics as well as the human activity, which may significantly affect the energy and water balance of the area leading to local-scale climate modifications in the atmosphere of cities. As a result, the so-called *urban climate* develops (e.g., *Oke*, 1987). The residents are affected directly to the alterations taking place in the *urban canopy layer* (a layer of air between the average height of the buildings and the street level). The most significant modification is the change in the thermal environment (the *urban heat island* phenomenon, UHI), as well as in the human bioclimatic (thermal comfort) conditions influenced by the thermal environment and other weather parameters.

The importance of the investigation of these issues is supported that in cases of some of the already loading or unfavorable weather situations, the city still adheres to these effects. For example, at heat wave situations in cities the nocturnal cooling weakens, thus the periods characterized by significant physiological load are extended.

Within larger settlements due to the intra-urban heterogeneity of the physical attributes of the surface, the thermal modifying effect is also different. It can be assumed that in many respects, the interactions between the urban parameters and thermal comfort as well as some elements of the weather phenomena within the city are not yet known sufficiently. These interactions can only be analyzed properly using detailed and long-term (several years) measurements, like detection and analysis of the characteristics of these urban thermal patterns. This analysis can be performed with the help of a *monitoring network* installed representatively and in appropriate density. For automatic monitoring network set up in the urban canopy layer, there can be found some international – mainly U.S., Japan, and Taiwan – examples, while in Europe there are very few of these, and none of them are aimed at the detection of patterns of human comfort conditions. A network began to be build from 1999 on with temperature sensors located from the center in different directions radially in London (*Watkins et al.*, 2002), while in Florence, there is a system with temperature-humidity sensors operating since 2004, whose elements observe the thermal features of the city's various built-up districts (*Petralli et al.*, 2013). The most complex network (utilizing meteorological stations and sensors) so far was started up in 2011 in Birmingham. Its development is now in progress and its elements are installed at higher density in the downtown area while less densely in the outskirts of the city (HiTEmp Project, 2014).

However, obviously it is not a realistic option to establish monitoring stations network to all major urban areas, therefore, in the long run, the presentation and prediction of the prevailing thermal comfort conditions in urban areas only through the proper downscaling of weather forecasting models is possible. Development of such a method, however, is only possible using representative and high resolution measurement data in space and time, as well as parameters characterizing the urban surface and geometry in an appropriate manner. The forecasting of weather processes in urban areas – at least in the structure and functioning of the models used – is similar to the issue of climate change prediction. Because urban areas significantly influence the local climate, in order to estimate the possible outcomes of climate change, these areas should be taken into account. At the same time – as the majority of the world's population already lives in cities –, if the urban areas are implemented to climate models in appropriate manner and they are transposed to the climate models, it will be possible to have correct forecasts for these areas in the future.

In the present paper, we aim to show the principle and practice of the siting and configuration of a representative urban human comfort monitoring system and its data processing. Furthermore, we aim to present the preliminary results related to the spatial distribution of the intra-urban human comfort conditions and their real-time visualization as a public information, and finally, to show the utilization possibilities of the results in the future.

2. Local climate zones (LCZ), station place selection, monitoring network

The main purpose of the LCZ system is the characterization of the local environment around a temperature measurement site in terms of its ability to influence the local thermal climate. Therefore, the number of types is not too large and their separation is based on objective, measurable parameters. LCZs are defined as "regions of uniform surface cover, structure, material, and human activity that span hundreds of meters to several kilometres in horizontal scale" (*Stewart* and *Oke*, 2012). Their names reflect the main characteristics of the types (*Table 1*).

The LCZ types can be distinguished by typical value ranges of measurable physical properties. These properties describe the surface geometry and cover (sky view factor, aspect ratio, fractions of building, pervious and impervious surfaces, height of roughness elements, terrain roughness class) as well as the thermal, radiative, and anthropogenic energy (surface admittance and albedo, anthropogenic heat output) features of the surface. As a result, the LCZ system consists of ten 'built' and seven 'land cover' LCZ types (*Table 1*). Although, originally it was not designed for mapping, mapping of the urban terrain the system can be efficiently used as to determine areas which are relatively homogeneous in surface properties and human activities.

In the context of the LCZ classification system, the UHI intensity is not an "urban-rural" temperature difference (ΔT_{u-r}), but a temperature difference between pairs of LCZ types ($\Delta T_{LCZ\ X-Y}$), that is an inter-zone temperature difference (*Stewart et al.*, 2013). Consequently, the usage of the system allows the objective comparison of the thermal reactions in different areas within a city and between cities (intra-urban and inter-urban comparisons).

Table 1. Names and codes of the LCZ types (after *Stewart* and *Oke*, 2012)

Built types		Land cover types	
LCZ 1	compact high-rise	LCZ A	dense trees
LCZ 2	compact mid-rise	LCZ B	scattered trees
LCZ 3	compact low-rise	LCZ C	bush, scrub
LCZ 4	open high-rise	LCZ D	low plants
LCZ 5	open mid-rise	LCZ E	bare rock / paved
LCZ 6	open low-rise	LCZ F	bare soil / sand
LCZ 7	lightweight low-rise	LCZ G	water
LCZ 8	large low-rise		
LCZ 9	sparsely built		
LCZ 10	heavy industry		

2.1. LCZs in Szeged

Szeged is located in the south-eastern part of Hungary (46°N, 20°E) at 79 m above sea level on a flat terrain with a population of 160,000 within an urbanized area of about 40 km^2. The area is in Köppen's climatic region Cfb with an annual mean temperature of 10.4 °C and an annual amount of precipitation of 497 mm (*Unger et al.*, 2001). The study area covers an 11.5 km × 8.5 km rectangle in and around Szeged (*Fig. 1*).

In order to apply the LCZ system in the study area, that is to delineate the types occurring therein, a recently developed automated method was used (*Lelovics et al.*, 2014). *Fig. 1.* shows the obtained seven 'built' and four 'land cover' LCZ types and their pattern in and around Szeged.

2.2. Installed and already existing stations

Within the framework of an EU project (URBAN-PATH Project, 2014) a monitoring network with 23 stations (air temperature, *T* and relative humidity, *RH*) was set up in Szeged. Additionally, data series from the stations of the

Hungarian Meteorological Service (HMS) are added. One of them is at the same place where the station D-1 is located (global radiation, G and wind speed, u) and the other is at the University of Szeged (station 5-1) (T, RH, G) (*Fig. 2*). Altogether, the whole network consists of 24 measurement sites.

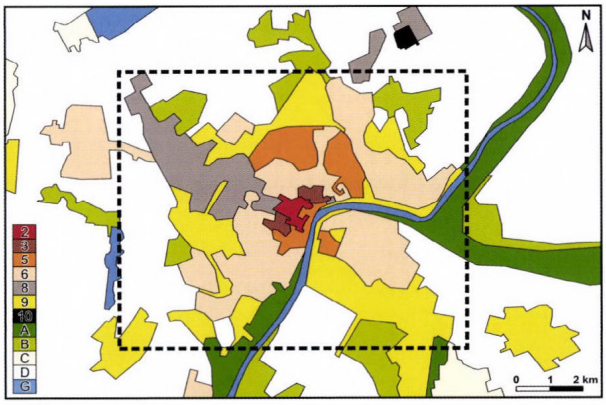

Fig. 1. The obtained LCZ map in Szeged (LCZ 2 – compact mid-rise, LCZ 3 – compact low-rise, LCZ 5 – open mid-rise, LCZ 6 – open low-rise, LCZ 8 – large low-rise, LCZ 9 – sparsely built, LCZ A – dense trees, LCZ B – scattered trees, LCZ C – bush, scrub, LCZ D – low plants, LCZ G – water) and the study area (broken line).

Fig. 2. Station locations of the urban monitoring network in Szeged with their notations (first number indicates the LCZ type, second one indicates the station number in a given LCZ type) (a – station, b – main road, c – water, d – urbanized area) (after *Lelovics et al.* 2014).

In order to have a representative urban human comfort monitoring network within the seven delineated 'built' LCZ areas, the siting and configuration of 22 stations from the above mentioned 24 ones were based on: (i) the distance of the site from the border of the LCZ zone within it was located; (ii) the ability of the selected network geometry to reproduce the spatial distribution of mean temperature surplus pattern estimated by an empirical model (*Balázs et al.*, 2009); (iii) the site's representativeness of its microenvironment; and (iv) the site's suitability for instrument installation. Thus, in summary, two stations (D-1, D-2) represent the rural area, while the other 22 stations the different built-up areas of the city (*Lelovics et al.*, 2014) (*Fig. 2*).

2.3. Measuring equipments

In each monitoring station, the measurement is provided by a Sensirion SHT25 sensor in a radiation protection screen (220×310 mm) at the end of a 60 cm console. The accuracy of the sensor is 0.4 °C and 3% for the temperature and relative humidity, respectively. The radiation protection shield is the same as the model used by the HMS. The consoles are mounted on lamp posts at a height of 4 m above the ground for security reasons. As the air in the urban canyon is well-mixed, the temperature measured at this height is representative for the lower air layers too (but not for the air near the wall or ground) (*Nakamura* and *Oke,* 1988). At the beginning of the console, there are two boxes (*Fig. 3*). The upper one contains the central processor, data storage (microSD) card, GPRS/EDGE/3G modem, battery, and charger. The lower box is utilized in the case of 20 stations where the local electricity provider has made it possible to use the power for the station, and it contains only a separate power switch. At the remaining 4 stations, there is direct access to the power so they do not need any additional boxes.

Fig. 3. One of the stations of the monitoring network on a lamp post (temperature and relative humidity sensors are inside of the radiation shield cylinder).

The system time of the stations (and the whole monitoring system) is in UTC regularly synchronized by the main server. Most of the stations (17 items) have continuous power supply, but seven stations have power supply only when the city lights are on. These seven stations use the power of built in batteries during daytime or at power failure. These stations can operate up to 10 days using only battery power. The stations measure the parameters every minute, and they send the readings with some technical information (battery voltage, temperature inside the box, sensor status) into the main server (Dell PowerEdge T420 tower server) every 10 minutes. If there is no mobile internet connection or the main server does not receive the data, the station tries to send it repeatedly until it succeeded. If the station's battery level is low, the station increases the time between two data transfer to decrease the power consumption. One station (D-1) is located in the garden of the HMS station in order to provide calibration information for the network.

3. Data processing

3.1. Calculation of the human bioclimatological index (PET)

The human (bioclimatological) comfort sensation is formed as the complex effect of air temperature, air humidity, radiation and wind conditions. In order to characterize this comfort sensation, one of the rational indices, the physiologically equivalent temperature (*PET*) is used, which is defined as 'the temperature (in °C) of a standardized fictitious environment (where the mean radiation temperature is the air temperature, vapor pressure is 12 hPa, and wind speed is 0.1 ms^{-1}), in which the body, in order to maintain its energy balance, gives the same physiological responses like in the complex real-world conditions' (*Mayer* and *Höppe*, 1987).

The PET value categories were initially defined according to thermal sensations and physiological stress levels of Central European people, where the comfortable thermal heat sensation (no stress level) are indicated by a range of 18–23 °C (*Matzarakis* and *Mayer,* 1996). Furthermore, ranges of 13–18 °C and 23–29 °C mean slightly cool and slightly warm sensations, that is slightly cool stress and slightly heat stress levels, respectively, etc.

For the calculation of the PET index, an algorithm, the multilayer perceptron (MLP) network structure (*Haykin*, 1999) was developed (*Fig. 4*). It consists of neurons organized in layers. The neuron's differentiable outputs have non-linearity, which ensure that the output of the network is a continuous differentiable function of the weights. The output layer can be linear or non-linear. Even in the simplest case when an MLP contains only one hidden layer, it implements nonlinear mapping in his parameters. MLP use the error backpropagation learning algorithm, which is an iterative learning process based on an instantaneous gradient.

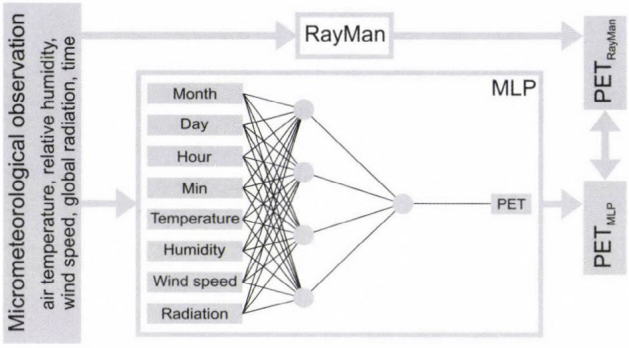

Fig. 4. Flow chart of the development of the MLP

In our case, the input data (air temperature, relative humidity, wind speed, global radiation, time) are derived from the results of the field measurements carried out in different urban microenvironments in Szeged between 2009 and 2013 (e.g., *Kántor* and *Unger,* 2010; *Égerházi et al.*, 2012a, 2012b) (*Fig. 4*). The target output data for the learning was a PET dataset calculated from the same input by the widely used RayMan software (*Matzarakis et al.,* 2007). The MLP model always has one hidden layer and MLP has several parameters that need to be set. They are training time, learning rate, hidden layers, and neurons in the layers. The training time was 1500 epochs, the learning rate started from 0.3 and it was reduced in each step. This helps to stop the network from diverging from the target output as well as to improve the general performance. The number of hidden layers and the nodes in each layer were generated automatically by the WEKA data mining software (*Hall et al.*, 2009). The MLP with these options was applied for predicting the PET index.

3.2. Estimation of the wind and global radiation

For PET calculation in one site in the urban area, the wind speed and radiation data measured there would be ideal. In contrary, if the aim is the monitoring of the thermal comfort conditions in local scale, the direct measurement is not appropriate as the wind speed and radiation measured on site are highly affected by several micro scale phenomena like the arrangement of the nearby obstacles and their effect for the shading and wind flow. Moreover, the deployment of expensive wind and radiation sensors in every urban monitoring site is also not practical because of safety and financial reasons. By virtue of these reasons we used mean wind speed (u_{UCL}) in the urban canopy layer and the undisturbed global radiation (G). The height of the UCL is Szeged in assumed about 30 meters based on the available building database.

As we mentioned, in the study area, the global radiation data are available from the two HMS stations (sites D-1 and 5-1, see Section 2.3). For every monitoring sites, we used the nearest measured global radiation data.

Application of the different forms of logarithmic wind profile (*Oke*, 1987; *Foken*, 2008) for the reduction of the wind speed is prevalent in several thermal comfort studies (*Spagnolo* and *de Dear*, 2003; *Bröde et al.*, 2012). However, this method is questionable if the sum of the roughness length (z_0) and the displacement height (z_d) are higher than the height where we want to calculate the wind speed, because the logarithmic approximation gives 0 ms^{-1} in these cases (*Oke*, 1987; *Foken*, 2008). Therefore, in our study we had to find another solution, because the values of the roughness parameters in urban area (*Gál* and *Unger*, 2009) exceed this limitation. For the estimation of the mean wind speed in UCL, we applied a new method developed for this purpose, however it is mainly based on the power law equation (*Counihan*, 1975):

$$u_1 = u_2 \cdot \left(\frac{z_1}{z_2} \right)^{\alpha}, \tag{1}$$

where u_1 and u_2 are the wind speeds at z_1 and z_2 heights, respectively, and α is estimated as a function of z_0:

$$\alpha \approx \frac{1}{\ln\left(\frac{\sqrt{z_1 \cdot z_2}}{z_0} \right)}. \tag{2}$$

Firstly, we used the Roughness Mapping Tool developed by *Gál* and *Unger* (2013). This is a standalone software for calculation the roughness parameters (z_0, z_d) using building and tree crown database. With this software we calculated z_0 and z_d at the monitoring sites and 8 additional areas. These additional areas are the sites of the earlier thermal comfort studies in Szeged between 2009 and 2012 (*Égerházi et al.*, 2012a, 2012b; *Kántor et al.*, 2011, 2012), and for these areas 59 523 individual wind speed readings are available. We calculated the 10-minute average wind speeds (u_{UCL}) from the 1-minute data of these field measurements and compared them to the 10 minute average wind speed data (u_{10}) from the HMS station. We assumed that u_{UCL} is constant inside the UCL and is equal to u_{10}. Finally, we got 1615 data pairs after filtering out the no- and very weak wind situations ($u<1$ ms^{-1}).

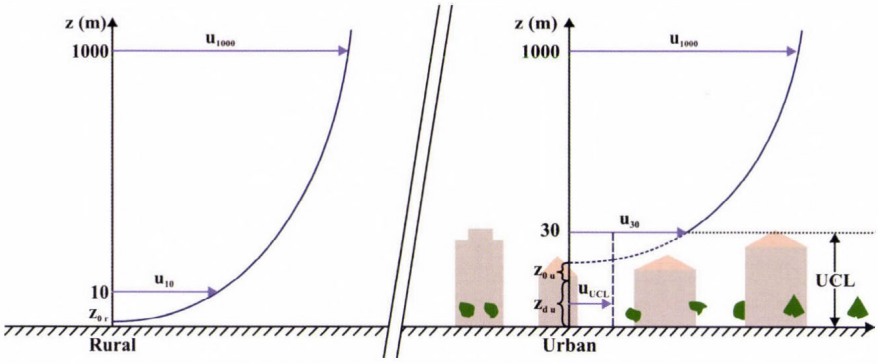

Fig. 5. Concept of the wind speed reduction (for explanation of symbols see the text).

Secondly, the wind speed at a height 1000 m (u_{1000}) was calculated from u_{10} using the logarithmic formula assuming that this u_{1000} value is the regional wind speed unaffected by the drag of the surface (*Fig. 5*). As a next step we determined the wind speed at the top of the UCL (u_{30}) and we calculated a constant (k) with the minimization of the mean square error (MSE) (*Scharf*, 1991) which describes the difference between u_{30} and the measured u_{UCL} (*Fig. 5*). This constant is 0.3331 (MSE=0.3284).

Finally, we obtained the following formula for the wind reduction:

$$u_{UCL} = u_{10} \cdot \left(\frac{1000}{10}\right)^{\alpha_1} \cdot \left(\frac{30 - z_{du}}{1000 - z_{du}}\right)^{\alpha_2} \cdot k \,, \tag{1}$$

where

$$\alpha_1 \approx \frac{1}{\ln\left(\frac{\sqrt{10 \cdot 1000}}{z_{0r}}\right)} \quad \alpha_2 \approx \frac{1}{\ln\left(\frac{\sqrt{(1000 - z_{du}) \cdot (30 - z_{du})}}{z_{0u}}\right)},$$

and subscripts r and u mark the rural and urban sites.

In Equation (1) all value are constants for a given station inside the urban area, except the u_{10} what is measured in the rural station, therefore a complex wind reduction constant (R) was calculated for each monitoring site (*Table 2*) from the constants in this equation. We used this value to calculate the wind speed for the stations from the wind speed measured at D-1 (rural) station at the same time as the time of the PET calculation.

Table 2. Displacement height (z_d), roughness length (z_0), and complex wind reduction constant (R) at urban stations

Station ID	z_d (m)	z_0 (m)	R
2–1	8.7183	1.7455	0.2932
3–1	6.3586	1.4968	0.3116
5–1	6.0872	1.6751	0.3065
5–2	4.6924	2.2986	0.2937
5–3	7.6809	2.0346	0.2887
5–4	5.7750	2.8261	0.2765
6–1	1.7582	0.6740	0.3663
6–2	1.4402	0.4290	0.3856
6–3	1.0717	0.3134	0.3982
6–4	2.6706	0.8682	0.3521
6–5	3.4694	1.0783	0.3392
6–6	3.1466	0.9509	0.3463
6–7	1.5964	0.4782	0.3809
6–8	3.1734	1.1458	0.3372
6–9	1.5275	0.4108	0.3870
6–10	1.2339	0.5226	0.3784
8–1	1.8155	0.2798	0.4001
8–2	2.1910	0.2509	0.4028
9–1	0.1703	0.2000	0.4157
9–2	0.7589	0.2199	0.4111
9–3	0.2805	0.2000	0.4154
9–4	0.7641	0.2177	0.4115

3.3. Operational data processing and display

After the transmission of the station data into the main server every 10 minutes, the automatic data procession system creates the final two (site and spatial) databases (*Fig. 6*) in order to make it possible to present these data as charts and maps on the public homepage of the project (urban-path.hu). Using this public display system, all of the measured and calculated parameters can be accessed a way that the time of the maps and charts can be freely modified by the visitors.

Data received from the monitoring network are stored in one text file per day on the server, and also stored in a MySQL database. Every 10 minutes a Java software calculates the PET value describing the human comfort conditions (see Section 3.1.) for each station using the temperature and relative humidity values measured there, as well as global radiation and wind speed data measured at the

HMS stations (*Fig. 6*). The results of this calculation are also stored in the MySQL database (*Fig. 6*). On the homepage the data, stored in the MySQL database are displayed by charts using PHP scripts.

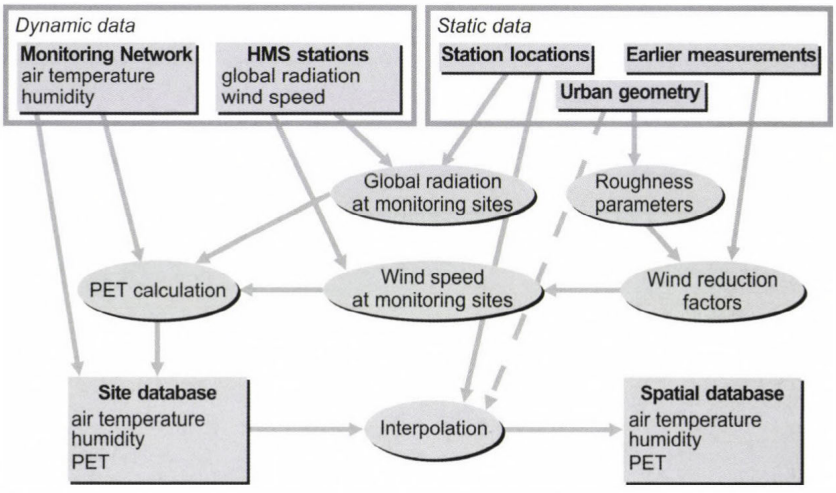

Fig. 6. Flow chart of the automatic data processing of the monitoring system.

For the automatic interpolation of the spatial patterns of the measured and calculated data, a Java software was developed. This program applies simple linear interpolation for a 500 m resolution grid of the study area using the data of the three nearest station of each grid point. In order to avoid the incorrect interpolation in the edge of the study area, the two rural stations are considered as background stations, thus, at the bordering (non-urban) grid points we used the data of the nearest rural station, and all of these points were added to the original measurement points for the interpolation (*Fig. 6*). The coordinates of the grid points and stations are in the Unified Hungarian Projection, but at the end of the interpolation they were converted to WGS84 latitude and longitude coordinates, because it is more appropriate for the further processing (drawing maps with GrADS, comparing the measurements with weather prediction models). At the first hand, we applied a weighting constant (currently it is 1) in the interpolation. After further investigations, we will alter this constant using the statistical connection between the surface parameters (e.g., built-up ratio, SVF, green area, water surface) and the measured temperature, relative humidity, or PET values in order to increase the precision of the interpolation (*Fig. 6*). The final patterns are stored in another, spatial database, which is

technically a NetCDF file. The public project homepage presents these patterns as maps created by GrADS and PHP scripts.

4. Intra-urban variation of the measured and calculated parameters

In this section, the intra-urban differences in the thermal and human comfort conditions are illustrated in selecting time periods, when the weather conditions promoted the microclimatic effects of the spatially varied surface features.

4.1. Temperature data series – comparison of LCZs' thermal reactions

The distinct thermal behavior of the different LCZ areas is shown during a 48 h cloudless period between March 29 and 31, 2014 (from morning to morning) as an example. This period is characterized as a pleasant spring weather. According to the data of the rural HMS station, the insolation was undisturbed during the daylight hours with maximum values of 750–780 Wm^{-2}. The air movement was moderate (0–3 ms^{-1}) except of the first few (daytime) hours (~4–5 ms^{-1}). The days were rather warm with maximum values of 18–20 °C, but the mornings were a bit chilly with the minimum values of 2–4 °C because of the intense nocturnal cooling provided by the cloudless sky.

In order to compare the temperature variations of LCZs during the 48 h period, the areal averages were calculated for every LCZ area. As the number of stations located at these areas is different because of the different areal extent of LCZs (from one station in LCZ 2 to ten in LCZ 6, see *Fig. 2*), the *T*-averages are calculated based on original data with different number of sites. As a result seven temperature series are compared ($\Delta T_{LCZ\ X-Y}$), in accordance with the number of LCZs in the study area (except 'heavy industry' (*Fig. 7*).

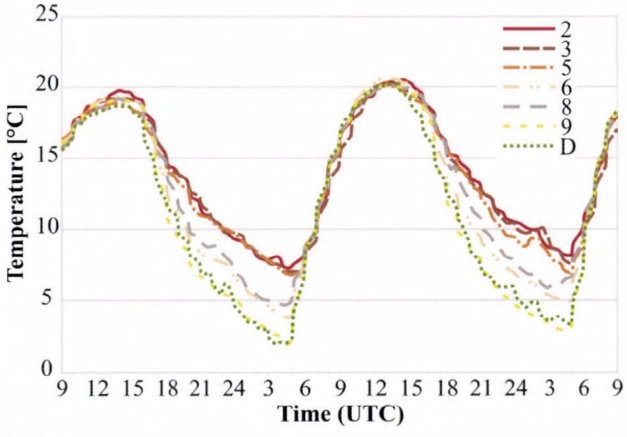

Fig. 7. Temporal variation of the mean LCZ temperatures during a 48 h period (March 29–31, 2014).

As *Fig. 7* shows, the *T*-curves follow the regular shape of the daily temperature cycle in spring, that is warming in the daytime until early afternoon (~8–10 hours) then cooling until dawn (14–16 hours). As expected, LCZ 2 area is the warmest and LCZ 9 and LCZ D types are the coolest, but this is really prevalent at night, as in the daytime the curves move almost together. The largest temperature differences occur in the nocturnal hours: for example, at 4.30 UTC, $\Delta T_{LCZ\ 2\text{–}D} \sim 5$ °C, $\Delta T_{LCZ\ 5\text{–}D} \sim 4.5$ °C, but $\Delta T_{LCZ\ 8\text{–}D} \sim 2{,}5$ °C only, while $\Delta T_{LCZ\ 9\text{–}D} \sim 0$ °C at both nights. This can be explained by the slower cooling of the built-up areas compared to the open and more vegetated rural areas because of the radiation processes at the mentioned weather conditions.

4.2. Maps on temperature, relative humidity, and human comfort

During the processing of incoming data (see Section 3), high resolution maps are produced automatically showing the spatial structures of the thermal, humidity, and human comfort conditions, which appear on the project website continuously updated in 10-minute intervals (online) from June 2014.

As an example, in the case of air temperature and relative humidity, we present the situations in the evening hours (*Fig. 8*). That day was also a typical nice spring one with some cloud drift, so the global radiation was a bit disturbed, therefore in the most intensive period, it varied between 550 and 780 Wm ^{2}. The temperature reached 19°C at the rural HMS station and it was about 10 °C at 20:00 UTC. The daytime wind speed was 2–3 ms^{-1}, then it decreased to about 1 ms^{-1} in the evening.

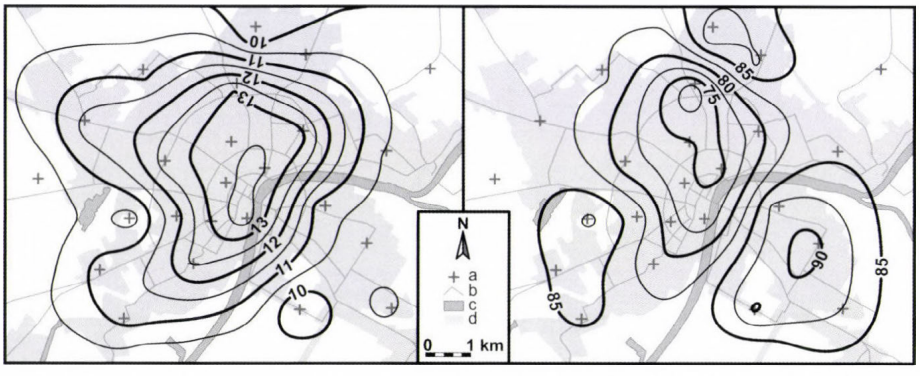

Fig. 8. Intra-urban patterns of temperature (°C) and relative humidity (%) at 20:00 UTC, April 7, 2014 (a – station, b – main road, c – water, d – urbanized area).

The *T*-pattern shows a typical 'island-like' shape with a maximum of over 13.5 °C in the inner city. The values decrease toward the outskirts to about 10 °C (as mentioned above in the case of rural HMS stations). A small deviation from the quasi-concentric shape can be found in the western parts of the city, where small lakes and large green areas are predominant. An opposite case can be experienced for the RH: the largest values (85–90%) occur in the periphery and the smallest ones (under 75%) in the inner parts stretching a bit toward the hosing estates in the north-eastern parts of the city. The shape of the temperature pattern is mostly similar to the results of the previous UHI measurement campaign in Szeged (*Unger et al.*, 2001; *Balázs et al.*, 2009), thus the selection of the sites was really representative.

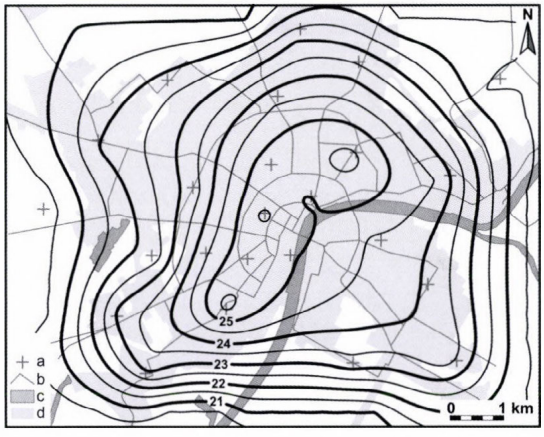

Fig. 9. Intra-urban pattern of human comfort conditions (PET °C) at 12:00 UTC, April 7, 2014 (a – station, b – main road, c – water, d – urbanized area).

In the case of human comfort conditions, the *PET*-pattern for the daytime (12:00 UTC) is presented. At that time, the distribution of temperature (not shown) is almost homogeneous in the study area (with a variation of less than 0.5 °C around 17 °C), but in the *PET* values a range of 20.5–25.5 °C occurs. Accordingly, there is comfortable thermal heat sensation (no stress level) in outer parts of the city (below 23 °C *PET*), and much of the city has been experiencing a very slightly warm sensation (slight heat stress level) (from 23 to 25.5 °C *PET* in the inner parts). Consequently, already in this nice and not too warm early spring day, the environmental conditions in the inner urban parts can be a bit loading for the people. This can be explained by the altered wind conditions (lower wind speeds in the inner urban parts) with rather uniform insolation. This (thermal) load could be strengthened by the fact that after the colder winter days, the thermal contrast (e.g., stronger sunshine) is rather large for the unprepared (not accustomed) people staying outdoors.

5. Conclusions and outlook

Based on this study, the following conclusions can be drawn in accordance with the aims set in Section 1.

Besides the two already existing measurement points, 22 additional sites were selected within the seven delineated local climate zones in Szeged in order to develop a representative urban human comfort monitoring network and information system.

The incoming data (*T*, *RH* from 24 stations, *G*, *T*, and *RH* from the urban HMS station, as well as *G* and *v* from the two HMS stations) were processed by the following steps: firstly, G estimation for each station where it is not measured, then wind reduction for each station using roughness parameters and logarithmic wind profile, and final adjustment using previous street-level wind measurements. Secondly, PET calculation from the four meteorological parameters with a neural network method (MLP) was processed, followed by a linear interpolation of the measured and calculated parameters into a regular grid with 500 m resolution.

As public information, the maps about the thermal and human comfort conditions, and additionally, different graphs about the temporal variations of *T*, *RH*, and PET value appear in 10-minute time steps as a real-time visualization on the project homepage (URBAN-PATH Project, 2014).

According to the preliminary outcomes as case studies, the largest intra-urban thermal differences between the LCZ areas in a two-day period occurred in the nocturnal hours reaching even 5 °C in early spring. These results confirm the findings of *Stewart* and *Oke* (2012), that is the thermal influence of any change or difference in landscapes (e.g., the different levels of urbanization) are better demonstrated using LCZ difference concept than a simple but generally not clear urban-rural approach, and additionally, it provides an opportunity for intra- and inter-urban comparisons. In the spatial distribution of human comfort conditions, there are distinct differences in the strength of the loading or favorable environmental conditions between the neighborhoods during the daytime. As the inhabitants can meet large differences even within relatively short distances, the urban areas can not be considered homogeneous from this respect.

In summary, as a result of the infrastructure development and related research in the frame of the URBAN-PATH project, an operating urban human comfort monitoring network and information system was established in Szeged.

The utilization possibilities of the results in the future are related to the high-resolution weather prediction models which can be applied in the urban environments – these are real alternatives of urban climate measurement networks –, but their results are not adequate enough so far (*Case et al.*, 2008; *Chen et al.*, 2011; *Salamanca et al.*, 2011). Real time predictions of urban meteorological environment are based not only on the attributes of static urban parameters (built-up ratio, sky-view factor, building heights, etc.), because these data are basically constant in the prognostic time-scales. On the other hand, the

actual weather of a given urban region strongly depends on physical processes working in macro- and meso-scales. The mentioned processes can be taken into account only using a well-defined, telescopic downscaling method with the help of a high resolution numerical weather prediction model (such as WRF). Today these high resolution models are directly able to predict the urban meteorological effects and give adequate data for a complex urban weather prediction system. Nevertheless, the basic urban surface data sets and their attributes which are needed to make a successful forecast will have to be specified. Since the urban weather factors mainly work on meso-γ and micro-α scales, the applied numerical model will be able to run with 300 m horizontal resolution and dense vertical layering. Based on the mentioned challenges, it is important to implement a high-resolution urban static database into the WRF system moreover, the global and local (urban) meteorological data assimilation procedures are required. An WRF-based urban meteorological prediction system can be able to give fundamental data for some new research aspects such as military, urban planning, public health, etc., applications.

Acknowledgements: The study was supported by the Hungary-Serbia IPA Cross-border Co-operation Programme (HUSRB/1203/122/166 – URBAN-PATH), in case of the second author by the Hungarian Scientific Research Fund (OTKA PD-100352) and by the János Bolyai Research Scholarship of the Hungarian Academy of Sciences, and in case of the fourth author by the TÁMOP 4.2.4. A/2-11-1-2012-0001 „National Excellence Program – Elaborating and operating an inland student and researcher personal support system convergence program", which project was subsidized by the EU and co-financed by the European Social Fund.

References

Balázs, B., Unger, J., Gál, T., Sümeghy, Z., Geiger, J., and *Szegedi, S.*, 2009: Simulation of the mean urban heat island using 2D surface parameters: empirical modeling, verification and extension. *Meteorol. Appl. 16,* 275–287.

Bröde, P., Fiala, D., Błażejczyk, K., Holmér, I., Jendritzky, G., Kampmann, B., Tinz, B., and *Havenith, G.*, 2012: Deriving the operational procedure for the Universal Thermal Climate Index (UTCI). *Int. J. Biometeorol. 56,* 481–494.

Case, J., Crosson, W., Kumar, S.V., Lapenta, W.M., and *Peters-Lidard, C.D.*, 2008: Impacts of high-resolution land surface initialization on regional sensible weather forecasts from the WRF model. *J. Hydromet. 9,* 1249–1266.

Chen, F., Kusaka, H., Bornstein, R., Ching, J., Grimmond, C.S.B., Grossman-Clarke, S., Loridan, T., Manning, K.W., Martilli, A., Miao, S., Sailor, D., Salamanca, F.P., Taha, H., Tewari, M., Wang, X., Wyszogrodzki, A.A., and *Zhang, C.*, 2011: The integrated WRF/urban modelling system: development, evaluation, and applications to urban environmental problems. *Int. J. Climatol. 31,* 273–288.

Counihan, J., 1975: Adiabatic atmospheric boundary layers: A review and analysis of data from the period 1880-1972. *Atmos. Environ. 9,* 871–905.

Égerházi, L., Kántor, N., Takács, Á., and *Unger, J.*, 2012a: Patterns of attendance and thermal conditions on a pedestrian street. Proceed of the 8th Int. Conf. on Urban Climate. Dublin, Ireland, Paper no. 170.

Égerházi, L., Kántor, N., Takács, Á., Gál, T., and *Unger, J.*, 2012b: Thermal stress maps validation with on-site measurements in a playground. Proceed of the 8th Int. Conf. on Urban Climate. Dublin, Ireland, Paper no. 169.

Foken, T., 2008: Angewandte Meteorologie. Springer, Berlin–Heidelberg.
Gál, T. and *Unger, J.*, 2009: Detection of ventilation paths using high-resolution roughness parameter mapping in a large urban area. *Build. Environ. 44*, 198–206.
Gál, T. and *Unger, J.*, 2013: Calculation of the aerodynamical roughness parameters using building and tree-crown database. In (eds: *Pajtókné Tari I, Tóth A.)* Changing Earth, Changing Society, Changing Learning – The role of renewable energy in regional development Int. Conf. Eger, Hungary, 43–48.
Hall, M., Frank, E., Holmes, G., Pfahringer, B., Reutemann, P., and *Witten, I.H.*, 2009: The WEKA data mining software: an update. *ACM SIGKDD Explorations Newsletter 11*, 10–18.
Haykin, S., 1999: Neural Networks: a comprehensive foundation (2nd ed.). Prentice Hall, Upper Saddle River, NJ.
HiTemp Project, 2014: High Density Measurements within the Urban Environment. http://www.birmingham.ac.uk/schools/gees/centres/bucl/hitemp/index.aspx. Last accessed: April 10, 2014.
Kántor, N. and *Unger, J.*, 2010: Benefits and opportunities of adapting GIS in thermal comfort studies in resting places: An urban park as an example. *Landsc. Urban Plan. 98*, 36–46.
Kántor, N., Gulyás, Á., Égerházi, L., and *Unger, J.*, 2011: Assessments of the outdoor thermal conditions in Szeged, Hungary: thermal sensation ranges for local residents. In (eds: *Gerdes, A., Kottmeier, C.* and *Wagner, A.*) Climate and Construction Int. Conf. Karlsruhe, Germany, 181–190.
Kántor, N., Égerházi, L., and *Unger, J.*, 2012: Subjective estimation of thermal environment in recreational urban spaces—Part 1: investigations in Szeged, Hungary. *Int. J. Biometeorol. 56*, 1075–1088.
Lelovics, E., Unger, J., Gál, T., and *Gál, C.V.*, 2014: Design of an urban monitoring network based on Local Climate Zone mapping and temperature pattern modeling. *Climate Res.* (doi: 10.3354/cr01220)
Matzarakis, A. and *Mayer, H.*, 1996: Another kind of environmental stress: thermal stress. *WHO Newsletter 18*, 7–10.
Matzarakis, A., Rutz, F. and *Mayer, H.*, 2007: Modelling radiation fluxes in simple and complex environments—application of the RayMan model. *Int. J. Biometeorol. 51*, 323–334.
Mayer, H. and *Höppe, P.*, 1987: Thermal comfort of man in different urban environments. *Theor. Appl. Climatol. 38*, 43–49.
Nakamura, Y. and *Oke, T.R.*, 1988: Wind, temperature and stability conditions in an east-west oriented urban canyon. *Atmos. Environ. 22*, 2691–2700
Oke, T.R., 1987: Boundary Layer Climates. (2nd ed.) Routledge, University Press, Cambridge.
Petralli, M., Masetti, L., Brandani, G., and *Orlandini, S.*, 2013: Urban planning indicators: useful tools to measure the effect of urbanization and vegetation on summer air temperatures. *Int. J. Climatol. 34*, 1236–1244.
Salamanca, F., Martilli, A., Tewari, M., and *Chen, F.*, 2011: A study of the urban boundary layer using different urban parameterizations and high-resolution urban canopy parameters with WRF. *J. Appl. Meteorol. Climatol. 50*, 1107–1128.
Scharf, L.L., 1991: Statistical signal processing. Vol. 98. Reading, MA: Addison-Wesley.
Spagnolo, J. and *de Dear, R.*, 2003: A human thermal climatology of subtropical Sydney. *Int. J. Climatol. 23*, 1383–1395.
Stewart, I.D. and *Oke, T.R.*, 2012: Local Climate Zones for urban temperature studies. *Bull. Am. Meteorol. Soc. 93*, 1879–1900.
Stewart, I.D., Oke, T.R., and *Krayenhoff, E.S.*, 2014: Evaluation of the 'local climate zone' scheme using temperature observations and model simulations. *Int. J. Climatol. 34*, 1062–1080.
Unger, J., Sümeghy, Z., Gulyás, Á., Bottyán Z. and *Mucsi, L.*, 2001: Land-use and meteorological aspects of the urban heat island. *Meteorol. Appl. 8*, 189–194.
URBAN-PATH Project, 2014: Evaluations and Public Display of Urban Patterns of Human Thermal Conditions. http://urban-path.hu/. Last accessed: April 20, 2014.
Watkins, R., Palmer, J., Kolokotroni, M. and *Littlefair, P.*, 2002: The London heat island: Results from summertime monitoring. *Build. Serv. Eng. Res. Technol. 23*, 97–106.

IDŐJÁRÁS

Quarterly Journal of the Hungarian Meteorological Service
Vol. 119, No. 3, July – September, 2015, pp. 355–378

Regional air quality models and the regulation of atmospheric emissions

Bernard E.A. Fisher*[1], Charles Chemel [2], Ranjeet S. Sokhi [3], Xavier V. Francis [4], Keith J. Vincent [5], Anthony J. Dore [6], Stephen Griffiths [7], Paul Sutton [8], and Raymond D. Wright [9]

[1] *Retired from Environment Agency, Reading, UK beafisher@cantab.net*
Permanent address: Little Beeches, Headley Road, Leatherhead KT22 8PT, UK

[2] *National Centre for Atmospheric Science, Centre for Atmospheric and Instrumentation Research, University of Hertfordshire, Hatfield, UK c.chemel@herts.ac.uk*

[3] *Centre for Atmospheric and Instrumentation Research, University of Hertfordshire, Hatfield, UK r.s.sokhi@herts.ac.uk*

[4] *Centre for Atmospheric and Instrumentation Research, University of Hertfordshire, Hatfield, UK X.Francis@herts.ac.uk*

[5] *Ricardo-AEA, Harwell, UK Keith.Vincent@ricardo-aea.co.uk*

[6] *Centre for Ecology and Hydrology, Penicuik, UK tony.dore@ceh.ac.uk*

[7] *E.ON Technologies, Ratcliffe-on-Soar, UK Stephen.Griffiths@eon.com*

[8] *RWE npower, Swindon, UK paul.sutton@rwenpower.com*

[9] *Spacefleet Ltd, UK rdw@spacefleet.co.uk*

**Corresponding author*

(Manuscript received in final form October 13, 2014)

Abstract—This paper investigates regional air quality model performance and the regulation of atmospheric emissions. Although evaluation of regional models cannot be reduced to a set of rules, the paper shows ways of developing better understanding of model performance. It draws on studies in recent years by the Environment Agency to quantify the uncertainty in predictions of regional air quality models. It is argued that a decision by a regulator on how to use a regional air quality model should be based on both operational evaluation (involving comparison with observation) and diagnostic

evaluation (for developing understanding of the model), using operational and diagnostic metrics. Operational and diagnostic evaluations were undertaken, using a 'constructor' (CMAQ) and a 'seer' type (TRACK-ADMS) regional air quality model, for the secondary pollutants PM_{10}, $PM_{2.5}$ and ozone, though for episodic ozone it was not possible to define an appropriate performance metric.

Neither type of model showed clearly better performance when applied to long-term average concentrations. There was not enough information to set a minimum margin of error in operational evaluations but margins of 20% or more are to be expected. Unlike operational metrics there is no obvious way of deriving diagnostic metrics. However a footprint diagnostic metric was shown to be a way to reveal the behaviour of PM_{10} and $PM_{2.5}$ in both types of model. It is therefore suggested that seer models are used to reveal the structure of a model's underlying mathematical equations from which diagnostic metrics can be formed.

In the absence of an objective basis for setting acceptance criteria for models, it is proposed that the underlying pragmatic principle should be to use whatever has comparable accuracy with the best existing international practice. For regulatory applications, the error expected in current types of air quality models should be a consideration in any decision made on the basis of models.

Key-words: Inter-comparison, regional air quality, model, footprint, metric, diagnostic, operational, evaluation, seer, constructor

1. Introduction

This paper addresses the question "When is a regional air quality model good enough to be the basis for making a decision about emission reductions to meet limit values?", accepting that the use of an environmental model may only be part of the decision making process. Model evaluation studies involve selecting appropriate metrics or diagnostics (parameters summarising key aspects of the behaviour of a model), and showing that the model can predict the metrics with appropriate accuracy compared with observations.

Regional model development has made considerable progress in recent decades and complex air quality models are essential for assessing secondary pollutants, such as wet deposition, ozone and particulate matter. However just because regional models are the only tools for assessing secondary pollutants, such as ozone and particulate matter, this does not ensure that they are adequate to make decisions about emission reductions.

The paper draws on studies in recent years by the Environment Agency to quantify the uncertainty in predictions of regional air quality models, the latest of which is the CREMO, Comparison of Regional Models, project. The results of the project are described in a number of reports (*Derwent*, 2013; *Fisher*, 2013; *Hayman et al.*, 2013a, 2013b, 2013c, and 2013d). These are used to draw conclusions about whether regional air quality models describing atmospheric concentrations over some 100's to a few 1000 kilometres, are an adequate basis for making decisions about emission reductions to meet environmental criteria.

2. General discussion of environmental models

The way environmental models have been developed and used has been discussed in the literature (*Edwards*, 2010). One can refer to attempts to ensure that models are used properly (*Pilkey-Jarvis* and *Pilkey*, 2008). Air quality models include parameters which are assigned values for the problem in hand, to distinguish them from dependent variables, such as pollutant concentration or deposition. Parameters are usually mathematical functions of coefficients and dependent variables, representing a physical process.

It is rare for there to be sufficient observational data to be able to test exhaustively the behaviour of an environmental model. More often than not for policy applications, one is interested in the behaviour of an environmental system under conditions which have never occurred in nature and one is therefore investigating model scenarios which cannot be explicitly tested. In such situations the qualitative behaviour of the system described by the mathematical model is the only realistic goal. The environmental model can generally be approximated by a set of time dependent non-linear ordinary differential equations. In regional air quality models the synoptic meteorological conditions describe the motion of air masses crossing the main source regions. Under steady synoptic conditions regional pollutant concentrations may build up or decay. Assuming steady meteorological conditions persist for long enough, the solution of the set of mathematical equations tends in time towards a stationary point, though in nature the long time limits are not necessarily reached as meteorological conditions are never steady. However the behavior at stationary points under such idealistic conditions reveals something about the structure of the mathematical system, even if such conditions do not occur in reality. Of special interest are the specific parameter values at points where the qualitative behaviour changes, say from a tendency to decay from initial values to the growth in concentration (see later for a suspected example for ozone of a bifurcation). For this reason two broad categories of model can be distinguished: (1) those which reveal the underlying structure of the mathematical system, and (2) those which try to emulate the full complexity of the environmental system.

Edwards (2010) describes these two broad modelling approaches in relation to climate modelling: in type (1) *model seers*[1] use models to understand and explore the climate system with emphasis on its sensitivity to changing variables and processes. In type (2) *model constructors* seek to capture the full complexity of the climate system, which can then be used for various applications, promoted by the power of modern computing. Constructors seek to include more realism, including all known physical processes that influence the climate. Seers tend to focus on modelling the most fundamental and understood processes and to use a variety of models. The 'state of the art' for seers depends

[1] Definition. A *seer* is one who has insight. The common implication that a seer can predict the future is not relevant in the context of this paper.

on the model application. For constructors a single 'state of the art' model exists, which uses the most up to date observations as input and evaluation, and contains the most detailed and physically realistic parameterisations. This does not separate good from bad modelling practice but illustrates two different strategies for extending knowledge. Seers are generally interested in simple models, which promote understanding, while constructors ignore simple models and focus on complex comprehensive models. Regulators prefer a single model which can be regarded as 'fit for purpose' for making a policy decision, but one conclusion from this paper is not to rely on such a narrow approach to regional modelling.

3. Advances in air pollution assessment

Regulators, such as the Environment Agency in the U.K., need to know whether a model can be used for decision making and this discussion has prompted model comparison exercises, starting with the comparison of dispersion models (*Hall et al.*, 2000a, 2000b) describing concentrations in the near-field out to 20 km from a source, and relatively simple acid deposition assessment models (*Abbott et al.*, 2003), where the model inter-comparison was used to gain understanding of model uncertainty. This paper focuses on the secondary pollutants, particulate matter (PM)[2], both PM_{10} and $PM_{2.5}$ and ozone (O_3). The last decade or so has seen an enormous increase in the sophistication of computer programs, making calculations of secondary pollutants more accessible. The practical implementation of the US Environmental Protection Agency (USEPA) supported CMAQ (Community Multi-scale Air Quality) modelling system, which follows the constructor approach, has been notable. Documentation on CMAQ is available from the official CMAQ website (http://www.cmaq-model.org) [accessed 21 May 2013]. Regulators therefore need to be able to assess the capabilities of different types of air quality models with different levels of sophistication. This has promoted the constructors' approach. However, just because regional models are the only way of assessing secondary pollutants, this does not mean that they are good enough for regulation (*Pilkey-Jarvis* and *Pilkey*, 2008).

Secondary $PM_{2.5}$ is generated on a regional scale, so that the $PM_{2.5}$ concentration is a mixture of local and regional components. Regional models are the only way of assessing the impact of individual sources on the regional component of the $PM_{2.5}$ concentration and of estimating the population exposure. The contribution from local sources is not included within the regional component, because only concentration variations over regional scales, typically

[2] PM_{10} particulate matter less than or equal to 10 microns (50% cut off);
$PM_{2.5}$ particulate matter less than or equal to 2.5 microns (50% cut off).

5 km or more, are treated in regional models such as CMAQ. A correction factor to take account of local sources needs to be included.

Regulators face a problem when applying complex, constructor models, such as CMAQ. In principle it is desirable that the results of a calculation can be replicated. However this becomes increasingly difficult as models become more complex. The detailed configuration may be difficult to set up on different computer platforms and decisions about which input data sets and options to apply become complicated to document.

Comparison of model predictions against observations is known as 'operational' evaluation. 'Diagnostic' assessment involves understanding the behaviour and response of a model system (*Dennis et al.*, 2010). Following the broad model categorisation described in Section 2, seers tend to consider 'diagnostic' evaluation, while constructors tend to focus mainly on the 'operational' evaluation of models. The operational performance of different types of regional models has been compared in the Model Evaluation Exercise for the UK Department for Environment, Food and Rural Affairs (Defra) (*Carslaw* 2011a, 2011b, and 2011c) and the Air Quality Modelling Evaluation International Initiative, AQMEII, (http://aqmeii.jrc.ec.europa.eu/ [accessed 21 May, 2013]). *Dore et al.* (2013) presented results of the Defra Model Evaluation Exercise which encompassed a wider set of models than comparisons described in this paper. Phase one of the AQMEII intercomparison (*Solazzo et al.*, 2012) involved 10 regional models. Four models were applied to both the European and North American domains; five models were applied to just the European domain and one model was applied to the North American domain. In the second phase of AQMEII (the Air Quality Model Evaluation International Inter-comparison) the earlier regional model inter-comparison assessment was extended to on-line air quality models in which the air quality and meteorological models were coupled together. The PM_{10} and $PM_{2.5}$ concentrations simulated by eight on-line coupled models, run by seventeen independent groups from Europe and North America, were compared with each other and with observations (*Im et al.*, 2014).

In HTAP, the taskforce on the Hemispheric Transport of Air Pollutants, modelling inter-comparison, the predictions of the change in surface ozone as a result of continental scale changes in emissions were compared in 14 global chemical transport models. In this case *Wild et al.* (2012) did not use a seer model to understand the result, but rather used a simple scaling model to represent the source-receptor relationships found from the results in the full models. One global transport model was used to investigate the range of emission changes over which this simple, linearised model is accurate enough for practical, policy applications.

Generally the constructionist models used in the CREMO, AQMEII and HTAP inter-comparisons are too complex for it to be possible to diagnose which

factors have greatest influence on a model's performance. For particulate matter, model prediction was disappointing suggesting it is difficult to include all factors affecting concentrations.

Seer and constructor models have been used to evaluate policy decisions in the areas of air quality and acid deposition. Examples of a seer model in the UK include the semi-empirical TRACK-ADMS model, which is much simpler than CMAQ (*Abbott et al.* 2003; *Abbott et al.,* 2007) and was used to show that the average PM_{10} concentration would have been 3 $\mu g\ m^{-3}$ higher in 2005 without the industrial policy intervention of the Environment Agency between 1990 and 2005 (*Vincent* and *Abbott,* 2008). Using the more complex, constructor model CMAQ, *Chemel et al.* (2014) estimated that the major industrial sources in the UK made up between 10 to 20% of the $PM_{2.5}$ concentration depending on location in 2006.

The type of a model used at the policy stage may not be the same as that used in the scientific stages of model evaluation. Instead it could involve model emulation.[3] As an example of the emulation methodology, a statistical emulation of the moderately complex constructor model, The Air Pollution Model (TAPM)[4] was used to estimate the consequences on human health, expressed as the number of life years lost, for one year's emission from a coal-fired power station (*Fisher et al.,* 2010). A range of emission conditions were evaluated without re-running TAPM for every set of conditions.

Simple, order of magnitude estimates, sometimes called 'back of envelope' calculations, can be considered to be a type of seer model. Provided they predict approximately similar responses to input changes as more complex, constructor models there is justification for using them in integrated assessments of air quality policy. This does not mean that the constructor models should be neglected by regulators and left to specialists. The constructor model provides the essential test bed for exploring understanding of the response of a model to changes in input over a wide range of conditions. Thus for regulators both the model *seer* and the model *constructor* approaches have important roles.

---

[3] For an explanation of an emulator, see http://mucm.aston.ac.uk/MUCM/MUCMToolkit/index.php?page=MetaOverviewEmulators.html [accessed 21 May, 2013]. If a computer simulation is computationally expensive, so that evaluating a constructor model for a choice of inputs takes a significant amount of computing time, one may be limited to evaluating the model at a small number of different input data sets. However one may want to know model predictions at a large number of different input values. One can deal with this problem by building an emulator: a statistical model of the model, constructed from a fairly small number of runs of the constructor model. The emulator will predict both output values, and report uncertainty in any prediction. In the Managing Uncertainty in Computer Models (MUCM) project, a toolkit for constructing Gaussian process emulators is described in which all parameter values and their interactions have uncertainty described by Gaussian functions. Gaussian functions possess convenient properties, making emulator formulation easy.

[4] The moderately complex meso-scale model, TAPM, was applied with UK emissions and meteorology in 2003 to illustrate the approach. The use of TAPM was an efficient way to generate a set of results distributed through parameter space. It would not have been practical at the time to have generated enough CMAQ results to build an emulator.

4. Model evaluation protocols and metrics

In the CREMO project, different versions of the constructor model CMAQ were compared with three air quality models developed in the UK which may be regarded as seer models: the Fine Resolution Atmosphere Multi-Pollutant Exchange (FRAME) model for acid deposition (*Dore et al.* 2007), the Trajectory model with Atmospheric Chemical Kinetics–Atmospheric Dispersion Modelling System (TRACK-ADMS) model for annual audits (*Abbott et al.,* 2007) and the Ozone Source–Receptor Model (OSRM) for ozone (*Hayman et al.*, 2010). An Environment Agency report (*Hayman et al.*, 2013a) lists the sites, measurements and methods available in the UK for evaluating models against observations, as well as summarising the models. The aim was to establish whether the models met acceptance criteria as part of an evaluation protocol and not to establish which model had the best performance judged against observations.

Defra (*Derwent et al.*, 2010), and informally the USEPA (*Dennis et al.*, 2010), have published protocols for operational model evaluation using familiar statistical measures. Benchmarking procedures (*Thunis et al.*, 2011a) have also been produced. The optimal set-up (the set-up requiring the lowest computer resource and least preparation) for running constructor models efficiently over a year or more, to answer a policy question or a regulatory issue, cannot be specified precisely. The process involves setting up (1) emissions, (2) initial and boundary conditions, (3) running a meso-model to determine the meteorological fields, and then (4) running a chemical transport model, such as CMAQ. Although a model complies with an operational evaluation protocol, the model should not be used under emissions or meteorological conditions which have not occurred during the testing of the model.

The acceptance criteria set in the Ambient Air Quality Directive (*EC,* 2008) also set operational performance limits and are of great importance, because they impose compliance requirements on EU countries. The Directive allows models which satisfy the criteria to be used for air quality assessment to reduce the number of sampling sites, to prepare plans and abatement measures and to determine where the pollution is coming from. The guidance published by *FAIRMODE* (2011) and the guidance on NO_2 (*Denby,* 2011) interpret the Directive, elaborating on text in the Directive, such as 'relative directive error', but also describing its limitations.

In the Defra Model Evaluation Protocol (*Derwent et al.*, 2010) predictions of the model should be accepted if the percentage of model predictions within a factor of two (*FAC2*) of the observations is greater than 50 per cent. The normalised mean bias (*NMB*) is defined as:

$$NMB = \frac{\sum_{i=1}^{N} M_i - O_i}{\sum_{i=1}^{N} O_i}, \tag{1}$$

where N is the number of observations, M_i are the calculated values, O_i are the observed values. The *NMB* should satisfy $-0.2 \leq NMB \leq 0.2$ in the Defra Model Evaluation Protocol. The *NMB* puts a higher weighting on model performance at higher concentrations, a distortion, but one which might be reasonable, given the greater concern over the occurrence of high concentrations. It would also be important to consider carefully the quality of the observations and the size of the sample N, the number of observed–calculated pairs.

A comparison of seer regional transport models (*Abbott et al.,* 2003) suggested that these simpler types of models could meet the *FAC2* criterion when calculating acid deposition. The set of possible statistical measures used to evaluate the constructor model CMAQ (*Chemel et al.,* 2010) included the percentage within a factor of two (*FAC2*) and the normalised mean bias (*NMB*). As part of the model intercomparison within CREMO (*Chemel et al.*, 2011), all the models considered (CMAQ v4.6, CMAQ v4.7, TRACK-ADMS and FRAME) were shown to satisfy the *FAC2* criterion, that 50 per cent of the modelled results should be within a factor of two of the annual mean concentrations for *all* the species considered. In contrast, none of the models satisfied the criterion that the normalised mean bias *NMB* should be in the range –20 to 20 per cent, for *all* the species considered, which included PM_{10}.

An *acceptance* criterion for ozone could refer to the annual average ozone concentration or to the peak ozone level during episodes. The annual average ozone depends largely on domain boundary conditions and removal within the domain, while episodic ozone concentrations rely on regional generation within the domain. It is therefore necessary to distinguish between an acceptance criterion for shorter periods, such as episodes, and an acceptance criterion for annual average ozone. There is no commonly accepted agreement over the best choice of metric in the operational evaluation of regional ozone models. There are examples of diagnostic ozone metrics in the review by *Middleton et al.* (2007), while *Rao et al.* (2011) argue in favour of the seasonal average as the most suitable operational metric.

5. Diagnostic evaluation

5.1. Footprint metric

A systematic procedure for setting a diagnostic evaluation protocol cannot be defined as this involves understanding model behaviour. A regulator is primarily interested in attributing concentrations to emissions. Thus diagnostic evaluation in the CREMO project was focused on the differences in the footprint of sources calculated by different regional models used for regulation. A 'footprint' metric is a response function, showing how concentrations or deposition are influenced spatially by emissions from a single specified source, such as a power station. Footprints are obtained from the difference between the concentration or

deposition, when all sources are included, and the concentration or deposition, when all sources, except for the specified source under consideration, are included. In the seer air quality models discussed in this paper, the individual footprints can be calculated directly. The footprint of secondary pollutants, such as particulate matter, depend directly on model parameters determining the formation by chemical reactions and removal by wet and dry deposition, which eventually lead to complete removal from the atmosphere after a number of days. In constructor models, such as CMAQ, the footprint determined after much computation appears to be distantly related to the original equations although the same removal processes influence behaviour. Consideration of the footprint metric can therefore link the performance of a seer type of regional model to the constructor type of model.

A footprint metric has two purposes: (a) it is a diagnostic of a seer or constructor model type, showing the change in concentration from the emission at a point source leading to understanding of the overall system behavior; and (b) for regulatory purposes, it shows how emission reductions may change concentrations.

A quantitative approach to evaluating footprints is to consider the distance dependent structure of the footprint of a single source (*Fisher et al.*, 2011). The weighted average concentration given by the average concentration along a typical trajectory, excluding dilution arising from horizontal dispersion, is obtained by multiplying the concentration by the distance from the source. This footprint metric is defined by:

$$\frac{r}{2\pi}\int_0^{2\pi} C(r,\theta)d\theta \tag{2}$$

where $C(r, \theta)$ is the concentration at a distance r from the specified source in a direction θ.

In CREMO the footprint profiles were normalised by the value of the near-field concentration, 30 km from the source, and this is illustrated in the profiles in the smaller figures in *Fig. 1*. The dependence of the PM_{10} and $PM_{2.5}$ concentrations along a radial trajectory does not decrease rapidly with distance because of the gradual production of secondary aerosol in the atmosphere. A numerical diagnostic can be defined as the distance between the point source and the point at which the radial average secondary PM_{10} or $PM_{2.5}$ concentration takes its maximum value. This diagnostic summarises the influence of the source on secondary aerosol formation.

The average dependence of the concentration with distance shown in *Fig. 1* (Eq. (2) without the distance r in the numerator) does decay rapidly with distance, because the average concentration contains a factor proportional to the inverse of the distance from the source ($1/r$) arising from the spread of air mass trajectories.

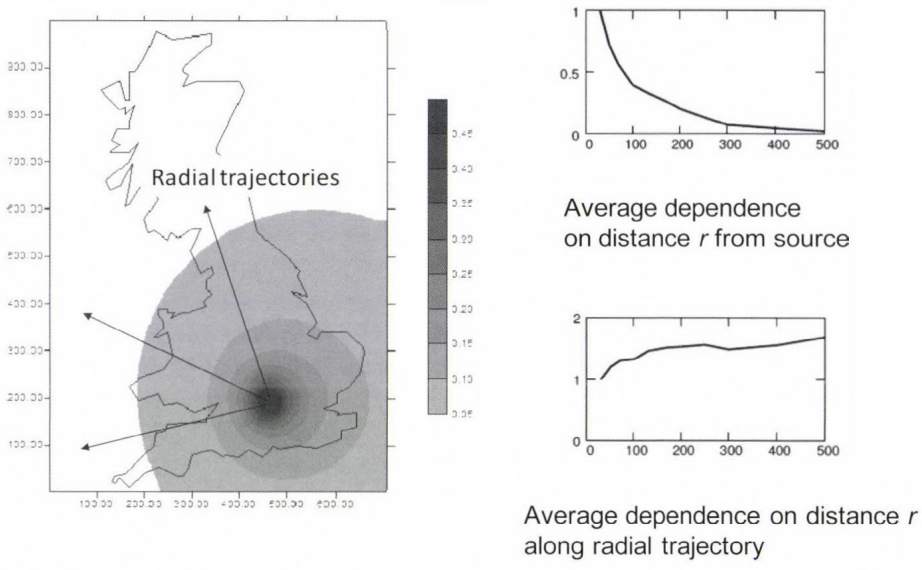

Fig. 1. Schematic illustration of the annual average PM_{10} concentration footprint in μgm^{-3} from a major stationary point source such as a power station. The main picture shows contours of the concentrations of PM_{10} in μgm^{-3}, with distances along the axes in kilometres. The *top* small right hand figure shows the concentration along a typical, radial trajectory as a function of distance in kilometres, normalised by the value of the near-field concentration 30km from the source. The *bottom* small right hand figure shows the average weighted concentration along a radial trajectory, excluding dilution arising from horizontal dispersion by multiplying the concentration by the distance from the source (Eq. (2)).

When making policy decisions, a regulator should understand the underlying structure of the model used in the assessment, for which the first step is to understand how the model responds to emission changes. As the next step in diagnostic evaluation using footprints, a regulator needs to know whether footprints can be aggregated to assess a source control strategy. This means that if Δq_i is the reduction in the source strength of the ith source under the control strategy, the reduction in concentration under the control strategy is approximately equal to ΔC, where:

$$\Delta C = \sum_i \Delta q_i G_i \tag{3}$$

and G_i is the footprint of the ith source of unit source strength. If Eq. (3) is a reasonable approximation, a reduction strategy can follow a sequential change in emissions, tracking in order which emission reductions are most effective.

5.2. Episode metric

The occurrence of photochemical episodes, when high ozone concentrations are generated, suggests the need to be aware of a variety of possible behaviours. Under steady meteorological conditions, ozone would be expected to tend towards a limit, which is the long-term solution of a system of ordinary differential equations for a given choice of VOC emission strengths. Under some conditions, corresponding to lower VOC emission rates under strong winds and high atmospheric dilution, the ozone limit value would be expected to be close to the initial ozone concentration close to the background ozone concentration. This represents an approximate balance between the production and destruction of ozone over the domain. Under other conditions, corresponding to higher VOC emission rates under light winds and low dilution, the limit ozone value may be far from the initial state, corresponding to the build-up of ozone in an anticyclonic episode. The large difference in the limiting ozone concentration between these two emission and meteorological situations corresponds to a bifurcation in the steady-state behaviour of the differential equations describing the ozone system. This does not imply any discontinuity in ozone concentration, but differences in the limit values of the solution of the underlying differential equations. A large change in the limiting ozone concentration occurs for a small change in emissions near a bifurcation, so a sensitivity analysis would break down near the bifurcation point.

The occurrence of ozone episodes will to some extent influence the long-term average ozone concentration, although the occurrence of episodes may vary considerably from year to year depending on weather conditions. Ozone formation can be attributed to specific sources during an episode using constructor models. An ozone footprint during an episode has been calculated using the CMAQ model (*Yu et al.*, 2008) by investigating changes in ozone formation when the emissions from a specified source are altered. The 'integrated downwind ozone production' (IDOP) described by *Derwent* and *Nelson* (2003) is a footprint metric during an episode. IDOP describes how much ozone is produced in the downwind environment under ideal ozone producing conditions by each VOC species of a specified stationary source from selected runs of the Photochemical Trajectory Model (*Derwent et al.*, 2009), which one could class as a seer model. Using IDOP as a metric is a convenient, precautionary approach to regulation when screening VOC emissions. In cases when the IDOP approach suggests that an emission is not acceptable, more complex models of a seer type, such as OSRM, or of a

constructor type, such as CMAQ, need to be applied to test the conclusion. An alternative metric to IDOP is whether a 30% reduction in emissions of VOC or NOx suppresses the formation of an ozone episode.

5.3. Diagnostic evaluation of individual processes

Another kind of diagnostic evaluation involves the behaviour of individual processes within a model, although it is not always possible to compare individual processes exactly when they are embedded within a complex model. When *Derwent* (2013) compared six chemical mechanisms (CRI, CB-05, CBM-4, SAPRC-99, SAPRC-07 and OSRM) within the Photochemical Trajectory Model (PTM), he found that the differences in the details of the chemical reaction scheme are not the most important factor in explaining differences between the predictions of ozone.

The Integrated Process Rate analysis of the CMAQ model undertaken by *Francis et al.* (2011) was used to understand the causes of an episode of high ozone over south-east England in 2003. The contributions of cloud processes, chemical processes, advection, diffusion, vertical advection, vertical diffusion, horizontal advection and dry deposition, at different model heights were considered. For this episode, in a south-east England domain, meteorological processes were shown to have the greatest influence.

6. Examples of operational evaluation

In this section some examples of the operational evaluation of constructor and seer models are described. The seer model TRACK-ADMS was developed to enable the Environment Agency to assess contributions from major industrial sources (*Abbott* and *Vincent* 2007; *Abbott et al.*, 2003; *Vincent* and *Abbott,* 2008). TRACK-ADMS assumes simplified meteorology to calculate the long-term average atmospheric concentration. It contains some degree of data assimilation which improves predictions (by applying a bias correction). The model is suited to calculating the contributions from large industrial sources and has been subject to uncertainty analysis by undertaking a Monte Carlo analysis of the variation in output over plausible ranges of input parameters. Its limitation is that one cannot be sure that the choice of parameter input values used to evaluate the model, is appropriate in future emission scenarios when emissions and boundary conditions over the model domain may be very different from the ones used to test the model.

Table 1 from *Chemel et al.* (2011) shows an example from the CREMO project of calculating PM_{10} concentrations across the UK, comparing the performance of the CMAQ model, with a resolution set of 5 km, against the model TRACK-ADMS, with a resolution of 1 km. Observations from some 40 rural and background sites in the UK Automatic Urban and Rural Network

(AURN) are used in the evaluation, for which no correction for local sources is applied. Many more parameters need to be specified in the CMAQ model compared with TRACK-ADMS leading to more opportunities for errors to arise in the input data.

Table 1. Comparison of performance in predicting annual average PM_{10} concentration at rural AURN sites in the UK in 2003, for which the local contribution should be minimal, for two versions of a constructor model, and a seer model

Model metric PM_{10} for 2003	**CMAQ v4.6**	**CMAQ v4.7**	**TRACK-ADMS**
FAC2 (%)	88.2	100.0	100.0
r (correlation coefficient)	0.09	0.0	0.45
NMB	–0.33	–0.09	–0.20
Single power station contribution (%)	0.34	0.28	0.28

Based on the *NMB* metric, no systematic difference can be seen between the performance of the two versions of the CMAQ model, of the constructor type, and that of the simpler, seer model TRACK-ADMS. A negative *NMB* bias implies a model under-prediction and so a margin of error should be included in model predictions. Results in *Table 1* suggest that the margin of error for PM_{10} is about 20%.

There is not sufficient observational data in 2006 in the UK on which to test the performance of regional model predictions of $PM_{2.5}$. However the CMAQ model has also been used to simulate air quality over North America and Europe for the year 2006 (*Appel et al.,* 2012) as part of the AQMEII project (*Galmarini* and *Rao,* 2011). *Table 2* shows the seasonal, domain averaged, normalised mean biases (*NMB*) of daily average $PM_{2.5}$ concentrations from the CMAQ model for the North American Air Quality System network and the European AirBase network in the year 2006. As far as possible, the CMAQ model configurations were similar for North America and Europe, with both simulations utilising version 4.7.1 of CMAQ. The North American simulation used 34 vertical layers and a 12 km horizontal grid spacing, while the European simulation used 34 vertical layers and an 18 km horizontal grid spacing covering most of Europe. The overestimate of $PM_{2.5}$ at North American sites is thought to arise from an overestimate in the unspeciated $PM_{2.5}$ mass (*Appel et al.,* 2012), which makes up a significant proportion of the $PM_{2.5}$ mass in version 4.7.1 of the CMAQ model. Improvements to the way this component is treated are incorporated in later versions of CMAQ. If one considers all the models for

which predictions were available in AQMEII, then generally there appears to be significant under-prediction of both PM_{10} and $PM_{2.5}$ (*Schere et al.,* 2012).

Table 3 shows the seasonal, domain-wide normalised mean biases of daily average PM_{10} concentrations for the North American Air Quality System and European AirBase networks from the CMAQ model. The model performance for $PM_{2.5}$ and PM_{10}, especially for the European domain, shows large under-prediction and occurs in other constructor models where the finest grid resolution is some kilometres or more, not just in CMAQ (*Solazzo et al.,* 2012).

Table 2. NMB of daily average $PM_{2.5}$ comparisons between predictions and observations in different seasons of 2006 over North America and Europe made under AQMEII (*Appel et al.* 2012) using the CMAQ model

Season and domain	Approximate number of sites	*NMB*
Winter, North America	958	0.304
Winter, Europe	160	–0.550
Spring, North America	958	0.189
Spring, Europe	160	–0.369
Summer, North America	958	–0.046
Summer, Europe	160	–0.372
Autumn, North America	958	0.363
Autumn, Europe	160	–0.242

Table 3. NMB of daily average PM_{10} comparisons between predictions and observations for different seasons in 2006 over North America and Europe made under AQMEII (*Appel et al.* 2012) using the CMAQ model

Season and domain	Approximate number of sites	*NMB*
Winter, North America	956	–0.479
Winter, Europe	1000	–0.648
Spring, North America	956	–0.565
Spring, Europe	1000	–0.562
Summer, North America	956	–0.574
Summer, Europe	1000	–0.612
Autumn, North America	956	–0.465
Autumn, Europe	1000	–0.468

The general tendency for constructor models with realistic chemistry and transport to under-predict particulate concentrations can be readily interpreted as either (1) due to the omission of local combustion source contributions in models with grid resolution of 5 km or more, or (2) due to the neglect or to the inaccurate estimate of the emissions of non-combustion, windblown or re-suspended dust (especially for the coarse fraction of particulate, the difference between PM_{10} and $PM_{2.5}$) or (3) inaccuracies in the instrumentation or the site description (rural, background *etc.*) in the observational network.

In constructor models, such as CMAQ, short-term average concentrations, such as daily concentrations, can be calculated. In *Table 4* from *Chemel et al.* (2010), the performance of CMAQ v4.6 is shown for the daily variation of the two main secondary species of interest, ozone and PM_{10}[5]. The model performance for daytime ozone concentrations over a year is seen to be superior to that of PM_{10}.

Table 4. Comparison of performance in predicting the daily maximum ozone and daily mean PM_{10} concentrations at AURN sites in the UK in 2003 for CMAQ v4.6

CMAQ v4.6 metric	**Maximum daily running eight-hour mean ozone**	**Daily mean PM_{10}**
NMB	0.05	–0.34
r (correlation coefficient)	0.69	0.47
FAC2 (%)	76.7	26.8
Number of sites	~40	~40

The CMAQ ozone *NMB* in *Table 4* for the UK in 2003 is within ±0.1. The ozone predictions in 2003 from the OSRM Lagrangian trajectory model for the UK in 2003, described by *Hayman et al.* (2010), also satisfy this performance measure. The AQMEII project provided CMAQ performance statistics for ozone for the many hundreds of ozone monitoring sites in Europe and North America. The *NMB* for daytime ozone over a year is generally within ±0.1, apart from during the summer season in Europe. Given the similar level of model performance from diverse models, a *NMB* of within ±0.1 appears to be achievable for the daytime ozone concentrations over a year with the current generation of photochemical models.

[5] The paper by Chemel *et al.* (2010) contains many more performance statistics than those summarised in *Table 4*. The daily PM_{10} *NMB* is equivalent to the annual average PM_{10} *NMB* in *Table 1* apart from rounding errors.

Using the seer OSRM and constructor CMAQ models, the impact of an oil refinery in southern England, with VOC emissions ~0.2 kg/s and NOx emissions ~0.2 kg/s, on annual average ozone concentrations in 2003 was assessed in CREMO. The predicted change in the annual average ozone concentration along a horizontal transect through the refinery (*Hayman et al.*, 2013d) shows that the emissions from the refinery led to a decrease in ozone on average in both models (of magnitude <0.2 μg m^{-3}) out to distances of a few hundred kilometres. The decrease is thought to be caused by the reaction of ozone with NO releases. The similarity in the operational performance of the OSRM and CMAQ models gives confidence in the simpler, seer OSRM model, which was designed to develop national policy for regulating ozone. However a full understanding of the performance of regional models over the complete range of conditions of interest cannot be based purely on operational performance metrics. Diagnostic evaluation is also required.

7. Examples of diagnostic evaluation

The modelling of the $PM_{2.5}$ and PM_{10} footprint from a power station ought be better than the regional predictions discussed in the previous section, because (1) there is no locally derived coarse particulate, (2) the primary source strength, which consists largely of inorganic compounds, is better known and (3) the plume chemistry without secondary organics is simpler. Examples from CREMO of the footprint of particulate matter from a power station source, are given in *Figs. 2* and *3* using the distance weighted footprint introduced schematically in Figure 1. The average concentration along a radial trajectory is normalised by the concentration in the near field, 30 km from the source.

Footprints used in diagnostic evaluations cannot be compared directly with observations. However they are useful for diagnosing how models are treating processes within the model. In *Fig. 2* the distance-dependent weightings of the annual average PM_{10} concentration in a power station footprint are compared for three types of models. Broadly the models show little dependence on distance suggesting that the removal by wet and dry deposition is largely in balance with production by chemical transformation. The detailed behaviour is different, presumably because of differences in details of the models' structure, parameters and the input data sets, even for the two models whose structure is similar (CMAQ v4.6 and CMAQ v4.7). *Sutton et al.* (2013) showed that apparently small differences in the temporal profile of ammonia emissions over the year in 2003 (although the spatial distribution of the annual total ammonia emission was identical) can make differences to the prediction of the annual spatial distribution of components of $PM_{2.5}$ and of acid deposition. This suggests that differences in the set-up of model runs can make differences to the spatial distribution, even if the

models themselves (CMAQ v4.6 and CMAQ v4.7) are formulated in a similar way and demonstrate similar behaviour.

The distance-dependent weighting of the sulphur deposition from a power station shows a general decrease out to distance of 500km, while the distance-dependent weighting of the nitrogen deposition shows an increase out to the same distance[6].

In *Fig. 3*, the distance-dependent weightings of $PM_{2.5}$ and NO_2 for different kinds of sources investigated in CREMO are shown. Different distance dependencies are demonstrated. Small-scale variations in the plots may be the result of edge effects in the domains from which the footprints are plotted.

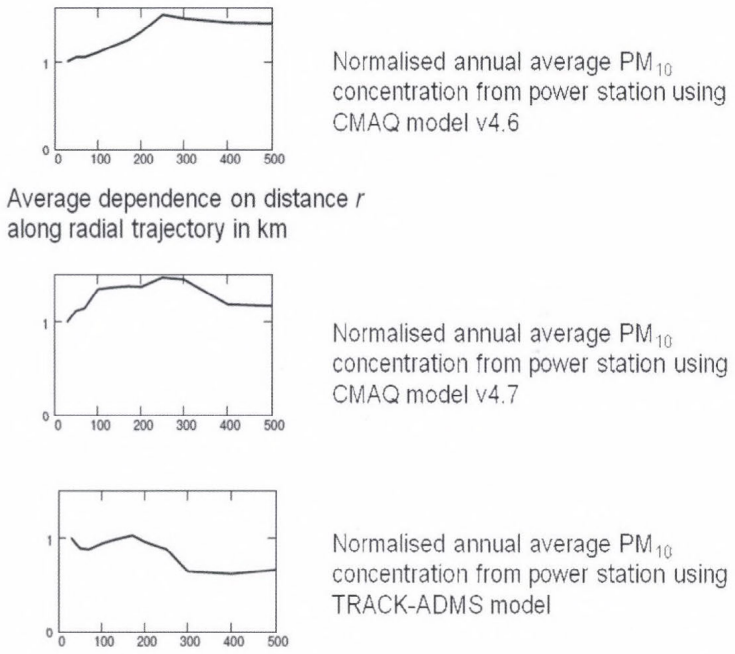

Fig. 2. Dependence of the PM_{10} concentration on distance in kilometres along a radial trajectory, derived from the footprint of a power station source in central southern England, using Eq. (2), normalised by the value of the concentration near the source at 30km, for two versions of the constructor model CMAQ (v4.6 and v4.7), *top two figures*, and for the seer model TRACK-ADMS, *bottom figure*.

[6] The deposition footprints are not shown in this paper.

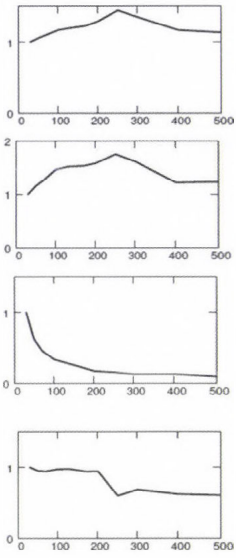

Fig. 3. Top two figures: Normalised dependence of the $PM_{2.5}$ concentration on distance in kilometres along a radial trajectory, derived from the footprint of a power station source, using Eq. (2), for two versions of the constructor model CMAQ (v4.6 and v4.7). *Bottom two figures*: Normalised dependence of the NO_2 concentration on distance in kilometres for Heathrow Airport and normalised dependence of the $PM_{2.5}$ concentration on distance in kilometres for an oil refinery in southern England from results of the constructor model CMAQ v4.6. Different distance dependencies are demonstrated in the footprints.

The EMEP model (NMI, 2010) is a constructor model and has been used to derive the contribution from individual countries to the regional concentration of $PM_{2.5}$ over Europe using grid cells of dimension 50 km×50 km. A diagnostic metric is the set of individual country footprints for a 15 per cent change in emissions, equivalent to the annual country-to-grid source–receptor matrices, see http://www.emep.int/SR_data/index_sr.html [accessed 21 May 2013]. *Fig. 4* shows the circumferentially averaged footprint of the UK centred on the middle of a grid cell in central England. The footprint is plotted at distances greater than 150 km from the centre of the country, because the national footprint of $PM_{2.5}$ concentration is distorted by the irregular distribution of sources over the country. The EMEP footprint for the UK is compared with the footprint from the typical power station analysed in CREMO. It is seen that, out to distances of 500 km, the balance between production and loss is approximately maintained in both the footprint calculations. As expected, atmospheric loss mechanisms from wet and dry deposition begin to dominate beyond this distance. The footprints are expressed in concentration units. The maximum $PM_{2.5}$ concentrations in the two cases are about 0.8 and 0.2 μgm^{-3}, respectively.

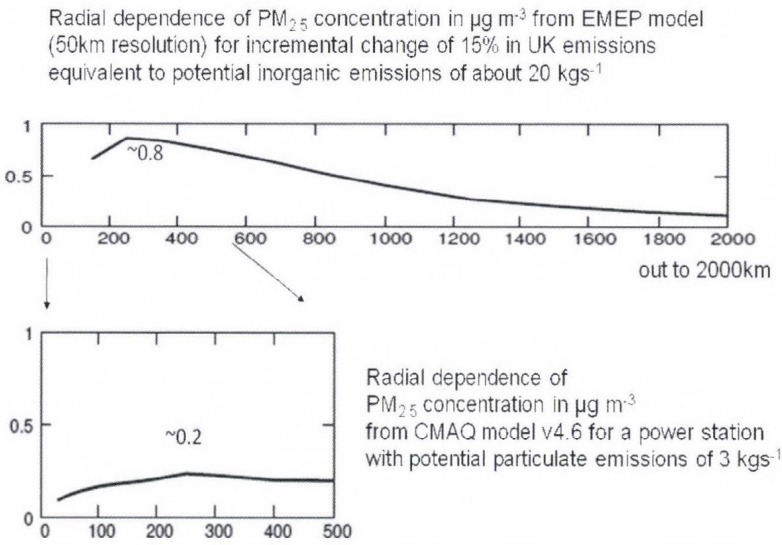

Fig. 4. Top: Dependence of the $PM_{2.5}$ concentration in μgm^{-3} on distance in kilometres, in 2003, along a radial trajectory starting in central England, based on a 15% reduction in UK emissions, based on the EMEP model (Klein *et al.* 2011). *Bottom:* Dependence of $PM_{2.5}$ concentration in μgm^{-3} on distance in 2003, along a radial trajectory, from the footprint of a power station source. Notional potential source strengths for the two types of sources (in kgs^{-1}) and the maximum values of the $PM_{2.5}$ concentrations in the two calculations (0.8 and 0.2 μgm^{-3}) are shown.

Although the species profiles (SO_2 : NOx: NH_3) of the UK emissions and a single coal-fired power station source are different, an approximate estimate can be made of the dominant precursor emissions, using the sum of primary, precursor species (SO_2 + NOx + NH3 + primary $PM_{2.5}$). Although only rough estimates, there is consistency in magnitude in the two cases. The 15% incremental change in UK emissions is six times the power station source strength and gives roughly four times the maximum $PM_{2.5}$ concentration of the power station. The distance-dependent weighting is different in detail. This may be a result of the different spatial resolution of the two models or the result of detailed differences in the treatment of particle formation in the two models.

The footprint is seen to be a valuable metric for diagnosing the behaviour of both constructor and seer air quality models. There is no objective way of deriving diagnostic metrics, though the structure of seer models are likely to indicate aspects of both types of models from which diagnostic metrics can be formulated.

8. Conclusions

The evaluation of models is thus not a wholly objective procedure i.e. it cannot be reduced to a set of rules. However it can be made more systematic by the use of checklists (*Risbey et al.*, 2001) and by systematically evaluating the performance of air quality models, as described by *Thunis et al.* (2011a,b) and *FAIRMODE* (2011) and illustrated by *Chemel et al.* (2010) and *Pederzoli et al.* (2011). Moreover if consistency is shown between the predictions of models which have been developed for performance (the model constructors' approach) and models used to develop understanding (the model seers' approach), then this gives greater confidence in the decisions made.

The operational and diagnostic evaluation of regional air quality models of the seer and constructor type for regulating secondary atmospheric pollutants, such ozone, PM_{10} and $PM_{2.5}$ have been illustrated. There was no clear separation between the operational performance of a seer and a constructor regional air quality model, using observational data sets and the commonly applied operational metrics *FAC*2 and *NMB*. A margin of error shown by operational evaluations of a model should be added to the predictions when the model is used to show compliance with a limit value. However it is not possible from the results of operational evaluations shown in this paper to set a minimum margin of error though this could be at least 20% for annual average concentrations of PM_{10} and $PM_{2.5}$. For long-term average ozone the margin of error appears to be smaller, but interest is really in episodic ozone for which no generally accepted metric has been agreed.

Diagnostic evaluation is needed to justify the use of regional air quality models under conditions where no observational data is available. Although widely applied metrics based on statistical variables are used in operational evaluation, no commonly agreed, standard set of diagnostics exists, which can be used to understand the performance of constructionist regional models. However it is hoped that the continued use of seer models will generate metrics for diagnostic evaluation on a case by case basis.

The footprint metric is shown to be a useful diagnostic for both user and constructor models. The footprint shows similar behaviour in the regional seer and constructor air quality models analysed. It illustrates clearly the balance between the production and loss of PM_{10} and $PM_{2.5}$ from a specified point source, such as a power station, out to distances of 500km beyond which removal processes dominate. For ozone the system behaviour is fundamentally different in episodic and non-episodic conditions. Unlike operational metrics there is no obvious way of deriving diagnostic metrics. However seer models are likely to reveal directly the structure of a model's underlying mathematical equations from which diagnostic metrics can be formed.

Acknowledgements: The principal author acknowledges valuable discussions held with colleagues within the context of the CREMO project when he was working at the Environment Agency and under the letter of agreement between Defra, the Environment Agency and the US Environmental Protection Agency establishing cooperation on exposure science. The CREMO project was supported by the Environment Agency of England under contract (20073/R&D SC060037). The partners included the University of Hertfordshire, AEA Technology, the Joint Environment Programme of the power industry, CEH Edinburgh, RD Scientific and Hayman Atmospheric Consulting. Some of these organisations made significant contributions in kind to the work programme. Results of this work may not necessarily reflect the views of the Environment Agency or any individual CREMO participant and no official endorsement should be inferred.

References

Abbott, J., Hayman, G., Vincent, K., Metcalfe, S., Dore, T., Skeffington, R., Whitehead, P., Whyatt, D., Passant, N. and *Woodfield, M.*, 2003: Uncertainty in acid deposition modelling and critical loads. *Environment Agency Technical Report P4-083(5)/1.* Bristol: Environment Agency.

Abbott, J.A., Vincent, K.J. and *Stedman, J.R.*, 2007: Methods for auditing the contribution of Environment Agency regulated processes to pollution. *Environment Agency Science Report SC030172/SR2.* Bristol: Environment Agency. https://publications.environment-agency.gov.uk/skeleton/publications/ViewPublication.aspx?id=b839fd39-b1db-4fdd-9d8a-40e3ee476c19 [accessed May 21, 2013].

Abbott, J. and *Vincent, K.*, 2007: Auditing the contribution of Environment Agency regulated processes to pollution. *Environment Agency Science Report SC030172/SR3.* Bristol: Environment Agency.https://publications.environment-agency.gov.uk/skeleton/publications/ViewPublication.aspx?id=65c9d2a8-87f9-4a2e-b67e-a69c5b244905 [accessed May 21, 2013].

Appel, W., Chemel, C., Roselle, S.J., Francis, X.V., Hu, R.-M., Sokhi, R.S., Rao, S.T. and *Galmarini, S.*, 2012: Examination of the Community Multiscale Air Quality (CMAQ) model performance over the North American and European domains. *Atmos. Environ. 53*,142–155.

Carslaw, D., 2011a: Defra urban model evaluation analysis – Phase 1. London: Defra. Available from: http://uk-air.defra.gov.uk/library/reports?report_id=654 [accessed May 21, 2013].

Carslaw, D., 2011b: Defra regional and transboundary model evaluation analysis – Phase 1. London: Defra. Available from: http://uk-air.defra.gov.uk/library/reports?report_id=653 [accessed May 21, 2013].

Carslaw, D., 2011c: Defra deposition model evaluation analysis – Phase 1. London: Defra. Available from: http://uk-air.defra.gov.uk/library/reports?report_id=652 [accessed May 21, 2013].

Chemel, C., Sokhi, R.S., Yu, Y., Hayman, G.D., Vincent, K.J., Dore, A.J., Tang, Y.S., Prain, H.D. and *Fisher, B.E.A.*, 2010: Evaluation of a CMAQ simulation at high resolution over the UK for the calendar year 2003. *Atmos. Environ. 44*, 2927–2939.

Chemel, C., Sokhi, R.S., Dore, A.J., Sutton, P., Vincent, K.J., Griffiths, S.J., Hayman, G.D., Wright, R., Baggaley, M., Hallsworth, S., Prain, H.D. and *Fisher, B.E.A.*, 2011: Predictions of UK regulated power station contributions to regional air pollution and deposition: a model comparison exercise. *J. Air Waste Manage. Ass. 61*, 1236–1245.

Chemel, C., Fisher B.E.A., Kong X., Francis X.V., Sokhi R.S., Good N., Collins W.J. and *Folberth G.A.*, 2014: Application of chemical transport model CMAQ to policy decisions regarding $PM_{2.5}$ in the UK. *Atmos. Environ. 82*, 410-417.

Denby, B., 2011: Guide on modelling nitrogen dioxide (NO_2) for air quality assessment and planning relevant to the European Air Quality Directive. Result of activities in the Forum for Air Quality Modelling in Europe. *FAIRMODE Working Group 1, Version 4.6. ETC/ACM Technical Paper 2011/15.* Bilthoven, The Netherlands, European Topic Centre on Air Pollution and Climate Change Mitigation, RIVM.

Dennis, R., Fox, T., Fuentes, M., Gilliland, A., Hanna, S., Hogrefe, C., Irwin, J., Rao, S.T., Scheffe, R., Schere, K., Steyn, D. and *Venkatram, A.*, 2010: A framework for evaluating regional-scale numerical photochemical modeling systems. *Environ. Fluid Mech. 10*, 471–489.

Derwent, R. and *Nelson, N.*, 2003: Development of a reactivity index for the control of the emissions of organic compounds. *R&D Technical Report P4-105 RC8309*. Bristol: Environment Agency.

Derwent, R., Witham, C., Redington, A., Jenkin, M., Stedman, J., Yardley, R. and *Hayman, G.*, 2009: Particulate matter at a rural location in southern England during 2006: Model sensitivities to precursor emissions. *Atmos. Environ. 43*, 689–696.

Derwent, D., Fraser, A., Abbott, J., Jenkin, M., Willis, P. and *Murrells, T.*, 2010: Evaluating the performance of air quality models. *Report prepared for the UK Department for Environment, Food and Rural Affairs*, Issue 3/June 2010. London: Defra. Available from:http://uk-air.defra.gov.uk/reports/cat05/1006241607_100608_MIP_Final_Version.pdf [accessed May 21, 2013].

Derwent, R.D., 2013: Chemical mechanism choice: impacts of ozone precursor emissions reductions in the United Kingdom on episodic peak ozone in the United Kingdom. *Environment Agency Report SC060037e/R*. Bristol: Environment Agency. https://publications.environment-agency.gov.uk/skeleton/publications/ViewPublication.aspx?id=cf825d8d-f061-44cb-9293-51b96939d244 [Accessed May 20, 2013].

Dore A.J., Vieno, M., Tang, Y.S., Dragosits, U., Dosio, A., Weston, K.J. and *Sutton, M.A.*, 2007: Modelling the atmospheric transport and deposition of sulphur and nitrogen over the United Kingdom and assessment of the influence of SO_2 emissions from international shipping. *Atmos. Environ. 41*, 2355–2367.

Dore, A.J., Carslaw, D., Chemel, C., Derwent, R.G., Fisher, B.E.A., Griffiths, S.J., Lawrence, S., Metcalfe, S.E., Redington, A., Simpson, D., Sokhi, R., Sutton, P., Vieno, M. and *Whyatt, J.D.*, 2013: Evaluation and inter-comparison of acid deposition models for the UK. *Air Pollution Modeling and its Application XXII* (ed. D G. Steyn, P.J.H. Builtjes and R.M.A. Timmermans), pp 505-10. Dordrecht: Springer.

EC, 2008: Directive 2008/50/EC of the European Parliament and of the Council of 21 May 2008 on Ambient air quality and cleaner air for Europe. *Official Journal of the European Union, L152*, 11 June 2008, 1–44.

Edwards, P.N., 2010: A vast machine Computer models, climate data and the politics of global warming, The MIT Press, Cambridge Massachusetts, London, England.

FAIRMODE (Forum for Air Quality Modelling in Europe), 2011: The application of models under the European Union's Air Quality Directive: A technical reference guide. *Technical Report No 10/2011*. Copenhagen: European Environment Agency. Available from: http://www.eea.europa.eu/publications/fairmode [accessed May 21, 2013].

Fisher, B.E.A., 2013: Comparison of simple and advanced regional models (CREMO): Outcomes for the Environment Agency. *Environment Agency Report SC060037/R*. Bristol: Environment Agency.https://publications.environment-agency.gov.uk/skeleton/publications/ViewPublication.aspx?id=cf825d8d-f061-44cb-9293-51b96939d244 [Accessed May 20, 2013].

Fisher, B., Chemel, C., Hu, R.-M. and *Sokhi, R.*, 2010: Emulating complex calculations for regulatory decisions. *Air Pollution Modeling and its Application XX*, (ed. D.G. Steyn and S.T. Rao), pp. 195–199. Dordrecht: Springer.

Fisher, B. E. A., Chemel, C., Francis, X.V., Hu, R.-M., Sokhi, R.S., Hayman, G.D., Vincent, K.J., Dore, A.J., Griffiths, S., Sutton, P. and *Wright, R.D.*, 2011: Diagnostic evaluation of complex and simple atmospheric chemical transport models by considering single source impacts in the UK. *Air Pollution Modeling and its Application XXI*, (ed.D.G. Steyn and S. Trini Castelli), pp 427–431. Dordrecht: Springer.

Francis, X., Chemel, C., Sokhi ,R.S., Norton, E.G., Ricketts, H. and *Fisher, B.*, 2011: Mechanisms responsible for the build-up of ozone over South East England during the August 2003 heat wave. *Atmos. Environ. 45*, 6880–6890.

Galmarini S. and *Rao S.T.*, 2011: The AQMEII two-continent Regional Air Quality Model evaluation study: Fueling ideas with unprecedented data. *Atmos. Environ. 45*, 2464.

Hall, D.J., Spanton, A.M., Dunkerley, F., Bennett, M. and *Griffiths, R.F.*, 2000a: A review of dispersion model inter-comparison studies using ISC, R91, AERMOD and ADMS. *Environment Agency Technical Report P353*, Environment Agency, Bristol.

Hall, D.J., Spanton, A.M., Dunkerley, F., Bennett, M. and *Griffiths, R.F.*, 2000b: An inter-comparison of the AERMOD and ADMS and ISC dispersion models for regulatory applications. *Environment Agency Technical Report P362*, Environment Agency, Bristol.

Hayman, G.D., Abbott, J., Davies, T., Thomson, C.L., Jenkin, M.E., Thetford, R. and *Fitzgerald, P.*, 2010: The Ozone Source–Receptor Model: a UK ozone policy tool. *Atmos. Environ. 44*, 4283–4297.

Hayman, G., Sokhi, R., Chemel, C., Griffiths, S., Vincent, K., Dore, A.J., Sutton, P. and *Wright, R.*, 2013a: Comparison of simple and advanced regional models (CREMO): Model evaluation protocol. *Environment Agency Report SC060037a/R.* Bristol: Environment Agency. https://publications.environment-agency.gov.uk/skeleton/publications/ViewPublication.aspx?id=cf825d8d-f061-44cb-9293-51b96939d244 [Accessed May 20, 2013].

Hayman, G., Sokhi, R., Chemel, C., Griffiths, S., Vincent, K., Dore, A.J., Sutton, P. and *Wright, D.R.*, 2013b: Comparison of simple and advanced regional models (CREMO): Model evaluation report. *Environment Agency Report SC060037b/R.* Bristol: Environment Agency.https://publications.environment-agency.gov.uk/skeleton/publications/ViewPublication.aspx?id=cf825d8d-f061-44cb-9293-51b96939d244 [Accessed May 20, 2013].

Hayman, G., Sokhi, R., Chemel, C., Griffiths, S., Vincent, K., Dore, A.J., Sutton, P. and *Wright, R.*, 2013c: Comparison of simple and advanced regional models (CREMO): Ozone diagnostics. *Environment Agency Report SC060037c/R.* Bristol: Environment Agency.https://publications.environment-agency.gov.uk/skeleton/publications/ViewPublication.aspx?id=cf825d8d-f061-44cb-9293-51b96939d244 [Accessed May 20, 2013].

Hayman, G., Sokhi, R., Chemel, C., Griffiths, S., Vincent, K., Dore, A.J., Sutton, P. and *Wright, R.*, 2013d. Comparison of simple and advanced regional models (CREMO): Model evaluation: Ground-level ozone. *Environment Agency Report SC060037d/R.* Bristol: Environment Agency. https://publications.environment-agency.gov.uk/skeleton/publications/ViewPublication.aspx?id=cf825d8d-f061-44cb-9293-51b96939d244 [Accessed 20 May 2013].

Im, U., Bianconi, R., Solazzo, E., Kioutsioukis, I., Badia, A., Balzarini, A., Baró, R., Bellasio, R., Brunner, D., Chemel, C., Curci, G., van der Gon, H.D., Flemming, J., Forkel, R., Giordano, L., Jiménez-Guerrero, P., Hirtl, M., Hodzic, A., Honzak, L., Jorba, O., Knote, C., Makar, P.A., Manders-Groot, A., Neal, L., Pérez, J.L., Pirovano, G., Pouliot, G., San Jose, R., Savage, N., Schroder, W., Sokhi, R.S., Syrakov, D., Torian, A., Tuccella, P., Wang, K., Werhahn, J., Wolke, R., Zabkar, R., Zhang, Y., Zhang, J., Hogrefe, C. and *Galmarini, S.*, 2014. Evaluation of operational online-coupled regional air quality models over Europe and North America in the context of AQMEII phase 2. Part II: Particulate matter., *Atmos. Environ.* http://dx.doi.org/10.1016/j.atmosenv.2014.08.072

Klein, H., Gauss M., Nyiri A. and *Steensen B.M.*, 2011: Transboundary air pollution by main pollutants (S, N, O_3) and PM: The United Kingdom. *MSC-W Data Note 1/2011.* Oslo: Norwegian Meteorological Institute.

Middleton, D.R., Luhana L. and *Sokhi R.S.*, 2007: Overview of indicators for estimating the contribution of Environment Agency regulated sources to regional ozone. *Environment Agency Report SC030171/SR3.* Bristol: Environment Agency.

NMI, 2010: Transboundary acidification, eutrophication and ground-level ozone in Europe for 2008. *EMEP Status Report 2010.* Oslo: Norwegian Meteorological Institute. Available from: http://emep.int/publ/reports/2010/status_report_1_2010.pdf [accessed May 21, 2013].

Pederzoli, A., Thunis, P., Georgieva, E., Borge, R. and *Carruthers, D.*, 2011: Performance criteria for the benchmarking of air quality model regulatory applications: the 'target' approach.*14th Conference on Harmonisation within Atmospheric Dispersion Modelling for Regulatory Purposes*, 2–6 October 2011, Kos, Greece.

Pilkey-Jarvis, L. and *Pilkey, O.H.*, 2008: Useless arithmetic: ten points to ponder when using mathematical models in environmental decision making. *Public Administration Review 68*, 470–479.

Rao, S.T., Porter, P.S., Mobley, J.D. and *Hurley, F.*, 2011: Understanding the spatio-temporal variability in air pollution concentrations, *EM*, the Air and Waste Management Association Magazine for Environmental Managers, November 2011, 42–48.

Risbey, J., Van Der Sluijs, J.P., Ravetz, J. and *Jannsen, P.*, 2001: A check list for quality assurance in environmental modelling. *Report Number NW&S-E-2001-11.* Utrecht: Department of Science, Technology and Society, Utrecht University. Available from: http://www.nusap.net/downloads/reports/E2001-11.pdf.

Schere, K., Vautard, R., Solazzo, E., Hogrefe, C. and *Galmarini, S.*, 2012: Results and lessons learned from Phase 1 of the AQMEII. *EM*, the Air and Waste Management Association Magazine for Environmental Managers, July 2012, 30–37.

Solazzo, E., Bianconi, R., Pirovano, G., Matthias, V., Vautard, R., Moran, M.D., Appel, K.W., Bessagnet, B., Brandt, J., Christensen, J.H., Chemel, C., Coll, I., Ferreira, J., Forkel, R., Francis, X.V., Grell, G., Grossi, P., Hansen, A.B., Miranda, A.I., Nopmongcol, U., Prank, M., Sartelet, K.N., Schaap, M., Silver, J.D., Sokhi, R.S., Vira, J., Werhahn, J., Wolkem, R., Yarwood, G., Zhang, J., Rao, S.T. and *Galmarini, S.*, 2012: Operational model evaluation for particulate matter in Europe and North America in the context of AQMEII. *Atmos. Environ. 53*, 75–92.

Sutton, P., Chemel, C., Griffiths, S. and *Sokhi, R.S.*, 2013: Investigation, using CMAQ, of sensitivity of air quality modelling to input ammonia emissions. *Air Pollution Modeling and its Application XXII* (ed. D G. Steyn, P.J.H. Builtjes and R.M.A. Timmermans), pp 571-6. Dordrecht: Springer.*Thunis, P., Georgieva, E.* and *Galmarini, S.*, 2011a: A procedure for air quality models benchmarking. Version 2. Ispra, Italy: European Commission, Joint Research Centre. Available from: http://fairmode.ew.eea.europa.eu/models-benchmarking-sg4. [accessed July 2, 2013].

Thunis, P., Georgieva, E. and *Pederzoli, A.*, 2011b: The DELTA tool and Benchmarking report template. Concepts and user guide. Version 2. Ispra, Italy: European Commission Joint Research Centre. Available from: http://fairmode.ew.eea.europa.eu/models-benchmarking-sg4 [accessed July 2, 2013].

Vincent, K. and *Abbott, J.*, 2008: Air quality and deposition benefits from Environment Agency regulation. *Environment Agency Science Report SC060108*. Bristol: Environment Agency. https://publications.environment-agency.gov.uk/skeleton/publications/ViewPublication.aspx?id=a98e1cd3-7d34-40ef-8f68-2e401db1bfa4 [accessed May 20, 2013].

Wild, O., Fiore, A.M., Shindell, D.T., Doherty, R.M., Collins, W.J., Dentener, F.J., Schultz, M.G., Gong, S., MacKenzie, I.A., Zeng, G., Hess, P., Duncan, B.N., Bergmann, D.J., Szopa, S., Jonson, J.E., T. J. Keating, T.J. and *Zuber, A.*, 2012: Modelling future changes in surface ozone: a parameterized approach. *Atmos. Chem. Phys. 12*, 2037–2054.

Yu, Y., Sokhi, R.S., Kitwiroon, N., Middleton, D.R. and *Fisher, B.*, 2008: Performance characteristics of MM5–SMOKE–CMAQ for a summer photochemical episode in southeast England, United Kingdom. *Atmos. Environ. 42*, 4870–4883.

IDŐJÁRÁS

Quarterly Journal of the Hungarian Meteorological Service
Vol. 119, No. 3, July – September, 2015, pp. 379–398

Combined closure single-column atmospheric boundary layer model

Árpád Bordás* and **Tamás Weidinger**

Department of Meteorology, Eötvös Loránd University,
P.O. Box 32, H-1518 Budapest, Hungary;

**Corresponding author E-mail: abordas@caesar.elte.hu*

(Manuscript received in final form March 20, 2015)

Abstract—This paper presents a development of the first order combined closure (local and nonlocal) single-column atmospheric boundary layer model. The model simulates the turbulent mixing of sensible heat, moisture, and momentum as a split between small scale (subgrid) and large scale (supergrid) processes according to the estimated ratio between local and nonlocal mixing. To verify the validity of the model, an evaluation process was conducted. The evaluation process included controlled offline numerical experiments and tests using the Wangara Experiment database. The obtained vertical profiles and estimated boundary layer heights are in good agreement with the Wangara observation data. Furthermore, uncertainty range affected by the choice of profile functions when estimating the ratio between local and nonlocal mixing processes was analyzed.

Key-worlds: atmospheric boundary layer, turbulent mixing, single-column model, combined (local and nonlocal) approach, Wangara Experiment

1. Introduction

Almost all human and biological activities take place in the atmospheric boundary layer (ABL), where the direct effects of the Earth's surface are noticeable. Therefore, the description of the boundary layer characteristics as well as the simulation of the turbulent mixing processes in the ABL are important for weather prediction, air pollution, and environmental modeling. When neglecting horizontal advection, the governing ABL equations in single-column (1D) form for the northern hemisphere are:

$$\frac{\partial \theta}{\partial t} = -\frac{\partial \left(\overline{w'\theta'}\right)}{\partial z}, \tag{1}$$

$$\frac{\partial q}{\partial t} = -\frac{\partial \left(\overline{w'q'}\right)}{\partial z}, \tag{2}$$

$$\frac{\partial u}{\partial t} = f\left(v - v_g\right) - \frac{\partial \left(\overline{u'w'}\right)}{\partial z}, \tag{3}$$

$$\frac{\partial v}{\partial t} = -f\left(u - u_g\right) - \frac{\partial \left(\overline{v'w'}\right)}{\partial z}, \tag{4}$$

where θ is the potential temperature, q is the specific humidity, u and v are the horizontal wind velocity components, u_g and v_g are the corresponding geostrophic wind components, $\overline{w'\theta'}$, $\overline{w'q'}$, $\overline{u'w'}$, and $\overline{v'w'}$ represent vertical fluxes, f denotes the Coriolis parameter, and z is the vertical coordinate.

Single-column ABL models differ in the main mixing assumption and the approach to the closure problem (*Stull*, 1988; *Foken*, 2006). The choice of a model depends on the aim of investigation and on the modelers' conception. Assuming that the turbulence is analogous to molecular diffusion, different types of first and higher order local closure procedures were developed. This approach is reasonable during conditions of stable and neutral static stability, when the scale of turbulent motion is much smaller than the scale of mean motion. In the convective ABL, where the boundary layer is directly affected by the solar heating of the surface, much of the mixing is caused by buoyant plumes originating in the surface layer and rising to the top of the boundary layer. When using nonlocal mixing schemes (*Blackadar* 1978; *Zhang* and *Anthes*, 1982; *Fiedler* and *Moeng*, 1985), the effects of local mixing during convective conditions are neglected and turbulent mixing is simulated by different size discrete convective elements. To simulate both local (small scale) and nonlocal (large scale) mixing processes simultaneously, combined closure (local and nonlocal) mixing schemes (*Stull*, 1984; *Pleim* and *Chang*, 1992 *Pleim*, 2007a; *Bordás*, 2008) were developed.

Single-column models are very useful tools in ABL investigation. Such models are comprehensive enough to illustrate basic ABL characteristics, simulate boundary layer processes (*Holtslag* and *Boville*, 1993), and compare different parameterization processes (*Alapaty et al.*, 1997; *Bosveld et al.*, 2014). Nesting 1D models in 3D environment, such as MM5 (*Berg* and *Zhong*, 2005; *Pleim*, 2007b) and WRF (*Hu et al.*, 2010; *Shin* and *Hong*, 2011; *Xie et al.*, 2012; *Kleczek et al.*, 2014), we can provide detailed and accurate information of the ABL structure.

The aim of our study is to represent the designed first order single-column ABL model (mixing concept, calculation of turbulent mixing rates, and estimation of the ABL height), which employs a combined (local and nonlocal) mixing scheme, as well as to introduce the model evaluation process done by controlled offline numerical experiments and the Wangara Experiment database. In stable and neutral static conditions, turbulent mixing is simulated as a subgrid (local) process. In unstable conditions, depending on the calculated ratio between local and nonlocal mixing of heat, the model simulates turbulent mixing of sensible heat, moisture, and momentum as a split between small scale and large scale processes. In addition, we analyzed how the type of profile function affected the uncertainty range when estimating the local versus nonlocal character of the turbulent mixing.

2. Estimation of the local to nonlocal mixing ratio

For the combined modeling of the boundary layer processes, it is necessary to define the explicit local and nonlocal vertical fluxes. Many ABL models (*Troen* and *Mahrt*, 1986; *Holtslag* and *Boville*, 1993; *Noh et al.* 2003, *Hong et al.*, 2006) simulate the nonlocal mixing of the different prognostic variables (c; θ, q, u, v) including gradient adjustment term (γ_c) into eddy diffusivity equation as:

$$-\frac{\partial\left(\overline{w'c'}\right)}{\partial z}=\frac{\partial}{\partial z}\left[K_c\left(\frac{\partial c}{\partial z}-\gamma_c\right)\right], \tag{5}$$

where K_c denotes the vertical eddy diffusivity for the quantity of interest. The gradient adjustment term, representing nonlocal influences on the turbulent mixing, can be estimated as (*Holtslag* and *Boville*, 1993):

$$\gamma_c=a\frac{w_*\left(\overline{w'c'}\right)_0}{w_m^2 h}, \tag{6}$$

where $\left(\overline{w'c'}\right)_0$ is the surface kinematic flux of the transported variable, w_* represents the convective velocity scale, $w_m=u_*/\Phi_m$ (where u_* is the friction velocity and Φ_m denotes the profile function for momentum), h denotes the height of the boundary layer, and a is a semi-empirical constant. Under neutral static conditions for which $w_*=0$, the gradient adjustment term vanishes. This approach is most valid for heat, since surface heat flux is the source and driver of convective turbulence. For other quantities, the surface heat flux is replaced by the surface flux of the transported quantity. However, nonlocal effects may

be driven by mechanisms completely unrelated to convective turbulence. For quantities that have no upward surface fluxes, these models revert to the local eddy diffusivity model.

Following *Pleim* (2007a) from Eq. (5), we can define the ratio between local and nonlocal heat mixing fluxes (R) as:

$$R = \frac{K_h \left| \partial\theta / \partial z \right|}{K_h \gamma_h}. \tag{7}$$

When estimating this ratio, it is possible to obtain information about the physical characteristics of the convective boundary layer applicable to any prognostic variable. The surface sensible heat flux can be approximated as:

$$\left(\overline{w'\theta'}\right)_0 = -\kappa \frac{u_* z_s}{\Phi_h} \frac{\partial\theta}{\partial z}, \tag{8}$$

where z_s is the thickness of the surface layer ($z_s = 0.1h$), and Φ_h denotes the profile function for heat. The convective velocity scale, defined by *Troen* and *Mahrt* (1986) as $w_* = \left[\beta\left(\overline{w'\theta_v'}\right)_0 h\right]^{1/3}$, is estimated in the form:

$$w_* = u_* \kappa^{-\frac{1}{3}} \left(-\frac{h}{L}\right)^{\frac{1}{3}}, \tag{9}$$

where L represents the Monin-Obukhov length scale, and κ is the von Kármán constant. The Monin-Obukhov length scale is calculated as:

$$L = -\frac{u_*^3}{\beta\kappa\left(\overline{w'\theta'}\right)_0}, \tag{10}$$

where β denotes the buoyancy parameter ($\beta = g / T_0$, g is the acceleration due to gravity, and T_0 is the average temperature in the surface layer). According to Eq. (6) to Eq. (10), the ratio between local and nonlocal mixing can be expressed as:

$$R = \left[0.1a\kappa^{\frac{2}{3}} \left(-\frac{h}{L}\right)^{\frac{1}{3}} \frac{\Phi_m^2}{\Phi_h}\right]^{-1}. \tag{11}$$

It can also be linked to the ratio of the nonlocal flux to the total flux (f_{conv}), defined by *Pleim* (2007a), as:

$$f_{conv} = \frac{1}{R+1}. \tag{12}$$

The local versus nonlocal turbulent mixing ratio (R) defined by Eq. (11) behaves as a function of stability ($-h/L$) and depends on the choice of profile functions for momentum and heat (Φ_m^2 / Φ_h). Comparing different profile functions, we can analyze the uncertainty caused by the choice of profile functions. *Table 1* lists four often used profile functions for unstable stratification, intervals of definition, and the von Kármán constant used by different authors. The detailed comparison of the profile functions for both stable and unstable conditions, as well as the effects of uncertainties on the calculation of surface layer fluxes are provided by *Weidinger et al.* (2000), *Ács* and *Kovács* (2001), *Arya* (2001), and *Kramm et al.* (2013). *Fig. 1* illustrates how Φ_m^2 / Φ_h, obtained by the listed profile functions, depends as a function of non-dimensional height (z/L). For *Dyer*'s (1974) profile functions, Φ_m^2 / Φ_h equals 1 throughout the interval of definition ($-1 \le z/L \le 0$). When using the *Businger et al.* (1971) functions, Φ_m^2 / Φ_h is greater than 1, while when applying the *Dyer* and *Bradley* (1982) functions, Φ_m^2 / Φ_h is smaller than 1. For both universal function types, Φ_m^2 / Φ_h is decreasing about 30% in the first part of the considered interval of definition ($-1 \le z/L \le 0$) and is nearly constant in the second part of the considered interval ($-2 \le z/L \le -1$). For the *Zilitinkevich* and *Chalikov* (1968) functions, Φ_m^2 / Φ_h is decreasing rapidly in the total interval of definition ($-1.2 \le z/L \le 0$).

As the aim of the subsequent analysis was to determine whether and to what extent the choice of profile function type influenced the uncertainty range, we used the *Dyer*-type profile functions for which Φ_m^2 / Φ_h equals 1 in the interval of definition, and set the von Kármán constant to 0.41. The semi-empirical constant a (see Eq. (6) and Eq. (11)) was set to 7.2 (*Holtslag* and *Boville*, 1993). *Fig. 2* shows how the ratio between local to nonlocal mixing processes (R) behaves as a function of stability. To estimate the uncertainty range caused by using different profile functions, the value of the semi-empirical constant a was varied by ± 15% and ± 25%. The obtained results are also presented in *Fig. 2*. For $R = 1$, the local and nonlocal mixing processes are in balance. When the value is higher than 1, it is the local processes that dominate, while when the value is lower than 1, it is the nonlocal processes that prevail. Due to the inverse proportion between R and a, when the value of the semi empirical constant is increasing, the effects of local mixing processes are decreasing. Nonlocal processes became dominant for very unstable conditions ($-h/L > 10$). During extremely convective conditions ($-h/L = 30$), the value of R is not lower than 0.65. Our results verify the combined mixing range of the unstable ABL. The uncertainty range is not significantly affected by the choice of profile function type in estimation of the ratio between local versus nonlocal mixing.

Table 1. Some frequently used profile functions in the case of unstable stratification,

intervals of definition, and estimation of the von Kármán constant

	profile function	interval	*k*
Zilitinkevich and *Chalikov* (1968)	$\Phi_m = \Phi_h = 1 + 1.45\frac{z}{L}$ $\Phi_m = \Phi_h = 0.417\left(-\frac{z}{L}\right)^{-}$	$-0.16 \le \frac{z}{L} \le 0$ $-1.2 \le \frac{z}{L} \le -0.1$	0.43
Businger et al. (1971)	$\Phi_m = \left(1-15\frac{z}{L}\right)^{-\frac{1}{4}}$ $\Phi_h = 0.74\left(1-9\frac{z}{L}\right)^{-\frac{1}{2}}$	$-2 \le \frac{z}{L} \le 0$	0.35
Dyer (1974)	$\Phi_m = \left(1-16\frac{z}{L}\right)^{-\frac{1}{4}}$ $\Phi_h = \left(1-16\frac{z}{L}\right)^{-\frac{1}{2}}$	$-1 \le \frac{z}{L} \le 0$	0.41
Dyer and *Bradley* (1982)	$\Phi_m = \left(1-28\frac{z}{L}\right)^{-\frac{1}{4}}$ $\Phi_h = \left(1-14\frac{z}{L}\right)^{-\frac{1}{2}}$	$-4 \le \frac{z}{L} \le 0$	0.4

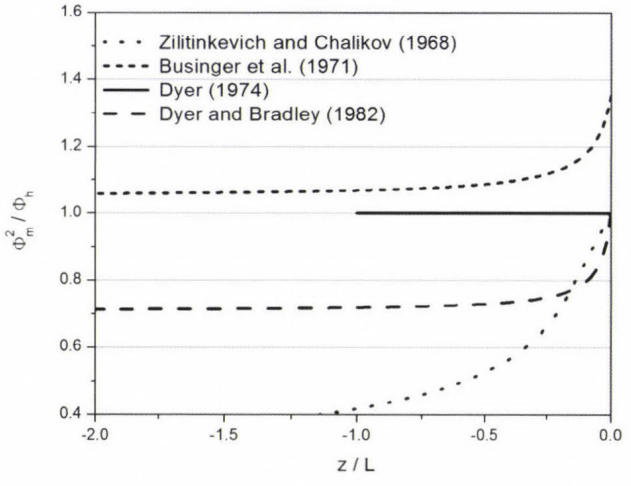

Fig. 1. Φ_m^2 / Φ_h as a function of non-dimensional height (z/L) using different universal functions.

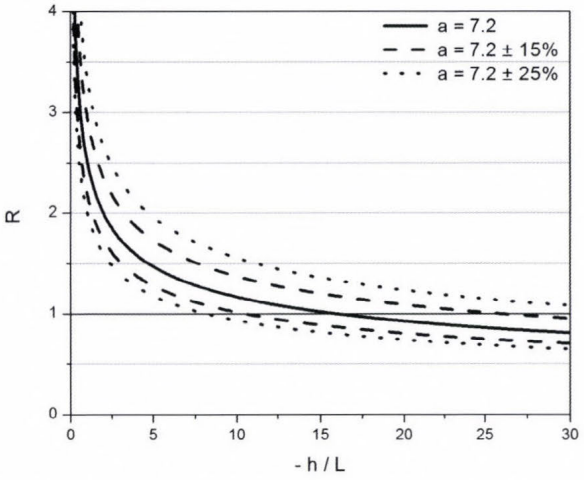

Fig. 2. The ratio between local and nonlocal turbulent mixing processes (R) as a function of stability.

3. Model description

3.1. Mixing concept

The model designed by the authors describes turbulent mixing during stable and neutral static conditions employing the standard eddy diffusion scheme. For unstable conditions, the model calculates the ratio between local and nonlocal mixing processes (R, defined by Eq. (11)) in every time step. According to the calculated ratio, turbulent mixing of sensible heat, moisture, and momentum are simulated as a split between local and nonlocal mixing processes employing a combined (local and nonlocal) closure mixing scheme (*Bordás*, 2008). Stability is defined by the bulk Richardson number method for the lowest model layer. The inclusion of the nonlocal mixing components of momentum can provide more realistic wind profiles for unstable conditions (*Frech* and *Mahrt*, 1995 *Brown* and *Grant*, 1997). However, it is not yet clear how the inclusion of the nonlocal mixing of momentum can improve general properties of a boundary layer model (*Noh et al.*, 2003).

The mixing scheme (*Bordás*, 2008) used for simulating turbulent mixing during unstable conditions combines the local eddy diffusion scheme and the nonlocal Blackadar scheme (*Blackadar,* 1978). The Blackadar scheme describes nonlocal mixing, transporting material directly from the lowest model layer to every other layer and symmetrically from each layer back to the surface layer as it is shown in *Fig. 3*. The explicit value of nonlocal exchange of the prognostic variable at layer i can be calculated as $M(c_1 - c_i)$, where $M\,[\mathrm{s}^{-1}]$ is the convective

mixing rate. Such a model was applied as one of the mixing schemes in MM4 (*Zhang* and *Anthes*, 1982) and MM5 (*Zhang* and *Zheng*, 2004; *Berg* and *Zhong*, 2005) models to simulate boundary layer processes during free convection.

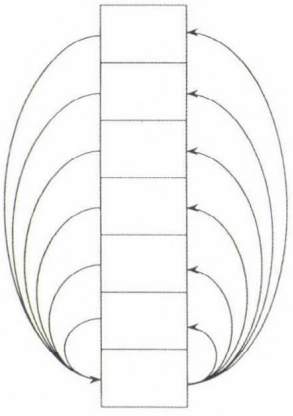

Fig. 3. Schematic representation of the Blackadar mixing scheme.

Since the total mixing is simulated as a split between local and nonlocal mixing components, we estimate the weighted vertical eddy diffusivity for heat and momentum (K'_{hm}) and the weighted upward mixing rate (M') as:

$$K'_{hm} = \frac{R}{R+1} K_{hm} = (1 - f_{conv}) K_{hm}, \tag{13}$$

and

$$M' = \frac{1}{R+1} M = f_{conv} M . \tag{14}$$

At either extremes ($R \to \infty$ or $R = 0$), the mixing reverts to the simple eddy diffusivity scheme and Blackadar scheme, respectively.

3.2. Calculation of the vertical eddy diffusivity and convective mixing rate

The model defines vertical eddy diffusivity for heat and momentum (K_{hm}) by boundary layer scaling, similarly to *Hotlsag* and *Boville* (1993) as:

$$K_{hm}(z) = \kappa \frac{u_* z}{\Phi_{hm}(z/L)} \left(1 - \frac{z}{h}\right)^2, \tag{15}$$

where Φ_{hm} is the corresponding profile function. The convective mixing rate (M) used for any prognostic variable was calculated according to *Pleim* (2007a) as:

$$M = -\frac{1}{h - z_1} \frac{F_{h1}}{\theta_v(z_2) - \theta_v(z_1)}, \tag{16}$$

where F_{h1} is the sensible heat flux in the lowest model layer, $\theta_v(z_2)$ and $\theta_v(z_1)$ represent the virtual potential temperature at the top and bottom of the lowest model layer, respectively, and z_1 is the height of the lowest model level. The sensible heat flux in the lowest layer was defined as:

$$F_{h1} = -K_{h1} \frac{\theta_v(z_2) - \theta_v(z_1)}{\Delta z_1}, \tag{17}$$

where K_{h1} denotes the vertical eddy diffusivity for heat in the lowest model layer estimated from the surface layer theory as in Eq. (16) and Δz_1 represents the thickness of the lowest model layer. Combining Eq. (17) and Eq. (18), the convective mixing rate can be calculated as:

$$M = \frac{K_{h1}}{(h - z_1)\Delta z_1}. \tag{18}$$

3.3. Determination of the ABL height

The height of the ABL, one of the mean characteristics of the boundary layer, shows a strong diurnal variation. The model determines the ABL height by specifying a critical value of the bulk Richardson number (Ri_b), defined by:

$$h = Ri_b \frac{u(h)^2 + v(h)^2}{\beta\left[\theta_v(h) - \theta_s\right]}, \tag{19}$$

where $u(h)$ and $v(h)$ are the horizontal wind velocity components at h, $\theta_v(h)$ is the virtual potential temperature at h, and θ_s is an appropriate temperature of air near the surface. The near surface potential temperature (θ_s) is calculated as (*Troen* and *Mahrt*, 1986):

$$\theta_s = \theta_v(z_1) + b\frac{\left(\overline{w'\theta_v'}\right)_0}{w_m}, \tag{20}$$

where b is a semi-empirical constant (b = 8.5, *Holtslag et al.*, 1990). The top of the ABL is diagnosed as the height where the bulk Richardson number is equal to the critical Richardson number.

4. Model evaluation

Model evaluation plays an important role in model development. A good ABL model should be able to predict realistic vertical profiles of temperature, humidity, and winds, as well as simulate the morning growth, maximum height, and evening collapse of the boundary layer. During the evaluation process, our model was tested by controlled offline numerical experiments, where initial conditions and forcing were specified. Furthermore, the model tests were performed using the Wangara observational data. The model runs were done with equally spaced vertical layers in z coordinates. Stability was defined by the surface layer bulk Richardson number as: $Ri_0 > 0.01$ for stable conditions, $-0.01 \leq Ri_0 \leq 0.01$ for neutral static conditions, and $Ri_0 < -0.01$ for the unstable boundary layer. For the test runs, *Dyer*'s (1974) profile functions were used, and the semi empirical constant a necessary to estimate ratio between local and nonlocal mixing processes (see Eq. (12)) was set to 7.2 (*Holtslag* and *Boville*, 1993). The top of the ABL is diagnosed as the height where the bulk Richardson number is equal to the critical Richardson number, which value was set to 0.25 (*Holtslag et al.*, 1990).

4.1. Controlled offline numerical experiments

The controlled offline experiments were performed for a dry atmosphere with a defined initial potential temperature (θ) and horizontal wind (u and v) profiles. The constant potential temperature increase of the lowest model level was determined with a magnitude of 0.16 K/h (*Nieuwstadt et al.*, 1992), the roughness length was set to 0.1 m, and the geostrophic wind components were u_g = 10 m/s and v_g = 0 m/s at all levels.

The simulated potential temperature profiles after the 4th and 8ht hour of integration obtained by estimating the ratio between local and nonlocal mixing processes (R) in every time step are presented in *Fig. 4*. The vertical model resolution was 50 m. The simulated profiles show a downward gradient from the ground up to 2/3 of the ABL height. *Fig. 5* compares profiles shown in *Fig. 4* (varying R), profiles obtained assuming that during unstable conditions the local and nonlocal mixing processes are in equilibrium ($R = 1$), and profiles simulated

by the local eddy diffusivity scheme ($R \to \infty$). As expected, the defined weak forcing local mixing processes were dominant and the profiles obtained by the varying ratio between local and nonlocal mixing processes showed a more local than a nonlocal character.

Fig. 6 describes the time evolution of the ABL height simulated by different vertical model resolutions (25 m, 50 m, and 100 m) by the varying ratio between local and nonlocal mixing processes. Since weak forcing was used in the simulation, the ABL height increased slowly. The estimation of the boundary layer height was independent of vertical resolution. Performed controlled numerical experiments showed that simulated potential temperature (θ) as well as horizontal wind (u and v) profiles were also free of vertical model resolution. The profiles obtained for eastward (u) and northward (v) wind components simulated after the 4th and 8th hours of integration by varying R are presented in *Fig. 7*. Model runs were done by 50 m vertical resolution. *Fig. 8* compares the horizontal wind profiles simulated by the eddy diffusivity scheme ($R \to \infty$), constant ($R = 1$), and varying ratio between local and nonlocal processes (profiles shown in *Fig. 7*). The differences among combined closure profiles are negligible. These profiles simulate slightly higher v wind speeds in the mixed layer and slightly lower u wind speeds near the top of the ABL than profiles obtained by local closure approach.

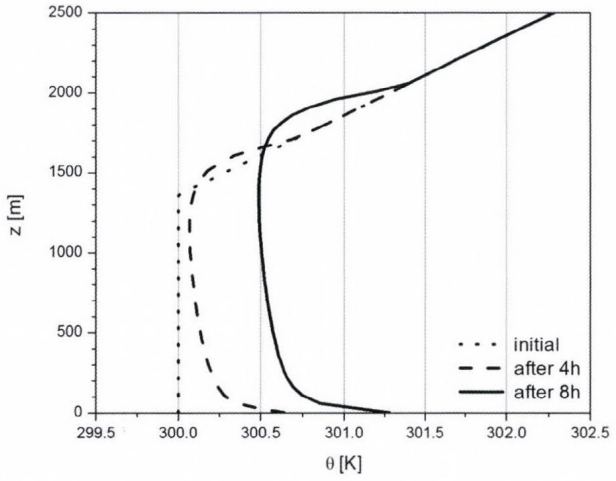

Fig. 4. Potential temperature profile at initial time and simulated after the 4th and 8th hour of integration.

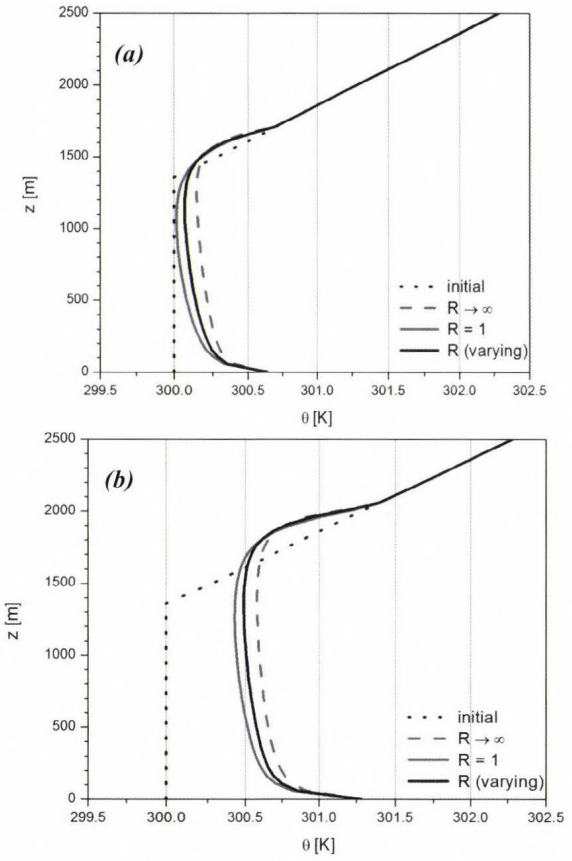

Fig. 5. Potential temperature profiles at initial time and simulated after the 4th *(a)* and 8th *(b)* hour of integration by different mixing approaches.

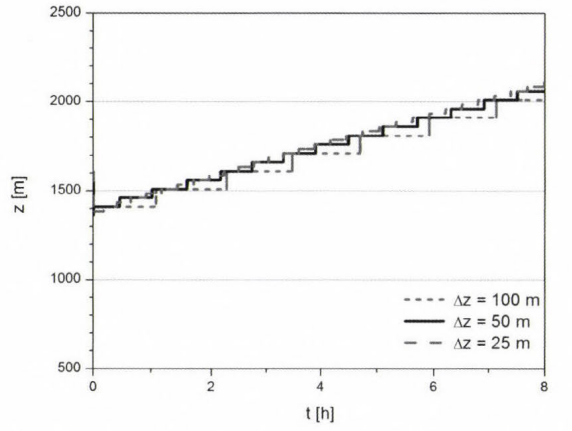

Fig. 6. Time evolution of the ABL height obtained by different vertical resolutions.

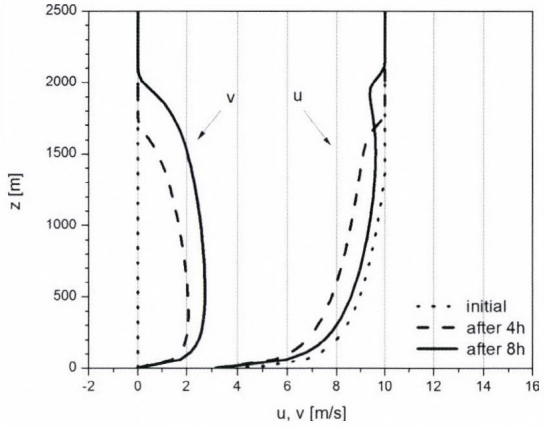

Fig. 7. Horizontal wind profiles at initial time and simulated after the 4th and 8th hour of integration.

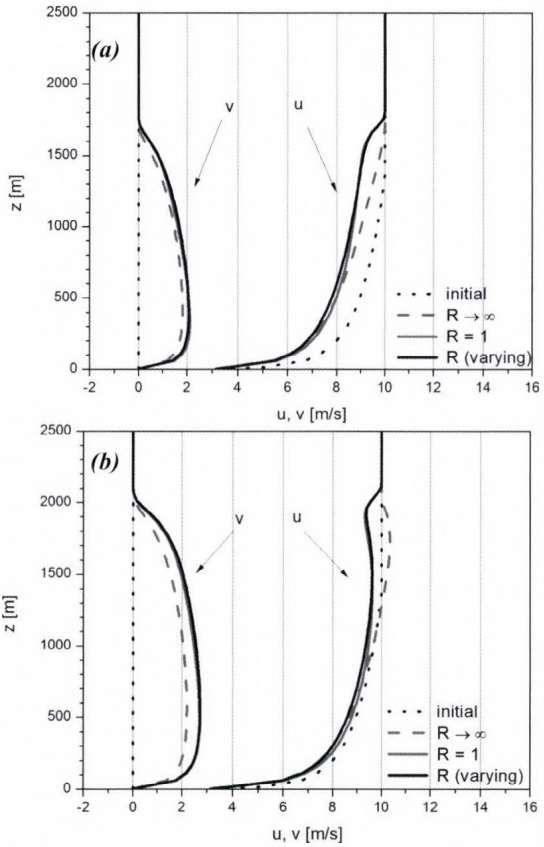

Fig. 8. Horizontal wind profiles at initial time and simulated after the 4th *(a)* and 8th *(b)* hour of integration by different mixing approaches.

4.2. Comparison with the Wangara observations

The Wangara campaign (*Clarke et al.*, 1971; *Hess et al.*, 1981) was one of the first field experiments to define the universal characteristics of the ABL. It was conducted in July and August 1967 near Hay (New South Wales, Australia). The name "Wangara" was taken from an Aboriginal word for "west wind", which was the primary focus of the experiment. The area was selected because of its flatness, small slope, and all-weather accessibility. The observational site was located over a sparsely and uniformly vegetated region close to a desert. Over such areas, errors arising from the insufficient representation of vegetation-atmosphere interactions should be at a minimum during simulations. The high density of the observational network and the availability of many meteorological parameters (pilot balloons were released hourly, radiosonde every three hours) made the Wangara database very popular for model comparison and evaluation studies.

Our model tests were done using the data for day 33 (August 16) of the Wangara database. This particular day has been used quite often as a test case for different types of ABL models (*Yamada* and *Mellor*, 1975; *Pleim* and *Xiu*, 1995; *Alpaty et al.*, 1997; *Xue et al.*, 2001.; *Cara-Lyn et al.*, 2010) because the sky was clear the whole day and horizontal advection was very weak. Our model calculations were done by a 50 m vertical model resolution. The vertical resolution of the Wangara data is 50 m from the land surface to 1000 m, and 100 m from 1000 m to 2000 m. The initial profiles for the potential temperature (θ), water vapor mixing ratio (q), and horizontal wind components (u, v) were the observed values at 0900 LT (local time). The time variation of these quantities at the lowest model level were set explicitly as a lower boundary condition in the model. The virtual potential temperature was calculated using measured and simulated data for potential temperature and water vapor mixing ratio. According to *Yamada* and *Mellor* (1975), the roughness length was set to 0.01 m.

Observed and modeled (by varying R) virtual potential temperature profiles at four times during day 33 are shown in *Fig. 9*. The profile at 0900 LT shows a stable boundary layer. By 1200 LT, the inversion was dissipated and a convective layer was formed in both vertical profiles. The predicted top of the ABL is slightly underestimated. From 1200 LT to 1500 LT, the mean mixed layer warmed up by about 2 K. At 1800 LT, the profiles show a formed surface inversion with a well mixed residual layer.

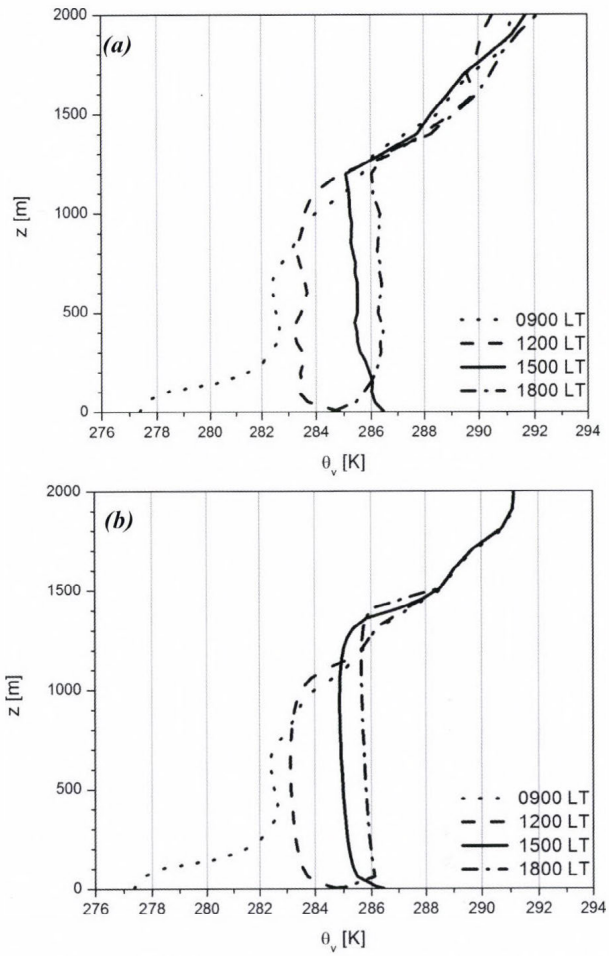

Fig. 9. The Wangara observational *(a)* and modeled *(b)* virtual potential temperature profiles.

Fig. 10 compares the virtual potential temperature profiles obtained by the eddy diffusivity scheme ($R \to \infty$), a combined mixing scheme with constant ($R = 1$), and a varying (varying R) ratio between mixing processes at 1200 LT and 1500 LT. The predicted profiles for 1200 LT are very close to the observations. At lower altitudes it is the combined closure profiles, while near the top of the boundary layer it is the local closure profile that fit the Wangara data better. The differences between the simulated and observed profiles for 1500 LT are higher. In the lower part of the boundary layer, the best fit was obtained by the local closure profile. The combined closure profiles, on the other hand, estimate the height of the boundary layer better.

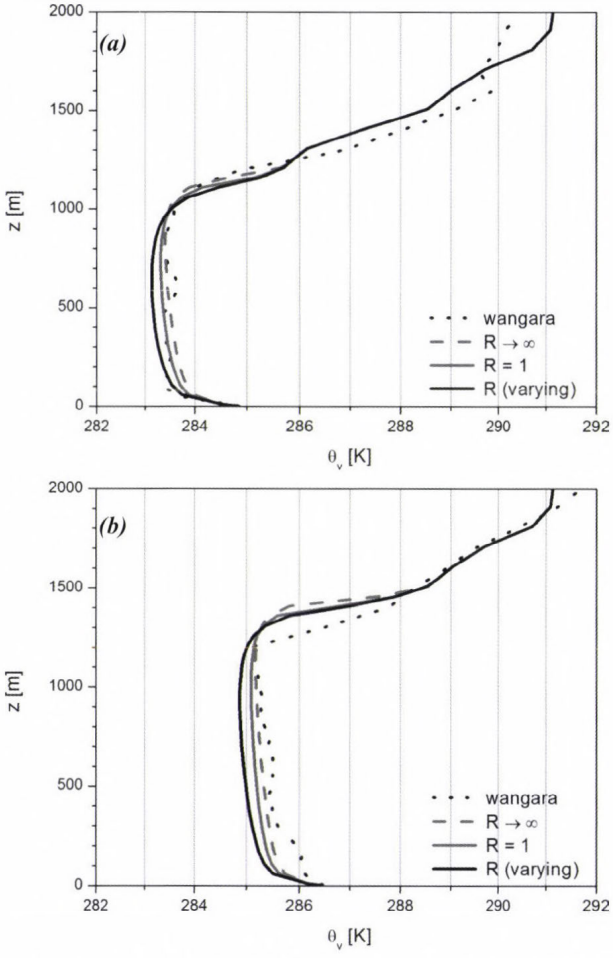

Fig. 10. Comparison of simulated and observational virtual temperature profiles at 1200 LT *(a)* and 1500 LT *(b)*.

The observed and modeled ABL heights are presented in *Fig. 11.* The observations were estimated using two methods from radiosonde measurements: as reported by *Yamada* and *Mellor* (1975), and by applying the determination process described in Section 3.3. The time resolution of the three ($R \to \infty, R = 1$, and varying R) modeled ABL heights is one hour. The modeled and observed heights agree very well in timing of rise, and they also predict the collapse of the ABL. At 1800 LT, when the ground-based inversion was developed, the first observational method actually represents the top of the residual layer.

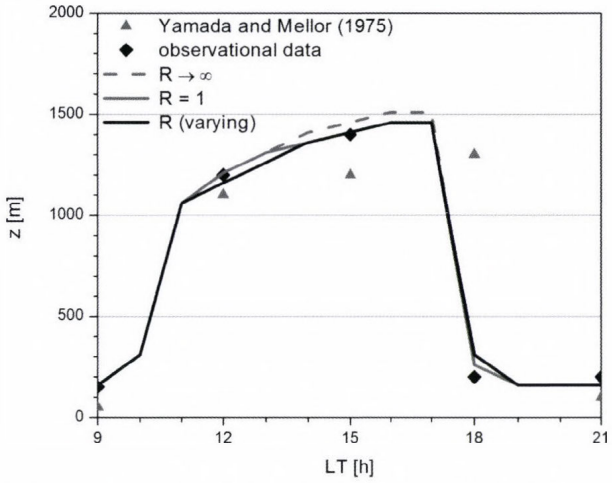

Fig. 11. Temporal evolution of the estimated and predicted height of the ABL for the Wangara simulation.

Fig. 12 compares the observed and the three predicted ($R \to \infty$, $R = 1$, and varying R) horizontal wind profiles at 1200 LT and 1800 LT. Geostrophic wind profiles were estimated from a parabolic fit to the thermal wind data as suggested by *Yamada* and *Mellor* (1975). As a function of height and time, the resulting geostrophic winds were supplied to the model as input. The differences between the modeled profiles are very small, with the highest difference being approximately 0.5 m/s. These profiles show similar features to the observations. For 1200 LT, the v profiles fit well, while the u profiles underestimate the observational data. Underestimation is explicit from 800 m to the top of the boundary layer at 1150 m. The predicted winds at 1800 LT are close to the observations. The simulated u profiles slightly underestimate, while v profiles at lower altitudes overestimate the measured data. The average difference between the estimated and measured values is about 1 m/s. The differences between the observed and simulated profiles may be due to the uncertainty in geostrophic wind estimation (*Yamada* and *Mellor*, 1975).

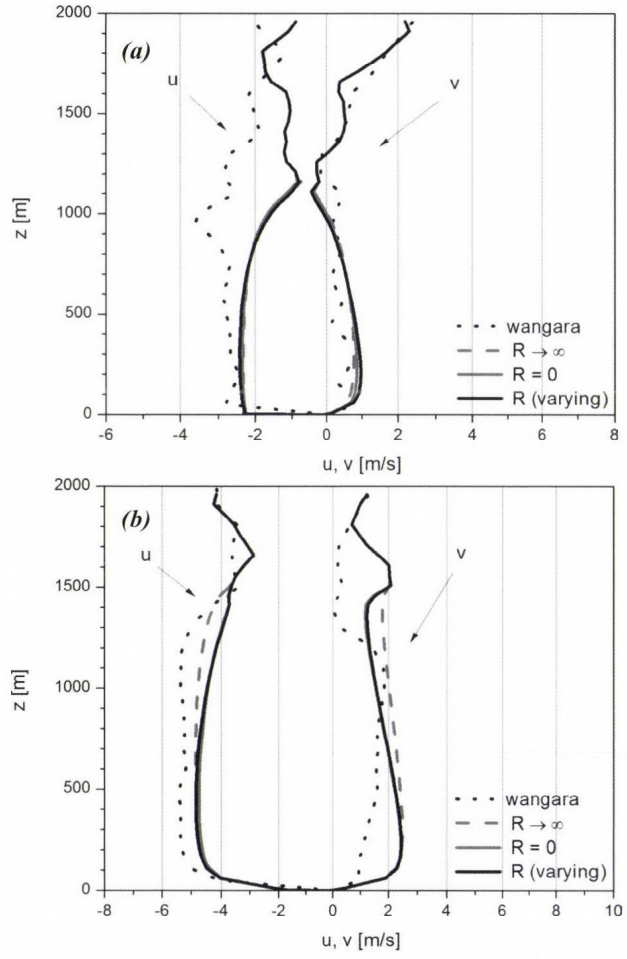

Fig. 12. Observed and simulated horizontal wind profiles at 1200 LT *(a)* and 1800 LT *(b)*.

5. Summary

This paper presents a first order single-column (1D) ABL model with a combined closure approach. In order to describe ABL properties as accurately as possible, the model calculates the local to nonlocal mixing ratio in every time step. According to the current ratio, the model simulates the turbulent mixing of prognostic variables as a split between small scale and large scale components. The obtained mixing ratio values verify the combined character of the turbulent mixing during unstable conditions. It was also proven that the uncertainty range caused by the choice of profile function types does not have a significant bearing on the obtained results.

In order to verify the validity of the model, controlled offline numerical experiments were conducted. These experiments showed that the designed model is able to simulate realistic potential temperature and wind profiles, and indicate differences among local and combined closure. A comparison with the Wangara Experiment data demonstrated a good agreement between the measured and simulated vertical profiles and it also provided a reasonably accurate estimation of the ABL height during the temporal evolution and collapse. The next step in our work is to incorporate the presented single column model into the WRF model and compare the obtained model outputs with other first and higher order profiles simulated in 1D and 3D environments.

Acknowledgements: The authors thank the European Union and the European Social Fund for their financial support (grant agreement no. TÁMOP-4.2.1.B-11/2/KMR-2011-0001 "Critical infrastructure defense research") during the preparation of this paper. The financial support of the Hungarian Scientific Research Foundation (OTKA, project no. K83909, and no. NN109679) is also greatly appreciated.

References

Ács, F. and *Kovács, M.*, 2001: The surface aerodynamic transfer parameterization method SAPA: description and performance analyses. *Időjárás 105*, 165–182.

Alapaty, K., Pleim, J.E., Raman, S., Niyogi, D.S., and *Byune, D.W.*, 1997: Simulation of atmospheric boundary layer processes using local- and nonlocal-closure schemes. *J. Appl. Meteorol. 36*, 214–233.

Arya, P.S., 2001: Introduction to micrometeorology. Academic Press, San Diego.

Berg, L.K. and *Zhong, S.*, 2005: Sensitivity of MM5-simulated boundary layer characteristics to turbulence parameterizations. *J. Appl. Meteorol. 44*, 1467–1483.

Blackadar, A. K., 1978: Modeling pollutant transfer during daytime convection. 4th Symposium on Atmospheric Turbulence, Diffusion and Air Quality. Reno, NV, USA, 443–447.

Bordás, Á., 2008: One-column vertical turbulent mixing model for the atmospheric convective layer. *Phys. Scr. T132*, 5.

Bosveld, F.C., Baas, P., Steeneveld, G.-J., Holtslag, A.A.M., Angevine, W.M., Bazile, E., de Bruijn, E.I.F., Deacu, D., Edwards, J.M., Ek, M., Larson, V.E., Pleim, J.E., Matthias Raschendorfer, M., and *Svensson, G.*, 2014: The third GABLS intercomparison case for evaluation studies of boundary-layer models. Part B: results and process understanding. *Bound.-Lay. Meteorol. 152*, 157–187.

Brown, A.R. and *Grant, A.L.M.*, 1997: Non-local mixing of momentum in the convective boundary layer a review of flux-profile relationships. *Bound.-Lay. Meteorol. 84*, 1–22.

Businger, J.A., Wyngaard, J.C., Izumi, Y., and *Bradley, E.F.*, 1971: Flux-profile relationships in the atmospheric surface layer. *J. Atmos. Sci. 28*, 181–189.

Cara-Lyn L., Randall, D., and *Yamaguchi, T.*, 2010: A higher-order closure model with an explicit PBL top. *J. Atmos. Sci. 67*, 834–850.

Clarke, R.H., Dyer, A.J., Brook, R.R., Reid, D.G., and *Troup, A.J.*, 1971: The Wangara Experiment: boundary layer data. *Tech. Paper No. 19*, CSIRO, Div. Meteor. Phys.

Dyer, A. J., 1974: A review of flux-profile relationships. *Bound.-Lay. Meteorol. 7*, 363–372.

Dyer, A.F. and *Bradley, E.F.*, 1982: An alternative analysis of flux-gradient relationships at the 1967 ITCE. *Bound.-Lay. Meteorol. 22*, 3–19.

Fiedler, B.H. and *Moeng, C.-H.*, 1985: A practical integral closure model for mean vertical transport of a scalar in a convective boundary layer. *J. Atmos. Sci. 42*, 359–363.

Foken, T., 2006: Angewandte Meteorologie, Mikrometeorologische Methoden. Springer, Heidelberg.

Frech, M. and *Mahrt, L.*, 1995: A two-scale mixing formulation for the atmospheric boundary layer. *Bound.-Lay. Meteorol. 73*, 91–104.

Hess, G.D., Hicks, B.B., and *Yamada, T.*, 1981: The impact of the Wangara Experiment. *Bound.-Lay. Meteorol. 20*, 135–174.

Holtslag, A.A.M. and *Boville, B.A.*, 1993: Local versus nonlocal boundary-layer diffusion in a global climate model. *J. Climate 6*, 1825–1842.

Holtslag, A.A.M., De Bruin, E.I.F., and *Pan, H.-L.*, 1990: A high resolution air mass transformation model for short-range weather forecasting. *Mon. Weather Rev. 118*, 1561–1575.

Hong, S.-Y., Noh, Y., and *Dudhia, J.*, 2006: A new vertical diffusion package with an explicit treatment of entrainment process. *Mon. Weather Rev. 134*, 2318–2341.

Hu, X.-M., Nielsen-Gammon, J.W., and *Zhang, F.*, 2010: Evaluation of three boundary layer schemes in the WRF model. *J. Appl. Metorolol Climate 49*, 1831–1844.

Kleczek, M.A., Steeneveld, G.-J., and *Holtslag, A.A.M.*, 2014: Evaluation of the Weather Research and Forecasting mesoscale model for GABLS3: impact of boundary-layer schemes, boundary conditions and spin-up. *Bound.-Lay. Meteorol. 152*, 213–243.

Kramm, G., Amaya, D.J., Foken, T., and *Mölders, N.*, 2013: Hans A. Panofsky's Integral Similarity Function – At Fifty, *Atmos. Climate Sci. 3*, 581–594.

Noh, Y., Cheon, W.G., Hong, S.Y., and *Raasch, S.*, 2003: Improvement of the K-profile model for the planetary boundary layer based on large eddy simulation data. *Bound.-Lay. Meteorol. 107*, 401–427.

Nieuwstadt, F.T.M., Mason, P.J., Moeng, C.-H., and *Schumann, U.*, 1992: Large Eddy Simulations of the Convective Boundary Layer: A Comparison of Four Computer Codes. In Turbulent Shear Flows Vol. 8, Springer, 343–367.

Pleim, J.E., 2007a: A combined local and nonlocal closure model for the atmospheric boundary layer. Part I: model decription and testing. *J. Appl. Metorol. Climate 46*, 1383–1395.

Pleim, J.E., 2007b: A combined local and nonlocal closure model for the atmospheric boundary layer. Part II: application and evaluation in a mesoscale meteorological model. *J. Appl. Metorol. Climate 46*, 1396–1409.

Pleim, J.E. and *Chang, J.S.*, 1992: A non-local closure model for vertical mixing in the convective boundary layer. *Atmos. Environ. 26A*, 965–981.

Pleim, J.E. and *Xiu, A.*, 1995: Development and testing of a surface flux and planetary boundary layer model for application in mesoscale models. *J. Appl. Meteorol. 34*, 16–34.

Shin, H.H. and *Hong, S.–Y.*, 2011: Intercomparison of Planetary Boundary-Layer Parametrizations in the WRF Model for a Single Day from CASES-99. *Bound.-Lay. Meteorol. 139*, 261–281.

Stull, R.B., 1984: Transilient tubulence theory. Part I: The concept of eddy-mixing across finite distances. *J. Atmos. Sci. 41*, 3351–3367.

Stull, R.B., 1988: An introduction to Boundary layer meteorology. Kluwer Academic Publ., Dordrecht.

Troen, I.B. and *Mahrt, L.*, 1986: A simple model of the atmospheric boundary layer; sensitivity to surface evaporation. *Bound.-Lay. Meteorol. 37*, 129–148.

Weidinger, T., Pinto, J., and *Hotváth, L.*, 2000: Effects of uncertainties in universal functions, roughness length, and displacement height on the calculation of surface layer fluxes. *Meterorol. Z. 9*, 139–154.

Xie, B., Fung, J.C.H, Chan, A., and *Lau, A.*, 2012: Evaluation of nonlocal and local planetary boundary layer schemes in the WRF model. *J. Geophys. Res. 117*, D12103.

Xue, M., Droegemeier, K. K., Wong, V., Shapiro, A., Brewster, K., Carr, F., Weber, D., Liu, Y., and *Wang, D.*, 2001: The advanced regional prediction system (ARPS) – a multi-scale nonhydrostatic atmospheric simulation and prediction tool. Part II: model physics and applications. *Meteorol. Atmos. Phys. 76*, 143–165.

Yamada, T. and *Mellor, G.*, 1975: A simulation of the Wangara atmospheric boundary layer data. *J. Atom. Sci. 32*, 23099–2329.

Zilitinkevich, S.S. and *Chalikov, D.V.*, 1968. Determining the universal wind-velocity and temperature profiles in the atmospheric boundary layer. *Izv. Atmospheric and Oceanic Physics 4*, 2949–302. (English version 1659–170.)

Zhang, D. and *Anthes, R.A.*, 1982: A high-resolution model of the planetary layer – sensitivity tests and comparison with SESAME-79 data. *J. Appl. Meteor. 21*, 1594–1609.

Zhang, D.L. and *Zheng, W.Z.*, 2004: Diurnal cycles of surface winds and temperatures as simulated by five boundary layer parameterizations, *J. Appl. Meteor. 43*, 157–169.

IDŐJÁRÁS

Quarterly Journal of the Hungarian Meteorological Service
Vol. 119, No. 3, July – September, 2015, pp. 399–408

Effects of atmospheric ions on human well-being in indoor environment

Levente Herczeg* and **Norbert Érces**

Department of Building Service Engineering and Process Engineering
Budapest University of Technology and Economics
Műegyetem rkp. 3, H-1111, Budapest

*Corresponding author E-mail: l.herczeg@hfhc.hu

(Manuscript received in final form October 15, 2014)

Abtract—People spend a significant part of their days in buildings or in a box within some kind of means of transport. It is one of the main issues in our fast-paced world that typifies the twentieth and twenty-first centuries. Consequently, suitable environment creation plays an increasingly important part, which has significant influence on human comfort, health, and productivity as well. It turns out in pursuance of developments in various heating, ventilation and air conditioning (HVAC) systems that human comfort is affected not only by air temperature, humidity, and draught but also by meteorological, physiological, and psychological parameters. Airborne particles, so-called atmospheric ions assessments have been carried out in the course of these investigations. This paper presents effects of atmospheric ions on indoor environment and the occupants.

Key-words: atmospheric ions, human well-being, air quality, comfort spaces, measurement technique

1. Introduction

The comfort in closed spaces is usually understood as thermal, air quality, acoustical, and illumination engineering comfort. The office plays a special role in providing adequate comfort as workers spend a longer time in closed spaces performing intellectual work. In the air-conditioning of comfort spaces, the primary task is to provide a pleasant indoor microclimate for the people staying in the room. In addition to thermal comfort, air quality is also regulated by international requirements and standards. In the occupied zone, a sufficient

amount of fresh air of appropriate quality must be provided for the people staying in the room. Hungarian technical regulations do not fully cover these aspects yet, hence the complaints frequently heard from employees working in air-conditioned spaces are the air has an unpleasant 'smell', they experience 'lack of air' or perhaps have headaches (*Kajtár* and *Hrustinszky*, 2001, 2002, 2003; *Kajtár* and *Herczeg*, 2012; *Kalmár* and *Kalmár,* 2013) In addition to the impact on human's health- and comfort factors, extensive studies were carried out on the effect of atmospheric ions.

2. Physical attributes of atmospheric ions

According to Henri Hess (1802–1850), a Swiss chemist, every type of gases contains electrically – positively or negatively – charged particles called ions. One singular ion carries 4.77·10-10 electrostatic values (ESV) charge. Under this force, ions will migrate in an electric field according to the type of their charge. Basically, two types of ions are distinguished: small or molecular ions and large, i.e., Langevin ions. Certainly dimensional differences can be observed in regard to ion velocity as well. Under normal air conditions, small ions are moving at 1–2 cm/s, and large ones at 0.01–0.005 cm/s, depending on their size. Velocity of negatively charged ions is usually higher than in case of positive ones.

In nature, ions are formed because of the radiation of sun, cosmic rays, and fluctuations of radioactivity within the lithosphere on the Earth. Highly ionized gases are approaching the Earth surface due to a capillary action generated by wind suction. Considering the total number of ions in the air, it is in the order of 60%. Stage of atmospheric ionization is simultaneously influenced by other natural processes which attempt to destroy or neutralize the ions.

The most important factors and processes are:

- bonds between oppositely charged ions,
- neutral ions creation, aggregation with condensation centers,
- large ions creation, and
- absorption by solid or liquid conductors (*Kérdő et al.,* 1972).

2.1. Determination of the number of atmospheric ions

Positively and negatively charged atmospheric ions in the air usually measured with the Ebert counter or with a modified version of that. The examined air sample is forced trough a cylindrical condenser with an electrode pole fitted in the middle. This electrode is oppositely charged than ions which should be measured, and only sufficiently high-speed ions are able to reach it. In the course of collision, pole subtracts electrons equally to the charge of ions. Based on the quantity of electrical discharges and the airflow measured by a damping plate, the number of ions can be determined in a given amount of air.

The ion concentration depends significantly on the time of day, weather conditions, and location, moreover the number of occupants and their activity (*Yaglou,*1935).

3. Effects of atmospheric ions on human physiology

First interdisciplinary study of biological and medical influents of ionized air was published by *Dessauer* in 1931. In the course of their assessments, ionized air was conducted directly on the face of participants through a funnel. Exposure had been taking 15–60 minutes, at concentration of 10^6 ions/cm^3. It was clearly established that positive and negative ions had different effects on human health, amongst healthy participants and inpatients too. Positive ions induced discomfort, headache, rising blood pressure and respiratory rate. Moreover, they generate occasionally a feeling of being sick. Negative ions had opposite influences which led to sense of refreshment and decreased blood-pressure.

Effects of atmospheric ions were evaluated in a more cautious way in a research had been carried out by Harvard School of Public Health in 1933. In the course of investigations, ions formed by small molecules were dispersed into the experimental space with a velocity of 1.3 cm/s. Concentrations of positive and negative ions were continuously varying between 5000–1 500 000 ions/cm^3. Applied ionizer could produce simultaneously positive and negative ions. Temperature in the experimental room was set according to the personal demands. Air-change rate was 35, without usage of a humidifier.

Examination series were divided into three groups:

- normal ground state,
- 2–4 hours after breakfast, and
- 3–5 hours after an easy lunch.

During the investigation, variations in metabolism, breathing, pulse rate, blood pressure, and body temperature were recorded in regard to each test persons, who aged from 10 to 68 years. The group of 60 participants was observed during 141, one or more hour long experiments under influence of ionized air. It was established that intake air can normalize body processes, i.e., accelerate physiological changes if personal results are above or below the normal rate. Significant influences of positive and negative charges could not be determined. However, based on evaluation of subjective physiological effects, the following statements can be made: exposure to positive ionization causes headache, nose and throat irritation. Negative ionization led to a feeling of being calm. A small group of test persons reported sense of freshness, especially affected by negative ionization (*Yaglou et al.,* 1933).

4. Measuring investigations of atmospheric ions

4.1. Description of measurements

To purpose of this chapter is to present how ion number is varying and what the influence of that is on occupants being in different places. Since 1930s, several measurements have been taken in areas in towns, subway stations, and residential enclosures, in order to answer these questions.

Under conditions of natural ion climate which is beneficial to health, numbers of positive and negative ions are equal to each other in terms of scale, and concentration of biological effective ions is in the range of 500–4000 ions/cm^3. Due to changes generated by civilisation, atmospheric ion concentration rates scattered in cities and industrial areas are fundamental. Number of large ions will be significantly increased by polluted air. Consequently small, biological effective, negatively charged ions are almost completely disappearing. Several studies were carried out by *Yaglou* and *Benjamin* between 1930 and 1934 in relation of various meteorological parameters. Seasonal phenomena, influences of temperature, humidity, clouds, precipitation, and changes in atmospheric pressure were also taken into consideration. Results from the three-year-long assessments show adequate similarity, presenting definite minimum ion concentration in winter, and maximum in summer. Winter of 1930–31 was extremely cold. Therefore, results for this period had been deleted afterwards. Indoor level of ionisation was lower than in outdoor air during winter and springtime of 1932–33. In summertime this deviation could not be observed. In comparison with measurements at Pacific, Atlantic, and Indian Oceans (1915–16), corresponding variation in ion concentrations was established. However, comparing results had not been considered sufficient to provide an adequate basis in regard to both land and water surface measurements. Related to the connection between yearly changes and ionization, no conclusions were made as further measurements had been considered inaccurate. Ion concentration influenced by air temperature and humidity was evaluated in a more adequate way. Increased wind velocity leads to a consequent decrease in ion concentration at any time of the year, independently from temperature levels. Low concentration of small ions starts to be appreciable below air temperature of 21 °C. Thus, minimal concentration in winter becomes out of question as the humidity is at the highest level and temperature is at the lowest level simultaneously. Presence of high ion concentration can be noticed at relative humidity of 75%, independently of temperature parameters. Ion concentration level is varied with both cloudy and partly cloudy weather. In fact, clouds which cover the sky completely or partly will decrease ion concentration significantly. There is similar effect both of light and moderate rain. Heavy rain and storms accompanied by lighting and very heavy precipitations will increase the level of negative ion

concentration definitely. If storm approaches its peak, this can reach the level of the zenith point of ion concentration 3000–3150 ions/cm^3. Indoor ion concentration depends considerably both on the amount and duration of precipitation and the direction of the wind. A few hours of light or moderate rain has no major impact on indoor ion concentration.

Number of ions formed by surface radioactivity is influenced by barometric effect which can be measured near the ground. If Earth's capillaries are under a decreased pressure, more ions will be released. This kind of "ground breathing" becomes heavy at an increased level of pressure. However, these are not significant changes.

4.2. Measurement results in Hungary

Obviously, studies on atmospheric ionization have been made in Hungary too. István Kérdő candidates of medicine, and Ferenc Sváb electrical engineer had been performed two assessments, in Budapest on October 12, 1970 and in Stuttgart on July 28, 1972 (*Kérdő et al.*, 1972). Results of their studies are presented in *Table 1*.

Table 1. Variation of atmospheric ion number in urban area (*Kérdő et al.*, 1972)

Location	**Temperature [^{0}C]**	**Relative humidity [%]**	**n+ [ions/cm^3]**	**n- [ions/cm^3]**	**n+/n- [-]**
Budapest, 200 m far from Danube	21–18	56–62	120–130	–	–
North, 14 km far from Budapest	21	60	250–300	120–140	2.08–2.14
Budapest, Nyugati square	21	60	120–140	20–30	6.00–4.67
Budapest, Jászai Mari square	18	–	50–100	10–20	5.00
Budapest, Boráros square	18	–	130–170	20–40	6.50–4.25
Budapest, Nagyvárad square	18	–	100–130	20–30	5.00–4.33
Stuttgart, Entrance of Wagenburg tunnel	20	61	300–500	20	15–25
Stuttgart, Kriegsberg road	20	61	200–220	30–40	6.67–5.50
Stuttgart,Bosch Hospital, 115 m altitude	20	–	270–290	20–30	13.5–9.67
Stuttgart, TV Tower	20	–	110–130	120–130	0.92–1.00

The above mentioned phenomena can be observed, i.e., number of negatively charged ions could be considered negligible or non-measurable in higher polluted environment. However, results measured in the TV tower of Stuttgart verified the theory that unipolarity is near to one in clean environment, so positively and negatively charged ions are dimensionally equated to each other. It shows the importance of negative ions, which can primary affect the physiological parameter, one of the earlier mentioned factors influencing human comfort.

4.3. Recent researches

After the first, remarkable researches in the 1930s which had been processed without achieving a real breakthrough, in the 1960s a new attempt was made in order to define effects of atmospheric ions on occupants in residential spaces. In the course of investigations it was discovered, that a significant amount of positively and negatively charged ions could be generated by humidifiers and vaporizers in the air conditioning devices. As it can be seen in *Table 1*, in case of TV Tower of Stuttgart, natural ions are approximately balanced, but usually more positively charged ions can be found in a cubic centimeter. In general, this number is below 1000 ions/cm^3 in a clean, natural environment. It can be observed that certain human activities, especially ones accompanied by a considerable heat load form positively charged ions. Therefore, man got used to the presence of positive ions more likely. In accordance with the study presented above, this could also give an explanation for the favorable effects of negative ions on human well-being, as the surplus of negatively charged ions could create a perceptible change in well-being. However, this statement was handled with care, even after the study of *Jennings* in 1964 (*Jennings* and *Givoni*, 1964) . As previous investigations, this was also performed in an artificial environment, where ion concentration in air could be increased above the natural level. All the experiments had been performed in the research lab chamber for environmental studies of American Society for Engineering Education (ASEE) which is a room with internal size of 7.5×3.5×2.55 meters. Both indoor air temperature and humidity were controlled by an air conditioning device. In the room, four ion generators were installed. Likewise in the 1930s, adjustable devices could be set for producing or counting either positive or negation ions. The pilot studies showed that there was no direct correlation between the ion concentration in the room and the number of ionizators, since two generators could produce the same high level of ion concentration as the four together. Still simultaneous use of the four devices were considered practical, in order to ensure homogeneity.

In the course of the assessment, 16 people (12 woman and 4 men) were employed as test persons. Before the ionization, each of them has gone through a general physical examination. Initial studies were performed between July 19 and 22, at a relative humidity of 50%. These were reproduced between July 25

and February 2, also at the same humidity level but at a temperature level of 30.5 °C in order to observe the reactions of the same test persons at mild heat stress. Both measurement series were remade between April 19 and May 26. Two groups of 6–8 persons were established and observed in the daytime and at night during each investigation. Three levels of ionization were distinguished:

- basic, when ionizators did not worked,
- negative ionization,
- positive ionization.

In the course of examinations, a special attention was paid to ensure random change in the three levels, in order to avoid any effects of the different ionization statuses. Ionizators had been operating at maximum output which resulted significant increasing in ion concentration day by day. *Table 2* shows the variation of the ion levels in the examination room with respect of different ionization statuses.

Table 2. Variation of ion levels in the examination room

Ion polarity	25.5 ^{0}C, 50% relative humidity		30.5 ^{0}C, 50% relative humidity	
	Average level [ions/cm^3]	**Constant deviation [ions/cm^3]**	**Average level [ions/cm^3]**	**Constant deviation [ions/cm^3]**
		Basic points		
Positive	277	79	393	46
Negative	118	45	194	30
		Measured levels		
Positive	12245	1350	14819	1586
Negative	4766	587	5494	897

It can be observed, that 10 °C rise in temperature causes higher level ion concentration in the room. Approximately, it is increased by 1650 ions/cm^3 in ionized status and by 190 ions/cm^3 in basic. This change was considered a marginal one during the examination. In the course of the examination test persons were allowed to read, play games, and listen to the radio as well. It was

permitted to discuss only their well-being. Each test person had to fill a summary questionnaire about well-being during the three-hour-long time of observation, which contained scales of overall thermal comfort, sensible perspiration, pleasantness, tiredness, humidity sensation, air movement, and personal feelings or moods. Sensitivity of estimates is confirmed by the fact that human factors bring individual results. Moreover, subjective sense of human comfort could be influenced by the points of begin and end of the measuring period, the part of the day, and the actual season. If change caused by these "distortive" parameters occurs at the same time as an ionization process, evaluation will be more complicated. It can be said without presenting the enormous amount of results, that neither of test persons prefers the status of negative over-ionization (see *Table 2*) in such a determined way as the basic level of negative ion concentration in the room.

Furthermore, it can be established that if effect of ionization even exists, it must be far too slight to be significant. However, it comes up as a question, how occupants in the room are influenced by this comparatively insignificance (*Jennings* and *Givoni,* 1964).

5. Summary of the measurement results

Researchers could get any definite results in the course of evaluation trough the method of significance analysis. During estimation of pleasantness, some evidence was found in the evening teams for the rejection of the hypotheses.

By taking all the groups into consideration, during the assessments at temperature of 30.5 °C, a probability of P=0.03 was determined. There is a question of how ionization affects the groups at a different level during daytime and at night. Mood votes could not provide adequate information to prove the existence of the ionization effect. This lack of information was obtained also in regard to tiredness votes.

Authors are aware of the fact that the statistical methods which used by them is not the only way to evaluate such an assessment. Nevertheless, effect of ionization probably could not be proved by other methods in a more accurate way either. Influence on different people is not so significant at the measured level of temperature and ion concentration that it should be remarkable from technical point of view.

By summarizing the results it can be declared, that ionization has no significant effect on occupant's well-being and health in residential spaces. All the studies declared that there was some detectable effect, but it was not evaluated exactly. However, air conditioning developers keep on being engaged in this issue, and in the course of technological innovation, more researches were made in the field of ionization in regard to different technologies and building structures.

6. Practical usage of ion air conditioning

It was observed, that filters in air handling devices deionize the air almost completely, but cheaper window air conditioners generate a surplus of positive charge. Reinforced concrete building structures cause further problems, whereas due to the shadow effect of the iron structure, small air ions can not even enter the building or they become neutralized shortly after the entering. This is also caused by that floating condensation seed particles can be separated really gently from the indoor air. Deionization could be generated in that case as well, when plastic parts of the building envelope get electrostatic charge. If the process of air conditioning is assumed optimal from the point of view of ionization, corresponding level of ion concentration should be ensured in an artificial way. It causes further difficulties, that air ionization in central air handling units can not be considered a practical method, whereas ions will be quickly neutralized in the ducts of the distribution system. It was proved by measurements that a three-meter-long metal air duct can completely deionized the air flowing inside. According to the experiences, efficient level of ionization can be achieved if the ioniser is placed into the air inlet. It was a signal result, that number of floating bacteria was decreased significantly by ionizators in the air of bandage, surgical, and operating rooms of hospitals. Surplus of positive ion concentration was measured in an average room with central heating in ten minutes after the room was properly aired. Based on the assessment it can be established, that it is sufficient to provide only the negative ion supplements.

In addition to the buildings, measurements were conducted in different vehicles, in driver cabins of buses and cars, and in cabins of dockyard cranes. Similar results were obtained in regard both to the train set of Budapest Metro and to Russian researches. Rate of unipolarity was not influenced significantly in the course of travelling underground and above ground. Surplus positive ion concentration was measured in the cabins of dockyard cranes even if the window was open. In summertime improved, ion concentration was detected only if a moderate breeze was blowing.

References

Dessauer, F., 1931: Zehn Jahre Forschung auf dem Physikalisch Medizinischen Grengebiet. G. Thieme Leipzi. (In Deutsch)

Jennings, B.H. and *Givoni, B.*, 1964: Enviroment Reactions in the 80F to 105F Zone. *ASHRAE Trans. V. 65,* 115–136.

Kajtár, L. and *Hrustinszky, T.*, 2001: Measurements of Indoor Air Quality and Emission of Indoor Materials. International Conference on Health, Comfort and Productivity vs. Cost Effective Operation of HVACR proceedings, Sttrbské Pleso, Slovakia.

Kajtár, L. and *Hrustinszky, T.*, 2002: Measurements of Indoor Air Quality and Emission of Indoor Materials. Proceedings of the third conference on mechanical engineering1. Budapest, Hungary, 362–366.

Kajtár, L. and *Hrustinszky, T.* 2003: Investigation of indoor air quality and emission of indoor used materials in Hungary. 7th International Conference Healthy Buildings, 2003. Singapore, Proceedings 3. 752–757.

Kalmár, F. and *Kalmár, T.*, 2013*:* Alternative personalized ventilation. *Energ. Bulidings 65*, 37–44.

Kérdő I., Hay Gy., and *Sváb F.*, 1972: Problems of Ion Climatisation. Budapest.

Yaglou, C.P., Benjamin, L.C. and *Brandt. A.D.*, 1933: Physiologic Changes During Exposure to Ionized Air. *ASHRAE Transactions*. 357–372.

Yaglou, C.P., 1935: Observations of Phyisical Efficiency in Ionized Air. *J. Ind. Hygiene 17*,280–282.

IDŐJÁRÁS

Quarterly Journal of the Hungarian Meteorological Service
Vol. 119, No. 3, July – September, 2015, pp. 409–423

A multivariate linear regression model of mean maximum urban heat island: a case study of Beregszász (Berehove), Ukraine

Elemér László and **Sándor Szegedi**

Department of Meteorology, University of Debrecen
Egyetem tér 1, H-4043 Debrecen, Hungary

Corresponding author E-mail: laszlo.elemer@science.unideb.hu

(Manuscript received in final form December 12, 2014)

Abstract—The aim of the research presented in this study is to elaborate a multivariate linear regression model that describes the spatial structure of the mean maximal development urban heat island (UHI) formed under favorable synoptic conditions on the basis of surface parameters. Temperature data were gathered in a small town, Beregszász, Zakarpattia, Ukraine. As a first step, a one-year-long UHI measurement campaign has been carried out using mobile techniques in order to obtain data for the description of the UHI in the study area. Two surface parameters (ratio of non-evaporating surfaces in the environment of the measurement sites and distance of measurement sites from the center of the settlement) have been selected first. The two surface parameters had to be quantified next. On this basis, relationships between surface parameters as independent variables and UHI intensities as dependent variables could be traced by performing a multivariate linear regression. Results have showed that the two chosen parameters have strong impact on UHI development in our study area. Spatial structure and intensity of UHI can be estimated with an accuracy of 0.4 °C within the built-up area of the town using our MLR model. The high resolution surface parameter database and the UHI estimating model enable the prediction of heat load of smaller spaces and town parts. This procedure helps the reduction of heat load and the determination of the location of green areas important for urban planning as well.

Key-words: multivariate linear regression model, non-evaporating surfaces, urban heat island

1. Introduction

Settlements differ from natural environment significantly, due to altered surface geometry, different composition, and structure of urban atmosphere. Anthropogenic heat emissions should be taken into consideration as well (*Oke,* 1997). As a result, a local or meso gamma scale phenomenon, the urban climate develops (*Arnfiled,* 2003; *Oke,* 1973; *Orlanski,* 1975). Built-up areas are characterized by higher air and surface temperatures than close-to-natural areas in their neighborhood what is called urban heat island (UHI). The thermal difference between the town center and its rural environment determines the intensity of the urban heat island. UHI intensities have a special diurnal and annual course with maxima 3–5 hours after sunset and in late summer – early autumn (*Landsberg,* 1981). Additionally, UHI intensities change according to synoptic conditions as well: clear skies with calm weather are advantageous for the development of a strong UHI. This way, synoptic conditions determine the UHI intensities at a given point of time, while maximal (or potential) intensities can develop under favorable synoptic conditions. These factors are dynamic conditions of UHI development. Spatial pattern of the absolute or the mean maximal UHI is determined by static factors, the characteristics of the urban surface (*Bottyán* and *Unger*, 2003; *Bottyán et al.,* 2005*; Chen et al.,* 2011; *Ginnaros et al.,* 2013). Therefore, for studying the effects of static conditions on the spatial structure of UHI, favorable synoptic conditions are suitable. Investigations on heat islands give important information for town-planning (*Kuttler,* 1998), because the phenomenon influences the comfort sense of town dwellers (negatively in summer, positively in winter) essentially, alters the composition of urban vegetation, and can cause phenologic phase shifting (*Oke,* 1975).

Beyond determination of the characteristics of urban heat islands, recent studies focus on examination of their evolving factors in big cities. Our study area, Beregszász (Berehove) with its population of 26,000 belongs to the group of settlements which gain much less attention from this aspect. However, a high ratio of the population of Central and Eastern Europe live in small settlements, where heat islands can develop (*Fig. 1*), but there are much less studies in that field. Additionally, many rapidly growing independent suburbs of cities fall into that size category as well.

The main aim of the study presented here is to analyze the relationships between spatial structure of UHI and its formative surface parameters. There are many surface parameters that have an effect on UHI development. The hypothesis was that the most important parameters are the distance of a given site in the settlement from the geometrical center and the ratio of non-evaporating surfaces in that site.

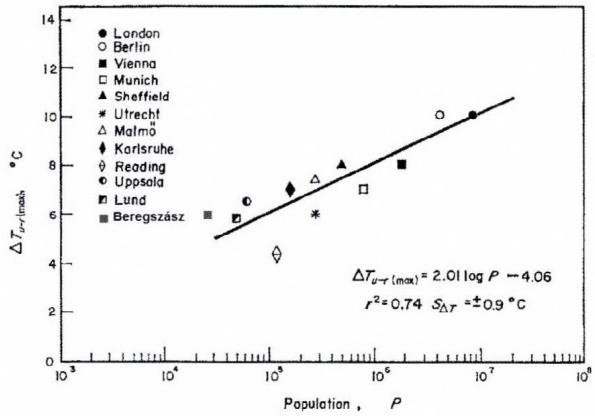

Fig. 1. Relationship between maximum observed heat island intensity ($T_{u\text{-}r(max)}$) and population *(P)* for European settlements indicating the position of Beregszász from this aspect (modified after *Oke,* 1973).

Other aim of our studies is to build an empirical estimating model for the spatial pattern of the mean maximal development UHI using the before mentioned surface parameters. The model could make possible the description of the spatial structure of the mean maximal development UHI for settlements of that size and structure category. Results can provide basic information on spatial pattern of the thermal excess in a given small settlement for spatial planning, forming urban spaces and green areas to utilize the advantages and prevent the drawbacks of the heat island phenomenon.

The examination of effects of surface parameters on UHI development requires high resolution spatial temperature data gathered under synoptic conditions what makes possible the strong development of UHI. For this reason, measurements were carried out under anticyclone synoptic conditions with clear skies and calm weather.

While examination of satellite images (*Bartholy et al.,* 2009) are more capable for heat islands of big cities (*Oke,* 1975; *Park,* 1986; *Kislov* and *Konstantinov,* 2011; *Lee* and *Baik,* 2010) (e.g., New York, Montréal, Moscow, Soul, Budapest), in the case of Beregszász, due to its size, the adaptation of a mobile measurement method (*Elansky et al.,* 2012) used by researchers of the University of Szeged (*Unger et al.,* 2000) and Debrecen (*Szegedi,* 2000) seemed to be adequate. The difference between the two methods is that satellite images make possible the determination of heat surplus in surface temperatures, while the latter one allows the measurement of heat excess in air temperatures.

Our mobile temperature measurements have provided abundant data for the characterization of UHI in Beregszász (Berehove). On this base, a multivariate linear regression model can be applied to analyze the role of some surface parameters in development of UHI in our study area.

2. Study area and methods

2.1. Location and climate of Beregszász (Berehove)

Beregszász (Berehove) (48.1°N, 22.3°E) lies 117 m above sea level. The southwestern part of the town can be found on a flat, alluvial plain, only occasionally interrupted by small hills. The town is situated on an almost flat terrain without great water bodies, what is advantageous from the aspect of the examination of the spatial development of urban heat island. It is located in the Zakarpattia Oblast (province) in Western Ukraine, near to the Hungarian border. It is the administrative center of the Berehivskyi Raion (district) with a population of 26,000.

The climate normal was calculated based on the Climate of the Carpathian Region Project dataset *(Lakatos et al., 2013)*. The town and its environment belong to Köppen's climate region Cfb on the basis of the climate parameters (*Table 1.*). The annual course of precipitation reaches its maximum in June and July. Prevailing wind direction is north-easterly.

Table 1. Annual and monthly means and sums of meteorological parameters at the weather station of Beregszász (Berehove), 1961–2010 (*Anon,* 1992; *Lakatos et al.,* 2013).

Beregszász (Berehove)	
Annual mean temperature (˚C)	9.8
Temperature range (˚C)	21.8
Mean temperature in January (°C)	–2.7
Mean temperature in July (˚C)	20.2
Annual mean precipitation (mm)	682
Annual mean wind speed (m s^{-1})	2.1
Sunshine duration per year (h)	1998

2.2. UHI measurements

Since the spatial pattern of the heat island is influenced by different urban morphological types significantly (*Szegedi,* 2006; *Unger et al.*, 2004; *Molnár et al., 2006*), we had to integrate the highly complex urban morphology into our model. Along a measurement route 42 measurement sites were selected, which are representative on one hand and quite smoothly cover the settlement on the other hand (*Fig. 2*). Temperature data was gathered 36 times along the route using mobile measurement techniques from January to December in 2005 by

Marguca V. and Kakas M. A measurement session was carried out using mobile measurement techniques in 2010 as well (n=10), under meteorological conditions advantageous for UHI development. This dataset was used as independent data in validating the established empirical model.

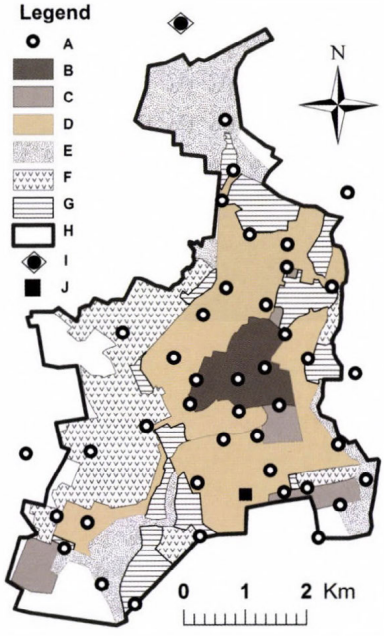

Fig. 2. UHI measurement sites (**A**) and urban morphological types in Beregszász (Berehove):**B**–historical town center with 3–5 storied buildings, **C**– 5–8 storied apartment houses, **D**—1-2 storied detached houses, **E**—open low-rise built-up area, **F**—industrial area, **G**—green areas inside the town, **H**—border of the study area, **I**—rural measurement site (reference point), **J**—weather station.

Measurement days were chosen according to the weather conditions within the decades: nights with rain and/or strong winds were excluded, since these conditions prevent the development of UHI. Measurements started approximately 3 hours after sunset, when heat island development is the most dynamic. Temperatures were recorded manually at each measurement site (*Table 2*).

Table 2. Observed meteorological parameters during the UHI measurements at the weather station of Beregszász (WMO station code is 33634; 48.19°N, 22.64°E, 122 m above sea level)

Measurement date	Air temperature (°C)		Cloudiness (octas)	Wind speed ($m\ s^{-1}$)		UHI max	UHI mean
2005	19 : 00	01 : 00	19 : 00	19 : 00	01 : 00		
January 5	2.8	3.5	7	0	0	0.9	0.5
January 17	–2.1	–3.1	0	0	1	5.0	1.6
January 25	–1.3	–1.4	4	1	2	2.2	1.2
February 4	–5.1	–5.4	2	2	3	4.1	3.0
February 16	0.3	0.8	0	0	1	1.8	1.1
February 21	2.6	1.1	1	1	0	4.0	1.7
March 3	–1.4	–0.8	2	2	1	0.9	0.4
March 15	3.5	1.6	6	1	0	2.2	1.0
March 22	0.1	1.4	0	2	1	2.6	1.5
April 5	9.3	8.1	0	0	1	4.9	2.7
April 18	11.3	10.4	8	3	4	0.5	0.3
April 27	10.4	12.6	0	0	1	2.8	1.6
May 5	13.7	12.8	4	1	2	0.9	0.7
May 12	8.0	5.3	0	0	1	1.7	0.9
May 23	19.4	17.8	0	0	0	3.9	2.1
June 07	12.8	12.2	0	1	0	1.9	1.3
June 14	17.1	15.5	0	0	0	4.6	1.4
June 22	20.1	19.0	7	2	3	2.0	1.1
July 8	18.2	16.9	0	1	0	4.9	2.4
July 18	23.4	22.3	0	1	0	2.1	1.6
July 21	15.5	14.1	0	1	1	4.9	1.4
August 2	23.2	22.7	0	0	1	3.3	1.9
August 12	18.1	17.7	0	0	0	2.3	1.4
August 22	20.2	19.6	6	2	3	0.8	0.4
September 6	12.7	12.0	0	0	1	4.5	2.6
September 13	18.5	16.6	0	1	0	1.7	0.9
September 22	14.2	15.9	0	0	2	6.6	4.1
October 04	14.9	16.7	1	0	1	3.6	1.6
October 11	9.0	8.1	0	0	0	3.9	1.7
October 25	14.4	13.9	7	2	3	1.7	0.3
November 03	3.3	1.5	0	1	0	4.2	2.5
November 15	7.7	7.4	8	3	4	1.4	0.6
November 22	–2.2	–3.0	0	0	1	2.7	1.8
December 07	5.1	4.3	5	1	3	0.7	0.4
December 13	0.6	0.5	6	0	1	1.0	0.6
December 21	–5.0	–5.9	1	2	1	3.2	2.5

From the numerous methods developed for urban climate examinations, mobile techniques were used in order to get abundant comparable data for Debrecen and settlements involved in the research. Sensors of a digital thermometer were mounted on a car (with a resolution of 0.1 °C) at a height of 1.5 m, which is a common practice in UHI measurements. An important problem is that measurements should be carried out at exactly the same time in each grid. This is impossible using mobile techniques. The difference between the first and the last grid is 90 minutes, which is a considerable time span from the aspect of the change of temperatures in the different parts of the city. In order to get comparable temperature data during the measurements, we visited each grid two times: first on the way to the end of the route (the reference site, measurement site 42) and the second time on the way back. In this way we gained two temperature values for each grid. Since on the way back we visited the grids in reversed order, calculating the averages for the grids we gained values for the same time (the reference time). The reference time was four hours after sunset, since according to the literature, heat island intensity reaches its maximum 3–5 hours after sunset. Since the aim of the research was to trace the spatial pattern of urban heat island, only favorable conditions for heat island development were taken into consideration during the first campaign: measurements were carried out in anticyclone conditions. *Fig. 2* shows locations of measurement sites. UHI intensities (Δt values) were calculated using the following formula:

$$\Delta t = t_{urban} - t_{rural} \,, \tag{1}$$

where t_{urban} means temperature values measured at urban sites and t_{rural} means temperatures measured at the reference site outside the town.

2.3. Determination of surface parameters

The role of two surface parameters (presumably the most important ones) influencing the heat island development have been examined in the present study.

These are:

— Ratio of non-evaporating surfaces *(NES)* in the environment of measurement sites;

— Distance between measurement sites and the geometrical center (48.20°N, 22.64°E) of the town. Distances between measurement sites and the geometrical center of the town (km) were calculated, and distances were determined for the grid points of the network of the town as well.

Since non-evaporating surfaces store more heat during daytime than the close-to-natural evaporating surfaces, the air above built-up areas is warmer than over their surroundings. For this reason, quantification of the ratio of non-evaporating surfaces is necessary.

Close-to-natural evaporating areas are surfaces covered by vegetation (wood, shrub, lawn etc.) or bare soil. Non-evaporating surfaces are mainly artificial objects (buildings, pavements, other constructions). We have found that satellite images are the most suitable for parameter estimation. Thus, the ratio of non-evaporating surfaces was assessed visually using high-resolution, true color images of Google Earth. A grid network of 15.4×15.4 m was set on the images with the measurement points at the centers of the grids, and characteristic surface types for each grid were determined. The land cover was determined at 109,500 points with a spatial resolution of 15.4×15.4 m, which gives more detailed data than a grid network with 500×500 m resolution used by other researchers *(Kislov et al.,* 2011; *Unger et al.*, 2000).

It was an important question to decide what size of environment of measurement points influences the heat island intensity most strongly. We have tested four variations by statistical analysis:

—NES_1 – 9 grid points represent an area of 2134 m^2 around the measurement point;

—NES_2 – 25 grid points cover an area of 5930 m^2;

—NES_3 – 49 grid points represent an area of 11,621 m^2 around the measurement point;

—NES_4 –81 grid points cover an area of 19,210 m^2.

As a first step, the size of the environment, which influences the heat island intensity most strongly around the measurement sites was determined statistically. For this reason, *NES* values of the 4 chosen areas were correlated with the mean maximal heat island intensities of measurement sites, and significant correlation was found in every case (*Table 3*).

Table 3. Connection between the ratio of non-evaporating surfaces (*NES*) and UHI intensities, *r*– correlation coefficient

Period	NES_1 *r*	NES_2 *r*	NES_3 *r*	NES_4 *r*	Sign. level
Δt-annual	0.57	0.64	**0.70**	0.67	1%
Δt/heating	0.56	0.64	**0.69**	0.67	1%
Δt/non-heating	0.54	0.59	**0.68**	0.61	1%

The strongest relationship was found between NES_3 and the UHI, so the 11,621 m^2 area influences heat island intensities of Beregszász most remarkably. Maps were completed on the basis of the ratio of non-evaporating surfaces in Surfer 8.0 (*Fig. 3*). This statistical software offers several types of interpolation methods, from which we have chosen the widely used Kriging-procedure. Ratio of non-evaporating surfaces reaches its maximum in the center of the town, however, there are some patches with high ratio of artificial (non-evaporating) surface cover around the center near the edges of the settlement. They are industrial areas and housing estates. The distance of the measurement points from the town center was determined by using the differences of coordinates of the previously mentioned grids.

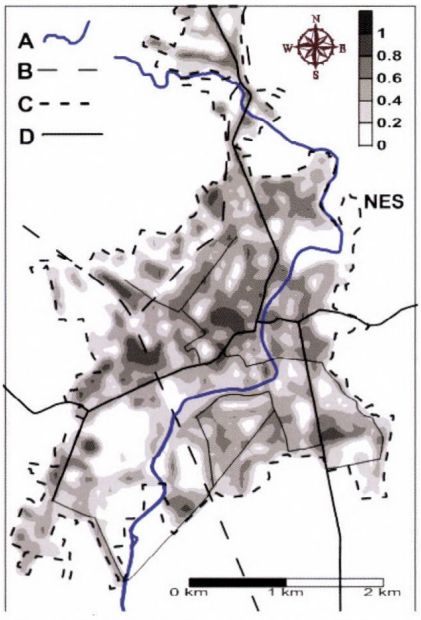

Fig. 3. Spatial pattern of the of non-evaporating surfaces in Beregszász: A– Vérke canal, B–railroad line, C– border of built-up area, D– main road line.

Correlations between variations of *NES* (NES_1-NES_4) and distances from the geometrical center of the town were determined. In this way, possible linear dependence between explanatory variables was traced. In the case of dependence between explanatory variables, one of them was ignored in order to create an independent system of explanatory variables. This method

minimized the possible multicollinearity (M) of explanatory variables incorporated into the model. Value of M shows the magnitude of the non-separable effect of factor variables. In this way, the coefficient of multiple determination can be divided into the partial effect of each factor variable and the joint effect of the factor variables. In our case, the value of M was 0.37 which cannot be regarded as significant. This value was tested using the variance inflation factor (VIF):

$$VIF_i = \frac{1}{1 - R_i^2} \,. \tag{2}$$

This factor shows how many times greater the actual variance of the estimated coefficient of variable i is than it would be with the complete exclusion of multicollinearity. Value of VIF in our case is 1.58 suggesting slight multicollinearity that determines the estimation strength of the model not significantly.

2.4. The statistical model applied

Beside basic statistical analysis (average, correlation), we have attempted to build an empirical model to investigate relationships between heat island intensities and surface parameters. We have applied the multivariate linear regression (MLR) method in the model, which is deemed to be advisable for solving similar kind of problems by other researcher's (*Bottyán et al.*, 2005; *Hjort et al.*,2011; *Szymanowski* and *Kryza,* 2012).The MLR equation is

$$Y = a + b_1 X_1 + b_2 X_2 + ... + b_i X_i \,, \; i=1,2,\ldots,n \tag{3}$$

where Y is the dependent variable, a is a constant, X_i is independent variable, b_i is the partial regression coefficient of independent variable number, and n is the number of independent variables taken into consideration (*Ezekiel* and *Fox,* 1959).

Fitting of the multiple regression equation was performed using the method of least squares. Calculations were carried out using SPSS software pack. Establishment of the linear model was made suing the software SPSS applying the Enter method. Kolmogorov–Smirnov tests proved that distribution of dependent and independent variables involved in the model is not different significantly from normal distribution what is a condition of correlation and regression calculations.

3. Results and discussion

3.1. Characteristics of the mean maximal UHI

Mean maximal diurnal UHI intensities culminated in the center of the settlement of Beregszász with 2.3 °C during the studied period, while maximal observed UHI intensity reached 6.1°C, in accordance with the results of *Oke* (1973). Development of the UHI is supported by high ratio of non-evaporating surfaces, compact built-up structure with two storied buildings, and high traffic density beside the central part of studied area.

A map of mean maximal UHI intensities have been prepared by calculating the average maximal UHI intensities for each measurement sites (*Fig. 2*). The following main characteristics of the UHI can be determined (*Molnár et al.*, 2006; *Molnár, 2007*):

- Highest mean maximal UHI intensities over 2.3 °C form the "peak" in the center of the town.
- Thermal excess decreases gradually from the center towards the outskirts of the town. The phenomenon "plateau" cannot be identified due to the small size of the settlement, presumably.
- Thermal excess over 1 °C on the slopes of the low mountain ridge bordering the town from the East is linked to the UHI.
- Low intensity fringes (around 1 °C) of the UHI of Beregszász reach the small, previously independent villages around the town (Beregardó on the north and Búcsú on the southwest) and a housing estate on the southeastern border of the town.
- Mean maximal UHI intensities around the weather station of Beregszász reach 1.2 °C what should be taken into consideration in the processing of datasets measured there.
- Low intensity borders of the mean maximal UHI reaches far over the borders of the built-up area of the town due to the impacts of airflows.

3.2. Structure of the multivariate model

Our main aim was to elaborate a universal model for estimation of spatial pattern of mean maximal heat islands on the base of meteorological and morphological data of Beregszász.

The input parameters of the multivariable model are

- heat island intensity as a dependent variable (°C),
- ratio of non-evaporating surfaces as an independent variable (*NES* – given in %), and
- distance of measurement sites from the geometrical center of the town as an independent variable (D – given in meters).

The following model equation has been created for the spatial structure of annual mean maximal heat island intensity using multivariate regression process of SPSS software:

$$\Delta t_{annual} = 1.642 - 0.00026 \times D + 0.54 \times NES \,. \tag{4}$$

It has been proved that the two parameters play an important role in development of the temperature excess (r^2=0,766). The value of D partial correlation coefficient is prominent in the model (r^2=0,766), since it is much higher than the other parameter (NES – r=0.477), which means that it may play much more important role in the formation of UHI. Spatial structure of UHI in Beregszász has been described on the base of UHI intensities calculated by the model. It can clearly be seen in the map that ratio of non-evaporating surfaces determines the alteration of air temperature much obviously in the built-up area than on the outskirts (*Fig. 4*). Where *NES* values are above 40%, isotherm lines run parallel with them, otherwise isotherm lines diverge. The reason for this is the irregular shape of the borderline between the built-up and close-to-natural areas in the town, probably.

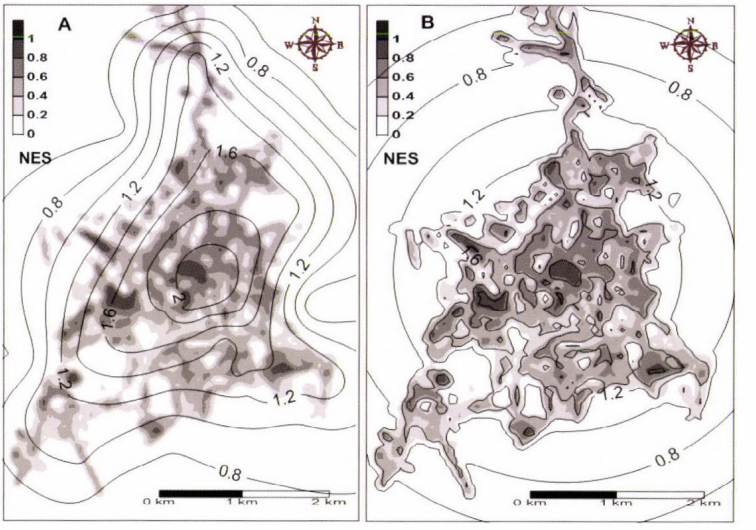

Fig. 4. Spatial structure of non-evaporating surfaces, measured (A) and estimated (B) mean maximal UHI intensities (difference between isotherms is 0.2 °C) for the studied period.

Empirical estimation model equations were created for the summer period (April 16 – October 15), winter period (October 16 – April 15), and sunny (under 4 octas) and cloudy days (over 4 octas).

Differences can be found in the empirical model of heat island intensities in the heating and non-heating periods. Values of r^2 indicate that the two built-up factors determinate the „strength" of heat excess developed in the town relatively weakly in the winter period. *Table 4.* presents the multivariate linear regression equations created for heating and non-heating periods. The disparity of partial correlation coefficients emphasizes the higher importance of distance from the center probably in the cold season, since decreasing evaporation rates weaken the impact of evaporating surfaces on the energy balance in the heating season.

Table 4. The multivariate regression equations of heat island intensities at measurement sites, the surface parameters influencing them, and the partial correlation coefficients built in the equations for Beregszász. r^2 is the coefficient of multiple determination, the other applied notations are the same as in *Table 3.*

	Equation of multivariate linear regression	*r2*	**Partial correlation coefficients**	
			D	***NES***
Δt/heating	$=1.652-0.000274\times D+0.709\times NES$	0.650	–0.665	0.513
Δt/non-heating	$=1.679-0.000273\times D+0.319\times NES$	0.732	–0.737	0.309

Correlation analysis was carried out to verify our model. Mean maximal UHI intensity values estimated by the model were correlated to mean maximal UHI intensities calculated on the base of results of a campaign of ten measurements carried out in 2010. There is a significant connection between the two datasets ($r=0.86$, $n=41$) at a level of significance of 0.1. Maximal error of the model was 0.4 °C, standard deviation of error was under 0.2 °C.

4. Conclusions

Our attempt to elaborate a model describing the spatial pattern of UHI in a small town has proved to be successful from methodological aspects. The multivariate linear regression model created by the integration of two surface factors as ratio of non-evaporating surfaces and distance of measurement points from the

settlement center describes the structure of UHI in our study area well. A part of spatial pattern of thermal excess developed in the built-up area could not be interpreted by the regression model, what can be a result of measurement bias on one hand and factors not taken into consideration in the model on the other hand. A continuation of this research for this reason could be to integrate new surface parameters into the model like sky view factor (SVF) and aspect ratio (H/W), which can have a significant impact on UHI formation as well.

According to literature and our previous examinations, the limit of the development of urban heat island is under 1,000 inhabitants. Our results provide better knowledge on spatial structure of UHI in small settlements. It is important, since small settlements have different structures from cities making it impossible to study the spatial and temporal characteristics of those heat islands on the basis of simple extrapolation of results for big cities.

Most advantageous location of new buildings and green areas can be found using UHI maps. Human comfort conditions of public spaces could be improved by the establishment of smaller parks in central areas of the town, while heating energy demand could be decreased by more compact built-up in residential areas. This way our results could be applied in spatial planning.

Acknowledgements:The authors are grateful to anonymous reviewer for providing valuable comments this study. The authors wish to special thanks to Molnár József, Kakas Mónika, and Marguca Viola. The publication is supported by the Arany János Közalapítvány a Tudományért.

References

Arnfield J.A., 2003: Two decades of urban climate research: A review of turbulence, exchanges of energy and water, and the urban heat island. *Int. J. Climatol, 23,* 1–26.

Atkinson B.W., 2003: Numerical modelling of urban heat-island intensity. *Bound.-Lay. Meteorol. 109,* 285–310.

Anon, 1992: Climatological normals (CLINO) for the period 1961–1990. *WMO/OMM-No. 847.*

Chen F., Kusaka H., Bornstein R., Ching J., Grimmond S., Grossman-Clarke S., Loridan T, Manning K., Martilli A., Miao S., Sailor D., Salamanca FP., Taha H., Tewari M., Wang X., Wyszogrodzki A., Zhang C., 2011: The integrated WRF/urban modelling system: development, evaluation, and applications to urban environmental problems. *Int. J. Climatol., 31*, 273–288.

Bartholy J., Pongrácz R., Lelovics E., and *Dezső Zs.*, 2009: Comparison of urban heat island effect using ground-based and satellite measurements. *Acta Climatologica et Chronologica Universitatis Szegediensis. 42-43*, 7–15.

Bottyán Z. and *Unger J.*, 2003: A multiple linear statistical model for estimating mean maximum urban heat island. *Theor. Appl.Climatol. 75,* 233–243.

Bottyán Z., Kircsi A., Szegedi S., and *Unger J.*, 2005: The relationship between built-up areas and the spatial development of the mean maximum urban heat island in Debrecen, Hungary, *Int. J. Climatol.25*, 405–418.

Elansky, N.F., Lavrova, O.V., Moklov, I.I., and *Rakin A.A.*, 2012: Heat island structure over Russian towns based on mobile laboratory observation. *Doklady Earth Siciences 443*, Part 1, 420–425.

Ezekiel, M. and *Fox, K.A.*, 1959: Methods of correlation and regression analysis: Linear and curvilinear. John Wiley, Oxford, England.

Giannaros, T.M., Melas, D., Daglis, I.A., Keramitsoglou, I., and *Kourtidis, K.,* 2013: Numerical study of the urban heat island over Athens (Greece) with the WRF model. *Atmos. Environ. 73*, 103–111.

Hjort, J., Suomi, J., and *Käyhkö, J.,* 2011: Spatial prediction of urban-rural temperatures using statistical methods", *Theor. Appl. Climatol. 106*, 139–152.

Kislov, A.V. and *Konstantinov, P.I.,* 2011: Detailed spatial modeling of temperature in Moscow. *Meteorol. Gidrol., 5*. 300–306.

Kuttler, W., 1998: Stadtklima. In Stadtökologie (eds: Sukopp, H. und Wittig, R.) Gustav Fischer, Stuttgart-Jena-Lübeck-Ulm,. 125–167.

Molnár J., Kakas M., and *Marguca V.*, 2006: A beregszászi hősziget intenzitásának és térbeli szerkezetének vizsgálata (Examination of intensity and the spatial structure of maximum heat island in Beregszász (Berehove), Ukraine). In Kiss A, Mezősi G, Sümeghy Z (szerk): Táj, környezet és társadalom. Ünnepi tanulmányok Keveiné Bárány Ilona professzor asszony tiszteletére. SZTE Éghajlattani és Tájföldrajzi Tanszék, Természeti Földrajzi és Geoinformatikai Tanszék, Szeged, 509-518. (*in Hungarian*)

Molnár J., 2007: A városi hősziget és annak kapcsolata a főbb felszínparaméterekkel Beregszász példáján. In Tóth Tamás, Bíróné Kircsi Andrea (szerk.) Kedvező széllel Kunhegyestől Debrecenig: Tiszteletkötet Dr. Tar Károly 60. születésnapjára. Debrecen: Magyar Szélenergia Társaság, 2007. pp. 225-233. (*in Hungarian*)

Lakatos M., Szentimrey T., Bihari Z., and *Szalai S.,* 2013: Creation of a homogenized climate database for the Carpathian region by applying the MASH procedure and the preliminary analysis of the data. *Időjárás 117*, 143–158.

Landsberg, H.E., 1981: The Urban Climate. Academic Press: New York.

Lee, S.H., Baik, J.J., 2010: Statistical and dynamical characteristics of the urban heat island intensity in Seoul. *Theor. Appl. Climatol. 100*, 227–237

Oke, T.R., 1973: City size and the urban heat island. *Atmos. Environ. 7*, 769–779

Oke, T.R., and *Maxwell, G.B.,* 1975: Urban heat island dynamics in Montreal and Vancouver. *Atmos. Environ. 9*, 191–200.

Oke, T.R., 1997: Urban climates and global environmental change. In (eds.: R.D Thompson. and Perry) Applied Climatology. Routledge, London and New York, 273–287.

Orlanski, I. 1975: A rational subdivision of scales for atmospheric processes"*Bull. Amer. Meteor. Soc., 56,* 527–530.

Park, H.S., 1986: Features of the heat island in Seoul and its surrounding cities. *Atmos. Environ. 20,* 1859–1866.

Szymanowski, M. and *Kryza, M.,* 2012: Local regression models for spatial interpolation of urban heat island– an example from Wroclaw, SW Poland. *Theor. Appl. Climatol. 108,* 53-71.

Szegedi S., 2000: Spatial structure of urban heat island in Debrecen. *In 3rd European Conference on Applied Climatology,* Pisa, Italy, 16–20 October; CD-ROM

Szegedi S., 2006: Heat islands in small and medium sized towns in Hungary. *Proceedings of Sixth International Conference on Urban Climate,* Gothenburg, Sweden, 439–442.

Unger J., Sümeghy Z., Gulyás, Á., Bottyán Z., and *Mucsi L.,* 2000: Land-use and meteorological aspects of the urban heat island. *Meteorol. Appl. 8,* 189–194.

Unger J., Bottyán Z., Sümeghy, Z., and *Gulyás A.,* 2004: Connection between urban heat island and surface parameters: measurements and modeling. *Időjárás 108*, 173–194.

INSTRUCTIONS TO AUTHORS OF *IDŐJÁRÁS*

The purpose of the journal is to publish papers in any field of meteorology and atmosphere related scientific areas. These may be

- research papers on new results of scientific investigations,
- critical review articles summarizing the current state of art of a certain topic,
- short contributions dealing with a particular question.

Some issues contain "News" and "Book review", therefore, such contributions are also welcome. The papers must be in American English and should be checked by a native speaker if necessary.

Authors are requested to send their manuscripts to

Editor-in Chief of IDŐJÁRÁS
P.O. Box 38, H-1525 Budapest, Hungary
E-mail: journal.idojaras@met.hu

including all illustrations. MS Word format is preferred in electronic submission. Papers will then be reviewed normally by two independent referees, who remain unidentified for the author(s). The Editor-in-Chief will inform the author(s) whether or not the paper is acceptable for publication, and what modifications, if any, are necessary.

Please, follow the order given below when typing manuscripts.

Title page: should consist of the title, the name(s) of the author(s), their affiliation(s) including full postal and e-mail address(es). In case of more than one author, the corresponding author must be identified.

Abstract: should contain the purpose, the applied data and methods as well as the basic conclusion(s) of the paper.

Key-words: must be included (from 5 to 10) to help to classify the topic.

Text: has to be typed in single spacing on an A4 size paper using 14 pt Times New Roman font if possible. Use of S.I. units are expected, and the use of negative exponent is preferred to fractional sign. Mathematical formulae are expected to be as simple as possible and numbered in parentheses at the right margin.

All publications cited in the text should be presented in the *list of references*, arranged in alphabetical order. For an article: name(s) of author(s) in Italics, year, title of article, name of journal, volume, number (the latter two in Italics) and pages. E.g., *Nathan, K.K.,* 1986: A note on the relationship between photosynthetically active radiation and cloud amount. *Időjárás 90,* 10-13. For a book: name(s) of author(s), year, title of the book (all in Italics except the year), publisher and place of publication. E.g., *Junge, C.E.,* 1963: *Air Chemistry and Radioactivity.* Academic Press, New York and London. Reference in the text should contain the name(s) of the author(s) in Italics and year of publication. E.g., in the case of one author: *Miller* (1989); in the case of two authors: *Gamov* and *Cleveland* (1973); and if there are more than two authors: *Smith et al.* (1990). If the name of the author cannot be fitted into the text: *(Miller,* 1989); etc. When referring papers published in the same year by the same author, letters a, b, c, etc. should follow the year of publication.

Tables should be marked by Arabic numbers and printed in separate sheets with their numbers and legends given below them. Avoid too lengthy or complicated tables, or tables duplicating results given in other form in the manuscript (e.g., graphs).

Figures should also be marked with Arabic numbers and printed in black and white or color (under special arrangement) in separate sheets with their numbers and captions given below them. JPG, TIF, GIF, BMP or PNG formats should be used for electronic artwork submission.

More information for authors is available: journal.idojaras@met.hu

Published by the Hungarian Meteorological Service

Budapest, Hungary

INDEX 26 361

HU ISSN 0324-6329

IDŐJÁRÁS

QUARTERLY JOURNAL
OF THE HUNGARIAN METEOROLOGICAL SERVICE

CONTENTS

****

VOL. 119 * NO. 4 * OCTOBER – DECEMBER 2015

IDŐJÁRÁS

Quarterly Journal of the Hungarian Meteorological Service

Editorial Office: Kitaibel P.u. 1, H-1024 Budapest, Hungary
P.O. Box 38, H-1525 Budapest, Hungary
E-mail: journal.idojaras@met.hu
Fax: (36-1) 346-4669

Indexed and abstracted in Science Citation Index Expanded™ and Journal Citation Reports/Science Edition
Covered in the abstract and citation database SCOPUS®

Subscription by mail:
IDŐJÁRÁS, P.O. Box 38, H-1525 Budapest, Hungary
E-mail: journal.idojaras@met.hu

IDŐJÁRÁS

Quarterly Journal of the Hungarian Meteorological Service
Vol. 119, No. 4, October – December, 2015, pp. 425–441

Climatic threats determining future adaptive forest management – a case study of Zala County

Borbála Gálos[1]*, Ernő Führer[2], Kornél Czimber[3], Krisztina Gulyás[1], András Bidló[1], Andreas Hänsler[4], Daniela Jacob[4], and Csaba Mátyás[1]

[1] *Institute of Environmental and Earth Sciences, Faculty of Forestry, University of West Hungary, Bajcsy-Zs. u. 4, 9400 Sopron, Hungary*

[2] *National Agricultural Research and Innovation Centre, Forest Research Institute, Paprét 17, 9400 Sopron, Hungary*

[3] *Institute of Geomatics and Civil Engineering, Faculty of Forestry, University of West Hungary, Bajcsy-Zs. u. 4, 9400 Sopron, Hungary*

[4] *Climate Service Center 2.0, Germany – eine Einrichtung am Helmholtz-Zentrum Geesthacht, Fischertwiete 1, 20095 Hamburg, Germany*

** Corresponding authors E-mail: galos.borbala@emk.nyme.hu*

(Manuscript received in final form May 20, 2015)

Abstract— Research of future climate tendencies is a precondition for appropriate climate change adaptation strategies in forestry and agriculture. The aim of this paper is to investigate the expected probability and magnitude of threatening climate conditions that are of primary importance in terms of forest management. Until 2100, precipitation and temperature results of an ensemble of 12 regional climate model simulations as well as derived indicators (e.g., Forestry Aridity Index and Ellenberg's climate quotient) have been analyzed for the A1B emission scenario. For the case study area in Southwest Hungary (Zala County), projections indicate an increasing tendency of warming and drying of summers towards the end of the 21st century. In the period 2071–2100, decrease of summer precipitation sum may exceed 25% compared to 1981–2010. Both extreme droughts and heavy precipitation events are expected to be more frequent. Consequently, the already observed climate change impacts and damages in forestry are very likely to occur with higher probability and severity. Including these results, a GIS-based "Agroclimate" decision support system is under development that contains a coherent data chain from climate change simulations, through impact assessments to adaptation support in order to provide quantified information on the possible yield potential and production risk for sustainable forest management.

Key-words: regional climate modeling, climate change impact, forest ecosystem, adaptation, decision support

1. Introduction

1.1. Climatic extremes threatening forests in the Carpathian Basin

The Carpathian Basin is considered to be highly sensitive and vulnerable to climate change and the related increase of the probability and intensity of extreme events. Droughts are recurrent features in the climate of the region, and relatively high amounts of precipitation is required to recover from a severe dry period (*Antofie et al.,* 2015). For the high drought risk, climate change, land cover changes, and intensive land use jointly are responsible (*Spinoni et al.,* 2013).

Precipitation is the determining and limiting factor of the distribution of climate dependent tree species in the forest/grassland transition zone ("xeric limits"; *Mátyás,* 2009) in Eastern-Central Europe and Southeast Europe. Primarily consecutive drought periods threaten the survival and adaptation of forest ecosystems (*Mátyás,* 2009; *Mátyás et al.,* 2010). In the last 50 years, the frequency, severity, and duration of extremely dry and warm weather events have increased (*Szinell et al.,* 1998; *Spinoni et al.,* 2013), their impacts on the most sensitive tree species are already visible.

Summer droughts of the last decades (especially in 1983–1995 and 2000–2003) have led to vitality loss of beech forests and to the drastic reduction of their climatically suitable niche in Hungary (*Berki et al.,* 2009). Health status decline has been observed also in sessile oak stands (*Berki et al.,* 2014). Under drier climate conditions, *Führer et al.,* (2013) found less organic matter production of above-ground dendromass. Climatic extremes are being observed to affect the water uptake of forests from groundwater and the whole water balance of forested catchments (*Gribovszki,* 2014). As result of a drought induced damage chain, increasing number of pests and diseases has been detected in beech and oak forests (*Lakatos* and *Molnár,* 2009; *Csóka* and *Hirka* 2011). Lack of adaptation may lead to increasing forest die-back and mortality (*Mátyás et al.,* 2010; *Czúcz et al.,* 2011; *Rasztovits et al.,* 2014; *Hlásny et al.,* 2014).

1.2. Projected climate tendencies

Regional climate change projections largely agree in a statistically significant warming in all seasons over Europe (*Christensen et al.,* 2007; *Jacob et al.,* 2008; *van der Linden* and *Mitchell,* 2009). The annual precipitation sum shows an increase in the northern and a decrease in the southern regions towards the end of the 21st century. In the transition zone, changes are smaller and statistically not significant (*Kjellström et al.,* 2011). This zone is projected to shift northwards in summer resulting in a decrease of the precipitation amount in the Carpathian Basin, whereas the southward shift of the transition zone in winter may lead to precipitation increase (*Bartholy et al.,* 2007, 2008; *Jacob et al.,*

2008). Projected increase of warm extremes as well as of drought frequency, magnitude, and length are statistically the most significant in the Southern European regions, whereas the risk of wet extremes is the most pronounced in the northernmost areas of the continent (*Heinrich* and *Gobiet,* 2011). In the Carpathian Basin, more irregular rainfall can lead both to more frequent heavy precipitation events and severe droughts (*Gálos et al.,* 2007; *Szépszó,* 2008; *Pongrácz et al.,* 2014). Recently, in the frame of the World Climate Research Program Coordinated Regional Downscaling Experiment (EURO-CORDEX) initiative, new regional climate projections have been provided for Europe in higher horizontal resolution (*Jacob et al.,* 2013). The results of the multi-model ensemble confirm the above introduced tendencies, the magnitude and the main spatial patterns of the expected climate change, however, they show more spatial details (*Jacob et al.,* 2013; *Vautard et al.,* 2013, 2014).

1.3. Decision support system development

In Hungary, silvicultural technologies and species preferences are prescribed by binding regulation based on climate conditions that are assumed to be constant over time. Severe droughts of the last decades and observed tree mortality shed light on the need to rethink forest management planning. Reliable projections of health status, production, growth, and yield are essential for the next decades in order to decide about sustainable tree species preference and to assess the economic impacts of possible species changes. The "Agroclimate" decision support system will provide coherent, GIS-supported information about the most important regional and local risks and adaptation options for three climate-dependent sectors (forestry, rainfed agriculture, and animal husbandry on nature-close pastures; *Mátyás et al.,* 2013). In the first step, Zala County in Southwest Hungary was selected as pilot region.

This paper introduces the climate part of the decision support system. The aim is to analyze future climate projections that are providing input for the assessment of forest responses to climate change. Special focus is on the expected probability and magnitude of threatening climate conditions that are of primary importance in terms of forest management (Section 3). Examples are shown for application of regional climate model outputs for impact research in the GIS-supported system (Section 4).

2. Sources of climate information and methods for analyzing

2.1. Applied climate data and models

For the period 1961–2010, daily observation series of temperature and precipitation have been used. The gridded data are available from the CARPATCLIM EU-project (www.carpatclim-eu.org, *Lakatos et al.,* 2013) in

$0.1° \times 0.1°$ horizontal resolution. In the project, the MASH (Multiple Analysis of Series for Homogenization; *Szentimrey,* 2011) procedure has been used for homogenization of long-term observation series. Interpolation of the homogenized time series was carried out by applying the MISH (Meteorological Interpolation based on Surface Homogenized data basis; *Szentimrey* and *Bihari,* 2007) method. Since the target region of the CARPATCLIM project does not cover the whole Zala County, data from further stations of the Hungarian Meteorological Service were also involved in the investigations.

For the 21st century, results of 12 regional climate model simulations have been analyzed that were created in the frame of the ENSEMBLES EU FP6 project (www.ensembles-eu.org). The data are accessible at daily time scale, in $0.22° \times 0.22°$ spatial resolution. The models are already validated (*Jacob et al.,* 2008), their uncertainties (related to the model, scenario, boundaries, and the variability of the climate system; *Prein et al.*, 2011) have been investigated and evaluated in many research projects (e.g., *Christensen et al.,* 2007). This ensemble of regional climate change projections for the SRES A1B emission scenario (IPCC, 2007) are considered as state-of-the-art for European climate impact assessments, so far.

2.2. Methods of analyzing

Climate model results have been included in the GIS-based decision support system, transformed into a common grid applying the DigiTerra Map GIS software and its newly developed Climate Database Query Module (*Czimber,* 2014). Inclusion of all available information (e.g., elevation, hydrology, soil and climate conditions, and satellite images of land use, land cover, and forest inventory data) into a geoinformatic system allows the integrated data processing of the different raster and vector layers. It is possible to query data from the database and the map, and to make geostatistical analyses. For finding spatial correlations and developing functions for impact assessments, the latest image processing technologies (fuzzy membership functions based and maximum likelihood classifiers) has been used.

Applying the Climate Database Query Module, monthly, seasonal, and annual temperature means and precipitation sums as well as their means over the vegetation period have been determined using the daily time series of 12 different regional climate models. For calculating general extreme indices (e.g., total number of summer days, hot days, frost days, dry days, heavy precipitation days), minimum and maximum temperatures from 6 models are available. Moderate and severe dry summers have been defined based on *Gálos et al.* (2007). *Table 1* contains the variables and derived indices selected and investigated in this paper.

Table 1. Climate variables and indices analyzed in this study

Temperature means (*T*)	• annual, seasonal, monthly, vegetation period
Derived extreme indices from daily temperature minima (*Tmin*) and temperature maxima (*Tmax*)	• extremely hot days (*Tmax* ≥ 35 °C) • hot days (T*max* ≥ 30 °C) • frost days (*Tmin* < 0 °C) • ice days (*Tmax* < 0 °C)
Precipitation sums (*P*)	• annual, seasonal, monthly, vegetation period
Derived extreme indices from daily precipitation sums	• wet days ($P \geq 20$ mm day^{-1})
Ellenberg's climate quotient (*EQ*; *Ellenberg,* 1988)	$EQ = \frac{T_{July}}{P_{Annual}} * 1000$
Forestry aridity index (*FAI*; *Führer*, 2010)	$FAI = \frac{T_{July-August}}{P_{May-July} + P_{July-August}} * 100$

Projected climate conditions have been analyzed for three 30-year time periods in the 21st century: 2011–2040, 2041–2070, and 2071–2100, respectively. Expected changes of temperature and precipitation as well as of the probability and severity of climate extremes have been determined relative to the reference period 1981–2010.

Results of an ensemble of different regional climate model simulations have been considered rather than one single climate projection. In this way, the spread and robustness of the projections as well as the likelihood of the possible changes can be evaluated (it is not possible to state a concrete value for future climate change in a specific region). According to the IPCC, the change has been categorized as "likely" when 66% of all changes projected through the various models lie within this range.

3. Climate tendencies in Zala County

3.1. Observed climate

Based on meteorological observations, Zala County can be characterized by 10.4 °C annual mean temperature and 717 mm annual precipitation sum for the time period 1981–2010 that has been applied as reference of the projected climate change (*Table 2*). Summer is the warmest (19.7 °C) and wettest (241 mm), whereas winter is the coldest (0.5 °C) and driest (121 mm) among the seasons.

Table 2. Observed temperature and precipitation in Zala County for the time period 1981–2010

	Temperature mean [°C]	Precipitation sum [mm]
Annual	10.4	717
Spring	10.6	162
Summer	19.6	241
Autumn	10.5	193
Winter	0.5	121
Vegetation period	15.9	494

Measured data of Zalaegerszeg (in Zala County) indicate that in the last decade, almost all summers were warmer than the average of 1981–2010 (*Fig. 1*). Extremely dry periods (at the beginning of the 1990s, 2000s, and 2010s) can be clearly detected that could induce the reported drought damages in forestry (Section 1.1). Summers with precipitation sum below the 30-year mean often have extreme high temperatures as well (*Fig. 1*). Observed tendencies of general climate indices (*Table 1*) show that frequency of hot days ($Tmax \geq 30$ °C) and extremely hot days ($Tmax \geq 35$ °C) increased during the investigated time period (*Fig. 2*). Whereas there was only 1 year in the last 8 years when the total number of frost days ($Tmin < 0$ °C) exceeded the long term mean (*Fig. 2*), which indicates the recent warming of the region.

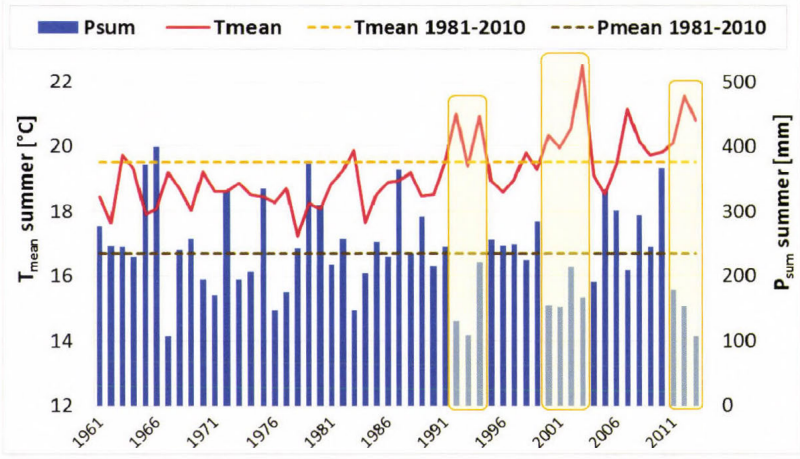

Fig. 1. Summer (June-July-August) temperature means and precipitation sums observed in Zalaegerszeg in the time period 1961–2013.

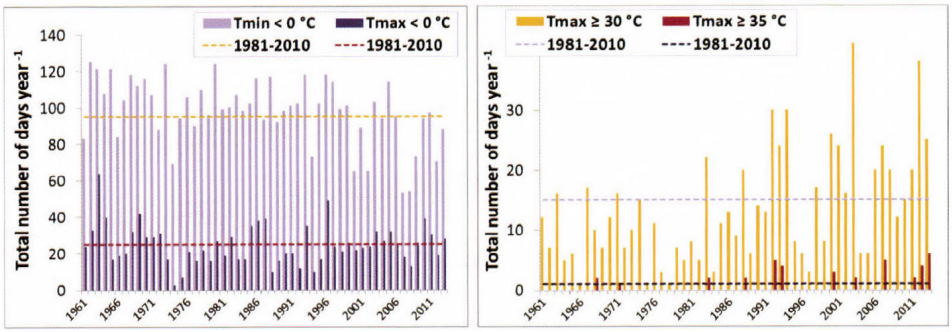

Fig. 2. Left part: total number of frost days (*Tmin* < 0 °C) and ice days (*Tmax* < 0 °C), right part: total number of hot days (*Tmax* ≥ 30 °C) and extremely hot days (*Tmax* ≥ 35 °C) observed in Zalaegerszeg.

3.2. Projected changes of temperature means and precipitation sums

Regional climate model simulations agree on a significant increase of temperature for all investigated time periods. Annual temperature means are "likely" to be 0.5–1.5 °C higher in 2011–2040, 1.5–2.8 °C higher in 2041–2070, and 2.4–4.2 °C higher in 2071–2100 relative to the time period 1981–2010 (*Fig. 3, Table 2*). The magnitude of warming is expected to increase in all seasons towards the end of the century. Summer temperature means shows the largest changes (for the mean projection of change by up to +3.9 °C in 2071–2100 compared to the reference period), whereas the smallest warming is projected for spring.

Change of annual precipitation sum is not significant, simulation results show a relatively large spread in magnitude and uncertainty in sign (*Fig. 3*). However, the inter-annual distribution of precipitation may change. The winter precipitation amount can be 12% larger for the period 2071–2100. Together with the higher temperatures, more rain is expected instead of snow.

Summers are projected to be significantly drier towards the end of the century. Considering the mean of the simulated changes, decrease of the precipitation sum can exceed the 7%, 12%, and 25%, respectively, in the analyzed 30-year future time periods compared to 1981–2010 (*Fig. 3*). In this case, Zala County might be characterized by similar summer precipitation conditions for the end of the century, like one of the driest regions in Hungary now. From forestry point of view it is important, that less precipitation is projected for the vegetation period, as well. For spring and autumn, expected changes are smaller and less clear in sign. The bandwidth of climate projections is the largest in summer and in the far future time period for both temperature and precipitation.

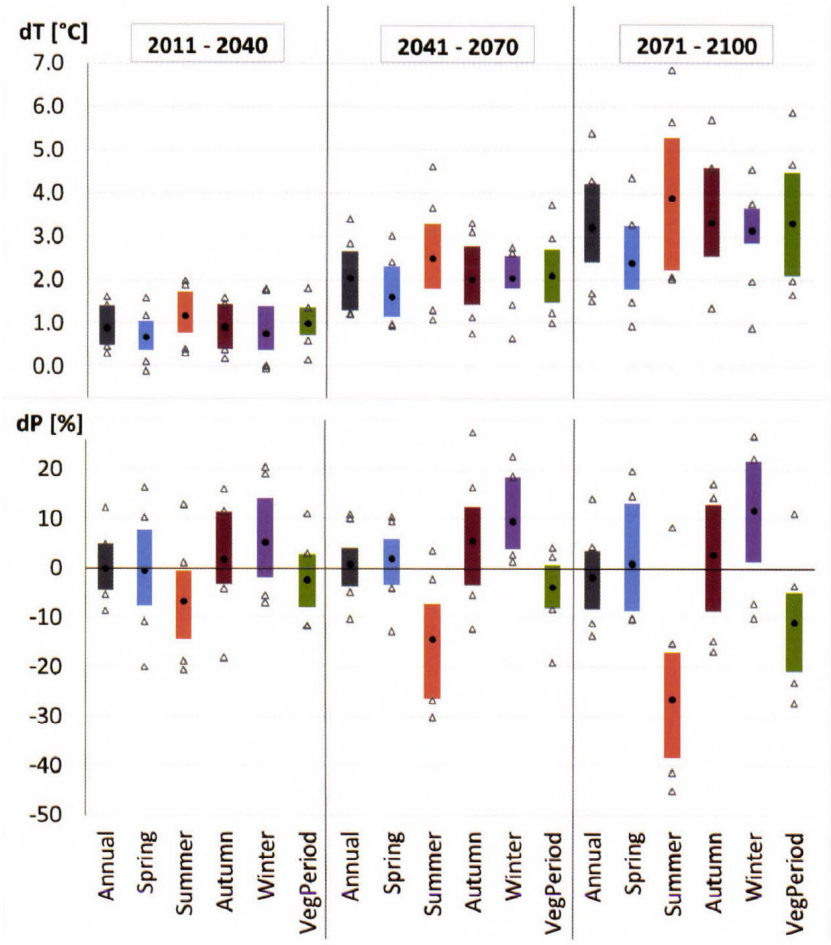

Fig. 3. Projected change of the temperature means (*dT*; top) and precipitation sums (*dP*; bottom) for the 30-year periods in Zala County. Columns: 66% of all projected changes fall within this range. Filled dots: mean projection of 12 regional climate models. Empty dots: bandwidth of all projected changes.

3.3. *Projected changes of the probability of temperature and precipitation extremes*

Additionally to the increase of the 30-year mean temperature, the distribution of its daily values is projected to shift into the warmer direction. That can lead to higher probability of extremely warm days and to less extremely cold days (*Fig. 4*). The "likely" range of the simulation results shows a clear signal in sign. Considering the mean of the projected changes, the total number of hot days

(*Tmax*≥30 °C) can increase by 17 days/year for the middle of the 21st century compared to 1981–2010. It would mean that the period when daily temperature maximums are greater than 30 °C may last 1 month/year. In the time period 1981–2010, only 1 extremely hot day/year (*Tmax*≥35 °C) in average was observed (*Fig. 2*). This amount might be 20 days/year higher by the end of the century. The total number of frost days may decrease by up to 1 month/year for 2071–2100 relative to the reference time period (*Fig. 4*).

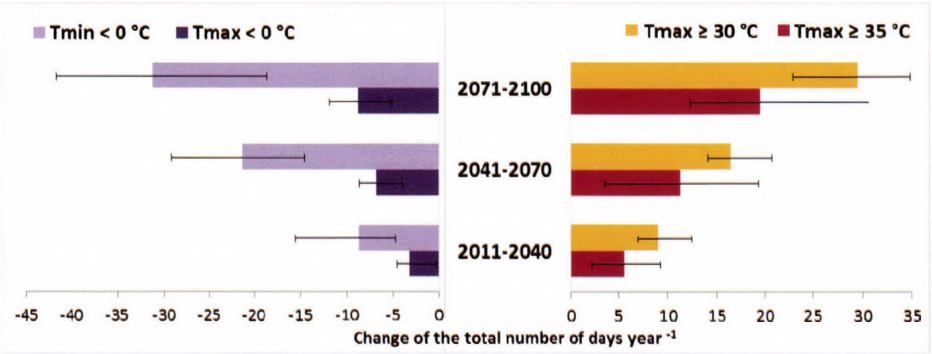

Fig. 4. Left part: mean annual change of the total number of frost days (*Tmin* < 0 °C) and ice days (*Tmax* < 0 °C); right part change of the total number of hot days (*Tmax* ≥ 30 °C) and extremely hot days (*Tmax* ≥ 35 °C) for the 30-year periods in Zala County based on the mean projection of 6 regional climate models. Error bars: 66% of all projected changes fall within this range.

Simulation results show that the change of the temporal distribution of precipitation can result in more intense precipitation events, especially in autumn and winter (*Fig. 5*). The bandwidth of the projections is relatively large on annual timescale, but for 2041–2100, more than 66% of the climate models agree in the direction of the change.

The total number of summer droughts is expected to increase. Not only the probability but also the severity of these events can be higher for the end of the 21st century (*Fig. 6*). For 2071–2100, more than half of the 30-year period can be extremely dry. Consequently, the consecutive dry periods may last longer compared to the end of the 20th century (*Gálos et al.,* 2014). More frequent warm extremes (*Fig. 4*) strengthen the effects of dry conditions due to the higher atmospheric evaporative demand.

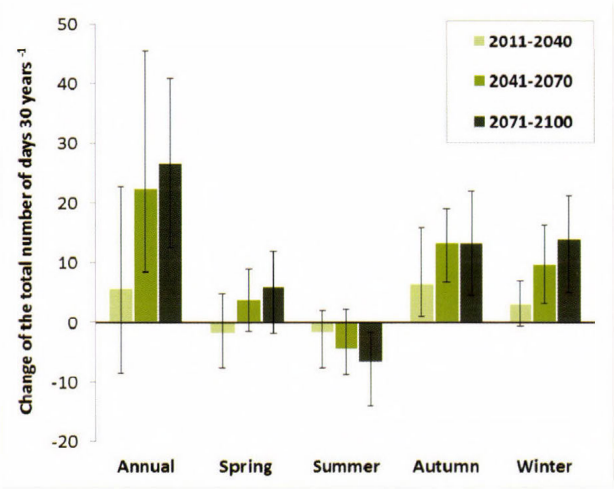

Fig. 5. Change of the total number of wet days ($P > 20$ mm day^{-1}) for the 30-year periods in Zala County based on the mean projection of 12 regional climate models. Error bars: 66% of all projected changes fall within this range.

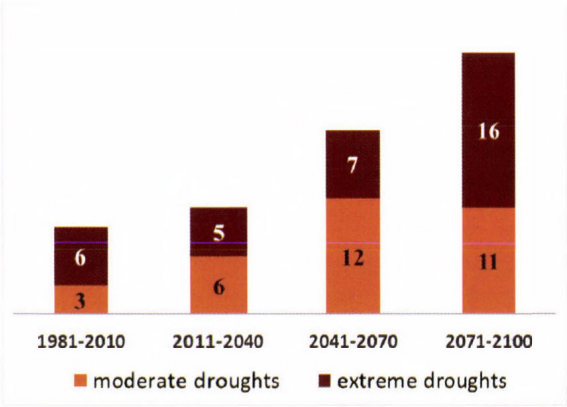

Fig. 6. Total number of summer droughts for the investigated time periods in Zala County (for 1981-2010: observed data, for the future time periods: observed data + simulated changes based on the mean projection of 12 regional climate models. Drought definition is based on *Gálos et al.*, 2007).

4. Application of the results for decision support in the forestry sector

Long term climate projections introduced in Section 3 provide information for two main user-groups: for climate impact researchers and for end users in the affected sectors.

4.1. Climate information for impact research in forestry

In terms of forest management, projection of forest yield conditions is highly important. Their estimation on a geoinformatic basis requires correlations between growth and vitality of species and the determining climatic factors. Different approaches are simultaneously applied in the *D*ecision *S*upport *S*ystem.

- *Forest yield potential.* The Ellenberg's climate quotient (*EQ*; *Ellenberg,* 1988; *Table 1*) has been used for instance to estimate the yield potential of beech. *Fig. 7* shows that beech sites with warmer and dryer conditions (indicated by higher *EQ* values) can be characterized by lower yield potential. Yield potentials with the same *EQ* values show large standard deviation that can be explained by the effect of other site conditions, in particular by soil texture and topsoil layer thickness (*Bidló,* 2014). Connection of yield potential and locally determined drought index may be interpreted also as a series of data predicting yield change over time. Projected increase of *EQ* values by 7.7 units for the end of the 21st century (*Table 3*) would mean a yield potential loss of beech (*Fig. 7*).

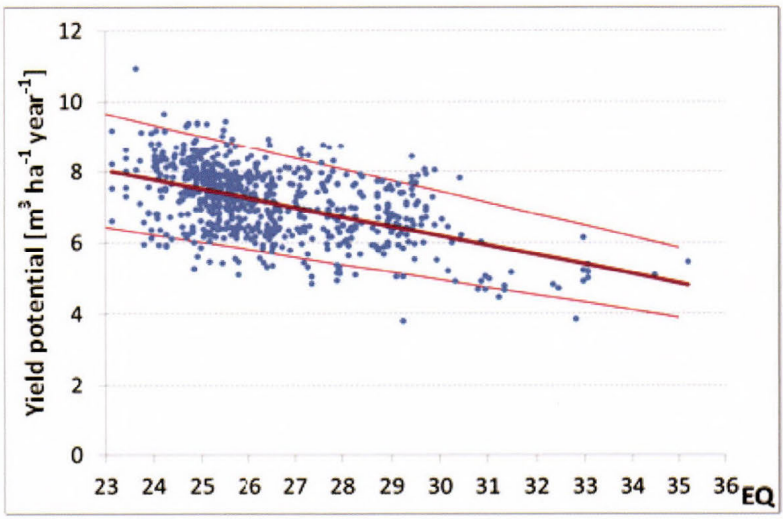

Fig. 7. Yield potential of beech forests in Southwest Hungary calculated as mean annual increment at age 80, in function of long-term values of the Ellenberg's climate quotient (*EQ*). Limiting lines stand for ±20% error (*Veperdi*, 2014).

Table 3. Ellenberg's climate quotient (*EQ*) and its projected change (*dEQ*) for the 30-year time periods in the entire Zala County based on the results of 12 regional climate models. Likely range: 66% of all projections fall within this range

	EQ	***dEQ*** (reference period: 1981–2010)		
Time period	**1981-2010**	**2011–2040**	**2041–2070**	**2071–2100**
Mean over the time period	28.5	+2.1	+3.9	+7.7
Likely range of changes		–1 – +4.9	+0.6 – +5.7	+2.4 – +11.6

- *Climate extremes and their effect on mortality.* Effects of extremes are determining the vitality of forest stands rather than average climate conditions. Projected increase of probability and severity of droughts (*Fig. 6*) overwrites the projections of yield potential functions. Consecutive periods characterized by *EQ* values above a threshold are the basis for modeling present and future tree species distribution as well as tree mortality induced by drought stress (*Móricz et al.,* 2013; *Rasztovits et al.,* 2014).
- *Genetically directed adaptation.* Survival of forest populations is also influenced by genetic factors. Increase of *EQ* indicate the increment decline beech due to suboptimal adaptation (*Horváth* and *Mátyás*, 2014). According to the climate tolerance limit, genetic diversity of oak stands may drastically decline (*Borovics* and *Mátyás,* 2013).

In addition to projections of yield, a number of other important aspects of the climate impact research in forestry will be imported into the decision support system such as:

- *Forest climate zones and production capacity.* Among the site conditions, climate is changing the most dynamically. Therefore for decision support, appropriate determination of climate tendencies and forestry climate categories are essential. Contrary to the climate classification derived from the forest inventory database, a meteorology-based forestry aridity index (*FAI*) has been developed (*Führer*, 2010; *Table 1*) and applied to assess the ecological and economic impacts climate change (*Führer et al.,* 2011, 2013). *FAI* considers not only the distribution and vitality of tree species but also their complex relationships with growth and production.
- *Changes of the forestry climate classes* in Zala County also refer to the more frequent and severe drought periods in the last 30 years (*Fig. 2*). For 1981–2010, most of the climatically suitable areas of beech changed to hornbeam-oak compared to 1961–1990 (*Fig. 8*). In case of the projected

temperature increase and precipitation decrease for May-August (*Fig. 3*), climate conditions are assumed to be favorable for sessile oak – turkey oak rather than for beech in the case study region (*Fig. 8*).

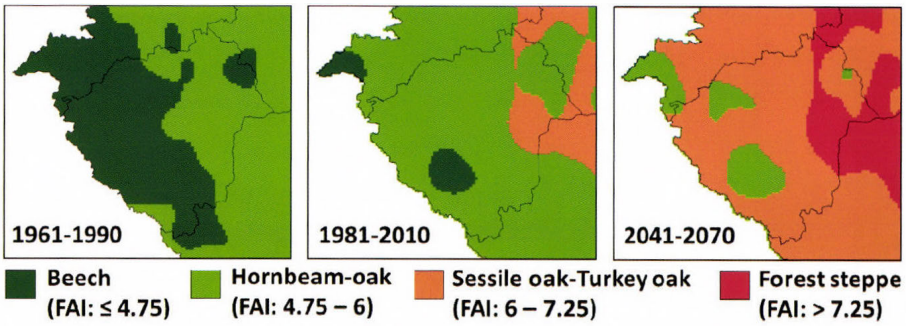

Fig. 8. Climatically suitable areas of different forests derived from the *FAI*-based forestry climate classification (*Führer,* 2010). For 1961–1990 and 1981–2010: observed data, for 2041–2070: observed data + simulated changes based on the mean projection of 12 regional climate models.

- *Water cycle of forested catchments*. Monthly temperature means and precipitation sums are the input of water balance models. The tendency towards a warmer and drier climate (*Fig. 3*) may result in a larger amount of annual evapotranspiration in Zala County, whereas the runoff may decrease to the one third by end of the century (*Csáki et al.,* 2014). Distribution of daily precipitation and its projected changes are used for deriving rainfall interception functions (*Zagyvainé Kiss et al.,* 2014).
- *Soil conditions*. More frequent heavy precipitation days or extreme winds may lead to the decrease of the topsoil layer thickness through higher erosion and deflation risks (*Bidló et al.*, 2014).
- *Potential biotic damages, pests and diseases*. For projecting the frequency of biotic damages as well as the appearance of new insects and diseases, more complex analyses are essential (*Csóka* and *Hirka,* 2011), these cannot be directly derived from the climate input.
- *Wildlife management in forests*. From the projected change of the probability distribution of temperature and from the related reduction of snowfall and snow cover, consequences are drawn for the game damage risks.

4.2. Decision support for end users

Forest management planning needs concrete and quantified information about the possible change of the yield potential, including the economic consequences of premature harvesting due to stability loss on the level of forest sub-compartments, in order to make decisions on species preference. It is a challenge for the decision support system to translate and interpret projected climate change (including the range and likelihood of the simulation results) as well as the standard deviation of the possible impacts as a quantified risk factor, so far.

5. Summary

Long term climate projections have been analyzed that serves as basis of climate impact research and adaptation support in forestry, focusing on the expected probability and magnitude of threatening climate conditions. In the case study region (Zala County in Southwest Hungary), simulation results of an ensemble of regional climate models indicate a significant warming in all seasons towards the end of the 21st century (by up to 3.9 °C for summer in 2071–2100). Both increasing frequency of warm temperature extremes and less cold extremes confirm the warming tendency. Although the mean annual values of precipitation remain almost constant, in winter an increase, whereas in summer a decrease of precipitation can be expected. The latter can exceed 25% until the end of the century in Zala County compared to the climate baseline period 1981–2010. Warmer and drier conditions in summer can result in an increase of the probability and severity of droughts. Heavy precipitation days can be more frequent, especially in autumn and winter. Magnitude of all simulated changes is expected to increase towards the end of the century.

These climate projections have been included as one of the basic datasets in the GIS-based "Agroclimate" decision support system. From the climate input, general climate indices (e.g., hot days, extremely hot days, wet days) and forestry climate indicators (e.g., Ellenberg's climate quotinent; *Ellenberg,* 1988 and forestry aridity index; *Führer,* 2010) are derived. They are used to develop correlation functions for forest growth, yield potential, and production as well as to model many other variables such as species distribution, water and carbon cycle of forests, etc. (see Section 4). Results of climate impact assessments indicate that in case of projected warming and drying of summers, the already observed damages in forestry are very likely to occur with higher probability and severity.

The geoinformatic system allows the integrated data processing and the complex investigation of the climate influenced processes in forest ecosystems. In this way, the GIS-supported climate services can provide a basis of new scientific results in impact research.

However, there is still a gap between provided climate information and required data for impact assessments regarding to the spatial and temporal resolution and the appropriate bias correction methods. Forest responses are also influenced by other factors (e.g., site conditions beyond climate, biotic damages and adaptive capacity) that have been shown to contribute to the relatively large standard deviation of the estimated impacts. The main challenge is to interpret the different bandwidths and uncertainties and to provide a quantified risk factor regarding to possible climate change impacts for end-users in forest management planning.

Climate impact research is being continued in the frame of the "Agroclimate-2" project, where results are planned to be extended to country scale and to the climate-dependent sectors of agriculture by continuous update with recent data and climate projections.

Acknowledgements: Climate data are derived from the regional climate model simulation results of the EU FP6 Integrated Project ENSEMBLES (Contract number 505539; www.ensembles-eu.org). The authors thank to the regional climate modeling group of the Climate Service Center 2.0 Germany for the scientific background. Development of the decision support system is supported by the "Agroclimate" (TÁMOP-4.2.2.A-11/1/KONV) and "Agroclimate-2" (VKSZ_12-1-2013-0034) EU-national joint founded research projects.

References

Antofie, T., Naumann, G., Spinoni, J., and *Vogt, J.,* 2015: Estimating the water needed to end the drought or reduce the drought severity. *Hydrol. Earth Syst. Sc. 19,* 177–193.

Bartholy, J., Pongrácz, R., and *Gelybó, Gy.,* 2007: Regional climate change expected in Hungary for 2071-2100. *Appl.Ecol. Environ. Res. 5,* 1–17.

Bartholy J., Pongrácz R., Gelybó Gy., and *Szabó P.,* 2008: Analysis of expected climate change in the Carpathian basin using the PRUDENCE results. *Időjárás 112,* 249–264.

Berki, I., Rasztovits, E., Móricz, N., and *Mátyás, Cs.,* 2009: Determination of the drought tolerance limit of beech forests and forecasting their future distribution in Hungary. *Cereal Res. Commun. 37,* 613–616.

Berki, I., Rasztovits, E., and *Móricz, N.,* 2014: Erdőállományok egészségi állapotának értékelése – egy új megközelítés. *Erdészettudományi Közlemények 4,*149–155. (in Hungarian)

Bidló, A., Horváth, A., and *Gálos, B.,* 2014: Változó termőhely – változatlan erdők? In (Eds. *Bidló, A., Horváth, A.,* and *Szűcs, P.*) Nyugat-magyarországi Egyetem, Erdőmérnöki Kar, IV. Kari Tudományos Konferencia. NymE Erdőmérnöki Kar Sopron. (in Hungarian)

Bidló, A., 2014: Termőhelyi változás hatása a fatermésre. In: (*Bidló, A., Király, A.,* and *Mátyás Cs.,* (szerk)) Agrárklíma. Nyugat-magyarországi Egyetem Kiadó Sopron. (in Hungarian)

Borovics, A., and *Mátyás, C., 2013:* Decline of genetic diversity of sessile oak at the retracting (xeric) limits. *Ann. Forest Sci. 70,* 835–844.

Csáki, P., Kalicz, P., Brolly, G., Csóka, G., Czimber, K., and *Gribovszki, Z,.* 2014: Hydrological Impacts of Various Land Cover Types in the Context of Climate Change for Zala County. *Acta Silv. Lign. Hung. 10,* 117–131.

Christensen, J.H., Carter, T.R., Rummukainen, M., and *Amanatidis G.,* 2007: Evaluating the performance and utility of regional climate models: the PRUDENCE project. *Clim. Change 81,* 1–6.

Czúcz, B., Gálhidy, L., and *Mátyás, Cs.,* 2011: Present and forecasted xeric climatic limits of beech and sessile oak distribution at low altitudes in Central Europe. *Ann. Forest Sci. 68,* 9–108.

Csóka, G., and *Hirka, A.*, 2011: Alien and invasive forest insects in Hungary (A review). Biotic Risks and Climate Changes in Forest. *Berichte Freiburger Forstliche Forschung 89,* 54–60.

Czimber, K., 2014: Geoadat orientált döntéstámogató rendszer fejlesztése a klímaváltozás hatásainak elemzéséhez. In: ((Szerk.: *Márkus B.* Térinformatika) Székesfehérvár, 309–318. (in Hungarian)

Ellenberg, H., 1988: Vegetation ecology of Central Europe. 4th ed., Cambridge University Press, Cambridge.

Fischer, E.M. and *Schär, C.*, 2010: Consistent geographical patterns of changes in high-impact European heatwaves. *Nature Geosci. 3,* 398–403.

Führer, E., 2010: Tree growth and the climate (in Hungarian). *"Klíma-21" Füzetek, 61,* 98–107.

Führer, E., Horváth, L., Jagodics, A., Machon, A., and *Szabados, I.*, 2011: Application of a new aridity index in Hungarian forestry practice. *Időjárás, 115,* 205–216.

Führer, E., Jagodics, A., Juhász, I., Marosi, Gy., and *Horváth, L.*, 2013: Ecological and economical impacts of climate change on Hungarian forestry practice. *Időjárás 117,* 159–174.

Gálos, B., Lorenz, Ph., and *Jacob D.*, 2007: Will dry events occur more often in Hungary in the future? *Environ. Res. Lett. 2.* 034006.

Gálos, B., Antal, V., Czimber, K., and *Mátyás, Cs.*, 2014: Forest ecosystems, sewage works and droughts – possibilities for climate change adaptation. In (Eds.: *Santamarta J.C., Hernandez-Gutiérrez L.E.*, and *Arraiza M.P.*,) Natural Hazards and Climate Change/Riesgos Naturales y Cambio Climático. Madrid: Colegio de Ingenieros de Montes.

Gribovszki, Z., 2014: Diurnal Method for Evapotranspiration Estimation from Soil Moisture Profile. *Acta Silv. Lign. Hung. 10,* 67–75.

Heinrich, G. and *Gobiet, A.*, 2011: The future of dry and wet spells in Europe: A comprehensive study based on the ENSEMBLES regional climate models. *Int. J. Climatol.* 32, 1951–1970.

Hlásny, T., Mátyás, Cs., Seidl, R., Kulla, L., Mergaicová, K., Trombik, J., Dobor, L., Barcza, Z., and *Konopka, B.*, 2014: Climate change increases the drought risk in Central European forests: What are the options for adaptation? *Lesn. Cas. For. J. 60,* 5–18.

Horváth, A. and *Mátyás, Cs.*, 2014: Növedékcsökkenés előrevetítése egy bükk származási kísérlet alapján. *Erdészettudományi Közlemények 4,* 91–99. (in Hungarian)

IPCC, 2007: Climate change 2007: Synthesis Report. Contribution of Working Groups I, II and III to the Fourth Assessment Report of the Intergovernmental Panel on Climate Change (Pachauri, R.K. and Reisinger, A., eds.), IPCC, Geneva, Switzerland. pp 104. http//:www.ipcc.ch.

Jacob, D., Kotova, L., Lorenz, P., Moseley, Ch., and *Pfeifer, S.*, 2008: Regional climate modeling activities in relation to the CLAVIER project. *Időjárás 112,* 141–153.

Jacob, D., et 38 coauthors EURO–CORDEX, 2013: New high–resolution climate change projections for European impact research. *Reg. Environ. Change 14*, 563–578.

Kjellström, E., Nikulin, G., Hansson, U., Strandberg, G., and *Ullerstig, A.*, 2011: 21st century changes in the European climate: uncertainties derived from an ensemble of regional climate model simulations. *Tellus 63A,* 24–40.

Lakatos, M., Szentimrey, T., Bihari, Z., and *Szalai, S.*, 2013: Creation of a homogenized climate database for the Carpathian region by applying the MASH procedure and the preliminary analysis of the data. *Időjárás 117,* 143–158.

Lakatos, F., and *Molnár, M.*, 2009: Mass mortality of beech on Southwest Hungary. *Acta Silv. Lign. Hung. 5,* 75–82.

van der Linden, P., and *Mitchell, J.F.B.*, eds., 2009: ENSEMBLES: Climate Change and its Impacts: Summary of research and results from the ENSEMBLES project. Met Office Hadley Centre, FitzRoy Road, Exeter EX1 3PB, UK.

Mátyás, Cs., 2009: Ecological perspectives of climate change in Europe's continental, drought-threatened Southeast. In (Eds. *Groisman, P.Y.*, and *Ivanov, S.*) Regional aspects of climate-terrestrial-hydrologic interactions in non-boreal Eastern Europe. NATO Science Series, Springer Verl. 31–42.

Mátyás, Cs., Berki, I., Czúcz, B., Gálos, B., Móricz, N., and *Rasztovits, E.*, 2010: Future of beech in Southeast Europe from the perspective of evolutionary ecology. *Acta Silv. Lign. Hung. 6,* 91–110.

Mátyás, Cs., Gálos, B., Berki, I., Bidló, A., Drüszler, Á., Eredics, A., Illés, G., Móricz, N., Rasztovits, E., and *Czimber, K.*, 2013: A Decision Support System for Climate Change Adaptation in Rainfed Sectors of Agriculture for Central Europe. *Geophys. Res. Abstracts 15,* EGU2013-2942.

Móricz, N., Rasztovits, E., Gálos, B., Berki, I., Eredics, A., and *Loibl, W.,* 2013: Modeling the Potential Distribution of Three Climate Zonal Tree Species for Present and Future Climate in Hungary. *Acta Silv. Lign. Hung. 9,* 85–96.

Pongrácz, R., Bartholy, J., and *Kis, A.,* 2014: Estimation of future precipitation conditions for Hungary with special focus on dry periods. *Időjárás 118,* 305–321.

Prein, A.F., Gobiet, A., and *Truhetz, H.,* 2011: Analysis of uncertainty in large scale climate change projections over Europe. *Meteorol. Z. 20,* 383–395.

Rasztovits, E., Berki, I., Mátyás, Cs., Czimber, K., Pötzelsberger, E., and *Móricz, N.,* 2014: The incorporation of extreme drought events improves models for beech persistence at its distribution limit. *Annals For. Sci. 71,* 201–210.

Spinoni, J., Antofie, T., Barbosa, P., Bihari, Z., Lakatos, M., Szalai, S., Szentimrey, T., and *Vogt, J.,* 2013: An overview of drought events in the Carpathian Region in 1961–2010, *Adv. Sci. Res. 10,* 21–32.

Szentimrey, T., 2011: Manual of homogenization software MASHv3.03. *Hungarian Meteorological Service.*

Szentimrey, T., and *Bihari, Z.,* 2007: Mathematical background of the spatial interpolation methods and the software MISH (Meteorological Interpolation based on Surface Homogenized Data Basis). *Proceedings from the Conference on Spatial Interpolation in Climatology and Meteorology,* Budapest, Hungary, 2004, COST Action 719, COST Office, 17–27.

Szépszó, G., 2008: Regional change of climate extremes in Hungary based on different regional climate models of the PRUDENCE project. *Időjárás 112,* 265–83.

Szinell, Cs., Bussay, A., and *Szentimrey, T.,* 1998: Drought tendencies in Hungary. *Int. J. Climatol. 18,* 1479–1491.

Vautard, R., et 25 coauthors 2013: The simulation of European heat waves from an ensemble of regional climate models within the EURO–CORDEX project. *Clim. Dynam. 41,* 2555–2575.

Vautard, R., Gobiet, A., Sobolowski, S., Kjellström, E., Stegehuis, A., Watkiss, P., Mendlik, T., Landgren, O., Nikulin, G., Teichmann, C., and *Jacob, D.,* 2014: The European climate under a 2 °C global warming. *Environ. Res. Lett. 9,* 034006

Veperdi, G., 2014: Az erdőállományok növekedésmenetének és természeti kockázatainak változásai. In: (Szerk. *Bidló, A., Király, A.,* and *Mátyás Cs.,*) Agrárklíma. Nyugat-magyarországi Egyetem Kiadó Sopron. (in Hungarian)

Zagyvainé Kiss, K.A., Kalicz, P., Csáfordi, P., and *Gribovszki, Z.,* 2014: Forest litter interception model for a sessile oak forest. *Acta Silv. Lign. Hung. 10,* 91–101.

IDŐJÁRÁS

Quarterly Journal of the Hungarian Meteorological Service
Vol. 119, No. 4, October – December, 2015, pp. 443–474

A new hail size forecasting technique by using numerical modeling of hailstorms: A case study in Hungary

Kálmán Csirmaz

Hungarian Meteorological Service Storm Warning Observatory
Vitorlás u. 17. H-8600 Siófok, Hungary
csirmaz.k@met.hu

(Manuscript received in final form March 30, 2015)

Abstract—A new forecasting method for maximum size of hail stones is presented in this paper by using the outputs of a high-resolution, non-hydrostatic numerical weather prediction model (NWP). The method was tested applying simulations of a real case supercell storm producing damaging hail with the Weather, Research and Forecasting (WRF) model. Numerical simulations were made with two distinct horizontal resolutions, 2 km and 100 m, applying nesting technique to assess the effect of the resolution on the storm microphysical properties and the maximum size of the hail stones on the surface. The WRF was able to simulate the main observed characteristics of the supercell on both resolutions. However, the numerical simulation with finer resolution gave better agreement with the radar observation and the observed maximum hail size on the surface. It was found that the horizontal resolution has significant influence on the magnitude and evolution of the microphysical processes in the storm. The numerical simulation with finer resolution produced not only significantly larger maximum mixing ratios of graupel/hail than the 2 km one did, but the volume integrated content of graupel/hail particles in the storm was also larger in the case of finer resolution. This difference can be attributed to the stronger updraft in the case of 100 m resolution. The analysis of various production shows that graupel/hail particles were mainly formed by the heterogeneous freezing of supercooled rain drops and by the freezing of rain drops due to the collision with cloud ice in the midlevels (between 3 and 8 km). Subsequent accretion of graupel/hail particles occurred by the collision with cloud and rain water. Larger graupel/hail content aloft in the case of finer simulation resulted in larger surface mixing ratios which directly led to larger maximum hail sizes on the ground.

Key-words: supercell, hail, WRF

1. Introduction

Hail is a threatening atmospheric phenomenon and storms with hail on the ground (hereafter hailstorms) frequently cause large fraction of weather-related damages. The annual crop losses often reach several hundreds of million dollars (*Changnon et al.,* 2000) in the USA. Hungary is an exposed region, as well: in the 70s, the hail-related annual insurance charges in Baranya county – before the installation of the hail suppression system – totaled to 100–200 million forints. Therefore, prediction of hail on the ground – especially its existence and a characteristic diameter of hailstones –, is a crucial segment of mesoscale forecasts and warning systems. The difficulties of forecasting hail come from the large spatial and temporal variability of hailfalls and relatively low frequency of their occurrence over a certain point of the ground. This makes the verification and validation of any forecasting techniques quite complicated.

The first methods were based on statistical relationships between the observed state of the atmosphere and the existence and size of the hail on the ground (e.g., *Fawbush* and *Miller*, 1953; *Miller*, 1972). From the sixties-seventies, as the capacity of computers had gradually improved, it became possible to explicitly simulate the hail formation and growth in thunderstorms producing hail on the ground. The initial attempts were one-dimensional steady-state "jet" models (e.g., *Simpson* and *Wiggert*, 1969; *Weinstein*, 1972; *Zoltán* and *Geresdi*, 1984) and one-dimensional, time-dependent models (*Ogura* and *Takashi*, 1971; *Wisner et al.*, 1972; *Ćurić* and *Janc*, 1989 and 1993). Since that time, the statistical methods for forecasting hail have been coupled with one-dimensional cloud models to evaluate the maximum updraft speed (e.g., *Renick* and *Maxwell*, 1977; *Moore* and *Pino*, 1990) or complex microphysics schemes have been combined with simple steady-state cumulus models (e.g., *Brimelow et al.*, 2002, *Brimelow* and *Reuter*, 2006; *Geresdi et al.*, 2004 etc.). The development of two- or three-dimensional, time-dependent cloud models enabled the more reliable simulations and complex analyses of the microphysical processes and their relationships to the airflow in and around multi- and supercell storms (*Orville* and *Kopp*, 1977; *Takahashi*, 1976; *Johnson et al.*, 1993 and 1995; *Geresdi*, 1990 and 1996). However, these models involve bulk microphysics schemes, therefore, they are not able to explicitly compute the evolution of hydrometeor sizes, but only the parameters of their preset size distributions. Though detailed spectral (bin) microphysical models work with size categories, they are computationally more expensive (*Farley* and *Orville,* 1986; *Farley,* 1987 a,b; *Geresdi*, 1998), which inhibits their wide-spread application in multidimensional microphysical numerical experiments and operational application.

Due to the appearance of the new generation of mesoscale, non-hydrostatic models, such as the Weather Research and Forecasting Model (WRF – *Skamarock et al.*, 2008), three-dimensional, real-data simulations of hailstorms became routinely executable in an operational manner via their complex bulk

microphysical schemes. Moreover, using this type of numerical models, explicit prediction of hail or other hydrometeor categories on the ground is also possible. Still, to date, there is barely known any hail forecasting methods based upon the explicit microphysical outputs of mesoscale numerical weather prediction models (NWP). Though *Milbrandt* and *Yau* (2006) developed a method to estimate the maximum size of hailstones at the surface based on the three-moment size distribution of the hail category predicted by NWP, they did not suggest that method as a possible way for operationally forecasting the existence and size of hail stones. In this paper, the description and results of recently developed method about the forecast of the maximum hail size is presented.

The effect of resolution on the morphology of thunderstorms has been thoroughly studied (e.g., *Grabowski et al.*, 1998; *Adlerman* and *Droegemeier,* 2002; *Petch et al.*, 2002). It was found that the properties of the simulated mesoscale phenomena were very sensitive to the applied horizontal resolution of the model. In relation with this issue, numerous experiments were made to determine the "ideal" resolution to a physically consistent cloud-resolving model regime. *Bryan et al.* (2003), for example, found that a horizontal resolution of about 100 m is necessary for a correct simulation of an idealized squall line case. *Craig* and *Dörnback* (2008) proposed that the horizontal resolution of a consistent mesoscale simulation should be determined by either of horizontal scale of a buoyant bubble or the buoyancy height which requires tens of meters of resolution. *Friori et al.* (2010) examined the effects of resolution and various turbulence schemes on the morphology of a supercell by numerical simulation of idealized cases, and they found the values of storm-scale properties to converge at horizontal resolution of 200 m. To summarize, simulation with horizontal resolution on the order of hundreds of meters is necessary in order to obtain physically as consistent results as possible regarding the microphysical properties of a hailstorm.

Supercells, as effective hail-producing storms, occurs over Hungary every year mainly during the warm season (*Horváth* and *Geresdi*, 2003), and there were successful attempts to simulate them with state-of-the-art NWP's (*Horváth* and *Geresdi*, 2003; *Horváth et. al.*, 2009; *Putsay et al.*, 2011). However, these studies did not cover the microphysical aspects of the simulations. Therefore, in this paper, a detailed analysis of microphysical processes focusing on the formation and growth of solid hydrometeors (graupel/hail) is given. The analysis was performed, on one hand, on a coarser model grid with O (1 km) grid spacing corresponding to the present-day, operationally applied resolution in NWP forecasts and, on the other hand, on a high-resolution domain with O (100 m) grid distance which yields physically the most consistent cloud-resolving simulation. The comparison of the storm's microphysical properties on the two distinct grids is also carried out to study the effect of the resolution on the hydrometeor fields in the storm. In Section 2, the methodology of the research and the method for assessing hail-size on the ground are shown. In

Section 3, we describe the details of a case study, and the results of the numerical simulations and hail-size calculations are presented. Summary and plans for future work are given in Section 4.

2. *Methodology*

2.1. Description of the modeling environment

The simulations were carried out with the WRF-ARW non-hydrostatic mesoscale numerical model version 3.1.1 (*Skamarock et al.*, 2008) using nested domains with different horizontal resolutions. The largest domain (Domain 1) has a resolution of 6 km and it covers an area of 700 km × 850 km in the Carpathian Basin. The second, smaller domain (Nest 1) includes Hungary, too, but it has 2 km resolution and covers a region of 450 km × 360 km. The smallest domain (Nest 2) is embedded in Nest 1. This domain is used to focus on the particular storm, therefore its horizontal resolution is 100 m and covers only an area of 44 km × 30 km. This resolution was chosen according to the results published by *Bryan et al.* (2003). They found that – in the case of idealized boundary conditions – the simulated properties of a squall line showed convergence if the horizontal resolution was equal to or less than 100 m. This means that the further decrease of horizontal grid distances hardly affects the output of the numerical model. It is supposed that the above-mentioned conclusion of *Bryan et al.* (2003) is valid for the supercell case presented in this paper, too. The vertical resolution was the same in each nest: 37 terrain-following levels were applied with larger vertical resolution near to the surface and with stretched resolution at higher altitudes. The lowest model level was about ten meters above the ground and the top of the domain was at 50 hPa. All in all, we performed one model run on three domains (Domain 1, Nest 1 and Nest 2) connected via one-way nesting technique, but only the results on Nest 1 and Nest 2 were evaluated. We consider the model run on Nest 1 and Nest 2 as distinct simulations, therefore, hereafter we are referring to these simulations as Simulation1 (Nest 1) and Simulation2 (Nest 2). See *Fig. 1* for the location of domains of the simulations.

The formation and evolution of different types of hydrometeor species was simulated by the Thompson's one-moment bulk microphysical scheme (*Thompson et al.*, 2004) adapted from the Reisner scheme (*Reisner et al.*, 1998). The Thompson's parametrization is a state-of-the-art Simulation of the microphysical processes, especially in the case of mixed phase clouds. This scheme allows us to study the characteristics of different types of ice particles in severe thunderstorms. The scheme involves prognostic equations of mixing ratios for five different species: cloud water, cloud ice (cloud particles), snow, rain, and graupel/hail (precipitation particles). The parametrization does not include hail as a distinct category but larger graupel particles computed implicitly by the model can be

treated as hailstones[1]. Grell's cumulus parameterization scheme (*Grell* and *Dévényi*, 2002) is used to simulate the formation of convective clouds. In the cases of larger resolution (i.e., Simulation1 and Simulation2), this parameterization scheme was switched off and the model was let to develop the convection directly. Independently of the horizontal resolution, the Mellor-Yamada-Janjic's (MYJ – *Mellor* and *Yamada*, 1982) planetary boundary layer (PBL) parametrization scheme is activated coupled horizontally with Smagorinsky's first order closure treatment for the sub-grid diffusion. A proper selection from the schemes describing the turbulence is crucial. The main problem about the choosing of the appropriate scheme is that different resolutions need different treatments of the turbulence. As the horizontal resolution is increased from 2 km to 100 m, the averaged momentum equations of the model begin to resolve the boundary layer eddies (large eddy simulation – hereafter LES). This range of resolution is named "terra incongnita" by *Wyngaard* (2004). Eddies in this size interval possess the main fraction of the turbulent energy spectrum regarding cumulus convection. Nevertheless, a Simulation in "terra incongnita" is not able to adequately resolve the energy-containing eddies based on subgrid diffusion closure with a scalar diffusivity. Instead, *Wyngaard* (2004) suggested that a tenzor of three-dimension scalar diffusivity coefficients should be applied in such Simulations. In addition, for a nested, real data case simulated by WRF, *Talbot et al.* (2012) showed that applying LES in "terra incognita" yielded mixed results in the model performance. In addition, they found that the results on the nest with ultra-fine resolution (on the order of 100 m's) were even more sensitive to the lateral boundary conditions and to the initial forcing (represented by the analysis) than to the chosen turbulence closure. These are the reason why the same schemes – the MYL-scheme for handling the vertical diffusion and the Smagorinsky first order scheme for parameterization of the horizontal eddy diffusivity coefficients – were used both in the case of Simulation1 and Simulation2.

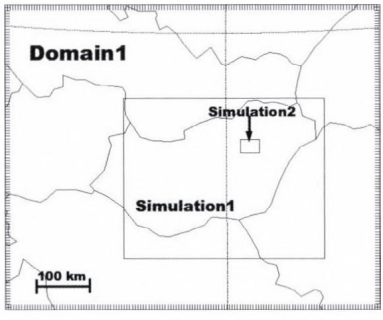

Fig. 1. Location of Domain1 and the nests of Simulation1 and Simulation2 in the WRF model run.

1 In this case, implicit means that the scheme only returns with the mixing ratio of graupel/hail in a grid box. However, upon this quantity and the size distribution, hypothetical and possible particle sizes with their concentration can be assessed.

Initial and lateral boundary conditions for Domain 1, Nest 1, and Nest 2 were provided by the ECMWF global model, by the outputs of Domain 1, and by the outputs of Nest 1, respectively. (The WRF model outputs were generated in every 5 minutes in the case of Simulation1, and in every 1 minute both in Simulation2 and Simulation1 during the time interval when the storm was in the volume defined by Nest 1. Analyses and hail-size calculations were performed on the model's terrain-following eta-system. For the plotting of vertical cross sections, the data were transformed into a Cartesian system with height above the mean sea level as a vertical coordinate.

2.2. Description of the data collected for validation

The results of the numerical model and that of the recently developed hail size forecasting method are intended to compare with observation data. The reliability of the forecast of maximum hail size depends both on the quality of the model output and on the accuracy of the method used on the calculation of the maximum hail size from the model output. Therefore, for the validation of the forecast of maximum hail stone size, such a case was chosen where the model was able to simulate the characteristics of a severe storm correctly, and surface observation data about the size of the hail stones were available. Database of well-documented cases of severe hailstorms was searched to find the appropriate case. This means that, besides the data of hail existence, data on the hailstone sizes should be also available. In the eighties a hail pad network operated in the southern parts of Hungary associated with the hail suppression activity. Unfortunately, this type of hail size measurements was ceased in the early 90's. Since then, there have been no directly observed, quantitative data about the hailstone sizes on the surface, but only qualitative and indirectly observed data about the characteristics of the hailstones are available. The source of data is the followings: 1) Online sources of falling hailstones on various commercial and amateur meteorological sites where extensive documentation of significant severe weather events can be found. These documentations were done mostly by voluntary people who uploaded their photos and videos of hailstones to these sites. These sources, though to a limited extent, can be used for verification. 2) Radar observation data which are not suitable for direct evaluation of hailstone sizes at the ground due to the uncertain relation between the observed reflectivity and hail stone size. However, high reflectivity itself can indicate the existence of hail or perhaps severe hail. Therefore, comparison between the measured and simulated reflectivity is also performed in order to evaluate the model's ability to reproduce the microphysical characteristics of real storms. The simulated radar intensity was calculated by the NCAR Command Language (NCL) post-processing module of WRF-ARW.

2.3. *Description of the hail-size calculation method*

Forecasting of maximum hail-size is based on the followings: the model computes the graupel/hail mixing ratios on the three-dimensional model grid at every time step. These calculations are carried out by taking the size following gamma size distribution of graupel/hail particles (*Fig. 2*) defined by the scheme (see *Thompson et al.*, 2004) at the lowest model level (η=0.997):

$$N(D) = N_0 D e^{-\lambda D}, \tag{1}$$

where D is the diameter of graupel/hail particles (they are supposed to be spherical objects)

$$N_0 = 2.38\left[\frac{\pi\rho_g}{q\rho_a}\right]^{0.92}, \tag{2}$$

where is ρ_g the density of a graupel/hail particle (400 kgm^{-3}) and ρ_a is the density of air.

The λ parameter can be obtained from the mixing ratio via the following relationship:

$$q = \frac{1}{\rho_a}\int_0^{\infty} N_0 \frac{D^3\pi}{6} \rho_g D e^{-\lambda D} dD \tag{3}$$

After calculating the integral on the right hand side of Eq. (3), the λ parameter can be given in an explicit form:

$$\lambda = \left[\frac{4N_0\pi\rho_g}{q\rho_a}\right]^{0.2}. \tag{4}$$

The number concentration of graupel/hail particles can be computed via the following equation:

$$n = \int_0^{\infty} N_0 D e^{-\lambda D} dD = \frac{N_0}{\lambda^2}. \tag{5}$$

A definite integral of Eq. (5) between X and ∞ gives the number concentration of particles larger than X. The algorithm of hail size forecast is based on the following equation:

$$n_X = \int_X^{\infty} N_0 D e^{-\lambda D} dD = N_0 \frac{e^{-\lambda X}}{\lambda^2}(\lambda X + 1), \tag{6}$$

where n_x is a predefined threshold number concentration of graupel/hail particles. The Newton-Raphson iteration technique was used to calculate the value of the variable X, the diameter of graupel/hail particles which concentration is equal to n_x. The value of this threshold number concentration was chosen to be equal to 10^{-4} m^{-3} (*Milbrandt* and *Yau*, 2006). This value means that there is exactly one hail stone in a volume of column with height of 1 m and with cross section of 100 m × 100 m^2. The hail stones of lower concentration than the threshold are very difficult to detect. Therefore, X can be defined as maximum observable (possible) hail size.

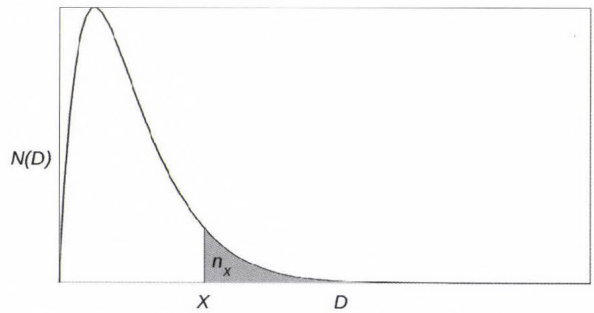

Fig. 2. The gamma distribution of graupel/hail particles used in the Thompson's scheme. D on the abscissa represents the graupel diameter, $N(D)*dD$ along the y-axis is the number concentration of graupel in the infinitesimal D, $D+dD$ interval. X denotes the diameter above which the concentration is equal to n_x. See text for further description.

3. Results

3.1. *Case study: synoptic features and observation data*

On June 7, 2009, an isolated supercell passed through the northeastern part of Hungary, produced large hail (the maximum hail stone diameter was reported to be about the size of a tennis ball) causing severe hail-related damages in several locations. The synoptic feature of this event was characterized by a quasi-stationary waving cold front at northwest of Hungary (*Fig. 3a*). East of the front, over Hungary, warm and moist air advected from the south at low-levels. At upper-levels, at the western part of Hungary, the front is accompanied by a trough (not shown) moving slowly eastward. Downstream of the trough, high

wind speeds prevailed aloft (~30 m/s at 500 hPa). These conditions resulted in considerable instability and significant vertical wind shear: ~1000 J/kg convective available potential energy values and 25–30 m/s as magnitudes of vector differences between winds at the surface and 6 km (*Fig. 3b*). These parameters are good indicators regarding the large chance of developing supercells (*Thompson et al.*, 2003).

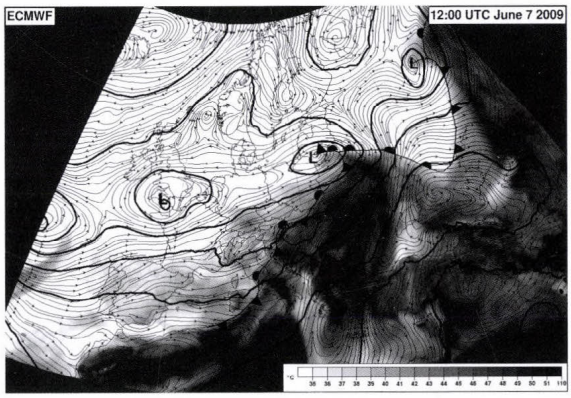

Fig. 3a. The synoptic situation of the waving front over Central Europe at 12:00 UTC, on June 7, 2009 according to the ECWMF analysis. Shading represents the equivalent potential temperature field (in Celsius) at 850 hPa, black solid lines denote the geopotential height of the 850 hPa pressure level (contoured with 40 m intervals), streamlines denote the wind at 850 hPa. Letter L denotes low heights (low pressures).

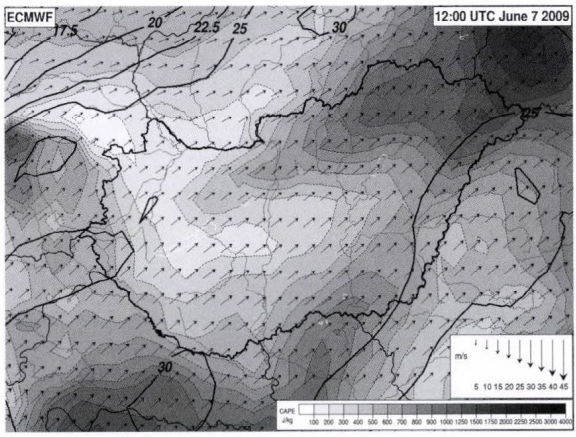

Fig. 3b. Convective available potential energy (shaded), 0–6 km vertical wind shear (magnitude of the vector difference, m/s, solid black lines), and 0–6 km mean wind (black arrows) at 12:00 UTC, on June 7, 2009 above Hungary according to the ECWMF 12:00 UTC analysis.

According to composite radar images generated in every 15th minute, the supercell developed at 12:30 UTC over the central part of Hungary, then rapidly propagated (with an average speed of 75 km/h) northeastward, passed north of Nyíregyháza, left the country at 14:30 UTC, and dissipated at 16:30 UTC in Ukraine. Thus, its lifetime reached three and a half hours. The reflectivity inside the hail storm reached its maximum value of 67.5 dBz at 13:45 UTC (*Fig. 4*). Based on news reports, the cell caused the most hail-related damages along the line of Tiszavasvári-Nyírszőlős-Kemecse-Nyírbogdány-Demecser-Berkesz villages (see their location in *Fig. 4*). Voluntary observers reported maximum hailstone size of around 4 cm (*Fig. 5*).

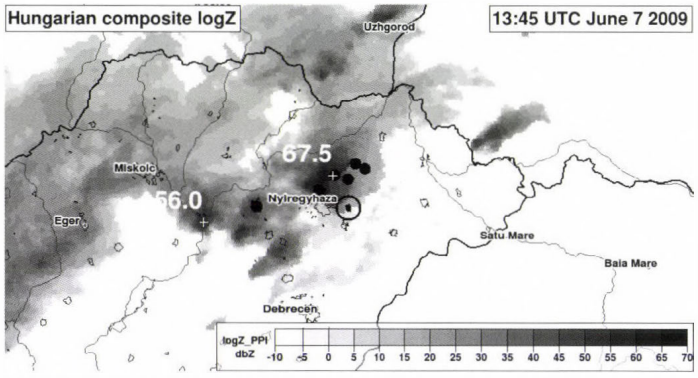

Fig. 4. Observed radar picture of the simulated thunderstorm at 13:45 UTC, on June 7, 2009. Shading represents the intensity in dBz, which is the column maximum reflectivity. Maximum values are indicated by white numbers. Villages exposed to large, damaging hail are denoted by dots. The location of the closest radar site (Napkor) is depicted by a black circle. The direction of propagation of the storm is denoted by a black arrow.

Fig. 5. Observed typical hail sizes in the villages (see text) crossed by the supercell on June 7, 2009. (Source: idokep.hu)

Analysis of reflectivity and radial velocity data proved that the hailstorm was a supercell with considerable rotational features. The storm moved along slightly north to the location of the radar at Napkor, east of Nyíregyháza (as seen in *Fig. 4*). According to the results of the analysis of Doppler radar data (*Fig. 6*), the storm did not showed features of low-level rotation in its development phase (from its formation at around 12:30 UTC to 14:30 UTC). However, considerable midlevel vortex (not shown) and, as a sign of highly sheared environment, a significant weak-echo region (WER) with high-reflectivity regions aloft on its downshear (to the east) side (not shown) were detected. After the storm passed Napkor, between 13:45 and 14:00 UTC, a well-visible hook echo feature developed on its southern side accompanied by a bounded weak echo region (BWER), and a vault extended on its downshear flank. At the same time, a low-level vortex (depicted by a rectangle in *Fig. 6*) formed around the hook echo region. According to *Lemon* and *Doswell* (1979), these features suggest that the hailstorm – during the long period of its lifetime – behaved as a supercell storm.

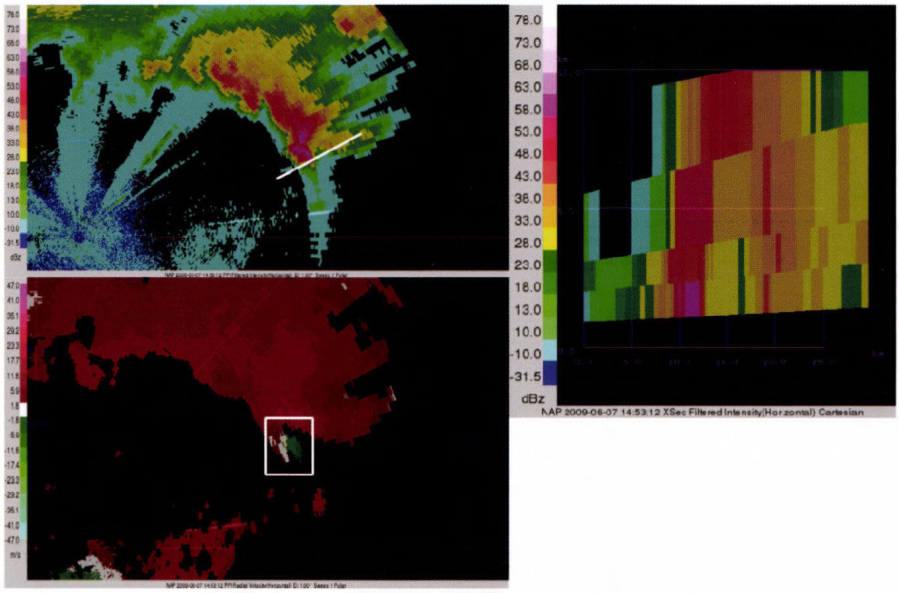

Fig. 6. PPI reflectivity (upper left), storm-relative radial velocity (lower left) at an elevation angle of 1 degree and vertical cross section of reflectivity (right) through the storm observed by the Napkor radar at 14:53 UTC, on June 7, 2009. Circles in the pictures on the left depict distances of 30 km, 48 km, and 115 km from the radar. The white line in the PPI denotes the orientation of the cross-section on the right. In the radial wind picture, red colors indicate approach, greenish colors mean drawing-away. The rectangle on the left lower picture encloses the area of significant radial shear, i. e., the location of a mesocyclone which has an altitude of around 1 km.

3.2. Results of numerical Simulation

The Simulations of WRF were initialized at 06:00 UTC, June 7, 2009 from the 00:00 UTC, June 7, 2009 ECMWF run, and was run until 18:00 UTC, June 7, 2009. The finest, 100 m grid (Simulation2) extended to a 44 km × 30 km area (440 × 300 horizontal grid points) was located in the path of storm formed in Simulation1.

3.2.1. Verification

The simulated reflectivity data on both grids at a given time are shown in *Fig. 7*. The reflectivity structure of the simulated thunderstorm is similar to that of the observed one (*Fig. 4*): an isolated high-reflectivity core with a significant gradient at the southern part of the cell and a much smoother gradient downstream with an accompanying larger scale weak-reflectivity pattern can be observed both in *Fig. 4.* and *Fig. 7.* These features indicate the presence of a supercell with rotating mesocyclone in a highly sheared environment.

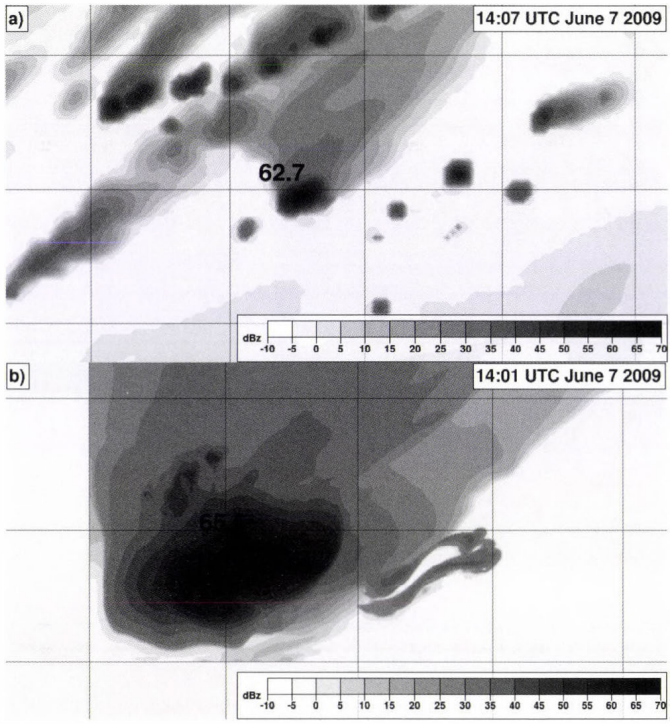

Fig. 7. Calculated column-maximum reflectivity in dBz a) in Simulation1 at 14:07 UTC and b) in Simulation2 at 14:01 UTC, June 7, 2009. The numbers denote the maximum values. The square boxes represent 25 km × 25 km and 10 km × 10 km areas in a) and in b), respectively.

Time evolution of both simulated and observed maximum values of reflectivity can be seen in *Fig. 8a*, which shows that Simulation1 underestimated the intensity of the cell throughout its lifetime. In the case of Simulation2, the cell entered Nest 2 has a maximum reflectivity of 62 dBz, and five minutes later it reached 66 dBz. These values are much closer to the observed ones than the simulated reflectivity values in the case of Simulation1. Note, that data for this high reflectivity core are only available between 13:45 and 14:30 UTC in Simulation2, because Nest 2 was rather small (only 44 km × 30 km), and the fast-moving cell (at a speed of about 55 km/h) quickly passed it.

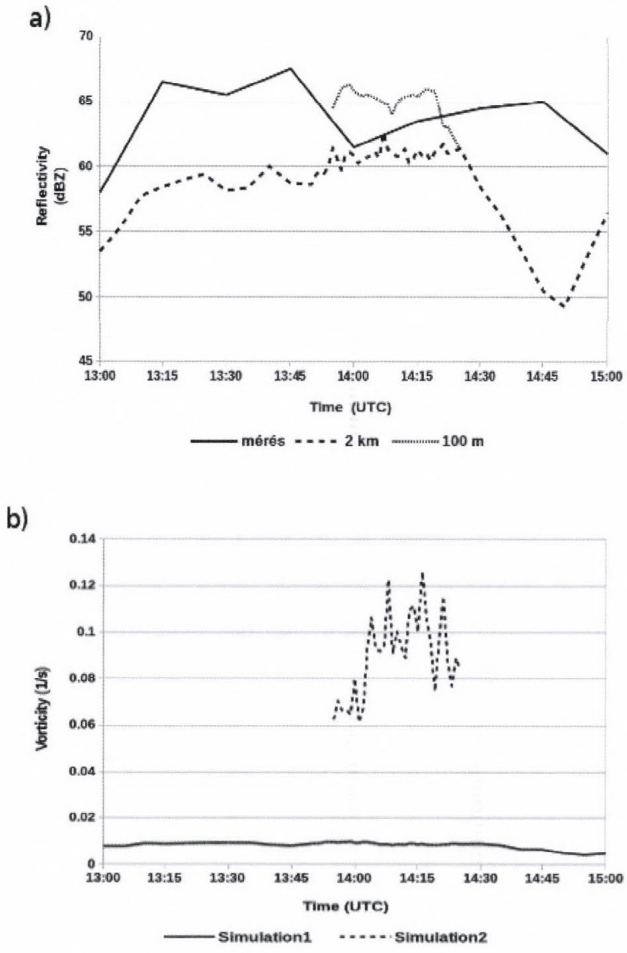

Fig. 8. Time evolution of a) the observed and simulated maximum reflectivities and b) the maximum relative vertical vorticity in the supercell in the case of Simulation1 and Simulation2 on June 7, 2009.

In order to assess the model's capability of simulating the dynamics and related structures of the supercell, spatial and temporal evolution of the vertical vorticity field were also investigated. *Fig. 8b* shows the time evolution of maximum midlevel (between 3 and 7 km) vertical vorticities. In the case of Simulation1, the maximum vertical vorticity remains near to 0.01 1/s (or slightly below). On the other hand, the supercell in Simulation2 developed a much more intense vortex with values larger than 0.06 1/s (for a short time even larger than 0.1 1/s). Horizontal cross-sections of vertical vorticity field around the simulated cell at a certain time step, together with other ultimate parameters, are plotted in *Fig. 9*. The cross sections are given at the height of 5 km, thus they characterize the midlevel structure of the storm. In the case of Simulation1 (*Fig. 9a*), an area of a strong updraft with vertical velocities between 20 and 30 m/s is coupled with moderately strong positive vertical vorticity in such a way, that the maximum of vertical vorticity lies on the right flank of maximum updraft velocities. This configuration corresponds well with both the observational (*Lemon* and *Doswell*, 1979) and simulated (*Klemp*, 1987) structures of supercells. The intensity of vertical vorticity hardly reaches the value of 0.01 1/s, which is a threshold for the formation of a mesocyclone (*Doswell*, 1996). The accompanying storm-relative streamlines show no pure vortices (the streamlines are curved but not enclosed). However, the areas of downdraft (indicated by the rainwater at the surface) and the updraft are horizontally well separated, which is a necessary condition for long-lived thunderstorms (*Browning*, 1968). Similar structure developed in the case of Simulation2 (*Fig. 9b*). The features are more obvious than in the case of Simulation1. The vertical vorticity is more intense (with maximum value of 0.05 1/s); the closing streamlines depict a true cyclonic vortex to the right of the updraft and a pure anticyclonic vortex deep in the precipitation zone; and the surface rain mixing ratio is much higher (above 10 g/kg), as well. It can be concluded that both Simulations were able to catch the essential structure of supercell, but the Simulation with finer resolution generated a cell with much more expressed features.

3.2.2. Comparison and evaluation of microphysical properties and production terms of graupel/hail of Simulation1 and Simulation2

The time evolution of maximum in-storm values of mixing ratios of all hydrometeor categories (cloud water, cloud ice, rain, snow, and graupel/hail) in Simulation1 and Simulation2 are plotted in *Figs. 10a* and *b*. The spatial resolution seems to have a significant effect on the amount of the precipitation particles. The simulation with finer resolution produced larger maximum mixing ratios of graupel/hail particles and that of rain water (*Fig. 10a*). The mean maximum mixing ratios of these precipitation species are 3–4 g/kg and 5–7 g/kg higher in the case of Simulation2 than in the case of Simulation1. No significant differences were found in the case of maximum mixing ratio of the snow. If we

assess the differences in cloud particle mass (cloud water and ice) and relative humidity maximum between the two resolutions (*Fig. 10b*), then the following conclusions can be drawn: while Simulation1 and Simulation2 give similar maximum cloud water mixing ratios (~2–4 g/kg), the maximum value of cloud ice mixing ratio is significantly larger in the case of Simulation1, than in Simulation2 (~0.4–0.6 g/kg versus ~0.2 g/kg). The obtained in-cloud (above 3km) maximum water vapor mixing ratio was about 6–7 g/kg on both grids with a bit higher value on the 100 m resolution grid.

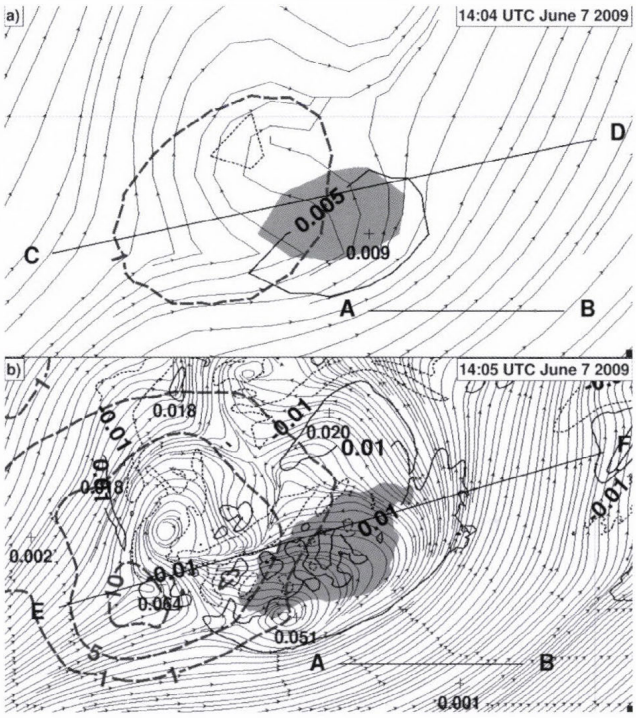

Fig. 9. Simulated horizontal, storm-relative streamlines; relative vertical vorticity (light solid contour of positive values; light dashed contours of negative values); vertical velocity (grey shaded area above the value of 20 m/s) at z=5 km, and rainwater mixing ratio (dark grey bold dashed contours of 1, 5, and 10 g/kg) at z=50 m.
a) in Simulation1 at 14:04 UTC on, June 7, 2009. As for vertical vorticity, only the 0.005 1/s and –0.005 1/s isolines are shown. The length of AB line is 10 km. The CD line represents the horizontal orientation of the vertical cross section in *Figs. 13a* and *b*, and *Figs. 14a* and *b*.
b) in Simulation2 at 1405 UTC on, June 7, 2009. As for vertical vorticity, only the 0.01 1/s and –0.01 1/s isolines are shown. The length of AB line is 2,5 km. The EF line represents the horizontal orientation of the vertical cross section in *Figs. 13c* and *d*, and *Figs. 14c* and *d*.
In both pictures, the local maximum values of vertical vorticity (1/s) are indicated by numbers.

The microphysical processes regarding the formation of graupel/hail in the cloud were analyzed by plotting the time evolution of the production terms of graupel/hail mass. The following production terms are included in the Tompson's scheme (without the melting): deposition/sublimation of water vapor onto/from the graupel/hail surface (gde), conversion of snow into graupel/hail due to riming (sgc), freezing of supercooled rainwater (frz), collision of rainwater and snow (rcs), collection/accretion of graupel/hail by cloud water (gcw), collision of rainwater and graupel/hail (rcg), freezing of rainwater by its collision with cloud ice (rci), and graupel/hail production due to ice multiplication during riming process (ihm) (*Hallet* and *Mossop*, 1974). These production terms were averaged around the location of the maximum mixing ratio of graupel/hail in a volume, which involves 3×3 (in Simulation1) and 60×60 (in Simulation2) grid points horizontally (each represents a 6 km × 6 km square) and 3 grid points vertically (in both simulations). Note, that results of Simulation2 are plotted only between 13:55 and 14:25 UTC because this was the time period when the cell stayed inside of Nest 2.

Time evolution of the production terms in *Figs. 10c* and *d* show that the larger amount of graupel/hail in the case of Simulation2 is the consequence of the considerably larger freezing rate of rainwater (the difference between Simulation2 and Simulation1 is about an order of one magnitude). Subsequently, the amount of graupel/hail further increased due to the more efficient accretion by supercooled cloud water drops (this latter production term is two times larger in Simulation2 than in Simulation1). The riming of cloud ice by cloud water acts as a strong sink of cloud ice (much more efficient than cloud ice-rain collision). Because the formation of snow is more efficient due this process in Simulation2 than in Simulation1 (not shown), more cloud ice particles remain in the latter case. As a consequence, the graupel/hail production due to rain-ice collision is significantly larger in Simulation1 than in Simulation2. The height of maximum graupel/hail mixing ratio is larger in Simulation2 than in Simulation2 during the first half of the 13:55–14:25 UTC time period (slightly below 7 km in Simulation1 and between 7–8 km in Simulation2). After this time period, it rapidly decreases below 5 km in Simulation2 (in Simulation1 the decrease is gradual).The larger height of maximum in Simulation2 can be attributed to the larger vertical velocities (see next paragraph), which can transport the graupel/hail mass to higher altitudes.

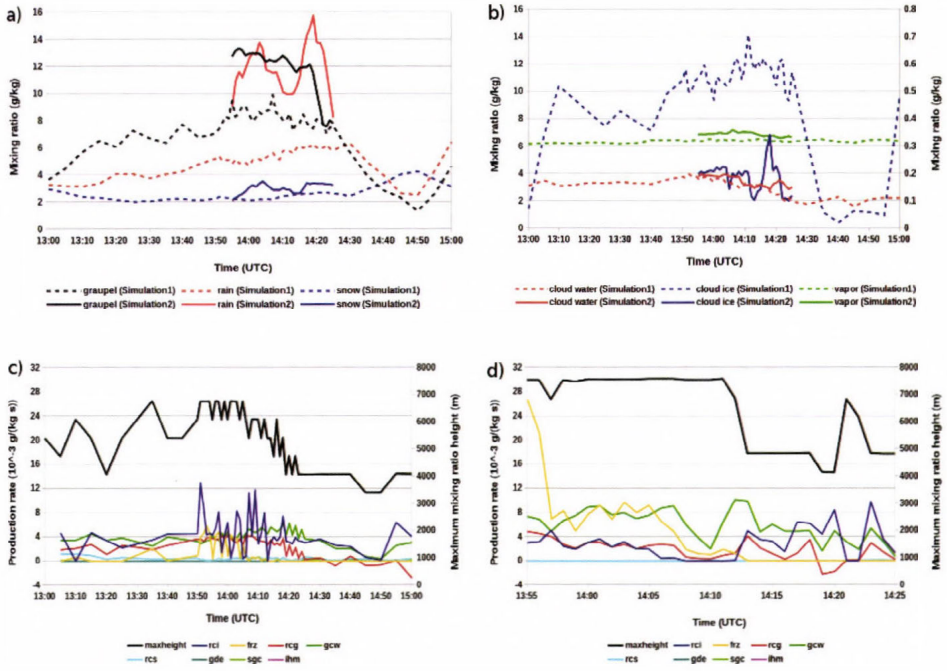

Fig. 10. Time evolution of maximum in-storm values of a) precipitation particles (graupel, rain, and snow in g/kg), b) cloud particle mixing ratios (g/kg) of both nests. c) and d) shows the tendency of graupel production terms (in mg/kg s) averaged around the maximum graupel mixing ratio (see text) in Simulation1 and Simulation2, respectively. For the description of abbreviations in the legend of c) and d) see text. Curve maxheight represents the height (above ground level) of the maximum graupel mixing ratio.

Maximum of updraft and downdraft velocities in the vicinity of the maximum mixing ratio of graupel/hail and the time evolution of maximum graupel/hail mixing ratio on the surface are plotted in *Fig. 11*. In the case of the updraft, vicinity means that the maximum values are chosen from a volume contains $3 \times 3 \times 5$ and $11 \times 11 \times 5$ grid points around the location of the graupel/hail maximum in Simulation1 and Simulation2, respectively. The maximum value of downdraft was taken from a volume contains the location of maximum graupel/hail mixing ratio on the surface. The bottom of this volume is on the surface, its horizontal extension is the same as it was mentioned above. The depth of the volume is 6 km. The maximum vertical velocity was larger in the case of Simulation2 (peaked at around 35 m/s) than in Simulation1 (below 30 m/s, around 25 m/s) almost all the time during the simulation. This difference could explain why maximum graupel/hail mixing ratios aloft is greater in Simulation2. The stronger updraft could hold up larger amount of graupel/hail

aloft, and the larger vertical velocity might resulted in larger upward vapor flux, which subsequently could promote the enhanced production of rainwater and graupel/hail. Furthermore, due to larger condensation rate, more latent heat is released which could further intensify the updraft. The strong relation between the updraft intensity and the maximum mixing ratios of precipitation particles aloft is clearly visible by comparing the plots in *Fig. 11* and *Fig. 10a*. These figures show that the time evolution of the maximum of mixing ratios (both rain and graupel/hail) and maximum of updraft velocities run parallel. On the surface, the maximum of graupel/hail mixing ratio is considerably larger in Simulation2 than in Simulation1. Sometimes this difference is as large as one order of magnitude (~2–3 g/kg in Simulation2 and 0.3–0.6 g/kg in Simulation1). This is the consequence of the larger maximum mixing ratio of graupel/hail aloft in Simulation2. The larger amount of graupel/hail aloft generates stronger downdraft by loading, evaporative cooling, and melting effects. This is the reason why stronger downdraft developed in the case of Simulation2 than in the case of Simulation1 (~10–15 m/s versus ~5 m/s).

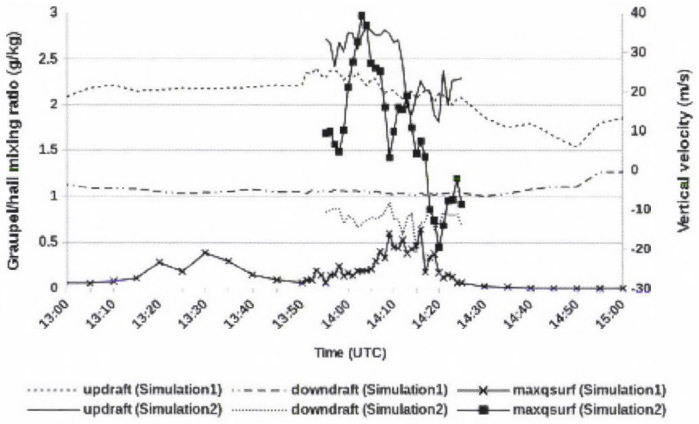

Fig. 11. Time evolution of maximum updrafts and downdrafts (m/s) and the mixing ratios of graupel particles at the lowest model level (g/kg) in the simulated cells in both cases.

It is important to clarify, whether these above mentioned differences between the results of Simulation1 and Simulation2 on the surface are valid also for the volume integrated values of graupel/hail mixing ratios, or they represent the differences only for the maximum values. This problem is critical if the amount of the hail on surfaces is intended to be forecast. Time evolutions of graupel/hail mixing ratios integrated over a square of 196 km^2 are plotted in *Fig. 12*. The location of the center of this square is fitted to the grid point where the mixing ratio of the graupel/hail has maximum value on the surface. *Fig. 12*

also shows the time evolution of the extent of the region where the graupel/hail mixing ratio exceeded 0.001 g/kg on the surface. The comparison of the curves shows, that not only the maximum graupel/hail mixing ratio is larger in Simulation2, but the total amount of graupel/hail mass is also significantly greater. In the case of the areas where the mixing ratio of the graupel/hail is larger than 1 mg/kg, the difference between the two Simulations is not significant, yet Simulation1 gives larger area during a relatively long time period.

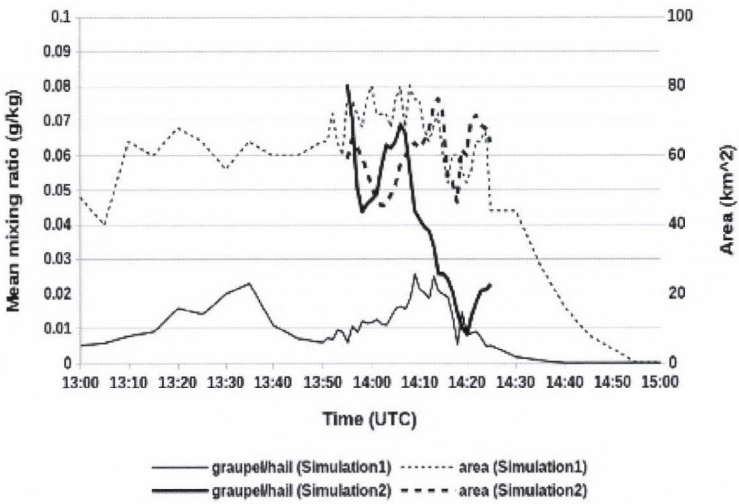

Fig. 12. Time evolution of mean values of graupel particle mixing ratios (g/kg) and the area of graupel mixing ratios above 0.001 g/kg (km^2) at the lowest model level in the simulated cells in both nests for the June 7, 2009 case.

The influence of the spatial resolution on the microphysical properties of the simulated thunderstorm is shown by vertical cross sections of the storm. *Figs. 13a-d* show the cross section calculated in Simulation1 and in Simulation2, respectively. The morphology of the thunderstorm is clearly visible in the case of both resolutions: (i) the horizontally separated updraft and downdraft regions; the rearward tilted updraft region; (ii) the mid-level maximum of the graupel/hail mixing ratios at mid-level; (iii) the WER (in Simulation2, even a slight BWER structure visible at $z = 4$ km – see *Fig. 13d*) at low altitudes due to the intense updraft; (iv) the fall-out of graupel/hail and rain in the rear side of downdraft; (v) the downwind advection of the graupel/hail, snow, and cloud ice (right side of the cross sections) aloft forming an anvil-like structure.

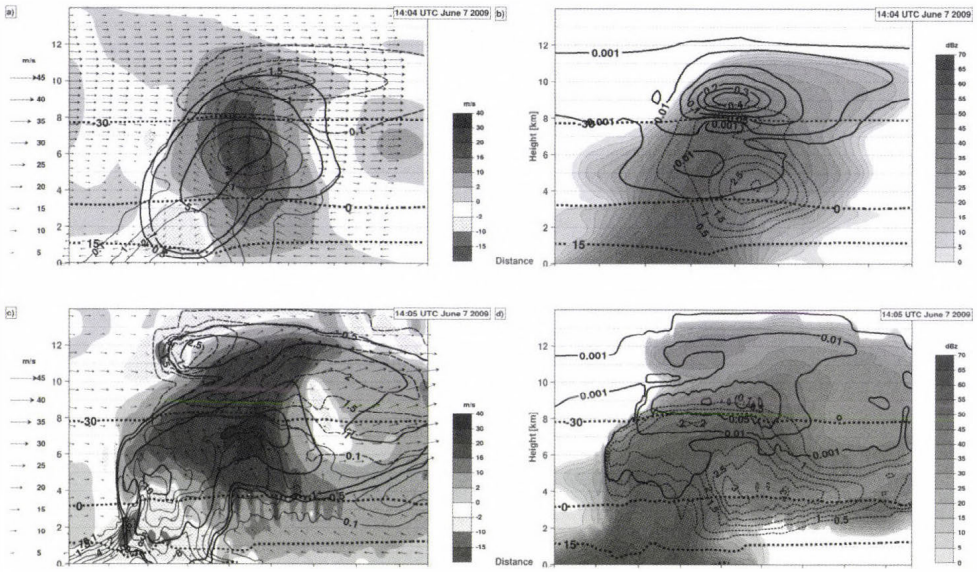

Fig. 13. Vertical cross sections of the thunderstorm in Simulation1 at 14:04 UTC and in Simulation2 at 14:05 UTC on June 7, 2009. The vertical dimension is in km unit. Cross sections in a) and b) were created by Simulation1 and marked by the CD line in *Fig. 9a*. Cross sections in c) and d) were created by Simulation2 and marked by the EF line in *Fig. 9b*. The displayed quantities are the followings:
a) and c): vertical wind speed (shaded), storm-relative streamlines in the plane of the cross section (arrows), graupel mixing ratio (thick solid contours of 0.5, 1, 5, 7.5, 10 g/kg and above 10 g/kg with intervals of 5 g/kg), rainwater mixing ratio (light solid contours of 0.1, 1, and 2 g/kg and above 2 g/kg with intervals of 2 g/kg), and snow mixing ratio (light dashed contours of 0.1, 1 g/kg and above 1 g/kg with intervals of 0.5 g/kg). Thick dashed lines denote the isolines of 15, 0, and –30 °C.
b) and d): simulated radar reflectivity (dBz units), cloud ice mixing ratio (thick solid contours of 0.001, 0.01, and 0.05 g/kg, 0.1 g/kg, and above 0.1 g/kg with intervals of 0.1 g/kg), cloud water mixing ratio (dashed light contours with intervals of 0.5 g/kg), and the isolines of the 0 and –30 °C temperatures (dashed thick contours). Thick dashed lines denote the isolines of 15, 0, and –30 °C.

Nevertheless, the differences between the two cases are also apparent. The updraft intensity in the case of finer resolution is much greater than on the coarser grid (30–40 m/s maximum of updraft velocity in Simulation2 versus 20–30 m/s in Simulation1). The differences in the cloud dynamics correspond to the height of the cloud top. It is about 14 km in the case of Simulation2 and around 12 km in the case of Simulation1 (the cloud ice isoline of 1 mg/kg is defined as an upper boundary of the cloud). The maximum of graupel/hail mixing ratio is between 10–15 g/kg and between 7.5–10 g/kg in Simulation2 (*Fig. 13c*) and in Simulation1 (*Fig. 13a*), respectively. The altitudes of the maximum of graupel/hail mixing ratio are also different in the two cases (~7–8 km versus ~6–

7 km). The mixing ratio of graupel/hail particles on the surface is an important characteristic of the morphology, too. While the isoline of 1 g/kg graupel/hail mixing ratio reaches the surface in Simulation2, even the bottom of the isoline of 0.5 g/kg is above the surface in the case of Simulation1. This means that – in agreements with the previous findings upon the time evolutions in *Fig. 11*, the fine-resolution storm produced considerably greater graupel/hail mixing ratio values on the surface than its coarse-resolution counterpart does. This result has consequences on the the maximum possible hail-size (see Section 3.2.3. for details). In both cases, the location of maximum of graupel/hail mixing ratio mass is in spatial correlation with the maximum of updraft velocity. The significant rearward advection of graupel/hail and rain results in rear-flank downdraft and mixed phase precipitation on the surface (*Figs. 13a* and *c*). The amount of the rain on the surface is almost twice larger in Simulation2 than in Simulation1 (9–10 g/kg versus 4–5 g/kg). Similarly to the previous findings, the high-resolution storm in Simulation2 produced larger simulated radar intensity (*Figs. 13b* and *d*) than in Simulation2 (above 60 dBz versus below 60 dB). It is a remarkable feature that the maximum radar reflectivity is at low-levels in both Simulations which can be attributed to the melting graupel/hail inducing great reflectivity. Considering the isolines of cloud water mixing ratio (*Figs. 13b* and *d*), their structures and maximum values are very similar (~3 g/kg). However, while in Simulation2, the isoline of 1.5 g/kg extends up to 8 km, the top of this isoline is at 6 km in Simulation1. This indicates that due to larger vertical velocities, the cloud water is transported to higher altitudes in Simulation2 than in Simulation1. The cloud ice content is significantly larger in Simulation1 (~0.4 g/kg maximum values) than in Simulation2 (~0.1 g/kg maximum values). In Simulation1, a secondary local maximum can be found at lower levels (between 5 and 6 km). This secondary peak in Simulation2 is absent. The higher amount of cloud ice in Simulation1 can be attributed to the fact that in that simulation, weaker updraft developed which resulted in smaller mean drop diameters. Then the smaller drops transported in sub-zero regions formed ice crystals instead of graupels.

The height of the 0 °C and –30 °C isotherms in *Fig. 13* inside the storms are similar in both cases (height of the 0 °C level is at ~3–4 km, the –30 °C level is at ~8 km). However, in Simulation2, the anomaly of these levels in the updraft region is somewhat larger than in Simulation1. This difference can be explained by the larger releasing latent heat of freezing and condensation in the case of Simulation2. More significant difference can be found if the shapes of the 15 °C isotherms are compared. The shape of this isotherm is affected by the latent heat of cooling due to melting and evaporation. A notable difference is, however, that the maximum of the height anomaly of this isotherm (reaching about several hundreds of meters and being slightly larger in Simulation2) is at the rear edge of the downdraft in Simulation2, while in Simulation1, it is located rather in the forward region of the downdraft.

Not only the intensity of updraft, but the strength of the downdraft is also strongly affected by the spatial resolution (*Figs. 13a* and *c*): the downdraft is more intense in Simulation2 than in Simulation1. The maximum value of downdraft is above 15 m/s in the case of Simulation2 and it is about 10 m/s in the case of Simulation1. Not only the maximum value of the downdraft is larger in the case of Simulation2, but the downdraft region is deeper, as well (~4 km versus ~3 km deep). The overlapping of the downdraft region, the height anomaly of the 15 °C isotherm, and the region where the graupel/hail mixing ratio is large suggest that the intensity of downdraft depends on the loading effect (represented by the sum of the mixing ratios of the precipitation elements – rain and graupel/hail particles) and on the cooling caused by the melting and evaporation of these species.

In order to identify the location and sources of the formation and growth of graupel/hail particles, production terms are plotted in *Fig. 14* in the same vertical cross sections as in *Fig. 13*. The following production terms are considered: (i) accretion of graupel/hail particles by rain drops; (ii) freezing of supercooled rain drops; (iii) freezing of supercooled rain drops due to the collision with cloud ice particles; (iv) riming of graupel/hail particles due collision with cloud drops; (v) collision between rain drops and snowflakes. The other sources, like evaporation/sublimation, snow-graupel/hail conversion through riming, and ice multiplication were found to be negligible comparing to the other, above mentioned terms (see *Fig. 15* for discussion). *Fig. 14* shows that most of the graupel/hail particles were formed in cloud volume between the altitudes of 3 km and 9 km. The vertical extension of this volume does not depend on the applied spatial resolution. Above and below that layer, the existence of graupel/hail is mainly due to the advection/convection and fall-out processes. The midlevel accretion rates of graupel/hail particles (*Figs. 14a* and *c*) by rain are similar in Simulation1 and Simulation2 ($\sim 10 \cdot 10^{-3}$ g/(kg·s)). However, the maximum of the riming rates of graupel/hail particles by cloud water (*Figs. 14a* and *c*) was significantly larger in the case of Simulation2 than in the case of Simulation1. ($\sim 15 \cdot 10^{-3}$ g/(kg·s) versus $\sim 10 \cdot 10^{-3}$ g/(kg·s)), which is a direct consequence of greater transport of cloud water by stronger updraft (refer to *Figs. 13b* and *d*). The larger amount of the rain between the melting level and the surface in Simulation2 (refer to *Fig. 13a* versus *Fig. 13c*) is the consequence of the melting of larger graupel/hail content. The collision between rain and snow much less efficiently produces graupel/hail particles than freezing of the rain drops. In Simulation2, it operates only in the right flank of the midlevel updraft, under the forward sheared anvil, where the snow begins to descend and can encounter to some amounts of rain. However, in the case of Simulation1, besides the anvil region, there is another and more significant maximum of this process in the updraft at around 7 km, as well.

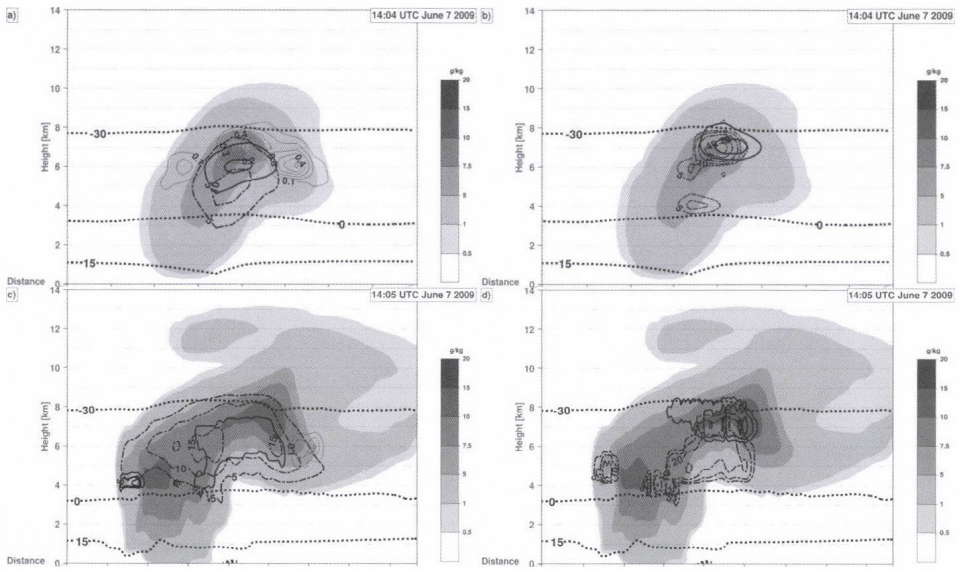

Fig. 14. Vertical cross sections of graupel production terms through the simulated thunderstorm on June 7, 2009 a) and b) in the case of Simulation1 at 14:04 UTC, c) and d) in the case of Simulation2 at 14:05 UTC. The orientation of cross sections is identical to the ones in *Fig. 13* (marked in *Fig. 9*). The displayed quantities are the followings:
a) and c) Shading represents the graupel mixing ratio (scale and legend are displayed in the pictures), thick solid lines show the values of production due to rain and graupel collision (contoured with intervals of $10 \cdot 10^{-3}$ g/(kg·s) and the minimum value is $5 \cdot 10^{-3}$ g/(kg·s)), the thick dot-dashed lines depict the accretion rate of cloud water by graupel (with contour intervals of $5 \cdot 10^{-3}$ g/(kg·s)), the light solid lines represent the collision between rain and snow (with contour intervals of $0.1 \cdot 10^{-3}$ g/(kg·s)) Thick dashed contours represent the isolines of 15, 0 and –30 °C.
b) and d) Shading represents the graupel mixing ratio (the scale and legend is displayed in the pictures), thick solid lines represent the freezing process of supercooled rainwater (contoured with intervals of $10 \cdot 10^{-3}$ g/(kg·s) and the minimum value is $5 \cdot 10^{-3}$ g/(kg·s)), the light dot-dashed lines show the production rate due to collision between rain and cloud ice (contoured with intervals of $10 \cdot 10^{-3}$ g/(kg·s), and the minimum value is $5 \cdot 10^{-3}$ g/(kg·s)). The thick dashed contours represent the isolines of 15, 0 and –30 °C.

The production rate by collision between supercooled rain drops and cloud ice particles (*Figs. 14b* and *d*) is two times smaller in the case of Simulation2 than in the case of Simulation1. This can be due to the larger cloud ice content aloft in Simulation1 (refer to *Fig. 13b*). A local maximum of this production rate can be also observed just above the melting level. This stems from the fact, that the ice crystals can form due to the break of the small ice fragments from the surface of the graupel/hail particles due to the collision between the graupel/hail particles and water drops (ice multiplication – *Hallet* and *Mossop*, 1974). The graupel/hail formation due to the freezing of the supercooled rain drops mostly occur in the region between the height of 6 and 8 km. The freezing rate is about two times larger in the case of Simulation2 than in the case of Simulation1 (~20–$30 \cdot 10^{-3}$ g/(kg·s) versus ~10–$15 \cdot 10^{-3}$ g/(kg·s)).

Time evolution of the volume integrated values of the above mentioned production terms were also investigated. The storm was divided into three volumes: (i) 8–14 km, (ii) 3–8 km, and (iii) 0 (surface) – 3 km. Production terms integrated over these volume characterize the microphysical processes in the low-, mid-, and upper-level parts of the storm. Results are summarized in *Fig. 15*. *Figs. 15a* and *b*, imply a clear evidence, that above $z = 8$ km, the graupel/hail mainly forms by the freezing of supercooled rain water and grows by collecting of supercooled cloud water. Another important process affecting the mixing ratio of graupel/hail is the transport by the vertical velocity (not shown) from lower elevations. Analysis of the plots in *Figs. 15a* and *b* shows that the sum of production terms integrated in time is much lesser than the graupel/hail mass formed in this volume, therefore, there has to be other sources than the productions of it. In the model, the only other source is the transport by convection. This confirms that besides the microphysical processes, the three-dimensional advection also plays important role in the evolution of the three dimensional structure of the graupel/hail particles. Due to the larger updraft in the case of Simulation2, significantly more graupel/hail particles can accumulate in the region above the height of 8km. The stronger convection of the cloud drops results in more efficient graupel/hail formation by freezing and larger riming rate as well.

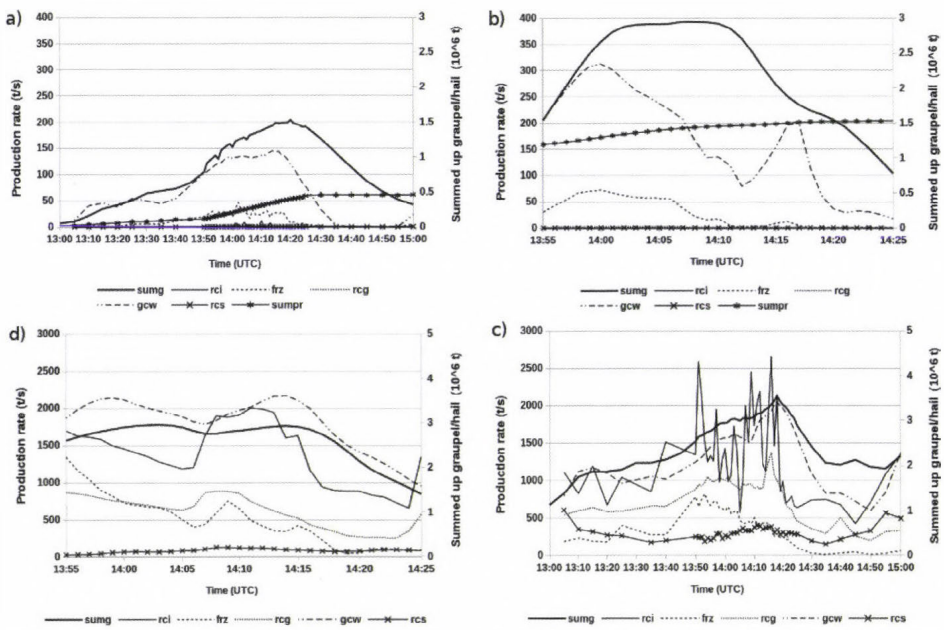

Fig. 15 a)-d). Time evolution of graupel production terms (in t/s), and graupel mass integrated over the volume of the storm a) between 8 and 14 km altitudes in the case of Simulation1, b) between 8 and 14 km altitudes in the case of Simulation2, c) between 3 and 8 km altitudes in the case of Simulation1, d) between 3 and 8km altitudes in the case of Simulation2. Abbreviations are the same as in *Figs. 10 c* and *d*. Curve sumg represents the total graupel content (in 10^6 t). While curve sumpr in a) and b) depicts the sum of all production terms integrated in time (in 10^6 t).

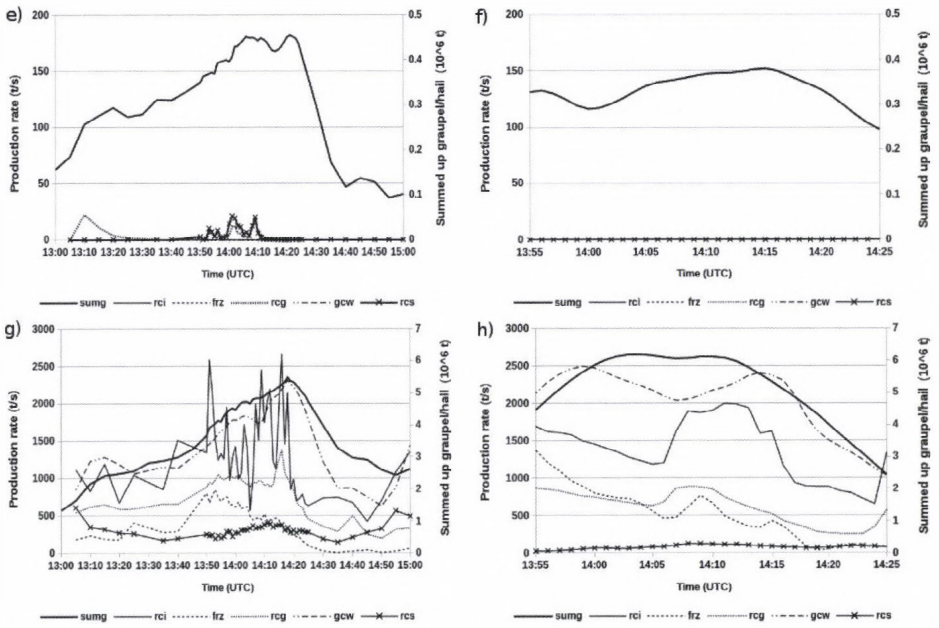

Fig. 15 e)-h). Time evolution of graupel production terms (in t/s), and graupel mass integrated over the volume of the storm e) between 3 km and the surface in the case of Simulation1, f) between 3 km and the surface in the case of Simulation2, g) over the whole column of the storm in the case of Simulation1, h) over the whole column of the storm in the case of Simulation2. Abbreviations are the same as in *Figs. 10 c* and *d*. Curve sumg represents the total graupel content (in 10^6 t).

Most of the graupel/hail content can be found in the middle region (between 3 and 8 km) in both cases (*Figs. 15c* and *d*). While the maximum of the graupel/hail mixing ratio was larger in the case of Simulation2 than in the case of Simulation1, the difference between the volume integrated values is nearly the opposite: the maximum of the volume integrated graupel/hail mass is between $3 \cdot 10^6$ and $4 \cdot 10^6$ T in Simulation1, while in Simulation2 it remains below $3 \cdot 10^6$ T during the Simulation. Most of graupel/hail particles formed by heterogeneous freezing of rain drops and freezing of supercooled rain drops due to collision with cloud ice. The latter process shows a rather hectic behavior with large jumps in intensity in Simulation1 with larger maximum than in Simulation2. This difference between the Simulations can be attributed to the greater cloud ice content in midlevels in Simulation1 (see again *Figs. 13b* and *d*). Formation of the graupel/hail particles was significantly affected by the horizontal resolution. As for the heterogeneous freezing of supercooled rain drops, Simulation2 produced similar rates as Simulation1. The amount of

graupel/hail formed by collision of snowflakes and rain drops was negligible in the case of Simulation2, however, in Simulation1, especially in the first minutes of the period, the snow-rain interaction played non-negligible role in creating graupel/hail (it even exceeds the production rate of the freezing of rain) and was more significant than in Simulation2 throughout the period. Subsequent growth of graupel/hail was largely driven by the accretion processes (accretion by cloud water and rain drops). In both simulations, accretion of graupel/hail by cloud water was more efficient than by rain water.

In the low-level region of the storm, below $z = 3$ km, which is the melting layer, positive values of graupel production are negligible according to *Figs. 15e* and *f*, and there is only one sink term: the sublimation of graupel particles. Production due to collision processes with rain and cloud drops is exactly zero, because in the melting region, all the liquid water amount collided with graupel particles is instantaneously shed to form rain drops. In the case of the total graupel/hail amount in this layer, Simulation1 exceeds the values of Simulation2 at the main part of the integration. This means that the cell in Simulation1 produced more graupel/hail at lower levels than its high-resolution counterpart, though this relation is not valid for the mean graupel/hail values at the surface according to the previous results (see *Fig. 12*). One explanation of this contradiction is that under a certain threshold of mixing ratio, all the graupel/hail particles melt during its falling. If this threshold is exceeded – this could be the case in Simulation2, where we found higher maximum values –, then there is some amount of solid particles which do not melt and, therefore, reach the surface. Based on these results, we can state that compared to its coarser counterpart, the finer resolution Simulation created a storm which produced higher low-level maximum values of graupel/hail mixing ratio but less total graupel/hail content than the storm simulated on the coarser resolution.

Figs. 15g and *h* shows that the total amount of graupel/hail formed in the whole cloud volume only slightly depends on the horizontal resolution ($6 \cdot 10^6$T in the case of Simulation2 versus $5.5 \cdot 10^6$ T in the case of Simulation1). In both cases, most of the graupel/hail particles formed by freezing of supercooled rain due to collision with cloud ice and due to heterogeneous freezing. In both Simulations, the first process is dominant over the second one. While in Simulation1 there is a non-negligible contribution to graupel/hail production by the rain-snow collision, this process has a negligible effect in the case of Simulation2. The graupel/hail particles subsequently grow by collision with cloud and rain water. The accretion by cloud water was more efficient than by rain water, in both simulations.

3.2.3. Results of the maximum hail size calculation method

According to Eqs. (4) and (6), the maximum size of the graupel/hail particles is a function of their mixing ratio. The shape of this function is similar to that of

the square root function (*Fig. 16*). This means that the value of the maximum hail size is more sensitive to the mixing ratio if the value of the mixing ratio is small, and near linearly increases with the mixing ratio above the value of 4 g/kg. Because Simulation1 and Simulation2 cases gave different amounts of graupel/hail on the surface (*Fig. 11*), the maximum hail sizes are expected to be also significantly different. Time evolutions of the largest maximum hail size on the surface are plotted in *Fig. 17*. The figure shows that the maximum hail size calculated by Simulation1 was less than 2 cm during most of the Simulation time; it increases above 2 cm only in a short time period of 10 minutes. However, the forecast maximum hail size in Simulation2 is above 3 cm almost throughout the whole time period and comes near to maximum value of 5 cm. According to the photo documentations and inflicted damages described in Section 3.2.1., the implemented hail size method yielded diameters closer to the observations in the case of Simulation2 than in the case of Simulation1.

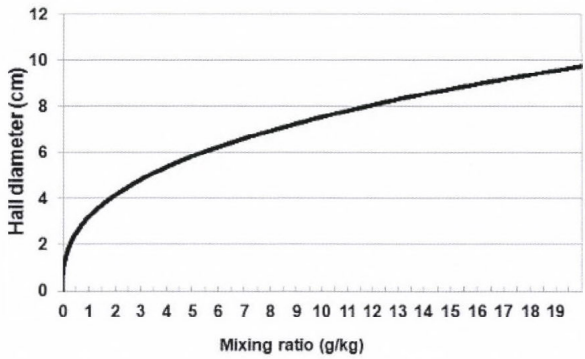

Fig. 16. The dependence of the hail size diameter (calculated by the method - cm) on the graupel mixing ratio (g/kg). The calculation was done in an environment of the following atmospheric conditions: T (temperature) = 25 °C, P (pressure) = 101000 Pa, r (water vapor mixing ratio) = 5 g/kg.

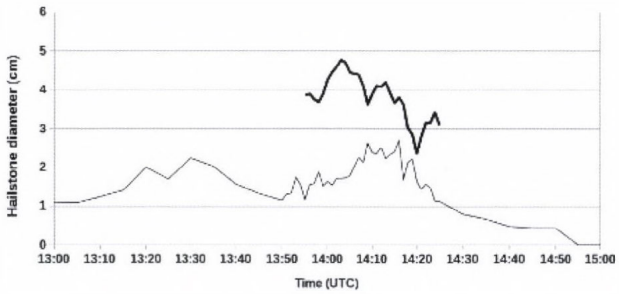

Fig. 17. Time evolution of the maximum hail size at the lowest model level. Light and thick solid lines denote the forecast maximum sizes in the case of Simulation1 and Simulation2, respectively. The units are cm (as diameters).

To illustrate the typical horizontal distribution of the expected hail sizes on the ground, horizontal cross sections of calculated hail sizes at the lowest model level are displayed at a given time in *Figs. 18a* and *b*. The maximum values in Simulation1 slightly exceeds 2.5 cm in one grid point which represents a 4 km^2 area. The maximum in-storm hail size in the finer simulation is above 4.5 cm on an area of roughly 1 km^2, and the isoline of 2.5 cm encloses an area of around 8 km^2, which is twice as high as in Simulation1. That is, the simulation with higher resolution resulted in not only larger maximum hail sizes, but the area exposed by these larger hail stones is also significantly larger in Simulation2 than in Simulation1.

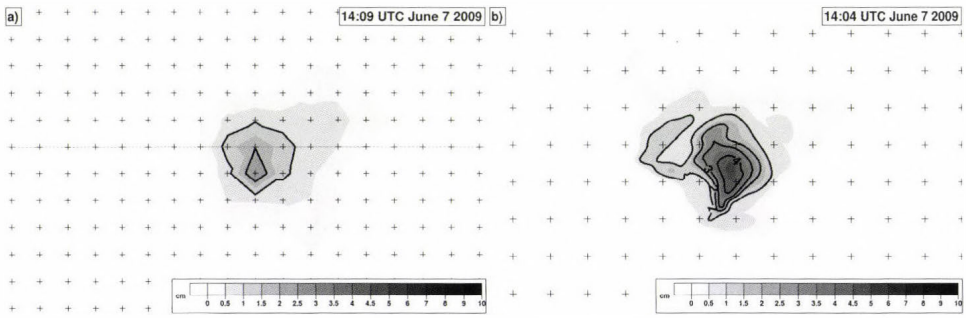

Fig. 18. Horizontal cross sections of the maximum hail sizes produced by the storm at the lowest model level a) Simulation1 at 14:09 UTC and b) Simulation2 at 14:04 UTC. The scale of the shading is as in the legend, its isolines are denoted by black solid lines. The distance between two neighboring crosses represents 2 km on both nests.

4. Summary and conclusion

In this paper, an algorithm was developed to evaluate a forecast method for the maximum hail size on the ground. The input data for this algorithm are given by WRF-ARW model with the Thompson's one-moment microphysical scheme, which treats graupel and hail as one hydrometeor category (graupel/hail). Besides that, a detailed analysis was made to reveal the dependence of microphysical processes (focusing on the graupel/hail formation and growth) on the horizontal resolution. The results were evaluated on two nests with horizontal resolution of 2 km (Simulation1) and 100 m (Simulation2). In order to better understand the mechanisms led to graupel/hail formation in the cloud, the production terms responsible for the graupel/hail formation and growth were also analyzed. A case study of a supercell produced large and damaging hail was selected to achieve these goals. Both Simulations were able to reproduce the main characteristics of the observed supercell, such as: radar reflectivity,

morphology, and vorticity fields. On the other hand, the details of these properties were significantly better simulated if the finer resolution was used.

The Simulation with finer resolution resulted in larger maximum values of graupel/hail and rain mixing ratios, but smaller maximum mixing ratios of cloud ice were calculated. The location of the maximum of graupel/hail mixing ratio was found in the updraft region between the heights of 5 and 8 km in both cases. The maximum values of cloud water and snow mixing ratio were found to be similar in both Simulations. Although the maximum of the graupel/hail mixing ratio was significantly larger in the case of Simulation2 than in the case of Simulation1, considering the total mass of graupel/hail particles in the storm, the two Simulations produced almost the same amount. The higher maximum values can be explained by the stronger updrafts occurred in the case of Simulation2. The stronger updraft resulted in more intense upward flux of water vapor, and it was able to held larger amount graupel/hail aloft. In addition, due to the stronger updraft in Simulation2, the maximum graupel/hail mixing ratio was located at higher altitudes than in Simulation1. The maximum of downdraft velocity was also larger in the case of Simulation2 due to the larger loading effect and cooling rate by melting and evaporation.

The graupel/hail in the storm formed mainly by the freezing of supercooled rain due to its collision with cloud ice, and secondly, by the heterogeneous freezing of supercooled rain. Nevertheless, the latter process was more intense in the finer Simulation than in its counterpart, while the rain-cloud ice collision at times was found more effective graupel/hail producer in Simulation1 than in Simulation2. This latter difference and the smaller maximum of graupel mixing ratio aloft, too, can be attributed to the larger amount of cloud ice remained in Simulation1, because the weaker updraft in that case produced smaller water drops which subsequently formed ice crystals instead of graupel particles. In addition, in the case of Simulation1, rain-snow collision resulted in significant amount of graupel/hail. The formed graupel/hail content subsequently grew mainly by the accretion by cloud water, and to a lesser extent, the accretion by rain water. However, the overall greater formation rate of graupel/hail resulted in more efficient accretion. The analysis of production terms in the various layers of the storm shows, that the most of the graupel/hail particles were formed between the height of 3 and 8 km, while above and below of this layer, the graupel/hail particles were mainly transported by the advection and by their fallout falling.

The application of both Simulations resulted in reasonable maximum hail size on the surface. However, significantly larger maximum hail size (around 4 cm) was forecast in the case of Simulation2 than in the case of Simulation1 (about 2 cm). In addition, the horizontal extent of the area with large hail size (above 2 cm) was about twice larger in the case of Simulation2than in the case of Simulation1.

The method for the forecast of maximum hail size can be applied not only in supercell cases but with ordinary and multicell storms, as well. Therefore, in the future, more case studies involving these types of storms must be elaborated to test the universal abilities of this method. In addition, numerical Simulation with other two-moment microphysics schemes (*Morrison et al.*, 2005; *Milbrandt* and *Yau*, 2005; etc.) which allow greater degree of freedom on the size distribution should be performed to investigate their effect on the surface. Though the Simulation on the 100 m resolution nest was performed with applying a PBL scheme, it is necessary to clarify whether using a LES closure in that range ("terra incognita") would lead to consistent results.

References

Adlerman E.J., and *Droegemeier, K.K.*, 2002: The sensitivity of numerically simulated cyclic mesocyclogenesis to variations in physical and computational parameters. *Mon. Weather Rev. 130*, 2671–2691.

Brimelow, J.C., Reuter, G.W., and *Poolman, E.P.*, 2002: Modeling maximum hail size in Alberta thunderstorms. *Weather Forecast. 17*, 1048–1062.

Brimelow, C. and *Reuter, G.W.*, 2006: Spatial Forecasts of Maximum Hail Size Using Prognostic Model Soundings and HAILCAST. *Weather Forecast. 21*, 206–219.

Browning, K.A., 1968: The organization of severe local storms. *Weather 23*, 429–434.

Bryan, G.H., Wyngaard, J.C., and *Fritsch, J.M.*, 2003: Resolution requirements for the simulation of deep moist convection. *Mon. Weather Rev. 131*, 2394–2416.

Changnon, S.A., Pielke, R.A. Jr., Changnon D., Sylves, R.T., and *Pulwarty, R.*, 2000: Human factors explain the increased losses from weather and climate extremes. *B. Am. Meteorol. Soc. 81*, 437–442.

Craig, C.G. and *Dörnbrack, A.*, 2008: Entrainment in cumulus clouds: What resolution is cloud-resolving? *J. Atmos. Sci. 65*, 3978–3988.

Ćurić, M., and *Janc, D.*, 1989: The behavior of a hailstone in a forced 1-D Cb cloud model. *Meteorol. Atmos. Phys.* 41, 45–54.

Ćurić, M., and *Janc, D.*, 1993: Predictive capability of a one-dimensional convective cloud model with forced lifting and a new entrainment formulation. *J. Appl. Meteorol. 32*, 1733–1740.

Doswell III, C.A., 1996: What is a supercell?. Preprints 18th Conf. Severe Local Storms (San Francisco, CA). Amer. Meteor. Soc, 641.

Farley, R.D. and *Orville, H.D.*, 1986: Numerical Modeling of Hailstorms and Hailstone Growth. Part I: Preliminary Model Verification and Sensitivity Tests. *J. Climate Appl. Meteorol. 25*, 2014–2035.

Farley, R.D., 1987a: Numerical Modeling of Hailstorms and Hailstone Growth. Part II: The Role of Low-Density Riming Growth in Hag Production. *J. Clim. Appl. Meteorol. 26*, 234–254.

Farley, R.D., 1987b: Numerical Modeling of Hailstorms and Hailstone Growth. Part III: Simulation of an Alberta Hailstorm—Natural and Seeded Cases. *J. Clim. Appl. Meteorol. 26*, 789–812.

Fawbush, E.J., and *R.C. Miller*, 1953: A method of forecasting hailstone size at the earth's surface. *Bull. Amer. Meteorol. Soc. 34*, 235–244.

Fiori, E., Parodi, A., and *Siccardi, F.*, 2010: Turbulence Closure Parameterization and Grid Spacing Effects in Simulated Supercell Storms. *J. Atmos. Sci. 67*, 3870–3890.

Geresdi, I., 1990: Two-dimensional simulation of a small hailstorm. *Időjárás 94*, 346–359.

Geresdi, I., 1996: Precipitation formation in a severe thunderstorm. *Atmos. Res. 41*, 71–81.

Geresdi, I., 1998: Idealized simulation of the Colorado hailstorm case: Comparison of bulk and detailed microphysics. *Atmos. Res. 45*, 237–252.

Geresdi, I., Horváth, Á., and *Mátyus, Á.*, 2004: Nowcasting of the precipitation type Part II: Forecast of thunderstorms and hailstone size. *Időjárás 108*, 33–49.

Grabowski, W.W., Wu, X., Moncrieff, M.W., and *Hall, W.D.,* 1998: Cloud-resolving modeling of tropical cloud systems during phase III of GATE. Part II: Effects of resolution and the third spatial dimension. *J. Atmos. Sci. 55*, 3264–3282.

Grell, G.A., and *Dévényi, D.,* 2002: A generalized approach to parameterizing convection combining ensemble and data assimilation techniques. *Geophys. Res. Lett., 29(14),* Article 1693.

Hallett, J., and *Mossop, S.C.,* 1974: Production of secondary ice particles during the riming process, *Nature 249*, 26–28.

Horváth, Á. and *Geresdi, I.,* 2003: Severe storms and nowcasting in the Carpathian Basin. *Atmos. Res., 67–68*, 319–332.

Horváth, Á., Geresdi, I., Németh, P., Csirmaz, K., and *Dombai, F.,* 2009: Numerical modeling of severe convective storms occurring in the Carpathian Basin. *Atmos. Res. 93*, 221–237.

Johnson, D.E., Wang, P.K., and *Straka, J.M.,* 1993: Numerical Simulations of the 2 August 1981 CCOPE Supercell Storm with and without Ice Microphysics. *J. Appl. Meteorol. 32*, 745–759.

Johnson, D.E., Wang, P.K., and *Straka, J.M.,* 1995: A study of microphysical processes in the 2 August 1981 CCOPE supercell storm. *Atmos. Res. 33*, 93–123.

Klemp, J.B., 1987: Dynamics of tornadic thunderstorms. *Annual Rev. Fluid Mech. 19*, 396–402.

Lemon, L.R., and *Doswell III, C.A.,* 1979: Severe thunderstorm evolution and mesocyclone structure as related to tornadogenesis. *Mon. Weather Rev. 107*, 1184–1197.

Mellor, G.L. and *Yamada, T.*, 1982: Development of a turbulence closure model for geophysical fluid problems. *Rev. Geophys. Space Phys.*, 20, 851–875.

Milbrandt, J.A. and *Yau, M.K.,* 2005: A multimoment bulk microphysics parameterization. Part I: Analysis of the role of the spectral shape parameter. *J. Atmos. Sci. 62*, 3051–3064.

Milbrandt, J.A. and *Yau, M.K.,* 2006: A Multimoment Bulk Microphysics Parameterization. Part III: Control simulation of a Hailstorm. *J. Atmos. Sci. 63*, 3114–3136.

Miller, R.C., 1972: Notes on analysis and severe-storm forecasting procedures of the Air Force Global Weather Central. Air Weather Service Tech. Rep. 200 (Rev.), Air Weather Service, Scott Air Force Base, IL, 190 pp. [Available from Air Weather Service Technical Library, 859 Buchanan St., Scott AFB, IL 62225-5118.]

Moore, J.T. and *Pino, J.P.,* 1990: An interactive method for estimating maximum hailstone size from forecast soundings. *Weather Forecast. 5*, 508–526.

Morrison, H., Curry, J.A., and *Khvorostyanov, V.I.,* 2005: A new double-moment microphysics parameterization for application in cloud and climate models, Part I: Description. *J. Atmos. Sci. 62*, 1665–1677.

Ogura, Y., and *Takahashi, T.,* 1971: Numerical simulation of the life cycle of a thunderstorm cell. *Mon. Weather Rev. 99*, 895–911.

Orville H.D. and *Kopp, F.J.,* 1977: Numerical simulation of the Life History of a Hailstorm. *J. Atmos. Sci. 34*, 1596–1618.

Petch, J.C., Brown, A.R., and *Gray, M.E.B.*, 2002: The impact of horizontal resolution on the simulations of convective development over land. *Q. J. Roy. Meteor. Soc. 128*, 2031–2044.

Putsay, M., Simon, A., Szenyán, I., Kerkmann, J., and *Horváth, Gy.,* 2011: Case study of the 20 May 2008 tornadic storm in Hungary — remote sensing features and NWP simulation. *Atmos. Res. 100*, 657–679.

Reisner, J., Rasmussen, R.M., and *Bruintjes, R.T.,* 1998: Explicit forecasting of supercooled liquid water in winter storms using the MM5 mesoscale model. *Q. J. Roy. Meteor. Soc. 124*, 1071–1107.

Renick, J.H., and *Maxwell, J.B.,* 1977: Forecasting hailfall in Alberta. Hail: A Review of Hail Science and Hail Suppression, Meteor. Monogr., No. 38, Amer. Meteor. Soc., 145–151.

Simpson, J. and *Wiggert, V.,* 1969: Models of precipitating cumulus towers. *Mon. Weather Rev.* 97, 471–489.

Skamarock, W.C., Klemp, J.B., Dudhia, J., Gill, D.O., Barker, D.M., Duda, M.G., Huang, X.-Y., Wang, W., and *Powers, J.G.*, 2008. A description of the advanced research WRF version 3. NCAR Technical Note NCAR/TN-475+STR, June 2008. 113.

Takahashi, T., 1976: Hail in an Axisymmetric Cloud Model. *J. Atmos. Sci. 33*, 1579–1601.

Talbot, C., Bou-Zeid, E., and *Smith, J.,* 2012: Nested Mesoscale Large-Eddy simulations with WRF: Performance in Real Test Cases. *J. Hydrometeor. 13*, 1421–1441.

Thompson, G., Rasmussen, R.M., and *Manning, K.*, 2004. Explicit forecasts of winter precipitation using an improved bulk microphysics scheme. Part-I: description and sensitivity analysis. *Mon. Weather Rev. 132*, 519–542.

Thompson, R.L., Edwards, R., Hart, J.A., Elmore, K.L., and *Markowski, P.*, 2003: Close proximity soundings within supercell environments obtained from the rapid update cycle. *Weather Forecast. 18*, 1243–1261.

Weinstein, A.I., 1972: Ice-Phase Seeding Potential for Cumulus Cloud Modification in the Western United States. *J. Appl. Meteor. 11*, 202–210.

Wisner, C., Orville, H.D., and *Myers, C.*, 1972: A Numerical Model of a Hail-Bearing Cloud. *J. Atmos. Sci., 29*, 1160–1181.

Wyngaard, J.C., 2004: Toward numerical modeling in the ''terra incognita''. *J. Atmos. Sci. 61*, 1816–1826.

Zoltán, Cs. and *Geresdi, I.*, 1984: A one-dimensional steady-state jet model for thunderclouds. *Időjárás 88*, 21–31.

IDŐJÁRÁS

Quarterly Journal of the Hungarian Meteorological Service
Vol. 119, No. 4, October – December, 2015, pp. 475–491

Examining the probable length in days of wet and dry spells in Khuzestan province

Seyed Hossein Mirmousavi

University of Zanjan, Faculty of Humanities,
University Blvd.,45371-38791, Iran
hossein.mousavi047@gmail.com

(Manuscript received in final form November 11, 2014)

Abstract—This study evaluated the probable length in days of dry and wet spells in Khuzestan province using daily rainfall data from 11 synoptic stations during the period 1990–2012. Transfer matrix calculations and model tests were performed using Matlab software. For interpolation maps, kriging in ARC GIS 10.2 software was used. Results indicated that the probability of dry days occurring in Khuzestan province increases from the south to the north. The highest probabilities of a two-day dry spell were 15% in the north and 12% in the northeast of the province. The probability of a 3-day dry spell in the north and northeast was 10%. Moving to the south and southwest of the province, the probability decreases, amounting to 6% in the southwest. Results of calculations of return periods of wet and dry days showed the probability of the dry-days return period increases from the north to the south. An investigation of the role of general circulation in the creation of wet and dry periods showed that 4 patterns are effective in their production.

Key-words: Markov chain, probability, dry and wet spells, Khuzestan Province.

1. Introduction

Wet spells and dry spells are two main physical characteristics of rainfall occurrence, and the volume of rainfall in a geographical area depends heavily on the distribution of such spells. It is, therefore, important to investigate the occurrence patterns of wet and dry spells scientifically through model-based analysis, that consists of studying the statistical properties of two common indicators, the spell length and spell frequency. Such studies are essential for agricultural planning, water resource management, and other interests such as fisheries, health, ecology, environment, etc. Several kinds of stochastic models

have been used to describe frequency distributions of spell lengths at spatial and temporal levels. The fitted probability distributions of spell lengths under the models are used to study the persistence properties of wet and dry spells. Since spell lengths govern the persistence properties of the daily precipitation process, it is desirable to use a criterion to select the best model from among a series of competitive models that is fitted successfully to the observed datasets.

In order to put our discussion into the proper perspective, we related our work to the existing literature. The model most frequently used to generate consecutive series of dry and wet days is the first-order, two-state, homogeneous Markov chain that has been applied by and is very popular among various researchers, *Todorovic* and *Woolhiser* (1974), *Berger* and *Goossens* (1983), *El_seed* (1987), *Haggstrom* (2002), *Bekele* (2002), *Anagnostopoulou et al.* (2003), *Alasseur et al.* (2004), *Ana* and *Paulo* (2007), *Asakereh* (2009), *Fischer et al.* (2013)). An essential improvement to the reproduction of short and long spells was made by *Berger* and *Goossens* (1983) and *Nobilis* (1986) using the higher order Markov chain and Eggenberger-Polya distribution. They found that short spells were best fitted by the fourth order Markov chain, whereas the Eggenberger-Polya distribution gave the best fit to the long series. *Deni* and *Jemain* (2008) proposed a model constituting two different geometric distributions. In the referred study, both geometric distributions were separated according to the length of dry spells. Results of the works suggested that mixed distribution, including the geometric one, could be promising in reproducing long dry periods. For wet spells, it was also observed that simple geometric distribution could be promising. Recently, following the idea of *Deca et al.* (2010), a mixture distribution based on a weighted sum of two geometric distributions, as well as that of one geometric and one Poisson distribution, was applied by *Mathugama* and *Peiris* (2011). The first model exhibits a good fit for dry spells, and the latter can be employed for wet periods. More recently, *Ababaei et al.* (2012) found that both the Markov chain of order two and negative binomial distribution can be used to estimate wet spells in Qazvin (Iran).

Khuzestan province is one of the most important agricultural areas in Iran. Due to successive droughts, farmers in this province have endured many losses. In this region, the incidence of consecutive dry days is a main factor in increasing the amount of damage to the agricultural sector (*Nadi et al.*, 2012). For this reason, it is necessary to carefully examine the consecutive dry days in the area. The present study examined in detail the ability of the Markov models to analyze the wet or dry condition of a given day in this area.

2. Data

In this study, daily rainfall data was collected from 11 meteorology stations. The period 1990–2012 was chosen for the evaluation of the model. A wet day

was defined as a 24-hour period with total rainfall exceeding 0.1 mm, and a dry day was defined as one with measurable precipitation <0.1 mm. The pressure data used were the NMC grid data in different windows over Europe and Middle East at the grid resolution 2.5°×2.5°. Several geopotential heights (500 hPa and sea level pressure (SLP)) were used. The selected area experienced a large part of the systems affecting Iran during the years (from 1970 to 2013) involved. This region is located within 20–60° N and 20–80° E. Data used from the NCEP site (www.ncep.noaa.gov) is provided.

3. Method

3.1. Markov chains

A Markov chain can be defined as a type of time-ordered probabilistic process that goes from one state to another according to the probabilistic transition rules that are determined by the current state only (*Haggstrom*, 2002). That is, the probability of a day being in a certain state (either wet or dry) is conditioned on the states of the previous periods, where the number of previous periods is termed as the order of the chain.

In the first-order, two-state Markov model, the current state is dependent solely upon the state of the previous period, while in the second–order, two-state Markov chains, the current state is determined by the states of the two previous periods (*Hakimi-Pour*, 1998).

When recording whether a measurable amount of rain has occurred over time at a particular location (2-state time series), data is in the form of a discrete state series. The most commonly used model for discrete state series is a low-order stationary Markov chain. Such models are used to predict the occurrence of certain sequences.

The states of the system are dry and wet. A wet state is defined as a 24-hour period measured from 8:30 a.m. with total rainfall exceeding some threshold amount (0.1 mm). Otherwise, the state is taken as dry (*Zarei* and *Shahkar*, 2002). The discrete state series of rainfall can be represented as X_1, X_2, X_3 , ……,.X_t for a t length sequence, where:

$$X_t = 0, \text{ if day } t \text{ is dry,}$$

$$X_t = 1, \text{ if day } t \text{ is wet.} \quad (1)$$

3.2. First-order Markov model

The probabilities of a first-order Markov chain are defined as:

$$P\{X_t = j \mid X_{t-1} = i\}\ i,j = 0,1\ . \tag{2}$$

The *transition probability* P_{ij}, (where $i, j = 0, 1$) is the probability that if the system is in state i at any observation, it will be in state j at the next observation. As probabilities, the numbers P_{ij} must all lie in the interval [0, 1]. Transitional probabilities for the first order can be expressed as follows:

$$Pij(t) = P\{X_t = j \mid X_{t-1} = i\}\ i,j = 0,1\ . \tag{3}$$

For any fixed i, $\{i = 0, 1\}$, we must have $P_{i0} + P_{i1} = 1$.

This expresses the fact that if the system is in one of the states at one observation, it will with certainty be in one of the two states at the next observation. With these transition probabilities, a 2×2 matrix $\mathbf{P} = \{P_{ij}\}^{T}$, called the transition matrix of the Markov process, can be formed where the sum of the entries in each column of **P** is one.

$$\mathbf{P} = \begin{pmatrix} p_{00} & p_{10} \\ p_{01} & p_{11} \end{pmatrix}. \tag{4}$$

The probability vectors $\boldsymbol{p}^{(n)}$ for $\boldsymbol{n} = 0, 1, 2, \ldots\ldots$ are said to be the state vectors of a Markov process, where $pi^{(n)}$ is the probability that the system is in the ith state at the nth observation. In particular, the state vector $\boldsymbol{p}^{(0)}$ is called the initial probability or initial state vector of the Markov process. If **P** is the transition matrix and $\boldsymbol{p}^{(n)}$ is the state vector at the nth observation, one can write:

$$\mathbf{P}^{(n+1)} = \boldsymbol{p}^{(n)}\mathbf{P} \tag{5}$$

Where $\boldsymbol{p}^{(n+1)}$ is the state vector at the $n+1$th observation. From this it follows that:

$$\mathbf{P}^{(n)} = \boldsymbol{p}^{(0)}\mathbf{P}^{n} \tag{6}$$

i.e., the initial state vector $\boldsymbol{p}^{(0)}$ and the transition matrix **P** determine the state vector $\boldsymbol{p}^{(n)}$ at the nth day. The nth step transition probabilities are called conditional probabilities and is denoted by $P_{ij}^{(n)}$, (where $i, j = 0, 1$) with $\mathbf{P}_{ij}^{(n)} \geq 0$, for n=0,1,2,3…., and:

$$\sum_{j=0}^{1} p_{ij}^{(n)} = 1 \ . \tag{7}$$

$\mathbf{P}^{(n)} = \boldsymbol{p}^{(0)} \mathbf{P}$ in matrix notation for the 1th order Markov chain can be written as (*Chynlar*, 2002):

$$\left(p_0^{(n)} p_1^{(n)}\right) = \left(p_0^{(0)} p_1^{(0)}\right) \begin{pmatrix} p_{00} & p_{10} \\ p_{01} & p_{11} \end{pmatrix} n \ . \tag{8}$$

Moreover, the calculation for the continuation of wet and dry days uses the following equation (*Berger* and *Goossens,* 1983):

$$P_m = \boldsymbol{p}^{m-1} \boldsymbol{q} \tag{9}$$

Return periods of dry and wet days, with the continuity of m-day, is calculated using the following equation:

$$T_m = \frac{1}{\boldsymbol{p}^{m-1} \boldsymbol{q}} \tag{10}$$

One of the main assumptions in Markov chains is stationarity. That is $P_{ij}(t)=P_{ij}$ for $t_k < t < t_{k+T}$ where T is the time interval taken to calculate the transitional probabilities. This assumes that the chance of rain remains constant within T day periods. The data was grouped into 2-day, 3-day, and 5-day groups and studied separately.

To evaluate the strength of the relationship between the occurrence of circulation patterns and rainfall, an index, called performance index (*PI*), is defined to measure the relative contribution of a particular pattern to the total rainfall amount. Specifically, the mean daily rainfall within cluster i is compared with the climatological mean daily rainfall, that is, (*Zhang*, 1995):

$$PI(i) = \frac{R_i/n_i}{R/n}, \tag{11}$$

where n_i is the number of days with pattern i; R_i is the total rainfall during those days; R is the total rainfall received during the study period, and n is the number of days in the study period. If *PI* is less than 1 in rainy weather, the pattern has no effect, and the placement of the pattern in the atmosphere of an area can be consecutive dry. If *PI* index is more than 1, consecutive wet days in the region will be created.

In order to assess the impact of dry periods on water resources and agricultural yield, linear regression and polynomial regression methods with the following equations were used:

$$\mu_{y|x} = \beta_0 + \beta_1 X \ . \tag{12}$$

$$Y = \beta_0 + \beta_1 X + \beta_2 X^2 + \ldots + \beta_{p-1} X^{p-1} + \varepsilon \ . \tag{13}$$

4. *Study area*

The province of Khuzestan, which occupies an area of 63,213 km^2 in southwestern Iran, is located between 48°E and 49.5°E longitudes and between 31°N and 32°N latitudes (*Fig. 1*). Topographic elevations in the province vary between 0 and 3740 m. The climate of the study area varies from arid to humid. The northern parts of the province experience cold weather, whereas the southern parts experience tropical weather. Summer is from April to September, whereas winter is from October to March. Annual mean of maximum summer temperatures in the province is about 50 °C (in July) and minimum winter temperature is 9 °C (in March). The annual amounts of rainfall are 165–200 mm in the southwest and 433–480 mm in the northeast, and about 70% of annual rainfall events occur from February to April (*Fig. 2*). The annual evaporation is 1500–2800 mm.

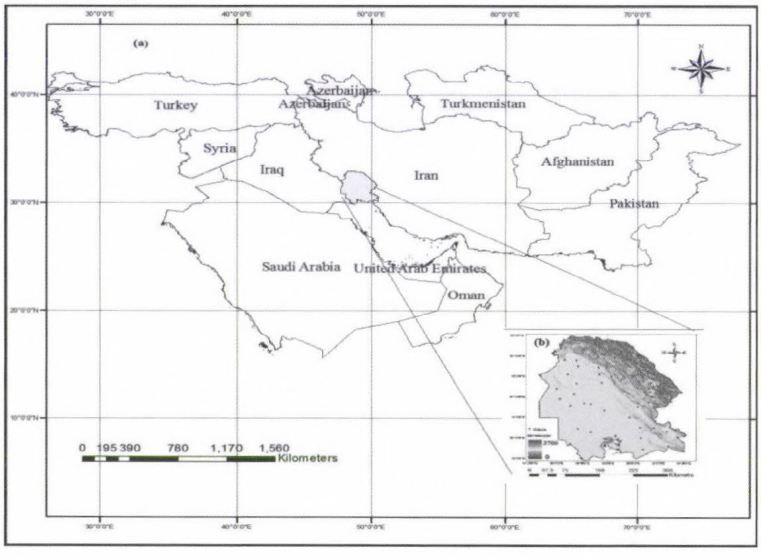

Fig. 1. Khuzestan province: (a) location in Iran; (b) Digital elevation model and locations of the studied stations.

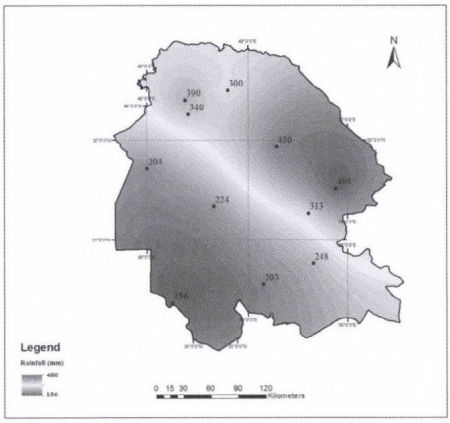

Fig. 2. Average annual rainfall in the Khuzestan Province.

5. *Results*

The calculation results showed that in Khuzestan province from the south to the north, the probability of dry days decreases. Maximum probability of dry days is found in the central and southwestern parts of the province (92%). This means that, on average, in the southwest part of the study area, 336 days per year are dry. The minimum probability of dry days was found in the northern region (74%). This means that in northern Khuzestan, on average, the probable number of dry days per year is 270. Overall, the average probability of dry days in Khuzestan province was 86%(*Fig. 3*).

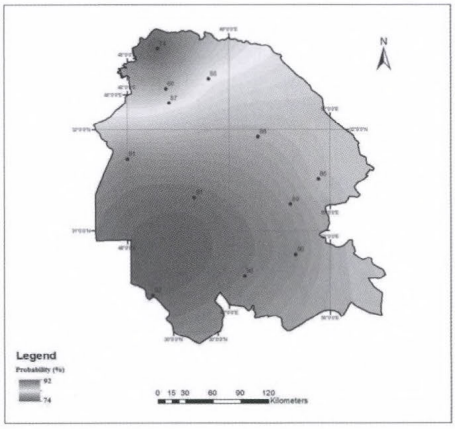

Fig. 3. Map of the dry day's probability (%).

An examination of the probability of a 2-day dry spell showed higher probabilities in the north (15%) and northeast (12%) than elsewhere in the study area. In the south and southwest, the probability of a 2-day dry spell is reduced so that in the southwest of the province, this rate reached the minimum amount of 6% (*Fig. 4*). Assessments showed that the probability for a 3-day dry spell in the north and northeast of the study area is approximately 10% and in the southwest of the province, the probability is equal to 6% (*Fig. 5*). Also, the probability of a dry spell lasting five days is less than that for a 3-day dry spell, so that the maximum value is in the northeast province (7%) and the minimum value is in the southern region at almost 2% (*Fig. 6*).

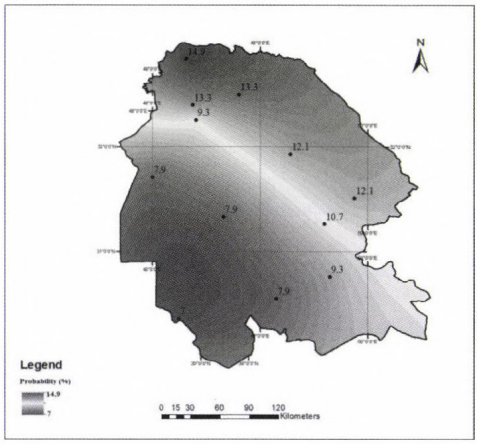

Fig. 4. Map probability of two days dry spell lengths (%).

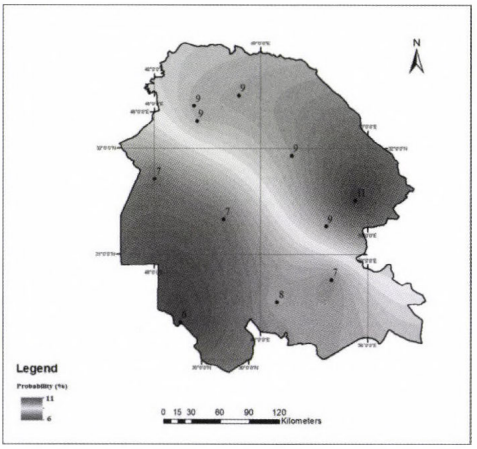

Fig. 5. Map probability of three days dry spell lengths (%).

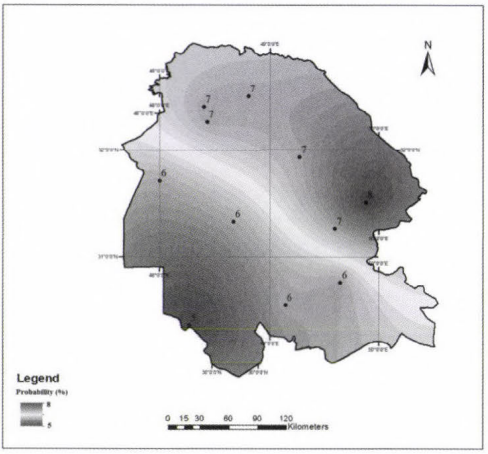

Fig. 6. Map probability of five days dry spell lengths (%).

5.1. Return period of 2-5-day dry spell

Calculating return periods of 2- to 5-day dry spells showed that the minimum length of a dry spell is 2 days, which occurred in the north and northeastern parts of Khuzestan province. This means that the probability of a dry spell lasting two days is higher in the north and northeast than in the south and southwest. Accordingly, the probable return period of a 2-day dry spell in the southwest of the province is, on average, 15 days, while in the north, the return period occurs once every 7 days. Studies have shown that most 2-day dry spells occur in the southwest of the province (*Fig. 7*).

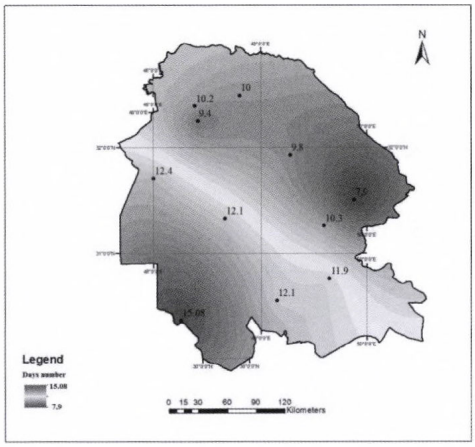

Fig. 7. Map of the persistence of a 2-day dry spell return period.

When the length of a dry spell increases to 3–5 days, the return period also increases; however, this data at the provincial level becomes a little slower. Evaluations showed that in the north and northeast of the province, the potential return period of the 3-day dry spell is once every 10 days, and the probability in the southwest province is once every 16 days (*Fig. 8*). The probability of the return period of a 5-day dry spell is much like that of a 3-day period. Every 17.5 days in the southern part of Khuzestan province and every 12.8 days in the northeast, the return period of a 5-day dry spell occurs (*Fig. 9*).

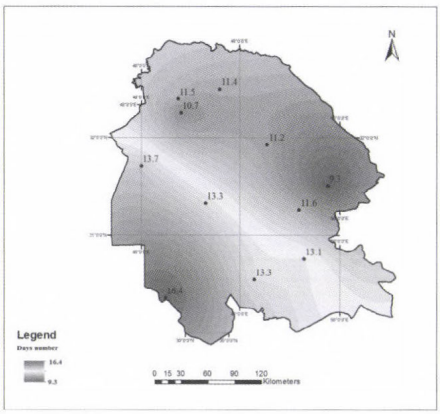

Fig. 8. Map of the persistence of a 3-day dry spell return period.

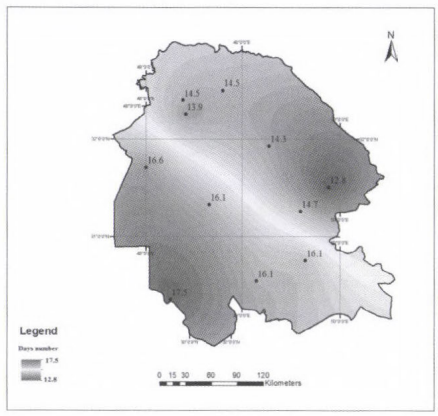

Fig. 9. Map of the persistence of a 5-day dry spell return period.

5.2. *Assessment of the relationship between the height and distribution of dry and wet spell lengths in days*

In order to assess the relationship between the height and distribution of consecutive dry days, simple linear regression was used. For this purpose, the elevation map of Khuzestan province was extracted using a 30-meter resolution satellite image (DEM) (*Fig. 10*). Then, using the Euclidean distance equation, 1200 elevation points were selected in Khuzestan province. Then, using kriging interpolation, the probabilities of lengths of dry spells in days for the 1200 selected points were extracted. The following regression equation was used to calculate the correlation ratio between the elevation and dry spell length in days:

$$y = 1E\text{-}07x^4 - 0.0001x^3 + 0.046x^2 - 7.146x + 377.88(12)\,, \qquad (14)$$

$$R^2 = 0.8394\,.$$

The results of the relation between the height and precipitation showed that, at a 99% confidence level, there is a strong correlation between these parameters. Based on this equation, correlation maps were drawn between elevation and dry spell lengths in days (*Fig. 11*). Exploration of this map indicated that the probability of dry days from the north to the south of the province is reduced. For wet spell lengths this situation is quite the contrary.

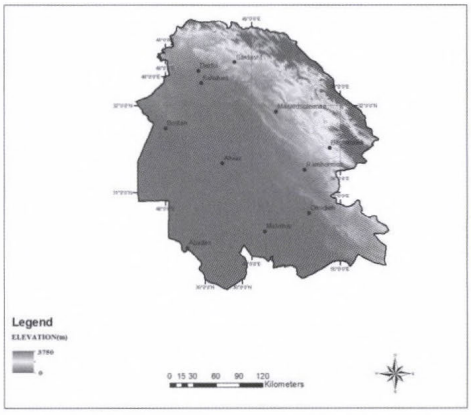

Fig 10. Elevation map of Khuzestan Province.

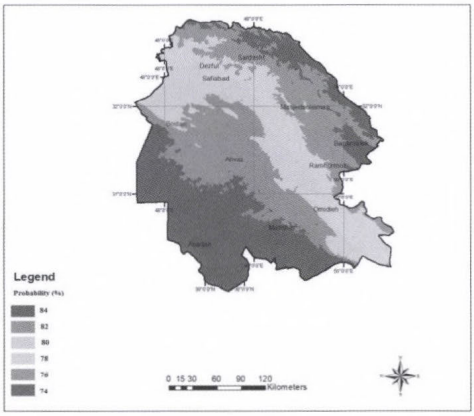

Fig. 11. Map of the relationship between the elevation and the length of dry spell.

5.3. Assessment of the relationship between the atmospheric circulation system and the probability of lengths of dry and wet spells in days

In order to assess the relationship between the atmospheric circulation patterns and the precipitation, the PI index was calculated and analyzed for 11 weather stations in the study area. This index specifies the conditional probability of rainfall in a circulation pattern. Results of PI, the role of each of the atmospheric circulation pattern showed the creation or lack of precipitation.

The results showed significant differences in the arrangement patterns of geopotential height of 500 hPa, sea level pressure, and circulation patterns in Iran. Analysis of atmospheric circulation systems showed three distinct patterns of rainfall in Iran.

5.4. Atmospheric circulation patterns for wet spell lengths

5.4.1. Pattern 1 (p1)

In Pattern 1, the 500 hPa geopotential height maps show a trough from northeastern Europe, to the southwest of Iraq. Because of the trough in the east, there is positive relative vorticity in this situation. Where there is sufficient moisture in the area, there is a chance of rain in this circulation pattern (*Fig. 12*-p1-A).

The map of the mean sea level pressure, the pressure of 1024 hPa, show deployment over Siberia. The pressure tabs stretch from the east-west to northwestern Europe. The low pressure from Saudi Arabia and North Africa in

the mid-latitudes extends to the East Mediterranean region. The results of the PI index indicated that this pattern has the greatest impact on the southwestern and western regions of Iran (Khuzestan province). The present pattern causes precipitation and wet events in much of the country (*Fig. 12*-p1-B and C).

5.4.2. Pattern 2 (p2)

The composite map of 500 hpa geopotential height indicated the presence of a trough over Russia that expands to the Mediterranean along the southwest (*Fig. 12*-p2-A). The trough from the southwest (Khuzestan province) entered Iran and caused a lot of rain in these areas. The PI in Khuzestan is relatively high (PI = 3), which indicates that this pattern causes wet periods (*Fig. 12*-p2-B and C).

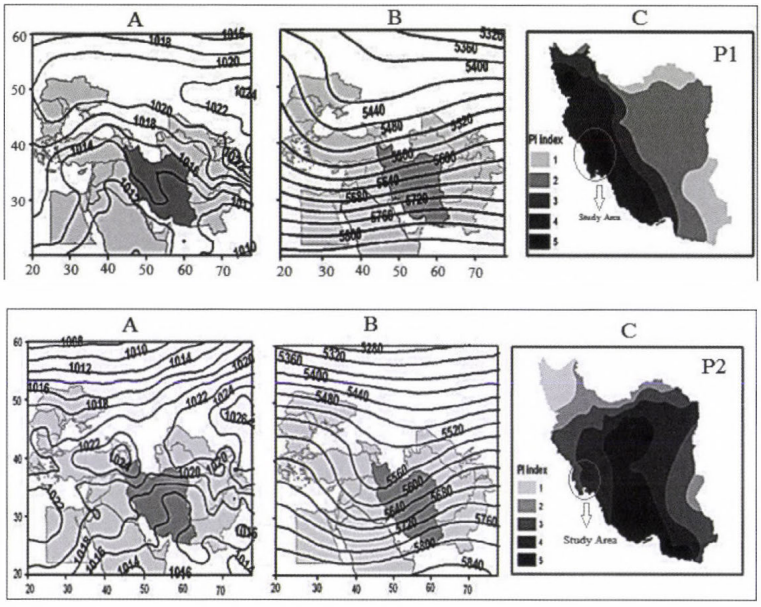

Fig. 12. Patterns of atmospheric circulation in Iran's Khuzestan province. A: 500 hPa mean geopotential height pattern ; B: mean sea level pressure pattern ;C: PI index pattern.

5.5. Atmospheric circulation patterns for dry spell lengths

5.5.1. Pattern 1 (p1)

The map of 500 hPa level showed a trough with a north-south direction expanding from the north of the Black Sea to the Red Sea. The eastern part of

the trough has affected the northern regions of Iran (*Fig. 13*-p1-A). In this pattern, high pressure (with a center of 1026 hPa) was seen over Siberia and Europe, and the 1020 hPa isobaric curves expanded on the Mediterranean, North Africa, and the southeast. Formation of this synoptic pattern caused drought in most parts of Iran (*Fig. 13*-p1-B). The PI Index calculation also shows that with the exception of the northwestern areas, the index rate is less than 1 in other parts of the country. This means that the implementation of this pattern in the study area causes dry conditions (*Fig. 13*-p1-C).

5.5.2. Pattern 2 (p2)

In this pattern, a trough over northwestern Europe and the eastern Mediterranean is located at the 500 hPa level. Most parts of Iran are dominated by high pressure (*Fig. 13*-p2-A), and atmospheric stability conditions prevail (*Fig. 13*-p2-B). The PI index calculation also showed that the index was less than 1 in most parts of the country and the province of Khuzestan, and dry conditions have occurred (*Fig. 13*-p2-c).

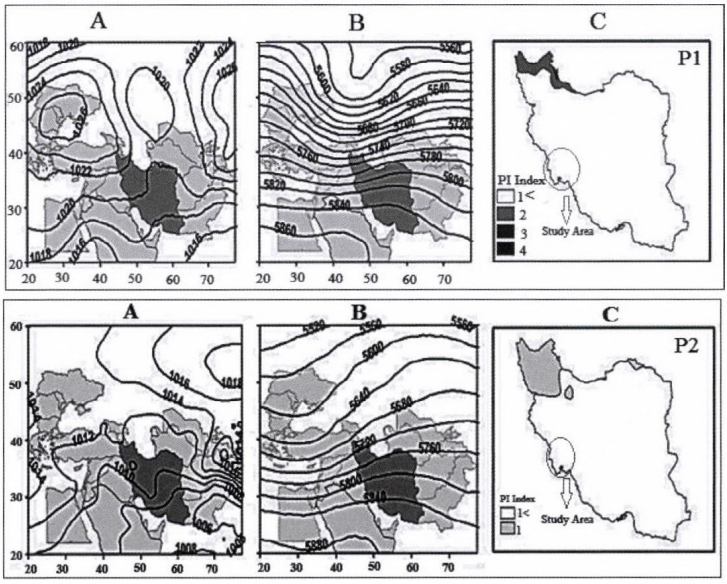

Fig. 13. Patterns of atmospheric circulation in Iran's Khuzestan province. A: 500 hPa mean geopotential height pattern ; B: mean sea level pressure pattern ;C: PI index pattern.

5.6. Evaluation of dry and wet periods

For the impact assessment of dry and wet periods in Khuzestan province, two sets of field data were used:

—data on groundwater levels in different parts of Khuzestan province,

—data on rainfed wheat yield in different parts of Khuzestan Province.

Data on groundwater levels and data relating to rainfed wheat yield were obtained from the Agricultural Research Center of Khuzestan Province. To evaluate the effects of dry days on water resources and agricultural products, 46 stations were selected. In order to evaluate the effect of the dry period, the water level and the correlation between these two parameters were studied, and linear regression and polynomial regression methods were used. The results of the correlation between the levels of the groundwater and the average probability of consecutive dry days in 46 selected stations showed that a significant, strong correlation exists between the mean probability of dry periods and the groundwater level. The degree of correlation is $R^2 = 0.93$ at a 99% confidence level (*Fig. 14*). This result shows that the groundwater is strongly influenced by dry periods.

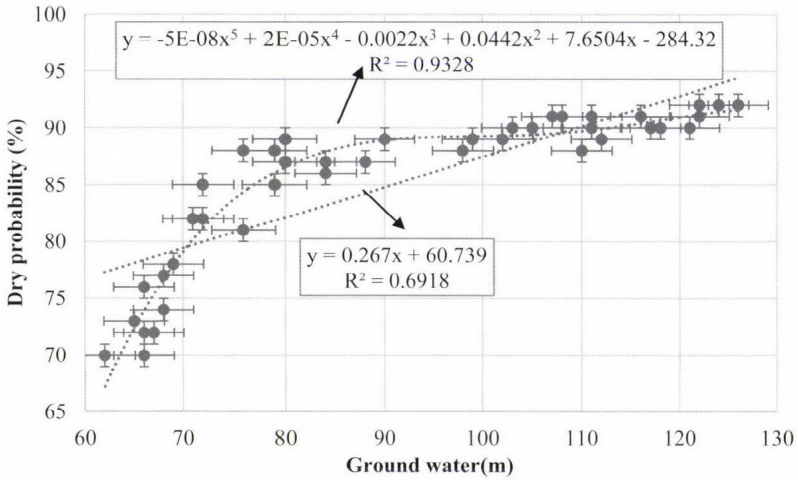

Fig. 14. Graph correlation between the average probability of dry periods and ground water levels.

In order to assess the impact of consecutive dry days on the yield of crops, rainfed wheat was selected, because it is the main crop of Khuzestan province, and its performance is subject to fluctuations in rainfall. The results of the regression relationship to calculate the average probability of dry days with an average annual yield of rainfed wheat in selected stations indicated the existence of a high correlation between these two parameters (at the 99% confidence level, $R^2 = 0.87$). Investigations showed that the yield of rainfed wheat is significantly reduced by increasing the probability of dry periods (*Fig. 15*).

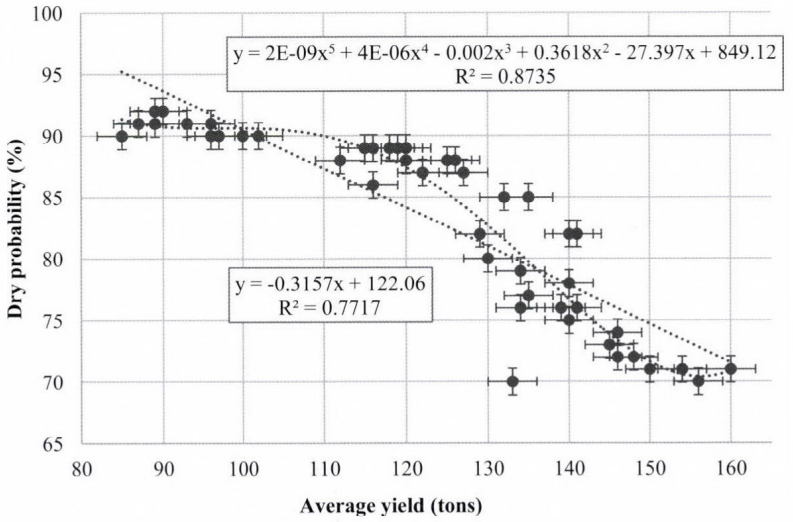

Fig. 15. Graph correlation between the average probability of dry periods and annual dryd wheat yield (tons).

6. Conclusions

The study of extreme precipitation events, such as floods and droughts, requires the analysis of wet and dry day sequences. The empirical frequency distribution does not provide a good insight into the probabilities of very long sequences of dry and wet spells, which are more important for practical purposes than short sequences. Statistical models give more reliable estimates. In this work, dry and wet spells were studied using the first-order Markov chain model. The daily precipitation data at 11 meteorological stations, being representative of different climate regimes in Khuzestan province, were analyzed. Wet or dry days were classified according to daily precipitation amounts of 1.0 mm.

Khuzestan province is one of the most important agricultural sectors with a variety of crops, and it plays an important role in supplying the needs of the country. This province is first in the country in cultivating cereals. Results of the current study showed that the probability of consecutive dry periods is high, in different parts of the province; moreover, water resources and agricultural performance are greatly affected by dry and wet periods, therefore, careful planning must be done in this area.

Results of the current study also indicate thaton the basis the generated sequences of wet and dry periods, the synoptic systems, and local factors (topography), four patterns were identified. Analysis of general circulation models of the atmosphere, and previous studies of this area by other researchers such as *Lashkari* (1996), *Alijani* (2002), *Hojatizadeh* (2002), and *Raziei et al.* (2008) confirm these conclusions. These patterns can predict extreme wet and dry periods.

References

Ababaei, B., Sohrabi, T.M., and *Mirzaei, F.*, 2012: Simulation of Rainfall Occurrence in Qazvin Synoptic Station Using Probability Models. *J. Nat. Geogr. Res. 79*, 111–122.

Alasseur, C., Husson, L., and *Perez-Fontan, F.,* 2004: Simulation of rain events time series with Markov model. Proc. of 15th IEEE International Symposium on Personal, Indoor and Mobile Radio Communications 4, 2801–2805.

Alijani, B., 2002: Variation of 500 hpa Flow Patterns Over Iran and Surrounding Areas and Their Relationship with Climate of Iran. *Theor. Appl. Climatol. 71*, 41–54.

Ana, A. and *Paulo, S.,* 2007: Prediction of SPI Drought class Transitions using Markov chain, *Water Resour. Manage. 21,* 1813–1827.

Anagnosropoulou, Chr., Maheras, P., Karakostas, T., and *Vafadis, M.*, 2003: Spatial and temporal Analysis of Dry Spell in Greece. *Theor. Appl. Climatol. 74*, 77–91.

Asakereh, H., 2009: A Study of the frequency and persistence of the possibility of rainy days in the city of Tabriz, using a Markov chain model. *Water Resour. Res.Iran. 2*, 46–56.

Bekele, E., 2002: Markov chain modeling and Enso influences on the rainfall seasons of Ethiopia. National Meteorological Services of Ethiopia. 25.

Berger, A. and *Goossens, C.*, 1983: Persistence of wet and dry spells at Uccle (Belgium). *J. Climatol. 3*. 21–34.

Chynlar, A., 2002: Introduction to Stochastic Processes, translated by Shahkar,G,H., BozorgNia,A,G., Tehran, Amirkabir University of Technology Institute of Scientific Publications.451.

Deni, S.M. and Jemain, A.A., 2008: Mixed log series geometric distribution for sequences of dry days. Atmos. Res. 92. 236–243.

Deka , S., Borah, M., and *Kakaty, S.C.* , 2010: Statistical modeling of wet and dry spell frequencies over North-East India. *J. Appl. Nat. Sci. 2*, 42–47.

*El Seed, A.G.,*1987: An application of Markov Chain Model for wet and dry spell probabilities at Juba in Southern Sudan.- *Geo J. Lib. 15*.420–424.

Fisher, B.M.C., Mul, M.L., and *Savenije, H.H.G.*, 2013: Determining spatial variability of dry spells: a Markov-based method, applied to the Makanya catchment, Tanzania. *Hydrol. Earth Syst. Sci. 17*, 2161–2170.

Hakimi-Pour, A., 1998: Application of the theory of Markov chain management decisions. Mashhad, Razavi Publications. 431.

Haggstrom, O., 2002: Finite Markov Chains and Algorithmic Applications. Cambridge University Press. 541.

Hojatizadeh, R., 2002: A Synoptic Investigation of Floods in Rivers of Western Zgros (With Emphasis on Karkheh, Karoon and Dez basins). Ph.D. Thesis. Supervisor Mohamad Reza Kaviani and Hassan Ghayour. Department of physical geography,University of Isfahan. Iran. 233.

Lashkari, H., 1996: The Synoptic Pattern of Heavy Precipitation Occurrences in Southwestern Iran. - Ph.D. Thesis, Supervisor Ghaemi,H., Department of physical geography, University of Tarbiat Modares, Iran.221.

Mathugama, S.C. and *Peiris, T.S.G.,* 2011: Critical Evaluation of Dry Spell Research. *Int. J. Basic Appl. Sci.. 11(6).*153–160.

Nadi, M., Jamei, M., Bazrafshan, J., and *Jannat Rostami, S.*, 2012: Evaluation of Different Methods for Interpolation of Mean Monthly and Annual Precipitation Data (Case Study: Khuzestan Province). *Phys. Geogr. Res. Quart. 44(4).* 117-130.

Nobolis, F., 1986: Dry spells in the Alpine country Austria. *J. Hydrol. 8,* 235–251.

Raziei, T., Mofidi, A., and *Zarrin, A.,* 2008:The 500 hPa Centers of Action and Atmospheric Circulation Patterns over Middle East and their Relationship with Precipitation in Iran.- *Iranian J. Earth Space Phys. 35.* 121–141.

Todorovic, P. and *Woolhiser, D,A.,* 1974: A statistic model of n-day Precipitation. *J. Appl. Meteorol. 14.* 17–24.

Zarei, H. and *Sahkar, G.H.,* 2002: Review the possibility of frequency of rainy days and dry areas Khoramdeh - Arak Zeshk. - The third seminar Probability and Stochastic Processes. University of Isfahan, 7 and 8. *134-142.*

Zhang, X., 1995: Regional climatic variability and climate change scenarios" Ph. D. Dissertation university of Lisbon.135.

IDŐJÁRÁS

Quarterly Journal of the Hungarian Meteorological Service
Vol. 119, No. 4, October – December, 2015, pp. 493–514

Mann–Kendall trend analysis of surface air temperatures and rainfall in Iraq

El-Sayed M. Robaa [1*] and **Zhian Al-Barazanji** [2]

[1] *Astronomy, Space Science and Meteorology Department, Faculty of Science, Cairo University, P.O. Box 12613, Giza, Egypt*
E-mail: d_robaa@hotmail.com
[2] *Department of Atmospheric Science, Faculty of Science, Al-Mustansiriyah University, Baghdad, Iraq*
E-mail: zhdilshad@gmail.com

** Corresponding author*

(Manuscript received in final form March 20, 2015)

Abstract—In this study, trends of the seasonal and annual maximum (T_{max}), minimum (T_{min}), and mean (T) air temperatures, as well as rainfall amounts (R_a) time series were investigated for eleven stations in Iraq for the period 1972–2011 (40 years). Four statistical tests including homogeneity, Mann–Kendall (MK), Sen's slope estimator and linear regression were used for the analysis. The results revealed that annual mean of T_{max}, T_{min}, and T time series showed statistically significant increasing trends over 81.8, 100, and 100% of the stations at the 0.001 level and they experienced an increase of 0.50, 0.67, and 0.58 °C/decade, respectively; while the annual rainfall has shown decreasing trends at 90.9% of the stations and it experienced a decrease of –20.50 mm/decade. Seasonally, the highest increase of T_{max}, T_{min}, and T values have been found over the extreme south of the country during summer at the rates of 1.47, 1.06, and 1.16 °C/decade, respectively, while the highest decrease of R_a values has been found in the northern part of the country during winter at the rate of –36.35 mm/decade.

Key-words: climate change, air temperature, rainfall, Mann-Kendall test, trends, Iraq

1. Introduction

The detection and attribution of global climate change resulting from anthropogenic activities are one of the main themes of current climatological research. Several studies of long-term time series of temperatures have been done on global scale (*Jones,* 1994; *Nicholls et al.,* 1996; *Watson et al.*, 1998; Jones *et al.*,1999; *Folland et al.,* 2001; *Eichner et al.,* 2003; *Rybski et al.*, 2006; *Efstathiou et al.,* 2011; *Varotsos et al.*, 2013) and regional scale (*Marco et al.,* 2003; *Arora et al.,* 2005; *Smadi*, 2006; *Chen et al.*, 2007; *Rebetez* and *Reinhard*, 2008; *Busuioc et al.*, 2010; *Tabari* and *Talaee*, 2011a; *Stephenson, et al.*, 2014). The main finding of the results have shown that the Earth's surface air temperature has increased by 0.6 °C – 0.8 °C during the 20th century. The increasing of the air temperature proved to be nonlinear and non-homogenous at global scale (*Croitoru et al.*, 2012). Associated with global warming, there are strong indications that rainfall changes are already taking place on both global (*Diaz et al.*, 1989; *Hulme et al.*, 1998; *Lambert et al.*, 2003; *Dore*, 2005) and regional scales (*Yu* and *Neil*, 1993*; Gemmer et al.*, 2004; *Smadi* and *Zghoul*, 2006; *Kayano* and *Sansıgolo,* 2008; *Busuioc et al.*, 2010; *Tannecia et al.*, 2014). There have not been any internationally published works on surface air temperature and rainfall changes over the past century in Iraq. The detailed analysis and understanding of trends of climate events in Iraq are important to reduce the climate-induced dryness and the impact of temperature extremes on society, agriculture and environment. Therefore, this study was carried out for analysing the seasonal and annual trends in mean maximum, minimum, and mean air temperatures, as well as rainfall amounts. The Mann-Kendall test, the Sen's slope estimator, and the linear regression in Iraq from 1972 to 2011 were used.

2. Study area and data

Iraq is located in southwest Asia between latitudes $29°5' - 37°22'$ N and longitudes $38°45' - 48°45'$ E. The surface of Iraq is 438,317 km^2 (*Fig. 1*). Topographically, Iraq is shaped like a basin, consisting of the Great Mesopotamian alluvial plain of the Tigris and Euphrates rivers. This plain is surrounded by mountains in the north and east, which can reach altitudes of 3611 m above sea level, and by desert areas in the south and west, which account for over 40 percent of the land area. Iraq is characterized by four distinct topographic features:

a. Mesopotamian plain. This alluvial plain occupies a quarter of the area of Iraq.

b. Desert plateau. This area is located in the west of Iraq and occupies about less than half of Iraq.

c. Mountainous region. This region is located in the northern and north-eastern part of Iraq.

d. Hilly region. This is a transition zone between the low-lying Mesopotamian plain in the south and the high mountains in the far north and north-eastern part of Iraq.

Diverse topography of Iraq plays an essential role in its climate. Being situated in the north part of the subtropical region, Iraq is characterized by relatively low winter temperature, dry and hot summer, and two short transitorial seasons (spring and autumn). It seems that the differences in temperature have great impacts on Iraq's extreme climate. Iraq lies within the northern temperate zone, but the climate is continental and subtropical. Winters are usually cool to cold, with an average daily temperature that might reach 16 °C dropping at night to 2 °C. Summers are dry and hot to extremely hot, with a temperature of over 43 °C during July and August, yet dropping at night to 26 °C (*Al-Ansari et al.,* 2013). The rainfall in Iraq is tracking the climate of the Mediterranean Sea. Most amount of rainfall falls during the seasons of winter, spring, and autumn, while summer is rainless. Average annual rainfall is 154 mm, and it ranges from less than 100 mm over 60% of the country in the south up to 1200 mm in the north-east (*Al-Ansari et al.,* 2013; *Al-Ansari* and *Knutsson*, 2011).

Climatic data were available over the 40-year period from 1972 until 2011 at eleven stations. The monthly mean daily values of measured mean minimum air temperature, T_{min} (°C), mean maximum air temperature, T_{max} (°C), mean air temperature T (°C), and total rainfall amount R_a (mm) at the eleven selected stations have been taken from the Iraq Meteorological Authority (IMA). The stations have been chosen based on data availability and to cover the whole area of Iraq. Site of each station has remained the same, with almost negligible change since the beginning of the data records. The selected stations and their geographical coordinates as well as the observation periods of temperature and rainfall are given in *Table 1* and *Fig. 1*. Three statistical techniques were used in this research: a homogeneity test, the widely used non-parametric Mann–Kendall test, and Sen's slope estimator. The homogeneity test of the data series was carried out by applying the Abbe-test (*Schoenwiese*, 1992; *Schaefer*, 1996). All data series were shown to be homogeneous at all stations. To estimate the slope of an existing trend, the Sen's nonparametric method (*Sen*, 1968) was also used. Whether or not a constant increasing or decreasing trend was occurring, the MK (*Kendall*, 1938, *Mann*, 1945, *Kendall*, 1975; *Zhang et al.*, 2001) test for trend was also applied. In this test, the significance levels are 0.001, 0.01, 0.05, and 0.1 (*Salmi et al.*, 2002, *Luo et al.*, 2008), from very high significance to non-significance. SPSS and Excel programs were used to analyze temporal and

spatial temperature and rainfall changes. The Excel template MAKESENS (*Salmi et al.*, 2002) was also used to detect trends by the MK test.

Table 1. List of the eleven meteorological stations in Iraq, their geographical coordinates, as well as the observation periods of the air temperature and rainfall at each station.

Stations	Latitude (N)	Longitude (E)	Elevation (m) above M.S.L	Observation period for air temperatures and rainfall
Mosul	36° 19′	43° 07′	223	1972–2011
Sulaymaniya	35° 32′	45° 26′	884.8	1972–2011
Kirkuk	35° 28′	44° 23′	330.8	1972–2011
Khanaqin	34° 16′	45° 17′	202	1972–2011
Baghdad	33° 19′	44° 25′	31.7	1972–2011
Rutba	33° 02′	40° 17′	630.8	1972–2011
Al-Hai	32° 01′	46° 02′	17	1972–2011
Diwaniya	31° 59′	44° 59′	20	1972–2011
Samawa	31° 19′	45° 17′	6	1972–2011
Nasiriya	31° 03′	46° 14′	5	1972–2011
Basra	30° 30′	47° 50′	2.4	1972–2011

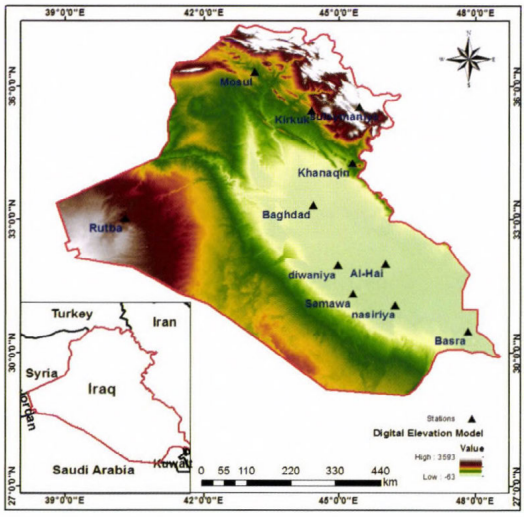

Fig. 1. Map of Iraq including the eleven selected stations.

3. Results and discussion

3.1. Trends of mean maximum temperature

Fig. 2 illustrates the annual anomalies of mean maximum temperature (T_{max}, °C) at the eleven selected stations in Iraq. Statistical properties of the seasonal and annual T_{max} series were tested and presented in *Table 2*. In winter, it can be clearly seen that 63.6, 27.3, and 9.1% of stations have experienced significant positive trend at the 0.01, 0.05, and 0.1 levels, respectively. According to the MK test. The trends range from 0.42 °C/decade at Basra in the south (significant at the 0.05 level) to 0.75 °C/decade at Sulaymaniya in the north (significant at the 0.01 level) (*Figs. 2.* and *6* and *Table 2*).

In spring, significant positive trends are observed for all stations (except Samawa, which has non-significant trend). It was found that 45.4, 27.3, and 18.2% of the stations have experienced significant positive trend at the 0.001, 0.01, and 0.1 levels, respectively, while the trends are not significant at only 9.1% of the stations. Trends ranged between 0.20 °C/decade at Samawa and 0.86 °C/decade at Khanaqin; the trend for Khanaqin is significant at the 0.001 level, while it is not significant for Samawa. During summer, all stations showed strong evidence of significant positive trend (except Kirkuk station which has non-significant trend). It can be seen that 45.4 and 45.5% of the stations have experienced significant positive trend at the 0.001 and 0.01 levels respectively, while the trends are not significant at only 9.1% of the stations. The trends range from 0.15 °C/decade (non-significant trend) at Kirkuk to 1.47 °C/decade (significant at the 0.001 level) at Basra (*Figs. 2* and *6* and *Table 2*).

On the contrary, negative and non-significant positive trend patterns dominated during autumn (*Table 2*). It can be seen that 9.1 and 9.1% of the stations have experienced significant positive trend at the 0.01 and 0.1 levels, respectively, while the trends are not significant at 72.7% of the stations. The trends range from –0.02 °C/decade at Diwaniya (non-significant trend) to 0.5 °C/decade at Basra (significant at the 0.05 level). From the beginning of 1972 until 1995, a cooling pattern was found at all stations, while subsequently warming pattern was identified until the end of the study period, and the change is statistically significant. The annual and seasonal trend analyses reveal that most warming in reference to T_{max} was observed in both winter (0.56 °C/decade) and spring (0.55 °C/decade), while the average trend over the whole country of Iraq was found to be 0.50 °C/decade. Annually, it was found that 81.8, 9.1, and 9.1% of the stations have experienced significant positive trend at the 0.001, 0.01 and 0.05 levels, respectively (*Figs. 2* and *6* and *Table 2*).

Table 2. Trends of maximum (T_{max}), minimum (T_{min}) and mean (T) temperatures (°C/decade), by Mann-Kendall Sen's test

Station	Element	Winter	Spring	Summer	Autumn	Annual
Mosul	T_{max}	0.53^{**}	0.43^{+}	0.33^{**}	0.25^{-}	0.36^{***}
	T_{min}	0.13^{-}	0.29^{+}	0.45^{***}	0.53^{**}	0.37^{***}
	T	0.30^{+}	0.39^{*}	0.38^{***}	0.47^{*}	0.36^{***}
Sulaymaniya	T_{max}	0.75^{**}	0.50^{**}	0.40^{**}	0.18^{-}	0.59^{***}
	T_{min}	0.75^{***}	0.59^{***}	0.64^{***}	0.41^{*}	0.62^{***}
	T	0.71^{***}	0.58^{**}	0.58^{***}	0.36^{*}	0.61^{***}
Kirkuk	T_{max}	0.48^{*}	0.42^{+}	0.15^{-}	0.01^{-}	0.26^{*}
	T_{min}	0.39^{**}	0.55^{***}	0.80^{***}	0.28^{-}	0.56^{***}
	T	0.44^{**}	0.51^{**}	0.56^{***}	0.17^{-}	0.43^{***}
Khanaqin	T_{max}	0.61^{**}	0.86^{***}	0.65^{***}	0.20^{-}	0.68^{***}
	T_{min}	0.39^{*}	0.91^{***}	1.04^{***}	0.83^{***}	0.81^{***}
	T	0.62^{**}	0.88^{***}	0.85^{***}	0.56^{***}	0.74^{***}
Baghdad	T_{max}	0.69^{**}	0.42^{**}	0.36^{**}	0.16^{-}	0.45^{***}
	T_{min}	0.57^{***}	0.78^{***}	1.06^{***}	0.72^{**}	0.79^{***}
	T	0.55^{**}	0.64^{***}	0.74^{***}	0.46^{**}	0.64^{***}
Rutba	T_{max}	0.49^{*}	0.41^{**}	0.48^{***}	0.18^{-}	0.44^{***}
	T_{min}	0.48^{**}	0.79^{***}	0.92^{***}	0.82^{***}	0.77^{***}
	T	0.51^{**}	0.66^{***}	0.69^{***}	0.57^{**}	0.58^{***}
Al - Hai	T_{max}	0.65^{**}	0.68^{***}	0.53^{***}	0.22^{-}	0.55^{***}
	T_{min}	0.67^{***}	1.03^{***}	0.97^{***}	0.65^{***}	0.86^{***}
	T	0.65^{***}	0.95^{***}	0.71^{***}	0.47^{**}	0.73^{***}
Diwaniya	T_{max}	0.57^{**}	0.50^{***}	0.35^{**}	-0.02^{-}	0.41^{***}
	T_{min}	0.63^{***}	0.71^{***}	1.00^{***}	0.87^{***}	0.84^{***}
	T	0.55^{**}	0.66^{***}	0.69^{***}	0.48^{**}	0.61^{***}
Samawa	T_{max}	0.43^{+}	0.20^{-}	0.34^{**}	0.08^{-}	0.30^{**}
	T_{min}	0.14^{-}	0.47^{***}	0.42^{**}	0.44^{*}	0.39^{***}
	T	0.34^{+}	0.35^{**}	0.36^{**}	0.25^{-}	0.31^{***}
Nasiriya	T_{max}	0.54^{**}	0.73^{***}	0.68^{***}	0.33^{+}	0.62^{***}
	T_{min}	0.36^{**}	0.79^{***}	0.82^{***}	0.50^{***}	0.63^{***}
	T	0.46^{**}	0.78^{***}	0.79^{***}	0.46^{**}	0.61^{***}
Basra	T_{max}	0.42^{*}	0.85^{***}	1.47^{***}	0.50^{**}	0.83^{***}
	T_{min}	0.37^{*}	0.85^{***}	0.86^{***}	0.72^{***}	0.71^{***}
	T	0.37^{*}	0.81^{***}	1.16^{***}	0.61^{***}	0.77^{***}
Average	$\boldsymbol{T_{max}}$	**0.56**	**0.55**	**0.52**	**0.19**	**0.50**
	$\boldsymbol{T_{min}}$	**0.44**	**0.71**	**0.82**	**0.62**	**0.67**
	$\boldsymbol{T}$	**0.50**	**0.66**	**0.68**	**0.44**	**0.58**

The significance levels tested are 0.001 (***), 0.01 (**), 0.05 (*), 0.1 (+), and >0.1 (–) (*Salmi et al.*, 2002).

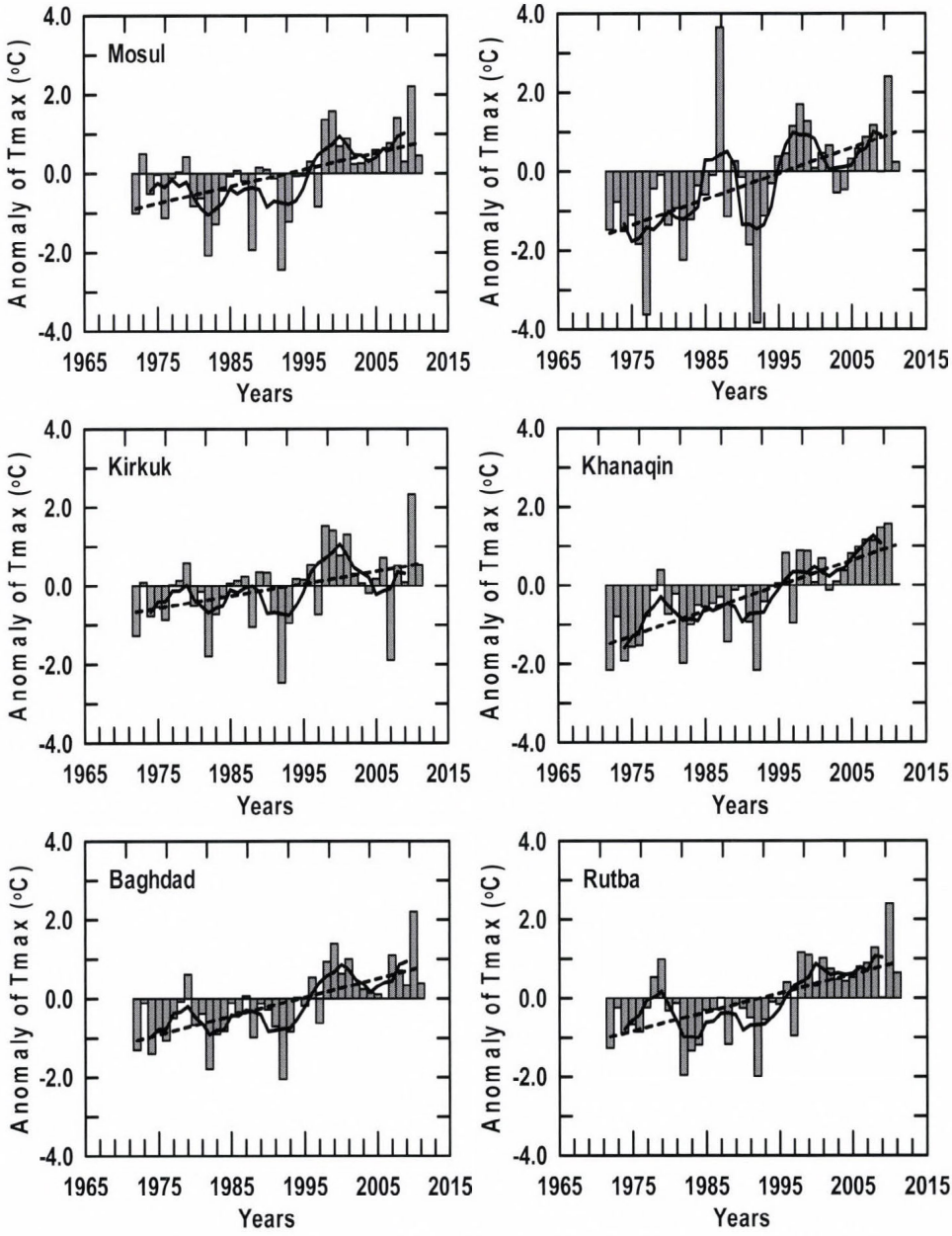

Fig. 2. Anomalies of maximum temperatures (T_{max} °C) for the eleven selected stations during the studied period (1972–2011), for the baseline (1982–2011) average. The bars indicate the anomalies of the years, the zigzag line represents five-year means, and the straight line indicates the long-term linear trends.

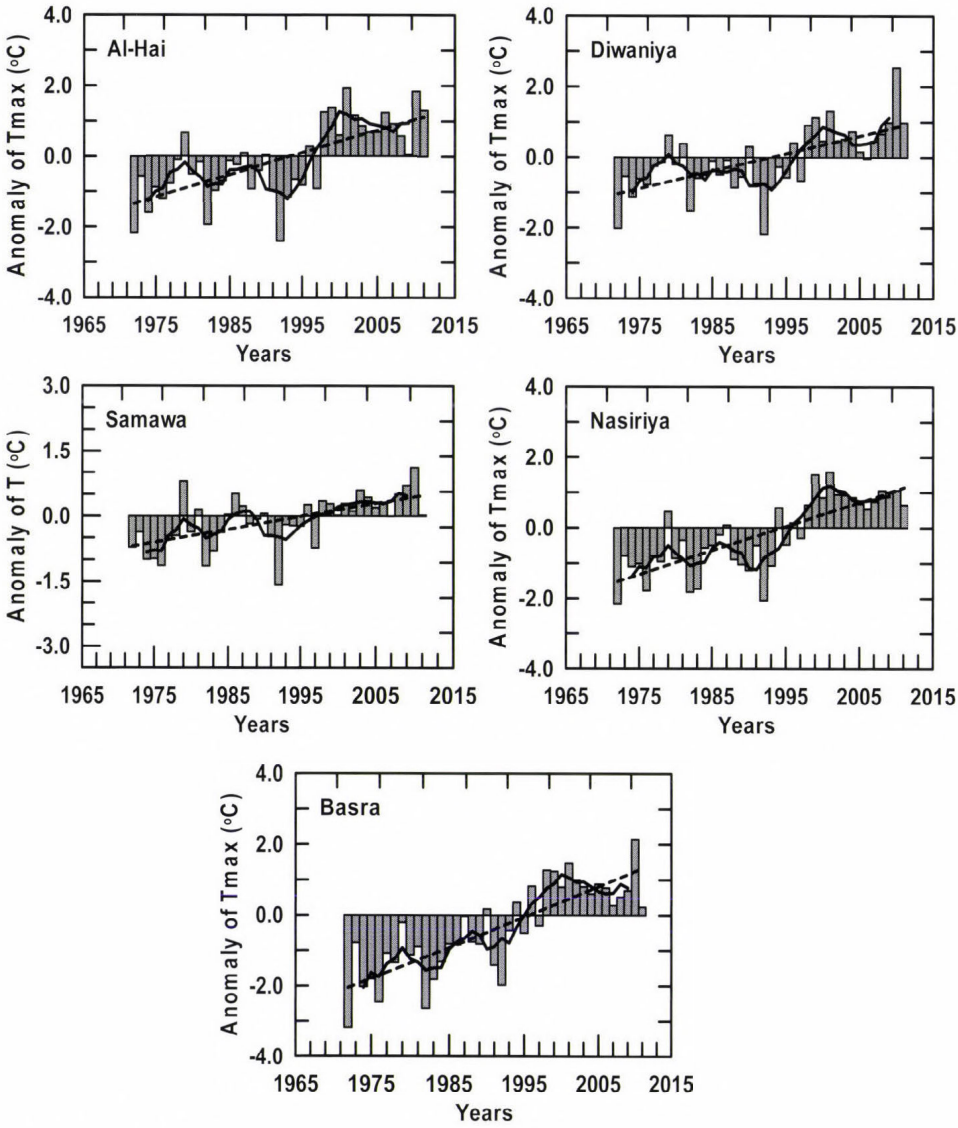

Fig. 2. (Continued).

In spring and summer, the significant positive trends of T_{max} are clearly observed with vider spatial distribution than winter and autumn. The strongest significant positive (1.47 °C/decade) and negative (–0.02 °C/decade) trends occurred in summer and autumn and reported at Basra and Diwaniya, respectively (*Fig. 6* and *Table 2*). It is clear that the long-term changes in

maximum temperature during winter, spring, and summer showed an increasing trend, which is statistically significant for the four last decades, while the autumn showed different pattern.

3.2. Trends of mean minimum temperature

Fig. 3 illustrates the annual anomalies of minimum temperature (T_{min}, °C) at the eleven selected stations in Iraq. Statistical properties of the seasonal and annual T_{min} series were tested using the Mann-Kendall test and presented in *Table 2*. It is clearly seen that all stations have experienced significant positive trend during winter, except for the two stations of Mosul and Samawa. It was found ,that 36.4, 27.3, and 18.2% of the stations have experienced significant positive trend during winter at the 0.001, 0.01, and 0.05 levels, respectively, while the trends are not significant at only 18.2% of the stations. The trends range from 0.13 °C/decade (non-significant trend) at Mosul to 0.75 °C/decade (significant at the 0.001 level) at Sulaymaniya. In spring, all stations have experienced significant positive trend. It was found that 90.9 and 9.1% of the stations had experienced significant positive trend at the 0.001 and 0.1 levels, respectively. Al-Hai, which is located in the southern part of the country, has experienced the highest positive trend (1.03 °C/decade), while Mosul in the northern part has experienced the lowest positive trend (0.29 °C/decade). Negative trends were not observed at the stations during this season. In summer, the trends were positive and significant at the 0.001 and 0.01 levels for 90.9 and 9.1% of the stations, respectively. It was found, that the trend values ranged between the lowest positive trend (0.42 °C/decade) at Kirkuk in the north to the highest positive trend (1.06 °C/decade) at Basra in the extreme south. In autumn, all stations have experienced significant positive trend (except Kirkuk). The trends range from 0.28 °C/decade (non-significant trend) at Kirkuk to 0.87 °C/decade (significant at the 0.001 level) at Diwaniya. It could be noticed, that 54.5, 18.2, and 18.2% of the stations have experienced significant positive trend during autumn at the 0.001, 0.01, and 0.05 levels, respectively, while the trends are not significant at only 9.1% of stations (*Figs. 3* and *6* and *Table 2*).

There is a general tendency for the warming trend during the study period. The annual and seasonal trend analyses reveal that most of the warming in reference to T_{min} was found in spring (0.71 °C/decade) and summer (0.82 °C/decade), respectively, while the average trend over the whole Iraq country is 0.67 °C/decade. Annually, it could be noticed that minimum temperature showed a significant positive trend in 100% of the stations at the 0.001 level, while there is not any stations in the whole Iraq which have significant/non-significant negative trend (*Figs. 3* and *6* and *Table 2*).

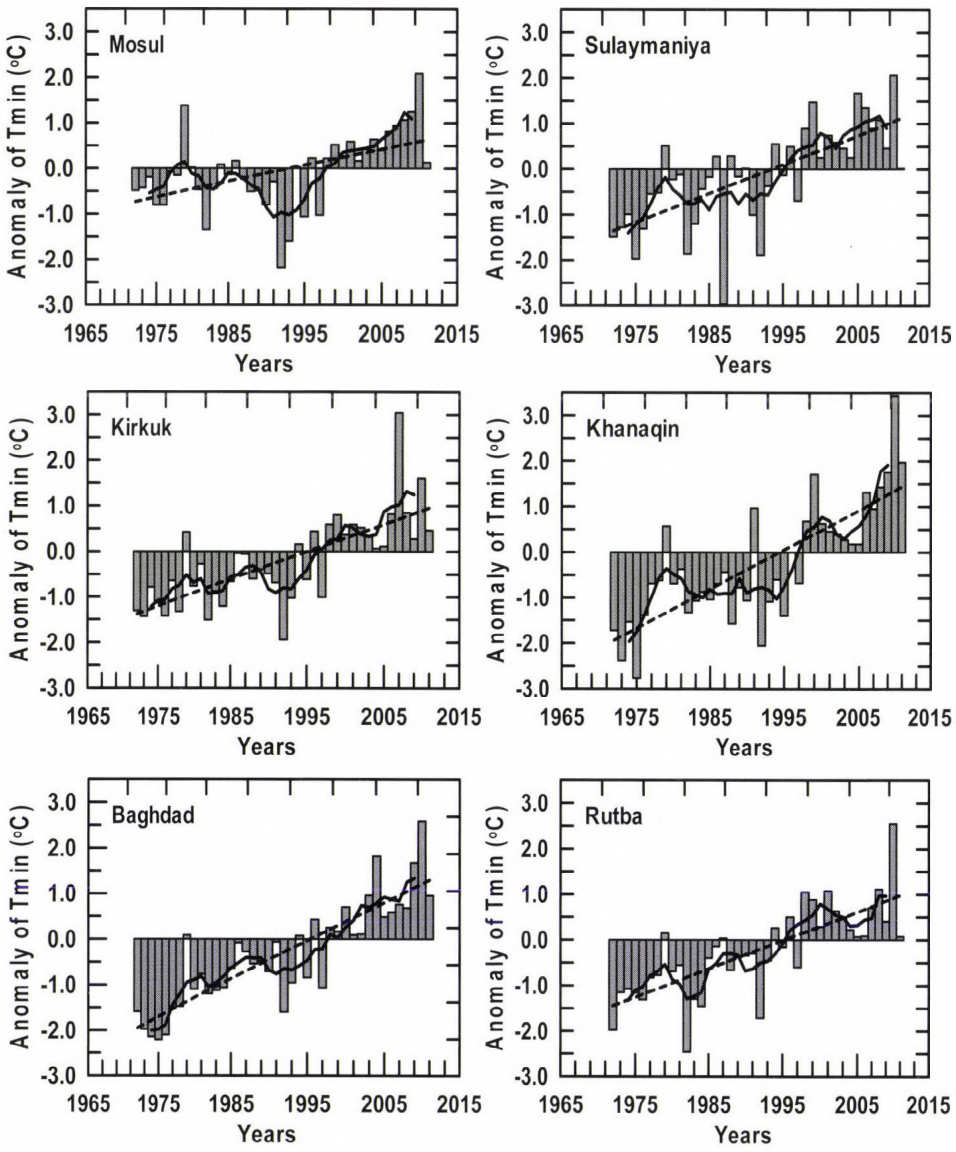

Fig. 3. Anomalies of minimum temperatures (T_{min}, °C) for the eleven selected stations during the studied period (1972–2011), for the baseline (1982–2011) average. The bars indicate the anomalies of the years, the zigzag line represents five-year means, and the straight line indicates the long-term linear trends.

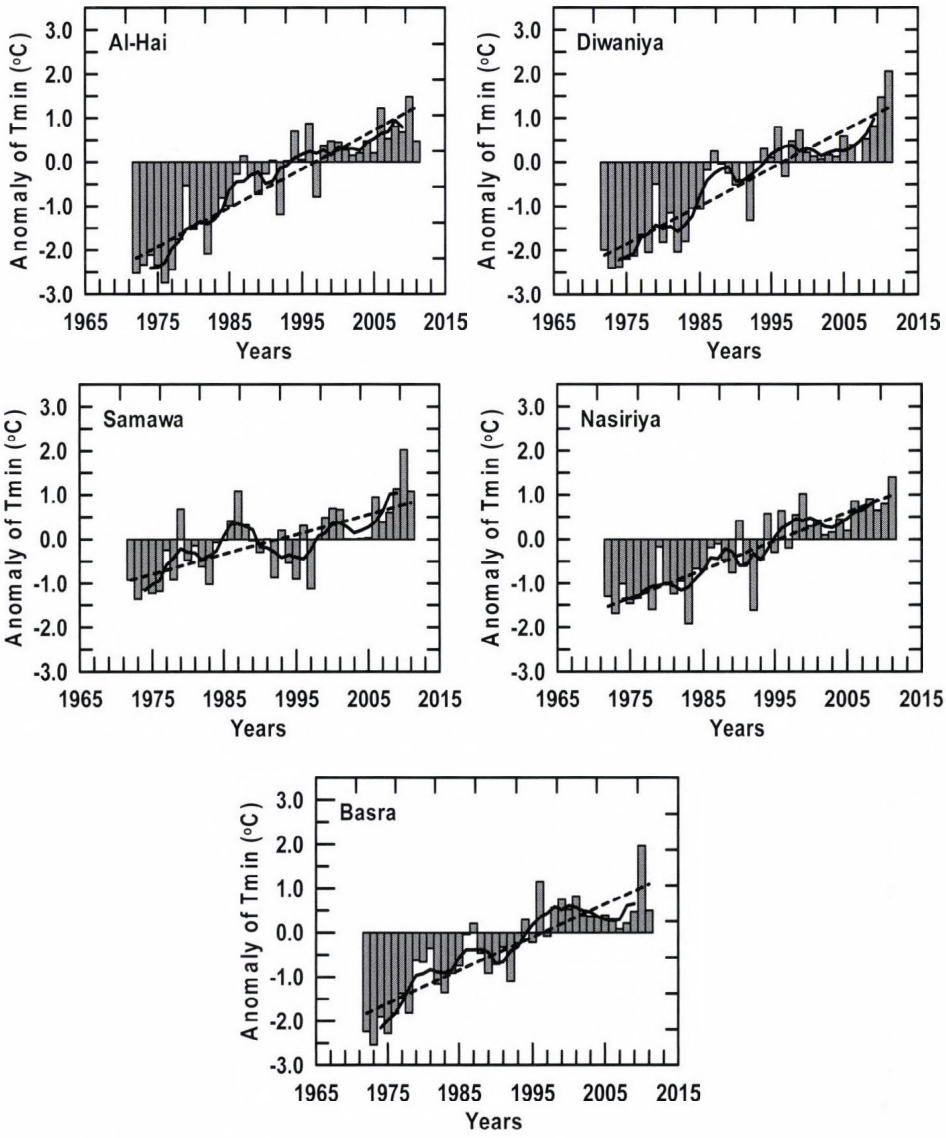

Fig. 3. (Continued).

3.3. Trends of mean temperature

Fig. 4 illustrates the annual anomalies of mean temperature (T, °C) at the eleven selected stations in Iraq. Statistical properties of the seasonal and annual T series were also tested and presented in *Table 2*. It was found, that according to the MK test for trend, all stations have experienced significant positive trends (warming pattern) of the annual mean temperature.

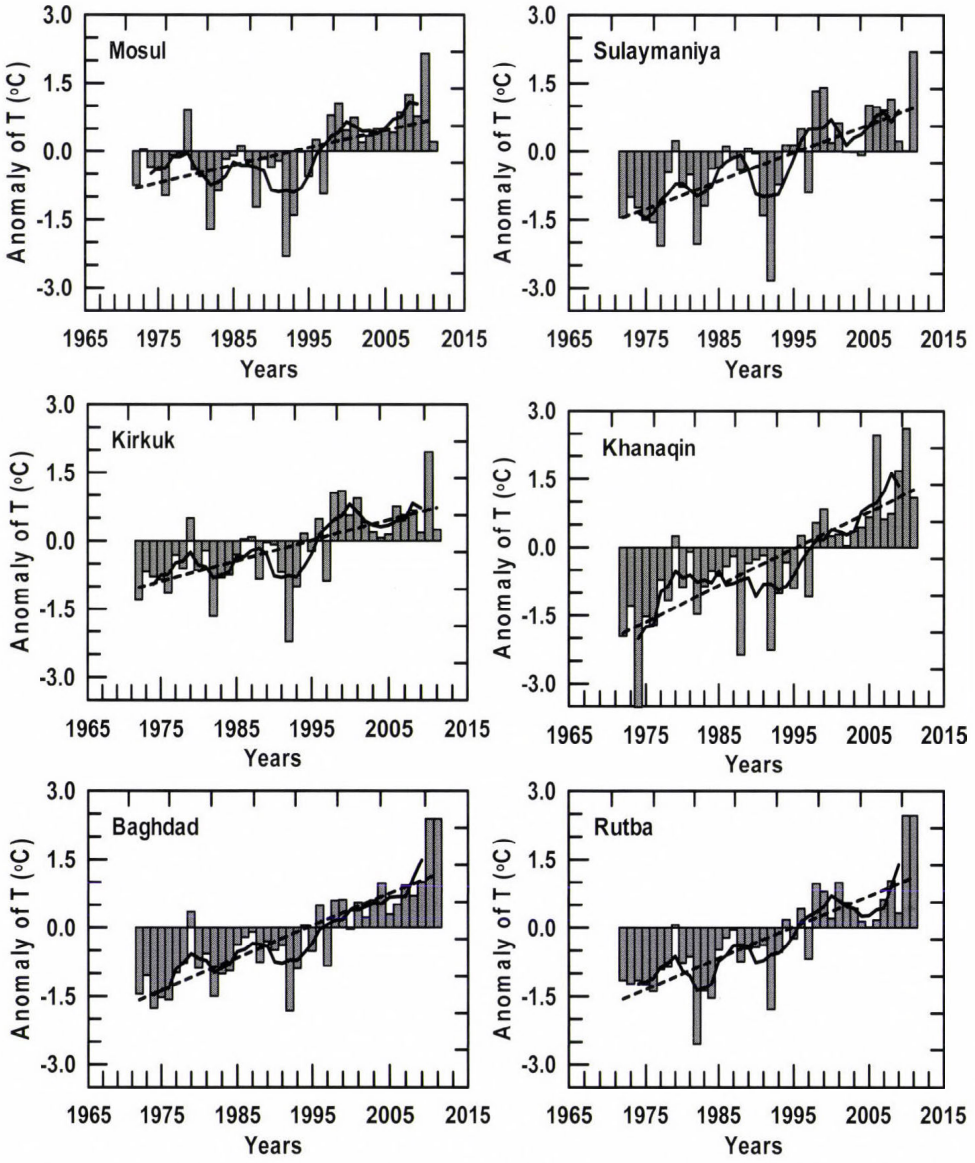

Fig. 4. Anomalies of mean temperatures (T, °C) for the eleven selected stations during the studied period (1972–2011), for the baseline (1982–2011) average. The bars indicate the anomalies of the years, the zigzag line represents five-year means, and the straight line indicates the long-term linear trends.

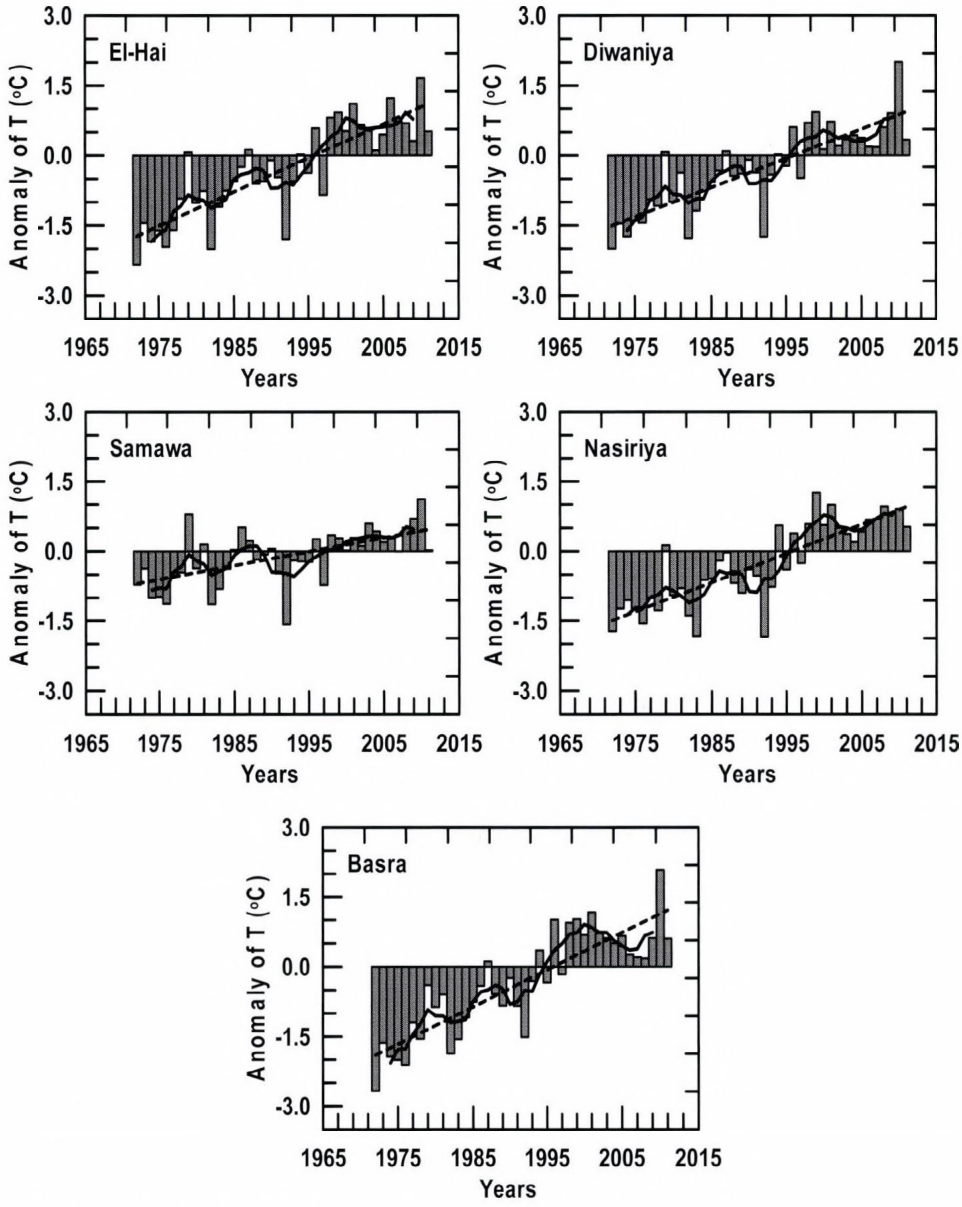

Fig. 4. (Continued).

In winter, all stations have experienced positive trend. It was found that 18.2, 54.5, 9.1, and 18.2% of the stations have experienced positive trend during winter at the 0.001, 0.01, 0.05, and 0.1 levels, respectively. Also, it can be noticed, that Mosul has the lowest and non-significant positive trend

(0.30 °C /decade), while Sulaymaniya has the highest significant positive trend (0.71 °C /decade) at the 0.001 level. During spring, ten stations show strong upward tendency trends, whereas 90.9% of the stations have experienced significant positive trend at the 0.001 level while 9.1% of the stations have positive trend at the 0.1 levels. It could be noticed, that the trends ranged between 0.35 °C/decade at Samawa and 0.95 °C/decade at Al-Hai; the trends for Samawa and Al-Hai are significant at the 0.01 and 0.001 levels, respectively (*Figs. 4* and *6* and *Table 2*).

All eleven stations also showed strong evidence of a significant positive trend during summer, while there is not any station with negative trend during this season. It could be noticed, that 90.9 and 9.1% of the stations have experienced strong significant positive trend at the 0.001 and 0.01 levels, respectively. Trends range between 0.36 °C/decade at Samawa and 1.16 °C/decade at Basra, and they are significant at the 0.01 and 0.001 levels, respectively. In autumn, the significant positive trend could be generally identified at all stations except for Kirkuk (0.17 °C/decade) and Samawa (0.25 °C/decade), which have non-significant trends, while Basra has the highest significant positive trend (0.61 °C/decade) at the significance level of 0.001. It was found that 18.2, 45.5, and 18.2% of the stations have experienced strong significant positive trend at the 0.001, 0.01, and 0.05 levels, respectively, and the trend is not significant at only 18.2% of the stations. Seasonally, there is not any stations in the whole Iraq which have significant/non-significant negative trend (*Figs. 4* and *6* and *Table 2*).

Annually, it is noticed that the mean temperature showed a significant positive trend at the 0.001 level for all stations, while there is not any stations in the whole Iraq which have significant/non-significant negative trend in the whole Iraq. It was also found, that the significant positive trends of T varied between the lowest value (0.31 °C/decade) at Samawa and the highest value (0.77 °C/decade) at Basra; the trends for both Samawa and Basra are significant at the 0.001 level (*Fig. 6* and *Table 2*).

The results are generally in agreement with those in many studies worldwide, which have shown a trend of increasing air temperature (*Jones* and *Moberg,* 2003; *Luterbacher et al.,* 2004; *Rebetez* and *Reinhard,* 2008; European Environment Agency reports (EEA), 2008; *Croitoru et al.*, 2012; *Piticar* and *Ristoiu*, 2012; *Ionita et al.*, 2013; *Croitoru* and *Piticar*, 2013; *Tannecia et al.*, 2014).

3.4. Trends of total rainfall

Total rainfall (R_a, mm), is the other important climate parameter in the present study. Statistical properties of the seasonal and annual R_a series at the eleven selected stations in Iraq were tested using the MK test and presented in *Table 3* and illustrated by *Fig. 5*.

Table 3. Trends of total rainfall amounts, Ra (mm/decade), by Mann- Kendall Sen's test

Station	Winter	Spring	Summer	Autumn	Annual
Mosul	−23.50^{+}	−3.45^{-}	0.00^{-}	−1.53^{-}	−32.25*
Sulaymaniya	−24.00^{-}	−3.50^{-}	0.00^{-}	0.39^{-}	−35.52^{-}
Kirkuk	−20.95^{-}	−7.69^{-}	0.00^{-}	−1.32^{-}	−36.06*
Khanaqin	−36.35**	−4.83^{-}	0.00^{-}	2.31^{-}	−41.96***
Baghdad	−9.85^{+}	0.65^{-}	0.00^{-}	0.51^{-}	−12.10*
Rutba	−11.75**	−2.29^{-}	0.00^{-}	0.47^{-}	−9.38^{-}
Al – Hai	−12.87^{+}	−0.91^{-}	0.00^{-}	−1.41^{-}	−24.72**
Diwaniya	−8.69^{+}	−0.61^{-}	0.00^{-}	1.81^{-}	−10.13^{-}
Samawa	−4.40^{-}	0.68^{-}	0.00^{-}	2.00^{-}	0.26^{-}
Nasiriya	−10.68^{+}	0.52^{-}	0.00^{-}	−0.04^{-}	−7.83^{-}
Basra	−7.27^{-}	0.67^{-}	0.00^{-}	0.29^{-}	−15.77*
Average	**−15.48**	**−1.89**	**0.00**	**0.32**	**−20.50**

The results distinctly revealed that, during winter, all stations have experienced negative trend. It was found that 18.2 and 45.4% of the stations have experienced significant negative trend during winter at the 0.01, 0.1 levels, respectively, while 36.4% of the stations have non-significant negative trend. The highest significant negative trend (–36.35 mm/decade) was found at Khanaqin, while the lowest negative trend (–4.4% mm/decade) was found at Samawa; the trend for Khanaqin is significant at the 0.01 level, while Samawa showed non-significant decreasing trend. During spring, only four stations (36.4% of stations) have experienced non-significant positive trend, while the remaining stations (63.6% of stations) have experienced non-significant negative trend. It could also noticed, that Samawa experienced the highest non-significant positive trend (0.68 mm/decade) while Kirkuk experienced the lowest non-significant negative trend (–7.69 mm/decade), see *Figs. 5* and *6* and *Table 3*.

In summer, the climate of Iraq is rainless and clear skies prevail. Therefore, all stations show no trend during this season. During autumn, only seven stations (63.6% of stations) have experienced non-significant positive trend, while the remaining four stations (36.4% of the stations) have experienced non-significant negative trend. It could be noticed that the highest positive trend during the autumn season (2.31 mm/decade) occurred at Khanaqin station, while the lowest negative trend (–1.53 mm/decade) occurred at Mosul station (*Figs. 5* and *6* and *Table 3*).

Annually, negative trends of total rainfall have been observed at all stations except Samawa, which showed non-significant positive trend (2.31 mm/decade). It was found that 9.1, 9.1, and 36.4% of the stations have experienced significant negative trend at the 0.001, 0.01, and 0.05 levels, respectively, while 36.4 and 9.1%

of the stations showed non-significant negative and positive trends respectively. The trends range from –7.83 mm/decade at Nasiriya to –41.96 mm/decade at Khanaqin; the trend for Khanaqin is significant at the 0.001 level, while Nasiriya showed non-significant negative trend (*Figs. 5* and *6* and *Table 3*).

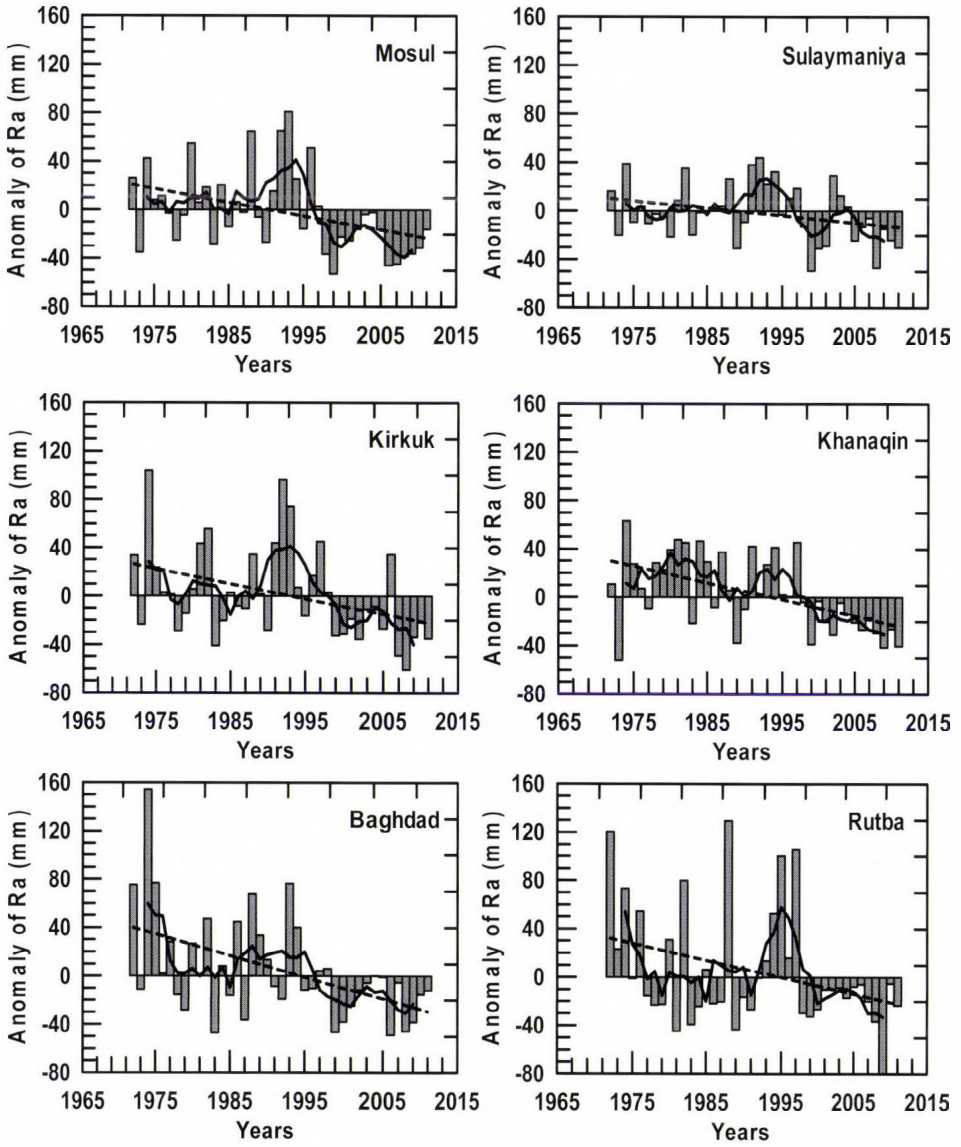

Fig. 5. Anomalies of the rainfall amount (*Ra*, mm) for the eleven selected stations during the studied period (1972–2011), for the baseline (1982–2011) average. The bars indicate the anomalies of the years, the zigzag line represents five-year means, and the straight line indicates the long-term linear trends.

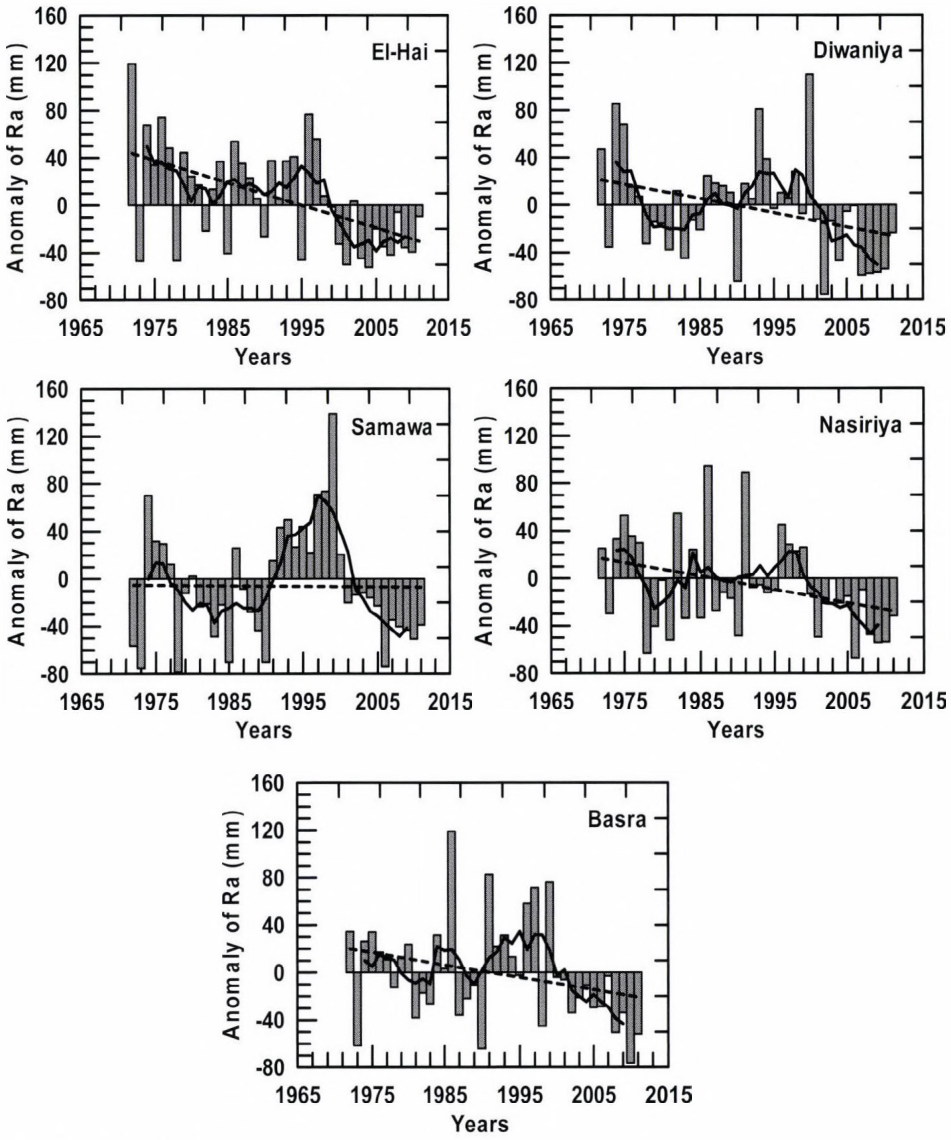

Fig. 5. (Continued).

It could be concluded, that the trends of R_a were negative over the whole country of Iraq except for Samawa, where the observed rainfall has slightly increased. The average rate of R_a decreased over the whole Iraq, and it has been found –15.48 mm/decade, –1.89 mm/decade, –0.32 mm/decade during winter,

spring, and autumn seasons, respectively, and –20.5 mm/decade annually, while no consistent changes were found during the summer season. Majority of the trends indicated reduced precipitation during winter. It is also noticed, that the rainfall showed a negative trend in 90.9% of the stations, but there is 9.1% of the stations with positive trend in the whole Iraq (see *Fig. 6* and *Table 3*). This result agrees with the findings of *Raziei et al.*, (2005) and *Tabari* and *Talaee* (2011b), who found a significant negative trend in the annual precipitation series in Iran.

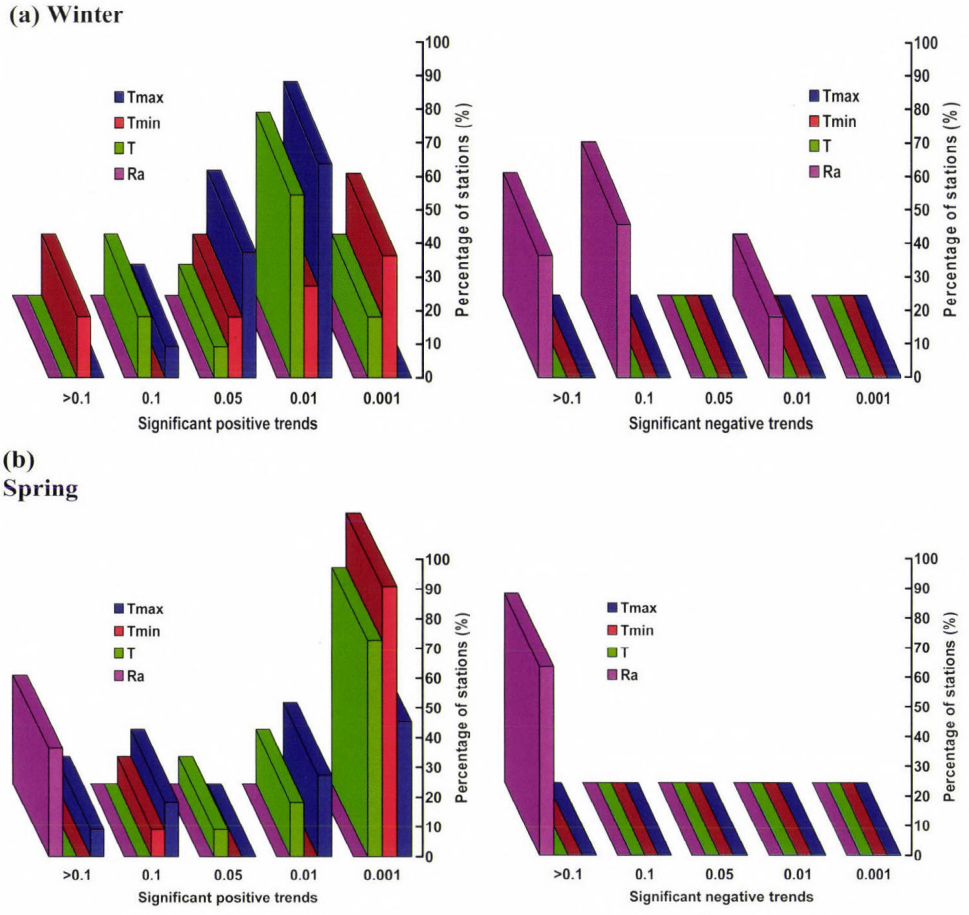

Fig. 6. The percentage of stations with significant positive and negative trends for T_{max}, T_{min}, T, and Ra by the Mann-Kendall test during (a) winter, (b) spring, (c) summer, (d) autumn, and (e) annual.

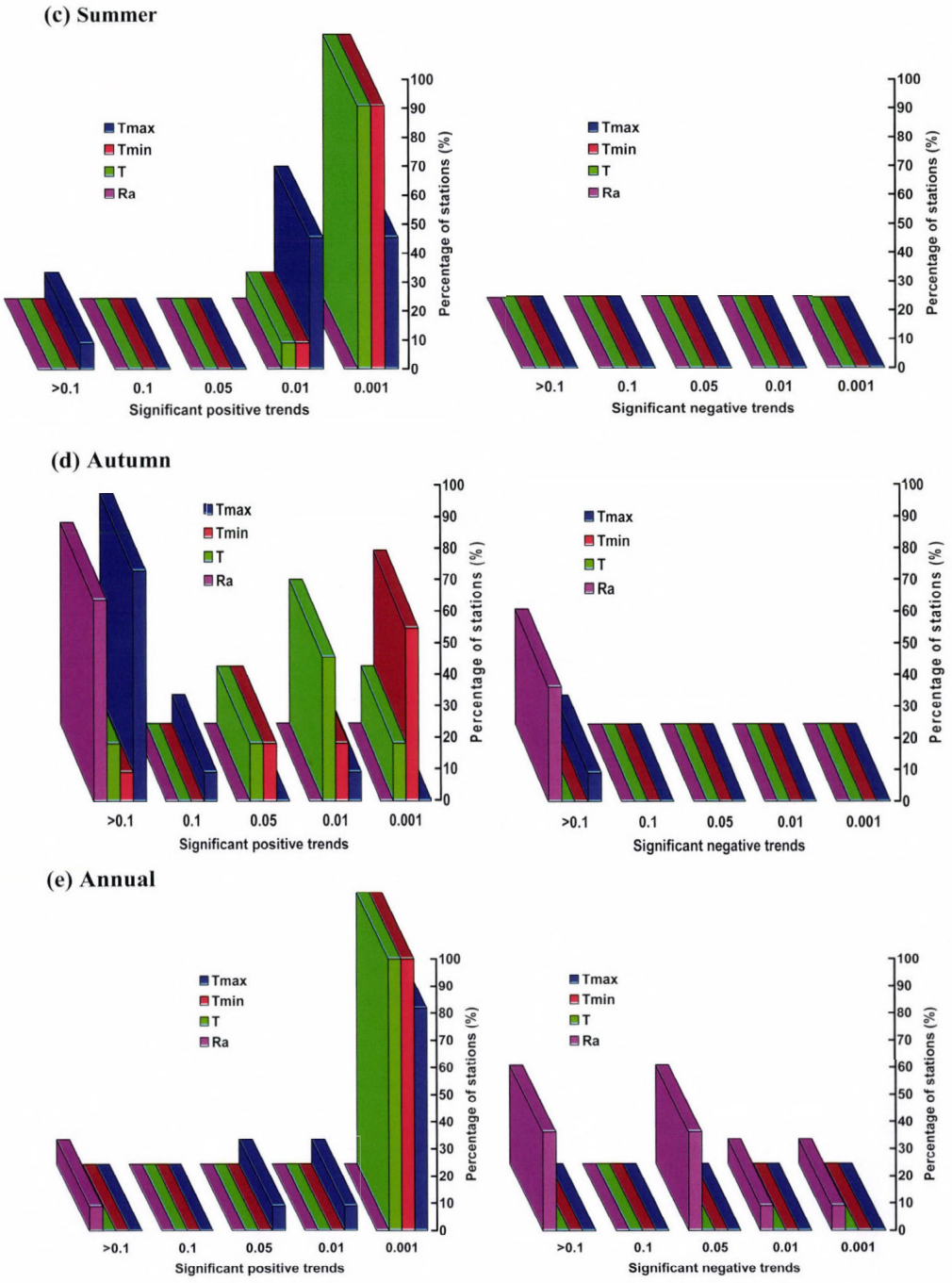

Fig. 6. (Continued).

4. Conclusions

The present study is mainly concerned with the changing trend of air temperatures and rainfall in Iraq. A complete set of measurements for maximum (T_{max}), minimum (T_{min}) and mean air temperatures (T) in addition to rainfall amounts (R_a) for the period 1972–2011 at 11 meteorological stations in Iraq have been used. Statistical tests including the Mann-Kendall test, the Sen's slope estimator, and linear regression were used for the analysis. Final results and conclusions could be summarized in the following points:

1. Annual mean of T_{max}, T_{min}, and T time series showed statistically significant increasing trends over 81.8, 100, and 100% of the stations at the 0.001 level, and they experienced an increase of 0.50, 0.67, and 0.58 °C/decade, respectively.
2. The significant positive trends of T_{max}, T_{min}, and T can be observed clearly during spring and summer than during winter and autumn.
3. There is not any stations which have significant or non-significant negative trend for air temperatures in the whole Iraq except Diwaniya, where the trend of T_{max} was weakly negative during autumn.
4. Annual rainfall has shown decreasing trends at all stations (except Samawa), and it experienced an decrease of –20.50 mm/decade.
5. Seasonally, the highest increase of T_{max}, T_{min}, and T values have been found at the extreme south of the country (Basra) during summer at the rates of 1.47, 1.06, and 1.16 °C/decade, respectively, while the lowest increase of the air temperatures prevail in the northern part of the country, especially at Kirkuk.
6. The highest decrease of R_a values has been found in the northern part of the country (Khanaqin) during winter at the rate of –36.35 mm/decade.
7. The warming pattern occurred shortly after 1995 at all stations.

Changes in air temperature and rainfall amounts will have significant impacts on biodiversity and food security in Iraq. Therefore, substantial reductions of heat-trapping gas emissions and adaptation strategies are crucial in Iraq.

References

Al-Ansari, N. and *Knutsson, S.*, 2011: Toward Prudent management of Water Resources in Iraq. *J.Adv. Sci. Engineer. Res. 1*, 53–67.

Al-Ansari, N., Al-Oun, S., Hadad, W., and Knutsson, S. 2013: Water loss in Mafraq Governorate, Jordan. Natural Sci. 5, 333–340.

Arora, M., Goel, N.K., and *Singh ,R.* 2005: Evaluation of temperature trends over India. *Hydrol. Sci. J. 50.*, 81–93.

Busuioc, A., Caian, M., Cheva, S., Bojariu, R., Boroneant, C., Baciu, M., and Dumitrescu, A., 2010: Climate variability and change in Romania. Ed. Pro Universitaria, Bucharest.

Chen, H., Guo, S., Chong-yu, X., and *Singh, V.P.,* 2007: Historical temporal trends of hydro-climatic variables and runoff response to climate variability and their relevance in water resource management in the Hanjiang basin. *J. Hydrol. 344*,171–184.

Croitoru, A.E., Holobaca, I.H., Lazar, C., Moldovan, F., and *Imbroane, A.,* 2012: Air temperature trend and the impact on winter wheat phenology in Romania. *Climatic Change 111*, 393–410.

Croitoru, A.E. and *Piticar, A.,* 2013: Changes in daily extreme temperatures in the extra-Carpathians regions of Romania. *Int. J. Climatol. 33,* 1987–2001.

Diaz, H.F., Bradley, R.S., and *Eischeid, J.K.,* 1989: Precipitation fluctuations over global land areas since the late 1800s. *J Geophis. Res. 94*, 1195–1210.

Dore, M.H.I., 2005: Climate change and changes in global precipitation patterns: what do we know. *Environ. Int. 31*, 1167–1181.

EEA. 2008: Impacts of Europe's changing climate -2008 indicator-based assessment. *EEA report 4*, 242.

Efstathiou, M.N., Tzanis, C., Cracknell, A., and *Varotsos, C.A.,* 2011: New features of the land and sea surface temperature anomalies. *Int. J. Remote Sens. 32*, 3231–3238.

Eichner, J.F., Koscielny-Bunde, E., Bunde, A., Havlin, S., and *Schellnhuber, .HJ.* (2003) Power-law persistence and trends in the atmosphere: A detailed study of long temperature records. *Phys. Rev. E., 68,* 046133.

Folland, C.K., Rayner, N.A., Brown, S.J., Smith, T.M., Shen, S.S.P., Parker, D.E., Macadam, I., Jones, P.D., Jones, R.N., Nicholls, N., and Sexton, D.M.H. 2001: Global temperature change and its uncertainties since 1861. Geophys. Res. Lett. 28, 2621–2624.

Gemmer, M., Becker, S., and *Jiang, T.* 2004: Observed monthly precipitation trends in China 1951–2002. *Theor. Appl. Climatol. 77*, 39–45.

Hulme, M., Osborn, T.J., and *Johns, T.C.*, 1998: Precipitation sensitivity to global warming: comparison of observations with HADCM2 simulations. *Geophys. Res. Lett. 25*, 3379–3382.

Ionita, M., Rimbu, N., Chelcea, S., and *Patruţ, S.,* 2013: Multidecadal variability of summer temperature over Romania and its relation with Atlantic Multidecadal Oscilation. *Theor. Appl. Climatol. 113*, 305–315.

Jones, P.D., 1994: Hemispheric surface air temperature variations: A reanalysis and an update to 1993. *J. Climate 7,* 1794–1802.

Jones, P.D., New, M., Parker, D.E., Martin, S., and *Rigor, I.G.*, 1999: Surface air temperature and its changes over the past 150 years. *Rev. Geophys. 37*,173–199.

Jones, P.D. and *Moberg, A.* 2003: Hemispheric and Large-Scale Surface Air Temperature Variations: An Extensive Revision and Update to 2001. *J. Climate 16,* 206–223.

Kayano, M.T. and *Sansıgolo, C.,* 2008: Interannual to decadal variations of precipitation and daily maximum and daily minimum temperatures in southern Brazil. *Theor. Appl. Climatol. 97*, 81–90.

Kendall, M.G., 1938: A new measure of rank correlation. *Biometrika 30*, 81–93.

Kendall, M.G., 1975: Rank Correlation Methods. 4th ed. Charles Griffin: London, UK; 272.

Lambert, F., Stott, P., and *Allen, M.,* 2003: Detection and attribution of changes in global terrestrial precipitation. *Geophys. Res. Abst. 5*, 06140.

Luo, Y., Liu, S., Fu, S.F., Liu, J., Wang, G., and *Zhou, G.,* 2008: Trends of precipitation in Beijiang River Basin, Guangdong Province, China. *Hydrological Proc. 22*, 2377–2386.

Luterbacher, J., Dietrich, D., Xoplaki, E., Grosjean, M., and *Wanner, H.,* 2004: European seasonal and annual temperature variability, trends, and extremes since 1500. *Science 303*,1499–1503.

Mann, H.B., 1945: Non-parametric tests against trend. *Econometrica 33*, 245–259.

Marco, G., Stefan, B., and *Tong. J.,* 2003: Detection and Visualization of Climate Trends in China. No. 15, Giessen, Nanjing Institute of Geography and Limnology, Chinese Academy of Science (CAS), 210008 Nanjing, PR China.

Nicholls, N., Gruza, G.V., Jouzel, J., Karl, T.R., Ogallo, L.A., and Parker, D.E., 1996: Observed climate variability and change. In (Eds.: Houghton, J.T., Filho, L.G.M., Callander, B.A., Harris,

N., Kattenberg, A., and Maskell, K.).Climate Change 1995: The Science of Climate Change. Cambridge University Press: Cambridge; 133–192.

Raziei, T., Arasteh, P.D., and *Saghafian, B.,* 2005: Annual rainfall trend in arid and semi-arid regions of Iran. ICID 21st European regional conference, Frankfurt (Oder) and Slubice-Germany and Poland.

Piticar, A. and *Ristoiu, D.* 2012: Analysis of air temperature evolution in Northeastern Romania and evidence of warming trend. *Carpathian J. Earth Environ. Sci. 7,* 97–106.

Rebetez, M. and *Reinhard, M.,* 2008: Monthly air temperature trends in Switzerland 1901–2000 and 1975–2004. *Theor. Appl. Climatol. 91*, 27–34.

Rybski, D., Bunde, A., Havlin, S., and *von Storch, H.,* 2006: Long-term persistence in climate and the detection problem. *Geophys. Re. . Lett. 33*, l06718.

Salmi, T., Maata, A., Antilla, P., Ruoho-Airola, T., and *Amnell, T.,* 2002: Detecting trends of annual values of atmospheric pollutants by the Mann–Kendall test and Sen's slope estimates – the Excel template application MAKESENS. Finnish Meteorological Institute, Helsinki, Finland.

Schaefer, D., 1996: Uni- und multivariate statistische Untersuchungen zu rezenten Klima¨anderungen in Sri Lanka. PhD thesis, Institute of Geography, Mainz University, Germany.

Schoenwiese, C., 1992: Praktische Statistik für Meteorologen und Geowissenschaftler, second ed. Gebrüder Borntraeger, Berlin and Stuttgart.

Sen, P.K., 1968: Estimates of the regression coefficient based on Kendall's tau. *J. Amer. Stat. Assoc. 63*, 1379–1389.

Smadi, M.M., 2006: Observed abrupt changes in minimum and maximum temperatures in Jordan in the 20th century. *Amer. J. Environ. Sci. 2,* 114–120.

Smadi, M.M. and *Zghoul, A.,*2006: A sudden change in rainfall characteristics in Amman, Jordan during the mid 1950s. *Amer. J. Environ. Sci. 2,* 84–91.

Stephenson, T.S., Vincent, L.A., Allen, T., Van Meerbeeck, C.J., McLean, N., Peterson, T.C., Taylor, M.A., Aaron-Morrison, A.P., Auguste, T., Bernard, D., Boekhoudt, J.R.I., Blenman, R.C., Braithwaite, G.C., Brown, G., Butler, M., Cumberbatch, C.J.M., Etienne-Leblanc, S., Lake, D.E., Martin, D.E., McDonald, J.L., Zaruela, M.O., Porter, A.O., Ramirez, M.S., Tamar, G.A., Roberts, B.A., Mitro, S.S., Shaw, A., Spence, J.M., Winter, A., and *Trotman, A.R.,* 2014: Changes in extreme temperature and precipitation in the Caribbean region, 1961–2010. *Int. J. Climatol. 34*. 2957–2971.

Tabari, H. and Talaee, H. P. 2011a: Recent trends of mean maximum and minimum air temperatures in the western half of Iran. *Meteor. Atmos. Phys. 111*, 121–131.

Tabari, H. and *Talaee, H.P.*, 2011b: Temporal variability of precipitation over Iran: 1966–2005. *J. Hydrol 396*, 313–320.

Yu, B. and *Neil, D.T.,* 1993: Long-term variations in regional rainfall in the south-west of Western Australia and the difference between average and high intensity rainfalls. *Int. J. Climatol. 13*, 77–88.

Varotsos, C.A., Efstathiou, M.N., Cracknell, A.P., 2013: On the scaling effect in global surface air temperature anomalies. *Atmos. Chem. Phys. 13*, 5243–5253.

Watson, R.T., Zinyowera, M.C., and *Moss, R.H.,* (eds) 1998: The Regional Impacts of Climate Change: An Assessment of Vulnerability. Cambridge University Press: Cambridge UK.

Zhang, X., Harvey, K.D., Hogg, W.D., and *Yuzyk, T.R.* 2001: Trends in Canadian streamflow. *Water Resour. Res. 37*, 987–998.

IDŐJÁRÁS

Quarterly Journal of the Hungarian Meteorological Service
Vol. 119, No. 4, October – December, 2015, pp. 515–535

Continentality in Europe according to various resolution regional climate models with A1B scenario in the 21st century

Beáta Szabó-Takács[1]*, **Aleš Farda**[1,3], **Pavel Zahradníček**[1,2], and **Petr Štěpánek**[1,2]

[1] *Global Change Research Centre AS CR, v.v.i.*
Bělidla 986/4a, 60300 Brno, Czech Republic

[2] *Czech Hydrometeorological Institute, branch Brno,*
Kroftova 43, 616 00 Brno, Czech Republic

[3] *Czech Hydrometeorological Institute,*
Na Šabatce 17, 143006 Prague, Czech Republic

* *Corresponding authors E-mail: szabo.b@czechglobe.cz*

(Manuscript received in final form January 8, 2015)

Abstract— The purpose of our research is to simulate the influence of the thermal properties of land surface on the Central European climate in the 21st century. The simulation is carried out with calculation of Gorczynsky and Conrad continentality indexes, respectively, as a function of annual temperature range. Seven different ENSEMBLES models (ARPÈGE, CNRM, DMI, ITCP, KNMI, MPI, and SMHI) with various resolutions perform the space difference of continentality between seven European regions with IPCC A1B emission scenario for two time slices: 2021–2050 and 2071–2100. Beside these models, ALADIN-Climate/CZ simulation is implemented in finer resolution and smaller CECILIA domain taking into consideration only the central European area. The bias correction of models is implemented using the European Climate Assessment and Dataset (ECA&D). The largest influence to the spread among the simulation results is due to the chosen global climate models (GCMs). The resolution differences do not play dominant role in the variance of the results against the domain size. There are not significant differences between the Gorczynsky and Conrad index values. The largest change in the climate type tendency is simulated in the Scandinavian region by the Gorczynsky approach. In central Europe, the climate becomes continental only according to CNRM result which correlates with its underestimation of precipitation and overestimation of temperature. The simulated continentality indexes and the predicted changes are presented here.

Key-words: continentality, Gorczynsky index, Conrad index, ENSEMBLES, climate change, E-OBS

1. Introduction

Continentality is a basic indicator of climate change. In the climate of central Europe, oceanic and continental climate effects are combined. The continental climate areas have great annual temperature range and moderate precipitation (*McBoyle* and *Steiner,* 1972), whilst the oceanic climate is more balanced. The reason of this basic difference comes from the different thermal properties of ocean and land surface. The oceans have larger heat capacity, whilst the inland has larger heat conduction, which depends on surface properties (*Nikiforova et al.*, 2013). The combination of heat capacity and thermal conductivity determines three important physical properties underlying climate: (i) the proportion of heat shared by the interface substances; (ii) the depth (soil, water) or height (atmosphere) to which heat flows or transported; (iii) the range of temperatures over diurnal and annual cycles (*Dirscoll* and *Yee Fong,* 1992). This phenomenon has an effect on several climatic elements like distribution of cloudiness, precipitation, etc., which impact the temperature anomaly. Different approaches are used to quantify continentality (*Gorczynsky,* 1922; *Johansson,* 1926; *Conrad* and *Pollak,* 1950; *Currey,* 1974; *Holmlund* and *Schneider,* 1997; *Sládek,* 2005; *Mikolaskova,* 2009).

The purpose of our work is to investigate the formation of the spatial differences of continentality in Central Europe using ENSEMBLES based on A1B SRES scenario in the 21th century. The A1B estimates the future world in perspective of technical change in energy system with the assumption that similar improvement rates apply to all energy supply and end use technologies (*Nakićenovíc,* 2000, *Solomon,* 2007).

The EU 6th Framework Programme project ENSEMBLES applies a probabilistic approach to climate changes at a regional scale (*Hewit* and *Griggs,* 2004) with downscaling global circulation models (GCM) to higher resolution regional climate models (*van der Linden* and *Mitchell,* 2009).

The sources of uncertainties in the ENSEMBLES predictions are the chosen GCM, RCM, downscaling technique, and natural variability. The choice of GCM significantly determines the initial and boundary conditions of RCMs. The source of differences in RCMs comes from the difference of the applied physical parameterizations to represent sub-grid effects. There are two basic downscaling techniques: dynamical and statistical. The dynamical downscaling is not able to improve the simulation skills of large-scale fields over those simulated by the GCM (*Dosio* and *Paruolo,* 2011), while the statistical relationship is developed for present day climate by statistical downscaling is assumed to be valid for future climate under different forcing condition (*Wilby et al.,* 1998). The natural variability, such as seasonal cycle of insolation, non-linear interplay of feedbacks, and random fluctuations in physical or chemical factors also has an effect on the uncertainties. *Déqué et al.* (2012) found that the natural variability produces significantly larger mean interannual spread in a given model than running an ensemble of the same size without considering

perturbing the parameters. According to *Kjellström et al.* (2011), the lower natural variability in ECHAM5 and smaller large-scale circulation changes in HadCM3 (ECHAM5-r2 and HadCM3-low) show larger warming in much of Europe than the larger one (ECHAM5-r3 and HadCM3-high).

2. Data and method

The calculations were implemented in the variable resolution ARPÈGE 4. atmospheric global climate model (AGCM), and in six different 25 km resolution regional climate models (RCMs) for the European area using Gorzynsky and Conrad indexes, respectively. The resolution of ARPÈGE is 50 km over Central Europe and decreases to 300 km at the antipodes. The ENSEMBLES models chosen for our study are shown in *Table 1*. They are representative selection of models with respect to GCMs/RCMs combination. The temperature anomaly and continentality were predicted for 2021–2050 and 2071–2100.

Table 1. The institute, reference, GCM, RCM, and resolution of chosen ENSEMBLES simulations

	INSTITUTE/ REFERENCE	**GCM**	**RCM**	**RESOULTION**
1	ARPÈGE *Gibelin* and *Déqué*, (2003)	ARPÈGE	-	50 km
2	CNRM/ *Déqué* (2007)	ARPÈGE	ALADIN	25 km
3	DMI/ *Christensen et al.* (1996)	ARPÈGE	HIRHAM	25 km
4	KNMI/ *Lenderink et al.* (2003)	ECHAM5-r3	RACMO	25 km
5	SMHI/ *Kjellström et al.* (2005)	ECHAM5-r3	RCA	25 km
6	MPI/ *Jacob* (2001)	ECHAM5-r3	REMO	25 km
7	ICTP/ *Giorgi et al.* (2004)	ECHAM5-r3	RegCM	25 km
8	CHMI/ *Farda et al.* (2007)	ARPÈGE	ALADIN/CZ	10 km

Since the models contain bias, it is necessary to correct their outputs. An important point in the correction is the availability of suitable reference data, e.g., observations or re-analyses. On the European level, the biggest database of daily meteorological station observations is the European Climate Assessment and Dataset (ECA&D). The ECA&D project (*Klein Tank et al.,* 2002) was initiated by the European Climate Support Network of EUMETNET in 2002, and it was coordinated by the Royal Netherlands Meteorological Institute

(KNMI). ECA&D daily database contains more than 31k quality controlled series of 12 climate variables at more than 7000 meteorological stations in 62 countries, from which about half of them are public (*Fig. 1*). Using the ECA&D blended daily station data, the E-OBS daily high-resolution gridded observational dataset was produced. The E-OBS (*Haylock et. al.,* 2008) is currently perhaps the best pan-European gridded dataset with the spatial resolution of 0.25° in longitude and latitude (or 0.22° on the rotated pole grid typical for many RCMs) covering the period from 1950.

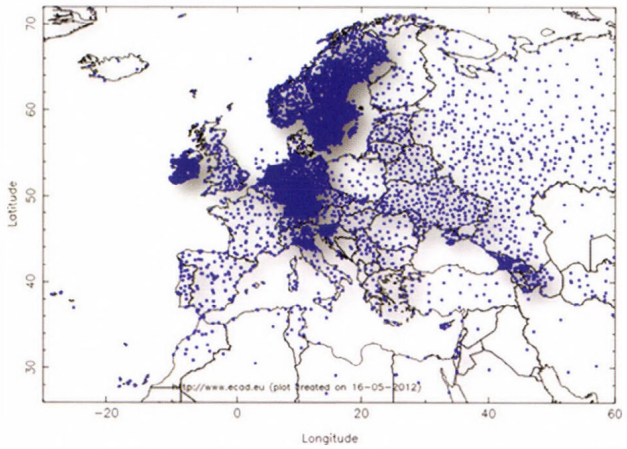

Fig. 1. Meteorological stations of ECA&D database.

The RCMs were corrected on the monthly scale. In the first step for each RCM grid point, the nearest E-OBS grid points were found. The differences of control run of RCM models and E-OBS database (applying reference period 1961–2000) were calculated for each month individually. Found differences were used for correcting the RCM outputs. It has been calculated for more than 14,000 grid points.

Considering the Central European area (Czech Republic (CR), Slovakia (SK), North-East Austria (AT)), the calculations were carried out with the 10 km resolution ALADIN/CZ RCM (*Fig. 2*). The regional climate model ALADIN - Climate/CZ is an adaptation of ALADIN numerical weather prediction model, version CY28T3. Within the EU FP6 project CECILIA, it was coupled with the GCM ARPEGE to provide a projection of future climate in two time slices, 2021–2050 and 2071–2100, according to the IPCC A1B emission scenario. Its description can be found, e.g., in *Farda et al.* (2007) or *Farda et al.* (2010). Before the analysis of the future climate, the model data were corrected, in daily

step, according to validation results carried out for the period 1961-2000. For this purpose (comparison with "truth"), the so-called technical series were recalculated from station data in the positions of grid points of the model (ALADIN-Climate/CZ grid at 10 km horizontal resolution, for the details about the method see, e.g., *Štěpánek et al.,* 2011a). All input station observations were quality controlled, homogenized in daily scale, and gaps in data were filled (for more information about the preprocessing of station data please refer to *Štěpánek et al.,* 2011b, 2013). According to the relationship between the RCM outputs and the recalculated station data (technical series for the grid points), outputs of A1B scenario integrations of the future climate were corrected applying an approach of *Déqué et al.* (2007) that is based on a variable correction using individual percentiles. The model outputs are fully compatible with the station (measured) data. As mentioned above, these data were processed at daily scale, from which final monthly values were then calculated. All data processing was performed by ProClimDB database software for processing of climatology datasets (free download is possible from www.climahom.eu).

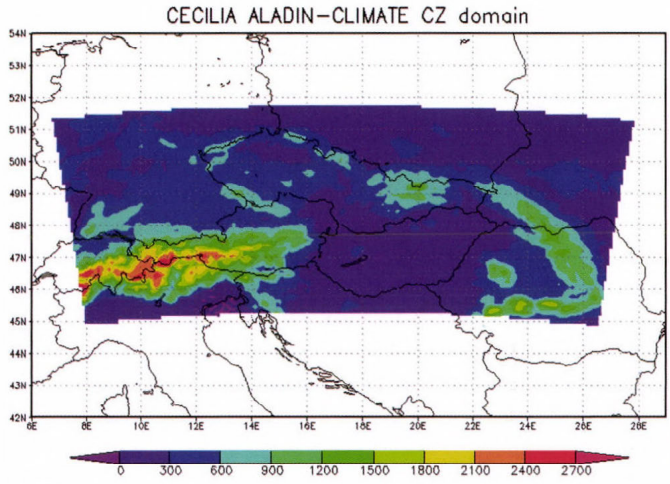

Fig. 2. Integration area with orography and used grid points details of model ALADIN-Climate/CZ as used in EC FP6 CECILIA project.

Owing to the higher density station network used for the correction, this dataset is expected to be subject of smaller interpolation error than E-OBS (*Hofstra et al.,* 2010).

The continentality index is calculated as a function of annual temperature anomaly divided by the sine of latitude to compensate for seasonal differences in radiation. The Gorzynsky index is most commonly used in Europe. It is computed by the equation:

$$k = \frac{1.7(A - 12\sin\theta)}{\sin\theta} = \frac{1.7A}{\sin\theta} - 20.4, \quad (1)$$

where A is the mean annual anomaly of temperature in °C, and θ is the latitude in degree. According to *Gorczynsky* (1922), the expression of $A=12\sin\theta$ corresponds well with observation over the ocean. The 1.7 constant is calculated from the assumption that Verchojansk, in eastern Siberia, is representative of 100% continentality (*Mikolaskova,* 2009). Based on the equation, the continentality can be divided into three categories: transitional maritime (k=0 to 33%), continental (k=33 to 66%), and extreme continental (k=67 to 100%) *Gorczynsky* (1922).

Conrad and *Pollak* (1950) found that the Gorczynsky approach gives negative values, which does not have physical meaning in some particular locations (e.g., Thorshvan at Faeroe Islands), hence they modified the equation with taking into account boundary conditions. The Conrad continentality index can be calculated by the equation:

$$k = \frac{1.7A}{\sin(\theta + 10)} - 14. \quad (2)$$

If the index value is 0, the climate is no longer influenced by continental surface, and if the value is 100, the climate is no longer influenced by maritime air masses (*Mikolaskova,* 2009). This index reaches better results in lower latitudes (e.g., 0), but its results are invalid in latitudes higher than 80.

The Pan-European domain originally designed for the ENSEMBLES project (*van der Linden* and *Mitchell,* 2009) is divided into seven regions for investigating the spatial differences of ENSEMBLES predicted annual temperature anomaly and continentality. The chosen regions are Southern Europe (1), Western Europe (2), Great Britain (3), Scandinavia (4), Central Europe (5), South-Eastern Europe (6), and Eastern Europe (7) represented in *Fig. 3*.

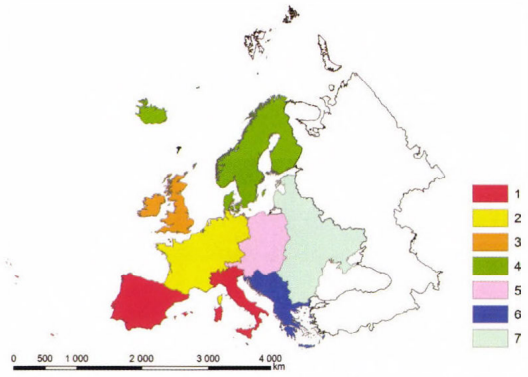

Fig. 3. Regions of ENSEMBLES domain: 1. South Europe, 2. Western Europe, 3. Great Britain, 4. Scandinavia, 5. Central Europe, 6. South-East Europe, and 7. East-Europe.

3. Results

3.1. Temperature anomaly

Table 2 shows the predicted mean annual temperature anomaly in the different regions in the 2021–2050 and 2071–2100 periods. The mean values denote that the temperature range increases eastward and toward the center of South Europe in both time periods. Increasing the distance from the Atlantic Ocean increases the temperature anomaly toward the east direction. The larger anomaly in South Europe can be explained with the topography, which modifies the intensity and depth of penetration of maritime influences. This block of wet maritime airmass is combined with rise of aridity which increases the temperature anomaly (*Dirscoll* and *Yee Fong*, 1992).

Table 2. Predicted mean annual temperature amplitudes T_{mean} in 2021–2050 (top) and 2071–2100 (bottom) for the defined regions: South Europe (1), Western Europe (2), Great Britain (3), Scandinavia (4), Central Europe (5), South-East Europe (6), East-Europe (7)

	Temperature amplitude in 2021–2050						
Region	**ARPÈGE** T_{mean}	**CNRM** T_{mean}	**DMI** T_{mean}	**ICTP** T_{mean}	**KNMI** T_{mean}	**MPI** T_{mean}	**SMHCI** T_{mean}
1	18.8	18.8	18.3	19.0	19.0	19.1	19.4
2	18.3	18.5	18.0	17.9	18.0	18.0	17.8
3	13.0	13.2	12.7	13.0	12.9	12.8	12.6
4	22.6	22.9	22.7	23.1	23.1	22.6	22.7
5	22.0	21.9	21.8	21.3	21.4	21.2	21.0
6	22.7	22.6	21.5	21.4	21.4	21.4	21.3
7	26.4	26.2	25.5	24.7	24.9	24.5	24.4
	Temperature amplitude in 2071–2100						
Region	**ARPÈGE** T_{mean}	**CNRM** T_{mean}	**DMI** T_{mean}	**ICTP** T_{mean}	**KNMI** T_{mean}	**MPI** T_{mean}	**SMHCI** T_{mean}
1	20.4	20.5	20.0	20.7	20.8	21.0	21.1
2	20.0	20.9	19.4	18.3	18.7	18.1	18.1
3	13.1	13.8	13.0	12.9	12.9	12.6	12.4
4	21.2	21.7	21.2	21.5	21.5	21.2	20.5
5	23.3	24.6	22.6	21.0	21.6	20.6	20.7
6	24.7	24.9	23.1	22.2	22.5	22.4	22.5
7	27.4	27.7	25.8	24.7	25.1	24.1	24.2

In 2021–2050, the spread among the predicted mean annual temperature anomalies are smaller than 0.3 in the Western Europe, Great-Britain, and Scandinavia regions (*Table 3a*). In the other regions, differences appear between ARPÈGE and ECHAM5-r3 driven RCMs results, respectively. The temperature range values are higher for RCMs forced by ARPÈGE except in South Europe. The ECHAM5 driver is coupled ocean-atmosphere GCM, while ARPÈGE is forced by the SST and sea-ice conditions of ERA40 (*Déqué* personal discussion) with added delta monthly anomaly from HadCM3 GCM (*Déqué,* 2007). The sea-ice extension is overestimated by HadCM3_ref, while it is underestimated by ECHAM5. Large-scale circulation in ECHAM5 is too zonal which transports the cool and moist air from the North Atlantic in summer (*Kjellström et al.,* 2011), and warm air is advected from the North Atlantic into the Baltic Sea region in winter combined with reduction of sea-ice albedo (*Meier et al.,* 2011). This too strong influence of the Atlantic Ocean on the surface temperature also contributes to the climate of the Central European regions, where it reduces the continental influences (*Plavcová* and *Kyselý*, 2011). The variability of the models is the largest in Scandinavia, which can also contribute to the SST and sea-ice condition caused natural variability.

The predicted change values are calculated by differences between the model predicted future (T_M) and E-OBS measured present (T_E) mean temperature anomalies. These values are negative in both RCMs in Scandinavia and in the ECHAM5 driven RCMs in Central and East Europe too, respectively. These negative values mean that the climate will be more balanced in the future than in the present. ARPÈGE has the largest positive differences in South-East Europe due to the increasing drought resulted from underestimating the precipitation in summer (*Gibelin* and *Déqué,* 2003; *Déqué,* 2007).

Compared with the 2021–2050 term, the mean annual temperature spread among the models increases in each regions in the 2071–2100 time period. Its largest value is 1.5 in Central Europe and the smallest is in Scandinavia region (*Table 3b*). In Central Europe, the mean annual temperature range increases in ARPÈGE driven RCMs and diminishes in ECHAM5 forced ones except KNMI compared with the 2021–2050 period. Moreover, the boundaries of the anomaly become slantwise to south-west north-east direction (not shown).

The mean annual temperature anomalies are also larger in RCMs forced with ARPÈGE except in South Europe. CNRM has the largest mean annual temperature anomalies and the highest predicted change in Central, South-East, and East Europe. SMHCI results the smallest mean annual temperature anomaly except in South Europe and Scandinavia. The variability of the models increases in each region in time with exception of Scandinavia area (not shown). Its value is higher in both time period due to the higher natural variability of the ECHAM5 forced RCMs (denoted by -r3). Because SSTs and sea-ice conditions are significant 'red noise' components (*Hasselmann,* 1976*; Rowell* and *Zwiers,* 1999),

the reduction of model variability in time refers to the fact that the signal (global warming) to noise (natural variability) is greater than in the former period.

In the most regions, the predicted change values increase with time (not shown). CNRM has the largest change values except in the Scandinavia area.

Table 3a. The spread of the simulated temperature amplitude of the models in 2021–2050 for the regions defined in *Table 2*

Spread of simulated temperature amplitude 2025-2050							
	1	**2**	**3**	**4**	**5**	**6**	**7**
ARPÈGE	18.8	18.3	13	22.6	22	22.7	26.4
CNRM	18.8	18.5	13.2	22.9	21.9	22.6	26.2
DMI	18.3	18	12.7	22.7	21.8	21.5	25.5
ICTP	19	17.9	13	23.1	21.3	21.4	24.7
KNMI	19	18	12.9	23.1	21.4	21.4	24.9
MPI	19.1	18	12.8	22.6	21.2	21.4	24.5
SMHCI	19.4	17.8	12.6	22.7	21	21.3	24.4
mean	**18.91**	**18.07**	**12.88**	**22.81**	**21.51**	**21.75**	**25.22**
spread	**0.33**	**0.24**	**0.20**	**0.21**	**0.38**	**0.61**	**0.81**

Table 3b. The spread of the simulated temperature amplitude of the models in 2071–2100 for the regions defined in *Table 2*

Spread of simulated temperature amplitude 2070–2100							
	1	**2**	**3**	**4**	**5**	**6**	**7**
ARPÈGE	20.4	20	13.1	21.2	23.3	24.7	27.4
CNRM	20.5	20.9	13.8	21.7	24.6	24.9	27.7
DMI	20	19.4	13	21.2	22.6	23.1	25.8
ICTP	20.7	18.3	12.9	21.5	21	22.2	24.7
KNMI	20.8	18.7	12.9	21.5	21.6	22.5	25.1
MPI	21	18.1	12.6	21.2	20.6	22.4	24.1
SMHCI	21.1	18.1	12.4	20.5	20.7	22.5	24.2
mean	**20.64**	**19.07**	**12.95**	**21.25**	**22.05**	**23.18**	**25.57**
spread	**0.37**	**1.07**	**0.44**	**0.38**	**1.50**	**1.13**	**1.46**

3.2. Gorczynsky index

The predicted mean Gorczynsky continentality indexes (Eq. (1)) in the 2021–2051 and 2071–2100 time slices are demonstrated in *Table 4*. According to the Gorczynsky index, the boundary of transitional maritime and continental climate is 33%. This boundary is near meridional in East Europe and against with *Mikolaskova,* 2009 results. Its direction is eastward in South-East and South Europe, respectively, in the 2021–2050 time slice (*Fig. 4*). The differences between the ARPÈGE and ECHAM5 driven model predicted indexes are analogous with the temperature amplitude ones.

In the 2021–2050 period, the climate is continental in South East and East Europe according to each model. The spread among the model results is smaller than 0.5 in Great Britain and Scandinavia, while it is greater than 1.0 in South East and East Europe (*Table 5a*).

The predicted change values are also negative in Scandinavia in case of each model and in Central and East Europe, respectively, in case of ECHAM5 forced RCMs (*Fig. 4*). The SMCHI has negative difference value in each region except for South- and South-East Europe, respectively, which relates with its smallest temperature anomaly values.

Correlating with temperature anomaly change, the Gorczynsky index depicts a sharp changing in the 2071–2100 period, where the continental climate slopes toward the north-east south-west direction. The continental climate recedes toward the southern direction in Scandinavia area, but increases in South and South-East Europe in both model cases. With exception of the Scandinavia area, index value increases in RCMs which are forced with ARPÈGE compared to the former period. In case of ECHAM5 driven RCMs, it decreases in more regions. The continentality rises in Central Europe only according to KNMI among ECHAM5 driven RCMs. In Central Europe, the continental climate predominates according to CNRM only where the index mean value is 34.5. CNRM has the largest mean annual temperature anomaly and the largest predicted change value in Central Europe in this period. *Christensen et al,* (2008) found that CNRM ALADIN has the largest positive temperature and negative precipitation biases from E-OBS observed data in Central European region compared with DMI, ICTP, KNMI, MPI, and SMHCI, when the RCMs were forced with ERA40. The spread among the model results is also the smallest in Scandinavia and Great Britain and the largest in South East and East Europe (*Table 5b*). The predicted change tendency is also analogous with the change of temperature range.

Table 4. Space differences of the predicted mean Gorczynsky index G_{mean} in 2021–2050 (top) and 2071–2100 (bottom) for the regions defined in *Table 2*

Gorczynsky index in 2021–2050							
Region	**ARPÈGE** G_{mean}	**CNRM** G_{mean}	**DMI** G_{mean}	**ICTP** G_{mean}	**KNMI** G_{mean}	**MPI** G_{mean}	**SMHCI** G_{mean}
1	28.4	28.5	27.1	29.1	29.1	29.2	29.9
2	21.5	21.8	20.8	20.6	20.6	20.6	20.2
3	7.1	7.5	6.6	7.0	7.0	6.7	6.4
4	22.8	23.2	22.9	23.6	23.7	22.8	22.8
5	28.7	28.4	28.1	27.2	27.2	26.9	26.3
6	37.2	36.7	34.0	33.8	33.8	33.7	33.6
7	39.2	38.8	37.2	35.3	35.7	34.9	34.6
Gorczynsky index in 2071–2100							
Region	**ARPÈGE** G_{mean}	**CNRM** G_{mean}	**DMI** G_{mean}	**ICTP** G_{mean}	**KNMI** G_{mean}	**MPI** G_{mean}	**SMHCI** G_{mean}
1	32.6	32.7	31.6	33.3	33.8	34.1	34.6
2	25.5	27.3	24.0	21.3	22.3	21.1	21.0
3	7.5	8.9	7.1	6.8	6.8	6.3	5.9
4	20.1	21.0	20.0	20.4	20.6	20.0	18.7
5	31.5	34.5	30.1	26.2	27.8	25.5	25.7
6	42.0	42.5	38.1	35.8	36.5	36.3	36.7
7	41.6	42.2	38.0	35.3	36.3	34.0	34.3

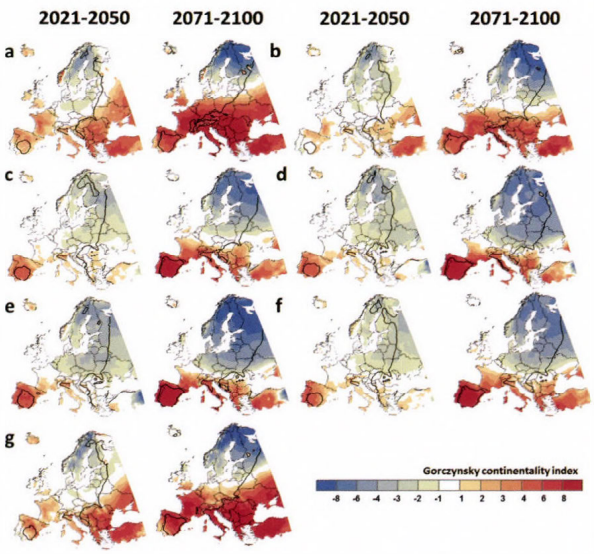

Fig. 4. Predicted changes of Gorczynsky indexes (a) CNRM, (b) DMI, (c) KNMI, (d) MPI, (e) SMHIRCA, (f) ICTP, and (g) ARPÈGE.

Table 5a. The spread of the simulated Gorczynsky index of the models in 2021–2050 for the regions defined in *Table 2*

Spread of simulated Gorczynsky index 2025-2050							
	1	**2**	**3**	**4**	**5**	**6**	**7**
ARPÈGE	28.4	21.5	7.1	22.8	28.7	37.2	39.2
CNRM	28.5	21.8	7.5	23.2	28.4	36.7	38.8
DMI	27.1	20.8	6.6	22.9	28.1	34	37.2
ICTP	29.1	20.6	7	23.6	27.2	33.8	35.3
KNMI	29.1	20.6	7	23.7	27.2	33.8	35.7
MPI	29.2	20.6	6.7	22.8	26.9	33.7	34.9
SMHCI	29.9	20.2	6.4	22.8	26.3	33.6	34.6
mean	**28.75**	**20.87**	**6.9**	**23.11**	**27.54**	**34.68**	**36.52**
spread	**0.88**	**0.56**	**0.36**	**0.39**	**0.87**	**1.55**	**1.88**

Table 5b. The spread of the simulated Gorczynsky index of the models in 2071–2100 for the regions defined in *Table 2*

Spread of simulated Gorczynsky index 2070-2100							
	1	**2**	**3**	**4**	**5**	**6**	**7**
ARPÈGE	32.6	25.5	7.5	20.1	31.5	42	41.6
CNRM	32.7	27.3	8.9	21	34.5	42.5	42.2
DMI	31.6	24	7.1	20	30.1	38.1	38
ICTP	33.3	21.3	6.8	20.4	26.2	35.8	35.3
KNMI	33.8	22.3	6.8	20.6	27.8	36.5	36.3
MPI	34.1	21.1	6.3	20	25.5	36.3	34
SMHCI	34.6	21	5.9	18.7	25.7	36.7	34.3
mean	**33.24**	**23.21**	**7.04**	**20.11**	**28.75**	**38.27**	**37.38**
spread	**1.02**	**2.46**	**0.96**	**0.72**	**3.04**	**2.81**	**3.36**

3.3. Conrad index

The mean Conrad index value is smaller than the Gorczynsky one in South, South-East, and East-Europe, respectively, according to each model (*Table 6*). The difference between the two indexes is the largest in Great-Britain due to the denominator and the smallest in East-Europe in the 2021–2050 period. In the 2071–2100 period, larger continental influence is predicted by the Conrad index than by the Gorczynsky in Scandinavia area, while the difference between the

two index is the smallest in Central Europe according to ARPÈGE driven and in East-Europe according to ECHAM5 driven RCMs, respectively. The predicted change of the Gorczynsky index is larger than the predicted change of the Conrad index in almost each region in both time periods (*Fig. 5*).

The distinction among the different GCM driven model results is analogous with the differences in the case of the temperature anomaly. The change of the Conrad index value in time is the same than in the case of the Gorczynsky index. Similarly to the Gorczynsky index, the largest Conrad index values are predicted by CNRM in Central, South-East and East Europe, respectively, in 2071–2100. The change of the modeled and measured difference values in time and the spread of the model results (*Table 7*) are also analogous with the Gorczynsky index ones.

Table 6. Space differences of the predicted mean Conrad index C_{mean} in 2021–2050 (top) and 2071–2100 (bottom) for the regions defined in *Table 2*

Conrad index in 2021–2050							
Region	**ARPÈGE** C_{mean}	**CNRM** C_{mean}	**DMI** C_{mean}	**ICTP** C_{mean}	**KNMI** C_{mean}	**MPI** C_{mean}	**SMHCI** C_{mean}
1	27.2	27.2	26.1	27.7	27.8	27.8	28.4
2	22.7	23.0	22.1	21.9	22.0	22.0	21.6
3	10.7	11.0	10.2	10.6	10.6	10.3	10.0
4	**26.3**	26.7	26.4	27.1	27.1	26.3	26.3
5	29.4	29.1	28.9	28.0	28.1	27.8	27.3
6	34.9	34.6	32.3	32.1	32.1	32.0	31.9
7	38.4	38.1	36.7	35.0	35.4	34.7	34.4
Conrad index in 2071–2100							
Region	**ARPÈGE** C_{mean}	**CNRM** C_{mean}	**DMI** C_{mean}	**ICTP** C_{mean}	**KNMI** C_{mean}	**MPI** C_{mean}	**SMHCI** C_{mean}
1	30.7	30.8	29.8	31.3	31.7	32.0	32.3
2	26.2	27.9	24.9	22.5	23.5	22.4	22.3
3	11.0	12.3	10.7	10.4	10.5	9.9	9.6
4	23.8	24.6	23.7	24.0	24.2	23.7	22.4
5	31.9	34.5	30.6	27.2	28.6	26.5	26.7
6	39.1	39.5	35.7	33.7	34.4	34.2	34.5
7	40.6	41.1	37.4	35.0	35.9	33.8	34.14

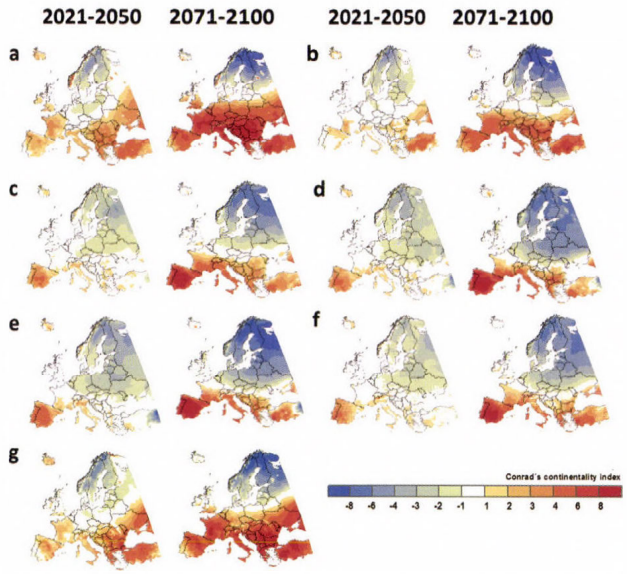

Fig. 5. Predicted changes of the Conrad indexes (a) CNRM, (b) DMI, (c) KNMI, (d) MPI, (e) SMHIRCA, (f) ICTP, and (g) ARPÈGE.

3.4. Central Europe

The continentality in Central Europe is detailed by the ALADIN-Climate/CZ (hereinafter referred to as CHMI) model with higher (10 km) horizontal resolution. The model has same dynamical core as CNRM, but they differ significantly in their physical package (*Skalak et al.,* 2008). Its physical package is detailed in *Farda et al.* (2010). CHMI is run in CECILIA domain which focuses on the Czech Republic and its vicinity. The results of simulated and observed Gorczynsky and Conrad indexes are presented in *Figs. 6* and *7*, respectively. *Table 8* shows the mean value and predicted change value of temperature amplitude, Gorczynsky index, and Conrad index, respectively in the 2021–2050 and 2071–2100 periods.

Table 7. The spread of the simulated Conrad index of the models in 2021–2050 (top) and in 2071–2100 (bottom) for the regions defined in *Table 2*

Spread of simulated Conrad index 2025–2050							
	1	**2**	**3**	**4**	**5**	**6**	**7**
ARPÈGE	27.2	22.7	10.7	26.3	29.4	34.9	38.4
CNRM	27.2	23	11	26.7	29.1	34.6	38.1
DMI	26.1	22.1	10.2	26.4	28.9	32.3	36.7
ICTP	27.7	21.9	10.6	27.1	28	32.1	35
KNMI	27.8	22	10.6	27.1	28.1	32.1	35.4
MPI	27.8	22	10.3	26.3	27.8	32	34.7
SMHCI	28.4	21.6	10	26.3	27.3	31.9	34.4
mean	**27.45**	**22.18**	**10.48**	**26.6**	**28.37**	**32.84**	**36.1**
spread	**0.72**	**0.48**	**0.33**	**0.36**	**0.76**	**1.31**	**1.64**
Spread of simulated Conrad index 2070–2100							
	1	**2**	**3**	**4**	**5**	**6**	**7**
ARPÈGE	30.7	26.2	11	23.8	31.9	39.1	40.6
CNRM	30.8	27.9	12.3	24.6	34.5	39.5	41.1
DMI	29.8	24.9	10.7	23.7	30.6	35.7	37.4
ICTP	31.3	22.5	10.4	24	27.2	33.7	35
KNMI	31.7	23.5	10.5	24.2	28.6	34.4	35.9
MPI	32	22.4	9.9	23.7	26.5	34.2	33.8
SMHCI	32.3	22.3	9.6	22.4	26.7	34.5	34.14
mean	**31.22**	**24.24**	**10.62**	**23.77**	**29.42**	**35.87**	**36.84**
spread	**0.86**	**2.17**	**0.87**	**0.68**	**3.02**	**2.42**	**2.98**

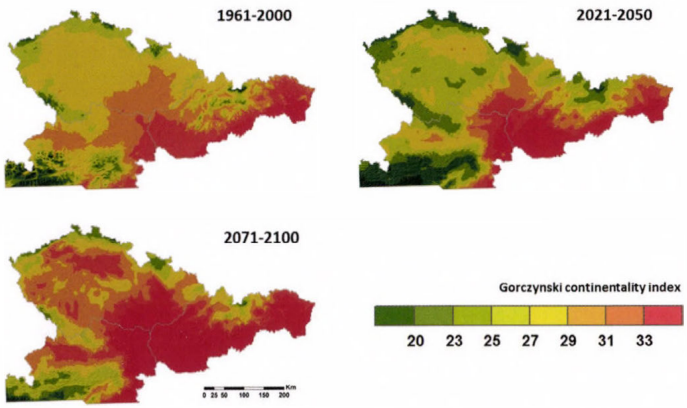

Fig. 6. ALADIN/CZ simulated and higher resolution observed Gorczynsky index in CECILIA domain.

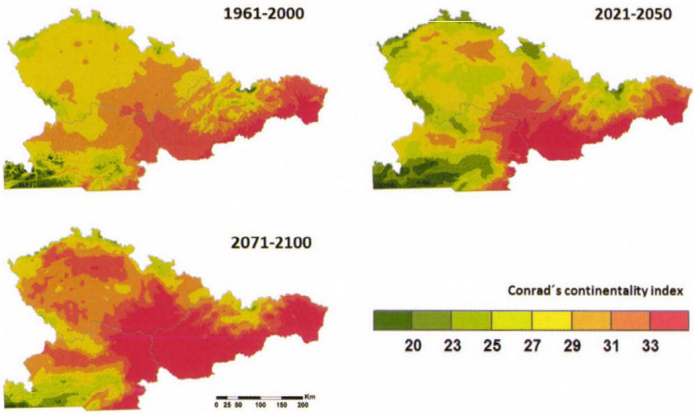

Fig. 7. ALADIN/CZ simulated and higher resolution observed Conrad index in CECILIA domain.

Table 8. The mean value and predicted changes of annual temperature amplitude, Gorczynsky and Conrad continentality indexes, respectively, predicted by the ALADIN-Climate/CZ model for the near and far future time slices, respectively

	ALADIN-CLIMATE/CZ			
	2021–2050		2071–2100	
	T_{MEAN}	T_M–T_E	T_{MEAN}	T_M–T_E
Temperature amplitude	21.3	–0.3	22.8	1.2
Gorczynsky index	27.6	–0.7	31.1	2.7
Conrad index	28.3	–0.6	31.4	2.4

Comparing the CHMI and ENSEMBLES model results, the differences are the smallest between CHMI and ICTP or KNMI values in 2021–2050, while in the further period the distinction is the smallest between the ARPÈGE and CHMI predicted continentality indexes. The predicted change value is negative in the near and positive in the far future, respectively, like in the DMI case. Based on the mean Gorczynsky index, the climate will be transitional maritime according to CHMI in Central Europe, which agrees with the other ENSEMBLES model results with the exception of the CNRM prediction to the 2071–2100 time slice.

The differences between the CNRM and CHMI predicted mean continentality values is 0.8 in the case of both indexes in the near future time slice, while the differences between the Gorczynsky and Conrad indexes are 3.4 and 3.1, respectively, in the far future period. Some factors which could be responsible for these differences are the large/small integrated area, higher/lower resolution, and the differences between the models. CHMI results positive precipitation bias due to high accumulation of snow in Central Europe during late winter and early spring in both of the 50 km and 10 km resolution cases (*Farda et al.,* 2007; *Skalak et al.,* 2008). This wetter feature of precipitation field corresponds well to the negative bias in winter and spring mean temperature. Furthermore, *Farda et al.* (2007) found that the smaller domain size enhances the precipitation due to the unrealistic generation of vertical velocity in the coupling zone of the model which affects directly even the interior of the rather limited domain.

4. Discussion

4.1. Effect of drivers

We found that the drivers have a significant effect on the spread of results. According to the ECHAM5 driven RCMs, the Atlantic Ocean has a strong influence on the surface temperature due to the too zonal large-scale circulation and underestimated sea-ice condition of the ECHAM5-r3 GCM. Thanks to this phenomenon, smaller continentality indexes were predicted by the ECHAM5 driven RCMs than the ARPÈGE forced ones in each regions except in South-Europe in both time periods.

4.2. Effect of model resolution

The higher resolution model provided finer details of the simulated field, but the resolution differences did not play dominant role in the difference from other RCM results. Small differences were found between the results of ARPÈGE 50 km and CNRM 25 km resolution models. The finer resolution ALADIN-Climate/CZ resulted similar results like ITCP or KNMI in the nearer future, while its results were closer to the ARPÈGE simulation in the far future case. The CHMI simulated mean continentality indexes decreased compared to the observed values in the 2021–2050 time period, while increased in the far future slice. The differences between the CNRM and CHMI results probably come from the positive wet bias of CHMI, which is persistent when smaller domain is used.

4.3. Impacts on continentality

Two different continentality indexes (Gorczynsky and Conrad, respectively) were calculated in function of annual temperature anomaly and sinus function of latitude. The mean annual temperature range rises with increasing distance from the ocean and with increasing aridity. Both continentality indexes strongly depend on the annual temperature range, and their spatial differences are well correlated with the space differences of temperature anomaly. The largest continental effect in South-Europe came from the block of maritime airmass caused by the Pyrenees. The continentality indexes decreased with time only in Scandinavia region. This phenomenon can be explained with the assumption of the melting of sea-ice which causes larger SST. Despite the fact that the maximum internal variability of RCMs is in the South-East European region (*Sanchez-Gomez, E. et al.,* 2009), the largest model variability was in the Scandinavia region in each model case. This maximum variability affected by the natural variability is caused by SST and sea-ice condition.

5. Conclusion

The future continental climate is simulated by applying two different continentality indexes: the Gorczynsky and Conrad, respectively. Both of them indicate the continentality as a function of the annual mean temperature anomaly and a sinus function of the latitude angle. The largest difference between their index values is caused by the boundary condition which is applied in the Conrad approach to avoid the insensible negative continentality values in lower latitudes. In our simulation, the isoline flows near meridionally only in East-Europe, and it flows to eastward direction in South-East and South Europe, respectively. The greatest change with time slice in isoline direction is in Scandinavia, where the climate becomes more balanced maritime despite the resulted larger model variability.

The core message of our research is whether Central Europe becomes more continental or maritime according to the A1B RCM scenarios in the 21st century?

The climate of Central Europe is predicted to be transitional maritime according to the mean Gorczynsky index of RCMs with exception of CNRM in the further time slice. This result might be explained by the experience that CNRM overestimates the monthly maximum temperature and underestimates the precipitation in Central Europe. The simulated continental influence will diminish compared to the observed state according to the ECHAM5 driven RCMs in Central Europe in both time slices. Although the boundary of maritime and continental climate run along east Austria, south-east Czech Republic, and mid-Slovakia according to the CHMI detailed Gorczynsky index, its mean value is below the continental boundary.

Acknowledgements: This research was supported by the Czech Grant Agency in the frame of the project: Global and regional climate model simulations in Central Europe in the 18th-20th centuries in comparison with observed and reconstructed climate, GACR P209/11/0956. Pavel Zahradníček was supported by project InterSucho (no. CZ.1.07/2.3.00/20.0248). We are thankful for the E-OBS data set from the EU-FP6 project ENSEMBLES (http://www.ensembles-eu.org) and the data provided by the ECA&D project (http://www.eca.knmi.nl). Data for Central Europe was performed within the CECILIA project, funded by the European Commission's 6th Framework Programme under contract number 037013.
We also would like to thank to the anonymous reviewers for their comments and suggestions.

References

Conrad, V. and *Pollak, L.W.*, 1950: Methods in climatology. 2nd edition. Harvard university press, Cambridge, Massachusetts.

Christensen, J.H., Christensen, O.B., Lopez, P., Van Meijgaard, E., and *Botzet, M.*, 1996: The HIRHAM4 regional atmospheric model. Scientific Report 96-4, The Danish Meteorological Institute, Copenhagen, Denmark.

Christensen, J.H., Boberg, F., Christensen, O.B., and *Lucas-Picher, P.*, 2008: On the need for bias correction of regional climate change projections of temperature and precipitation. *Geophys. Res. Lett. 35*, L20709.

Currey, D.R., 1974: Continentality of Extratropical Climates. *Ann. Ass. Amer. Geograph. 64*, 268–280.

Déqué, M., Rowell, D. P., Lüthi, D., Giorgi, F., Christensen, J.H., Rockel, B., Jacob, D., Kjellström, E., de Castro M., and *van den Hurk, B.*, 2007: An intercomparison of regional climate simulations for Europe: assessing uncertainties in model projections. *Climate Change* 81 (Suppl. 1), 53–70.

Déqué, M., Somot, S., Sanchez-Gomez, E., Goodess, C.M., Jacob, D., Lenderink G., and *Christensen, O.B.*, 2012: The spread amongst ENSEMBLES regional scenarios: regiona climate models, driving general circulation models and interannual variability. *Clim. Dynam. 38*, 951–964.

Dirscoll, D.M. and *Yee Fong, J.M.*, 1992: Continentality: A basic climatic parameter re-examined. *Int. J. Climat. 12*, 185–192.

Dosio, A. and *Paruolo, P.*, 2011: Bias correction of ENSEMBLES high-resolution climate change projections for use by impact models: Evaluation on the present climate. *J. Geophys. Res. 116*, D16106.

Farda, A. Štěpánek, P., Halenka, T., Skalák, P., and *Beld, M.*, 2007: Model ALADIN in climate mode forced with ERA40 reanalysis (course resolution experiment). *Meterologický časopis 10*, 123–130.

Farda, A., M. Dequé, S. Somot, A. Horányi, V. Spiridonov and *H. Tóth*, 2010: Model ALADIN as regional climate model for central and eastern Europe. *Stud. Geophys. Geod. 54*, 313–332.

Gibelin, A.-L., and *Déqué, M.*, 2003: Anthropogenic climate change over the Mediterranean region simulated by a global variable resolution model. *Clim. Dynam. 20*, 327–339.

Giorgi, F. Bi, X., and *Pal, J.S.*, 2004: Mean, interannual variability and trends in regional climate change experiment over Europe. I. Present-day climate (1961-1990). *Clim. Dyn*am. *22*, 733–756.

Gorczynsky, L., 1922: The calculation of the degree of continentality. *Mon. Weather Rev. 50*, 370.

Hasselmann, K., 1976: Stochastic climate models. Part I: Theory. *Tellus 28*, 473–485.

Haylock M.R., Hofstra, N., Klein Tank, A.M.G., Klok, E.J., Jones P.D., and *New, M.*, 2008: A European daily high-resolution gridded data set of surface temperature and precipitation for 1950–2006, *J. Geophys. Res. 113*, D20119.

Hewitt, C.D. and *Griggs, D.J.*, 2004: Ensembles-based predictions of climate changes and their impacts. *Eos Trans. AGU* 85, 566.

Hofstra, N., M. New, C. McSweeney, 2010: The infulence of interpolation and station network density on the distributions and trends of climate variables in gridded daily data. *Climate Dynam. 35*, 841–858.

Holmlund, P. and *Schneider, T.*, 1997: The effect of continentality on glacier response and mass balance. *Ann. Glaciology 24*, 272–276.

Jacob, D., 2001: A note to the simulation of the annual and inter-annual variability of the water budget over Baltic Sea drainage basin. *Meteorol. Atmos. Phys. 77*, 61–73.

Johansson, O.V., 1926: Uber die asymmetrie der meteorologischen Schwankungen. In.: Soc. Sci. Fennica, Commentationes Phys. Math., 3, 1ff

Kjellström, E., L. Bärring, S. Gollvik, U. Hansson, C. Jones, P. Samuelsson, M. Rummukainen, A. Ullerstig, U. Willén and *K. Wys*, 2005: A 140-year simulation of European climate with the new version of Rossby Central regional atmospheric climate model (RCA3). *SMHI Reports Meteorology and Climatology 108*, SMHI, SE-60176. Norrköping, Sweden.

Kjellström, E., G. Nikulin, U. Hansson, G. Strandberg and *A. Ullersting*, 2011: 21st century changes in the European climate: uncertainties derived from an ensemble of regional climate model simulations. *Tellus 63A*, 24–40.

Klein Tank, A.M.G., J. B. Wijngaard1, G. P. Können, R. Böhm, G. Demarée, A. Gocheva, M.Mileta, S. Pashiardis, L. Hejkrlik, C. Kern-Hansen, R. Heino, P. Bessemoulin, G. Müller-Westermeier, M. Tzanakou, S. Szalai, T. Pálsdóttir, D. Fitzgerald, S. Rubin, M. Capaldo, M. Maugeri, A. Leitass, A.Bukantis, R. Aberfeld, A. F. V. van Engelen, E. Forland, M. Mietus, F. Coelho, C. Mares, V.Razuvaev, E. Nieplova, T. Cegnar, J. Antonio López, B. Dahlström, A. Moberg, W. Kirchhofer, A. Ceylan, O. Pachaliuk, L. V. Alexander and P. Petrovic' 2002: Daily dataset of 20th century surface air temperature and precipitation series for the European climate asseessment. *Int. J. Climatol. 22*, 1441–1453.

Lenderink, G., B. van den Hurk, E. van Meijgaard, A. van Ulden and *H. Cuijpers*, 2003: Simulation of present-day climate in RACMO2: first results and model developments. *Technical Report TR-252*, Royal Netherlands Meteorological Institute.

van der Linden, P. and *Mitchell, J.F.B.* (eds.) 2009: ENSEMBLES: Climate Change and its Impacts: Summary of research and results from the ENSEMBLES project. Met Office Hadley Centre, FitzRoy Road, Exeter EX1 3PB, UK.

McBoyle, G.R., and *Steiner, D.*, 1972: A factor-analytic approach to the problem of continentally. *Geografiska Annaler Series* A, *Physical Geography, 54*, 12–27.

Meier, H.E.M., Höglund, A., Döscher, R., Andersson, H., Löptien, U., and *Kjellström, E.*,2011: Quality assessment of atmospheric surface fields over the Baltic Sea from an ensemble of regional climate model simulations with respect to ocean dynamics. *Oceanologia 53*, 193–227.

Mikolaskova, K., 2009: A regression evaluation of thermal continentality. *Geografie 4*, 350–361.

Nakicenovic, N. and *Swart, R.*, 2000: Special Report on Emissions Scenarios: A Special Report of Working Group III of the Intergovernmental Panel on Climate Change, Cambridge UK: Cambridge University Press.

Nikiforova, T., Savytskyi, M., Limam, K., Bosschaerts, W., and *Belarbi, R.*, 2013: Methods and results of experimental researches of thermal conductivity of soils. *Energy Procedia 42*, 775 – 783.

Placová, E. and *Kyselý, J.*, 2010: Evaluation of daily temperatures in Central Europe and their links to large-scale circulation in an ensemble of regional climate models. *Tellus 63A*, 763–781.

Rowell, D.P. and *Zwiers, F.W.*, 1999: The global distribution of sources of atmospheric decadal variability and mechanisms over the tropical Pacific and southern North America. *Clim. Dynam. 15*, 751–772.

Sanchez-Gomez, E., Somot, S., and *Déqué, M.*, 2009: Ability of an ensemble of regional climate models to reproduce weather regimes over Europe-Atlantic during the period 1961-2000. *Clim. Dynam. 33*, 723–736.

Skalak, P., Štěpánek, P., and *Farda, A.*, 2008: Validation of ALADIN-Climate/CZ for present climate (1961-1990) over the Czech Republic. *Idojaras 112*, 191–201.

Sládek, I., 2005: Návrh nové míry kontinentality klimatu. *Fyzickogeografický sborník, 3*,. 144–147. (In Slovak)

Solomon, S., Qin, D., Manning, M., 2007: Technical Summary. In: (Eds.: *S. Solomon, D. Qin, M. Manning, Z. Chen, M. Marquis, K. B. Averyt, M. Tignor* and *H. L. Miller.*) Climate Change 2007: The Physical Science Basis. Contribution of Working Group I to the Fourth Assessment Report of the Intergovernmental Panel on Climate Change. Cambridge University Press, Cambridge, United Kingdom and New York, NY, USA.

Štěpánek, P., Zahradníček, P., Brázdil, R., and *Tolasz, R.*. 2011a: Metodologie kontroly a homogenizace časových řad v klimatologii Český hydrometeorologický ústav: Praha. (in Czech).

Štěpánek, P., Zahradníček, P., and *Huth, R.,* 2011b: Interpolation techniques used for data quality control and calculation of technical series: an example of a Central European daily time series. *Időjárás 115*, 87–98.

Štěpánek, P., Zahradníček, P., and *Farda, A.,* 2013: Experiences with data quality control and homogenization of daily records of various meteorological elements in the Czech Republic in the period 1961–2010. *Időjárás 117*, 123–141.

Wilby R.L., Wigley, T.M.L., Conway, D., Jones, P.D., Hewitson, B.C., Main, J., and *Wilks, D.S.,* 1998: Statistical downscaling of general circulation model output, a comparison of Methods. *Water Resour. Res. 34*, 2995–3008.

IDŐJÁRÁS

Quarterly Journal of the Hungarian Meteorological Service
Vol. 119, No. 4, October – December, 2015, pp. 537–555

Estimation of solar and wind energy potential in the Hernád Valley

Károly Tar[1,2*], **Andrea Kircsi Bíróné**[1], **Blanka Bartók**[3], **Sándor Szegedi**[1], **István Lázár**[1], **Róbert Vass**[2], **Attila Bai**[4], and **Tamás Tóth**[1]

[1]*Department of Meteorology, University of Debrecen, Egyetem tér 1, H-4010 Debrecen, Hungary*

[2]*Institute of Tourism and Geography, College of Nyíregyháza, Sóstói út 31/b, H-4400 Nyíregyháza, Hungary*

[3]*Department of Geography in Hungarian, Babes-Bolyai University, Clinicilor 5-7, 400006 Cluj-Napoca, Romania*

[4]*Faculty of Applied Economics and Rural Development, University of Debrecen, Böszörményi u. 138, H-4032 Debrecen, Hungary*

** Corresponding authors E-mail: tarko47@gmail.com*

(Manuscript received in final form October 3, 2014)

Abstract—This paper focuses on the climatic conditions of the Hernád Valley with the purpose of exploring on what level the utilization of wind and solar energy is advanced or detained in the micro-region. For determination of wind and solar energy potential, an automatic weather station was mounted in the Hungarian section of the Hernád Valley located on a small hill 500 meters west from the settlement of Hidasnémeti.

Available long-term surface global radiation data do not represent our study area on regional scale. For this reason, daily global radiation datasets of the nearest weather station, the airport of Kosice has been used for the analyses. Diurnal and annual variation and spatial pattern of global radiation have been examined by combination of statistical analyses and geo-information/GIS methods.

Other important aim of the research is to describe the spatial characteristics of the wind energy potential related to orography in the Hernád Valley. Diurnal courses of different statistical parameters and the spatial pattern of wind speeds has been investigated on the base of our measured data. Since these data are not continuous, relationships between the diurnal average wind speeds of Kosice and Hidasnémeti were examined also. An attempt has been made to complete our diurnal average wind speed database by linear regression.

Finally, the social and economic conditions regarding solar and wind energy utilization are mentioned shortly in the paper.

Key-words: Hernád Valley, solar energy potential, wind profile, wind energy potential

1. Introduction

The Department of Meteorology, University of Debrecen carried out the research of the climatic and social-economic conditions of Hernád Valley in the frame of a scientific project between 2009 and 2012. The aim was to find optimal area for wind and solar energy, as well as biomass utilization. Our purpose is to work out a model wherein the complex evaluation of natural and social-economic conditions and effects can result in a sustainable and out-of-conflict land use, after all. The results of the research will be useful to work out a regional improvement strategy based on the use of renewable energy sources to help local decision process. Most important results of investigations on wind and solar climate and energy are summarized in this paper. Local conditions can serve as a good base for further development of solar energy utilization in the region. Solar energy can be introduced in some new fields like ecologic and silvicultural applications. Our examinations have showed also that in spite of temporal fluctuations, utilization of wind energy in the study area can be expedient and effective, especially in the case of application of low starting speed wind turbines. Citizens' opinion about instruments of utilization of solar and wind energy is positive, and they are open for such initiatives. Well prepared projects can be successful and can contribute to the development of the economy of the region.

This research intends to focus on the climatological conditions of the Hernád Valley micro-region with the purpose of exploring on what level they advance or detain the utilization of solar and wind energy.

As a first step, the exploration of the climatological endowments of the selected area based on climatological observations was carried out. It made possible the calculation of indexes, which describe the connections between weather types and the amount of utilizable wind and solar energy on one hand, the elaboration of a model, that helps the allocation of wind turbines and refining of relations, as well as describes the variations of wind speeds with height; and selection of plants optimal for biomass production in a given micro-region on the other hand. Social-economic studies focused on financial benefits and cost-efficiency indexes have been revealed, as well as social acceptance of renewable energy sources have been surveyed.

For determination of wind and solar energy potential, an automatic weather station was established in the Hungarian section of Hernád Valley on a small hill 500 meters west from the settlement of Hidasnémeti at N 48°30' and E 21°13' at a height of 175 meters above sea level (*Fig. 1*). The automatic weather station was mounted on a 20-meter high measurement mast which was equipped with a wind direction sensor at a height of 10 meters and two anemometers at heights of 10 and 20 meters among other instruments.

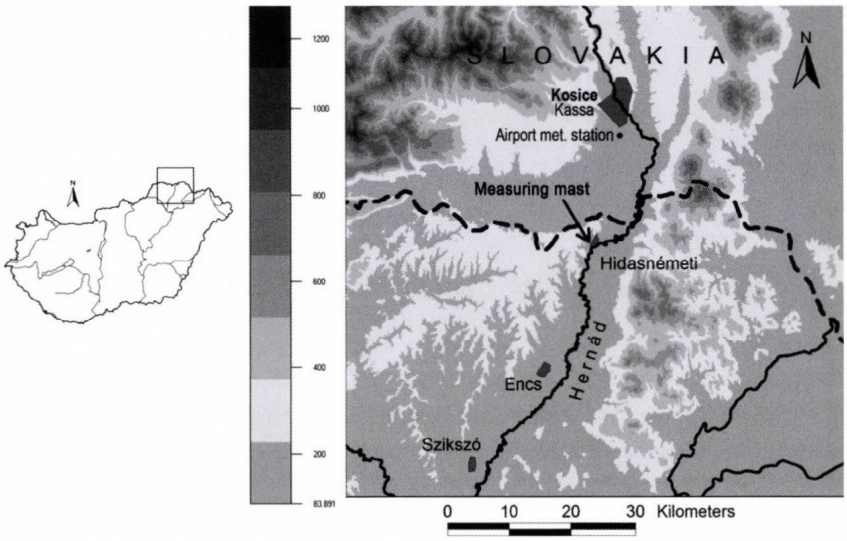

Fig. 1. Geographical situation of the meteorological measurements.

To survey the solar energy potential of the Hernád Valley, it is important to know the temporal and spatial pattern of global radiation of its region. It is determined by the Sun and the geometry of the relief; however, actual atmospheric conditions have an important effect on the amount of incoming solar radiation as well. Available surface global radiation data do not represents our study area on regional scale. For this reason, daily global radiation datasets of the nearest weather station, the airport of Kosice (48.667°N, 21.217°E, 231 m a.s.l.) have been used for the analyses.

Datasets have gone under statistic-climatological analyses, main statistic parameters have been determined, wind speed and direction frequency distributions have been prepared for both heights; hourly and diurnal average values of the parameter in the Hellman wind profile equation have been determined in the first stage of our wind climatological research. On this base, average diurnal courses and diurnal average wind speeds for levels higher than the measurements levels have been calculated, what is decisive from the aspect of the amount of potential wind energy. A statistic definition has been worked out for diurnal average specific wind power of a day of any period of time. Its comparative examination has been carried out as well.

However, the survey of wind potential of the Hernád Valley requires spatial extrapolation as well. The model used for this purpose is not our development, but there are not any examples for Hungarian adaptations of the WindSim 5.1 EV model yet. The model has a modular structure, and it generates the spatial distribution of average wind speeds influenced by orography in successive steps, what determines the prospective energy production of the chosen wind energy utilizing instrument practically. Turbulence parameters

influenced by orography and spatial patterns of wind speeds weighted on the base of average wind direction distribution have been determined for the Hernád Valley using both the results of our measurements and the one-year-long dataset from the airport of Kosice, eventually. Wind potential maps can be generated for any heights up to 200 meters. They can help the selection of optimal sites for wind energy utilization.

2. Examination of solar energy potential in the Hernád Valley

To determine the solar energy potential of the Hernád Valley the first step is to gain information on temporal and spatial pattern of global radiation of that region. Since there is not any Hungarian long-term surface radiation measurement stations in the environment of our study area, diurnal global radiation datasets of the nearest weather station, the airport of Kosice (Slovakia) have been used for the analyses.

Besides the pointwise measurements, ArcGIS geoinformation software has been used in order to analyze the spatial distribution of solar radiation in the Hernád Valley. In this case, the required input parameters have been determined using data measured there.

Changes in the global radiation are determined mainly by the geographical latitude. The other affecting factor is the air circulation having impact via cloudiness, amount of sunny hours and last but not least via transparency of the atmosphere (different air masses). Orography can also strongly modify the spatial and temporal pattern of global radiation. GIS programs are able to handle the surface characteristics with very high accuracy, but their weakness is that the meteorological conditions (cloudiness, water vapor content, etc.) are integrated indirectly using parameterizations (see Section 2.2).

Evaluation of global radiation data provides essential information for planning and economic analyses of solar energy utilization projects in the Hernád Valley. Examinations can be carried out for any point of the region by combination of statistical analyses and geoinformation methods.

2.1. Diurnal and annual courses of global radiation

Diurnal and annual courses of global radiation have been examined using the one-year-long dataset of the weather station of the airport of Kosice, located 25 km north from the settlement of Hidasnémeti. The raw database covers the period between May 2009 and April 2010, the hourly global radiation data are given in J/cm^2 (1 J/cm^2 = 2.778 W/m^2 hour). In the followings, the unit of W/m^2 will be used. Global radiation has a nearly symmetric curve with a maximum in June-July during the year. The curve reaches its minimum in the winter period in December, when the maximum is 367 W/m^2. There are higher maximal values in January and February, with 392 W/m^2 and 483 W/m^2, respectively. Values

increase gradually in the spring reaching 714 W/m^2 in March and even 900 W/m^2 in May. There is a gradual decrease in the autumn months, although values are a bit lower than in the spring: 739 W/m^2 in September, while 422 W/m^2 in November. Highest values of global radiation occur in the afternoon, in the summer months with maxima over 800 W/m^2 and average over 435 W/m^2 between 9 and 15 UTC. Annual course of global radiation has reached its maximum in July with 933 W/m^2 during the studied period.

Diurnal curves show a symmetric distribution also with a maximum at noon independently from the seasons. Only the amplitudes of the curves are different according to the seasons (*Fig. 2*). Minima occur in December with 143 W/m^2. Intensities reach 21 W/m^2 at 9 UTC in the morning and reach 64 W/m^2 by 15 UTC. Highest intensities occur at the summer solstice in June, when it reaches 609.3 W/m^2 at noon, 202.7 W/m^2 in the morning (6 UTC), and 109.7 W/m^2 and late afternoon (18 UTC).

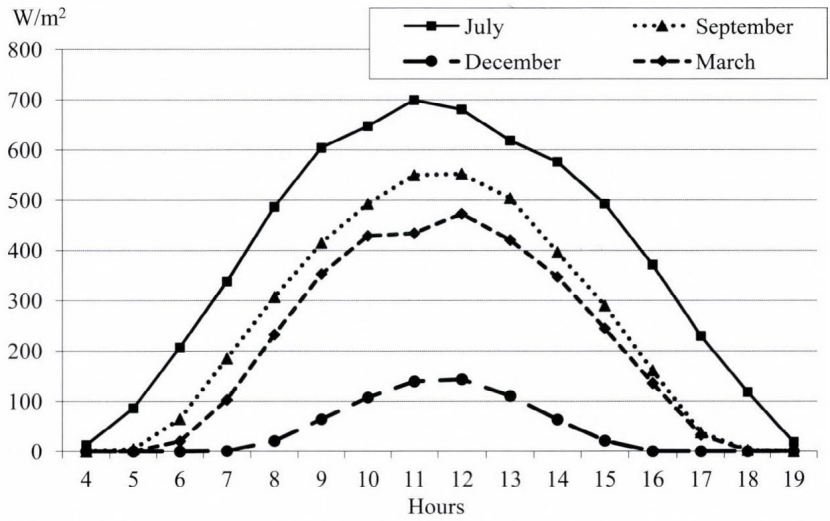

Fig. 2. Diurnal course of hourly average global radiation (W/m^2) at the weather station of Kosice during the 2009–2010 period.

Hourly values of global radiation are dependent on synoptic conditions which can change hour by hour significantly. Annual course of diurnal amounts of global radiation are presented in *Table 1*. It can be observed that values appear in 4 categories in the winter months, while they scatter in a much wider range in the summer period.

Table 1. Relative frequency of diurnal amounts of monthly global radiation (%) at the weather station of Kosice of the 2009–2010 period

W/m^2	Jan	Feb	Mar	Apr	May	June	July	Aug	Sept	Oct	Nov	Dec
0–500	22.6	3.6								6.5	**53.3**	32.3
501–1100	**51.6**	39.3		3.3					3.3	**35.5**	26.7	**54.8**
1101–2200	25.8	**46.4**	16.1	10.0	3.2	6.7		6.5	6.7	29.0	13.3	12.9
2201–3300		10.7	29.0	16.7	6.5	6.7	3.2	6.5	10.0	19.4	6.7	
3301–4400			**48.4**	23.3	3.2	16.7	12.9	19.4	**40.0**	9.7		
4401–5500			6.5	10.0	19.4	13.3	16.1	22.6	33.3			
5501–6600				**26.7**	29.0	**26.7**	16.1	**38.7**	6.7			
6601–7700				10.0	**32.3**	16.7	**38.7**	6.5				
7701–8800					6.5	13.3	12.9					

2.2. Examination of the spatial pattern of global radiation

On the base of point-like measurement data, high resolution radiation maps of the region have been elaborated using geoinformatic tools (Esri ArcGIS Solar radiation module). As the global radiation is determined by many factors, the module contains various setting options. One of the most important factors is the aspect and slope derived from the characteristics of the surface. This kind of information can be obtained from the input digital elevation model (DEM). The program recognizes the geographical latitude of the area even at the moment of loading the DEM, furthermore, the inclination angle of solar radiation can also be determined. The next step contains the time settings. The most important parameter is the sequence of the day in the given year. Based on this parameter, the inclination angel of the radiation, the way length of solar beam in the atmosphere, and the astronomical duration of sunshine can be determined. All these parameters of radiation presented above can be calculated exactly. In the following step, the input parameters refer to the atmospheric conditions like cloud cover, humidity, opacity, etc. Regarding these parameters in the module two, values can be adjusted, namely the proportion of diffuse radiation and the transmissivity of the atmosphere (τ). The values of proportion of diffuse radiation was taken from the PVGIS dataset (*http://re.jrc.ec.europa.eu*). The parameterization of transmissivity is elaborated based on measured global radiation values. The monthly radiation values are classified in function of standard deviation (σ) into three categories, namely $M \pm \sigma$ interval concerning situations with average radiation values, $M+2\sigma$ for situation with high values, and $M-2\sigma$ interval including the

situation of low global radiation. In order to determine a monthly τ parameter, an approximate τ was determined for each category weighted with the number of cases of the given category. In this way, an empirical τ parameter was calculated separately for each month (*Bartók et al.,* 2011).

Introducing the DEM of the region, the proportion of diffuse radiation, and the empirical τ parameter into the GIS Solar radiation module, high resolution global radiation maps were elaborated for different periods. Results regarding the period of May-August (warmest four months of the year) are presented in *Fig. 3*. Statistics of global radiation income (sum) of the region for the period between May and August are the following. The average is 501 kW/m^2, the minimum is 438 kW/m^2, the maximum is 563 kW/m^2, and the empiric standard deviation is 11 kW/m^2, respectively. The high resolution of the map makes it possible to evaluate radiation conditions of slopes of different expositions.

Evaluation of data of incoming global radiation provides essential information for planning and economic analyses of solar energy utilization projects planned in the Hernád Valley. Examinations like presented above can be carried out for any point of the region, where utilization of solar energy takes place by combination of statistical analyses and geoinformation methods. It is reasonable, since local features, especially orography, can modify the spatial and temporal pattern of global radiation remarkably.

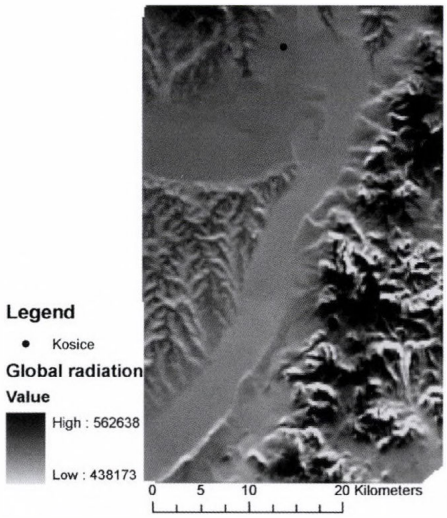

Fig. 3. Total global radiation (W/m^2) in the Hernád Valley for the period between May and August.

3. Determination of wind energy potential in the Hernád Valley

Besides the wind climatological research, other important aim of the research program was to describe the spatial characteristics of the wind energy potential related to orography in the Hernád Valley.

The data logger mounted on the measurement mast carried out measurements in every 10 seconds and calculated averages for 10-minute intervals. Resolution of the anemometer was 0.1 m/s, while wind directions have been recorded with a resolution of 1°. Measurements lasted from April 23, 2010 to April 27, 2012 with a time span of 24 month on the whole. Datasets had been tested before the statistical analyses and modeling. Time series have proved to be discontinuous due to rigorous weather conditions in the winter months. There have been lacks of data in December – February in the winter of 2010–2011, and once in July 2010. Lacks of data have not been complemented by statistical methods. This way we have gained wind data for 67% of the studied period.

3.1. Diurnal courses of different statistical parameters of wind speeds

Daily courses by 10-minute intervals of the average wind speeds, its standard deviation, variation coefficient, and the parameter in the Hellmann's wind profile (Eq. (1)) for the 525 days represented with wind measurement data of the before mentioned measurement period have been calculated for both heights. Mean diurnal course of wind speeds are presented in *Fig. 4*. Its maximum occurs between 13 and 15 UTC at both heights, while minima occur before dawn (3–4 UTC), what is in accordance with the basic characteristics of the wind climate of Hungary. Diurnal fluctuation is 1.6 m/s at 10 meters and 1.4 m/s at 20 meters, what refers to less changeable nature wind speeds of the higher level. Differences in the averages of the two levels do not exceed 0.4 m/s, with smaller differences in the day. Averages for the whole period are 3.2 and 3.4 m/s, respectively. Diurnal courses of variation coefficients (standard deviation/ average) are presented in *Fig. 5*. According to this, variability decreases in the day, especially at 10 meters.

Measurements carried out at two heights makes the determination of the α parameter possible in the equation of Hellmann:

$$\frac{v_2}{v_1} = \left(\frac{h_2}{h_1}\right)^{\alpha}, \tag{1}$$

where v_1 stands for the wind speed measured at height h_1, while v_2 is the wind speed at height h_2. The actual value of parameter α is a function of the roughness of the surface and the equilibrium conditions of the air near the

surface mainly. Due to the latter one it is temperature-dependent, therefore, it has a diurnal and seasonal course. Using α, wind speeds at higher levels can be estimated on the base of wind speeds measured at a given height.

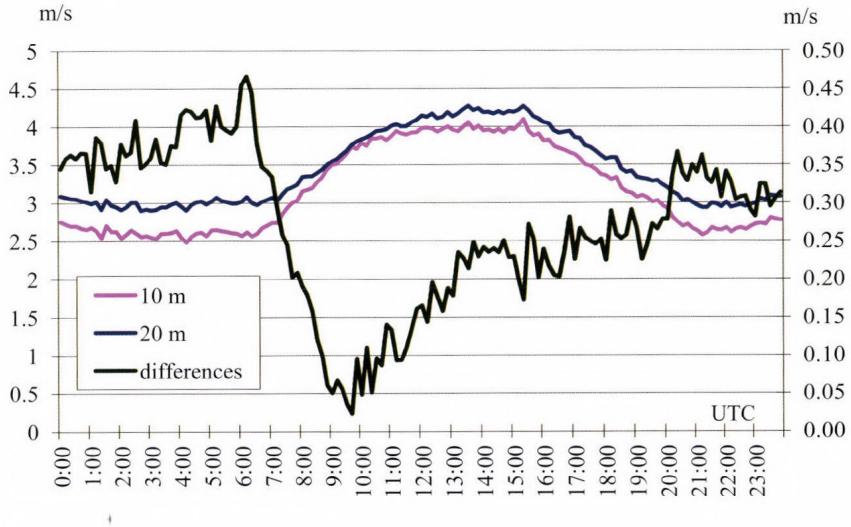

Fig. 4. 10-minute diurnal course of the average wind speeds and their differences.

Fig. 5. 10-minute diurnal course of the variation coefficient of wind speeds.

„Momentary" values of parameter α have been calculated from 10-minute wind speed averages at 10 and 20 meters using Eq. (1) for each day first, then averages for the points of time have been calculated. Diurnal course of parameter α follows the diurnal course of differences in hourly average wind speeds between the 10 and 20 meters levels, namely its value is raised between 4 and 6 in the dawn. Its average is 0.22, what is close to the value (0.25) proposed for calculations for the whole country (*Dobi* and *Mika*, 2007).

As it was mentioned before, α is temperature dependent via equilibrium conditions of the atmosphere. It means that low temperatures near the ground (atmospheric stability) leads to high values of α, while high temperatures close to the surface (atmospheric instability) cause low values of α (*Radics*, 2003). Its values are higher in the night according to other studies also (*Tar*, 2004, 2007), but its diurnal case is more regular than in our case: it can be considered as constant with a fluctuation of ± 0.05 from 21 to 6 UTC, while it decreases from 6 to 12–13 UTC and starts increasing later in the day. Fig. 6 shows a different diurnal course which could not be explained yet. It might be caused by the effect of orography or asymmetry of our data base (less winter days), or even data error cannot be excluded. To solve the problem, further examinations are required into this issue.

More regular diurnal course can be approached using hourly averages of the parameter. In such case, hourly average wind speeds for 10 and 20 meters have to be determined. After that, hourly average wind speeds for higher levels can be calculated with a better chance by Eq. (1). Diurnal course of hourly averages of wind speeds at heights of 20, 40, 60, and 80 meters have been calculated from 10-meter averages using the hourly values of the parameter. Results are presented in *Fig. 5* as well.

Comparison of values measured at 20 meters and values calculated for that height by the before mentioned method provide some information about the error of the Hellmann model. It can be seen that calculated values are higher by 0.1–0.4 m/s in each hour (0.2 m/s on average), what is 6.2% of the diurnal mean value (3.2 m/s). Higher differences occur between 1 and 7 UTC.

According to other authors and our previous examinations carried out in different parts of Hungary (*Kircsi* and *Tar*, 2008; *Tar*, 2009), there is a change in the average diurnal course of wind speeds at a height between 60 and 80 meters. Diurnal course is similar to that presented in *Fig. 4* at lower heights: it has a strong maximum at 13–14 UTC and a minimum in the night. At the same time there is an expressed minimum over that level in the early afternoon. Consequently, there have to be a so-called inflexion height, where diurnal course of (average) wind speeds is random. This hypothesis has been justified by statistical analyses. The inflexion height can be found at 50 meters at the weather stations examined so far (*Tar,* 2009). Unfortunately, inflexion height cannot be identified in *Fig. 6*. The reason for this requires further studies as well.

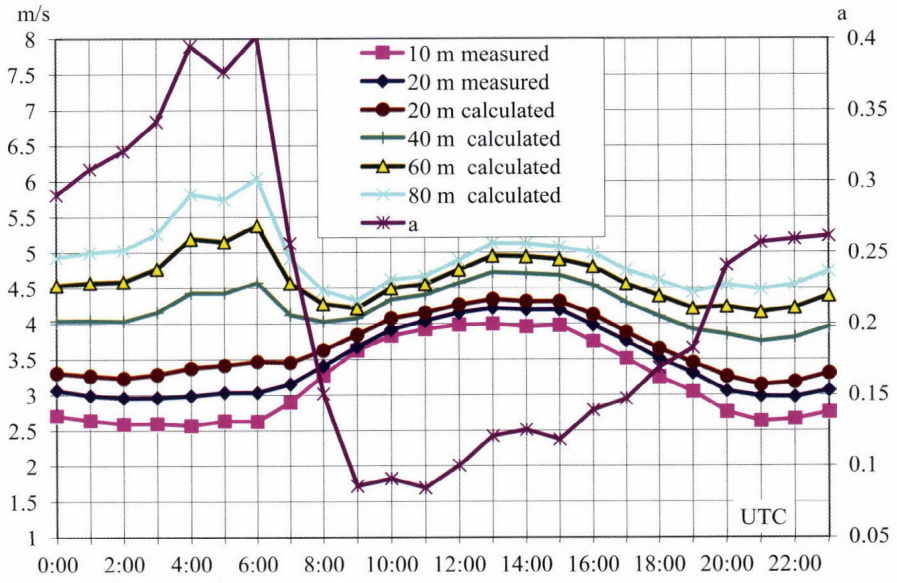

Fig. 6. Hourly average diurnal courses of the wind speeds measured and calculated for different heights and average diurnal course of the Hellmann exponent (α).

3.2. Examination of the spatial pattern of wind speeds

Speed of the air flowing over a solid surface is effected by internal and external friction, orography roughness of the surface, and artificial surface obstacles among other forces. In the case of regions with complex surface, models based on CFD analyses are used in engineering most frequently for revealing spatial patterns of wind speeds.

For wind potential survey of the Hernád Valley, the EV version of WindSim 5.1 software developed by the Norwegian VECTOR AS has been used. It is a wind farm planning tool based on computational fluid dynamic (CFD) simulations of wind flows over complex terrain. The core of the software pack is the PHOENICS software, which finite volume code based on solving the incompressible Reynolds-averaged Navier-Stokes equations (RANS) together with a two-equation turbulence model (k-epsilon turbulence model) (*Castro et al.,* 2003*; Lopez et al.,* 2007). This method favored due to their robustness and low computational costs.

The Reynolds averaged Navier-Stokes equations are used to simulate the turbulent flow field in the following way:

– continuity ($i = 1,2,3$):

$$\frac{\partial(u_i)}{\partial x_i} = 0. \tag{2}$$

– Reynolds-averaged Navier-Stokes equation ($i = 1,2,3$):

$$\rho\left(\frac{\partial \overline{u_i}}{\partial t} + \overline{u_j}\frac{\partial \overline{u_i}}{\partial x_j}\right) = -\frac{\partial \overline{p}}{\partial x_i} + \frac{\partial}{\partial x_j}\mu\left(\frac{\partial \overline{u_i}}{\partial x_j} + \frac{\partial \overline{u_j}}{\partial x_i}\right) - \frac{\partial \rho \overline{u_i' u_j'}}{\partial x_j}, \tag{3}$$

where u_i represents the velocity component, ρ is the density, p is the pressure, μ is the dynamic viscosity, and t is the time.

The software approaches the nonlinear dynamic equations describing mass-, momentum-, and energy transport by iteration.

The model has a modular structure and it approaches the spatial distribution of average wind speeds influenced by orography in several steps determining the prospective energy production of the chosen wind energy utilizing instruments practically.

The base of the running of the WindSim model is a digital terrain model. The digital terrain model used in our research has been derived from the SRTM (Shuttle Radar Topography Mission) database. It has been completed by an international consortium led by NGA (National Geospatial-Intelligence Agency) and NASA in February 2000 (*Farr et al.,* 2007). Elevation datasets of the SRTM database contain buildings, forests, and other roughness elements besides orography. For this reason, a roughness height homogeneous in space was given for the running of WindSim model. Roughness increasing effects of surface cover has not been considered in any other forms.

Before the wind climatological examinations, it had been presumable that the valley of the river has a strong effect on air movements in the study area. Northern-northeastern and the opposite southern-southeastern wind directions are the most frequent in the upper part of the Hernád Valley near the Hungarian-Slovakian border. Highest wind energy content belongs to these directions as well; therefore, they are the most important for establishment of wind energy utilization in the region. Turbulence intensity calculated on the base of standard deviation of wind speeds reaches its maximum when winds blow from the 135° SE and 270° W wind direction sectors.

Windenergy potential maps of the Hernád Valley have been generated using WindSim model for 3 heights above the surface (50, 80, and 110 meters). The numeric model has run with a grid number limited in space. The model area expands to 40 km N, E, S, and W from the measurement mast, so it spreads into the Slovakian part of the Hernád Valley. All orographic elements that have an impact on air movements have been taken into consideration from the Eperjes-

Tokaj Mountains on the east side, the ridges over 1,000 meters of the Slovak Ore Mountains in the northwest, the basin of Kosice and the Hernád Valley (*Kircsi,* 2011; *Bíróné Kircsi et al.,* 2011).

Verification of the result maps has not been carried out yet, estimations are not justified, but they can already be used for identification of areas suitable for wind energy utilization.

On the base of spatial distribution of wind speeds of the height of 50 meters it is visible (*Fig. 7a*) that the low laying basin of Kosice and the Hungarian section of the Hernád Valley is in wind shadow, so it is moderately windy. Annual average wind speeds exceed 5 m/s in the region of highest mountain ridges only. Irrespectively of this, the lower part of the Hernád Valley south of the settlement of Encs and the western side of the valley rising toward the Cserehát hills seems to be suitable for wind energy utilization. Highest wind speeds can be found over the peaks near Hejce and Vilmány.

Wind maps generated for heights of 80 and 110 meters are quite similar (*Figs. 7b* and *7c*), however, wind speed averages have not increased remarkably parallel with the height. The Hernád Valley is not the windiest region of Hungary, anyway. Wind potential in the study area makes possible to establish wind turbines with an axis height of about 100 meters at least.

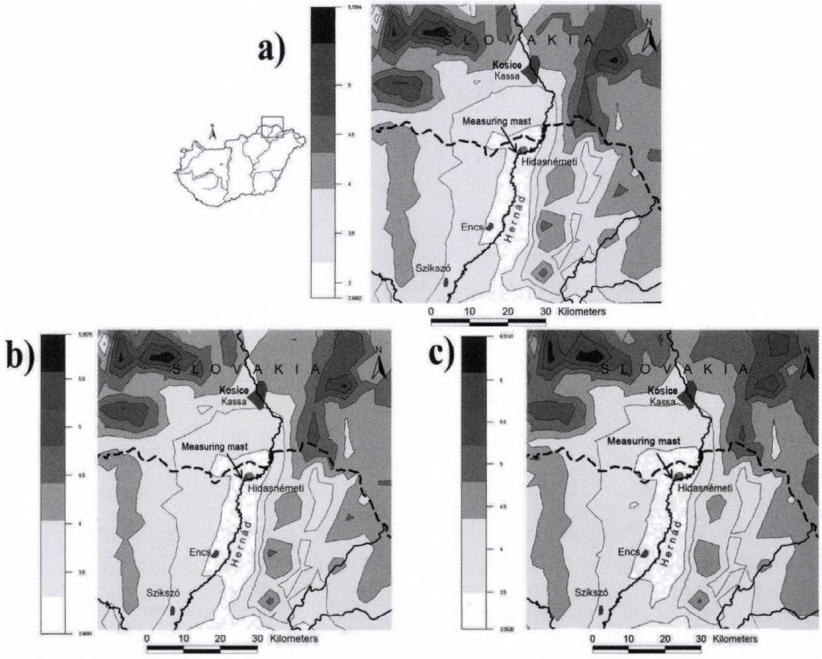

Fig 7. Modeled spatial distribution of wind speeds (m/s) 50 m (a), 80 m (b), and 110 meters (c) above the surface.

3.3. *Relationships between the diurnal average wind speeds of Kosice and Hidasnémeti*

Diurnal average wind speed data of the airport of Kosice for the studied period can be found at *http://ncdc.noaa.gov/oa/ncdc.html*, so they can be compared to our data measured at Hidasnémeti. It is a question anyway whether they are accurate or not. Accuracy of the wind speed datasets available at the homepage have been tested by comparison of base statistics of them and the purchased dataset. Our examinations have proved that they are data from the same weather station (*Tar,* 2012).

Diurnal average wind speed datasets of Kosice have been downloaded from the before mentioned homepage for the period between April 1, 2010 and October 31, 2011, what means 579 days. Our measurements cover 525 days, data for 54 days is missing. An attempt has been made to complete the diurnal average wind speed database by regression for both heights. *Figs. 8* and *9* show the relationships between the datasets available for both stations (525 days) with the two trend lines that fits best (they have the highest correlation index). Unfortunately, there is not any information on the height of the anemometer at the weather station of Kosice, but it is not important from the aspect of regression analyses. Linear trend has been selected for further analyses due to values of correlation index (R^2). T-test has showed that linear correlation coefficients differ significantly from 0. The significant correlation coefficients enable the generation of diurnal mean wind speeds to Hidasnémeti from data of Kosice with the help of regression equations without measurements.

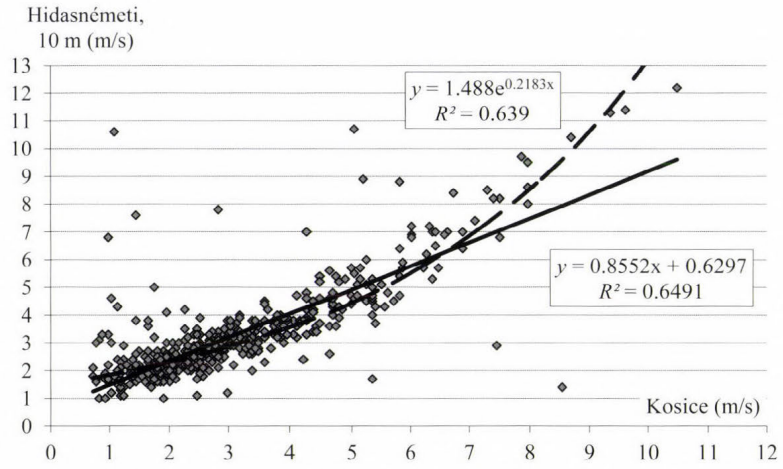

Fig. 8. Regression between datasets of diurnal average wind speeds of Kosice and Hidasnémeti at the height of 10 meters.

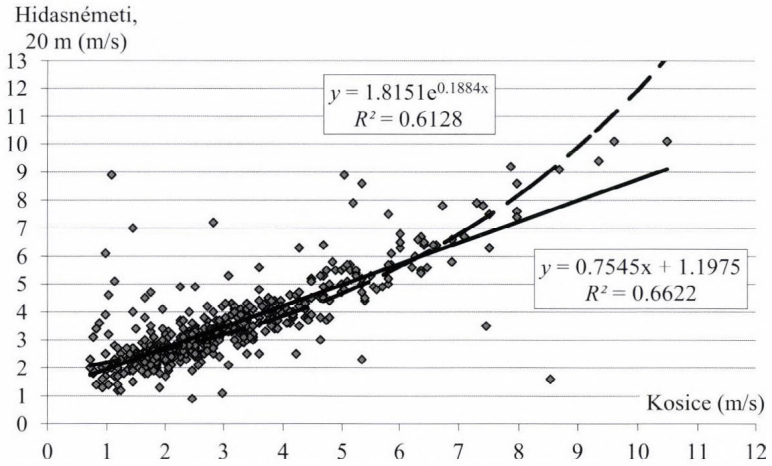

Fig. 9. Regression between datasets of diurnal average wind speeds of Kosice and Hidasnémeti at the height of 20 meters.

As a first step, datasets for 10 and 20 meters of Hidasnémeti have been reconstructed using regression equations $y = 0.8552x + 0.6297$ and $y = 0.7545x + 1.1975$ (where x stands for datasets of Kosice), in order to determine the error of the regression model. Mean relative error at 10 meters is 6.6%, standard deviation is rather high (33.3%), therefore variation coefficient is also high (5.04). Mean relative error at 20 meters is 5.7%, standard deviation is 30%, and variation coefficient is 5.27. Mean relative error is positive in 63.8% and 59.2% of all cases at 10 and 20 meters, what means that the model overestimates.

The most important statistical characteristics of the measured and estimated diurnal average wind speeds are given in *Table 2*. Variability (standard deviation, variation coefficient) of estimated, modeled values is lower than that of measured ones. Values of extremities like range have changed: the latter one has decreased from 11.2 to 8.4 at 10 meters and from 9.2 to 7.4 at 20 meters. Values of skewness and kurtosis show that modeled datasets are more regular, as it can be seen in *Fig. 10*.

The modus of the measured and estimated data falls into the 2–3 m/s interval at both heights according to *Fig. 10*. There is a higher frequency of occurrence by 3 and 2 % in the case of estimated data. It is visible as well, that frequency of values lower than the modus decreases at both heights, while frequency of values higher than the modus increases up to about the 6-7m/s interval together with the change of the coefficient of skewness (*Table 2*). However, homogeneity (χ^2) tests (*Vince,* 1975) have proved that measured and estimated values belong to the same distribution at both heights at a level of 99%.

More detailed results on the wind climatology of the study area can be found in *Tar* (2011a, b) and *Tar et al.* (2011).

Table 2. The most important statistical characteristics of the measured and estimated by regression diurnal average wind speeds at Hidasnémeti

	10 m		20 m	
	measured	**estimated**	**measured**	**estimated**
average	3.2	3.2	3.4	3.4
standard deviation.	1.71	1.38	1.49	1.22
coefficient of variation	0.54	0.44	0.44	0.35
minimum	1.0	1.2	0.9	1.7
maximum	12.2	9.6	10.1	9.1
lower quartile	2.1	2.2	2.4	2.6
median	2.7	2.8	3.0	3.1
upper quartile	3.6	3.8	4.0	4.0
skewness	2.20	1.42	1.63	1.42
kurtosis	6.03	2.30	3.29	2.30

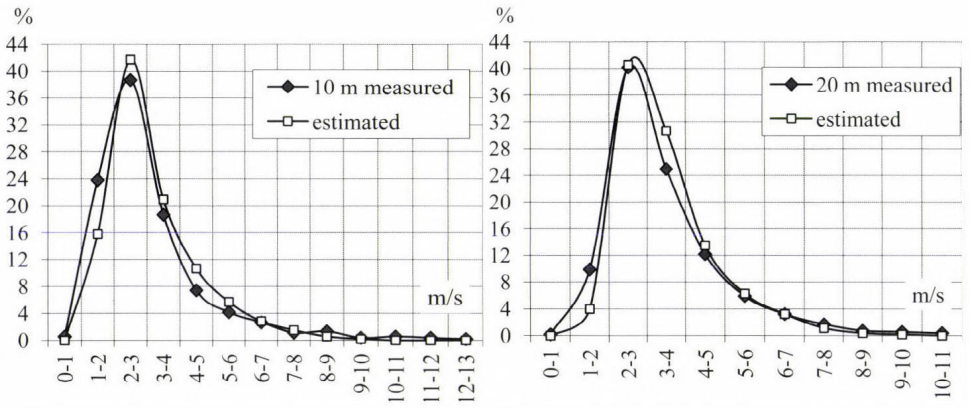

Fig. 10. Distribution of measured and estimated values of diurnal average wind speeds at 10 and 20 m heights at Hidasnémeti.

4. Supplementary investigations (biomass, social aspects)

The local support and biomass potential in the Hernád Valley were also examinated, because they are essentials for the future establishment of the renewables in the area. Results of an own questionnaire attitude survey show

that more than 80% of citizens (1,188 persons) questioned in 21 of the total 30 settlements have heard about wind and solar energy. Majority of citizens interviewed consider wind turbines, low capacity wind generators, and solar panels as acceptable, morally supportable, and realizable. However, only 10 % of citizens interviewed would tolerate a biomass burning power plant or a small heat generating power plant in their own settlement (*Tóth*, 2011; *Tóth* et al. 2012). Based on the estimations for biomass potential, about 125,000 tons of wood and herb biomass suitable for energy production is being produced annually in the study area after satisfying raw material and other demands. The estimated value of that mass is 4.4 billion forints, while bioenergy end products cost 7.8–8.6 billion forints. Approximately 75% of it remains in the region (*Bai*, 2012). All of these shows that not only solar and wind energy but bioenergy potential has also great importance in the Hernád Valley, but attitude of local inhabitants for bioenergy is not as positive as for the sun- and wind energy. Details of these results have already been published in another article.

5. Discussion

Solar energy potential of the Hernád Valley has been evaluated in the course of our examinations on the base of measured data by GIS tools. It can be stated that the region have significant solar energy potential with a total solar radiation income of 1204.8 kWh/m^2 measured at the weather station of Kosice during the studied period, what can be even higher in areas of advantageous exposition. This endowment can serve as a good base for further development of solar energy utilization in the region. Solar energy can be introduced in some new fields like ecologic and silvicultural applications.

Northerly and the opposite southerly winds are the most frequent in the upper part of the Hernád Valley near the Hungarian-Slovakian border. Highest wind speeds belong to northern-northeastern and southern-southeastern directions. Turbulence intensity calculated on the base of standard deviation of wind speeds reaches its maximum when winds blow from the southeastern and western wind directions. Wind energy potential maps of the Hernád Valley have been generated for heights of 50, 80, and 110 meters show that the Hungarian section of the Hernád Valley lays in wind shadow of the bordering mountain ridges. In the case of the model, the annual mean wind speeds weighted by wind direction distribution reach 2.8–3 m/s and 3.5–4 m/s in the northern and southern part of the Hungarian section of the Hernád Valley at heights of 50 and 110 meters. Energy content of air flows is low (nearly 60 W/m^2) at 50 meters. However, the lower part of the Hernád Valley, south of the settlement of Encs and the western side of the valley rising toward the Cserehát hills seem to be suitable for wind energy utilization. Highest wind speeds can be found over the

ridges over 1,000 meters bordering the basin of Kosice and the peaks in the Eperjes-Tokaj Mountains on the east side of the valley.

On the base of wind measurements carried out in Hidasnémeti between April 23, 2010 and April 27, 2012 it can be stated, that wind potential of the year 2011 was far behind the Hungarian annual average. It has been found that the software pack used for the spatial extrapolation of wind speeds is suitable for surveying wind energy potential of the Hernád Valley and its broader environment, and for fulfilling the tasks of the project (*Bíróné Kircsi* and *Vass*, 2011). Our examinations have showed that in spite of temporal fluctuations, utilization of wind energy in the study area can be expedient and effective, especially in the case of application of low starting speed wind turbines.

Not only solar and wind energy but bioenergy potential has also great importance in the Hernád Valley but the attitude of local inhabitants for bioenergy is not as positive as for the sun- and wind energy.

Acknowledgements: The authors thank the Hungarian Scientific Research Fund (OTKA K 75794) for the support of the research.

References

Bai, A., 2012: Az energetikai célú biomassza hasznosításának társadalmi-gazdasági kérdései a Hernád-völgyben. In: A megújuló energiaforrások hasznosításának természeti, társadalmi és gazdasági lehetőségei a Hernád-völgyben. Debreceni Egyetem Meteorológiai Tanszék, 47–60. (in Hungarian)

*Bartók, B., Imecs, Z.,*and *Tar, K.*, 2011: Modelling radiation conditions at Hernád Valley in GIS environment. *Collegium Geographicum 8, Special Edition,* Abel Publishing House, Cluj Napoca, 59–63.

Bíróné Kircsi, A., Tar, K., and *Lázár I.*, 2011: Módszer a szélenergia potenciál meghatározására a Hernád-völgy példáján. II. Környezet és energia konferencia, DAB Megújuló Energetikai Munkabizottság, Debreceni Egyetem Földtudományi Intézet, 160–166. (in Hungarian)

Bíróné Kircsi, A. and *Vass R.*, 2011: A térinformatika alkalmazása a Hernád-völgy szélenergia potenciáljának felmérésében. In: Az elmélet és a gyakorlat találkozása a térinformatikában. II. Térinformatikai konferencia és szakkiállítás, 311–318. (in Hungarian)

Castro, F., Palma, J.M.L.M, and *Lopes, A,S.*, 2003: Simulation of the Askervein flow. Part 1: Reynolds averaged Navier-Stokes equations (k-epsilon turbulence model). *Bound-lay. meteorol. 107*, 501–530.

Dobi, I. and *Mika, J.*, 2007: Adalékok a nap- és szélenergia felhasználásához az IPCC 2007. évi negyedik jelentéséhez kapcsolódva. Kedvező széllel Kunhegyestől Debrecenig. Tiszteletkötet Dr. Tar Károly 60. születésnapjára,101–109. (in Hungarian)

Farr, T.G., Rosen, P.A., Caro, E., Crippen, R., Duren, R., Hensley, S., Kobrick, M., Paller, M., Rodriguez, E., Roth, L., Seal, D., Shaffer, S., Shimada, J., Umland, J., Werner, M., Oskin, M., Burbank, D., and *Alsdorf, D.*, 2007: The shuttle radar topography mission. *Rev. geophys.* 45 art. No.-RG2004.

Kircsi, A. and *Tar, K.* (2008): Profile-tests for utilizing wind energy. *Acta Silvatica & Lignaria Hungarica 4*, 107–123.

Kircsi, A., 2011: The regional extrapolation of wind speed in the Hernád Valley. *Collegium Geographicum 8.* Special Edition, Abel Publishing House, Cluj Napoca, 73–77.

Lopes, A.S, Palma, J.M.L.M., and *Castro, F.A.*, 2007: Simulation of the asker vein flow. Part 2: Large-eddy simulations. *Bound-lay. meteorol. 125*, 85-108.

Radics, K., 2003: A szélenergia hasznosításának lehetőségei Magyarországon: hazánk szélklímája, a rendelkezésre álló szélenergia becslése és modellezése. Doktori (PhD) értekezés, ELTE, Budapest. (in Hungarian)

Tar, K., 2004: Becslési módszerek a magyarországi szélenergia potenciál meghatározására. *Magyar Energetika 12(4)*, 37–48. (in Hungarian)

Tar, K., 2007: Módszerek a magyarországi szélenergia potenciál becslésére. *Dissertationes Savarienses 44,* Societas Scentiarium Savariensis, Savaria University Press, Szombathely. (in Hungarian)

Tar, K., 2009: A potenciális szélenergia mennyiségének függése a magasságtól és kapcsolata a front-típusokkal. Változó Föld, változó társadalom, változó ismeretszerzés. Tudományos Konferencia, Eger, 148–158. (in Hungarian)

Tar, K., 2011a: Előtanulmány Hernád-völgy szélenergiájához. Geográfiai folyamatok térben és időben. Tanulmánykötet Dr. Hanusz Árpád 65. születésnapja tiszteletére. Nyíregyháza, 421–431. (in Hungarian)

Tar, K., 2011b: A Hernád-völgy szélenergiája.. In: (Eds. *Frisnyák, S., Gál, A.*) A magyarországi Hernád-völgy. Földrajzi tanulmányok. Nyíregyháza–Szerencs, 55–69 (in Hungarian)

Tar, K., 2012: Szélklimatológiai vizsgálatok a Hernád-völgyben. In: A megújuló energiaforrások hasznosításának természeti, társadalmi és gazdasági lehetőségei a Hernád-völgyben. Debreceni Egyetem Meteorológiai Tanszék, 21–31. (in Hungarian)

Tar, K., Kircsi, A., Szegedi, S., Tóth, T., Vass, R., and *Kapocska, L.*, 2011: Investigation of the wind power potential of the Hernád valley. *AGD Landsc. Environ. 5*, 93–107.

Tóth, T., 2011: A megújuló energiaforrások hasznosításának feltételei a Hernád völgyében. – In: A magyarországi Hernád-völgy. Földrajzi tanulmányok. Nyíregyházi Főiskola Természet-tudományi és Informatikai Kar Turizmus és Földrajztudományi Intézet, Nyíregyháza–Szerencs. 267–276. (in Hungarian)

Tóth, T., Szalontai, L., Spéder, F., and *Vass R.*, 2012: A biomassza hasznosításának társadalmi megítélése a Hernád völgyében. In: A megújuló energiaforrások hasznosításának természeti, társadalmi és gazdasági lehetőségei a Hernád-völgyben. Debreceni Egyetem Meteorológiai Tanszék, 61–72. (in Hungarian)

Vince, I., 1975: Matematikai statisztika ipari alkalmazásokkal. Műszaki Könyvkiadó, Budapest. (in Hungarian)

http://re.jrc.ec.europa.eu

http://ncdc.noaa.gov/oa/ncdc.html

IDŐJÁRÁS

VOLUME 119 * 2015

BUDAPEST, HUNGARY

AUTHOR INDEX

TABLE OF CONTENTS

I. Papers

II. News

SUBJECT INDEX

D

E

F

G

H

I

L

M

N

O

P

R

S

T

U

V

W

INSTRUCTIONS TO AUTHORS OF *IDŐJÁRÁS*

The purpose of the journal is to publish papers in any field of meteorology and atmosphere related scientific areas. These may be

- research papers on new results of scientific investigations,
- critical review articles summarizing the current state of art of a certain topic,
- short contributions dealing with a particular question.

Some issues contain "News" and "Book review", therefore, such contributions are also welcome. The papers must be in American English and should be checked by a native speaker if necessary.

Authors are requested to send their manuscripts to

Editor-in Chief of IDŐJÁRÁS
P.O. Box 38, H-1525 Budapest, Hungary
E-mail: journal.idojaras@met.hu

including all illustrations. MS Word format is preferred in electronic submission. Papers will then be reviewed normally by two independent referees, who remain unidentified for the author(s). The Editor-in-Chief will inform the author(s) whether or not the paper is acceptable for publication, and what modifications, if any, are necessary.

Please, follow the order given below when typing manuscripts.

Title page: should consist of the title, the name(s) of the author(s), their affiliation(s) including full postal and e-mail address(es). In case of more than one author, the corresponding author must be identified.

Abstract: should contain the purpose, the applied data and methods as well as the basic conclusion(s) of the paper.

Key-words: must be included (from 5 to 10) to help to classify the topic.

Text: has to be typed in single spacing on an A4 size paper using 14 pt Times New Roman font if possible. Use of S.I. units are expected, and the use of negative exponent is preferred to fractional sign. Mathematical formulae are expected to be as simple as possible and numbered in parentheses at the right margin.

All publications cited in the text should be presented in the *list of references*, arranged in alphabetical order. For an article: name(s) of author(s) in Italics, year, title of article, name of journal, volume, number (the latter two in Italics) and pages. E.g., *Nathan, K.K.,* 1986: A note on the relationship between photosynthetically active radiation and cloud amount. *Időjárás 90,* 10-13. For a book: name(s) of author(s), year, title of the book (all in Italics except the year), publisher and place of publication. E.g., *Junge, C.E.,* 1963: *Air Chemistry and Radioactivity.* Academic Press, New York and London. Reference in the text should contain the name(s) of the author(s) in Italics and year of publication. E.g., in the case of one author: *Miller* (1989); in the case of two authors: *Gamov* and *Cleveland* (1973); and if there are more than two authors: *Smith et al.* (1990). If the name of the author cannot be fitted into the text: *(Miller,* 1989); etc. When referring papers published in the same year by the same author, letters a, b, c, etc. should follow the year of publication.

Tables should be marked by Arabic numbers and printed in separate sheets with their numbers and legends given below them. Avoid too lengthy or complicated tables, or tables duplicating results given in other form in the manuscript (e.g., graphs).

Figures should also be marked with Arabic numbers and printed in black and white or color (under special arrangement) in separate sheets with their numbers and captions given below them. JPG, TIF, GIF, BMP or PNG formats should be used for electronic artwork submission.

More information for authors is available: journal.idojaras@met.hu

Published by the Hungarian Meteorological Service

Budapest, Hungary

INDEX 26 361

HU ISSN 0324-6329